

Copyright

by

Mohammed Awad Al-Juaied

2004

The Dissertation Committee for Mohammed Awad Al-Juaied Certifies that this is
the approved version of the following dissertation:

**Carbon Dioxide Removal from Natural Gas by Membranes in the Presence of
Heavy Hydrocarbons and by Aqueous Diglycolamine®/Morpholine**

Committee:

Gary T. Rochelle, Supervisor

William J. Koros, Co-Supervisor

Donald R Paul

Douglas R. Lloyd

R. Bruce Eldridge

Kamy Sepehrnoori

**Carbon Dioxide Removal from Natural Gas by Membranes in the Presence of
Heavy Hydrocarbons and by Aqueous Diglycolamine®/Morpholine**

by

Mohammed Awad Al-Juaied, B.Sc.; M.S.

Dissertation

Presented to the Faculty of the Graduate School of

The University of Texas at Austin

in Partial Fulfillment

of the Requirements

for the Degree of

Doctor of Philosophy

The University of Texas at Austin

May, 2004

UMI Number: 3143353

UMI[®]

UMI Microform 3143353

Copyright 2003 by ProQuest Information and Learning Company.

All rights reserved. This microform edition is protected against
unauthorized copying under Title 17, United States Code.

ProQuest Information and Learning Company
300 North Zeeb Road
PO Box 1346
Ann Arbor, MI 48106-1346

Dedication

To My Family

Acknowledgements

I would like to thank everyone who contributed to my education and experience throughout graduate school. I would like to express my gratitude to Professor Bill Koros and Professor Gary Rochelle for their guidance and support throughout this work. I am thankful for the chance to work for such professors.

I would also like to acknowledge Saudi Aramco who financially supported me during my four years at UT.

I would like to thank Dr. Paul for including me as part of his group from the time Dr. Koros left UT. I would like also to thank Dr. Sanchez and Dr. Peppas who provided me with the lab space. I would like also to thank my committee members, Dr. Eldridge, Sepehrnoori and Lloyd for their advice and suggestions. I want to thank Dr. Jim Critchfield of Huntsman Chemical who provided valuable feedback on my dissertation work. I want to express appreciation also for all the graduate students that worked in Dr. Rochelle's group and Dr. Koros's group during the time I spent at the University of Texas.

Finally I would like to thank my parents and my wife who have been with me throughout my college years.

Carbon Dioxide Removal from Natural Gas by Membranes in the Presence of Heavy Hydrocarbons and by Aqueous Diglycolamine®/Morpholine

Publication No. _____

Mohammed Al-Juaied, Ph.D.

The University of Texas at Austin, 2004

Supervisors: Gary T. Rochelle and W.J. Koros

Intrinsically defect-free asymmetric hollow fiber polyimide membrane modules were studied in the presence and absence of saturated and aromatic components. Results suggest that an essentially defect-free, non-nodular morphology offers advantages in stability under demanding operating conditions. Earlier work showed serious losses in performance of membranes comprised of similar materials, when the selective layer had a pronounced fused nodular nature as opposed to the intrinsically defect-free skin layers reported on here. Under some conditions for the ternary system, the permselectivity of the membrane is scarcely affected, while under other conditions, permselectivity is negatively affected by as much as 25%. In most cases, for the ternary feeds, significant depression in fluxes was observed due to competition between the CO₂, CH₄ and heavier hydrocarbons but the effect was even more pronounced for the toluene. In addition to steady state tests in the presence and absence of n-heptane and toluene, modules were conditioned for five days with ternary mixture of CO₂, CH₄ and one or the other of these heavy hydrocarbons. Following this conditioning process, the modules were studied with a simple binary 10% CO₂ /90 % CH₄ mixture. These conditioning studies provide insight into the fundamental effects induced in the membrane due to the long term exposure to the complex mixtures. Following exposure to the ternaries containing n-heptane, negligible CO₂ permeance increase was seen, while significantly increased permeances were seen under some conditions following toluene exposure even at low pressures of the ternary toluene/CO₂/CH₄

conditioning gas mixture. Although a more protracted process occurs in the case of heptane/CO₂/CH₄ at 35 °C and 500 ppm, a serious loss in selectivity occurs in the actual ternary tests after exposure for five days. The problem caused by 300 ppm toluene at 35 °C is more immediately apparent, but the ultimate selectivity loss is similar. In addition to the selectivity, in the presence of toluene the permeability is also depressed significantly, presumably due to a greater capability to toluene to compete for added free volume elements introduced in the conditioning process. The permeation enhancement due to toluene exposure is lost slowly when the module downstream is put under vacuum and the gas no longer in contact with the module for up to three weeks. The conditioning treatment has negligible effect at 55 °C, suggesting that the sorption affinity of toluene decreases with increasing temperature. It is seen from the sorption experiments that penetrant induced conditioning of toluene allows a significant increase in diffusivity than in solubility coefficients, thus allowing for higher permeability and lower selectivity.

Solubility, rate of absorption and NMR data were obtained for carbon dioxide in aqueous morpholine (MOR), diglycolamine® (DGA) and aqueous mixtures of MOR and DGA®. Solubility and rate data were acquired in a wetted wall contactor. 23.5 wt%, 65 wt% DGA and 11 wt% MOR/53 wt% DGA concentrations were studied at 298K to 333K. MOR forms an unstable carbamate upon reaction with CO₂ compared to DGA which forms a very stable carbamate. Morpholine at 11 wt% of the total amine increases the CO₂ equilibrium partial pressure by a factor of 5 to 7 at high loading. The working capacity of 11 wt% MOR/53 wt% DGA was found to be 10% smaller compared to 65 wt% DGA under the conditions studied. The heat of reaction of 11 wt% MOR/53 wt% DGA® was found to be comparable to the 65 wt% DGA. MOR was found also to be more volatile than DGA. The second order rate constant of DGA was found to increase linearly with loading by a factor of 5 over a loading range from 0 to 0.4. Experiments with 65 w% DGA, glycolic acid and potassium formate suggest that

rate constant increases with loading in the same way as in 65 wt% DGA. The second order rate constant for MOR ($k^{25C}_2=22000$ L/mol s) is four times greater than DGA ($k^{25C}_2=6600$ L/mol s). The MOR reaction with CO₂ was found to follow the zwitterion mechanism; DGA shows zwitterion mechanism in 25 wt% DGA and second order kinetics in 65 wt% DGA. Predictions made with a rigorous eddy diffusivity theory suggests that 11 wt% MOR/53 wt% DGA outperforms 65 wt% DGA of the same concentration by 50 % in terms of CO₂ absorption rate. The CO₂ enhancement decreases as CO₂ loading increases.

Table of Contents

List of Tables	xii
List of Figures	xviii
Chapter 1: Introduction to Gas Treating & Research Objective.....	1
1.1 Current Technologies for CO ₂ Removal from Natural Gas	1
1.2 CO ₂ Removal with Membranes.....	3
1.3 CO ₂ Removal with Amines	8
1.4 Natural Gas Sweetening with DGA	13
1.5 DGA Reclaimer Operations	15
1.6 Saudi Aramco Experience with DGA Units	18
Chapter 2: The Effects of Aliphatic and Aromatic Component Conditioning on the Permeation Behavior of Hollow Fiber Asymmetric Membranes	20
2.1 Experimental Methods	21
2.1.1 Materials.....	23
2.1.1.1 Polymer	23
2.1.1.2 Permeants	24
2.1.2 Module Housing.....	25
2.1.3 Pure Gas Permeation	26
2.1.4 Mixed Gas Permeation.....	28
2.1.5 Testing Procedure.....	32
2.2 Four Potential Deterioration Factors	34
2.2.1 Competition Effect	34
2.2.2 Plasticization	35
2.2.3 Swelling Induced Conditioning History Effect.....	36
2.2.4 Compaction	38
2.3 Results and Discussion.....	41
2.3.1 Comparison of Conditioning in Hollow Fiber Membranes at 200 psia <i>before and after Exposure</i>	41
2.3.2 Comparison of Conditioning in Hollow Fiber Membranes at 200 psia <i>during Exposure</i>	50
2.3.3 Comparison of Conditioning in Hollow Fiber Membranes at 600 psia <i>before and after Exposure</i>	57
2.3.4 Comparison of Conditioning in Hollow Fiber Membranes at 600 psia <i>during Exposure</i>	62
2.4 Defective vs. Defect-Free Fibers.....	66
2.5 Summary	69
Chapter 3: Sorption Results and Permeation Behavior Modelling and Analysis ..	74

3.1	Background	74
3.2	Gas Sorption Measurements.....	77
3.3	Results and Discussion.....	80
3.4	Sorption and Permeation Data Analysis.....	90
3.5	Conclusions	104
Chapter 4: Thermodynamics of Morpholine /Diglycolamine® / Water / Carbon Dioxide.....		
		106
4.1	Experimental Methods	108
4.2	Model Description.....	117
4.3	N ₂ O Solubility of Carbon Dioxide in Aqueous Solution of DGA, MOR, and MOR/DGA	121
4.4	Solubility of Carbon Dioxide in Aqueous Solution of DGA, MOR, and MOR/DGA	124
4.5	C13 NMR Data.....	128
4.6	N ₂ O Regression Results	140
4.7	Activity of Diglycolamine® and Morpholine in Aqueous Mixtures	141
4.8	Parameter Regression Results of CO ₂ Solubility and NMR Data.....	146
	4.8.1 DGA-CO ₂ system.....	146
	4.8.2 MOR-CO ₂ system.....	151
	4.8.3 MOR-DGA-CO ₂ system.....	156
4.9	Solvent Working Capacity	161
4.10	Regeneration Energy Requirements.....	162
4.11	Solvent Vaporization losses	165
4.12	Conclusions	166
Chapter 5: Absorption of Carbon Dioxide into Aqueous Diglycolamine®		
		168
5.1	Introduction	168
5.2	Experimental Methods	171
5.3	Physical Properties	171
5.4	Model Description.....	173
	5.4.1 Rigorous model	173
	5.4.2 Pseudo first order models.....	177
5.5	Results and Discussion.....	180
	5.5.1 CO ₂ reactive absorption into low-loading aqueous DGA solutions.....	180
	5.5.2 CO ₂ reactive absorption into partially loaded aqueous DGA solutions	192
	5.5.3 The influence of ionic strength on the rate constant for the reaction of diglycolamine and CO ₂	210
5.6	Conclusions	220

Chapter 6: Absorption of CO ₂ in Aqueous MOR and MOR/DGA® Blends	222
6.1 Introduction	222
6.2 Physical Properties	223
6.3 CO ₂ Absorption in Aqueous MOR.....	224
6.4 Rate Results with 11 wt% MOR/53 wt% DGA	230
6.5 Model Description.....	231
6.6 Rate Model Predictions	238
6.7 Sensitivity to Model Parameters	241
6.8 Deviation from Approximate Solutions	242
6.9 Conclusions	244
Chapter 7: Conclusions and Recommendations	246
7.1 Effects of Heavy Hydrocarbon Impurities on Hollow Fiber Membranes Performance in Natural Gas Separation	246
7.2 Carbon Dioxide Absorption and Solution Equilibrium in Morpholine and Diglycolamine	251
Appendix A: Modeling of Asymmetric Hollow Fiber Membrane Modules used for High-Pressure Natural Gas Purification	255
A.1 Model Development	258
A.2 Numerical Solution	261
A.3 Simulations Results and Discussion.....	266
A.4 Frame of Reference Model (FM) versus Diffusion Model (DM)	267
A.5 Effect of Feed Pressure	277
A.6 Effect of Membrane Thickness and Area.....	284
A.7 Effect of Permeate Pressure	290
A.8 Diffusion and Frame of Reference Models Comparisons	293
A.9 Conclusions	298
Appendix B: Program Documentation	300
Appendix C: Experimental Reproducibility and Replication	319
Appendix D: Equation for Compressibility Factors for Penetrants at 35 °C	327
Appendix E: Desorption Isotherm Sample Calculation.....	328
Appendix F: Working Equations for Sorption Isotherm Calculations	330
Appendix G: Polynomial Fitting Parameters for Permeation and Sorption Results	336
Appendix H: CO ₂ Solubility and Rate Data	339
Appendix I: Additional C13 NMR Data.....	369
Appendix J: ¹³ C NMR Sample Calculation.....	377
Bibliography	385
Vita.....	398

List of Tables

Table 1.1	Comparison of amine and membrane CO ₂ removal systems (William, 2002).....	2
Table 1.2	Common conditions found in natural gas plants (Newman, 1985)	14
Table 2.1	Reported gas permeabilites of Matrimid® at 25 ⁰ C (Clausi and Koros, 2000; Clausi, 1998).....	24
Table 2.2	Pure gas permeation results for hollow fiber membranes used in this work at 25 ⁰ C.	40
Table 2.3	Percent change in N ₂ , O ₂ and He permeance in Matrimid asymmetric hollow fiber over 42 days of aging at room temperature (Punsalan, 2001).	41
Table 2.4	Permeability of CO ₂ in the 10/90 CO ₂ /CH ₄ , at 35 ⁰ C illustrating the hysteretic behavior before conditioning, after conditioning to the 10/90 CO ₂ /CH ₄ +100 ppm toluene at 400 psia and after conditioning, followed by exposure to a vacuum source for 21 days.	69
Table 3.1	CH ₄ and CO ₂ / Matrimid® dual mode sorption parameters in unconditioned and conditioned samples with 10/90 CO ₂ /CH ₄ mixture at 600 psia and 35 ⁰ C.....	81
Table 3.2	CH ₄ and CO ₂ / Matrimid® dual mode sorption parameters in unconditioned and conditioned samples with 10/90 CO ₂ /CH ₄ + 300 ppm toluene mixture at 600 psia and 35 ⁰ C.....	84
Table 3.3	CH ₄ and CO ₂ / Matrimid® dual mode sorption parameters in unconditioned and conditioned samples with 10/90 CO ₂ /CH ₄ + 500 ppm n-heptane mixture at 600 psia and 35 ⁰ C.....	87
Table 3.4	Percent change in fractional free volume for CO ₂ and CH ₄ in conditioned samples with 10/90 CO ₂ /CH ₄ + 300 ppm toluene mixture at 200 psia, 600 psia and 35 ⁰ C.....	104
Table 4.1a	Default parameters for VLE program.....	119
Table 4.1b	Miscellaneous Constants for VLE program.....	120
Table 4.1c	Temperature dependent constants.....	120
Table 4.2	Temperature dependence of equilibrium constants, mole fraction based.....	121
Table 4.3	Henry's constant for N ₂ O in water in kPa.L/mol ⁻¹ at 25 ⁰ C and 40 ⁰ C.....	122
Table 4.4	N ₂ O solubility data in unloaded amine solutions.....	122
Table ** 4.5	CO ₂ Solubility in 65wt% DGA.....	125
Table ** 4.6	CO ₂ Solubility in 23.5wt% MOR.....	125

Table ** 4.7	CO ₂ Solubility in 11wt% MOR/53wt% DGA (65wt% Amine) ...	125
Table ** 4.8	Heat of Absorption of CO ₂ at various loading for 23.5 wt% MOR, 65 wt% DGA and 11 wt% MOR//53 wt% DGA	128
Table 4.9	Detailed ¹³ C NMR Results for 65 wt% DGA and 300K and loading 0.34 mol CO ₂ /mol DGA.....	134
Table 4.10	Detailed ¹³ C NMR Results for 65 wt% DGA and 313K and loading of 0.40 mol CO ₂ /mol MOR.....	135
Table 4.11	Detailed ¹³ C NMR Results for 23.5 wt% MOR/65 wt% DGA and 300K.....	135
Table 4.12	C13 NMR in 65wt% DGA.....	136
Table 4.13	C13 NMR in 23.5wt% MOR.....	136
Table 4.14	C13 NMR in 11wt% MOR/53wt% DGA.....	137
Table 4.15	Comparison of carbamate stability constants (Mole Fraction based*).....	139
Table 4.16	Heat of reaction of carbamate for 65 wt% DGA and 23.5 wt% MOR.....	140
Table 4.17	Parameter Values of the Henry's C constant.....	140
Table 4.18	Excess heat of mixing at infinite dilution and 25°C	143
Table 4.19	Fitted values of NRTL binary interaction parameters for MOR-H ₂ O system.....	145
Table 4.20	Non-Default parameters for the NRTL model.....	147
Table 4.21	Non-Default parameters for the NRTL model.....	152
Table 4.22.	Non-Default parameters for DGA-MOR mixed amine parameters.....	157
Table 4.23	Comparison of working capacities at 60 °C, P _{CO₂, rich} = 50 kPa, P _{CO₂,lean} = 10 ⁻³ kPa	161
Table 5.1	Van-Krevelen coefficients at 25 °C, 40 °C and 60 °C.	172
Table 5.2	Model Equations and Boundary Conditions.....	176
Table 5.3	65 wt% DGA/water and 25 wt% DGA/water subset of the experimental rate measurements at zero loading. Total pressures from 0-28 psig.....	182
Table 5.4	Kinetic data for DGA.....	187
Table 5.5	Analysis of importance of the kinetics at low and high loadings for 25 °C, 40 °C and 60 °C.....	198
Table 5.6	Results for the regression of D _{DGA} , D _{p,r} and k ₂	201
Table 5.7	Results for the fit of k ₂ as a function of μ	212
Table 5.8	65wt%DGA/water-glycolic acid experimental rate measurements at zero loading. Total pressures from 15-42 psig	214
Table 5.9	Measured values of Henry's constants and viscosities in glycolic acid-DGA solutions at 40 °C	216

Table 5.10	65 wt%DGA/water- potassium formate subset of the experimental rate measurements. Total pressures from 10-18 psig	217
Table 5.11	Measured values of Henry's constants and viscosities in potassium formate (CHKO ₂) solutions -DGA solutions.....	218
Table 5.12	Results for the fit of k ₂ as a function of μ for the results	221
Table 6.1	Rate of absorption data at zero loading into 23.5 wt% aqueous morpholine. Overall gas flowrates from 6.05 to 6.25 SLPM. Total pressures from 15-18 psig.....	225
Table 6.2	Bronsted Correlation of Morpholine Kinetics at 25°C	227
Table 6.3	Rate Data for the Morpholine (Rochelle et al., 2000)	229
Table 6.4	Rate of absorption into aqueous 11 wt% MOR/53 wt% DGA. Overall gas flowrates from 3.05 to 6.25 SLPM. Total pressures from 15-60 psig.....	230
Table 6.5	Model Equations and Boundary Conditions	233
Table 6.6	Results for the regression of Equation 6.13.....	237
Table A.1.	Fugacity based dual-mode and partial immobilization parameters of CO ₂ and CH ₄ at 35 °C in 6FDA-TADPO polypyrrolone Kamaruddin and Koros, 1997).....	266
Table A.2.	Default parameters for simulations.....	267
Table C.1	Experimental data of conditioning by 10/90 CO ₂ /CH ₄ mixture on CO ₂ permeance, CH ₄ permeance and the CO ₂ /CH ₄ selectivity at 200 psia and 35 °C. Sample # 1	319
Table C.2	Experimental data of conditioning by 10/90 CO ₂ /CH ₄ mixture on CO ₂ permeance, CH ₄ permeance and the CO ₂ /CH ₄ selectivity at 200 psia and 35 °C. Sample # 2	319
Table C.3	Experimental data of conditioning by 10/90 CO ₂ /CH ₄ + 500 ppm n-heptane mixture on CO ₂ permeance, CH ₄ permeance and the CO ₂ /CH ₄ selectivity at 200 psia and 35 °C. Sample # 1	320
Table C.4	Experimental data of conditioning by 10/90 CO ₂ /CH ₄ + 500 ppm n-heptane mixture CO ₂ permeance, CH ₄ permeance and the CO ₂ /CH ₄ selectivity at 200 psia and 35 °C. Sample # 2.....	320
Table C.5	Experimental data of conditioning by 10/90 CO ₂ /CH ₄ + 300 ppm n-heptane mixture on CO ₂ permeance, CH ₄ permeance and the CO ₂ /CH ₄ selectivity at 400 psia and 35 °C. Sample # 1	321
Table C.6	Experimental data of conditioning by 10/90 CO ₂ /CH ₄ + 300 ppm toluene mixture on CO ₂ permeance, CH ₄ permeance and the CO ₂ /CH ₄ selectivity at 200 psia and 35 °C. Sample # 1	321
Table C.7	Experimental data of conditioning by 10/90 CO ₂ /CH ₄ + 300 ppm toluene mixture on CO ₂ permeance, CH ₄ permeance and the CO ₂ /CH ₄ selectivity at 200 psia and 35 °C. Sample # 2.....	322

Table C.8	Experimental data of conditioning by 10/90 CO ₂ /CH ₄ + 300 ppm toluene mixture on CO ₂ permeance, CH ₄ permeance and the CO ₂ /CH ₄ selectivity at 600 psia and 35 °C. Sample # 1	322
Table C.9	Experimental data of conditioning by 10/90 CO ₂ /CH ₄ + 300 ppm toluene mixture on CO ₂ permeance, CH ₄ permeance and the CO ₂ /CH ₄ selectivity at 600 psia and 35 °C. Sample # 2	323
Table C.10	Experimental data of conditioning by 10/90 CO ₂ /CH ₄ + 500 ppm n-heptane mixture on CO ₂ permeance, CH ₄ permeance and the CO ₂ /CH ₄ selectivity at 600 psia and 35 °C. Sample # 1	323
Table C.11	Experimental data of conditioning by 10/90 CO ₂ /CH ₄ + 500 ppm n-heptane mixture on CO ₂ permeance, CH ₄ permeance and the CO ₂ /CH ₄ selectivity at 600 psia and 35 °C. Sample # 2	324
Table C.12	Experimental data of conditioning by 10/90 CO ₂ /CH ₄ mixture on CO ₂ permeance, CH ₄ permeance and the CO ₂ /CH ₄ selectivity at 600 psia and 35 °C. Sample # 1	324
Table C.13	Experimental data of conditioning by 10/90 CO ₂ /CH ₄ + 100 ppm toluene mixture on CO ₂ permeance, CH ₄ permeance and the CO ₂ /CH ₄ selectivity at 400 psia and 55 °C. Sample # 1	325
Table C.14	Experimental data of conditioning by 10/90 CO ₂ /CH ₄ + 300 ppm toluene mixture on CO ₂ permeance, CH ₄ permeance and the CO ₂ /CH ₄ selectivity at 200 psia and 55 °C. Sample # 1	325
Table C.15	Experimental data of conditioning by 10/90 CO ₂ /CH ₄ + 100 ppm toluene mixture on CO ₂ permeance, CH ₄ permeance and the CO ₂ /CH ₄ selectivity at 200 psia and 55 °C. Sample # 1	326
Table C.16	Experimental data of conditioning by 10/90 CO ₂ /CH ₄ + 500 ppm toluene mixture on CO ₂ permeance, CH ₄ permeance and the CO ₂ /CH ₄ selectivity at 200 psia and 55 °C. Sample # 1	326
Table E.1	Voltage Measurements	328
Table E.2	Pressure and moles desorbed calculations	328
Table E.3	Concentration Calculation, polymer sample volume = 0.239 cc.	329
Table F.1	Channel 1 Calibration	331
Table F.2	Channel 2 Calibration	332
Table F.3	Expansion – No ball.....	334
Table F.4:	Expansion – with ball (V _B = 0.719 cm ³).....	335
Table G.1	Summary of fitting parameters, A, B, C, D and E, for CO ₂ and CH ₄ in unconditioned and conditioned samples with 10/90 CO ₂ /CH ₄ mixture at 200 psia and 35 °C.....	336
Table G.2	Summary of fitting parameters, A, B, C, D and E, for CO ₂ and CH ₄ in unconditioned and conditioned samples with 10/90 CO ₂ /CH ₄ + 500 ppm n-heptane mixture at 200 psia and 35 °C.....	336

Table G.3	Summary of fitting parameters, A, B, C, D and E, for CO ₂ and CH ₄ in unconditioned and conditioned samples with 10/90 CO ₂ /CH ₄ + 300 ppm toluene mixture at 200 psia and 35 °C.....	336
Table G.4	Summary of fitting parameters, A, B, C, D and E, for CO ₂ and CH ₄ in unconditioned and conditioned samples with 10/90 CO ₂ /CH ₄ mixture at 600 psia and 35 °C.....	337
Table G.5	Summary of fitting parameters, A, B, C, D and E, for CO ₂ and CH ₄ in unconditioned and conditioned samples with 10/90 CO ₂ /CH ₄ + 500 ppm n-heptane mixture at 600 psia and 35 °C.....	337
Table G.6	Summary of fitting parameters, A, B, C, D and E, for CO ₂ and CH ₄ in unconditioned and conditioned samples with 10/90 CO ₂ /CH ₄ + 300 ppm toluene mixture at 600 psia and 35 °C.....	337
Table G.7	Summary of fitting parameters, A, B, C, D and E, for CO ₂ and CH ₄ in unconditioned and conditioned samples with 10/90 CO ₂ /CH ₄ at 600 psia and 35 °C.....	338
Table G.8	Summary of fitting parameters, A, B, C, D and E, for CO ₂ and CH ₄ in unconditioned and conditioned samples with 10/90 CO ₂ /CH ₄ + 300 ppm toluene mixture at 600 psia and 35 °C.....	338
Table G.9	Summary of fitting parameters, A, B, C, D and E, for CO ₂ and CH ₄ in unconditioned and conditioned samples with 10/90 CO ₂ /CH ₄ + 500 ppm n-heptane mixture at 600 psia and 35 °C.....	338
Table H.1	65 wt% DGA solubility and rate.....	339
Table H.2	23.5 wt% MOR solubility and rate.....	353
Table H.3	11 wt% MOR/53 wt% DGA solubility and rate.....	358
Table I.1	C13 NMR of 65 wt% DGA, Loading = 0.377 mol CO ₂ /mol DGA, T=27 °C.....	369
Table I.2	C13 NMR of 65 wt% DGA, Loading = 0.525 mol CO ₂ /mol DGA, T=27 °C.....	369
Table I.3	C13 NMR of 65 wt% DGA, Loading = 0.523 mol CO ₂ /mol DGA, T=40 °C.....	370
Table I.4	C13 NMR of 65 wt% DGA, Loading = 0.332 mol CO ₂ /mol DGA, T=60 °C.....	370
Table I.5	C13 NMR of 65 wt% DGA, Loading = 0.390 mol CO ₂ /mol DGA, T=40 °C.....	371
Table I.6	C13 NMR of 65 wt% DGA, Loading = 0.385 mol CO ₂ /mol DGA, T=60 °C.....	371
Table I.7	C13 NMR of 65 wt% DGA, Loading = 0.168 mol CO ₂ /mol DGA, T=27 °C.....	372
Table I.8	C13 NMR of 65 wt% DGA, Loading = 0.180 mol CO ₂ /mol DGA, T=60 °C.....	372
Table I.9	C13 NMR of 23.5 wt% MOR, Loading = 0.370 mol CO ₂ /mol MOR, T=27 °C.....	373

Table I.10	C13 NMR of 23.5 wt% MOR, Loading = 0.569 mol CO ₂ /mol MOR, T=27 °C.....	373
Table I.11	C13 NMR of 23.5 wt% MOR, Loading = 0.478 mol CO ₂ /mol MOR, T=27 °C.....	373
Table I.12	C13 NMR of 23.5 wt% MOR, Loading = 0.258 mol CO ₂ /mol MOR, T=27 °C.....	374
Table I.13	C13 NMR of 23.5 wt% MOR, Loading = 0.427 mol CO ₂ /mol MOR, T=27 °C.....	374
Table I.14	C13 NMR of 23.5 wt% MOR, Loading = 0.325 mol CO ₂ /mol MOR, T=27 °C.....	374
Table I.15	C13 NMR of 23.5 wt% MOR, Loading = 0.392 mol CO ₂ /mol MOR, T=40 °C.....	374
Table I.16	C13 NMR of 23.5 wt% MOR, Loading = 0.370 mol CO ₂ /mol MOR, T=40 °C.....	375
Table I.17	C13 NMR of 23.5 wt% MOR, Loading = 0.569 mol CO ₂ /mol MOR, T=40 °C.....	375
Table I.18	C13 NMR of 23.5 wt% MOR, Loading = 0.478 mol CO ₂ /mol MOR, T=40 °C.....	375
Table I.19	C13 NMR of 23.5 wt% MOR, Loading = 0.258 mol CO ₂ /mol MOR, T=40 °C.....	376
Table I.20	C13 NMR of 11 wt% MOR/53 wt% DGA, Loading = 0.364 mol CO ₂ /mol MOR, T=27 °C	376
Table I.21	C13 NMR of 11 wt% MOR/53 wt% DGA, Loading = 0.271 mol CO ₂ /mol MOR, T=27 °C	377
Table I.22	C13 NMR of 11 wt% MOR/53 wt% DGA, Loading = 0.521 mol CO ₂ /mol MOR, T=40 °C	377
Table I.23	C13 NMR of 11 wt% MOR/53 wt% DGA, Loading = 0.374 mol CO ₂ /mol MOR, T=40 °C	378
Table I.24	C13 NMR of 11 wt% MOR/53 wt% DGA, Loading = 0.285 mol CO ₂ /mol MOR, T=40 °C	379
Table I.25	C13 NMR of 11 wt% MOR/53 wt% DGA, Loading = 0.522 mol CO ₂ /mol MOR, T=60 °C	379
Table I.26	C13 NMR of 11 wt% MOR/53 wt% DGA, Loading = 0.285 mol CO ₂ /mol MOR, T=60 °C	380
Table I.27	C13 NMR of 11 wt% MOR/53 wt% DGA, Loading = 0.374 mol CO ₂ /mol MOR, T=60 °C	381

List of Figures

Figure 1.1	Illustration of a membrane separation operation.	3
Figure 1.2	Schematic of hollow fiber membrane showing skin and Support (Gunaidi, 2000).....	4
Figure 1.3	Relative Solubility of Some Typical Gas Components (Dortmundt, and Doshi, 1993; William, 2002).....	5
Figure 1.4	Hollow Fiber Membrane element (Dortmundt, and Doshi, 1993; William, 2002).....	6
Figure 1.5	Illustration of a absorption/stripping system for the removal of acid gases.....	10
Figure 1.6	Structures of common amines used in gas treating.....	11
Figure 1.7	A typical process flow diagram of a DGA® Agent reclaiming [Huntsman web site]	16
Figure 2.1	Repeat unit of Matrimid® 5218 polyimide.	23
Figure 2.2	Scanning Electron Micrograph of cross section of a Matrimid® asymmetric hollow fiber showing selective skin and porous support. The skin layer is shown in partially oblique view to illustrate its thin continuous nature (Gunaidi, 2000).	25
Figure 2.3	Shell-side feeding with the module construction.....	26
Figure 2.4	Schematic diagram of pure gas permeation testing	27
Figure 2.5	Schematic of gas permeation apparatus for hollow fiber modules.	29
Figure 2.6	Depiction of competition effect caused by a third component, C, in a membrane system. The symbols  depict unrelaxed volume elements accessible to both components A and B in the glassy polymer in the absence of a strongly condensable (e.g. toluene or n-heptane) component. During exposure to such “C” components, sorption and transport (i.e. permeation) pathways are precluded to A and B, thereby reducing their ternary gas permeation in comparison to binary feeds.	35
Figure 2.7	The effect of plasticizing: increase in the permeances of penetrants. In this case, besides any “competition” effects, additional swelling induced permeation pathways are made available to other components. The symbols  depict unrelaxed volume elements accessible to both components A and B in the glassy polymer in the absence of a strongly condensable (e.g. toluene or n-heptane) component. The additional arrows shown in the “during exposure” case illustrates the hypothetically possible higher flux of both A and B during plasticization.	36
Figure 2.8	The effect of conditioning is an increase in the permeances of penetrants. In this case, besides any “competition” effects,	

additional swelling induced permeation pathways are made available to other components. The symbols  depict unrelaxed volume elements accessible to both components A and B in the glassy polymer. The additional arrows show in the “after exposure” case illustrates the higher flux of both A and B due to conditioning.37

Figure 2.9 Depiction of the compaction effect.....39

Figure 2.10 Effect of conditioning of 10/90 CO₂/CH₄ mixture on a) the CO₂ permeability, and b) the CO₂/CH₄ selectivity at ~200 psia and 35 °C. Lines are “drawn by eye”.43

Figure 2.11 Effect of conditioning of 10/90 CO₂/CH₄ + 500 ppm n-heptane mixture on a) the CO₂ permeability, and b) the CO₂/CH₄ selectivity at 200 psia and 35 °C. Lines are “drawn by eye”.44

Figure 2.12 Effect of conditioning of 10/90 CO₂/CH₄ + 300 ppm toluene mixture on a) the CO₂ permeability, and b) the CO₂/CH₄ selectivity at 200 psia and 35 °C. Lines are “drawn by eye”.46

Figure 2.13 CO₂ and CH₄ Arrhenius plots of 10/90 CO₂/CH₄ mixture at 200 psia48

Figure 2.14 Effect of conditioning of 10/90 CO₂/CH₄ + 300 ppm toluene mixture on the a) CO₂ permeability, and b) CO₂/CH₄ selectivity at 200 psia and 55 °C. Lines are “drawn by eye”.49

Figure 2.15 Comparison of a) CO₂ permeability, and b) CO₂/CH₄ selectivity during exposure at 200 psia, and 35 °C for 10/90 CO₂/CH₄ mixture , 10/90 CO₂/CH₄ + 300 ppm toluene mixture, and 10/90 CO₂/CH₄ + 500 ppm n-heptane mixture.51

Figure 2.16 Comparison of a) CO₂ permeability, and b) CO₂/CH₄ selectivity during exposure at 200 psia, and 55 °C for 10/90 CO₂/CH₄ mixture , 10/90 CO₂/CH₄ + 300 ppm toluene mixture, and 10/90 CO₂/CH₄ + 500 ppm n-heptane mixture.53

Figure 2.17 Comparison of a) CO₂ permeability, and b) CO₂/CH₄ selectivity during exposure at 200 psia, 35 °C and 55 °C for 10/90 CO₂/CH₄ + 100 ppm toluene mixture.55

Figure 2.18 Comparison of a) CO₂ permeability, and b) CO₂/CH₄ selectivity during exposure at 400 psia, 35 °C and 55 °C for 10/90 CO₂/CH₄ + 100 ppm toluene mixture.56

Figure 2.19 Effect of conditioning of 10/90 CO₂/CH₄ mixture on a) the CO₂ permeability, and b) the CO₂/CH₄ selectivity at 600 psia and 35 °C. Lines are “drawn by eye”.58

Figure 2.20 Effect of conditioning of 10/90 CO₂/CH₄ + 500 ppm n-heptane mixture on a) the CO₂ permeability, and b) the CO₂/CH₄ selectivity at 600 psia and 35 °C. Lines are “drawn by eye”.60

Figure 2.21	Effect of conditioning of 10/90 CO ₂ /CH ₄ + 300 ppm toluene mixture on a) the CO ₂ permeability, and b) the CO ₂ /CH ₄ selectivity at 600 psia and 35 °C. Lines are “drawn by eye”.	61
Figure 2.22	Comparison of a) CO ₂ permeability, and b) CO ₂ /CH ₄ selectivity <i>during exposure</i> at 600 psia, 35 °C for 10/90 CO ₂ /CH ₄ mixture, 10/90 CO ₂ /CH ₄ + 300 ppm toluene mixture, and 10/90 CO ₂ /CH ₄ + 500 ppm n-heptane mixture.	63
Figure 2.23	Qualitative transport gap (free volume element) size distribution change after conditioning with 10/90 CO ₂ /CH ₄ + 300 ppm toluene mixture.	65
Figure 2.24	Hypothetical figure of the dense skin, and the defective morphology of an asymmetric hollow fiber. SEM of Matrimid asymmetric hollow fiber (taken by Seth Carruthers, 1999)	66
Figure 2.25	Comparison of CO ₂ /CH ₄ selectivity for defective and defect-free fibers during exposure at 35 °C for 10/90 CO ₂ /CH ₄ + 300 ppm toluene mixture.	68
Figure 3.1	Schematic of pressure decay apparatus	78
Figure 3.2	Effects of 10/90 CO ₂ /CH ₄ mixture exchange conditioning at 600 psia and 35 °C on a) CO ₂ sorption isotherms, and b) CH ₄ sorption isotherms for asymmetric hollow fibers of Matrimid® conditioned.	82
Figure 3.3	Effects of 10/90 CO ₂ /CH ₄ + 300 ppm toluene mixture exchange conditioning at 600 psia and 35 °C on a) CO ₂ sorption isotherms, and b) CH ₄ sorption isotherms for asymmetric hollow fibers of Matrimid® conditioned.	85
Figure 3.4	Effects of 10/90 CO ₂ /CH ₄ + 500 ppm n-heptane mixture exchange conditioning at 600 psia and 35 °C on a) CO ₂ sorption isotherms, and b) CH ₄ sorption isotherms for asymmetric hollow fibers of Matrimid® conditioned.	86
Figure 3.5	Solubility of CO ₂ and CH ₄ in conditioned samples with 10/90 CO ₂ /CH ₄ , 10/90 CO ₂ /CH ₄ + 300 ppm toluene and 10/90 CO ₂ /CH ₄ + 500 ppm n-heptane at 600 psia and 35 °C.	89
Figure 3.6	Change of a) CO ₂ local diffusion coefficient and b) CH ₄ local diffusion coefficient conditioned with 10/90 CO ₂ /CH ₄ mixture, 10/90 CO ₂ /CH ₄ + 500 ppm n-heptane mixture, and 10/90 CO ₂ /CH ₄ + 300 ppm toluene mixture at 200 psia and 35 °C. Lines are “drawn by eye”	94
Figure 3.7	Change of a) CO ₂ local diffusion coefficient and b) CH ₄ local diffusion coefficient conditioned with 10/90 CO ₂ /CH ₄ mixture, 10/90 CO ₂ /CH ₄ + 500 ppm n-heptane mixture, and 10/90 CO ₂ /CH ₄ + 300 ppm toluene mixture at 600 psia and 35 °C. Lines are “drawn by eye”	95

Figure 4.1	Detailed diagram of the wetted-wall column contactor.....	109
Figure 4.2	Flow diagram of the experimental setup.....	110
Figure 4.3	Flux interpolation to determine equilibrium solubility. Data points for absorption into 11 wt% MOR/53 wt% DGA at CO ₂ loading of 0.13 mol/mol amine and a temperature of 40 °C.	113
Figure 4.4	Schematic diagram of the N ₂ O experimental apparatus.	114
Figure 4.5	Solubility of nitrous oxide as a function of amine concentration.	124
Figure 4.6	Heat of Absorption of CO ₂ at various loading for 23.5 wt% MOR	126
Figure 4.7	Heat of Absorption of CO ₂ at various loading for 65 wt% DGA.	127
Figure 4.8	Heat of Absorption of CO ₂ at various loading for 23.5 wt% MOR/53 wt% DGA.	127
Figure 4.9	¹³ C NMR spectrum of 65 wt% DGA at 300K and 0.34 loading.	130
Figure 4.10	¹³ C NMR spectrum of 23.5 wt% MOR at 313K and 0.40 loading.	131
Figure 4.11	¹³ C NMR spectrum of 11 wt% MOR/53 wt% DGA at 300K and 0.52 loading.	132
Figure 4.12	Expanded ¹³ C NMR spectrum of 11 wt% MOR/53 wt% DGA at 300K and 0.52 loading.....	132
Figure 4.13	Expanded ¹³ C NMR spectrum of 11 wt% MOR/53 wt% DGA at 300K and 0.52 loading.....	133
Figure 4.14	Proton, ¹³ C and short range C-H correlation NMR spectra for 11 wt% MOR/53 wt% DGA at 300K and 0.52 moles/mol amine.....	134
Figure 4.15	Apparent carbamate stability constant for the 23.5wt% MOR and the 65wt% DGA with 0.1 to 0.5 moles CO ₂ /mol Amine.....	139
Figure 4.16	Results of Nitrous Oxide data Regression in unloaded solutions.	141
Figure 4.17	Data of Huey et al. (1991) reinterpreted as activity coefficients for the water / MOR system at elevated temperature.	143
Figure 4.18	Results of regression of the equilibrium partial pressure of MOR in MOR-H ₂ O mixture. Fitting the excess heat of mixing at 25 °C to -25 kJ/mol.....	145
Figure 4.19	Results of VLE and C13 NMR data regression of the DGA-CO ₂ system.	147
Figure 4.20	Results of regression of the equilibrium partial pressure of CO ₂ in 65wt% DGA system obtained in this work.	148
Figure 4.21	Results of regression of C13 NMR data in 65wt % DGA system at 25	149
Figure 4.22	Results of regression of C13 NMR data in 65wt % DGA system at 40 °C.	149
Figure 4.23	Results of regression of C13 NMR data in 65wt % DGA system at 60 °C.	150
Figure 4.24	Predicted speciation of CO ₂ in 65 wt% DGA at 40 °C.....	150

Figure 4.25	Results of VLE and NMR data regression of the MOR-CO ₂ system Fixing CO ₂ solubility to the N ₂ O Analogy.	151
Figure 4.26	Results of regression of the equilibrium partial pressure of CO ₂ in 23.5wt% DGA system.	153
Figure 4.27	Results of regression of C13 NMR data in MOR-CO ₂ system at 25 °C.	154
Figure 4.28	Results of regression of C13 NMR data in MOR-CO ₂ system at 40 °C.	154
Figure 4.29	Results of regression of C13 NMR data in MOR-CO ₂ system at 60 °C.	155
Figure 4.30	Predicted speciation of CO ₂ in 23.5 wt% MOR at 25 °C.	155
Figure 4.31	Results of model prediction for VLE and NMR data regression with no parameter adjustments of the DGA-MOR-CO ₂ system.	156
Figure 4.32	Results of VLE and NMR data regression of the DGA-CO ₂ system.	157
Figure 4.33	Results of VLE data regression of the 11 wt% MOR/53 wt% DGA system at 60 °C.	158
Figure 4.34	Results of regression of C13 NMR data in DGA-MOR-CO ₂ system at 25 °C.	159
Figure 4.35	Results of regression of C13 NMR data in DGA-MOR-CO ₂ system at 40 °C.	159
Figure 4.36	Results of regression of C13 NMR data in the 11 wt% MOR/53 wt% DGA system at 60 °C.	160
Figure 4.37	Predicted speciation of CO ₂ in 11 wt% MOR/53 wt% DGA at 40 °C.	160
Figure 4.38	CO ₂ partial pressure as a function of loading for the the 11 wt% MOR/53 wt% DGA system (solid lines) and 65 wt % DGA system (dashed lines) at 25 °C, 40 °C and 60 °C.	162
Figure 4.39	Heats of reaction of CO ₂ at various CO ₂ loading for 11 wt% MOR/53 wt% DGA (solid lines) and 65 wt % DGA (dashed lines) at 25 °C, 40 °C and 60 °C.	164
Figure 4.40	Vapor pressure of MOR over 11 wt% MOR/53 wt% DGA, and CO ₂ loading of 0.01 mol CO ₂ / mol amine.	166
Figure 5.1	Straight line fit for rate of CO ₂ absorption into aqueous 65 wt% diglycolamine solutions at low solution loading.	182
Figure 5.2	Second-order rate constant for the reaction between CO ₂ and 65wt% DGA using the rigorous model, from data at zero loading.	184
Figure 5.3	Comparison between the experimental and calculated interfacial fluxes of CO ₂ using the rigorous model for the 65 wt% DGA at zero loading.	185

Figure 5.4	Second-order rate constant for the reaction between CO ₂ and 25wt% DGA.	187
Figure 5.5	Second-order rate constant for the reaction between CO ₂ and DGA at zero loading.	188
Figure 5.6	Second-order rate constant for the reaction between CO ₂ and DGA.	189
Figure 5.7	Comparison between the data obtained in this work for the 65 wt% and 25 wt% DGA solution and Pacheco et al., (2000) for the 50 wt% DGA solution at low loading.	190
Figure 5.8	Second-order rate constant for the reaction between CO ₂ and 65 wt% DGA. at 25 °C.	193
Figure 5.9	Second-order rate constant for the reaction between CO ₂ and 65 wt% DGA. at 40 °C.	193
Figure 5.10	Second-order rate constant for the reaction between CO ₂ and 65 wt% DGA. at 60 °C.	194
Figure 5.11	Concentration gradients for absorption of carbon dioxide into 65 wt% DGA. Loading=0.115, k ₁ ^o =2.79E-3 m/s, P ⁱ /P [*] =392.0, T=313K.	196
Figure 5.12	Concentration gradients for absorption of carbon dioxide into 65 wt% DGA. Loading=0.385, k ₁ ^o =2.45E-3 m/s, P ⁱ /P [*] =28.5, T=313K.	196
Figure 5.13	Sensitivity of calculated CO ₂ flux to values of the diffusion coefficients of reactants and products and second order rate constant. 313 K, k ₁ ^o =2.74E-3 m/s, P _i =10P [*]	199
Figure 5.14	Effect of CO ₂ loading on the second rate constant at 25 °C, 40 °C and 60 °C for the system DGA- water-CO ₂ . Lines are model predictions.	201
Figure 5.15	Comparison between the measured and calculated interfacial fluxes of CO ₂ for the 65 wt% DGA at various CO ₂ loading.	202
Figure 5.16	Predicted activity coefficients for 65 wt% DGA at 313K	204
Figure 5.17	Predicted activity coefficients for 50 wt% DGA at 313K	204
Figure 5.18	Predicted activity coefficients for 25 wt% DGA at 313K	205
Figure 5.19	Effect of CO ₂ loading on the second rate constant calculated based on concentration and on activity at 40 °C for the system DGA- water-CO ₂ . Lines are model predictions.	207
Figure. 5.20	Normalized flux of 65wt% DGA and CO ₂ at low and high driving force at 313K.	208
Figure. 5.21	Normalized flux of 65wt% DGA and CO ₂ at low and high driving force at 298K.	209
Figure. 5.22	Normalized flux of 65wt% DGA and CO ₂ at low and high driving force at 313K.	209

Figure. 5.23	Normalized flux of 65wt% DGA and CO ₂ at low and high driving force at 333K.	210
Figure 5.24	Effect of ionic strength on the second rate constant at 25 °C, 40 °C and 60 °C for the system DGA- water-CO ₂	212
Figure 5.25	Normalized flux of 65wt% DGA and glycolic acid solvent at 40 °C.	215
Figure 5.26	Effect of glycolic acid on the second rate constant at 40 °C for the system DGA- water-CO ₂	215
Figure 5.27	Normalized flux of fresh 65wt% DGA and potassium formate solutions.....	218
Figure 5.28	Effect of potassium formate on the second rate constant at 25 °C and 40 °C for the system DGA- water-CO ₂	219
Figure 5.29	Effect of ionic strength on the second rate constant at 25 °C and 40 °C for the system DGA-water-CO ₂ , DGA-glycolic acid-water-CO ₂ , and the system DGA-potassium formate-water-CO ₂	220
Figure 6.1	Straight line fit for rate of CO ₂ absorption into aqueous 23.5 wt% MOR solutions at zero solution loading	226
Figure 6.2	Second order rate constant of MOR and carbon dioxide.....	227
Figure 6.3	Bronsted correlation of CO ₂ reaction rates with secondary amines at 25 °C. (Rochelle et al., 2000).....	228
Figure 6.4	Normalized flux of 11 wt% MOR/53 wt% DGA and CO ₂	231
Figure 6.5	Comparison of predicted and experimental fluxes for absorption of carbon dioxide into 11 wt% MOR/53 wt% DGA.....	235
Figure 6.6	Third-order rate constant for the reaction between CO ₂ and 11 wt% MOR/53 wt% DGA using the rigorous model, from data at zero loading.	236
Figure 6.7	Rigorous model fit of all MOR/DGA absorption data.	237
Figure 6.8	$k_{MOR-DGA}$ for absorption of carbon dioxide into 11 wt% MOR/53 wt% DGA at 25 °C, 40 °C and 60 °C.....	238
Figure 6.9	Normalized flux of CO ₂ in 11 wt% MOR/53 wt% DGA and 65 wt% DGA at 25 °C, $k_1^0=1.77E-3$ m/s, $P^i=10P^*$	239
Figure 6.10	Normalized flux of CO ₂ in 11 wt% MOR/53 wt% DGA and 65 wt% DGA at 40 °C, $k_1^0=1.77E-3$ m/s, $P^i=10P^*$	240
Figure 6.11	Normalized flux of CO ₂ in 11 wt% MOR/53 wt% DGA and 65 wt% DGA at 60 °C, $k_1^0=1.77E-3$ m/s, $P^i=10P^*$	240
Figure 6.12	Sensitivity of calculated CO ₂ flux to values of the diffusion coefficients of reactants and products and rate constants, 40 °C, $k_{ol}=1.77E-3$ m/s, $P^i=10P^*$	241
Figure 6.13	Comparison of rigorous model and PFO model for CO ₂ absorption at 40 °C, $k_1^0=1.77E-3$ m/s, $P^i=10P^*$	242

Figure 6.14	Comparison of rigorous model and PFO model for CO ₂ absorption rate at 40 °C, $k_1=2.74E-3$ m/s, $P^i=1.01P^*$243
Figure A.1	Simplified block diagram of carbon dioxide/methane separation in a countercurrent hollow-fiber module.258
Figure A.2	Effect of CO ₂ feed mole fraction on (a). ‘ \bar{r} ’; (b). CO ₂ average concentration inside the membrane; (c). CH ₄ average concentration inside the membrane.270
Figure A.3	Effect of CO ₂ feed mole fraction on (a). CO ₂ bulk flux contribution; (b). CH ₄ bulk flux contribution.....272
Figure A.4	Simulation of CO ₂ permeance for (a) 10/90 CO ₂ /CH ₄ feed (b) 50/50 CO ₂ /CH ₄ feed (b) 90/10 CO ₂ /CH ₄ feed as a function of axial position, considering the diffusion model (DM) and the frame of reference model (FM).274
Figure A.5	Simulation of CH ₄ permeance for (a) 10/90 CO ₂ /CH ₄ feed (b) 50/50 CO ₂ /CH ₄ feed (b) 90/10 CO ₂ /CH ₄ feed as a function of axial position, considering the diffusion model (DM) and the frame of reference model (FM).276
Figure A.6	Effect of total feed pressure on (a) average CO ₂ concentration inside the membrane (b) average CH ₄ concentration inside the membrane as a function of axial position, for 50/50 CO ₂ /CH ₄ feed considering the frame of reference model (FM).....279
Figure A.7	Simulation of average ‘ \bar{r} ’, the mass flux ratio of CO ₂ to CH ₄ in the membrane for (a) 10/90 CO ₂ /CH ₄ feed (b) 50/50 CO ₂ /CH ₄ feed (b) 90/10 CO ₂ /CH ₄ feed as a function of axial position, considering the frame of reference model (FM).282
Figure A.8	Bulk flux contribution of (a) CO ₂ (b) CH ₄ in 10/90 CO ₂ /CH ₄ , 50/50 CO ₂ /CH ₄ and 90/10 CO ₂ /CH ₄ feed as a function of total feed pressure.285
Figure A.9	Effect of membrane area on bulk flux contribution of CO ₂ and CH ₄ in 50/50 CO ₂ /CH ₄ feed.286
Figure A.10	Effect of membrane area on bulk flux contribution of CO ₂ and CH ₄ in 50/50 CO ₂ /CH ₄ feed as a function of axial position.287
Figure A.11	Effect of membrane thickness on bulk flux contribution of CO ₂ and CH ₄ in 50/50 CO ₂ /CH ₄ feed.....288
Figure A.12	Effect of of membrane thickness on bulk flux contribution of CO ₂ and CH ₄ in 50/50 CO ₂ /CH ₄ feed as a function of axial position. .289
Figure A.13	Effect of permeate pressure on (a). ‘ \bar{r} ’; (b). CO ₂ average concentration inside the membrane; (c). CH ₄ average concentration inside the membrane in 50/50 CO ₂ /CH ₄ feed.292
Figure A.14	Effect of permeate pressure on bulk flux contribution of CO ₂ and CH ₄ in 50/50 CO ₂ /CH ₄ feed in a hollow-fiber module, operating in countercurrent.293

Figure A.15	Percent stage cut and percent error ($[\% \text{ stage cut}_{\text{FM}} - \% \text{ stage cut}_{\text{DM}}] / [\% \text{ stage cut}_{\text{DM}}] \times 100\%$) as a function of feed pressure for (a). 10/90 CO ₂ /CH ₄ feed; (b). 50/50 CO ₂ /CH ₄ feed; (c). 90/10 CO ₂ /CH ₄ feed considering the frame of reference model (FM) and the diffusion model (DM).....	295
Figure A.16	Simulation of CH ₄ recovery as a function of feed pressure, in a hollow-fiber module, operating in countercurrent, considering the frame of reference model (FM) and the diffusion model (DM) for 10/90 CO ₂ /CH ₄ feed; 50/50 CO ₂ /CH ₄ feed; and. 90/10 CO ₂ /CH ₄ feed.....	296
Figure A.17	Simulation of CO ₂ /CH ₄ selectivity as a function of feed pressure for different permeate pressures, in a hollow-fiber module, operating in countercurrent, considering the frame of reference model (FM) and the diffusion model (DM) for (a). 10/90 CO ₂ /CH ₄ feed; and (b). 50/50 CO ₂ /CH ₄ feed.....	297
Figure F.1	Calibration curve for channel # 1	331
Figure F.2	Calibration curve for channel # 2	332

Chapter 1: Introduction to Gas Treating & Research Objective

Natural gas is a fuel that burns cleaner than many other traditional fossil fuels. It is used for heating, cooling, and production of electricity and it finds many uses in industry. Natural gas is more environmentally attractive than other fossil fuels because when burns it emits lower quantities of greenhouse gases than do other fossil fuels (Energy Information Administration, 2001). The composition of natural gas varies from one location to another. Common impurities in the natural gas streams include carbon dioxide, water vapor, hydrogen sulfide and nitrogen. These components are corrosive, and hydrogen sulfide is also toxic (Spillman, 1989); hence, removal of the contaminants is necessary to meet pipeline requirements. The pipeline specifications for these components are: <2% for CO₂, <4 ppm for H₂S, and <0.1 g/m³ for H₂O (Spillman, 1984; Fournie and Agostini, 1987; Bhide and Stern, 1993). Removal of the contaminants also increases the heating value of the transported gas.

1.1 Current Technologies for CO₂ Removal from Natural Gas

Various processes are used to condition raw natural gas to pipeline quality. Carbon dioxide and/or hydrogen sulfide removal can be accomplished via amines, or membranes. The choice of technology is dependent upon the needs of the gas processor (Rojey et al., 1997). Although membranes have proven their usefulness, membrane technology has to compete with amine technology. Advantages of membranes are low capital investment, ease of operation, low energy consumption, cost effectiveness even at low gas volumes and good weight and space efficiency. However, amine treatment is still an efficient method, but the

amine units are large and heavy. Table 1.1 compares amines and membranes for CO₂ removal systems. Despite all the advantages of membranes, it is still difficult to introduce membranes on a market where people are familiar with the conventional separation techniques. But given the number of commercial-scale membrane suppliers, there is a growing acceptance of membranes in industry.

Table 1.1 Comparison of amine and membrane CO₂ removal systems (William, 2002).

Operating Issues		
	Amines	Membranes
User Comfort Level	Very familiar	Still considered new technology
Hydrocarbon Losses	Very low	Losses depend upon conditions
Meets Low CO ₂ Spec.	Yes (ppm levels)	No (<2% economics are challenging)
Meets Low H ₂ S Spec.	Yes (<4 ppm)	Sometimes
Energy Consumption	Moderate to high	Low, unless compression used
Operating Cost	Moderate	Low to moderate
Maintenance Cost	Low to moderate	Low, unless compression used
Ease of Operation	Relatively complex	Relatively simple
Environmental Impact	Moderate	Low
Dehydration	Product gas saturated	Product gas dehydrated
Capital Cost Issues		
	Amines	Membranes
Delivery Time	Long for large systems	Modular construction is faster
On-Site Installation Time	Long	Short for skid-mounted equipment
Pretreatment Costs	Low	Low to moderate
Recycle Compression	Not used	Use depends upon conditions

A nice review on the advantages and disadvantages of membranes and amines are given by William (2002).

1.2 CO₂ Removal with Membranes

Membranes, thin barriers that allow preferential passage of certain substances, are currently available for CO₂ removal from natural gas streams. Figure 1.1 shows the simplest membrane operation.

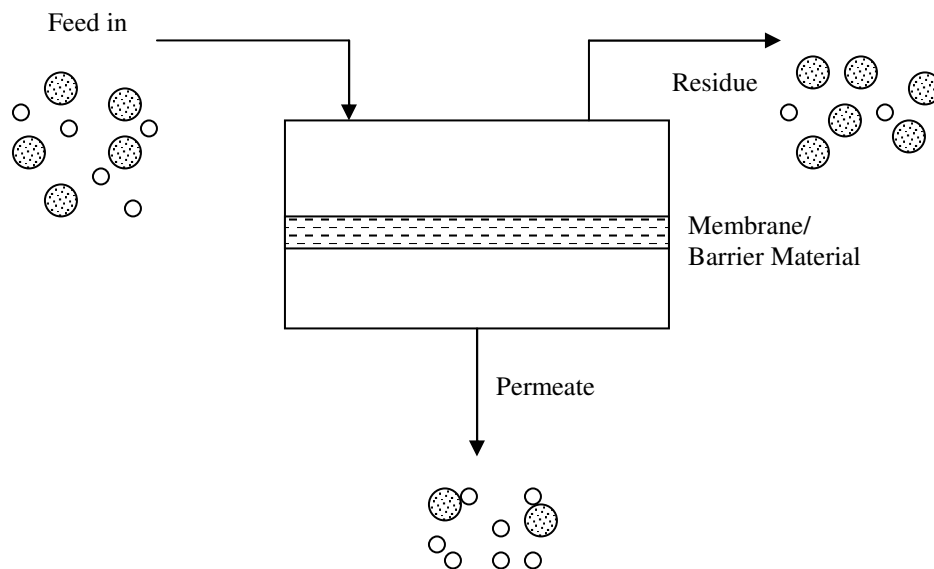


Figure 1.1 Illustration of a membrane separation operation.

The membrane materials that are currently available for natural gas conditioning are polymer based, for example, cellulose acetate, polyimides, polyamides, polysulfone, polycarbonates, and poly-etherimide. Polyimide has some potential in certain CO₂ removal applications, but it has not received sufficient testing to be used in large applications.

The most common types of membrane forms in use today for natural gas separation are of the spiral-wound type and the hollow-fiber type. The hollow fiber membranes consist of a very thin (0.1-1.0 micrometers, μm), nonporous "skin" or surface layer, combined with a much thicker microporous backing (100 to 200

μm). The separation of a gas mixture occurs in this skin, while the microporous substrate gives the membrane mechanical strength. Figure 1.2 shows the cross-section of hollow fiber membranes and the transition from the porous support to the dense-free skin.

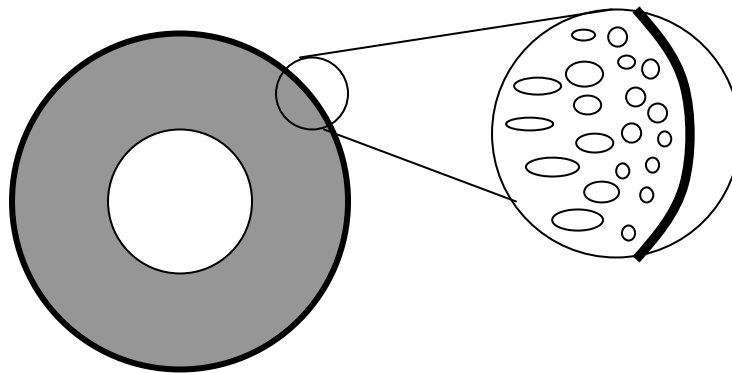


Figure 1.2 Schematic of hollow fiber membrane showing skin and Support (Gunaidi, 2000)

In these membranes, CO_2 dissolves into the thin surface layer and diffuses through the membrane more rapidly than methane or any of the other hydrocarbons present in natural gas. This is not a filtering type process; the gas molecules move through the membrane in a process based on solubility and diffusivity (Kesting and Fritzsche, 1993; Paul and Yampol'skii, 1994).

“Permeability” is defined as the rate at which gases and vapors can pass through the membrane. “Selectivity” defines the ratio between the permeation rates between different components in the gas stream. Permeability and selectivity are important factors when it comes to select membranes for gas treating. Permeability and selectivity usually have inverse relationship; the higher the permeability, the less membrane area is required for a given separation and therefore the lower the membrane cost. The higher the selectivity is the lower the

losses of methane and therefore the higher the volume of the product that can be recovered. Permeation rate is dependent on the solubility of a given gas component, molecular size and the operating conditions (Porter, 1990; Ho and Sirkar, 1992; William, 2002). Figure 1.3 shows the relative permeability of the components most commonly found in natural gas streams. Water permeates faster than other components including CO₂. This adds an advantage to membrane systems that can be used in gas dehydration while removing CO₂.

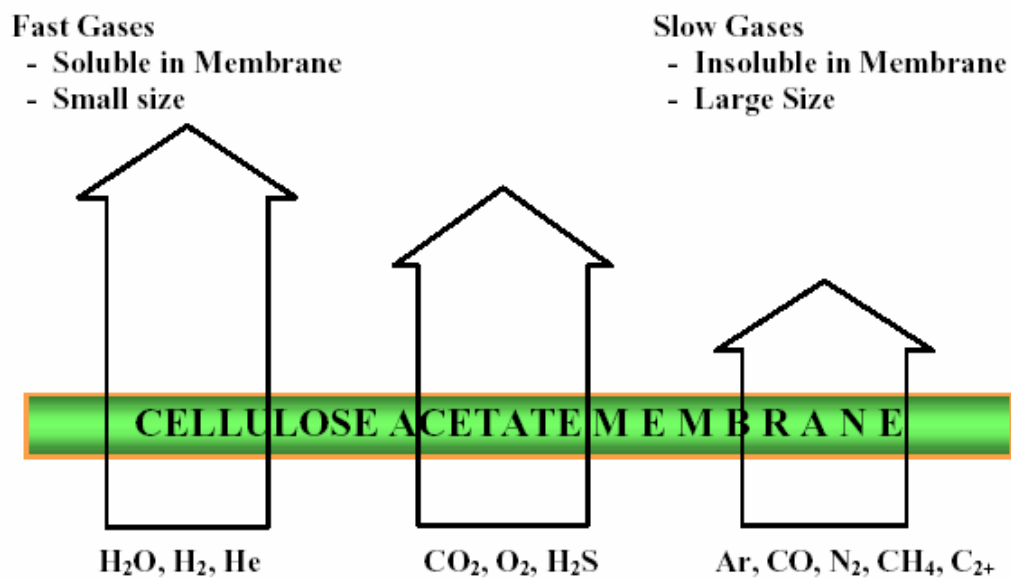


Figure 1.3 Relative Solubility of Some Typical Gas Components (Dortmundt, and Doshi, 1993; William, 2002)

The hollow fibers are typically combined into a bundle similar to a shell and tube heat exchanger. Figure 1.4 illustrates the hollow fiber membrane element. In hollow-fiber elements, very fine hollow fibers are wrapped around a central tube in a highly dense pattern. In this wrapping pattern, both open ends of the fiber end up at a permeate pot on one side of the element. Feed gas which is high in CO₂ concentration flows over and between the fibers, and the permeate stream which is

high in CO₂ concentration flows into the fibers. The permeated CO₂ then travels within the fibers until it reaches the permeate pot, where it mixes with CO₂ permeates from other fibers. The total permeate exits the element through a permeate pipe. The components that do not permeate are called residual gas and are low in CO₂ concentration (Dortmundt, and Doshi, 1993; William, 2002).

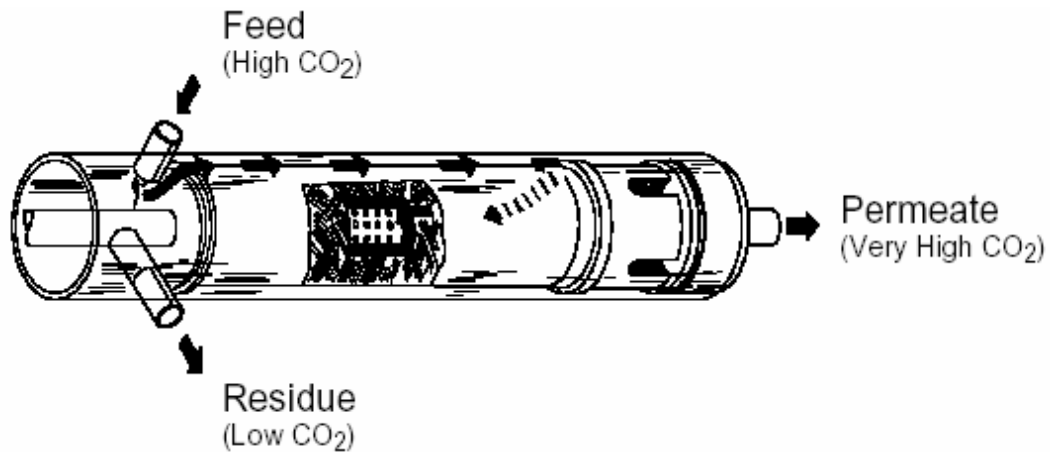


Figure 1.4 Hollow Fiber Membrane element (Dortmundt, and Doshi, 1993; William, 2002).

Membrane Pretreatment

The use of membranes in the past have shown the need for pretreatment of the feed stream when processing natural gas. Membrane life was found to be too short. Natural gas can contain a wide variety of contaminants that quickly reduce membrane effectiveness and force premature replacement of the elements. Substances commonly found in natural gas streams that will lower the performance of CO₂ removal membranes include:

- Liquids: Liquids cause swelling of the membranes and can destroy the membrane.

- Heavy hydrocarbons, approximately > C15: Significant levels of these compounds slowly coat the membrane surface, thus decreasing permeation rate. In addition, as found in this study hydrocarbons can cause swelling and loss in selectivity under some conditions.
- Particulate material: Particles can block the membrane flow area.
- Certain corrosion inhibitors and well additives: Some corrosion inhibitors and well additives are destructive to the membrane systems.

The pretreatment system must remove the above contaminants and must ensure that liquids do not form within the membrane. There are two cases where liquid hydrocarbons can form; in one case the gas cools down as a result of Joule-Thomson effect as CO₂ permeates through the membrane. The second case is when the CO₂ permeates and the gas becomes heavier in hydrocarbons and its dew point therefore increases through the membrane. To avoid condensation in the membrane sufficient heat must be applied. The pretreatment system must have a wide safety margin and be highly flexible to cope with unexpected circumstances. Heavy hydrocarbon content of a feed gas can vary widely from initial pre-start-up estimates and also from month to month during the plant's life. Large variations can happen between different wells in the same area. A reliable pretreatment system must take this variation into account and must be able to protect the membranes against a wide range of contaminants (Dortmundt and Doshi, 1993).

The impact of heavy hydrocarbons on the membrane system has remained poorly understood due to the complexity of these components and the difficulty in characterizing their effects experimentally. This thesis consists of two parts including this introduction. The first part of the dissertation aims to understand and model the effect of heavy hydrocarbons on the performance of the membranes. Previous work on membrane formation has led to successful synthesis and

modeling of reliable membranes for CO₂ removal from natural gas feeds. However, the tests performed in the laboratory on these membranes were contaminant free. In the actual field, membranes exhibit poorer performance. More work is needed to understand the key factors that undermine the gas separation ability of membranes in such applications. Therefore, the objectives of the first part of the dissertation are organized as follows;

- Chapter 2 presents the results and analysis of permeation experiments conducted with hollow fiber membranes which probe the glassy polymer environment with 10% CO₂/ 90% CH₄ feed gas and toluene and n-heptane molecules as a typical aromatic and parafinic hydrocarbons, respectively.
- Chapter 3 presents comparison of sorption behavior in asymmetric hollow fiber samples of Matrimid®. Exchange conditioning experiments are conducted to observe the response of the various polymer samples to the introduction of additional sites for sorption due to the conditioning process.
- Conclusions and recommendations are presented in Chapter 7.

1.3 CO₂ Removal with Amines

The most widely used gas treating process for acid gas removal in the natural gas and petroleum processing industries is the chemical solvent process, using the various alkanolamines. These processes use a solvent, either an alkanolamine or an alkali-salt (hot carbonate processes) in an aqueous solution, which reacts with the acid gas (H₂S and CO₂) to form a complex or bond. This complex is subsequently reversed in the regenerator at elevated temperatures and reduced acid gas partial pressures releasing the acid gas and regenerating the solvent for reuse. These are well suited for low pressure applications where the acid gas partial pressures are low and low levels of acid gas are desired in the

residue gas since their acid gas removal capacity is relatively high and insensitive to acid gas partial pressures as compared to physical solvents. The chemical solvent processes are generally characterized by a relatively high heat of acid gas absorption and require a substantial amount of heat for regeneration. A simplified flow schematic of a typical gas treating operation using amine solvents is shown in Figure 1.5.

A sour gas containing H_2S and/or CO_2 is introduced at the bottom of a high-pressure absorber where it rises and counter currently contacts an aqueous alkanolamine solution that is introduced at the top of the absorber. The CO_2 -rich amine solution that results is then pumped through heat exchangers where its temperature is raised. It is then introduced at the top of a stripper where it countercurrently contacts steam at an elevated temperature and reduced pressure. The steam strips the CO_2 and H_2S from solution and the lean alkanolamine solution is pumped through the heat exchanger, where it is cooled, and reintroduced at the top of absorber (LRGCC, 2003).

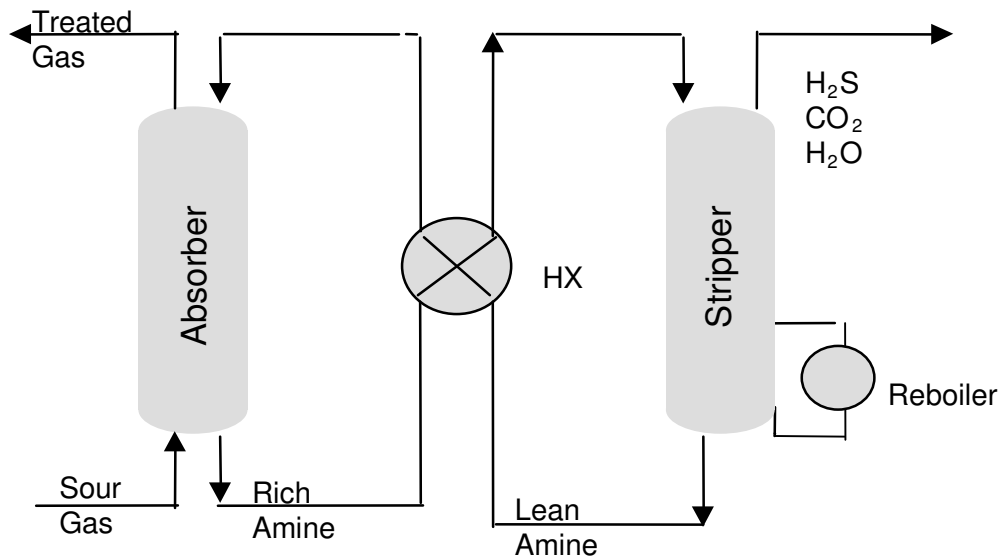


Figure 1.5 Illustration of a absorption/stripping system for the removal of acid gases.

The alkanolamines most commonly used in industrial applications are monoethanolamine (MEA), diethanolamine (DEA), methyldiethanolamine (MDEA), and diglycolamine (DGA). For higher CO_2 concentrations, physical solvents are employed that utilize a pressure-letdown to desorb the CO_2 from the rich solvent. The alkanolamines are classified by the degree of substitution on the central nitrogen; a single substitution denoting a primary amine, a double substitution, a secondary amine, and a triple substitution, a tertiary amine. Each of the alkanolamines has at least one hydroxyl group and one amino group. In general, the hydroxyl group serves to reduce the vapor pressure and increase water solubility, while the amino group provides the necessary alkalinity in water solutions to promote the reaction with acid gases. It is readily apparent looking at the molecular structure that the non-fully substituted alkanolamines have hydrogen atoms at the non-substituted valent sites on the central nitrogen. This structural characteristic plays an important role in the acid gas removal capabilities of the various treating solvents. Figure 1.6 shows the commonly used alkanolamines in the gas treating industry (LRGCC, 2003; Kohl and Nielsen, 1997).

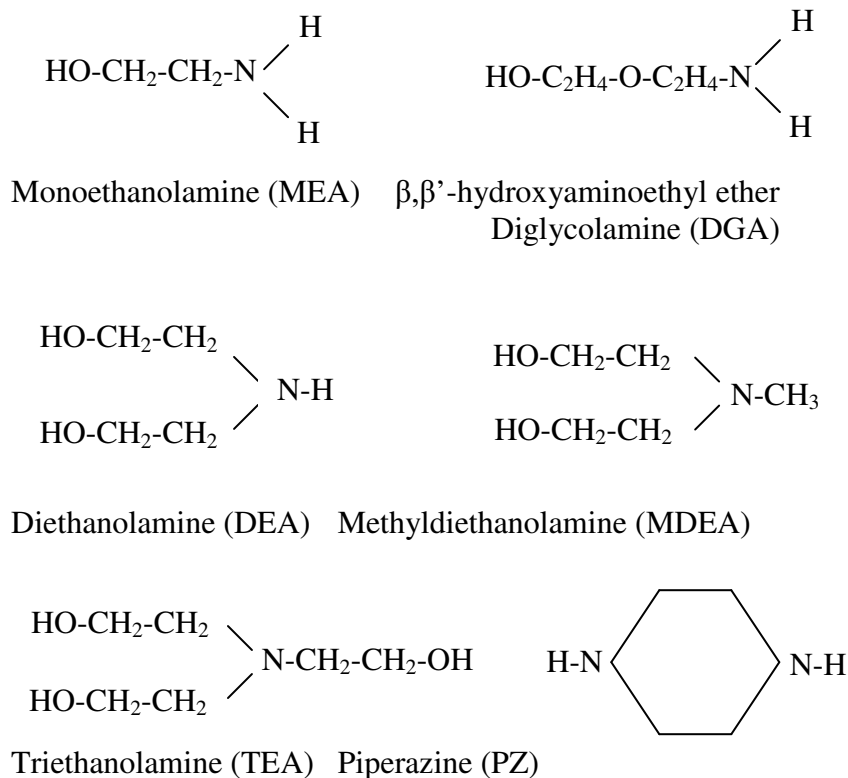


Figure 1.6 Structures of common amines used in gas treating.

H_2S and CO_2 are “acid gases” because they dissociate to form a weak acidic solution when they come into contact with water or an aqueous medium. The amines are weak organic bases. The acid gases and the amine base will combine chemically to form an acid base complex or “salt” in the treating solution. In the absorber column the acid gas absorption of H_2S is based only on “acid-base-reaction“. Regardless of the structure of the amine, H_2S reacts instantaneously with the primary, secondary, or tertiary amine via a direct proton transfer reaction as shown in Equation.1.1 below to form the hydrosulfide (LRGCC, 2003):

H₂S-reaction: Acid-base-reaction

Relative kinetics: instantaneous



For CO₂ removal the basis of chemistry is a combination of indirect “acid-base reaction” and direct “carbamate reaction”. The acid base reaction may occur with any of the alkanolamines regardless of the amine structure but it is kinetically slow because the carbonic acid dissociation step to the bicarbonate is relatively slow. The second reaction for CO₂, which results in the formation of the carbamate, is called the carbamate formation reaction and may only occur with the primary and secondary amines.

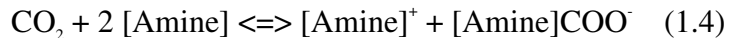
CO₂-reaction: Acid-base-reaction

Relative kinetics: slow

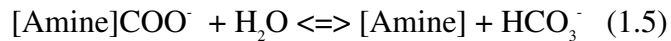


CO₂-reaction: Carbamate-reaction

Relative kinetics: fast



The rate of CO₂ absorption via the carbamate reaction is rapid, much faster than the CO₂ hydrolysis reaction, but somewhat slower than the H₂S absorption reaction. The stoichiometry of the carbamate reaction indicates that the capacity of the amine solution for CO₂ is limited to 0.5 mole of CO₂ per mole of amine if the only reaction product is the amine carbamate. However, the carbamate can undergo partial hydrolysis, as shown below in Equation 1.5, to form bicarbonate, regenerating free amine. Hence, CO₂ loading greater than 0.5 is possible through the hydrolysis of the carbamate intermediate to bicarbonate.



1.4 Natural Gas Sweetening with DGA

The Fluor Corporation patented the Diglycolamine process and DGA® agent was commercialized in the late sixties by Fluor and Jefferson Chemical company, a predecessor to Texaco Chemical Company and Huntsman Corporation. DGA is a primary amine, and its low vapor permits its use in higher concentrations, typically 50 to 60 weight percent, resulting in significant lower circulation rates and energy requirements. The advantages of DGA agent include (LRGCC, 2003):

- Capital and operating cost savings due to lower circulation requirements
- Removal of COS and CS₂
- High reactivity. The H₂S spec of ¼ grain can be generally obtained for applications with low operating pressures and high operating temperatures.
- Better mercaptan removal compared to other alkanolamines.
- Low freezing point; 50 wt% solution freezes at -30 °F, whereas 15 wt% MEA and 25wt% DEA solutions freeze at 25 and 21 °F, respectively.

Some of the disadvantages of DGA are:

- Nonselective removal in mixed acid gas systems.
- Absorbs aromatic compounds from inlet gas which complicates the sulfur recovery unit design, and
- Higher solvent cost relative to MEA and DEA.

Plants treating natural gas have DGA concentration ranging from 40 to 70 wt%. All of the natural gas sweetening plants are reducing H₂S concentration to less than 0.25 grains of H₂S/100 SCF. CO₂ concentration can also be reduced to less than 100 ppmv in most medium and high-pressure applications. Lower levels of CO₂ can be achieved when needed. Typical conditions found in natural gas plants are shown in Table 1.1

Table 1.2 Common conditions found in natural gas plants (Newman, 1985)

Range of Feed Gas Composition:

0.5–25 Mole % CO₂

0-33 Mole% H₂S

Range of Treating Pressures:

60-1150 psig

Range of Feed Gas Temperatures:

65-120 °F

Range of Treating Pressures:

60-1150 psig

Typical Treated Gas Quality:

	Low pressure	Medium ressure	High pressure
H ₂ S, ppmv	<4	<4	<4
CO ₂ , ppmv	>100	<100	<100

The acid gas loading of the rich DGA solution depends on three major factors; the DGA concentration, CO₂/H₂S ratio, and the material of construction. Plants treating natural gas with high CO₂/H₂S ratio generally operate with rich DGA acid gas loading of 0.35 to 0.40 moles of total acid gas/ mol DGA. Lean DGA loadings in these plants normally will be about 0.1 mol of acid gas/ mol DGA. Plants processing natural gas with low CO₂/H₂S ratios generally have loadings of 0.03 to 0.07 moles acid gas/mole DGA.

Natural gas containing low CO₂/H₂S ratio is considered less corrosive to process in amine sweetening systems. DGA plants, treating this type gas, typically use higher acid gas loadings in the rich DGA which, in conjunction with lower lean solution loadings, results in a significant increase in the net acid gas pickup per mole of DGA.

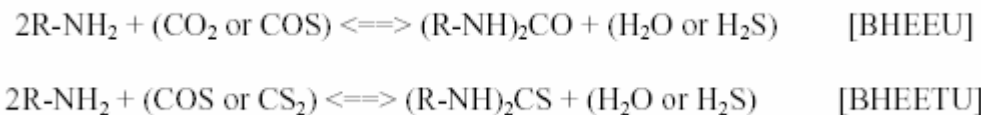
As is the case with loadings, the energy requirement to regenerate the DGA solution is also affected by the CO₂/H₂S ratio in the natural gas feeds. Plants operating with high CO₂/H₂S feed require less energy compared to feed with low CO₂/H₂S ratio. Plants operating with high CO₂/H₂S ratio may require 1.0 to 1.5

moles of water vapor per mole of acid gas in the regenerator overhead. Low CO₂/H₂S ratio of 0.2/1 may require 2.5 to 3.5 moles of water vapor per mole of total acid gas in the regenerator overhead. A reflux ratio of this magnitude is not unusual for low pressure treating plants which are required to produce natural gas with less than 0.25 grains of H₂S/100 SCF (Newman, 1985).

1.5 DGA Reclaimer Operations

The reclaimer is important in the operation of DGA plants. It reduces corrosion, foaming and fouling of the DGA® solution in the plant. It regenerates the DGA solution by removing the high boiling point and non-volatile acids and iron products from the DGA solution, concentrating them in the reclaimer as well as converting the chemical degradation product BHEEU back to DGA. A typical process flow diagram of a DGA® reclaimer is shown in Figure 1.7.

The major chemical degradation product of DGA solution in gas treating plants is N,N' bis(hydroxyethoxyethyl)urea (BHEEU). The reaction of two moles of DGA with 1 mole of either CO₂ or COS forms 1 mole of BUEEU. A second degradation product is thiourea or N,N' bis(hydroxyethoxyethyl)thiourea (BHEETU) which can also be formed by the reaction of 1 mole of either CS₂ or COS. Experience have shown that the dominant reaction with COS will be to form BHEEU. The reactions between CO₂, COS, or CS₂ and DGA are reversible in the temperature range of 340 to 360 °F. These reactions are shown below:



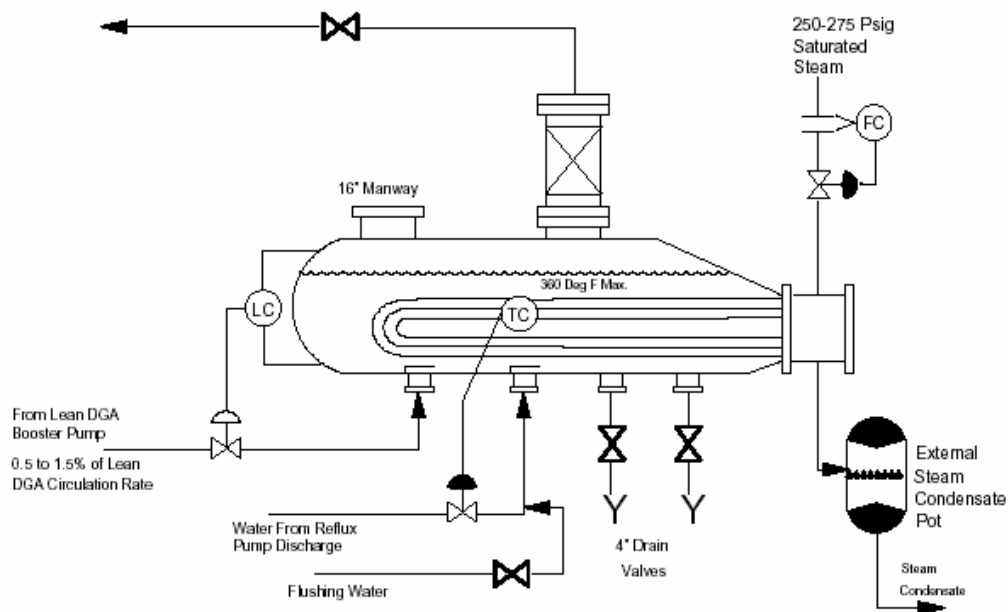


Figure 1.7 A typical process flow diagram of a DGA® Agent reclaimer [Huntsman web site]

The rate of conversion of BHEEU to DGA increases by increasing the reclaiming temperatures. Below temperatures of 340 °F the reaction of BHEEU to DGA is slow and at temperatures of 360 to 380 °F the reaction increases to acceptable rates.

In order to conserve energy, the hot lean DGA from the stripper reboiler is generally used as feed to the reclaimer. The reclaimer is filled with the hot lean amine solution until the heating tubes are fully immersed. A liquid level controller is used to maintain the liquid level above the heating tubes. A 250 psig saturated steam is used to bring up the kettle temperature to the operating temperature. Most of the overhead vapor initially at the start of each cycle will be water. As the cycle progresses, the amine will become more concentrated in the reclaimer bottoms and the amine concentration of the overhead stream will increase. As the solution becomes more concentrated in DGA, the temperature of the liquid in the reclaimer

will increase. Fresh make up feed are added via the level controller to maintain the liquid level above the heating tubes in the kettle.

The amine concentration will increase until the vapor composition approximately equals the composition of the circulation solution. The flow to the reclaimer is set when equilibrium is reached. This flow is controlled by the heat flux flowing to the tube bundle. In this case, the reclaimer can be operated with little attendance, except for temperature check up on occasional times. In order to maintain the same level of regeneration in the stripping still, it may be necessary to reduce the heat input to the reboiler. A small packed column is used for removal of any entrained liquids in the flashed vapors. The reclaimer overhead stream is returned to the bottom of the regenerator column to recover the heat from the reclaiming operation. Solids, sludge, heat stable salts, decomposition and degradation products accumulate in the reclaimer bottoms until the end of the reclaimer cycle, after that they are dumped. The length of the reclaimer cycle depends on the degree of solution contamination. Normal reclaiming cycles can vary from a few weeks to as long as three months or more. Samples of lean solution and the reclaimer liquid are analyzed periodically for contaminants. The BHEEU level in the lean amine solution should be kept at less than 3-5 percent. Increases in contaminant level vary from plant to plant; therefore, a history of reclaiming operations should be maintained. [Huntsman web site]

1.6 Saudi Aramco Experience with DGA Units

The largest gas plants which utilize DGA are located in Saudi Arabia. The choice of DGA as the sweetening agent for the Saudi gas plants was based on the following major criteria (Harruff, 1992):

- Removal of H₂S to pipeline specifications, <10 ppmwt.
- Removal of CO₂ to <300 ppmwt to facilitate ethane recovery.
- Be able to meet these specifications economically while operating with contactor pressures as low as 120-180 psig and inlet temperatures as high as 120-140°F.
- Be able to operate using air coolers alone with ambient temperatures as high as 126°F.
- Produce an acid gas stream capable of being used to make bright sulfur in downstream Claus units.

Over the first few years of operation, two plants noted that the lean amine concentration of morpholine (MOR) was rising. One study (Harruff, 1992) showed that BHEEU can thermally degrade into MOR in the reclaimer. There is no information in the open literature about the sweetening power of DGA/MOR blends. No off gas specifications have been observed; however, it is not known what the effect of MOR is on the plant performance. In order to establish the performance of the DGA treating process in the presence of MOR, thorough knowledge is required on the thermodynamics and kinetics of the reaction of CO₂ in DGA, MOR and DGA/MOR solutions. Therefore the objectives of the second part of the dissertation are organized as follows;

- Chapter 4 addresses the issues of MOR, DGA and MOR/DGA blend thermodynamics. Solubility data from the wetted wall column are combined with NMR data, physical solubility data and the electrolyte

NRTL model to predict the speciation of these solutions, the solvent working capacity, heat of reaction and solvent volatility.

- In Chapter 5, the aqueous DGA system is studied in a wetted wall column from 298K to 333K at loading from 0 to 0.4. Three models were used to model the absorption data; the rigorous mass transfer model developed by Bishnoi (2000), based on the eddy diffusivity theory, the pseudo first order (PFO) and interface pseudo first order (IPFO) approximations. The effect of ionic strength on the second order rate constant was also studied.
- In chapter 6, the kinetics of MOR are studied in a wetted wall column and found to be faster than DGA. The difference is attributed to MOR's cyclic nature. The behavior of rate enhancement for MOR/DGA blend is also shown. The rigorous model is shown to match absorption data from the wetted wall column. The model is also used to show what the important phenomena are at different operating conditions.
- Conclusions and recommendations are presented in Chapter 7.

Chapter 2: The Effects of Aliphatic and Aromatic Component Conditioning on the Permeation Behavior of Hollow Fiber Asymmetric Membranes

Membranes are used to separate a wide variety of gases, and separation of CO₂ from natural gas is one of the most important emerging applications of this technology. Most membrane-based gas separations are accomplished with asymmetric hollow fiber or spiral-wound modules, which provide a large amount of separation area per unit volume. Asymmetric fibers are comprised of a thin (500- 2000 Å) separating skin layer, which is supported on a second porous layer that is usually 50-200 µm thick. Ideally, the porous support has no effect on the permeation properties of the membrane (Spillman and Cooley, 1989; Kesting and Fritzsche, 1993; Porter, 1990; Ho and Sirkar, 1992; Paul and Yampol'skiy, 1994).

Natural gas streams contain numerous heavy hydrocarbons. A topic of concern in designing a reliable membrane system for natural gas purification involves the impact of such heavy hydrocarbon on the membranes. Very heavy hydrocarbon contamination is believed to be the cause of most membrane failures and loss in performance even at low mass fractions. Because of this, it is very important to carefully consider the required pretreatment requirements for membrane systems. The impact of these hydrocarbons on the membrane system has remained poorly understood due to the complexity of the components present and the difficulty in characterizing their effects experimentally. This chapter aims to understand the effect of heavy hydrocarbons on the performance of such membranes. Previous work on membrane formation has led to successful formation and modeling of reliable membrane structures for CO₂ removal for natural gas feeds (Clausi and Koros, 2000; Clausi, 1989; Thundiyil, 1998); however, the tests performed in the laboratory on these membranes were

contaminant-free. In actual field tests, membranes often exhibit poorer performance. Cellulose acetate membranes tend to show relatively low intrinsic CO₂/CH₄ selectivity, but have fair-to-good tolerance (with no loss in flux or CO₂/CH₄ selectivity) for contaminants such as benzene, toluene, and xylene in natural gas streams (Schell et al., 1989; Lee et al., 1988). On the other hand, for glassy polymeric membranes with intrinsically high selectivities, one study cites harsh performance decline in the range of 50% reduction in CO₂/CH₄ selectivity for polyimide films due to saturated concentrations of toluene or hexane in mixed gas feeds of CO₂/CH₄ (White et al., 1995). For a state-of-the-art polyimide asymmetric hollow fiber, one study (Gunaidi, 2000) showed serious losses in performance when the selective layer had a pronounced fused nodular nature, as compared to a truly integral dense skin. Nodule-like structures with sizes ranging from 300-1000 Å in diameter are often observed in conventional asymmetric membranes. These skin layers can be treated to fuse and plug defects in the nodular regime into an effectively defect free layer that is effective for gas separation in the absence of aggressive hydrocarbons such as considered here. More work is needed to understand the key factors that undermine the gas separation ability of membranes in such applications. The presence of hydrocarbons in the field, even in trace quantities, appears to be the culprit. Therefore, understanding the effect of heavy hydrocarbons is necessary for the development of more robust membranes for this application, and this study considers an intrinsically defect free skin that does not need defect-plugging treatment. Moreover, this study is the first of its kind to consider the effects of conditioning on defect-free asymmetric membranes.

2.1 Experimental Methods

The performance of a membrane is mainly characterized by the selectivity and permeability, or permeance. The permeance, P/l , is simply the pressure

normalized flux and is the preferred productivity measure for asymmetric membranes where the actual thickness of the selective skin layer is not clearly measurable. Using these parameters, the membrane-based natural gas purification process can be examined, based on determination of CO₂/CH₄ selectivity and permeances.

In order to understand the effect of the hydrocarbon's presence, one should compare the selectivity and permeances of the membranes from the same module. Testing with the same module minimizes the processing variability that could occur between modules. In addition, each fabricated module was only used at one state (one temperature and one hydrocarbon content) to avoid any hysteresis effect. Therefore, the experiments were completed by testing with two different sources of gases. The first source is a 10% CO₂/90% CH₄ tank without any hydrocarbons content. The second source has the same mixture of natural gas content, but with some hydrocarbons added as specified. Replicate runs were done by preparing multiple modules (usually 2) from each fiber state. See Appendix C.

For each module, the binary gas feed was used to determine the base case of the permeances and selectivities of the membrane fibers. Then, the same module was subjected to conditioning with ternary feeds. The module was tested again with the binary gas that did not contain any hydrocarbons. The results of these experiments were then compared to understand the effect of hydrocarbons. For the permeation tests, the variables for the experiments are temperature, feed pressure and hydrocarbon concentration in 10% CO₂/ 90% CH₄ feed gas. The investigated operating temperatures were 35⁰C and 55⁰C. The hydrocarbon contents in the feed gas stream were 100 ppm and 300 ppm for toluene and 300 ppm and 500 ppm for n-heptane. These numbers simulate the concentration at a typical natural gas field.

2.1.1 Materials

2.1.1.1 Polymer

Polyimides have been identified as materials with high selectivities and permeabilities for CO₂/CH₄ separation (Matsumoto and Xu, 1993; Kim et al., 1988; Kim et al., 1989; Tanaka et al., 1989; Stern et al., 1989; Coleman and Koros, 1990). In addition to high selectivities, polyimides possess high glass transition temperatures (T_g > 200⁰C). A polyimide that is available in the market is Matrimid® 5218. Its permeation properties, combined with its processability (i.e., solubility in common solvents) make it an attractive candidate for gas separation applications. Furthermore, its mechanical strength and high glass transition temperature, better suit it for more rigorous working environments than other noncellulosics such as polysulfone. Figure 2.1 shows the unit structure of this polyimide.

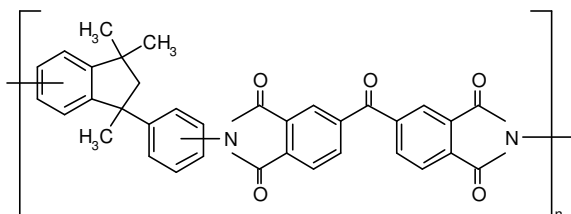


Figure 2.1 Repeat unit of Matrimid® 5218 polyimide.

The density of Matrimid® is 1.2 g/cm³. The polymer sample has a T_g at 305⁰C under differential scanning calorimetry (DSC-7, Perkin-Elmer) with a scan rate of 20⁰C/min. Various gas permeabilities of this polymer at 25⁰C are presented in Table 2.1.

Table 2.1 Reported gas permeabilites of Matrimid® at 25⁰C (Clausi and Koros, 2000; Clausi, 1998)

Polymer	P O ₂ (Barrer)*	P N ₂ (Barrer)*	P He (Barrer)*
Matrimid®5218	1.32	0.183	22.5

$$*1 \text{ Barrer} = 10^{-10} \left[\frac{cc(STP)cm}{cm^2 \text{ sec cmHg}} \right]$$

In the present study, these polymers are fabricated into asymmetric hollow fibers. The fibers were graciously provided by Dr. Seth Carruthers, Dr. David Wallace and Shabbir Husain. These hollow fiber membranes were produced in the laboratory using the phase-inversion method (Clausi and Koros, 2000; Clausi, 1998). Asymmetric membranes formed by this phase inversion techniques are generally said to be integrally skinned, since the porous substructure and skin layers are made from the same polymer in a single process. This particular process creates asymmetric membranes with a combination of adequate gas flux and excellent mechanical strength and essentially defect-free selective layers. Since the skin was formed in a defect-free condition, no post treatment was applied to these fibers. For this study, the fiber has an inner diameter (ID) of 100 μm and outer diameter (OD) of 250 μm. Figure 2.2 shows the scanning electron micrograph (SEM) of a fiber cross-section area.

2.1.1.2 Permeants

The mixed gas used were certified mixtures of 10% CO₂/ 90%CH₄, 10% CO₂/ 90%CH₄ + 100 ppm toluene, 10% CO₂/ 90%CH₄ + 300 ppm toluene, 10% CO₂/ 90%CH₄ + 300 ppm n-heptane and 10% CO₂/ 90%CH₄ + 500 ppm n-heptane. Gases were custom ordered through Air Liquide, Houston, TX.

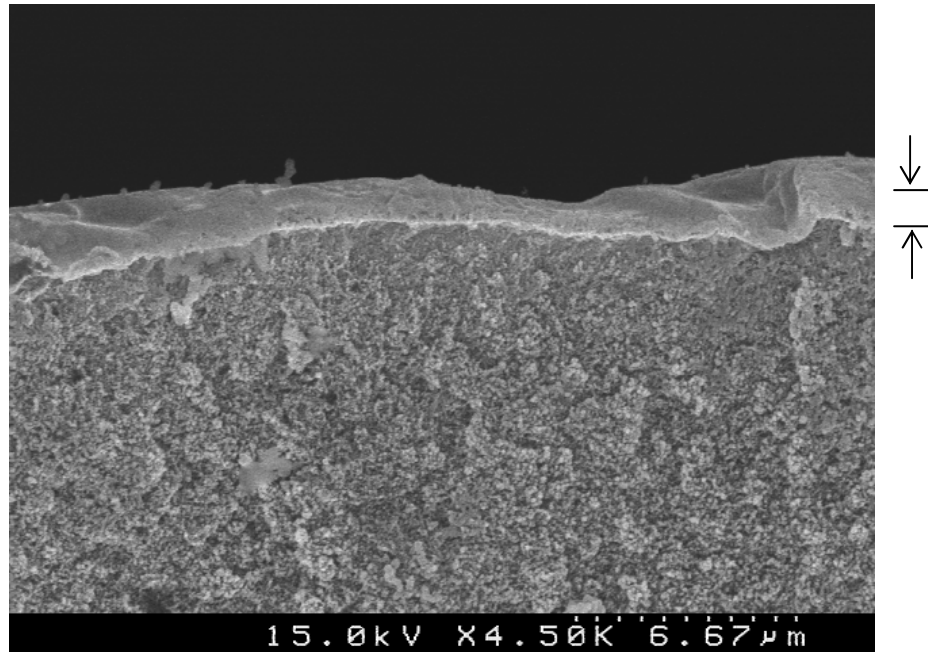


Figure 2.2 Scanning Electron Micrograph of cross section of a Matrimid® asymmetric hollow fiber showing selective skin and porous support. The skin layer is shown in partially oblique view to illustrate its thin continuous nature (Gunaidi, 2000).

2.1.2 Module Housing

The module housing is constructed of brass and 316 stainless steel (316 SS) Swagelok® and NPT fittings: two Swagelok® ¼” union tees (316 SS), one ¼” port connector (316 SS), two adapters for ¼” NPT female to ¼” union tees (brass), two adapters for ¼” NPT male to ¼” tubing (brass). Figure 2.3 shows the schematic diagram of the module housing. The selection of the housing material was based on cost and reusability.

To hold the fibers on the both ends at the NPT fittings, Stycast® 2651 epoxy resin was mixed with Catalyst 9 (Emerson & Cuming). Before the Stycast® was applied into the fitting, a PTFE tape is placed in between the fiber and the wall of the housing. The purpose of the PTFE tape was to prevent the epoxy from

dripping into the permeation area. Stycast® has good properties for this module housing because its high-pressure resistance ability and its appropriate viscosity for flowing into the fibers interspace. The resulting module has an active length for permeation of approximately 10.5 cm. In the experiment, usually 10 fibers are potted in a module to produce an active permeation area of 8.2 cm² per module. The module is designed to have a double-ended permeate flow. This design was to minimize the pressure drop effect that may occur in the permeate side (Thundyil et al., 1983). Shell side feeding is configured in the system to simulate the typical practice in the natural gas field.

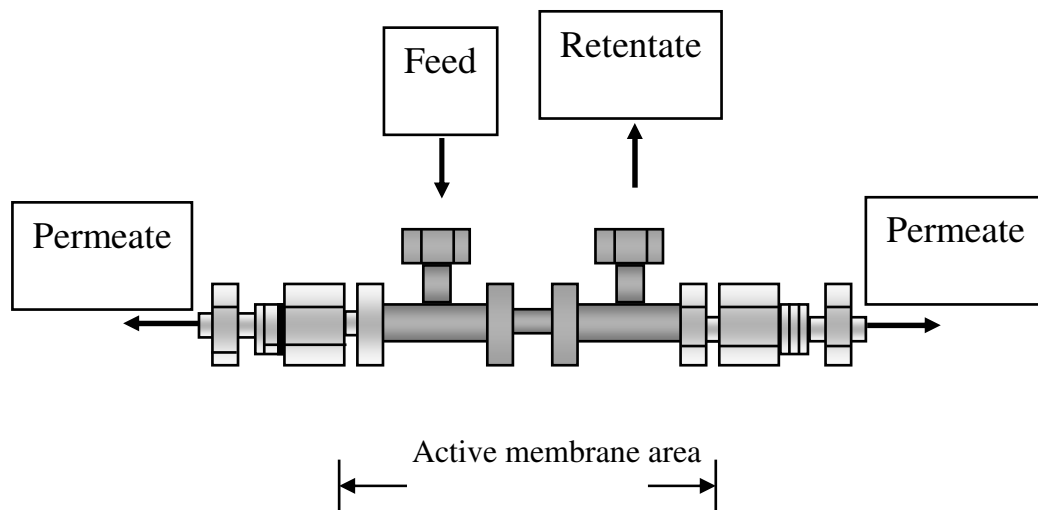


Figure 2.3 Shell-side feeding with the module construction.

2.1.3 Pure Gas Permeation

The skin integrity of the hollow fibers was confirmed by permeating oxygen, nitrogen and helium gases before testing with the natural gas components. The permeation technique utilized a bubble flow meter to measure the flux of the permeate. The equipment is shown schematically in Figure 2.4.

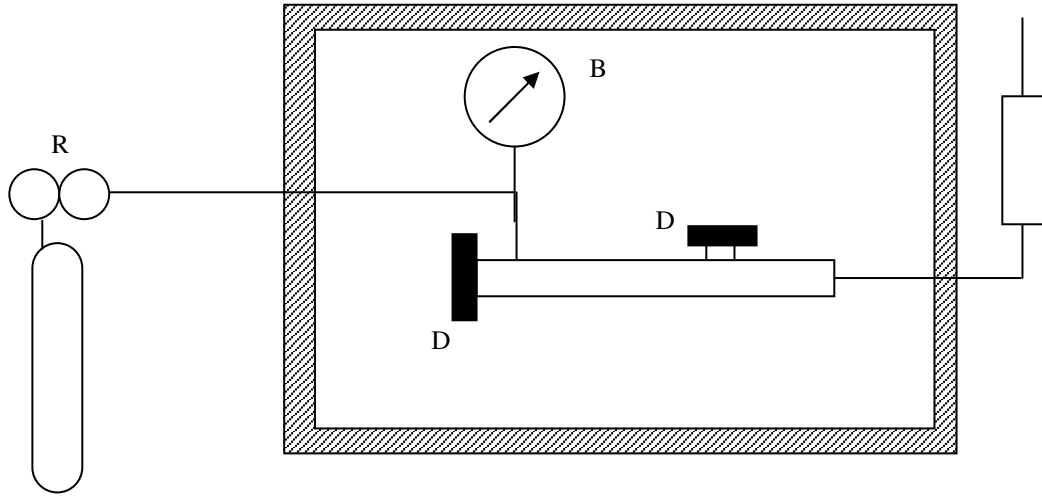


Figure 2.4 Schematic diagram of pure gas permeation testing

For pure gas permeation testing, the retentate flow and one of the permeate side is capped. The flux of the gas is then measured at other end of the permeate side by connecting it to a bubble flow meter. The permeance, P/l , for the pure gas component is then calculated by

$$\frac{P}{l} = \frac{5.28 \times 10^7 V}{(T)(A)(p_f - p_{atm})} \quad (2.1)$$

where:

P/l = Permeance [=] GPU

V = Permeate flow rate [=] cc(STP)/sec

T = Temperature [=] K

A = Membrane area [=] cm^2

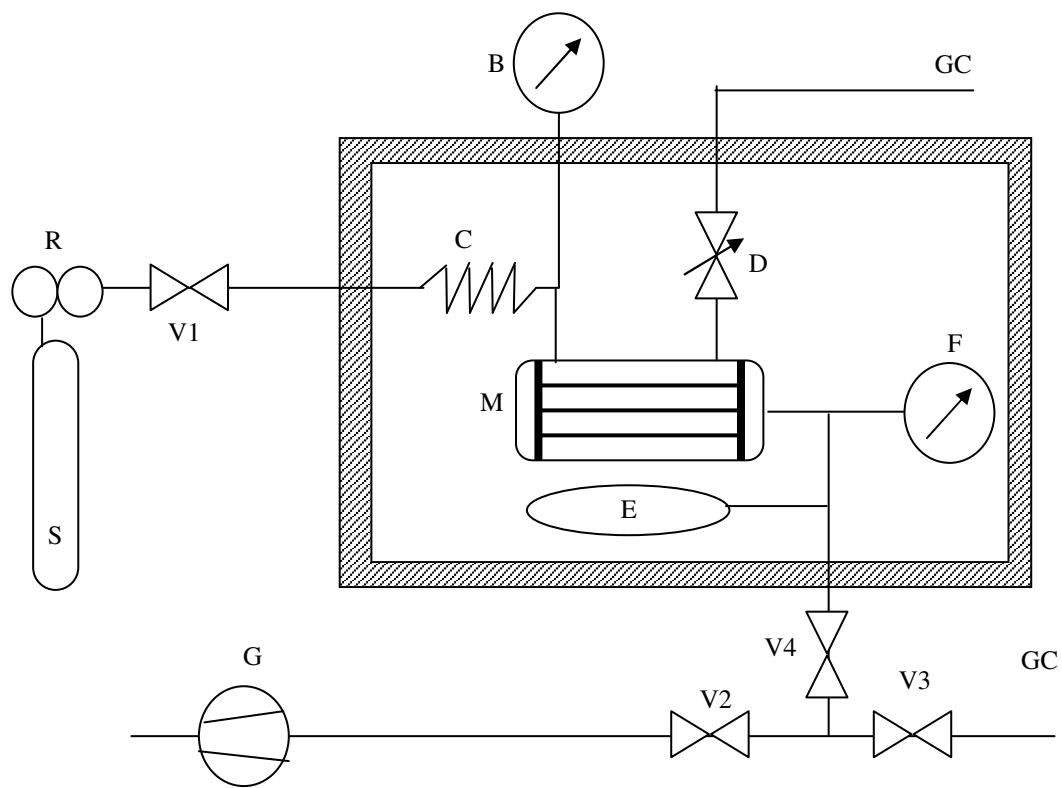
p_f = Feed pressure [=] psia

p_{atm} = Atmospheric pressure [=] psi

2.1.4 Mixed Gas Permeation

The permeability of hollow fibers was measured under vacuum permeate conditions. Figure 2.5 shows the schematic diagram of the permeation apparatus. The system is stationed in a temperature-controlled water bath using a circulating water bath (Model W2 water bath, and Model E3 circulator, Haake Buchler Instrument Inc., Saddle Brook, NJ). The feed pressure is measured using an Ashcroft® pressure gauge, which has 0 to 1000 psig pressure range (± 0.2 psi). A coiled stainless steel tubing of three meters was placed after the entrance in the water bath to ensure that thermal equilibration was reached. The system uses stainless steel tubing of 1/4" and 1/8" diameter with Swagelok® fittings and was also rated for 1500 psia pressure. The downstream volume was measured using volume expansion method and was determined to be 1029 cm³ (Gunaidi, 2000). A two stage mechanical vacuum pump (Model E2M2, Edwards Vacuum, Crawley, Sussex, England) was used to maintain vacuum (<0.01 mmHg) on the downstream side.

To ensure that the composition in the feed stream did not vary along the length, a stage cut (ratio of permeation rate to the retentate) of 1% was maintained. A Whitey® (SS-31EF4) screwed bonnet needle valve was used to regulate the retentate flow rate. In order to determine the permeability and selectivity of permeants in mixed gas permeation, it was necessary to measure the composition of at least two streams from the feed, residue and permeate streams. The composition measurements were accomplished by the installed gas chromatograph (Model 5880A, Hewlett Packard, Atlanta, GA).



- A: Supply Gas Cylinder
- F: Pressure Transducer
- B: Pressure Gauge G: Vacuum Pump
- C: Coiled Tubing V1-4: Valves
- D: Metering Valve M: Membrane
- E: Permeate Ballast Volume R: Pressure Regulator
- S: Gas Supply

Figure 2.5 Schematic of gas permeation apparatus for hollow fiber modules

The selectivity is determined from the compositions of feed and permeate streams

$$\alpha_{A/B} = \left(\frac{y_A}{y_B} \right) \left(\frac{x_B}{x_A} \right) \quad (2.2)$$

where y and x denote the mole fractions of components A and B in the permeate side and feed side, respectively. With mixed gas feeds, permeances were typically calculated using the component fluxes and the partial pressure (or fugacity) driving force

$$P_a = \frac{(2.94 \times 10^4)(V)(\ell) \left(\frac{dp_p}{dt} \right) y_a}{(T)(A) p_f x_a} \quad (2.3)$$

where

$$P_a = \text{Permeability} \quad [=] 1 \text{ Barrer} = 1 \times 10^{-10} \frac{\text{cc}(STP)\text{cm}}{\text{cm}^2 \text{sec cmHg}}$$

$$dp/dt = \text{rate of permeate rise} \quad [=] \text{ torr/min}$$

$$\ell = \text{Film thickness} \quad [=] \text{ mils}$$

$$T = \text{Temperature} \quad [=] \text{ Kelvin}$$

$$A = \text{Membrane surface area} \quad [=] \text{ cm}^2$$

$$p_f = \text{Feed pressure} \quad [=] \text{ cmHg}$$

$$y_a = \text{Feed composition of component a}$$

$$x_a = \text{Permeate composition of component a}$$

$$V = \text{Downstream volume} \quad [=] 1029 \text{ cm}^3$$

Thundyil (1998) developed recently a rigorous mathematical model which takes into account variation in compositions in the shell and the tube sides. He approximated the pressure drop in the tube-side by the expression:

$$\frac{d(p_T^2)}{dz} = \frac{25.6RT\mu}{\pi d_i^4} \frac{Q_T}{22400} \quad (2.4)$$

where p_i is the pressure in the tube-side, R is the ideal gas constant (8.3145 J·mol⁻¹·K⁻¹), T is absolute temperature (in K), μ is viscosity (in μP), d_i is the inner diameter of the membrane fiber, and Q_T is the flow rate in the tube-side (in cm³ (STP)/s). To calculate the permeance of each component, a finite element analysis was performed on a spreadsheet, where each discrete axial element along the fiber had a separate pressure driving force and flow rate. From Equation (2.4), the pressure drop for element j along the single fiber was calculated by

$$p_T(j) = \sqrt{p_T^2(j-1) - \frac{25.6RTQ_T(j)}{22400\pi d_i^4} \Delta z} \quad (2.5)$$

where Δz is the differential length of each element. Since the exit permeate pressure was known, an iterative technique (e.g., Solver in Excel[®]) was used to determine the permeate pressure profile by varying the midpoint axial permeate pressure until the calculated exit permeate pressure agrees with the measured exit permeate pressure within the specified error tolerance (<0.01%). The permeances were also iterated and were used to calculate the flow rate of each element and the resulting permeate pressure for each element using Equation (2.5) above. Additionally, the component permeances were related by the known permselectivity from the gas chromatography analysis. Both the component permeances and midpoint permeate pressure were simultaneously iterated and used to calculate the flow rates and permeate pressures until convergence. The component viscosities were estimated by the Lucas correlation, and the mixture viscosity was estimated by the Wilke method. Further details on the full mathematical model are described by Thundiyil (1998). The Excel[®] spreadsheet and iterative technique used to calculate the component permeances of our

membrane fibers were adapted from this model. Calculation of component permeances with this model differed slightly ($< 4\%$) from calculations using a simple mean Δp_i in Equation (2.3).

2.1.5 Testing Procedure

Before measurements were made, the module was placed under vacuum condition over night. The temperature of the circulating water bath is also adjusted to the desired setpoint. In this work, there are two sets of experiments depending on the conditioning pressure. The two sets are the **200 psia** conditioning pressure series and the **600 psia** conditioning pressure series. Conditioning pressure is defined as the pressure at which the membrane module is kept at by flowing a gas mixture for an extended period of time. **In this work, the conditioning time in most cases is at least five days.** The tests were then performed by starting the feed pressure at ~ 100 psia for the 200 psia conditioning pressure series and at ~ 200 psia for the 600 psia conditioning pressure series followed by, measuring the permeate pressure rise. To reduce the small variation in data among samples to a corresponding nondimensional form, plots of $P_{\text{CO}_2}/P_{\text{CO}_2}^{\text{ref}}$ against pressure or time were used. The permeances at ~ 100 psia and at ~ 200 psia for CO_2 before exposure for the 200 psia conditioning pressure series and for the 600 psia conditioning pressure series respectively were used as reference values for normalization.

Steady state was achieved in less than ten minutes for the thin selective layers. Once steady-state conditions were demonstrated, the vacuum pump valve (V2) was closed. This condition was verified by constancy of permeate flow rate and constancy of permeate composition for mixed gas feeds. The pressure increase in time, dp/dt , was then recorded by a SolTec® chart recorder. The fact that the short period of time is needed to reach steady state is due to the extremely thin thickness of the skin. In this work, the GC sampling and the dp/dt measurements were taken 30 minutes to one hour after the steady state has been verified. After

the permeate pressure has risen to 50 torr, the permeate gas is sampled into the gas chromatograph. From the gas composition and the pressure increase in time, dp/dt , the permeability and selectivity can be calculated. Two to three measurements were taken for the gas composition and the dp/dt and the average value is reported on here. Following the injection, the permeate volume is then pulled to vacuum, while the feed pressure is increased to 150 psia, and 200 psia for the 200 psia conditioning series and to 400 psia, and 600 psia for the 600 psia conditioning series. The above steps for permeability and selectivity measurements were then repeated at each designated feed pressure. This procedure of increasing the pressure from 100 to 200 psia for the 200 psia conditioning series and from 200 to 600 psia for the 600 psia conditioning series is termed ‘Pressurization’. It should be remembered that the measurements of permeances of CO_2 and CH_4 and selectivity is performed with the 10/90 CO_2/CH_4 binary gas mixture; therefore, the pressurization step is termed also as ‘Before exposure’ (meaning before exposure to the contaminant containing feed).

At the conditioning pressure, 200 psia for the 200 psia conditioning pressure series and 600 psia for the 600 psia conditioning pressure series, the 10/90 CO_2/CH_4 gas mixture was exchanged with the 10/90 CO_2/CH_4 in the presence of the hydrocarbon impurity as specified. This exchange and the subsequent exposure are termed ‘conditioning’ or ‘During exposure’ in this study. Clearly, a base case of ‘conditioning’ corresponds to exposure of the fibers to only the binary mixture. The module was then subjected to conditioning for *five days* period at the conditioning feed condition. During the conditioning period, also termed as ‘during exposure’ as noted earlier, the permeability and selectivity were measured as described above. After that, the ternary mixture was exchanged with the 10/90 CO_2/CH_4 and the permeability and selectivity were measured as described above to probe the effects caused by the heavy hydrocarbons. Feed pressures with 50 psia decreasing feed pressure decrements for the 200 psia

conditioning pressure series and with 200 psia decreasing feed pressure decrements for the 600 psia conditioning pressure series were then measured with the same method using the 10/90 CO₂/CH₄ binary mixture. Again, the CO₂ permeance and gas composition measurements were taken 30 minutes to one hour after the steady state has been achieved. This was done because we wanted to probe the “after effects” of conditioning and not to monitor any slow further collapse of the membrane in the presence of the 10/90 CO₂/CH₄ feed. This procedure of pressure decreasing is termed “Depressurization” or “After exposure”. These sets of experiments compare the pressure-permeability before exposure to that after exposure without evacuation of the membrane, thereby providing insight into the effects caused by the heavy hydrocarbons during exposure.

2.2 Four Potential Deterioration Factors

There are at least four possible non-ideal effects that the presence of hydrocarbons may cause in the selective skin layer of membrane used in natural gas purification processes. The four effects are: (i) competition, (ii) plasticization, (iii) conditioning and (iv) compaction.

2.2.1 Competition Effect

The term “competition” effect will be used in this study to mean a specific response caused by the presence of a penetrant, that inhibits the transport of the other components. The dual mode sorption theory suggests the competition effect should be most apparent for highly condensable feed components, like toluene (Chern et al., 1999). If this effect is present and *depresses* the CO₂/CH₄ selectivity, the selectivity should return to the original value upon removal of the preferentially sorbing penetrant. Figure 2.6 illustrates a cartoon representation of the competition effect in the presence of a strongly competitive (highly sorbing)

component like toluene. In this connection, the term “strong competitor” is taken to mean components whose critical temperature, T_c , is greater than the measurement temperature.

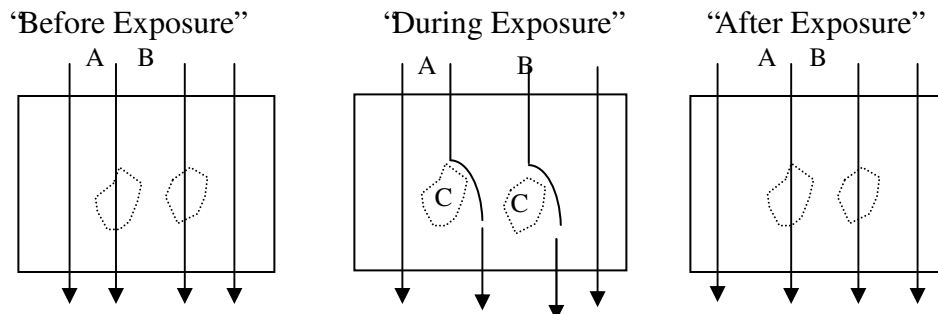


Figure 2.6 Depiction of competition effect caused by a third component, C, in a membrane system. The symbols  depict unrelaxed volume elements accessible to both components A and B in the glassy polymer in the absence of a strongly condensable (e.g. toluene or n-heptane) component. During exposure to such ‘C’ components, sorption and transport (i.e. permeation) pathways are precluded to A and B, thereby reducing their ternary gas permeation in comparison to binary feeds.

2.2.2 Plasticization

“Plasticization” is said to occur when the presence of a given component in a polymer matrix causes the diffusion, and hence permeation, of other components to *increase* compared to the case without that component present due to a swelling-induced facilitation of a local segmental motion.

A strongly sorbing component such as CO_2 or toluene can cause plasticization even in the absence of other penetrants. Plasticization is apparent as non-constant, upwardly inflecting permeability or permeance as a function of CO_2 or toluene feed pressure (Jordan and Koros, 1990; Jordan et al., 1990). The highly sorbing nature of toluene in aromatic polyimides was also expected to make it a potential plasticizing agent that would tend to increase the permeability or

permeance of both CO_2 and CH_4 . Since CH_4 is a larger molecule, facilitation of local segmental motions may promote its diffusion even more than it might assist the compact CO_2 ; however, the effect has not been well documented. Figure 2.7 depicts the plasticization effect. Fortunately, as will be documented in the results section, no evidence for strong plasticization by either CO_2 or toluene was seen over the range of conditions studied so far.

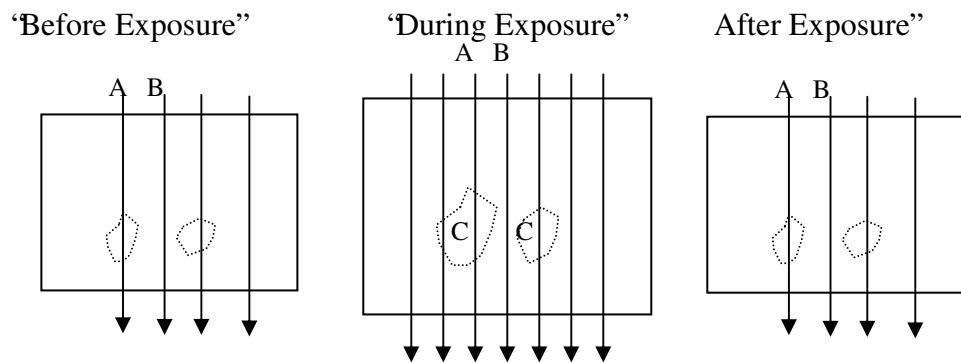


Figure 2.7 The effect of plasticizing: increase in the permeances of penetrants. In this case, besides any “competition” effects, additional swelling induced permeation pathways are made available to other components. The symbols  depict unrelaxed volume elements accessible to both components A and B in the glassy polymer in the absence of a strongly condensable (e.g. toluene or n-heptane) component. The additional arrows shown in the “during exposure” case illustrates the hypothetically possible higher flux of both A and B during plasticization.

2.2.3 Swelling Induced Conditioning History Effect

Since glassy polymers are known to be nonequilibrium materials, the manner in which the samples have been treated can affect their sorption and transport properties. Previous studies have shown that exposure to a highly sorbing gas like CO_2 at high pressures will cause an increase in sorption and dilation levels as compared to levels in an as-received or unconditioned sample (Jordan et al., 1990; Jordan and Koros, 1990). This phenomena has been explained in part by

attributing the increase in subsequent sorption and dilation levels to an increased number of subtle packing disruptions in the non-equilibrium polymer matrix, which makes it energetically easier for penetrant molecules to be sorbed and to diffuse. Figure 2.8 illustrates a cartoon representation of the conditioning effect in the presence of a strongly competitive (highly sorbing) component like toluene.

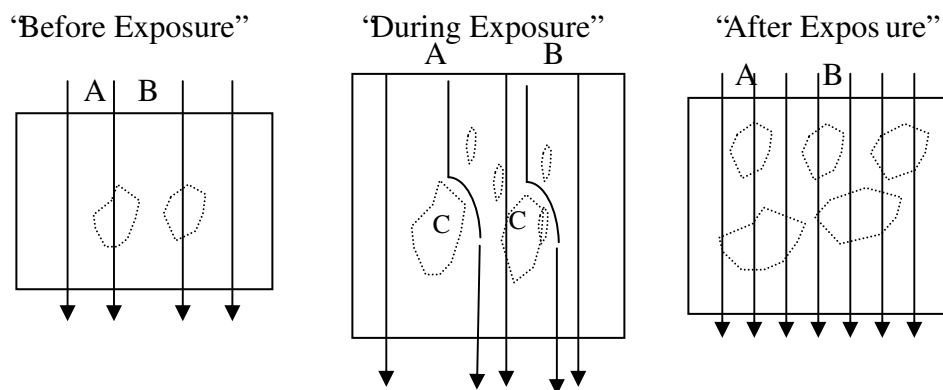


Figure 2.8 The effect of conditioning is an increase in the permeances of penetrants. In this case, besides any “competition” effects, additional swelling induced permeation pathways are made available to other components. The symbols  depict unrelaxed volume elements accessible to both components A and B in the glassy polymer. The additional arrows show in the “after exposure” case illustrates the higher flux of both A and B due to conditioning.

The swelling induced conditioning effect (SICE) is more pronounced if the secondary penetrant is introduced while the sample is still exposed to the conditioning agent, i.e. using a “gas exchange protocol. Less dramatic effects are apparent upon exposing a glassy sample to a highly sorbing penetrant at a pre-determined pressure; and then evacuating completely before exposure to the secondary penetrant since relaxation appears more facile in the absence of penetrant. Aromatic substances such as toluene are well known for their high condensability and therefore are suspected to act as potent “SICE” agents. Our

results show that, indeed, conditioning to toluene increases the transport properties of the membrane.

2.2.4 Compaction

Under catastrophic conditions, plasticized glassy structures exposed to high transmembrane pressure can have reduced moduli and undergo significant rearrangements of the super-molecular morphology leading to a denser microstructure (Gunaidi, 2000). In an asymmetric hollow-fiber membrane, which is comprised of dense and porous regions, the compaction can lead to subtle densification of the finely porous transition region between the more or less dense skin region and the highly porous support layer. This results in added mass transfer resistance to the membrane. Since this added resistance is associated with a porous medium (e.g. Knudsen selective), the effective observed overall selectivity of the combined skin, transition region and formerly “invisible” support resistance is biased to reflect greater contribution with its lower selectivity porous Knudsen properties. Such a change tends, therefore, to reduce permeance of all components but to most negatively impact the highest permeability components, thereby also reducing selectivity. Hence, the effect of compaction will be a decrease in the flux and decrease in the selectivity. Once a membrane is compacted, it is visualized as being deformed as shown schematically in Figure 2.9. A dramatic drop in modulus can accompany strong swelling and plasticization effects (Mulder, 1991; Jonsson, 1978). It is possible that the onset of strong skin plasticization may accompany modulus drop in the transition layer as well, so “catastrophic” failure and the onset of strong skin layer plasticization may occur under similar feed conditions. Fortunately, our results, shows no evidence for strong plasticization or compaction by either CO₂ or toluene as seen over the range of relatively aggressive conditions studied so far.

The asymmetric hollow fiber membranes used in this work are formed in a process known as ‘dry wet phase inversion’ which is, in essence, a solvent-nonsolvent quench (Clausi and Koros, 2000; Clausi, 1998). The resulting fibers consist of a thin selective layer over a nonselective porous support. Since membranes are formed very rapidly from solution, the dense selective layer is thought to consist of considerable excess free volume and is a highly out-of-equilibrium packing conformation. Therefore, there is a considerable driving force for densification of the selective layer of asymmetric membranes to an equilibrium packing density, which would result in a considerable loss in flux over time.

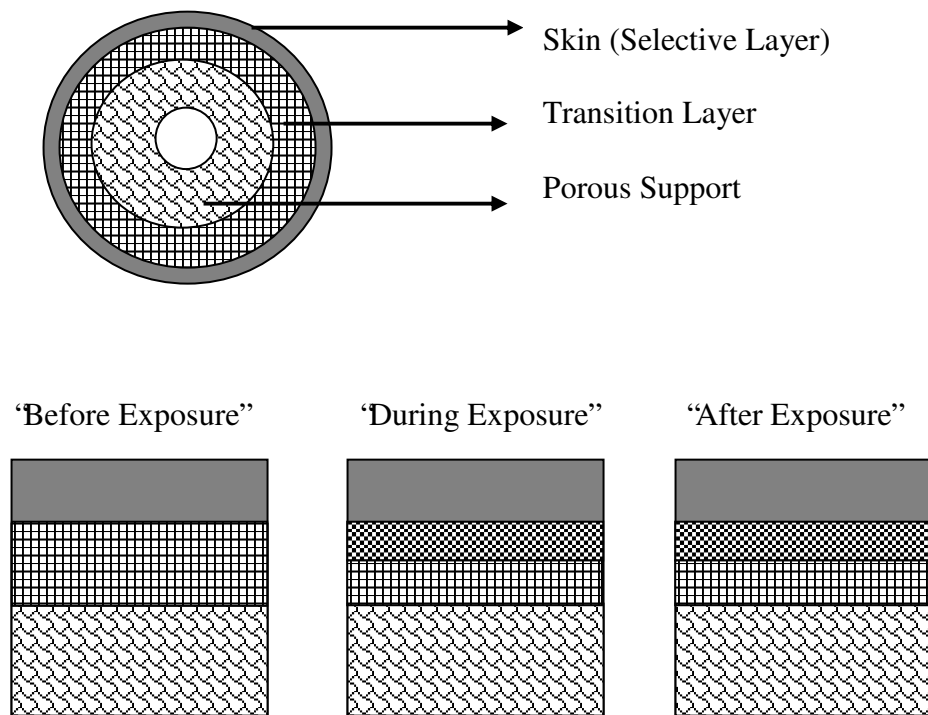


Figure 2.9 Depiction of the compaction effect.

To better understand the effect of hydrocarbon conditioning on the transport properties of membrane, the fibers were aged for two months following the formation process to avoid scatter in the results due to second-order differences in the process of aging. The permeabilities and selectivities of the O₂/N₂, He/N₂ gas pairs for the aged samples are shown in Table 2.2. There was little change in the permeabilities and permselectivities in the second two months.

Therefore, the majority of the physical aging in the unconditioned fibers occurred in the first three months following the membrane formation process. These results were expected since the majority of the volume relaxation occurs within a very short time period during physical aging (Punsalan, 2001). The reduction in permeability with time was due primarily to the densification of the polymer matrix. Punsalan (2001) studied the change in permeance of defect-free Matrimid asymmetric hollow fiber over a 42-day period of aging time. Table 2.3 shows the change in permeance over time for oxygen, nitrogen and helium.

Table 2.2 Pure gas permeation results for hollow fiber membranes used in this work at 25⁰C.

α_{O_2/N_2}	α_{He/N_2}	P/l_{O_2} (GPU)*	P/l_{N_2} (GPU)*	P/l_{He} (GPU)*
7.1	126	3.1	0.448	57

$$*1 \text{ GPU} = 10^{-6} \left[\frac{\text{cc}(STP)}{\text{cm}^2 \text{ seccmHg}} \right]$$

Table 2.3 Percent change in N₂, O₂ and He permeance in Matrimid asymmetric hollow fiber over 42 days of aging at room temperature (Punsalan, 2001).

Time, days	P/l			α	
	N ₂	O ₂	He	He/N ₂	O ₂ /N ₂
0	0.96	6.52	96.0	100	6.8
42	0.70	5.58	95.7	137	8.0

Samples were stored at room temperature in a plastic bag, to guard against complications from humidity that need to be removed prior to testing; however, this was adequate to produce a representative sample. In order to conserve gas, only ten fibers were potted in each module. The results presented below represent the average values based on two replicates.

2.3 Results and Discussion

2.3.1 Comparison of Conditioning in Hollow Fiber Membranes at 200 psia before and after Exposure

To establish a base case, the fibers were exposed to a simple binary 10/90 CO₂/CH₄ gas mixtures to show the conditioning effect of the CO₂ and CH₄ penetrants in hollow fiber membranes *in the absence of toluene or n-heptane*. The fibers were initially evacuated on the permeate side to remove any sorbed gases from the fibers. The feed pressure of the 10% CO₂/ 90% CH₄ was increased incrementally and the permeability was measured at each pressure increment. The feed was then maintained at the conditioning pressure for five days. After a five day period, the feed pressure of the conditioning mixture was reduced incrementally and the permeability measured at each pressure increment. An assumption in the measurement of conditioning effects has been that the hysteresis depends only on the maximum conditioning pressure. Therefore, the hysteresis was thought to be independent of the pathway used to reach the conditioning

pressure. Past studies have assumed that the extent of conditioning is strictly a function of the maximum exposure pressure for a specific polymer-penetrant pair (Coleman, 1990). Figure 2.10a shows the effect of conditioning of 10/90 CO₂/CH₄ at 200 psia and 35 °C on the CO₂ permeability. A “reduced” or “normalized” permeability is used to compare the relative permeability enhancements resulting from conditioning treatments in different fibers. The reduced permeability is the ratio of the permeability at each pressure to the permeability in the unconditioned sample at 110 psia. Note ($P_{CO_2/l}$) at 110 psia used for normalization corresponds to the permeance at 110 psia before exposure. This was selected as a reasonable value that showed negligible time dependence over a period of five days after reaching Fickian steady state.

As can be seen the maximum enhancement in CO₂ permeability was 3% relative to the unconditioned sample. The maximum enhancement in permeability in the conditioned sample occurred at lower pressures. The permeability of CO₂ and CH₄ decreases with pressure, which is typical of the dual mode behavior in glassy polymers. The CO₂ permeability enhancements following conditioning is probably a result of the loosening and reordering of the polymer matrix, which resulted in a slight increase in the CO₂ permeability. The selectivity of CO₂/CH₄ following 10/90 CO₂/CH₄ conditioning is shown in figure 2.10b. The selectivity of CO₂/CH₄ was slightly higher in the conditioned sample than in the unconditioned sample. However, it should be remembered that this slight increase in selectivity and CO₂ permeance is within the experimental error, and therefore the effects of conditioning at 200 psia with 10/90 CO₂/CH₄ on CO₂ and CH₄ permeances are negligible.

Typical experimental results, illustrating the effect of n-heptane in a natural gas field stream, are shown in Figure 2.11a and 2.11b. Figures 2.11a and 2.11b show the experimental results of the permeability and selectivity, respectively, of the CO₂/CH₄ separation at 35°C. Between exposure and prior to the “after

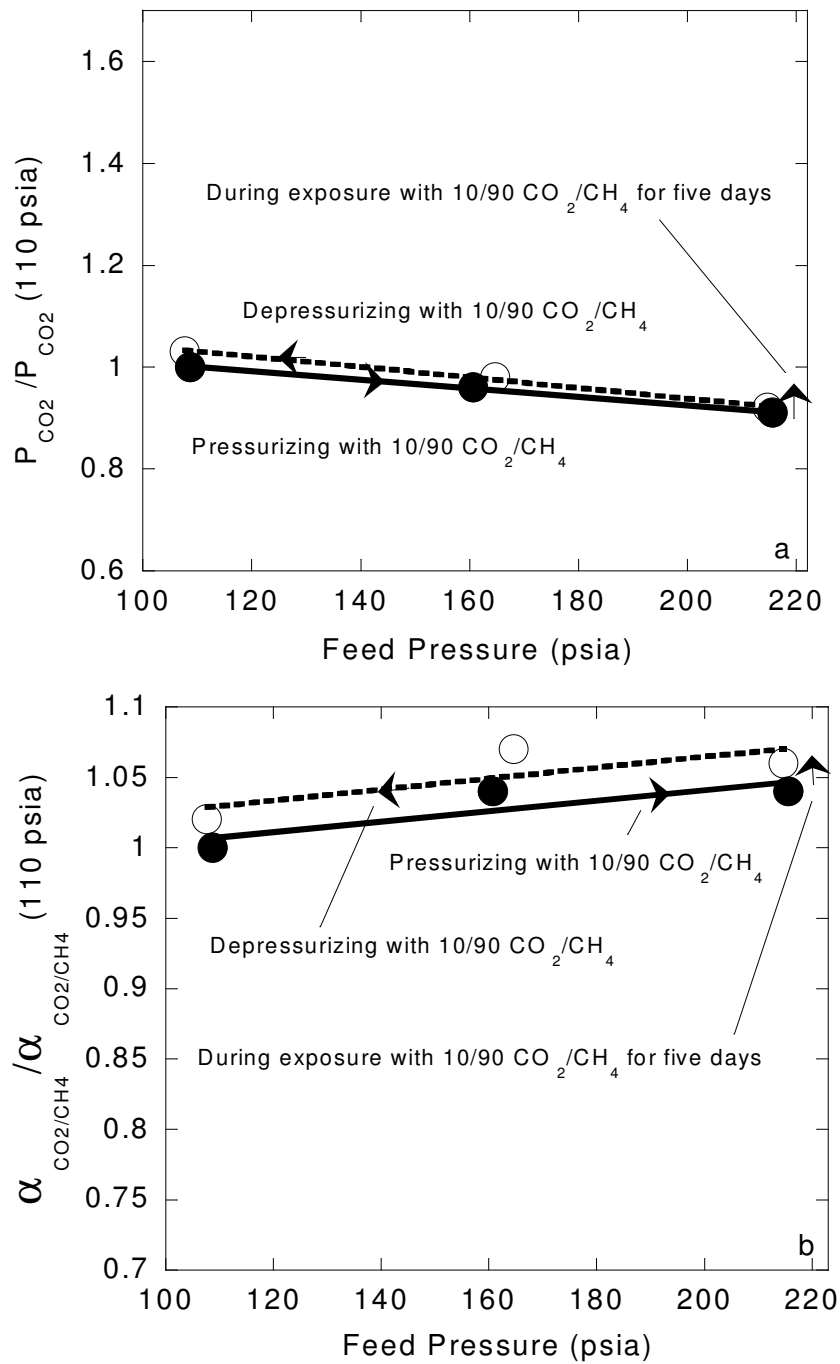


Figure 2.10 Effect of conditioning of 10/90 CO₂/CH₄ mixture on a) the CO₂ permeability, and b) the CO₂/CH₄ selectivity at ~200 psia and 35 °C. Lines are “drawn by eye”.

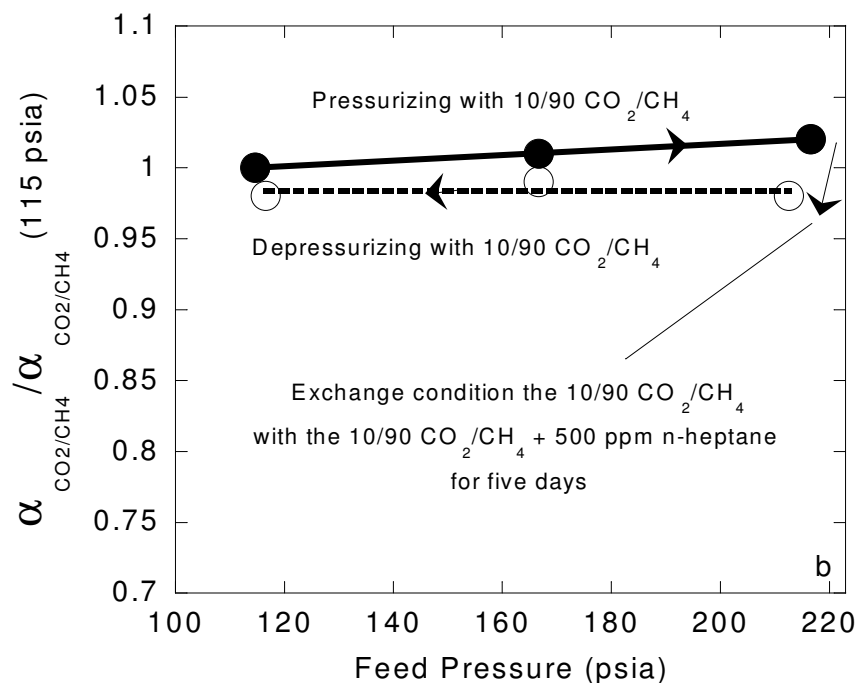
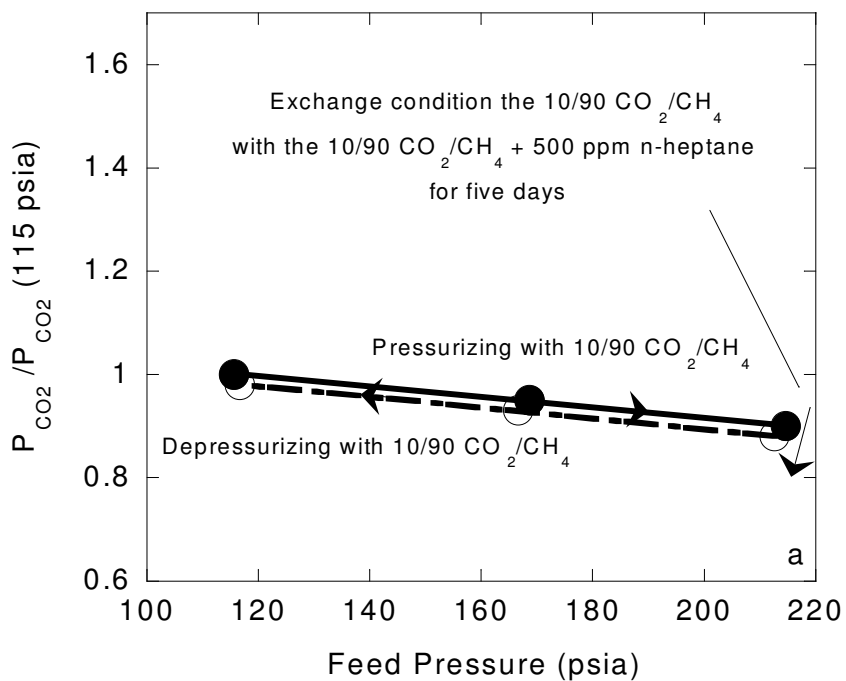


Figure 2.11 Effect of conditioning of 10/90 CO₂/CH₄ + 500 ppm n-heptane mixture on a) the CO₂ permeability, and b) the CO₂/CH₄ selectivity at 200 psia and 35 °C. Lines are “drawn by eye”.

exposure” experiments, vacuum condition was applied on the permeate side of the membrane, (two to three hours), at the constant temperature of the experiment. The procedure is a method to remove the residual hydrocarbons that may be present in the membranes as a result of the exposure testing for five days. In order to understand which of the four potential effects, see section 2.2, that the n-heptane causes, one has to look upon the permeability responses as well as the selectivity responses. Permeation studies with 500 ppm n-heptane in the 10% CO₂/ 90% CH₄ mixed gas feed indicate approximately a 2% decrease in CO₂ permeances with 2-3% loss in CO₂/CH₄ selectivity. After the n-heptane exposure, at 200 psia, the permeation behavior returned essentially to its original pattern. This recovery indicated that, the effect of n-heptane does not cause competition or major compaction or free volume plasticization induced facilitation of CH₄ versus CO₂ permeation. The small conditioning responses at 200 psia with the 300 ppm n-heptane were also similar to those with the 500 ppm n-heptane. Both the 300 ppm and the 500 ppm feed gas mixtures showed negligible conditioning effects at 200 psia.

In comparison to the n-heptane, one can see that the primary effect of exposure to toluene, is one of conditioning, (see section 2.2.3), since the permeance of CO₂ *exceeds* the permeance before exposure as can be seen in figure 2.12a. Clearly, there is difference in the conditioning ability of the aromatic versus the aliphatic component. Toluene conditioning increased the permeability of both the CO₂ and CH₄ in the polymer. Moreover, toluene conditioning resulted in a decrease in the permselectivity of CO₂/CH₄ as shown in Figure 2.12b. This decrease in permselectivity was due presumably to a decrease in diffusivity selectivity caused by a loosening of the polymer matrix. The conditioning induced increase in permeability was a result of an increase in diffusivity caused by a

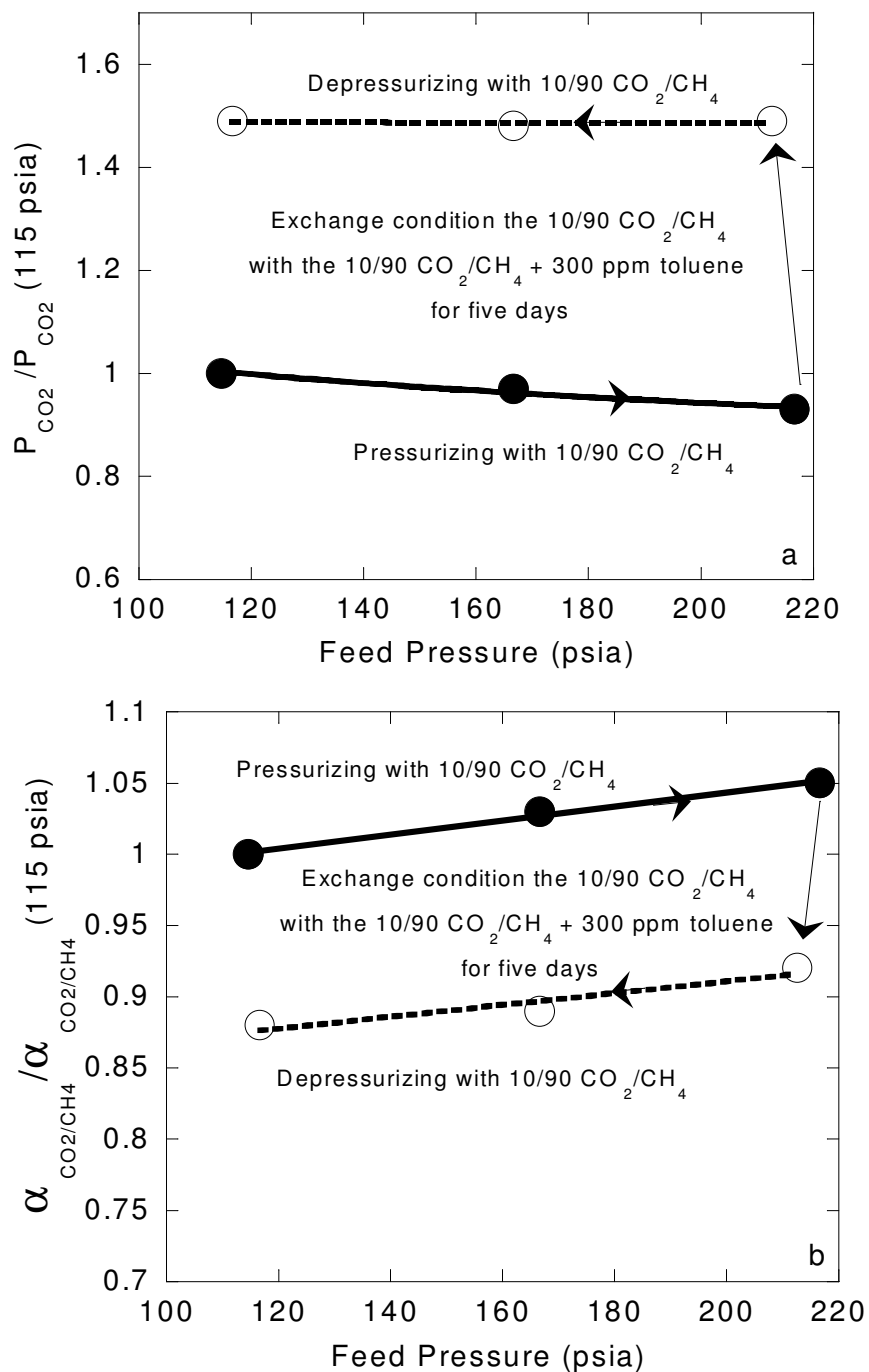


Figure 2.12 Effect of conditioning of 10/90 CO₂/CH₄ + 300 ppm toluene mixture on a) the CO₂ permeability, and b) the CO₂/CH₄ selectivity at 200 psia and 35 °C. Lines are “drawn by eye”.

decrease in the intersegmental resistance to mobility of the polymer chain. The loosening of the polymer matrix presumably tends to increase the size and frequency of adequately large transient gaps available for diffusive jumps. Transport conditioning will preferentially increase the diffusivity of the larger penetrant, CH₄ in this case, relative to the small penetrant, CO₂ in this case, and should result in a decrease in the diffusivity selectivity. These findings are in line with the sorption results as will be discussed in the next chapter. Exchange conditioning of the 10/90 CO₂/CH₄ and 300 ppm toluene with 10/90 CO₂/CH₄ gas mixture at 200 psia led to 50-60% increase in the CO₂ and CH₄ permeability relative to the permeability of the unconditioned sample with a corresponding 13% loss in CO₂/CH₄ permselectivity.

Mixed gas permeation experiments for the 10/90 CO₂/CH₄ were performed at 200 psia total feed pressure and 55 °C. As expected, with an increase in temperature an increase in permeability is observed, coupled with a decrease in selectivity, following the classical Arrhenius behavior. Since the temperature dependence of permeability is often modeled as an Arrhenius-type relationship, Arrhenius plots (log of permeance versus inverse absolute temperature) can be made and apparent activation energies for permeation can be obtained: $E_p = 14.5$ kJ/mol (for CO₂) and $E_p = 30.6$ kJ/mol (for CH₄). Figure 2.13 shows the Arrhenius plots for CO₂ and CH₄. The apparent activation energy for permeation is greater for CH₄ compared to CO₂, since apparent activation energy scales with penetrant diameter. This results in a declining selectivity with increasing temperature. The CO₂ permeance and CO₂/CH₄ selectivity were 11.6 GPU and 34.3 at 35 °C compared to 16.4 GPU and 23.4 at 55 °C respectively.

The effects of conditioning on the CO₂ permeability and CO₂/CH₄ selectivity at 55 °C and 200 psia are shown in figure 2.14. Since the sorption level decreases with temperature, it is reasonable that the conditioning effect is lower at 55 °C as compared to 35 °C. The results in Figure 2.14a suggest that the 10/90

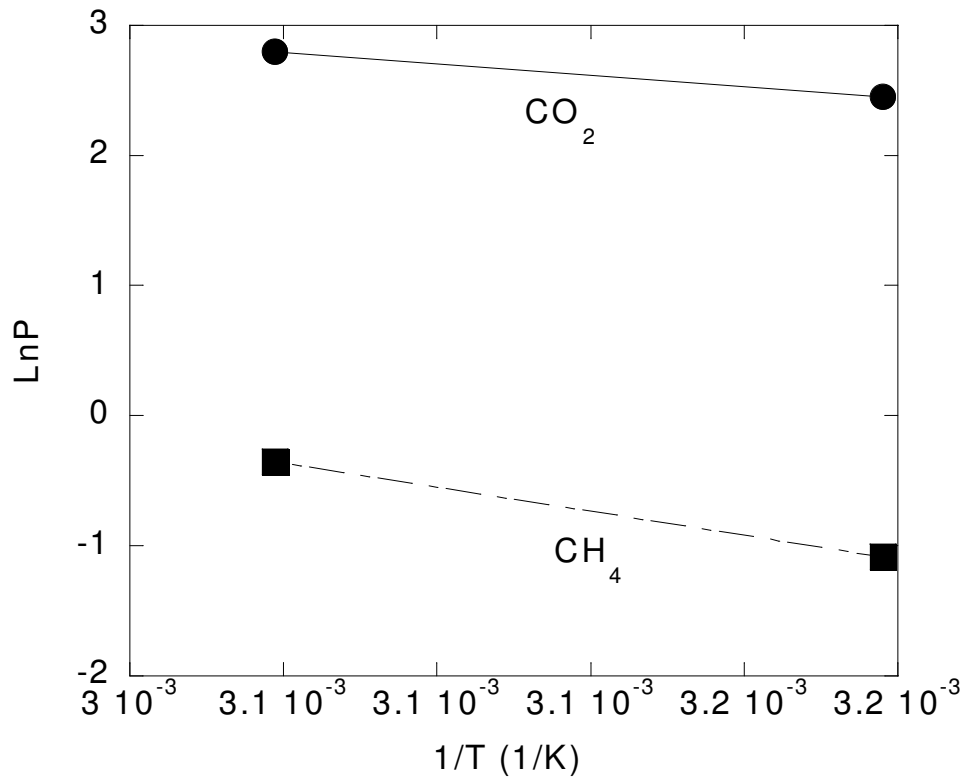


Figure 2.13 CO₂ and CH₄ Arrhenius plots of 10/90 CO₂/CH₄ mixture at 200 psia

CO₂/CH₄ and 300 ppm toluene conditioning is not an important factor at play. The maximum increase in permeability of CO₂ was 2% at 100 psia for the conditioned sample relative to the unconditioned sample. The selectivity of CO₂/CH₄ shown in Figure 2.14b was slightly higher in the conditioned sample than for the unconditioned sample. Similar results have been seen for the 10/90 CO₂/CH₄ + 500 ppm n-heptane mixture. The reported results, however, represent the average of duplicate permeators for each “state” (temperature and toluene exposure), so the trends, are believed to be correct and meaningful. This important result shows that pretreatment may not be a problem at the 300 ppm level if the feed is simply heated to 55 °C; however, the CO₂ flux is reduced during exposure as will be

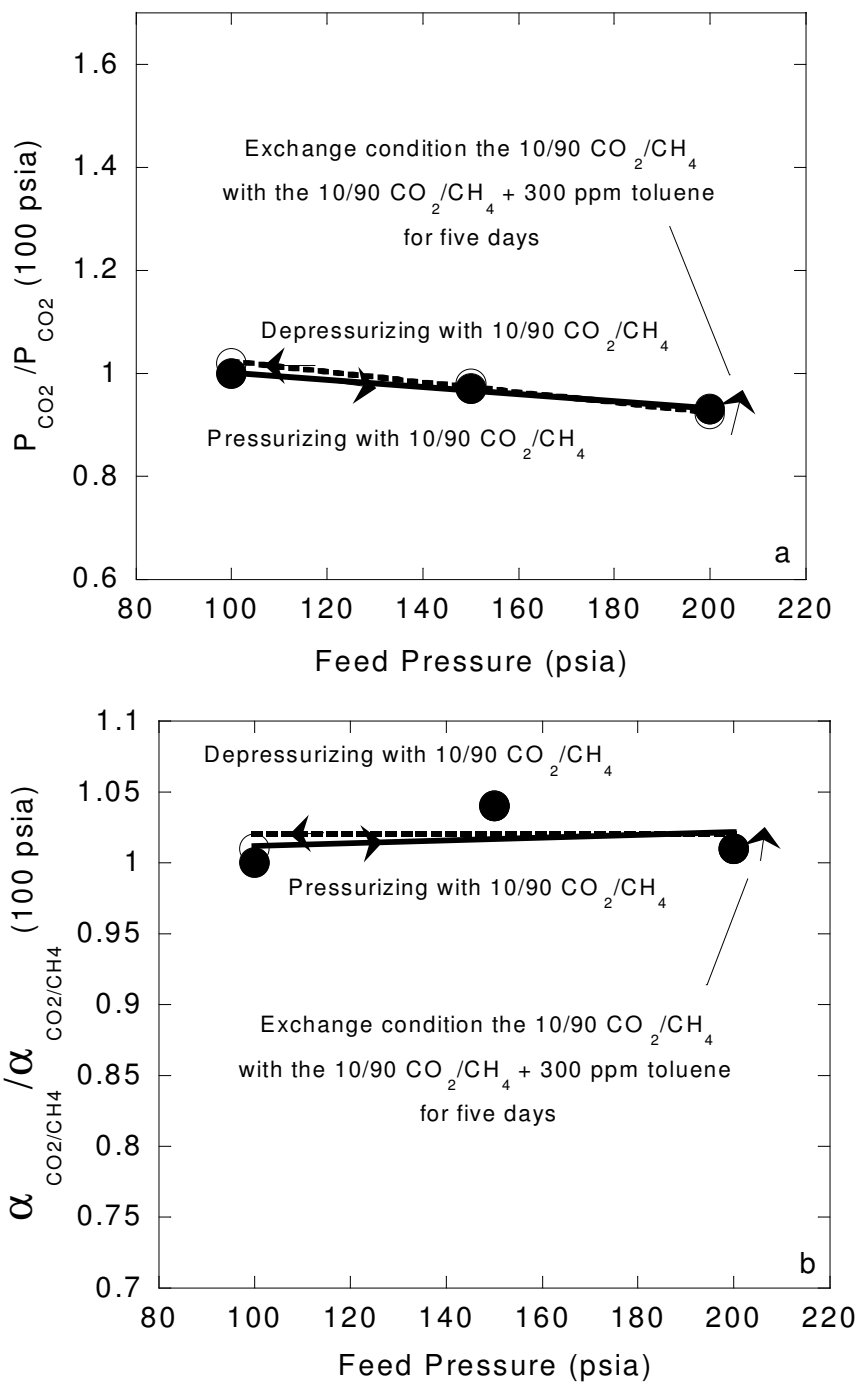


Figure 2.14 Effect of conditioning of 10/90 CO₂/CH₄ + 300 ppm toluene mixture on the a) CO₂ permeability, and b) CO₂/CH₄ selectivity at 200 psia and 55 °C. Lines are “drawn by eye”.

discussed later due to competition effects. This problem can be alleviated by using more fibers while preserving the selectivity by operating at 55 °C.

2.3.2 Comparison of Conditioning in Hollow Fiber Membranes at 200 psia during Exposure

As can be seen in Figure 2.15a, the CO₂ permeance in the 10/90 CO₂/CH₄ + 500 ppm n-heptane decreased by 23%, when compared to the 10/90 CO₂/CH₄ binary mixture. The CO₂ permeance in the 10/90 CO₂/CH₄ + 500 ppm n-heptane subsequently remains essentially constant during the five days period. The selectivity, as shown in figure 2.15b, decreased 5% during the five days of the experiment. Clearly, although possibly tolerable, pretreatment to remove even such paraffinic contaminants may be desirable if maximizing selectivity is crucial for a given application. On the other hand, the selectivity in the 10/90 CO₂/CH₄ + 300 ppm toluene decreased roughly 12% from the selectivity of the 10/90 CO₂/CH₄ base case. The permeance of CO₂ decreased 40% on the first day and then increased steadily to 67% relative to the CO₂ permeance of the 10/90 CO₂/CH₄. The small decrease of CO₂ permeance here during exposure in the case of the 10/90 CO₂/CH₄ + 500 ppm n-heptane suggested that, unlike toluene, the n-heptane does not compete strongly with the other components significantly to block transport through the membrane at the segmental scale. Toluene, on the other hand, appears to block permeation pathways such that the membranes are able to separate less efficiently. This may be due to competition with CO₂ and CH₄ for diffusion pathways and sorption sites in the gas mixture. Even at 300 ppm level, it appears that toluene has a sufficiently negative impact to make it necessary to reduce it to a lower level. The level required to render toluene no more problematic than n-heptane at 500 ppm would require more extensive study. Some investigation (discussed later) with 100 ppm toluene effectively is at this limit, but how 150, 200 or 250 ppm would behave cannot yet be predicted, since

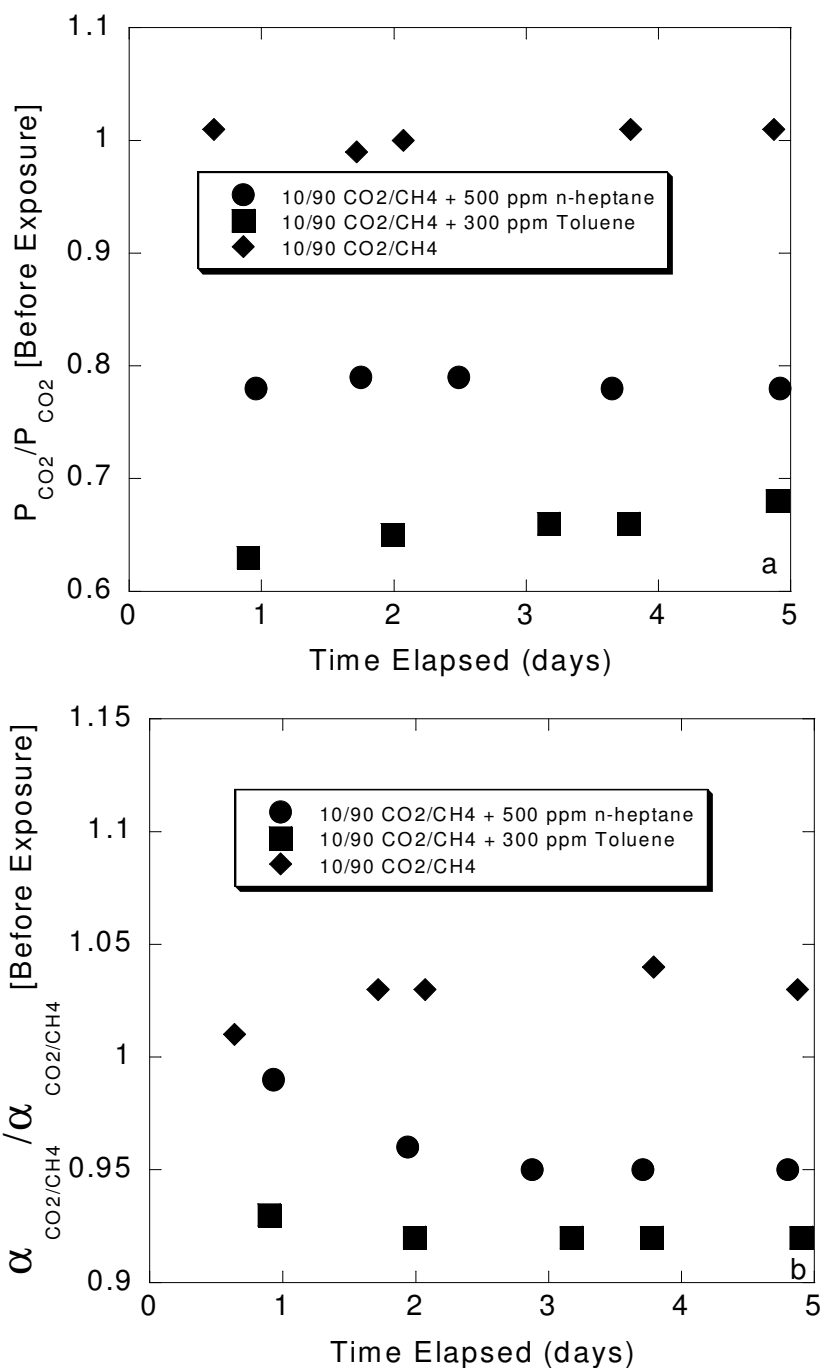


Figure 2.15 Comparison of a) CO₂ permeability, and b) CO₂/CH₄ selectivity during exposure at 200 psia, and 35 °C for 10/90 CO₂/CH₄ mixture, 10/90 CO₂/CH₄ + 300 ppm toluene mixture, and 10/90 CO₂/CH₄ + 500 ppm n-heptane mixture.

the operative phenomena are not well understood yet. Synergistically, negative effects of operating with different levels of these two penetrants also should be investigated, but this is an even more complex problem and was not a problem that was considered in the present work.

The reduced conditioning effect in the membranes is probably a result of the lower solubility level of n-heptane than the toluene at similar weight fractions. The decrease in selectivity was presumably due to a decrease in diffusivity selectivity caused by a loosening of the polymer matrix. There was 3% increase in selectivity after the exposure in the 10/90 CO₂/CH₄ mixtures with no significant changes in CO₂ permeability during the five-day period as can be seen in Figure 2.10a, so in the absence of hydrocarbons impurities, the binary CO₂/CH₄ feed does not have any negative impact on performance properties at the 200 psia feed pressure.

At 35 °C, the ‘reduced’ permeability, $P_{CO_2}/P_{CO_2}^{ref}$, was 5% smaller than at 55 °C at the same pressure for the 10/90 CO₂/CH₄ + 500 ppm n-heptane mixture relative to the 10/90 CO₂/CH₄ as shown in Figures 2.15a and 2.16a. Similar results are seen for the 10/90 CO₂/CH₄ + 300 ppm toluene mixture. The solubility of toluene exceeds that of n-heptane and causes a 12 % decrease in CO₂ permeability in 10/90 CO₂/CH₄ + 300 ppm toluene relative to the 10/90 CO₂/CH₄ + 500 ppm n-heptane mixture at 55 °C. The CO₂ permeability in 10/90 CO₂/CH₄ + 300 ppm toluene at 35 °C had a slightly *lower* CO₂ permeability than the 10/90 CO₂/CH₄ + 300 ppm toluene at 55 °C in the first two days as can be seen from Figures 2.15a and 2.16a. However, during the last three days, moderate increases in the CO₂ permeance (10%) were observed. More prolonged exposure (>5 days) to a pressurized feed gas with and without hydrocarbon impurities was not pursued; however, this type of study would be interesting, although it is beyond the scope of this work. In any case, the lack of significant changes in this period of time in the permselectivity of CO₂/CH₄ and CO₂ permeability for the 10/90 CO₂/CH₄ mixture

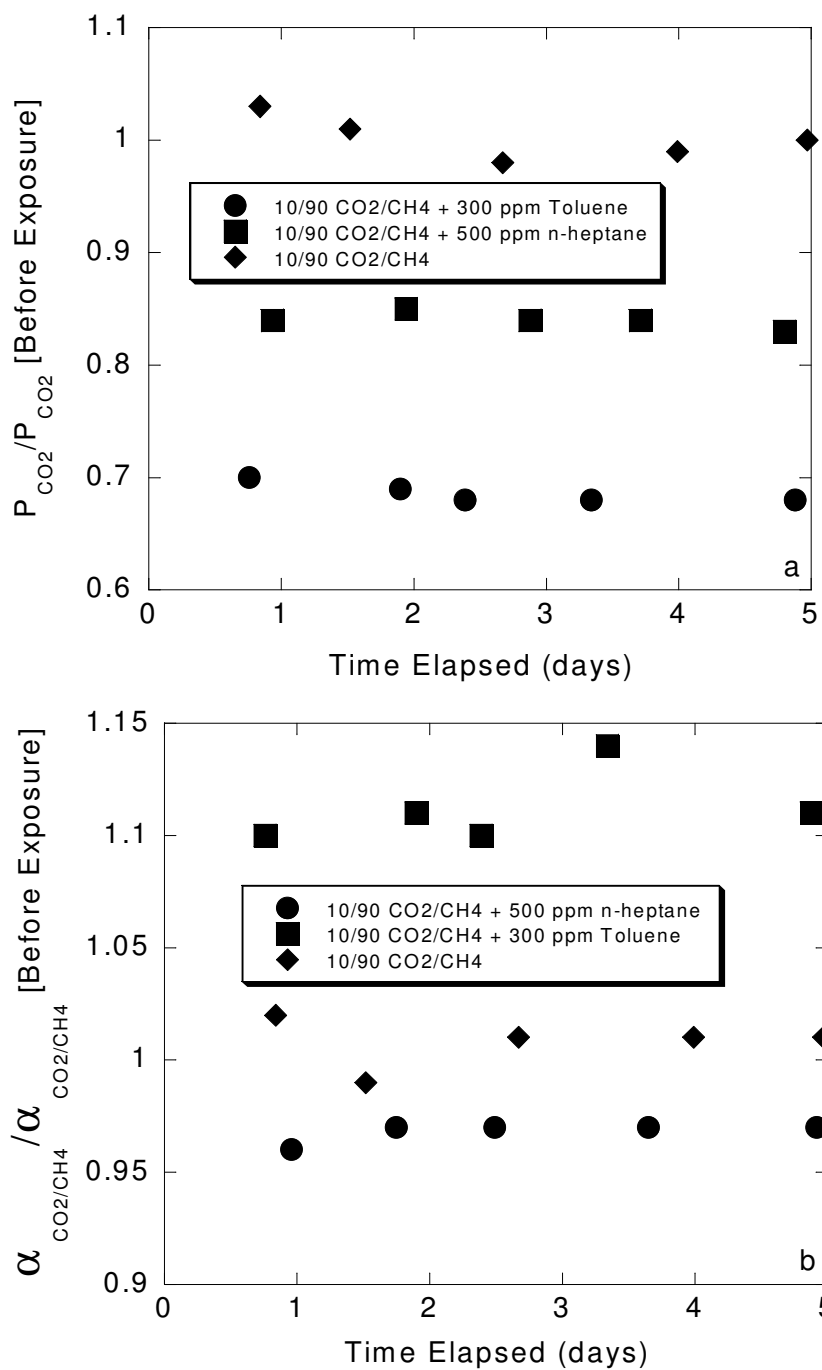


Figure 2.16 Comparison of a) CO₂ permeability, and b) CO₂/CH₄ selectivity during exposure at 200 psia, and 55 °C for 10/90 CO₂/CH₄ mixture , 10/90 CO₂/CH₄ + 300 ppm toluene mixture, and 10/90 CO₂/CH₄ + 500 ppm n-heptane mixture.

validates the characterization results of the membranes for these short term testing conditions.

The selectivity of CO₂/CH₄ in the 10/90 CO₂/CH₄ + 300 ppm toluene at 55 °C was 11% higher than in the 10/90 CO₂/CH₄ at the same temperature as can be seen in figure 2.16b. Increases in gas selectivity preclude notions that reductions in permeance are a result of the collapse of the substructure or that plasticization is a dominant feature. Collapse of the substructure would result in an additional resistance for mass transfer which is non-selective for gases since the mechanism for mass transfer is Knudsen instead of solution-diffusion. Ultimately, this would lead to an observed decline in gas selectivity (*which was not observed in fact*). The selectivity increase in the 10/90 CO₂/CH₄ + 300 ppm toluene is postulated to be caused by the “anti-plasticization” of toluene at high temperatures. The high temperature in the presence of toluene appears to strengthen the anti-plasticization characteristics of hollow fibers. In comparison to the toluene, the presence of n-heptane does not increase the selectivity, and currently the effects are not yet understood fundamentally; however, they are believed to be “real” and outside the experimental uncertainty.

Experiments with 10/90 CO₂/CH₄ + 100 ppm toluene were performed at 200 and 400 psia and at 35 °C and 55 °C to confirm the above results. Figures 2.17 and 2.18 show CO₂ permeance and CO₂/CH₄ selectivity during conditioning to the ternary mixture 10/90 CO₂/CH₄ + 100 ppm toluene at 200 psia, and 400 psia respectively. As can be seen in Figure 2.17a and 2.18a, at 35 °C the decrease in CO₂ permeance is larger than at 55 °C at the same toluene concentration, which is again consistent with expected lower sorption level of toluene with higher temperature. In addition, CO₂ permeability at 35 °C and 400 psia in the presence of 100 ppm toluene shows minimal creep indicating minimal if any permeation plasticization. It can also be seen from Figures 2.16a and 2.17a that the decrease in the CO₂ permeances at 300 ppm is larger than at 100 ppm, which is consistent

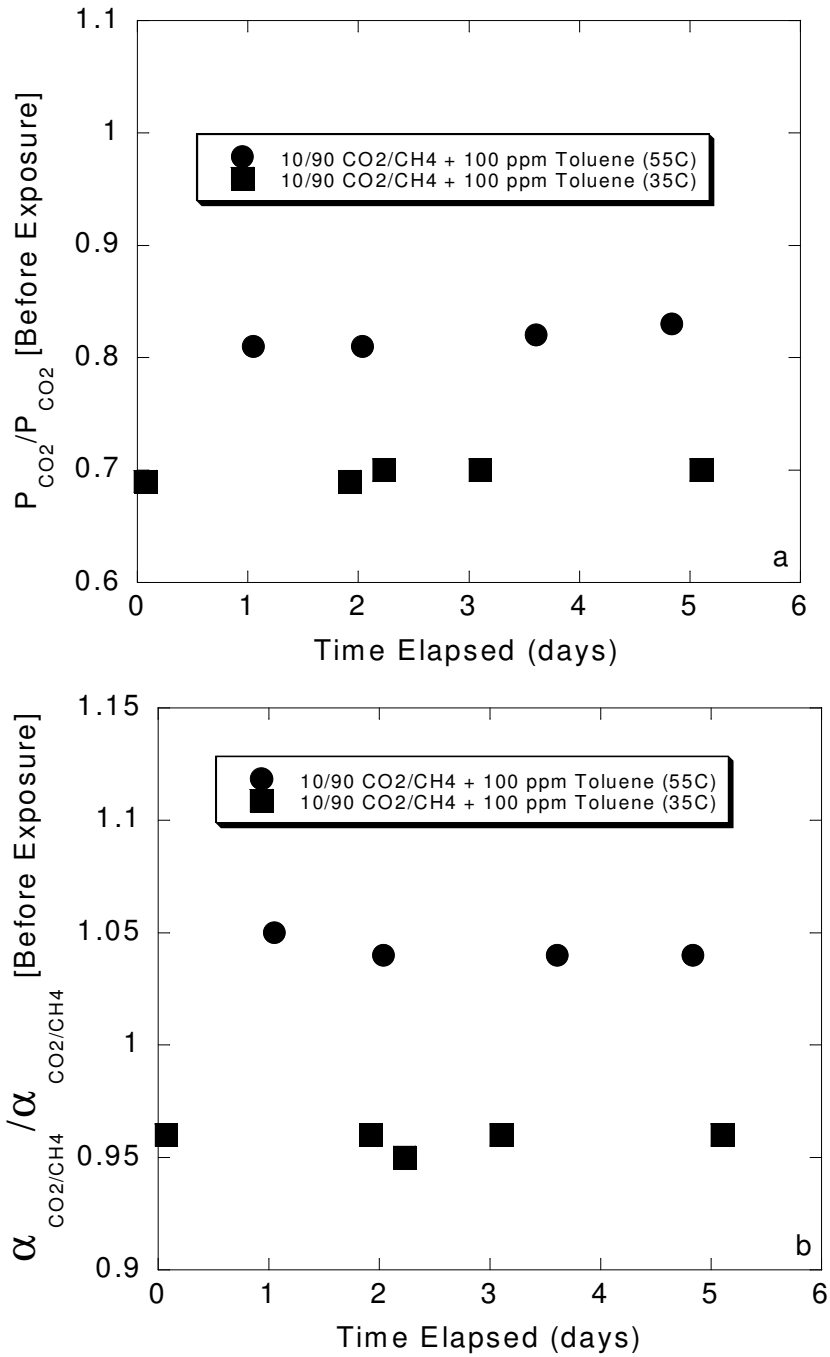


Figure 2.17 Comparison of a) CO₂ permeability, and b) CO₂/CH₄ selectivity during exposure at 200 psia, 35 °C and 55 °C for 10/90 CO₂/CH₄ + 100 ppm toluene mixture.

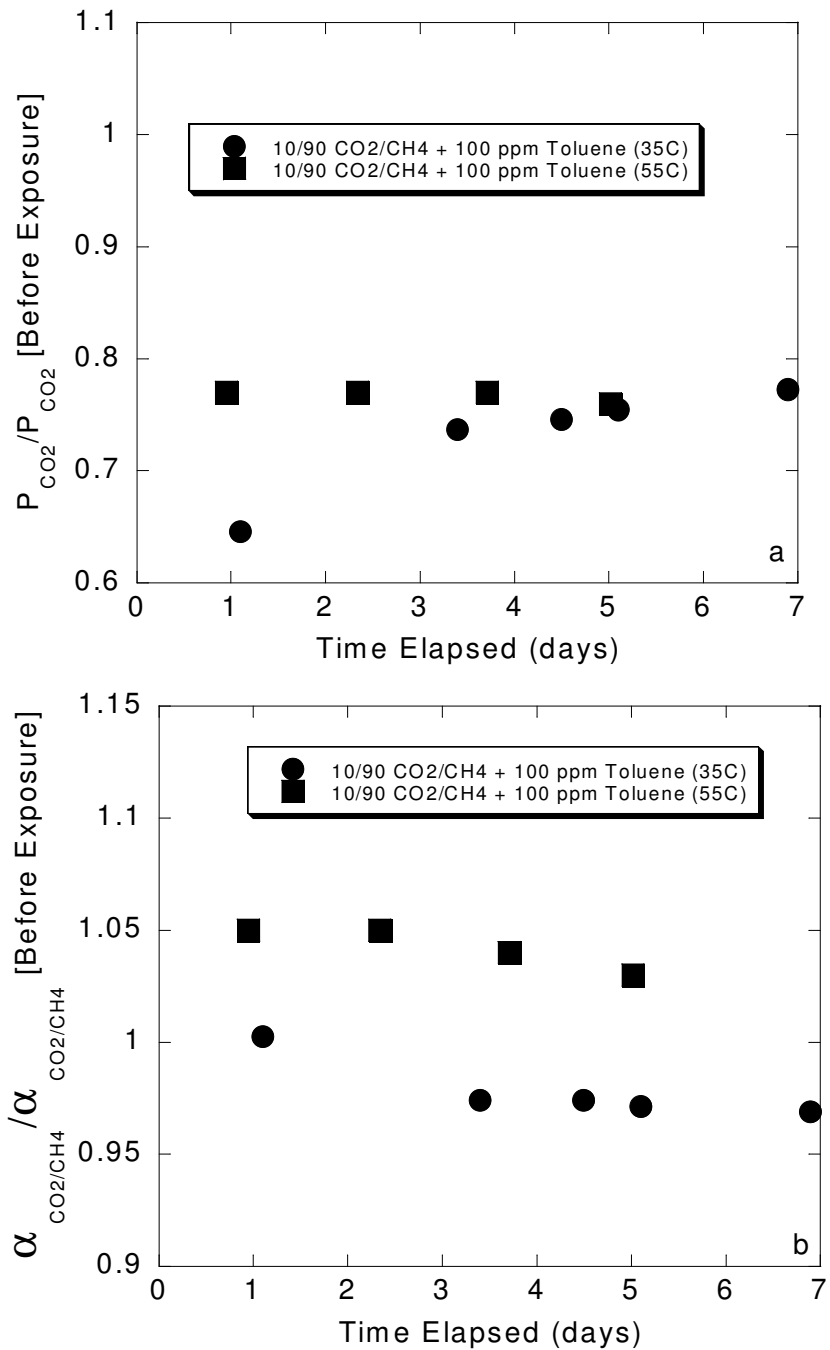


Figure 2.18 Comparison of a) CO₂ permeability, and b) CO₂/CH₄ selectivity during exposure at 400 psia, 35 °C and 55 °C for 10/90 CO₂/CH₄ + 100 ppm toluene mixture.

with the depressed CO₂ and CH₄ permeances at higher toluene concentrations due to expected “competition” between toluene for sorption and transport environments available to all three penetrants. Similar to the 10/90 CO₂/CH₄ + 300 ppm toluene results at 55 °C, the permselectivity of CO₂/CH₄ in the 10/90 CO₂/CH₄ + 100 ppm toluene at 200 psia, 400 psia and 55 °C increased approximately 5% relative the 10/90 CO₂/CH₄ base case. This, presumably, again reflects an effective “anti-plasticization” effect induced by the presence of toluene.

2.3.3 Comparison of Conditioning in Hollow Fiber Membranes at 600 psia before and after Exposure

In the previous sections, the effect on the transport properties for CO₂ and CH₄ caused by conditioning to 10/90 CO₂/CH₄ at 200 psia were discussed. The swelling conditioning effect of 10/90 CO₂/CH₄ on the transport properties on the hollow fiber membranes increased with increasing conditioning pressure as can be clearly seen by comparing Figures 2.10a and 2.19a. The increased permeability enhancements at 600 psia conditioning pressure compared to conditioning at 200 psia reflect an increase in sorption and penetrant induced swelling. At 200 psia conditioning pressure, the CO₂ partial pressure was too low to cause large swelling; however, at 600 psia exposure, the conditioning effects become much more apparent. The maximum increase in permeability of the conditioned sample in the 10/90 CO₂/CH₄ occurred at low pressures in both figures. In Figure 2.19a, the conditioning effect of 10/90 CO₂/CH₄ is reflected in 25% increase in the CO₂ permeance at 200 psia following depressurization. This increase in CO₂ permeance resulted in a 3 to 5% decrease in selectivity relative to the unconditioned sample as shown in Figure 2.19b. More importantly, however, is the dramatically larger negative impact on post exposure performance for the 600 psia conditioning. This is not completely surprising, since at the same temperature and weight fraction, the partial pressure of each respective hydrocarbon is three times higher at 600 psia

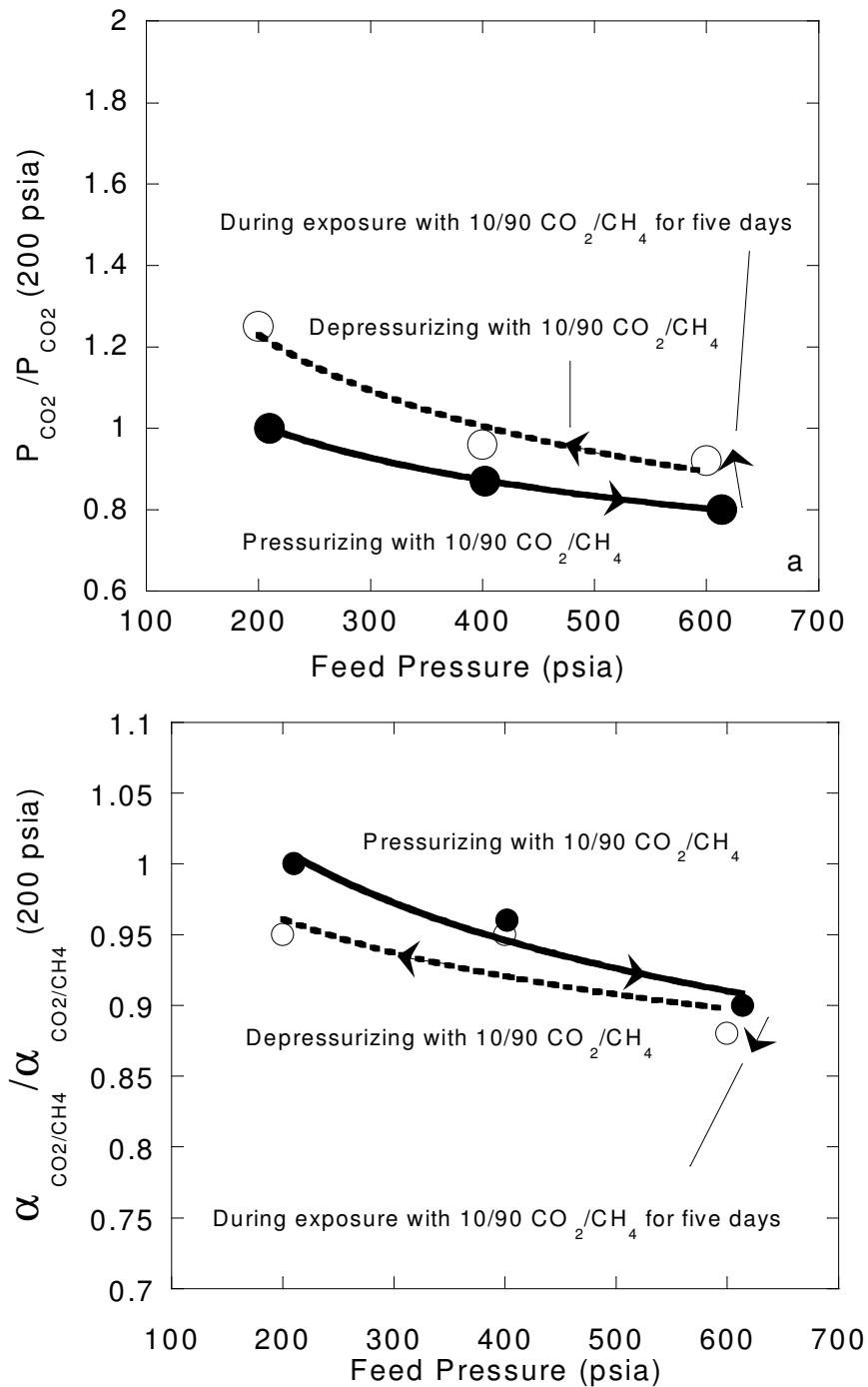


Figure 2.19 Effect of conditioning of 10/90 CO₂/CH₄ mixture on a) the CO₂ permeability, and b) the CO₂/CH₄ selectivity at 600 psia and 35 °C. Lines are “drawn by eye”.

versus 200 psia during the exposure conditioning process. Again, however, it is not possible yet to predict or model the observed effects due to the three times higher respective hydrocarbons partial pressures.

Specifically CO₂ permeability changes after exposure to n-heptane do not show additional swelling induced conditioning as measured by CO₂ permeation in the membrane compared to that seen only with the 10/90 CO₂/CH₄ binary (Figure 2.19). Nevertheless, significant effects are seen at 600 psia that are not apparent at 200 psia. Even, though CO₂ is affected like it was with no heavy hydrocarbons at 600 psia, the selectivity at 600 psia is much more negatively impacted. This suggests that CH₄ “detects” any subtle conditioning effect more sensitively than CO₂ does and makes CH₄ a sensitive probe of changes in the glass that are induced by conditioning. Permeation studies with 500 ppm n-heptane at 600 psia conditioning pressure in the 10% CO₂/ 90% CH₄ mixed gas feed indicate approximately 19% increase in CO₂ permeance with 11% loss in CO₂/CH₄ selectivity at 200 psia compared to the unconditioned sample as can be seen in Figures 2.20a and 2.20b respectively.

Figure 2.21a compares the CO₂ permeability, following conditioning with 10/90 CO₂/CH₄ + 300 ppm toluene, to the CO₂ permeability before the 10/90 CO₂/CH₄ + 300 ppm toluene exposure. While only CH₄ “senses” the subtle changes brought by exposure to heptane/CO₂/CH₄, CO₂ also shows a dramatic increase following exposure to toluene/CO₂/CH₄. Since the selectivity of the sample after exposure is not greatly different in either figure 2.21b or 2.20b, both CO₂ and CH₄ appear to be increased by roughly the same large extent. Exchange conditioning of the 10/90 CO₂/CH₄ + 300 ppm toluene with the 10/90 CO₂/CH₄ at 600 psia led to 116% increase in the CO₂ permeability relative to the permeability of the unconditioned sample with a corresponding 13% loss in CO₂/CH₄ permselectivity at 600 psia compared to the unconditioned sample. This increase in permeability was attributed to the increase in the subtle packing disruptions in

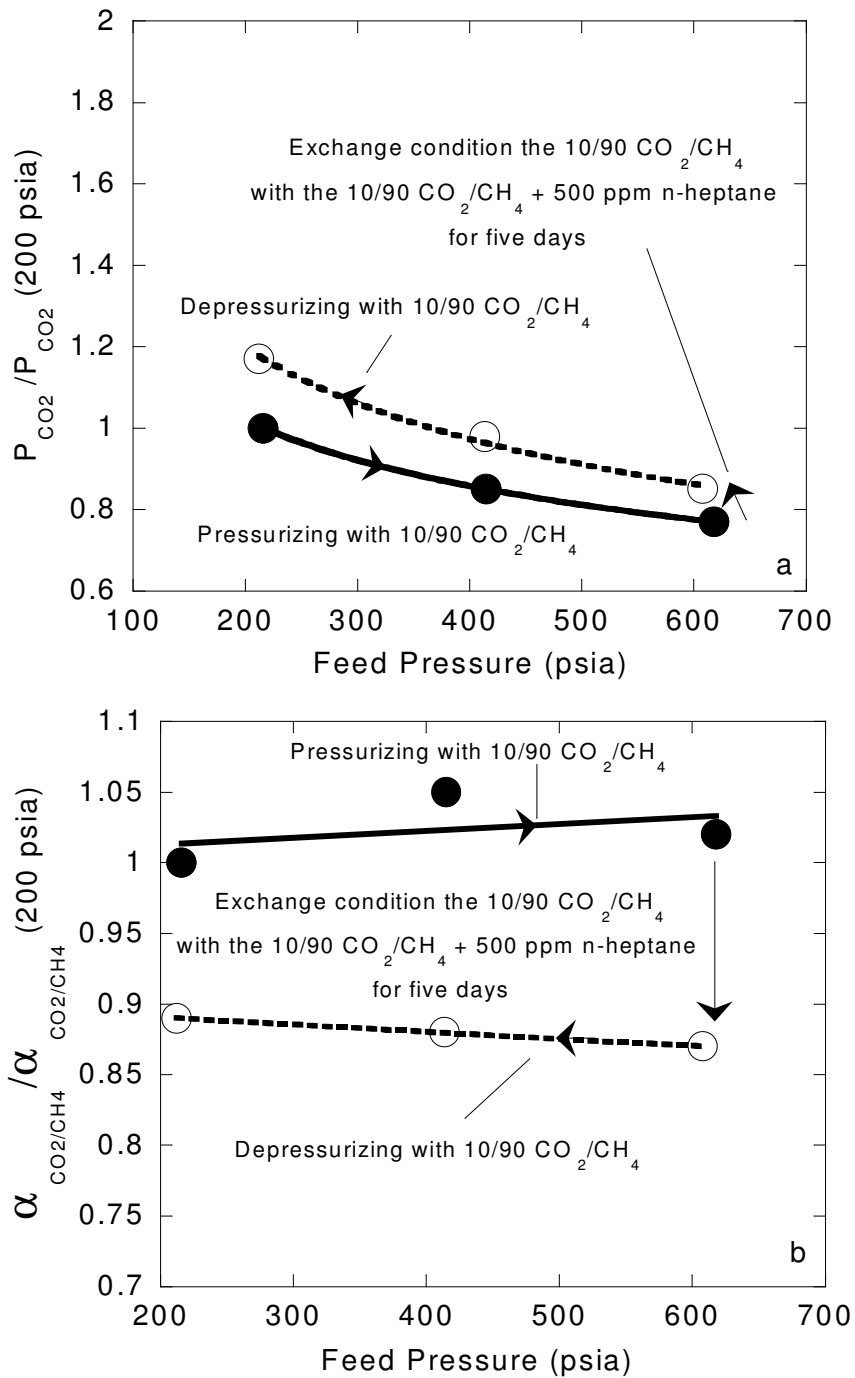


Figure 2.20 Effect of conditioning of 10/90 CO₂/CH₄ + 500 ppm n-heptane mixture on a) the CO₂ permeability, and b) the CO₂/CH₄ selectivity at 600 psia and 35 °C. Lines are “drawn by eye”.

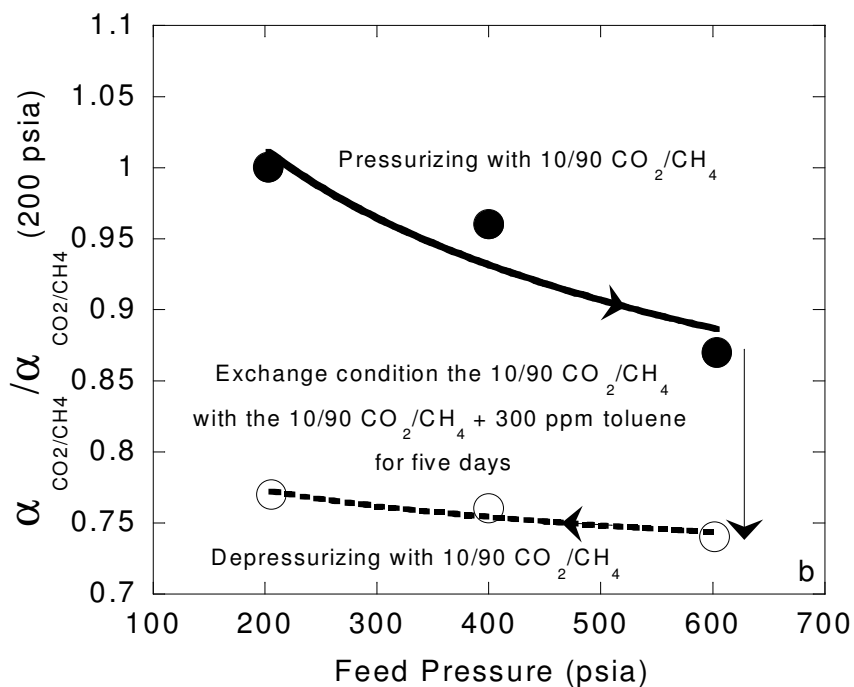
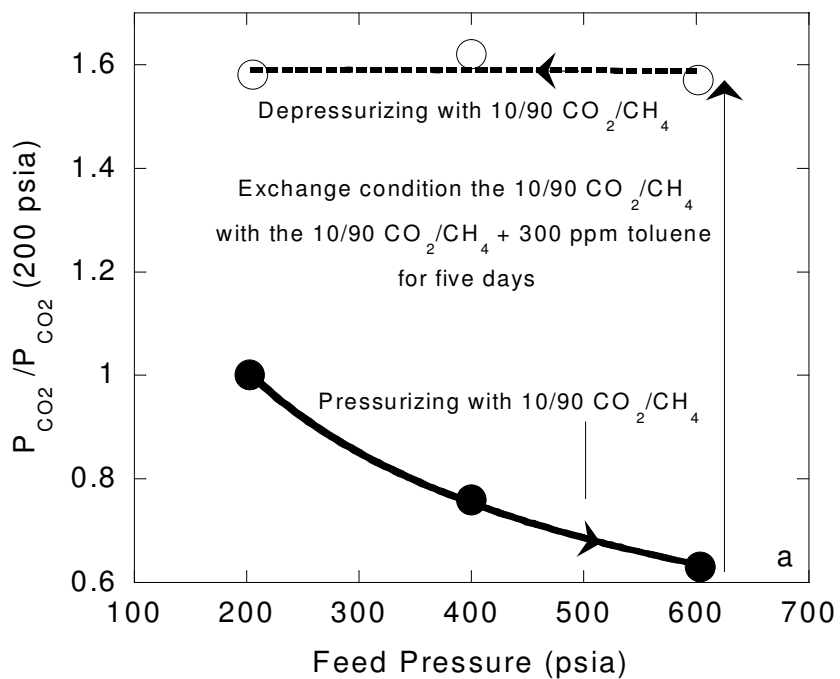


Figure 2.21 Effect of conditioning of 10/90 CO₂/CH₄ + 300 ppm toluene mixture on a) the CO₂ permeability, and b) the CO₂/CH₄ selectivity at 600 psia and 35 °C. Lines are “drawn by eye”.

the polymer caused by toluene swelling at 600 psia. The selectivity was also lower at 600 psia than at 200 psia.

Unfortunately, the hollow fiber membranes failed at 600 psia and 55 °C possibly due to stresses induced by the large swelling of the polymer matrix.

2.3.4 Comparison of Conditioning in Hollow Fiber Membranes at 600 psia during Exposure

Figure 2.22 shows CO₂ permeability and CO₂/CH₄ selectivity behavior **during** the exposure conditioning as a function of time. The reported experimental data in Figure 2.22 as well as other conditioning experiments **did** reflect steady state permeation properties of the hollow fiber membranes. The CO₂ permeability in the 10/90 CO₂/CH₄ mixture (in the absence of toluene or n-heptane) increased in the first day roughly by 10% relative to the CO₂ permeability at time zero and then leveled off with an increase between 10% and 15%. There was a slight increase in selectivity because CO₂ was being more selectively permeated by the membrane; presumably due to a favorable competition by CO₂ for any small addition of free volume. The results of Figure 2.22 indicates the absence of “short term” nonselective plasticization, but there is a longer term relaxation controlled “creep” that produces an increased CO₂ and CH₄ permeances at higher pressures. Both CO₂ and CH₄ permeabilities increased up to 15 % and 10% respectively at 600 psia following conditioning; however, CO₂ showed the largest increase. Therefore, the selectivity increased approximately 4% relative to the unconditioned sample.

The CO₂ permeance in the 10/90 CO₂/CH₄ + 500 ppm n-heptane shows a 10% decrease from the CO₂ permeance of the 10/90 CO₂/CH₄ conditioned sample. Compared to the unconditioned sample, CO₂ shows essentially no increases. This suggests that both n-heptane and CO₂ compete for the increased free volume introduced by n-heptane. Moreover, since CO₂ permeation in figure 2.20 increases by 20 % after removing n-heptane, the introduced free volume is definitely

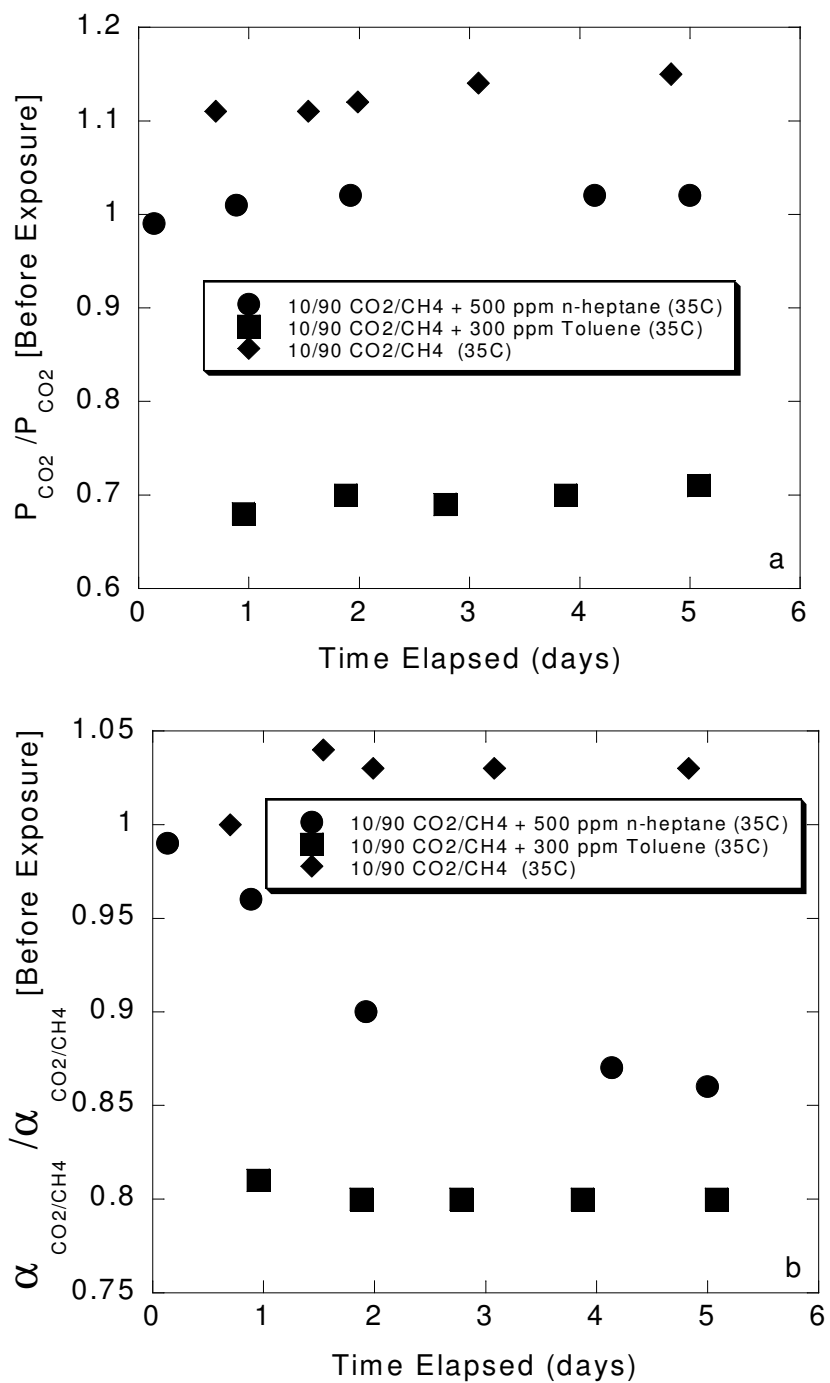


Figure 2.22 Comparison of a) CO₂ permeability, and b) CO₂/CH₄ selectivity *during exposure* at 600 psia, 35 °C for 10/90 CO₂/CH₄ mixture, 10/90 CO₂/CH₄ + 300 ppm toluene mixture, and 10/90 CO₂/CH₄ + 500 ppm n-heptane mixture.

“significant”. This surprising result in figure 2.22b, however, is that CH₄, (perhaps due to its high partial pressure) competes even more successfully, with heptane and CO₂, thereby reducing selectivity in a steady downward creep process. For the toluene containing stream during conditioning, the CO₂ permeance in the 10/90 CO₂/CH₄ + 300 ppm toluene shows a marked 40% decrease relative to the CO₂ permeance of the 10/90 CO₂/CH₄ conditioned sample. This suggests that neither the n-heptane nor the toluene ultimately compete strongly with CH₄; however, toluene appears to block permeation opportunities available to CO₂ such that the membranes are able to separate less efficiently. The abrupt drop in CO₂ permeance in the 10/90 CO₂/CH₄ + 300 ppm toluene at the beginning (< 1 day) may reflect the high affinity of the toluene to the membrane compared to n-heptane. A full explanation of the extremely complex processes at play in these conditioning phenomena will clearly need more studies.

This increase in CH₄ permeability was accompanied by a considerable gradual decrease in permselectivity. The selectivity decreased by 15% at the end of the five days relative to the selectivity in the unconditioned sample and appears to be approaching the same level as for toluene. A shift in free volume, caused by sorbing n-heptane facilitates, leads to an increase in the diffusion coefficient of CH₄ and only a moderate increase in CO₂ diffusion coefficient. Assuming a shift in the free volume distribution to high intersegmental spacings leads to lower selectivity. Normally, this would be expected to result in an increase in the diffusion coefficient and a decrease in the diffusivity selectivity.

The corresponding type of change believed to reflect the behavior seen for the reduced permselectivity of CO₂/CH₄ in figure 2.21a and 2.21b which was conditioned with the 10/90 CO₂/CH₄ + 300 ppm toluene at 600 psia is illustrated in Figure 2.23. Conditioning was found to result in 20% decreases in the CO₂/CH₄ permselectivities relative to the unconditioned sample. This decrease in selectivity can be attributed to increases in the subtle packing disruptions in the polymer as

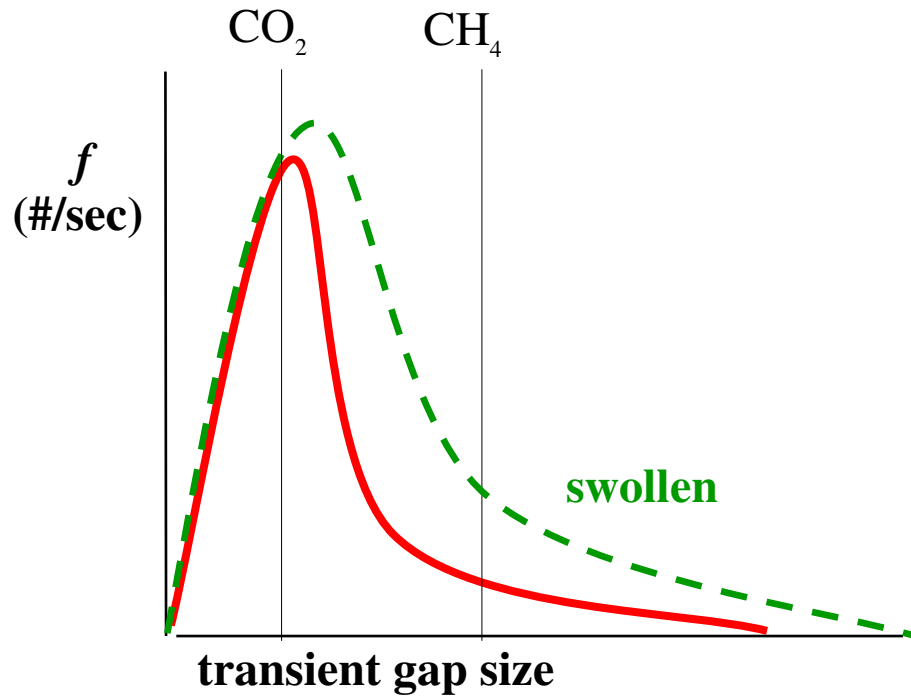


Figure 2.23 Qualitative transport gap (free volume element) size distribution change after conditioning with 10/90 CO₂/CH₄ + 300 ppm toluene mixture.

well as to a decrease in the diffusivity selectivity caused by toluene swelling. This decrease in selectivity does suggest a change in the free volume distribution as opposed to the n-heptane conditioning. In general, this is true since it shows a large increase in CO₂ “opportunities”, but a much larger percent increase in CH₄ “opportunities”.

In the presence of the hydrocarbons, it is believed that the decrease in selectivity after exposure to n-heptane and toluene at 600 psia conditioning pressure is because CH₄ is at its high partial pressure. As a result, this may out compete CO₂ as well as toluene or n-heptane. After removal of the conditioning hydrocarbon, the high CH₄ partial pressure makes the sorption level of CH₄ in the

high energy sites so large that CH₄ out compete CO₂ for jump opportunities and thus the selectivity decreases as seen in figures 2.22b.

2.4 Defective vs. Defect-Free Fibers

Figure 2.24 depicts simplified schematic morphologies and SEM of a defective nodular and defect free non-nodular asymmetric hollow fiber membrane skin layer. In practice, actual defects “caulked” using a variety of methods; however, the basic nodular morphology persists.

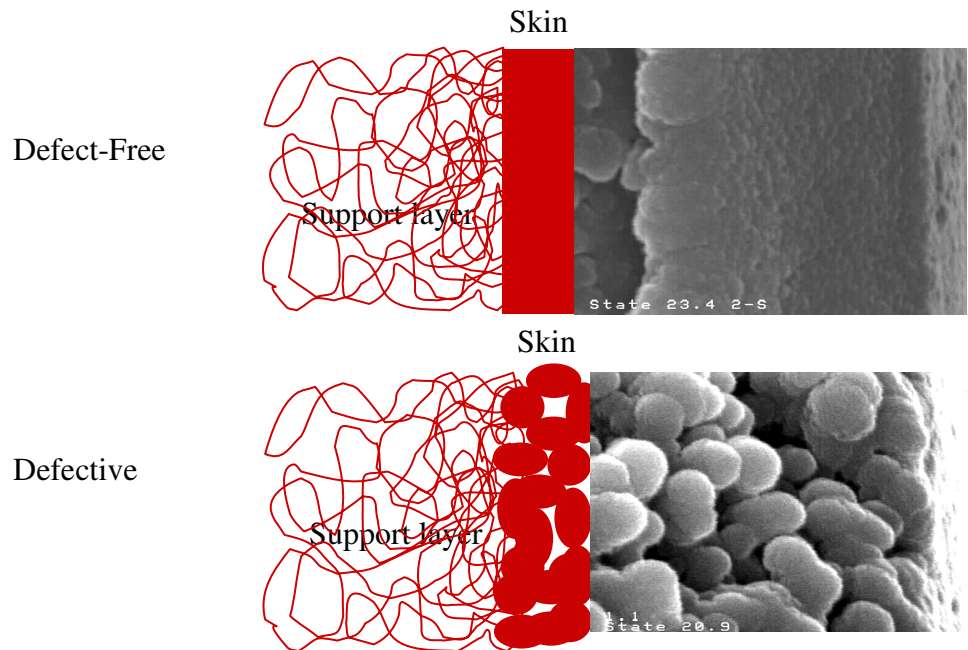


Figure 2.24 Hypothetical figure of the dense skin, and the defective morphology of an asymmetric hollow fiber. SEM of Matrimid asymmetric hollow fiber (taken by Seth Carruthers, 1999)

Although the “nodules” are depicted for simplicity as being spherical, they have poorly-defined shape and the nodules are thought to be interconnected by polymer chains that will be referred to as “tie chains” (Jordan et al., 1990). The tie chains are envisioned as keeping adjacent nodules “fused” together, with

negligible viscous flow through the volume between nodules. The gas molecules diffuse through the complex morphology occupied by the polymer chains in the nodules. The toluene presumably causes some swelling of the glassy matrix within the nodules, and might cause the nodules (or the internodular tie chain region) to become highly dilated. If such a hypothetical picture is valid, during exposure to a swelling agent, tie chains between the nodules may induce a variety of complex responses. If the toluene sorption level is high, many of the chains could presumably actually sufficiently swell and even disengage, thereby enabling viscous flow in the inter-nodular volume when 10/90 CO₂/CH₄ + 300 ppm toluene mixture is applied.

The hypothetical morphology of the *defect-free dense* skin is also shown in Figure 2.25. Although it is probably denser in structure than the defective structure, it is believed that the technique we used in the asymmetric membrane formation produces selective layers that may still contain *discontinuous* nanoscale pores during the phase separation (Carruthers, 2001). However, this structure is hypothesized to be capable of maintaining resistivity of the conditioning effect caused by toluene plasticization. The swelling of the polymer matrix may result in permeability enhancement as discussed earlier, but no catastrophic selectivity losses as typical of the inter-nodular failures mentioned above.

Using this concept, many of the anomalous results obtained for the module conditioning studies between the defective and defect free fibers can be rationalized. The data indicated in Figure 2.25 suggest that an essentially defect-free, non-nodular morphology offers advantages in stability under demanding operating conditions. Earlier work (Gunaidi, 2000) showed serious losses in performance of membranes comprised of the same polymer, when the selective layer had a pronounced fused nodular nature as opposed to the intrinsically defect-free skin layers reported on here.

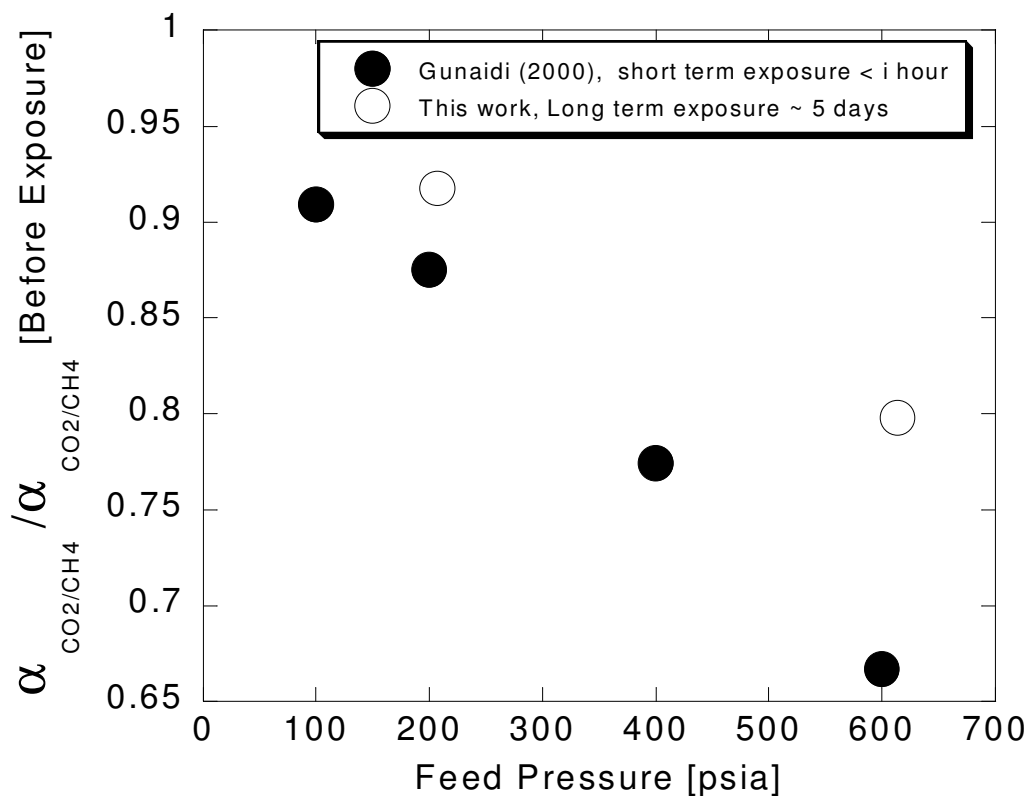


Figure 2.25 Comparison of CO₂/CH₄ selectivity for defective and defect-free fibers during exposure at 35 °C for 10/90 CO₂/CH₄ + 300 ppm toluene mixture.

When the module is depressurized and exposed to vacuum, the hypothetical excess volume introduced during conditioning can collapse to their unconditioned state as shown in Table 2.4.

Admittedly, it would be expected that packing defects induced by conditioning would be readily relaxed out of the fibers since there is both a short diffusional path of voids to the surface and a large driving force for volume recovery since the fibers are under vacuum. Hence, the defect-free fibers are able to ‘recover’ by diffusion, and the permeability approaches its original level (95% to 100% recovery) when the fibers are depressurized and the downstream is put under vacuum.

Table 2.4 Permeability of CO₂ in the 10/90 CO₂/CH₄, at 35' °C illustrating the hysteretic behavior before conditioning, after conditioning to the 10/90 CO₂/CH₄ +100 ppm toluene at 400 psia and after conditioning, followed by exposure to a vacuum source for 21 days.

	% change in CO ₂ permeance*	% change in selectivity*
After Exposure with 10/90 CO ₂ /CH ₄ +100 ppm toluene	+42.3	-7.8
After Exposure with 10/90 CO ₂ /CH ₄ +100 ppm toluene and 21 days under vacuum	+3.8	-1.8

*Original values of CO₂ permeance and selectivity are 11.1 GPU and 35.5 respectively.

2.5 Summary

The following conclusions can be made about the permeation experiments;

- Under the range of conditions studied here, our permeation results suggest the absence of strong plasticization or compaction of the asymmetric morphology by either CO₂ or toluene. The results suggest also the presence of competition consistent with dual mode theory. The competition effect is more pronounced for toluene compared to n-heptane. The permeation flux for CO₂ and CH₄ increased significantly following conditioning as high as 115% and 155% respectively. Heptane causes a slow and a more subtle set of changes; however, the ultimate loss in selectivity is similarly serious as toluene for 35 °C, 500 ppm level and 600 psia feed.
- Conditioning with 10/90 CO₂/CH₄ at 200 psia and 35 °C; CO₂ permeance increased 3% relative to the unconditioned sample. The increase in CO₂ permeance after conditioning is a direct result of the loosening and reordering of the polymer matrix. The selectivity of CO₂/CH₄ following conditioning was slightly higher by 2-3% in the conditioned sample than in

the unconditioned sample. These results showed that the conditioning effects of 10/90 CO₂/CH₄ mixture at 200 psia and 35 °C are negligible.

- Conditioning with 10/90 CO₂/CH₄ at 600 psia and 35 °C; The CO₂ permeance after conditioning with 10/90 CO₂/CH₄ gas mixture at 35 °C and 600 psia were higher by 10 to 25 % than before conditioning. The reason for this increase in CO₂ permeances is believed to be an increase in the number of hypothetical gaps due to an increase in the conditioning pressure. The selectivity is essentially unchanged. This is a surprising result, since the high CH₄ partial pressure enables CH₄ to effectively compete for newly introduced free volume due to large hydrocarbons like n-heptane and toluene. It appears that simple CO₂ conditioning does not introduce such large additional free volume packets as with the larger hydrocarbons. In this case, perhaps the intrinsic polymer affinity constants for CO₂ and CH₄ are still applicable. For the larger hydrocarbon conditioned cases, the larger “packing defects” may have lower affinity constants for CO₂ and even CH₄. Nevertheless, the large partial pressure of the CH₄ in the feed appears to still allow a large enough sorption in the langmuir sites to enable CH₄ to compete with CO₂ and the heavier hydrocarbons for newly introduced free volume.
- Conditioning with 10/90 CO₂/CH₄ + 500 ppm n-heptane at 200 psia and 35 °C; Conditioning the fibers with 10/90 CO₂/CH₄ + 500 ppm n-heptane at 200 psia does not change the transport properties of the membrane appreciably. The selectivity and permeability following conditioning remained essentially constant at their original values before conditioning. This shows that n-heptane does not cause compaction or free volume plasticization at this low level of exposure.
- Conditioning with 10/90 CO₂/CH₄ + 500 ppm n-heptane at 600 psia and 35 °C; Conditioning with 10/90 CO₂/CH₄ + 500 ppm n-heptane at 600 psia

and 35 showed 10 to 20% increase in CO₂ permeance following conditioning. The selectivity also decreased 10 to 20% compared to the unconditioned sample.

- Conditioning with 10/90 CO₂/CH₄ + 300 ppm toluene at 200 psia and 35 °C; Following conditioning with 10/90 CO₂/CH₄ + 300 ppm toluene at 200 psia and 35 showed large increases in CO₂ and CH₄ permeances compared to the original values before conditioning. The CO₂ permeance increased 60 to 80% following conditioning and selectivity decreased 12 to 15% relative to the unconditioned samples.
- Conditioning with 10/90 CO₂/CH₄ + 300 ppm toluene at 600 psia and 35 °C; Conditioning with 10/90 CO₂/CH₄ + 300 ppm toluene at 600 psia and 35 °C showed the maximum increase in CO₂ permeance in all the conditioning experiments considered. The conditioning treatment increased the CO₂ permeance 110% to 120%, CH₄ permeance 150% to 160% and decreased the selectivity 10% to 25% relative to the unconditioned samples. Toluene compared to n-heptane clearly swells the membrane. Because of toluene swelling the steric hindrance to chain motions is reduced, and therefore the size and the jumps frequency for CO₂ and CH₄ are increased.
- Conditioning with 10/90 CO₂/CH₄ + 300 ppm toluene at 200 psia and 55 °C; The conditioning experiments at 55 °C with the 10/90 CO₂/CH₄ + 300 ppm toluene at 200 psia showed negligible conditioning effects on the CO₂ permeance and selectivity *suggesting the decrease in toluene sorption level with temperature.*
- Conditioning with 10/90 CO₂/CH₄ + 300 ppm toluene at 600 psia and 55 °C; The membrane fails under these conditions and presumably due to stresses in the membrane and high CO₂ partial pressure.

- During Conditioning with 10/90 CO₂/CH₄ , 10/90 CO₂/CH₄ + 500 ppm n-heptane, and 10/90 CO₂/CH₄ + 300 ppm toluene 35 °C; The results showed that the presence of a third component (toluene or n-heptane) depresses the permeances of CO₂ and CH₄ and this is consistent with the dual mode theory. At 600 psia, the CO₂ permeance in the 10/90 CO₂/CH₄ + 500 ppm n-heptane decreased 10% and the CO₂ permeance in the 10/90 CO₂/CH₄ + 300 ppm toluene decreased 40% relative to the CO₂ permeance of the 10/90 CO₂/CH₄ conditioned sample. On the other hand, at 200 psia the CO₂ permeance decreased 15% to 20% in the the 10/90 CO₂/CH₄ + 500 ppm n-heptane and 35% to 40% in the the 10/90 CO₂/CH₄ + 300 ppm toluene. At 200 psia and 55 °C, the decrease in CO₂ permeance is 10% to 15% and 25% to 30% in the the 10/90 CO₂/CH₄ + 500 ppm n-heptane and the 10/90 CO₂/CH₄ + 300 ppm toluene mixtures respectively. This suggests the high affinity of membrane to toluene and that n-heptane does not strongly compete as toluene for sorption sites and permeation pathways. During conditioning to the 10/90 CO₂/CH₄ + 500 ppm n-heptane at 35 °C and 55 °C, the selectivity is depressed almost at the same level relative to the selectivity of the 10/90 CO₂/CH₄. However, during conditioning to the 10/90 CO₂/CH₄ + 300 ppm toluene the selectivity is increased at 55 °C while it decreased at 35 °C relative to the selectivity of the 10/90 CO₂/CH₄ base case.
- The hollow fiber membranes used in this work are defect free and showed distinct advantages compared to the defective fibers in terms of stability and separation efficiency under demanding conditions. The structure of theses fibers is denser than the defective fibers. This structure showed stronger conditioning resistivity. In this work, the toluene caused swelling in the polymer matrix resulting in large permeability enhancements but no

catastrophic failures in performance were observed as seen in the defective fibers.

- The defect free membrane is able to return to its original values of permeability and selectivity after depressurizing and when the module was put under vacuum for an adequate time to relax out excess free volume introduced during the hydrocarbon exposure conditioning.

Chapter 3: Sorption Results and Permeation Behavior Modelling and Analysis

In the preceding chapter, it was shown that the asymmetric hollow fiber membrane modules conditioned with 10/90 CO₂/CH₄ + 300 ppm toluene gas mixture have significantly enhanced CO₂ and CH₄ permeation rates as compared to their unconditioned values. Permeation increases as high as 116% and 154% are reported for CO₂ and CH₄ respectively for modules conditioned for five days at 600 psia with 10/90 CO₂/CH₄ + 300 ppm toluene gas mixture. On the other hand, the conditioning treatment with 10/90 CO₂/CH₄ + 500 ppm n-heptane gas mixture had negligible effect on the CO₂ and CH₄ permeation rates. The conditioning treatment caused reductions in permselectivity of 2-25% relative to the as-received samples for mixed gas feed streams of 10/90 CO₂/CH₄ + 300 ppm toluene and 10/90 CO₂/CH₄ + 500 ppm n-heptane, under the conditions studied. In this chapter, the sorption data are reported and analyzed along with the permeation data obtained in the previous chapter.

3.1 Background

The solubility of gases in glassy materials is usually described by the dual-mode sorption model (Chan et al., 1978; Vieth et al., 1976). This model idealizes sorption as occurring in two different environments, the dense well-packed region (as described by Henry's Law mode) as well as in non-equilibrium packing defects or "macrovoids" (as described by Langmuir mode).

Total sorption can be defined as:

$$C_A = C_{D_A} + C_{H_A} \quad (3.1)$$

Where $C_{D_A} = k_{D_A} p_A$ is also known as Henry's Law, and $C_{H_A} = \frac{C'_{H_A} b_A p_A}{1 + b_A p_A}$ models the Langmuir sorption. The parameter k_{D_A} is the Henry's Law constant that characterizes the sorption tendency in the normally densified regions of the glassy matrix, p_A is the partial pressure of component A, while b_A , characterizes the affinity of the penetrant for the Langmuir sites and C'_{H_A} is the Langmuir capacity constant.

It is generally accepted that penetrant-induced conditioning effects for glassy polymers give rise to added sorptive capacity compared to solubilities which may be anticipated in the first exposure of a glassy polymer to a high pressure gas. This phenomenon has been explained in the framework of dual mode sorption as an increased Langmuir sorption. It has also been found that the Langmuir capacity depends on prior gas exposure of the material (Jordan and Koros; 1990; Jordan, Koros and Fleming, 1990; Jordan, Henson and Koros, 1990). The results of these effects on sorption isotherms will be discussed in more detail later in terms of increases in a 'base case' Langmuir capacity, C'_H . Inherent in the dual mode model is the assumption that only the fraction of the total sorption attributed to dissolution into the polymer, C_D , is associated with the separation of chain segments to accommodate penetrant (Fleming and Koros, 1990; Koros and Hellums; 1990). It is also hypothesized that conditioning principally affects the Langmuir capacity parameter with little change in k_D or b .

Previous studies considered CO₂ conditioning effects for pressures as high as 900 psia at 35 °C (Fleming, 1988). Lasting effects of high pressure CO₂ exposure have been studied by Fleming (1988), Jordan (1990) and Pope (1991). It has been found that pre-exposure of high pressure CO₂ leads to subsequently higher gas sorption and permeation. The current explanation of this phenomenon, which has been termed "conditioning," is that highly sorbing species can cause

disruptions in the chain packing conformations in the polymer matrix. These disruptions may act as additional excess free volume sites, which can also accommodate penetrant molecules. It was further found that if a polymer sample is probed with sorption measurements while the sample is still swollen, in a procedure called “exchange conditioning”, even greater increases in solubility are observed. By comparing these results to the “conventionally conditioned” (evacuation of the sample in between preexposure and subsequent sorption probing) results, it can be inferred that although CO₂ conditioning results in semi-permanent increases in sorptive capacity, some additional excess free volume is lost when the conditioning agent is removed. While this analysis is useful in understanding the sorption of mixtures and swelling properties of CO₂, it also provides a means to observe the addition of excess free volume in glassy polymers, which is directly relevant to hydrocarbon conditioning in this study. While some work has been conducted on observing the conditioning effect of CO₂ on gas solubility in glassy polymers (Fleming, 1988; Jordan, 1990; Pope, 1991), no literature has been found to date on the effect of conditioning of heavy hydrocarbons on penetrant sorption and also the effects on apparent mobility.

Therefore, an objective of this chapter is to evaluate the conditioning effects of toluene and n-heptane on CO₂ and CH₄ gas sorption in hollow fiber membranes and to determine the magnitude of these effects. An additional objective is to connect the changes in sorption to changes in diffusivity of each penetrant and of one penetrant versus the others (e.g., D_{CO_2}/D_{CH_4}).

All fibers used in the measurements were from the same batch and were stored in a plastic bag + desiccant to prevent excessive moisture uptake. Each sorption isotherm represents a run conducted on a “virgin” sample, which has not previously exposed to high pressure gas. Sorption measurements have been made for 10/90 CO₂/CH₄ with and without the heavy hydrocarbons exposure to hollow fiber membranes at pressures as high as 600 psia at 35 °C. Therefore, at these

conditions the toluene or n-heptane activity approaches activity levels as high as those used in the permeation studies. The samples are tested at aging times of at least two months. Based on prior work in our group and elsewhere (Punsalan, 2001) is believed that aged samples have a much more stable morphology. By combining the sorption and permeability measurements as will be discussed later in this chapter, one can determine the change on the gas diffusivity for the gas/polymer system. Analysis of such data provides a substantially improved understanding of the rather complex interactions in gas/hydrocarbon/polymer systems.

3.2 Gas Sorption Measurements

Sorption measurements were measured by the pressure decay method (Koros and Paul, 1976). A schematic of a two-transducer pressure decay cell is shown in Figure 3.1. This design has been described in the literature and was successfully modified by adding a new valve (valve C in Figure 3.1) in order to be able to do ‘exchange conditioning’ procedure without evacuation of the sample between exposure and subsequent sorption probing. The sorption system was equipped with two 0-1000 psia temperature compensated pressure transducers (Model PA822-1M-16553, Schlumberger Statham, Oxnard, CA), the fittings were Nupro[®] SS-4H-V13 bellows valves. The transducers were excited by a 10V DC power supply (Model LCS-A-10, Lambda Group of Unitech, Melville, NY). The power supply and transducer output voltages were measured using a digital multimeter (Model 195A, Keithley, Cleveland, OH) with 100 point data logging used to take the average voltage reading at any given time. Measurements were made at 35⁰C by keeping the cells immersed in a circulation bath (Model W26 water bath and Model E3 circulator, Haake Buchler Instruments Inc., Saddle Brook, NJ). It is essential that the water level be maintained at exactly the same

level, as slight variations in temperature and pressure can cause variation in the transducer output.

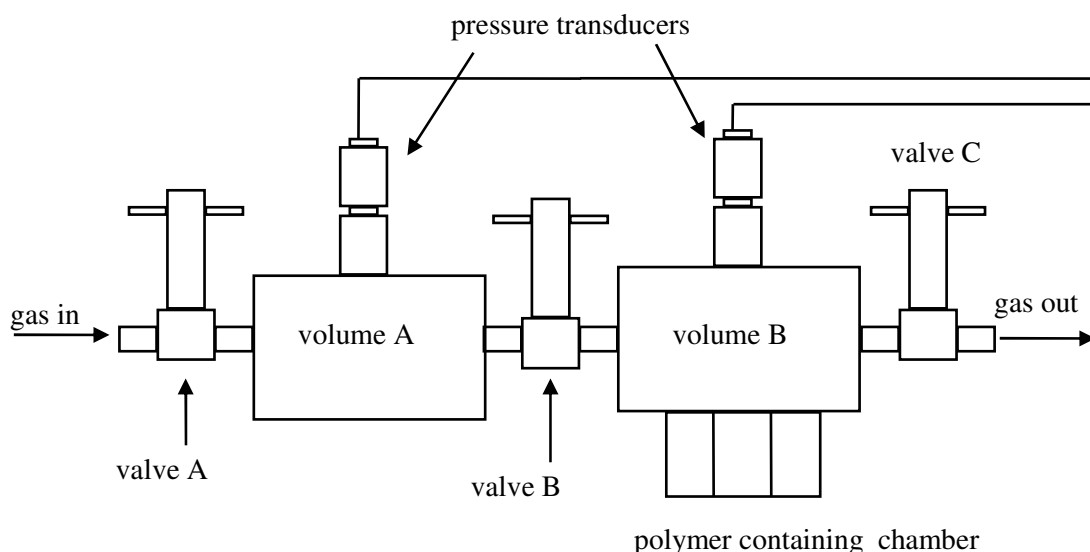


Figure 3.1 Schematic of pressure decay apparatus

The gas sorption measurement with this device is based on a rigorous mole balance. Initially, volumes A and B are evacuated and valves A, B and C are closed. An amount of CO_2/CH_4 gas mixture is injected into volume A and the pressure is monitored by the pressure transducer. Knowing the volume of chamber A, along with the compressibility, temperature, and pressure of the gas, the number of moles of gas in volume A is calculated. The gas is then introduced to the polymer in volume B by opening valve B. The pressure of volume B is monitored until no further change is seen. The number of moles remaining in volume B is calculated the same manner as for volume A. Then knowing the total number of moles of gas initially injected into the system, along with the number of remaining moles of gas in volume A and B, the amount of gas sorbed into the polymer is calculated. The reservoir and cell volumes were determined by the procedure shown in Appendix F. Statham pressure transducers (model PA822-1M-

16653) are used to measure the pressure and are powered by a Lauda 10DCV power source (Model LCS-A-1). The signal is measured with a Keithley 2000 Digital Multi-meter (DMM). The DMM is interfaced with a personal computer running National Instruments LabView™ software, which allows for visualization of the pressure decay and equilibrium and also for data collection. The resolution of the measurement is approximately ± 0.005 cc(STP) (Punsalan, 2001).

After the sorption measurement for the probe gas (CO_2 or CH_4) is performed, volumes A and B are evacuated and the mixed gas mixture is introduced. This work uses the following gas mixtures for conditioning experiments; 10/90 CO_2/CH_4 , 10/90 CO_2/CH_4 + 500 ppm n-heptane and 10/90 CO_2/CH_4 + 300 ppm toluene. The fibers were then conditioned for five days at the conditioning pressure used in the permeation experiments by closing valve B. Following conditioning, the probe gas is introduced through valves A and B at the same gas fugacity as in the gas mixture and by slowly opening valve C. The fugacity of CO_2 and CH_4 were calculated using the virial equation of state truncated after the second term (Smith and Van Ness, 1975). The gas compressibility is calculated from the equation of state shown in Appendix D. The probe gas is kept flowing for 15 to 30 minutes until all the components of the gas mixtures are displaced and then valves B and C are closed. The probe gas (CO_2 or CH_4) solubility is tested again. The gas in volume B is then introduced to volume A by opening valve B. It should be noted that the probe gas was depressurized gradually of approximately 10 psi and 50 psi increments for CO_2 and CH_4 sorption respectively. This is done to prevent "foaming" of the polymer, which is known to happen if a highly swelling penetrant is removed too quickly from a polymer sample (Fleming, 1988; Pope, 1991). The desorption steps are repeated until the pressure in volume B is close to zero. The total number of moles of gas sorbed following conditioning is then calculated. A sample calculation of the total number of moles is shown in Appendix E. From the total number of moles and the number

of moles desorbed in each single step, the desorption curve can be constructed. The sorption and desorption are then compared to see the effect of conditioning with CO₂/CH₄ mixture in the presence and absence of toluene and n-heptane.

The sorption system was initially tested for leaks after pressurizing to 900 psia CO₂ for more than five days. If the pressure deteriorates more than 5 psi, a leak exists and corrective action, such as tightening all fittings, is necessary. If no leaks are observed, the sorption system is presumed to have no detectable leaks as applicable and therefore it can be used for testing.

3.3 Results and Discussion

Since the magnitude of the conditioning effect was expected to be directly related to the level of the preswelling agent (toluene or n-heptane) in the 10/90 CO₂/CH₄ gas mixture used to condition the hollow fiber membranes, it was important to run the 10/90 CO₂/CH₄ case with no hydrocarbons (the base case). Shown in Figure 3.2 are CH₄ and CO₂ sorption isotherms for Matrimid® the hollow fiber membranes.

As is evident in both gases, the sorption isotherms increased only slightly over the 5 days “base case” conditioning period for either component. The higher - pressure regime of the sorption isotherm for the conditioned sample appears to be shifted a little bit upward compared to the unconditioned sample while sharing a similar slope. These trends are consistent with the dual mode sorption understanding of conditioning and suggest presumably an increase in the Langmuir capacity with negligible change in the Henry’s law constant as a result of gas conditioning. Table 3.1 shows the DMS model parameters determined for the experimental data from Figure 3.2.

Table 3.1 CH₄ and CO₂ / Matrimid® dual mode sorption parameters in unconditioned and conditioned samples with 10/90 CO₂/CH₄ mixture at 600 psia and 35 °C

Dual Mode Model Parameters	CO ₂		CH ₄	
	Unconditioned	Conditioned	Unconditioned	Conditioned
k_d [cc(STP)/cc psia] ($\times 10$)	0.17 (fixed)	0.17 (fixed)	0.02 (fixed)	0.02 (fixed)
b [psia ⁻¹] ($\times 10^2$)	0.07 (fixed)	0.07 (fixed)	0.01 (fixed)	0.01 (fixed)
C_H [cc(STP)/cc]	17.8 ± 0.19	18.6 ± 0.41	26.9 ± 0.13	27.5 ± 0.19
χ^2, R^2	0.87, 0.99	4.17, 0.99	0.68, 0.999	1.58, 0.99

To simplify interpretation of results, an unconstrained non-linear least squares fit to the DMS model is applied to all sorption data for a particular polymer-gas pair. Then an average of resulting Henry's law constants and the affinity constant are used for all data and are used as fixed parameter. This methodology is rationalized by the theory of dual mode sorption which postulates that k_D and b are intrinsic polymer/penetrant parameters and the relatively subtle effects studied here comply with the range of their applicability.

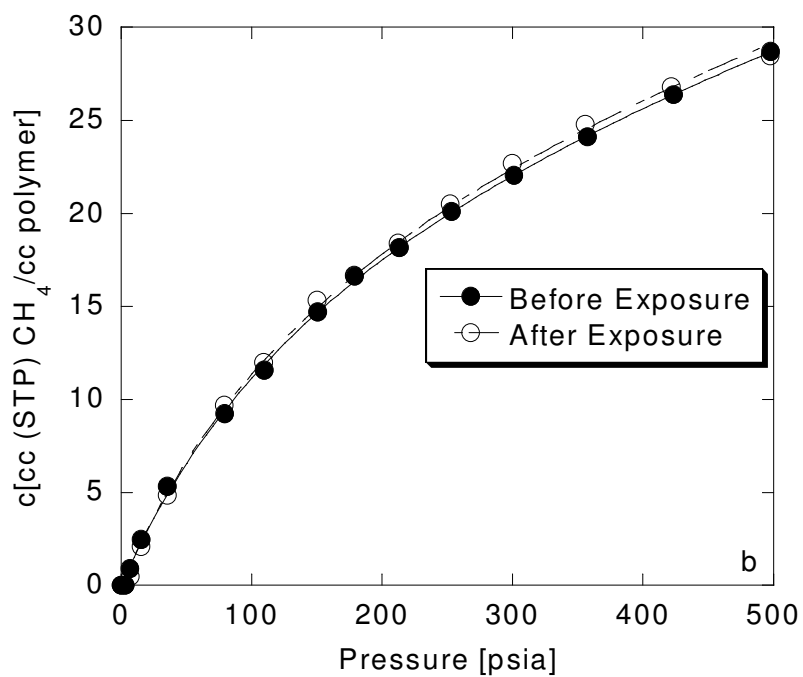
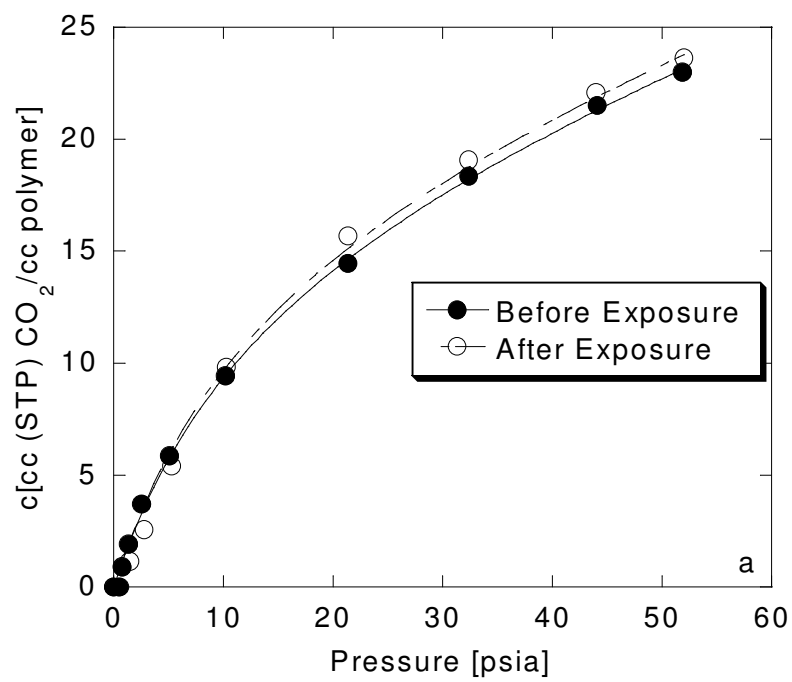


Figure 3.2 Effects of 10/90 CO₂/CH₄ mixture exchange conditioning at 600 psia and 35 °C on a) CO₂ sorption isotherms, and b) CH₄ sorption isotherms for asymmetric hollow fibers of Matrimid® conditioned.

Despite the added constraint on parameter determination, the resulting values for R2 are remarkably close to unity and the Chi-squared values are sufficiently low (Press et al., 1988) which suggests that the assumption of equal k_D 's and b's for conditioned and unconditioned samples is statistically reasonable. As reported in the above table, the increase in the Langmuir capacity constant is roughly only 1 cc(STP)/cc polymer for either gas; illustrating the minor effect of conditioning on sorption in the absence of the heavy hydrocarbons.

It was thought that conditioning the sample with the 10/90 CO₂/CH₄ with either toluene or n-heptane would give rise to a more swelled matrix, thus increasing the effects of conditioning. Therefore, it was expected that the sorption difference between the unconditioned and conditioned samples would be more, and in addition – the total sorption isotherms would shift more “upward” due to an increase in unrelaxed volume. To test this hypothesis - samples were conditioned with 10/90 CO₂/CH₄ + 300 ppm toluene over a period of five days, and then probed with CO₂ and CH₄ gases. The sorption results of these samples are shown in Figure 3.3 and the corresponding DMS parameters shown in Table 3.2. As expected, the increase in C'_H due to gas conditioning in these samples is slightly higher; however, the change in C'_H of 2.2 cc(STP)/cc polymer due to the five days conditioning period was smaller than might be expected based on the large increases seen in chapter 2 for the permeability of each component after hydrocarbon conditioning. The results in Table 3.2 show also that $\Delta C'_{H_{CO_2}} < \Delta C'_{H_{CH_4}}$ since $p_{CO_2} \gg p_{CH_4}$ due to the fact that CO₂ is being closer to its critical point. This shows that expectation of “filling up holes” may be too simplistic.

Table 3.2 CH₄ and CO₂ / Matrimid® dual mode sorption parameters in unconditioned and conditioned samples with 10/90 CO₂/CH₄ + 300 ppm toluene mixture at 600 psia and 35 °C

Dual Mode Model Parameters	CO ₂		CH ₄	
	Unconditioned	Conditioned	Unconditioned	Conditioned
k_d [cc(STP)/cc psia] ($\times 10$)	0.11 (fixed)	0.11 (fixed)	0.03 (fixed)	0.03 (fixed)
b [psia ⁻¹] ($\times 10^2$)	0.03 (fixed)	0.03 (fixed)	0.007 (fixed)	0.007 (fixed)
C_H [cc(STP)/cc]	27.1 ± 0.25	28.1 ± 0.49	14.0 ± 0.63	16.2 ± 0.38
χ^2, R^2	0.88,0.99	3.22,0.99	1.27,0.99	8.42,0.99

The samples conditioned with the 10/90 CO₂/CH₄ + 500 ppm n-heptane behaved similarly as the samples conditioned with the 10/90 CO₂/CH₄ + 300 ppm toluene. The results are shown in Figure 3.4 and the resulting dual mode parameters are reported in Table 3.3. The resulting values for R₂ are remarkably close to unity and the Chi-squared values are sufficiently low. Conditioning caused a slight increase in sorption capacity for both samples and, furthermore, this effect seems more pronounced in the 10/90 CO₂/CH₄ + 300 ppm toluene conditioned samples than the 10/90 CO₂/CH₄ + 500 ppm n-heptane conditioned samples. However, it should be noted that the uncertainty associated for that particular set of data is rather high with an error for CH' of 1.5 cc(STP)/cc polymer.

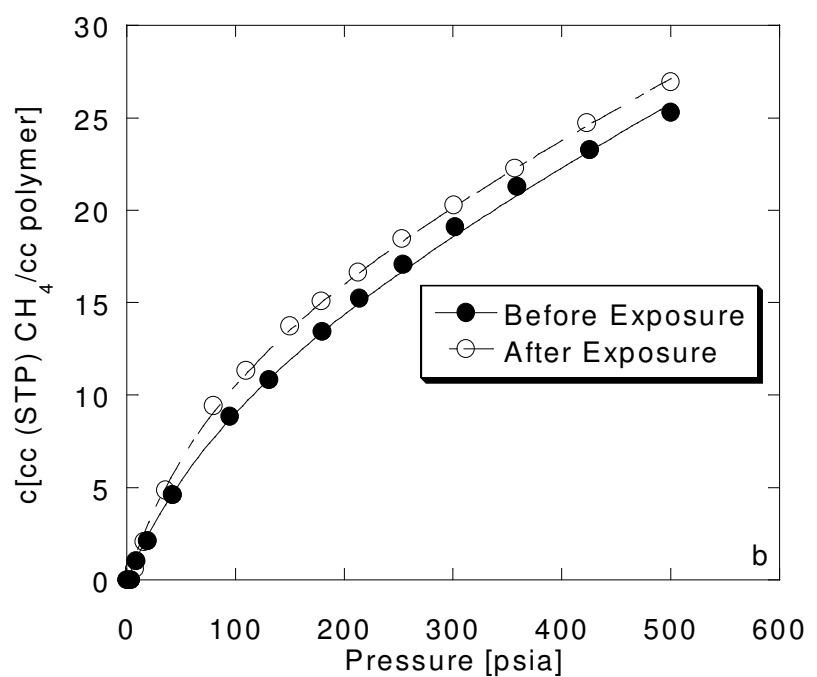
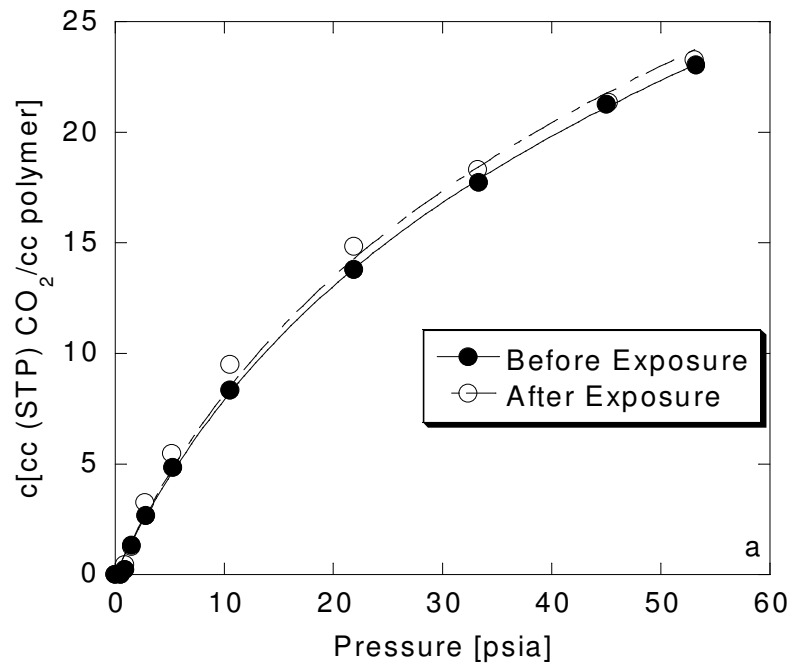


Figure 3.3 Effects of 10/90 CO₂/CH₄ + 300 ppm toluene mixture exchange conditioning at 600 psia and 35 °C on a) CO₂ sorption isotherms, and b) CH₄ sorption isotherms for asymmetric hollow fibers of Matrimid® conditioned.

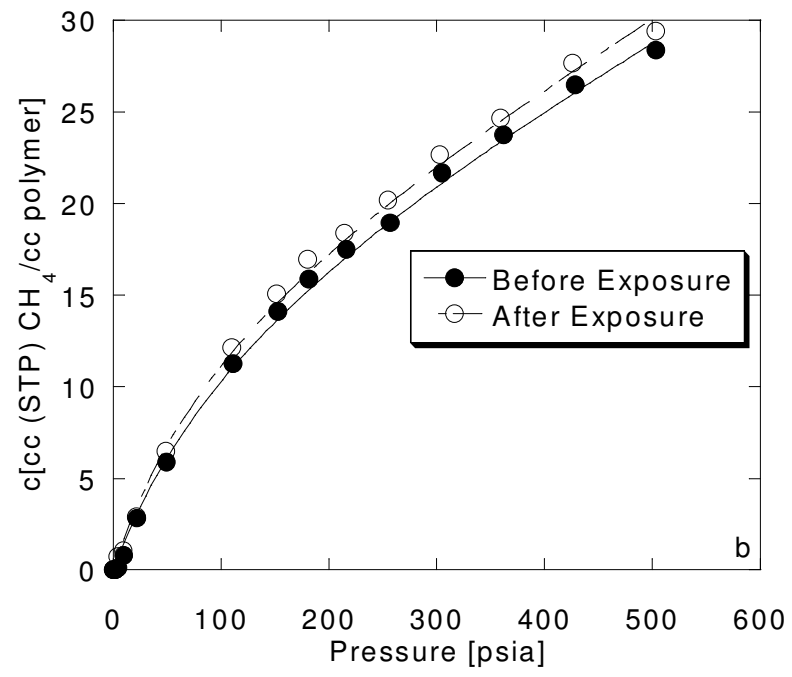
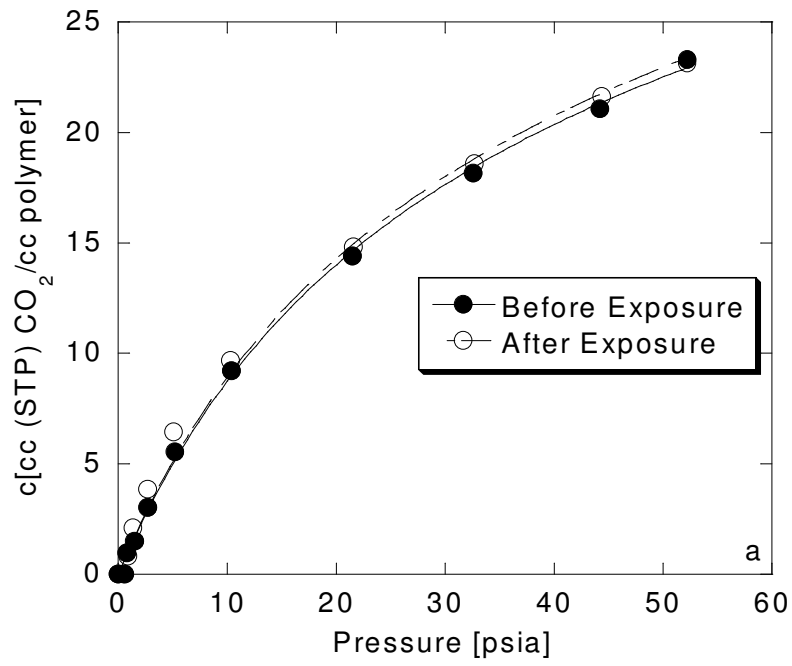


Figure 3.4 Effects of 10/90 CO₂/CH₄ + 500 ppm n-heptane mixture exchange conditioning at 600 psia and 35 °C on a) CO₂ sorption isotherms, and b) CH₄ sorption isotherms for asymmetric hollow fibers of Matrimid® conditioned.

Table 3.3 CH₄ and CO₂ / Matrimid® dual mode sorption parameters in unconditioned and conditioned samples with 10/90 CO₂/CH₄ + 500 ppm n-heptane mixture at 600 psia and 35 °C

Dual Mode Model Parameters	CO ₂		CH ₄	
	Unconditioned	Conditioned	Unconditioned	Conditioned
k_d [cc(STP)/cc psia] ($\times 10$)	0.05 (fixed)	0.05 (fixed)	0.03 (fixed)	0.03 (fixed)
b [psia ⁻¹] ($\times 10^2$)	0.04 (fixed)	0.04 (fixed)	0.007 (fixed)	0.007 (fixed)
C_H [cc(STP)/cc]	30.6 ± 0.27	31.4 ± 0.49	17.2 ± 0.19	18.8 ± 0.21
χ^2, R^2	1.03, 0.99	3.22, 0.99	2.08, 0.99	2.33, 0.99

This unusually high error is more than likely associated with the constraint that has been placed on the value of k_d and b . Therefore, it is difficult to draw a conclusion as if there is a large increase in the Langmuir sorptive capacity due to gas conditioning as a result of the 300 ppm toluene or the 500 ppm n-heptane in the 10/90 CO₂/CH₄ gas mixture. *In any case, the absolute value of the solubility coefficients for CO₂ and CH₄ as a function of pressure suggest that the gas conditioning affect the diffusion and diffusion selectivity much more than the solubility and solubility selectivity.* The solubility coefficient of a particular penetrant gas is equal to the concentration of gas penetrant in the polymer divided by its partial pressure in the gas phase;

$$S_i = C_i / p_i \quad (3.1)$$

The above sorption results after conditioning with 10/90 CO₂/CH₄, 10/90 CO₂/CH₄ + 500 ppm n-heptane and 10/90 CO₂/CH₄ + 300 ppm toluene can be reinterpreted in terms of Equation 3.1. Figure 3.5 and 3.6 shows the solubility

curve of CO₂ and CH₄ as a function of partial pressure at 35°C. The results again show that the solubility coefficient of CO₂ and CH₄ calculated using raw data are nearly close.

The separation factor of a membrane, if the downstream is held constant, for component i versus j , α_{ij} is defined by (Fleming, 1988);

$$\alpha_{ij} = P_i / P_j = [D_i / D_j] [S_i / S_j] \quad (3.2)$$

As indicated in equation 3.2, one can conveniently consider the overall selectivity to have two parts, a solubility $[S_i / S_j]$ coefficients and a mobility contribution $[D_i / D_j]$. This ratio, also called the ideal separation factor, is equal to the ratio of pure component permeabilities when external phase solution nonidealities are negligible and polymer phase plasticizing effects due to process stream components are not present.

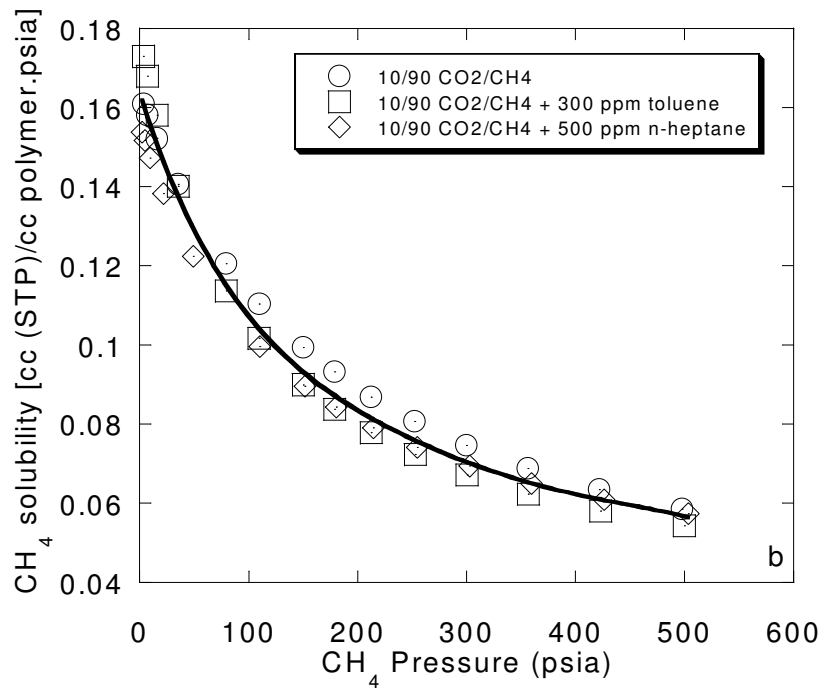
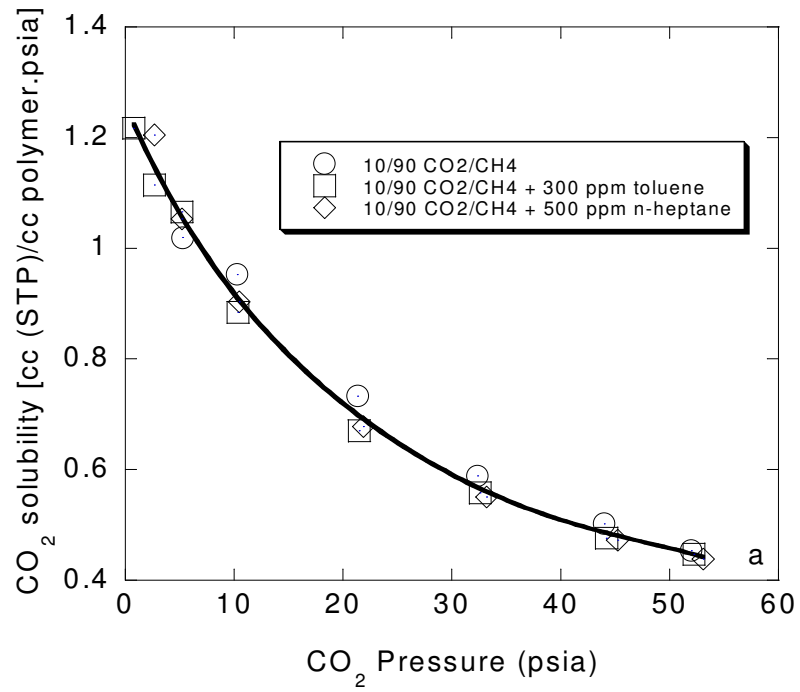


Figure 3.5 Solubility of CO₂ and CH₄ in conditioned samples with 10/90 CO₂/CH₄, 10/90 CO₂/CH₄ + 300 ppm toluene and 10/90 CO₂/CH₄ + 500 ppm n-heptane at 600 psia and 35 °C.

While these constraints seem restrictive, for many cases, they are often obeyed to a first approximation, and the data discussed in the following section have been collected in this way, so the data can be interpreted unambiguously in terms of equation 3.2.

3.4 Sorption and Permeation Data Analysis

Permeation through hollow fiber membranes can be described in terms of a simple one-dimensional diffusion model. The local flux of component i through the skin layer is given by the following expression (Crank, 1975):

$$N_i = -D_{eff}(C_t) \frac{dC_i}{dx} \quad (3.3)$$

where C_i is the concentration of component i , D_{eff} is the diffusion coefficient of component i and is a function of the total concentration, C_t and temperature. In this work, the total concentration is the sum of the concentration of CO₂ and CH₄.

The permeability can be defined as shown in equation 3.4 in terms of the steady state permeation flux through a membrane of thickness ℓ .

$$P = \frac{N}{\Delta p / \ell} \quad (3.4)$$

where N is the steady state flux, cc(STP)/(cm³.sec), and ΔP is the pressure difference between the upstream and downstream membrane faces (cm Hg). Substituting the expression for the flux given in equation 3.3 into equation 3.4 yields the permeability as a function of the local concentration gradient:

$$P = -D_{eff}(C) \frac{dC}{dx} \frac{1}{\Delta P} \quad (3.5)$$

Equation 3.5 can be rearranged and integrated for the appropriate boundary condition used in most of the experiments in this study: $C = C_2$ at $x = 0$ (upstream face of the membrane) and $C = 0$ at $x = \ell$ (downstream face of the membrane):

$$\int_0^\ell \frac{P}{\ell} dx = \int_0^{C_2} \left[\frac{D_{eff}(C) dC}{C_2} \right] \left[\frac{C_2}{p_2} \right] = \overline{SD} \quad (3.6)$$

where \overline{S} and \overline{D} are the average solubility and diffusivity coefficients (Koros, 1977).

The local diffusion coefficient can also be evaluated using equation 3.6, which allows analysis of permeability and solubility data to directly determine this coefficient at an arbitrarily selected upstream pressure p_2 , assuming the downstream pressure p_1 is negligible. Equation 3.7 is derived by applying the Liebnitz rule for differentiation under an integral sign to equation 3.6.

$$D_{eff}(C_i) = \left[P + p \left(\frac{dP}{dp} \right) \right]_{p_2} \left[\frac{dp}{dC} \right]_{p_2} \quad (3.7)$$

In state-of-the-art asymmetric membranes, the skin layer, ℓ , may be on the order of 1000 Angstroms thick and is thus difficult to reliably measure. Therefore, for the purpose of this calculation it is assumed that skin layer is 1000 Angstroms thick. We could also have assumed 1 cm instead. This should not greatly affect our conclusions since we are particularly interested in *relative diffusion coefficient changes* before and after conditioning and not in the absolute value of the diffusion coefficient. Since we are using permeance instead of permeability in equation 3.7, we multiply equation 3.7 by the skin thickness ℓ to obtain the diffusion

coefficient. Moreover, since we are dealing with virtually identical starting fibers, the analysis in terms of D/ℓ could also be done, but this will not change the key points here regarding changes in fundamental materials properties.

Figures 2.11-2.12 and Figures 2.20-2.21 show the CO₂ and CH₄ permeance results at 200 and at 600 psia and at 35 °C before and after conditioning to the 10/90 CO₂/CH₄, the 10/90 CO₂/CH₄ + 500 ppm n-heptane, and the 10/90 CO₂/CH₄ + 300 ppm toluene. A reduced permeability was used in the previous chapter to compare the relative permeability enhancements resulting from conditioning treatments in different fibers. In this chapter we use the actual CO₂ and CH₄ permeance results as a function of partial pressure of CO₂ and CH₄ in order to calculate $\frac{dP}{dp}$.

As can be seen in Figures 2.10-2.11 and Figures 2.19-2.20 for CO₂ and CH₄ before conditioning and after conditioning with the 10/90 CO₂/CH₄ and 10/90 CO₂/CH₄ + 500 ppm n-heptane, the permeance decreases with increasing pressure, which is typical of the dual mode behavior in glassy polymers. On the other hand after gas conditioning with the 10/90 CO₂/CH₄ + 300 ppm toluene mixture as can be seen in figures 2.12 and 2.21, the permeance is relatively independent of pressure. Although it is clear that the nature of the glassy polymer has been altered by the conditioning process, the reason for this difference in permeance slopes is not clear. For this reason, the permeance results were fitted with a polynomial equation in pressure instead of fitting the data to the dual mode-model. This approach avoids imposing model dependent constraints on the interpretation. The polynomial equation has the following form;

$$P = A + Bp + Cp^2 + Dp^3 \quad (3.8)$$

where A, B, C and D are the fitting parameters. Appendix G shows a summary of the fitting parameters for the CO₂ and CH₄ permeances at 35 °C before and after conditioning to the 10/90 CO₂/CH₄, the 10/90 CO₂/CH₄ + 500 ppm n-heptane, and the 10/90 CO₂/CH₄ + 300 ppm toluene at 200psia and 600 psia. The sorption results were also fitted with a four-term polynomial equation in pressure.

$$C = A + Bp + Cp^2 + Dp^3 \quad (3.9)$$

The fitting parameters are also summarized in Appendix G.

Using equation 3.9 and the fitting parameters for the sorption results, dC/dP can be calculated at each penetrant pressure. The permeance, P , and the tangent slope of the permeance versus the upstream pressure, dP/dp can be calculated readily from equation 3.8. Thus, we can now use equation 3.7 to get $D(c)$ versus c . Figures 3.6-3.7 show the percent change in the effective local diffusion coefficient of CO₂ and CH₄ at 35 °C conditioned with 10/90 CO₂/CH₄ mixture, 10/90 CO₂/CH₄ + 500 ppm n-heptane mixture, and 10/90 CO₂/CH₄ + 300 ppm toluene mixture relative to the diffusion coefficient before conditioning.

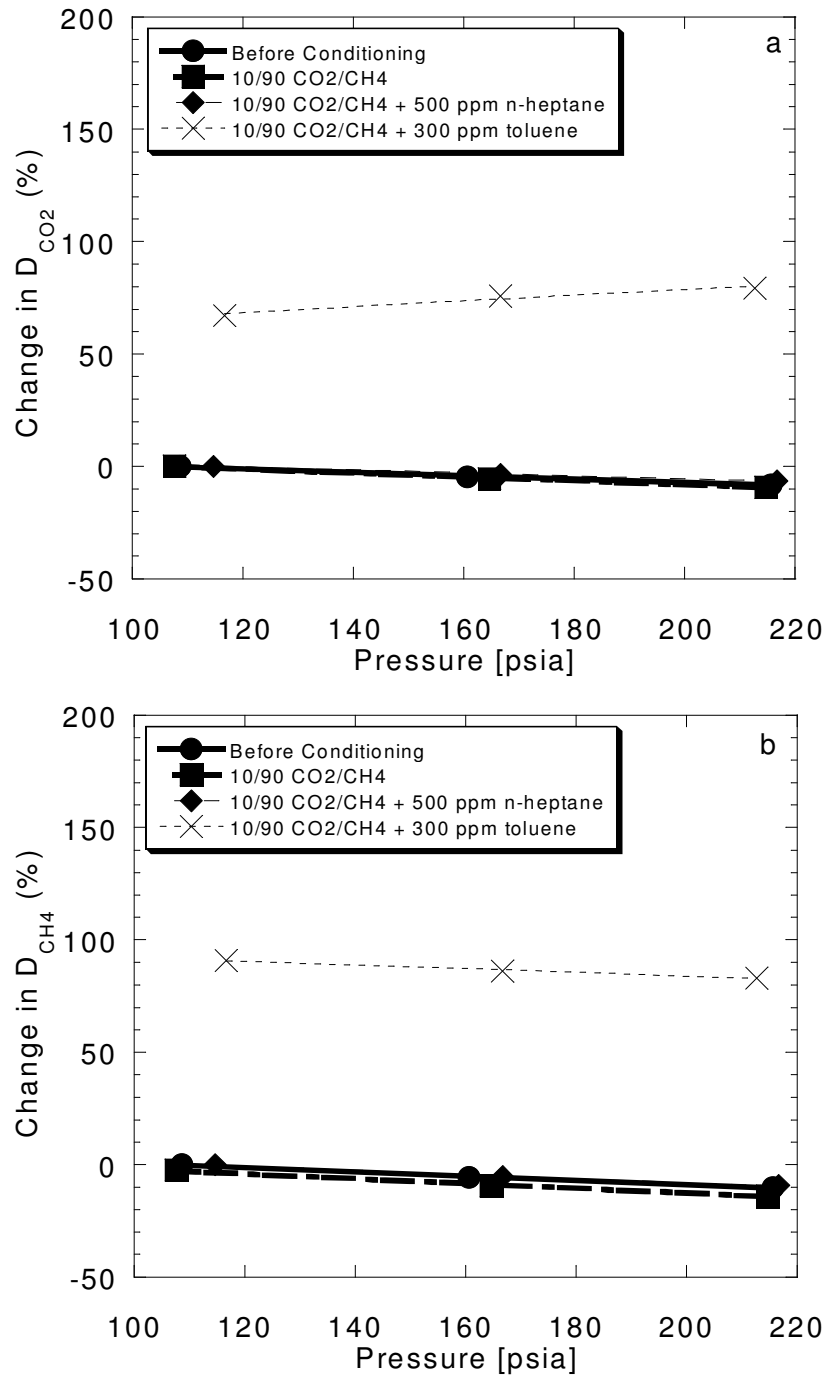


Figure 3.6 Change of a) CO₂ local diffusion coefficient and b) CH₄ local diffusion coefficient conditioned with 10/90 CO₂/CH₄ mixture, 10/90 CO₂/CH₄ + 500 ppm n-heptane mixture, and 10/90 CO₂/CH₄ + 300 ppm toluene mixture at 200 psia and 35 °C. Lines are “drawn by eye”

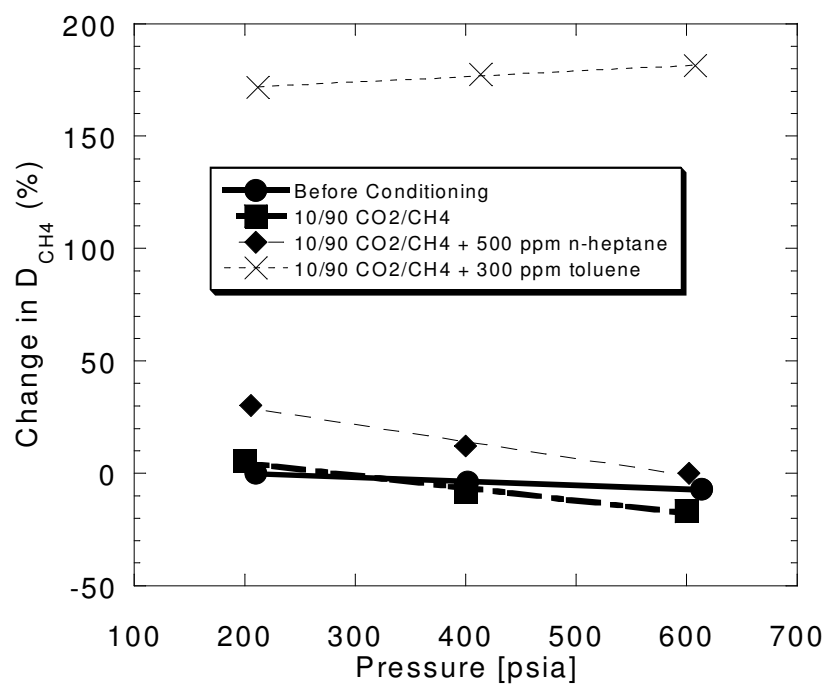
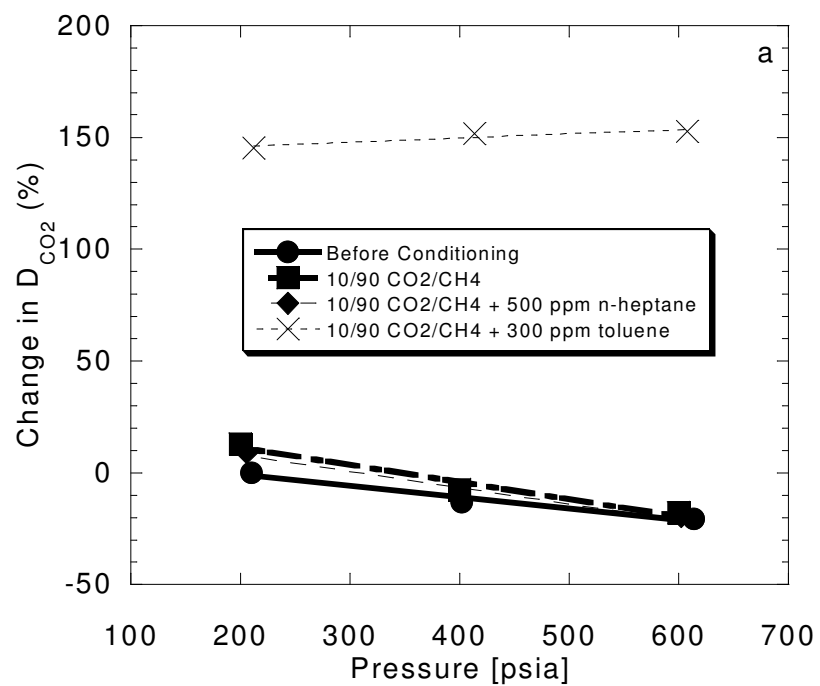


Figure 3.7 Change of a) CO_2 local diffusion coefficient and b) CH_4 local diffusion coefficient conditioned with 10/90 CO_2/CH_4 mixture, 10/90 CO_2/CH_4 + 500 ppm n-heptane mixture, and 10/90 CO_2/CH_4 + 300 ppm toluene mixture at 600 psia and 35 °C. Lines are “drawn by eye”

As noted earlier in the previous chapter, the 10/90 CO₂/CH₄ gas mixtures do not have the ability to produce a conditioning effect *at 200 psia* to the hollow fiber membranes compared to the 10/90 CO₂/CH₄ gas mixture in the presence of toluene. The permeabilities of both penetrants show virtually no increase after conditioning. The solubility selectivity of conditioned sample was essentially unchanged compared to the unconditioned samples. Since the permeability and the solubility selectivity is unaltered, changes in segmental packing and motion caused by the conditioning treatment of the 10/90 CO₂/CH₄ gas mixture at 35 °C and 200 psia are believed not to have affected the mobility selectivity of the conditioned matrix as can be seen in figures 3.6 for the CO₂ and CH₄.

For the case of conditioning with the 10/90 CO₂/CH₄ gas mixture at 35 °C and *600 psia*, reported earlier, the mixed gas permeabilities values of CO₂ and CH₄ after conditioning were higher than values before conditioning. This increase in the mixed gas values was discussed and explained earlier in the previous chapter in terms of an increase in the number of hypothetical gaps due to an increase in the conditioning pressure. Therefore, the larger increase in CO₂ and CH₄ permeabilities following the conditioning with the 10/90 CO₂/CH₄ gas mixtures for the hollow fiber membrane samples at 600 psia versus 200 psia seems reasonable. On the other hand, the overall selectivity is effectively constant. In addition, the conditioning treatment with the 10/90 CO₂/CH₄ causes no significant change in the solubility of either penetrant in the conditioned fibers. This suggests that the solubility selectivity should indeed remain essentially constant before and after conditioning. Therefore, since the solubility of both penetrants is not greatly affected after conditioning, and because diffusivity selectivity is the only other selectivity mechanism, the diffusivity selectivity is expected to increase. This result is shown in Figure 3.7a and 3.7b. The sorption and permeation measurements have shown that the major effect of the CO₂ conditioning treatment is to introduce residual packing disruptions in the matrix, without significantly

increasing the number of Langmuir sites present in the polymer. These subtle packing disruptions act as a source of locally available volume that reduces the amount by which the penetrant needs to dilate the matrix during sorption in order to be accommodated. This important conclusion shows that the idealized dual mode sorption vision of conditioning primarily affecting the Langmuir capacity constant, and hence K_j constant calculated by the following equation;

$$K_j = \frac{C'_{Hj} b_j}{k_{Dj}} \quad (3.10)$$

is simply not adequate to understand the full range of permeation and diffusion behavior. The C'_{Hj} in equation 3.10 is the Langmuir capacity constant, k_{Dj} is the Henry's law constant of component j which characterizes the sorption in the dense region of the polymer matrix; b_j is a constant that is a measure of the affinity of the penetrant to the Langmuir sites

Based on the preceding discussion, a natural question arises concerning the behavior of the CO₂ and CH₄ components in the 10/90 CO₂/CH₄, following a conditioning treatment with the 10/90 CO₂/CH₄ + 500 ppm n-heptane mixture at 200 psia and 600 psia. This issue was treated earlier in chapter 2. It was shown that the increase in CO₂ permeability was essentially negligible *in the presence of n-heptane at 200 and 600 psia*. In fact, CO₂ permeability is slightly lowered by the presence of n-heptane. In addition, the conditioning treatment resulted in tolerable losses in permselectivity as discussed in chapter 2. The net effect of the conditioning treatment is to produce small selectivity losses of 3% and 14% for conditioning pressure of 200 psia and 600 psia, respectively. Figure 3.6 and 3.7 show the hysteretic results of the CO₂ and CH₄ diffusion coefficient before and after conditioning for fibers that were conditioned with 10/90 CO₂/CH₄ + 500 ppm n-heptane mixture, at 200 psia and 600 psia for 5 days. A higher CH₄ diffusion coefficient was observed at 600 psia in the conditioned sample compared with that

in the unconditioned sample. Methane, itself cannot produce a hysteresis in permeability, but it can maintain a state of increased permeability in a film that has been conditioned by 10/90 CO₂/CH₄ + 500 ppm n-heptane at 600 psia. Similar to the methane, n-heptane does not have the ability to produce a similar conditioning effect by itself as the CO₂ does as can be seen by comparing the CO₂ diffusion coefficients results in Figure 3.7a after conditioning with 10/90 CO₂/CH₄ and 10/90 CO₂/CH₄ + 500 ppm n-heptane. Presumably, the conditioning effect caused by 10/90 CO₂/CH₄ + 500 ppm n-heptane was not completely lost, as the solubility of CH₄, was still high enough to prevent total consolidation of the matrix.

It is hypothesized that there is shift in the free volume distribution, as discussed in chapter 2, caused by sorbing n-heptane. This shift in free volume is more important in facilitating an increase in the diffusion coefficient of CH₄ and only a moderate increased CO₂ diffusion coefficient. Assuming a shift in the free volume distribution to high chains spacings leads to low selectivity. This is reasonable, since disruptions of the packing presumably make it easier to insert CH₄ between segments in a molecularly dissolved state. Normally, this would be expected to result in an increase in the diffusion coefficient of CH₄ and a decrease in the diffusivity selectivity. The solubility CO₂ and CH₄ of the conditioned sample increased slightly compared to the unconditioned samples as discussed in the previous section. The magnitude of this change is not much beyond the experimental accuracy of the equipment, so it is hard to say how significant this increase in solubility is. We currently believe that solubility of CO₂ and CH₄ is not greatly affected by the conditioning treatment in all three conditioning experiments with; 10/90 CO₂/CH₄ mixture, 10/90 CO₂/CH₄ + 500 ppm n-heptane mixture and 10/90 CO₂/CH₄ + 300 ppm toluene mixture. *Therefore, the increased CO₂ and CH₄ permeability observed at 600 psia is believed to be due to increases in the value of the diffusion coefficients.*

As discussed in chapter 2, the 10/90 CO₂/CH₄ + 300 ppm toluene mixture conditioning increases the permeability of CO₂ and CH₄ in exchange experiments with a 10/90 CO₂/CH₄, mixed gas feed. Unlike the 10/90 CO₂/CH₄ + 500 ppm n-heptane mixture, marked differences were seen for the CO₂ and CH₄ permeabilities after conditioning with the 10/90 CO₂/CH₄ + 300 ppm toluene. We currently believe that the ability of toluene, to induce and maintain conditioning in the glassy matrix is due primarily to its much higher solubility coefficient compared with n-heptane; however, additional more subtle penetrant polymer interaction and even shape factors of the flat toluene versus the linear n-heptane may be at play. Even the qualitative dependence of CO₂ and CH₄ permeabilities after conditioning is clearly different for the 10/90 CO₂/CH₄ + 300 ppm toluene as compared to the 10/90 CO₂/CH₄ + 500 ppm n-heptane conditioning which show typical dual-mode behavior in the conditioned samples.

This qualitative difference, which is suggestive of conditioning enhanced increases in CO₂ and CH₄ permeabilities is clearly not apparent for either the 10/90 CO₂/CH₄ or 10/90 CO₂/CH₄ + 500 ppm n-heptane mixtures. As discussed above in the context of the 10/90 CO₂/CH₄ and the 10/90 CO₂/CH₄ + 500 ppm n-heptane conditioning, the solubility is presumably unchanged. While the increase in the solubility of CO₂ and CH₄ following conditioning was qualitatively similar between the three gas conditioning mixtures, the relative increases are somewhat different. *Within the experimental accuracy, the increases in the gas solubility of CO₂ and CH₄ for the three cases studied, are identical.* Therefore, the CO₂ and CH₄ permeabilities enhancements are largely due to increases in the average diffusion coefficients. If one considers the CO₂ and CH₄, 300 ppm toluene exchange conditioned permeability data for the 200 psia conditioning pressure, the CO₂ and CH₄ diffusion coefficients calculated using equation 3.7 are higher by 75% and 87% for the CO₂ and CH₄ materials compared to the unconditioned, as-received samples (or the 500 ppm n-heptane conditioned samples) as shown in

Figure 3.5. These changes are significant, since conditioning of the samples at 200 psia with 10/90 CO₂/CH₄ or 10/90 CO₂/CH₄ + 500 ppm n-heptane has essentially *no ability* to condition the fibers.

In addition, fibers were exchange conditioned at 600 psia for five days with the 500 ppm n-heptane or 300 ppm toluene. Then, the 10/90 CO₂/CH₄ + 300 ppm toluene or 500 ppm n-heptane was completely replaced by 10/90 CO₂/CH₄ at 600 psia, and the fibers were maintained at this pressure for 1-2 hours to ensure that steady state had been reached. The results for the diffusion coefficient at 600 conditioning pressure are shown in Figs. 3.7. The conditioning treatment results in a 150% increase in CO₂ diffusion coefficient, and a 177% increase in CH₄ diffusion coefficient. The mobility selectivity is slightly decreased. As was the case at 200 psia, the conditioning treatment allows significant enhancement of the permeability at 600 psia without sacrificing selectivity. The latter fact, that selectivity is maintained suggests that CO₂ and CH₄ must somehow compete for additional jumps opportunities. This highly surprising result suggests that the simplistic arguments based on Figures 3.6 and 3.7 are not valid in actual mixed gas situations.

The CO₂ and CH₄ average diffusion coefficients enhancements are largely due to increases in the excess free volume generated during the conditioning treatment. Since the three samples were conditioned at a similar pressure, it is believed that the amount of free volume added to each of the matrices should be different. The increase in free volume for the samples conditioned with either the 10/90 CO₂/CH₄ or the 10/90 CO₂/CH₄ + 500 ppm n-heptane gas mixtures is significantly smaller than the free volume added for the sample conditioned with the 10/90 CO₂/CH₄ + 300 ppm toluene gas mixture. On the other hand, introduction of actual penetrant-scale defects is not suggested here since this mechanism will lead to increases in C'_H , which was not seen in our sorption

results. We are tempted by this view, since the membrane is not apparently damaged and with only slight loss in selectivity.

A useful way of interpreting the above results can also be seen in terms of the following expression for the effective local diffusion coefficient in systems that obey the dual mode model (Fleming, 1988):

$$D_{eff} = \frac{D_D [1 + FK / (1 + C_D b / k_D)^2]}{[1 + K / (1 + C_D b / k_D)^2]} \quad (3.11)$$

After conditioning, presumably C_H' remains constant from the sorption experiments, and hence K in equation 3.11. It is also hypothesized that conditioning does not affect k_D or b as discussed above. C_D , is the fraction of the total sorption attributed to dissolution into the polymer. The value of $F = D_H / D_D$, is typically small (< 0.1) for CO_2 and CH_4 . In the high pressure region, where $C_D b / k_D$, is large compared to unity, increases in D_{eff} is mainly due to increase in D_D as shown below in equation 3.12;

$$D_{eff} = D_D \quad (3.12)$$

At low pressures, $C_D b / k_D$, is small compared to unity and equation 3.11 reduces to equation 3.13:

$$D_{eff} = \frac{D_D [1 + FK]}{[1 + K]} \quad (3.13)$$

So increased values of D_D cause an increase in the local diffusion coefficient, since the other quantities remains constant. Therefore, the increased permeabilities after conditioning with the 10/90 CO_2/CH_4 subtle disruption or ‘loosening’ of the equilibrium packing is what causing the diffusivity referred to

as D_D , in equation 3.13 to increase by facilitating movement through the more open matrix. This can be understood, since the increase in C'_H or unrelaxed volume is presumably negligible.

This appears more descriptive of what actually happening, since the selectivity is essentially not much affected. Nevertheless, the number of jump opportunities increased for both CO₂ and CH₄, so D_D increased. The addition of toluene mostly involves filling up holes and reorganizing small holes to accommodate penetrants in low energy sites. The actual making of dissolved sorption sites will presumably not lead to huge holes after the toluene is removed. As a result, it is probable that all that happens is for the effective packing to slightly disturbed and few large (high energy) new gaps persists.

The large enhancements in the permeability of CO₂ and CH₄ following conditioning with the 10/90 CO₂/CH₄ +300 ppm toluene can be also rationalized by examining the free volume changes of the polymer. The free volume approach has proved particularly useful for a description of the effect of various factors on D_D in polymers above T_g through the corresponding changes in fractional free volume. In this work, the change in free volume will be reflected by a change in D_D since the toluene induced swelling effects are weak on the excess free volume of the polymer. According to Fujita (Fujita et al., 1961), the diffusion coefficient can be given by the expression for CO₂ and CH₄:

$$D_{CO_2}^* = RTA_d^{CO_2} \exp(-B_d^{CO_2}/v_f) \quad (3.14a)$$

$$D_{CH_4}^* = RTA_d^{CH_4} \exp(-B_d^{CH_4}/v_f) \quad (3.14b)$$

where R is the universal gas constant; T is the absolute temperature; v_f is the volume fraction of the free volume, i.e., the fractional free volume of the system comprised of penetrant and amorphous polymer; $A_d^{CO_2}$, $A_d^{CH_4}$, $B_d^{CO_2}$ and $B_d^{CH_4}$ are

characteristic parameters which depend on the size and shape of the penetrant molecules CO₂ and CH₄. The four parameters are taken to be independent of temperature and penetrant concentration. It is further assumed that the dependence of A_d and B_d on conditioning is negligible. Clearly, changes in the effective distribution of free volume shown speculatively in figure 2.23 may call this “zero order” assumption into question, but it still is a useful starting point for any such analysis. Denoting the diffusion coefficient before conditioning by D_u and the diffusion coefficient after conditioning by D_c , we can write the following;

$$\frac{v_{fc} - v_{fu}}{v_{fc}v_{fu}} = \ln \left[\frac{D_c}{D_u} \right] / B_d \quad (3.15)$$

With the further assumption that $B_d = 1$, the increase in the fractional volume can be calculated. Again, the last assumption is only a rather crude approximation for strongly interacting penetrants. B_d according to a more rigorous and complex treatment (Vrentas and Duda, 1977) depends on the size of the polymer jumping unit. Tables 3.4 show the percent increase in diffusion coefficient of CO₂ and CH₄ and the percent increase in the fractional free volume for samples conditioned with 10/90 CO₂/CH₄ + 300 ppm toluene at 200 psia, 600 psia and 35 °C.

The results in Table 3.4 enable us to draw some conclusions. The tendency of the D_D to increase with pressure or concentration (swelling effect) is interpreted on the basis of the higher fractional free volume of the liquid penetrant relative to the pure polymer (assuming additivity of volumes upon mixing). It follows that, in the 10/90 CO₂/CH₄ + 300 ppm toluene mixture, mutual enhancements of diffusion rates can be expected according to the relation;

$$v_f = v_{f0} + \gamma_{C_6H_6CH_3} v_{C_6H_6CH} + \gamma_{CO_2} v_{CO_2} + \gamma_{CH_4} v_{CH_4} \quad (3.16)$$

where v_{fo} is the fractional free volume of the pure polymer at some reference temperature T_s and pressure p_s . Furthermore, on the basis of the relative changes in the diffusivity suggests an increase in D_D for a given gas with the concentration of toluene in the polymer. If these phenomena can be merged with the traditional dual mode sorption and transport model for glassy polymers, modelling of conditioning and complex phenomena will be feasible. This would be a valuable focus for future work.

Table 3.4 Percent change in fractional free volume for CO₂ and CH₄ in conditioned samples with 10/90 CO₂/CH₄ + 300 ppm toluene mixture at 200 psia, 600 psia and 35 °C

Conditioning Pressure, psia	Component	% Change in diffusivity	% Change in fractional free volume
200	CO ₂	75	432
	CH ₄	87	447
600	CO ₂	150	501
	CH ₄	177	518

3.5 Conclusions

The following conclusions can be made about the sorption experiments;

- The solubility results indicate negligible increases in the solubility after conditioning with the three conditioning gas mixtures; 10/90 CO₂/CH₄, 10/90 CO₂/CH₄ + 500 ppm n-heptane, and 10/90 CO₂/CH₄ + 300 ppm toluene gas mixtures. These changes are within the experimental accuracy of the sorption equipment. Therefore, it is hard to draw a conclusion about the effect of conditioning on the solubility selectivity. It is believed that under the conditions studied, the solubility of CO₂ and CH₄ are not much affected by the conditioning treatment, so that the major contribution to the increased permeability following conditioning is an increase in diffusivity.

- Conditioning treatments had negligible effects on the Langmuir capacity constant, and therefore it affects diffusion in the dense matrix much more than in the free volume sites.
- The relative changes in the diffusion coefficient before and after conditioning for CO₂ and CH₄ have been found to be dependent on the conditioning pressure.
- The increases in diffusivity following conditioning with 10/90 CO₂/CH₄, and 10/90 CO₂/CH₄ + 500 ppm n-heptane were found to be negligible due to the weak conditioning effects on permeability.
- Conditioning increased the diffusion coefficients 115% and 155% for CO₂ and CH₄ respectively following conditioning with 10/90 CO₂/CH₄ + 300 ppm toluene at 35 °C and 600 psia. Similarly for samples conditioned with 10/90 CO₂/CH₄ + 300 ppm toluene at 35 °C and 200 psia, the diffusion coefficients increased 60% and 80% for CO₂ and CH₄ respectively.
- The largest increase in CO₂ and CH₄ permeabilities, at a given conditioning level, observed for samples conditioned with 10/90 CO₂/CH₄ + 300 ppm toluene is due to large increases in the fractional free volume at given conditioning pressure as compared to samples conditioned with 10/90 CO₂/CH₄ and 10/90 CO₂/CH₄ + 500 ppm n-heptane gas mixtures.

Chapter 4: Thermodynamics of Morpholine /Diglycolamine® / Water / Carbon Dioxide

The removal of acid gases by the amine process is accomplished by a chemical reaction. The alkanolamines most commonly used in industrial applications are monoethanolamine (MEA), diethanolamine (DEA), methyldiethanolamine (MDEA), and diglycolamine (DGA). DGA is a primary amine, and its low vapor pressures permits its use in higher concentrations, typically 50 to 60 weight percent, resulting in significantly lower circulation rates and energy requirements (LRGCC, 2003). DGA systems are normally installed with reclaimers to maintain solvent quality by reducing corrosion, foaming and degradation of the solvent. Research and experience have shown that DGA can thermally degrade in reclaimers to produce MOR (Harruff, 1992). The main objective of the present study is to determine thermodynamic characteristics of MOR/DGA/H₂O, MOR/H₂O and DGA/H₂O. This chapter explains how thermodynamics affects the performance of the CO₂ absorption process using DGA.

Thermodynamics of aqueous amine systems are crucial to understanding their industrial use to remove acid gas from process gas streams. The equilibrium partial pressure of acid gas above a solution of the amine defines pinch conditions for the absorber and stripper. Speciation of the amine and reaction products define the driving force for the forward and reverse reactions with CO₂. An understanding of this is important since the reactions are usually rate controlling. Furthermore, a consistent thermodynamic model can quantify the energy required for regenerating the solvent and solvent losses due to amine volatility.

Amine vaporization losses have become an important factor in operating gas plants due to increased chemical costs. Amine vaporization losses can be calculated based on vapor pressure data of the specific amine and the gas stream temperature and pressure. Using a consistent thermodynamic model, an estimate of amine losses can be obtained for the absorber, flash vent tanks and stripper. These are the three areas of vapor losses in alkanolamine treating systems.

The thermodynamic model provides information on the heats of absorption. Solvents with higher reactivity as indicated by higher forward reaction rate constants tend generally to have higher heats of absorption and therefore they may require more energy for regeneration and may be more difficult to regenerate. The amine reactivity of MOR, DGA and their blends is the subject of chapters 5 and 6.

The thermodynamic model can also provide information on the solvent capacity. The solvent capacity establishes the solvent circulation rate, which has a major impact on both plant investment and operating cost of the systems. The solvent circulation rate has a direct impact on the size of the absorber tower, piping system, circulation pumps, and size of the regenerator facilities. In general, 50 to 70% of the plant investment is directly associated with the magnitude of the solvent circulation rate.

A good amine solvent is the one that has higher CO₂ absorption capacity, faster CO₂ absorption rates, and lower vapor pressure. Therefore, these three most important cost factors – working capacity, regeneration energy duty and amine losses – will be discussed and estimated in this chapter.

Blended amine solvents have been studied by several researchers. Austgen (1989) studied the thermodynamics of MDEA blends with MEA, DEA and DGA using the electrolyte NRTL model. Posey (1996) improved the models by studying the activity coefficient of the amines at infinite dilution.

Pacheco et al. (2000) studied the absorption of CO₂ into aqueous DGA/MDEA blends. Glasscock (1990) and Critchfield (1988) have studied blends of DEA and MEA/MDEA. Littel et al. (1992 I&II) as well as many others have studied a variety of tertiary amines promoted by primary or secondary amines.

Specifically, this work will use the thermodynamic frameworks presented by Bishnoi and Rochelle (2000), Austgen et al. (1989) and Posey and Rochelle (1997). VLE data acquired by Martin et al. (1998) and Dingman et al. (1999) for the DGA system will be also used. The N₂O data obtained by Versteeg and Van Swaaij (1988) for the DGA and MOR systems will also be used in this work. A wetted wall column was used to measure CO₂ solubility. The solubility of N₂O in amine aqueous solutions was measured by using a solubility apparatus, similar to those presented by Al-Ghawas et al. (1989) and Haimour et al. (1984). The N₂O apparatus has been built in this work. The C13 NMR experiments were run on a Varian INOVA-500 machine. Parameters of the electrolyte NRTL model were adjusted in order to match the CO₂ solubility data, C13 NMR data, and the N₂O solubility data. The fitted model was then used to estimate the solvent working capacity, heat of reaction and vaporization losses for the DGA and the MOR/DGA blend systems.

4.1 Experimental Methods

Wetted Wall Column: Solubility of carbon dioxide was determined using a wetted-wall column (Figure 4.1). This contactor was designed and constructed by Mshewa (1995), then modified by Pacheco (1998). This apparatus was also used by Dang (2001), and Cullinane (2002). The column was constructed from a stainless-steel tube of 1.26 cm outside diameter with an exposed length of 9.1 cm. The interfacial area for mass transfer was 38.52 cm².

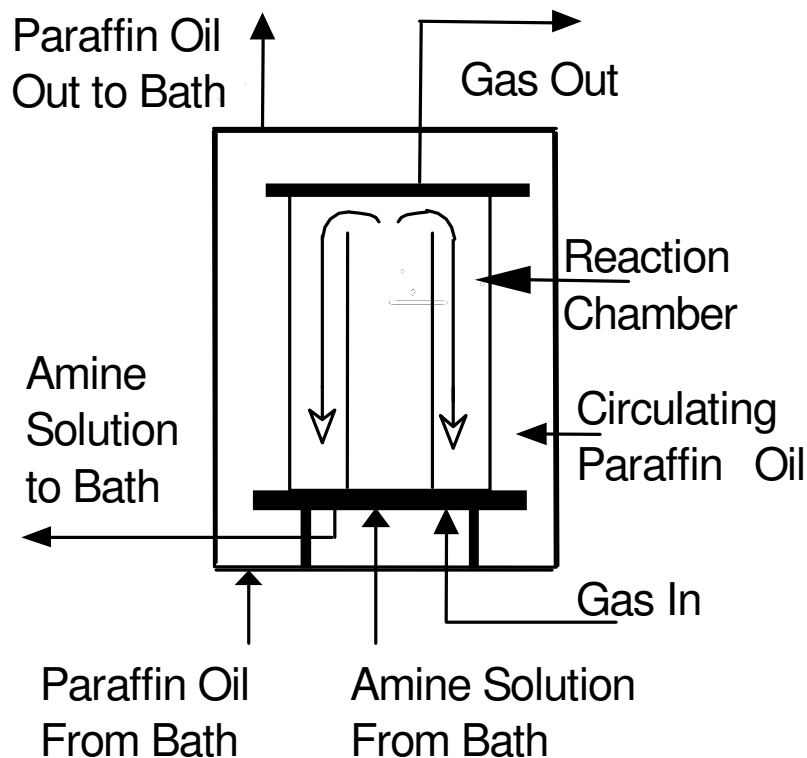


Figure 4.1 Detailed diagram of the wetted-wall column contactor.

Figure 4.2 represents the overall flow diagram of the experimental set up. The amine solution was contained in a 1000 cm³ stainless-steel reservoir in a heating bath at the temperature of the experiment. The gas stream fed to the contactor was either pure CO₂ or a mixture of N₂ and CO₂. This gas stream was presaturated with water at the temperature of the experiment. CO₂ gas concentration was determined continuously by two infrared analyzers (HORIBA model PIR- 2000) in series with ranges of 0-1 and 0-25% CO₂. The gas from the reactor was cooled by ice water to remove water from the gas phase to protect the CO₂ analyzer. The contactor was operated at a total pressure from 1 to 9 atm. The chemical solvent was circulated by a Cole-Parmer micropump.

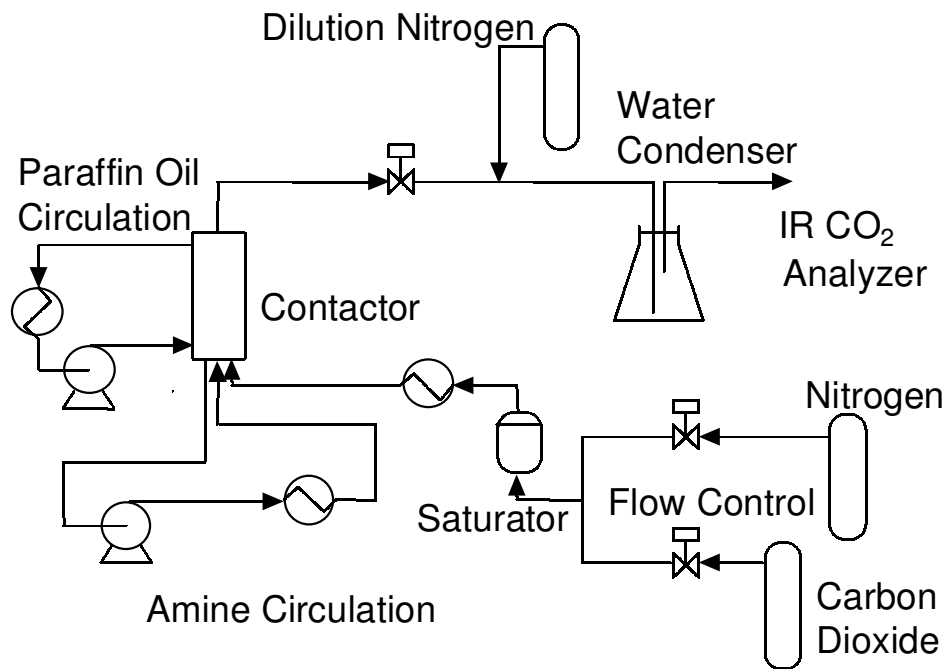


Figure 4.2 Flow diagram of the experimental setup.

The liquid flow rate was controlled at $2\text{-}3\text{ cm}^3/\text{s}$ to maintain a smooth liquid film. The liquid level at the bottom of the reactor was maintained at approximately the same point where the gas is fed. A small amount amine solution was added or withdrawn from the sample plot in order to keep the liquid level in the wetted wall column constant. J-type thermocouples were used in the solution inlet and outlet lines to the reactor for temperature measurement. Measurements of both CO_2 absorption and desorption were made with a continuously changing solution loading. Every 10-15 min the output of the analyzers, total pressure, and temperatures were recorded and a liquid sample was obtained to determine the CO_2 loading. The amount of total CO_2 (free CO_2 plus chemically combined) in the liquid phase was determined using a total carbon analyzer, model 525 from

Oceanography International Corporation. The CO₂ was carried by a nitrogen stream which bubbles through the acid solution to an infrared analyzer HORIBA model PIR-2000 with a range of 0-0.25% CO₂. This analyzer was calibrated using a standard solution of 7 mM sodium carbonate. Commercial grade DGA and MOR with a purity of not less than 99% were used in the experimental work.

In this work, at any given loading, both absorption and desorption rates were measured by variation of CO₂ partial pressure around the equilibrium partial pressure. When the flux is equal to zero, the partial pressure of CO₂ will be the equilibrium partial pressure of CO₂ at that loading. This point can be found by bracketing the absorption and desorption rates. Figure 4.3 gives an example with 11 wt% MOR/53 wt% DGA at CO₂ loading of 0.13 mol/mol amine and 40 °C. In figure 4.3, the interfacial pressure of CO₂, $P_{CO_2,int}$, was calculated by;

$$P_{CO_2,int} = P_{CO_2,b} - \text{flux} / k_g \quad (4.1)$$

where, $P_{CO_2,b}$ is the log mean CO₂ partial pressure in the gas phase, k_g is the gas film mass transfer coefficient. The gas film coefficient was determined by the absorption of sulfur dioxide into sodium hydroxide solutions (Bishnoi, 2002). The gas film mass transfer coefficient is given by:

$$Sh = 1.075 \left(Re \cdot Sc \cdot \frac{d}{h} \right)^{0.85} \quad (4.2)$$

where d is the hydraulic diameter of the annulus (0.44 cm), h is the length of the column (9.1 cm), Sh is Sherwood number, Re is Reynolds number and Sc is Schmidt number. Appendix H tabulates the detailed CO₂ solubility experimental data. While inferring the equilibrium partial pressure, only measurements close to equilibrium were considered. By applying the same method to every loading, CO₂ equilibrium partial pressure can be determined at a number of solution loading.

The liquid film mass transfer coefficient of the wetted wall column was measured by Mshewa (1995) and Pacheco (1998) by carbon dioxide desorption

from water and ethylene glycol mixtures. The model solves momentum balance equations (Bird et al., 1960) for a falling film to determine the film thickness (δ) and surface velocity (u_{surf}) where W is the wetted perimeter length.

$$\delta = \sqrt[3]{\frac{3\mu Q}{\rho g W}} \quad (4.3)$$

$$u_{\text{surf}} = \frac{\rho g \delta^2}{2\mu} \quad (4.4)$$

$$\tau = \frac{l}{u_{\text{surf}}} \quad (4.5)$$

The mass transfer coefficient is given as a function of $\eta = D\tau/\delta^2$, where τ is the surface contact time, and l is the length of the contactor ($l=9.1\text{cm}$). The contact area between liquid and gas phases is 38 cm^2 .

$$\Theta = \frac{[A]_{\text{L}}^{\text{L}} - [A]_{\text{b}}^{\text{L,out}}}{[A]_{\text{L}}^{\text{L}} - [A]_{\text{b}}^{\text{L,in}}} = 0.7857 \exp(-5.121\eta) + 0.1001 \exp(-39.21\eta) + 0.036 \exp(-105.6\eta) + 0.0181 \exp(-204.7\eta) \quad ; \text{ for } \eta > 0.01 \quad (4.6)$$

$$\Theta = \frac{[A]_{\text{L}}^{\text{L}} - [A]_{\text{b}}^{\text{L,out}}}{[A]_{\text{L}}^{\text{L}} - [A]_{\text{b}}^{\text{L,in}}} = 1 - 3 \sqrt{\frac{\eta}{\pi}} \quad ; \text{ for } \eta < 0.01 \quad (4.7)$$

$$k_{\text{L,A}}^{\circ} = \frac{Q_{\text{L}}}{a} (1 - \Theta) \quad (4.8)$$

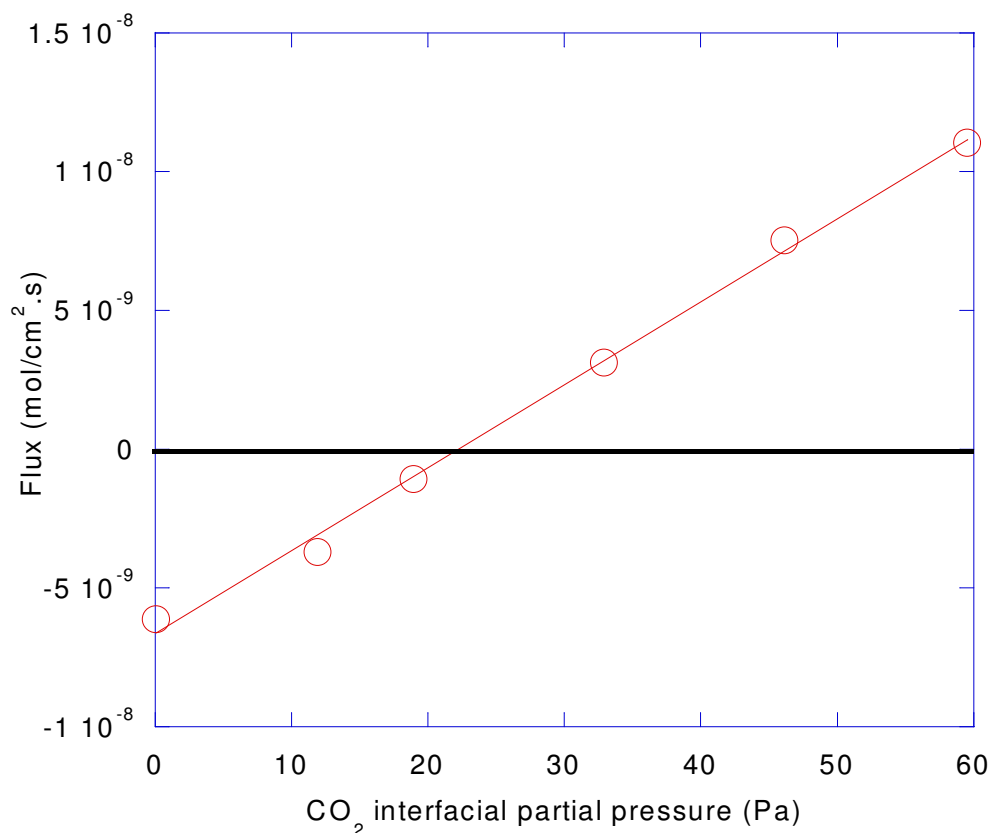


Figure 4.3 Flux interpolation to determine equilibrium solubility. Data points for absorption into 11 wt% MOR/53 wt% DGA at CO₂ loading of 0.13 mol/mol amine and a temperature of 40 °C.

NMR experiments were performed at UT's Department of Chemistry and Biochemistry NMR laboratory. ¹³C experiments were performed using D₂O solvent. All experiments were run at 27°C, 40 °C, and 60 °C on a Varian INOVA-500 machine. After the sample preparation step, small volume samples (< 5 mL) were sparged with CO₂ for ~ 15 minutes through a fine teflon line placed directly in the sample to almost the sample bottom. The NMR tubes were then flame sealed to prevent CO₂ from escaping the glass tube. The NMR spectrums were acquired with a relaxation delay of 5T₁ to ensure quantitative signals. T₁ is the relaxation time.

The N₂O solubility apparatus: The experimental apparatus used in the N₂O measurements is shown in figure 4.4.

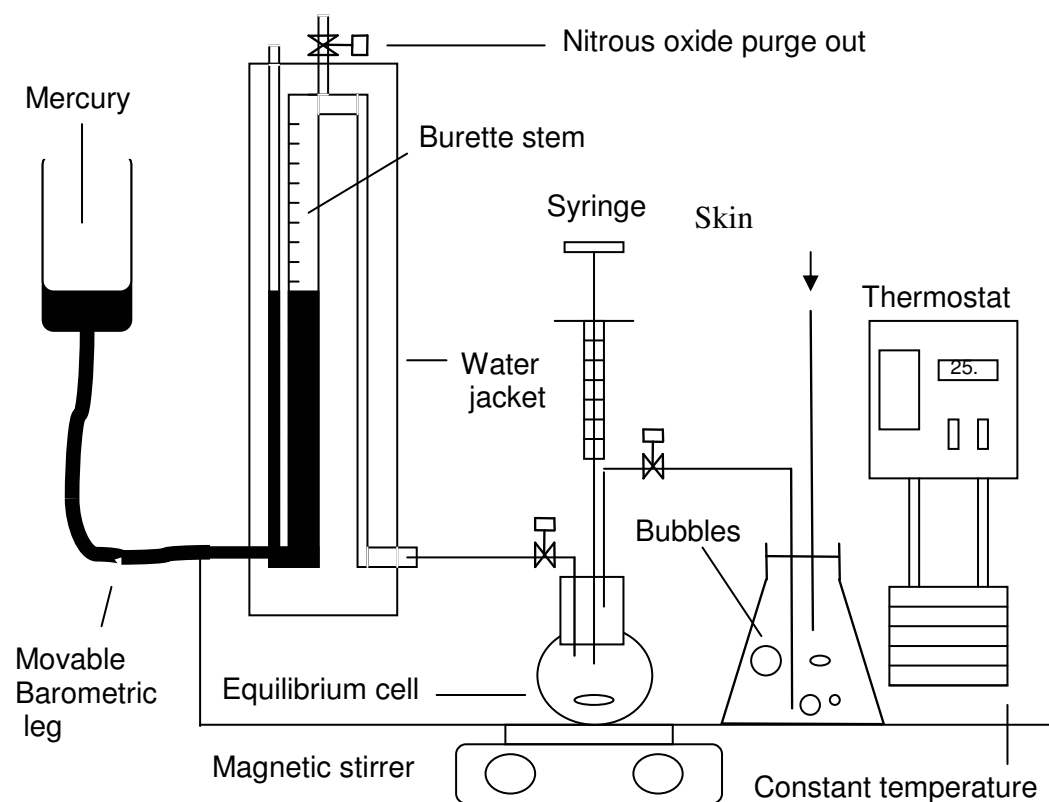


Figure 4.4 Schematic diagram of the N₂O experimental apparatus.

The principal of the operation of the apparatus is to displace a measured volume of gas into a liquid. The apparatus consists of a thick walled mercury reservoir (15 cm tall with a 5 cm ID) connected to Tygon tubing (1/4 inch ID), which was in turn connected to a glass tube open to the atmosphere, an inverted burette (graduated +/- 0.2 ml), and a second glass tube which is connected to the absorption flask via 9mm flange. The reservoir is open to the atmosphere and was attached to a 2 feet stand with clamp (2) and could be moved up and down the entire length of the stand to ensure that the pressure in the burette is always

atmospheric. The absorption flask was a 100 ml round bottom, with three necks of 24/40 Pyrex neck size. The middle neck allows for sample injection through a septum by a hypodermic syringe, one side neck has a water saturator maintained at the experiment temperature and allows for the N₂O gas flows to the system. The second side neck is connected to the displacement section by a flange and a rubber seal. The absorption flask is connected through plastic tubing to a second water saturator. The whole apparatus is kept at constant temperature inside a temperature-controlled water bath. The displacement section is jacketed using water as the circulating liquid. The accuracy of the temperature of the system is estimated to be +/-0.5 °C.

Testing procedure: The following steps should give a detailed procedure on how to operate this apparatus:

- Prior to the testing of a sample, the apparatus was purged with water saturated nitrous oxide for about 10 minutes. Both taps were then closed so that the nitrous oxide was sealed inside the apparatus.
- The movable barometric leg was adjusted to produce equal mercury levels in the two glass legs. By doing this, the pressure inside the apparatus was made equal to the surrounding atmospheric pressure.
- Solubility measurements are sensitive to air dissolved in the solution because as gas is absorbed, it displaces dissolved air. Since the method used measures the change in volume of the gas, concomitant desorption of air would introduce sizable error. To overcome this, all samples were vacuum degassed. Sample degassing should be done quickly to ensure that carbon dioxide removal from loaded solutions was minimal.

- A 20 mL sample was taken by syringe and weighed on an analytical balance.
- The sample was injected through the septum into the absorption flask while atmospheric pressure was maintained inside the system by adjustment of the movable leg.
- An important criteria of running this apparatus is deciding when equilibrium has been reached. This is done by taking gas volume measurements during the course of the experiment. Equilibrium was said to have been achieved when three identical gas volume measurements were in agreement to within ± 0.1 mL.

The solubility is calculated in terms of the Henry' s law constant as follows:

$$H_{N_2O} = P_{N_2O} / C_{N_2O}^* \quad (4.9)$$

where $C_{N_2O}^*$ is the equilibrium concentration of N_2O , which can be calculated from the total moles of gas absorbed in a volume of absorbing liquid.

The partial pressure of N_2O in the absorption apparatus can be calculated using Raoult' s law as follows;

$$P_{N_2O} = P_{total} - x_{H_2O}P_{H_2O} - x_{MOR}P_{MOR} - x_{DGA}P_{DGA} \quad (4.10)$$

where P_{total} is the total system pressure, x_{H_2O} , x_{MOR} and x_{DGA} are the mole fraction of H_2O , MOR and DGA respectively. P_{H_2O} , P_{MOR} and P_{DGA} are the vapor pressure of H_2O , MOR and DGA respectively. The vapor pressure of water was calculated using the following equation (Al-Ghawas et al, 1989):

$$P_{H_2O} = 1.33567 \times 10^6 \exp(-5243.04/T) \quad (4.11)$$

where P_{H_2O} is in bars, and T is in Kelvin.

The activity coefficient, γ_{N_2O} , is calculated by normalizing the N_2O solubility in the aqueous alkanolamine with the Henry's constant H_{N_2O,H_2O} , as shown in the following equation;

$$\gamma_{N_2O} = \frac{P_{N_2O}}{C_{N_2O}^* \cdot H_{N_2O,H_2O}} \quad (4.12)$$

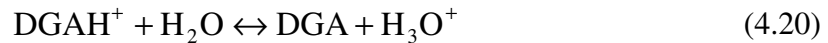
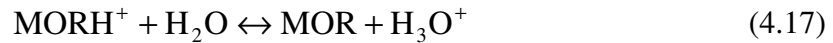
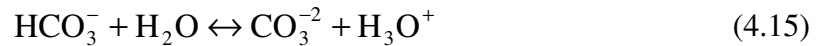
The Henry's constant of N_2O in water is given by the following equation (Versteeg and van Swaaij, 1988);

$$H_{N_2O,H_2O} = 8.5470 \times 10^6 \exp(-2284/T) \quad (4.13)$$

where H_{N_2O,H_2O} is in $\text{kPa} \cdot \text{m}^3 \cdot \text{kmol}^{-1}$, and T is in Kelvin.

4.2 Model Description

A flexible Fortran code for the solution and phase equilibrium of acid gas systems was developed by Austgen (1989). This code was modified to model MOR, DGA, and MOR/DGA blends. The model uses the Smith and Missen (1988) non-stoichiometric algorithm to speciate the liquid solution. Equilibrium constants were used to calculate the standard state chemical potentials using the method described by Austgen (1989). The following reactions and species are considered.



The total amount of water, carbon dioxide, MOR and DGA present in the liquid phase are specified. Equilibrium is first calculated in the liquid phase and

then vapor/liquid equilibrium is calculated for all molecular species (MOR, DGA, H₂O, CO₂).

Gas phase non-idealities are calculated using the SRK equation of state (Soave, 1972). Liquid phase non-idealities are calculated using the electrolyte NRTL model (Chen and Evans, 1986; Chen et al., 1982, Mock et al., 1986). The use of the electrolyte NRTL model in amine / acid gas systems has been described previously by Austgen (1989), Posey (1996) and Bishnoi and Rochelle (2000). This work most closely resembles that of Bishnoi and Rochelle (2000) with CO₂ referenced to infinite dilution in water. All ions are also referenced to infinite dilution in water. The MOR, DGA and H₂O are all referenced to the respective pure components at the system temperature. The reader is referred to Bishnoi and Rochelle (2000) for a more detailed description of the gas and liquid phase models used to account for non-ideality.

Tau parameters are defined in order to be consistent with the work of Bishnoi and Rochelle (2000). Tau parameters for molecule / molecule interactions are defined as:

$$\tau = A + \frac{B}{T} \quad (4.21)$$

Tau parameters for salt pair / molecule and molecule / salt pair are defined as:

$$\tau = A + B \left(\frac{1}{T} - \frac{1}{T_{ave}} \right) \quad (4.22)$$

Here, T is temperature in Kelvin and T_{ave} is 353.15K.

Default parameters consistent with Aspen PlusTM version 8.5 were used in this work. This is consistent with the work of Austgen (1989), Posey (1996) and Bishnoi and Rochelle (2000). A description of these defaults are given in Table 4.1a.

Table 4.1a Default parameters for VLE program

Parameter	A	B	α
molecule / molecule	0	0	0.2
water / salt pair	8.0	0	0.2
salt pair / water	-4.0	0	0.2
all molecule (other than water) / salt pair	15.0	0	0.1
all salt pair / molecule (other than water)	-8.0	0	0.1

Critical constants used by the SRK equation of state and the accentric factor were taken from the DIPPR database (Rowley et al., 1994). The Henry's law constant for CO₂ was fit by Chen et al. (1979). Brelvi-O'Connell parameters used in this work were obtained from the original work of Brelvi and O'Connell (1972). Critical compressibilities used in the Rackett model were obtained from the DIPPR database. The dielectric constant of MOR was assumed to be the same as MEA. Although this is purely an assumption, the mole fraction of MOR is so small that it will have a negligible effect on the calculated results. The Antoine equation for MOR was obtained from Stephenson and Malanowski (1987). Values of all these constants are documented in Tables 4.1b and 4.1c.

Table 4.1b Miscellaneous Constants for VLE program

Constant	Carbon Dioxide	Water	DGA®	MOR
Critical T (K)	304.2	647.3	699.0	618.0
Critical P (kPa)	7376	22090	4360	5340
Critical V (m ³ /mol)	9.4E-2	5.7E-2	0.33	0.2760
Accentric Factor	0.23	0.34	0.9693	0.3552
Rackett Z _{RA}	0.27	0.24	0.19	0.20
Brelvi-O'Connell	9.6E-2	-	-	-

Table 4.1c Temperature dependent constants

Henry's Law Constant (Pa / Mole Fraction) : $\ln H_x = A + B/T + C \ln(T) + DT$					
Carbon Dioxide	A	B	C	D	
	170.7126	-8477.711	-21.95743	0.005781	
Dielectric Constant : $D = A + B[1/T - 1/273.15]$					
	A	B			
H ₂ O	88.36	33030			
DGA	24.76	8989			
MOR (as MEA)	36.76	14836			
Antoine Equation (Pa) : $\ln P^{\text{SAT}} = A + B/T + C \ln T + D T^E$					
	A	B	C	D	E
H ₂ O	72.55	-7206.7	-7.1385	4.04E-6	2.0
DGA®	131.58	-14878	-14.614	6.1463E-18	6.0
MOR	87.958	-7860.7	-9.6344	5.676E-6	2.0

Equilibrium constants for reactions 4.14, 4.15, 4.16, 4.17 and 4.20 are documented in Table 4.2 along with their sources. The first and second dissociation constants of CO₂, the DGA protonation and water dissociation constants are unchanged from the work of Austgen (1989). The dissociation equilibrium constant for MOR is reported in Vistad et al. (2003) work and is based on molality scale. It is modified in this work in section 4.7 in order to treat MOR as a solvent rather than as a solute and also to change the equilibrium constant from the molality scale to the mole fraction scale.

Table 4.2 Temperature dependence of equilibrium constants, mole fraction based
 $\ln(K_x) = A + B/T + C \ln T + DT$

Eq No.	Equilibrium Constant	A	B	C	D	Value at 313 K	Source
14	$\frac{a_{\text{HCO}_3^-} a_{\text{H}_3\text{O}^+}}{a_{\text{CO}_2} a_{\text{H}_2\text{O}}^2}$	231.4	-12092	-36.78	0.0	8.55E-9	Posey (1996)
15	$\frac{a_{\text{H}_3\text{O}^+} a_{\text{CO}_3^{2-}}}{a_{\text{HCO}_3^-} a_{\text{H}_2\text{O}}}$	216.0	-12432	-35.48	0.0	1.04E-12	Posey (1996)
16	$\frac{a_{\text{H}_3\text{O}^+} a_{\text{OH}^-}}{a_{\text{H}_2\text{O}}^2}$	132.9	-13446	-22.48	0.0	9.15E-18	Posey (1996)
17	$\frac{a_{\text{MOR}} a_{\text{H}_3\text{O}^+}}{a_{\text{H}_2\text{O}} a_{\text{MORH}^+}}$	-4.06	-6445	0.0	0.0	1.97E-11	Vistad et al. (2003)
18	$\frac{a_{\text{MORCOO}^-} a_{\text{H}_3\text{O}^+}}{a_{\text{MOR}} a_{\text{CO}_2} a_{\text{H}_2\text{O}}}$	-7.9	-823	0.0	0.0	-10.5	This work
19	$\frac{a_{\text{DGACOO}^-} a_{\text{H}_3\text{O}^+}}{a_{\text{DGA}} a_{\text{CO}_2} a_{\text{H}_2\text{O}}}$	-24.9	5141	0.0	0.0	-8.5	This work
20	$\frac{a_{\text{DGA}} a_{\text{H}_3\text{O}^+}}{a_{\text{H}_2\text{O}} a_{\text{DGAH}^+}}$	1.69569	-8431.653	0.0	-0.50369E-2	2.25E-12	Austgen (1989)

4.3 N₂O Solubility of Carbon Dioxide in Aqueous Solution of DGA, MOR, and MOR/DGA

To validate the solubility apparatus and the experimental procedure, the solubility of N₂O in water was measured. The measured solubility of N₂O in water was 4260 and 5140 kPa m³ kmol⁻¹ for 25 °C and 40 °C, respectively. Data at 60 °C were obtained but were not reproducible. Previously published data at 60 °C show also some discrepancy. In Table 4.3, the comparison between the literature values for the solubility of N₂O in water and the values obtained in this study at 25 °C and at 40 °C is shown. As shown in Table 4.3, the measured solubility of N₂O in water is in good agreement with the literature values.

Table 4.3 Henry's constant for N₂O in water in kPa.L/mol⁻¹ at 25 °C and 40 °C

source	25 °C	40 °C
Joosten and Danckwerts (1972)	4151	
Browning and Weiland (1972)	4169	
Sada et al. (1994)	4116	
Markham and Kobe (1941)	4209	
Haimour and Sandall (1984)	4167	
Versteeg and van Swaaij, (1988)	4073	6136
Li and Lai (1995)		5725
Al-Ghawas et al. (1989)	3909	5020
This work	4260 ± 32	5140 ± 45

Versteeg and Van Swajj (1988) studied the solubility of nitrous oxide at DGA concentrations from 0 to 60 wt% at 298 to 318 K. They also studied the solubility of nitrous oxide in MOR solutions. Experiments were performed at concentrations from 0 to 30 wt% at 303 K. The effect of amine concentration is seen to lower the solubility of nitrous oxide in aqueous solutions. This may be seen in figure 4.5 where the solubility is plotted as the activity coefficient of nitrous oxide with a reference state of infinite dilution in water. The results are also summarized in Table 4.4.

Table 4.4 N₂O solubility data in unloaded amine solutions

Amine	Conc, mol/L	T, °C	H _{N₂O} , L-atm/gmol	Reference
DGA	0.19	303	47.8	Versteeg et al (1986)
DGA	0.40	303	46.9	Versteeg et al (1986)
DGA	0.80	303	46.3	Versteeg et al (1986)
DGA	1.63	303	49.8	Versteeg et al (1986)
DGA	2.28	303	50.2	Versteeg et al (1986)
DGA	3.25	303	54.0	Versteeg et al (1986)
DGA	3.26	303	55.4	Versteeg et al (1986)
DGA	0.21	298	40.6	Littel (1992)
DGA	0.41	298	41.9	Littel (1992)
DGA	0.81	298	42.5	Littel (1992)
DGA	1.61	298	43.6	Littel (1992)
DGA	2.44	298	46.6	Littel (1992)
DGA	3.24	298	49.8	Littel (1992)
DGA	4.67	298	53.3	Littel (1992)

DGA	6.13	298	60.8	Littel (1992)
DGA	6.14	298	59.2	Littel (1992)
DGA	0.19	303	48.6	Littel (1992)
DGA	0.40	303	47.7	Littel (1992)
DGA	0.79	303	47.1	Littel (1992)
DGA	1.63	303	50.6	Littel (1992)
DGA	2.28	303	51.1	Littel (1992)
DGA	3.25	303	54.9	Littel (1992)
DGA	3.26	303	56.4	Littel (1992)
DGA	0.20	318	69.2	Littel (1992)
DGA	0.36	318	70.3	Littel (1992)
DGA	0.91	318	68.9	Littel (1992)
DGA	1.83	318	69.2	Littel (1992)
DGA	2.58	318	72.3	Littel (1992)
DGA	3.59	318	75.4	Littel (1992)
DGA	3.64	318	74.1	Littel (1992)
DGA	0.20	333	90.8	Littel (1992)
DGA	0.41	333	88.7	Littel (1992)
DGA	0.80	333	89.9	Littel (1992)
DGA	1.71	333	91.4	Littel (1992)
DGA	2.32	333	89.6	Littel (1992)
DGA	2.49	333	92.3	Littel (1992)
DGA	3.25	333	86.5	Littel (1992)
DGA	3.54	333	85.7	Littel (1992)
MOR	0.20	303	47.2	Littel (1992)
MOR	0.48	303	47.8	Littel (1992)
MOR	0.78	303	48.6	Littel (1992)
MOR	1.59	303	46.2	Littel (1992)
MOR	2.19	303	46.1	Littel (1992)
MOR	3.11	303	48.3	Littel (1992)
MOR	3.24	303	46.9	Littel (1992)

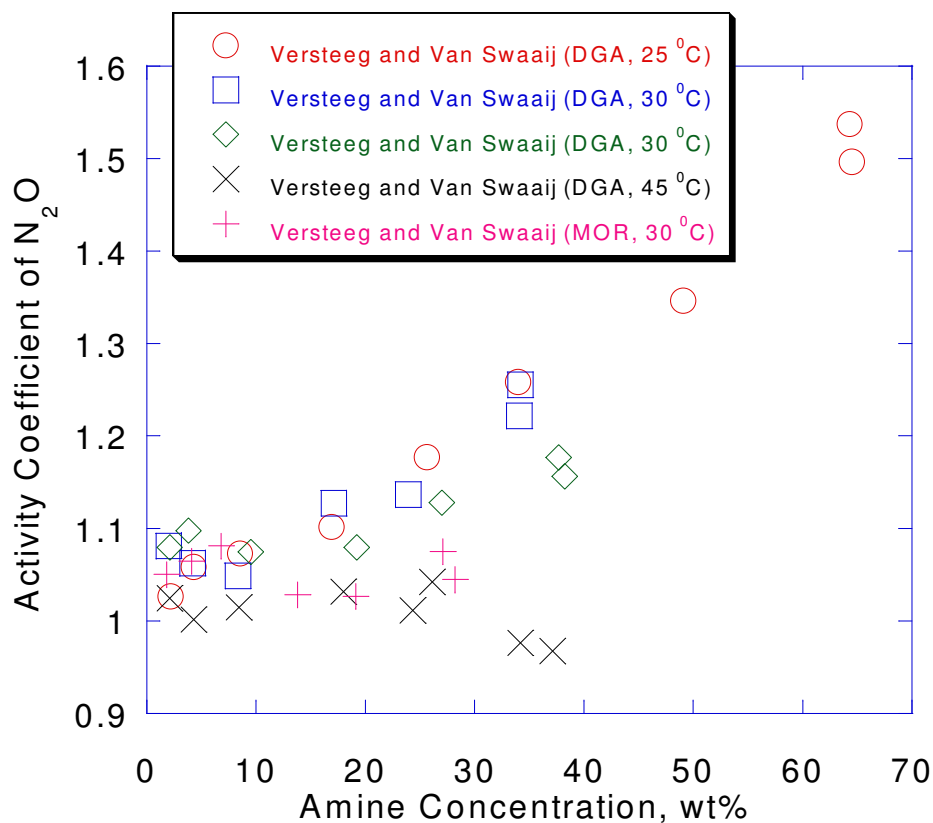


Figure 4.5 Solubility of nitrous oxide as a function of amine concentration.

4.4 Solubility of Carbon Dioxide in Aqueous Solution of DGA, MOR, and MOR/DGA

Data for CO₂ solubility in DGA/H₂O, MOR/H₂O, and MOR/DGA/H₂O solutions were obtained in this work. Data in 23.5wt% MOR, 65wt% DGA, and 11wt% MOR/53wt% DGA at 298, 313 and 333 K are given in Tables 4.5, 4.6, and 4.7. Throughout this work, loading is represented as moles CO₂/mole amine where the total concentration of amine is equal to the concentration of DGA plus the concentration of MOR.

Table ** 4.5 CO₂ Solubility in 65wt% DGA

T °C	Loading	P* _{CO2} (Pa)	T °C	Loading	P* _{CO2} (Pa)	T °C	Loading	P* _{CO2} (Pa)
24.2	0.23	15	41.2	0.10	10	58.5	0.11	145
23.8	0.43	735	39.5	0.23	75	60.2	0.24	795
			38.9	0.42	2120	59.6	0.42	14750

Table ** 4.6 CO₂ Solubility in 23.5wt% MOR

T °C	Loading	P* _{CO2} (Pa)	T °C	Loading	P* _{CO2} (Pa)	T °C	Loading	P* _{CO2} (Pa)
24.4	0.08	10				24.0	0.32	9540
39.8	0.08	35	39.8	0.21	1175	40.1	0.32	53700
60.0	0.08	250	59.5	0.21	6150			

Table ** 4.7 CO₂ Solubility in 11wt% MOR/53wt% DGA (65wt% Amine)

T °C	Loading	P* _{CO2} (Pa)	T °C	Loading	P* _{CO2} (Pa)	T °C	Loading	P* _{CO2} (Pa)
25.7	0.16	5	24.7	0.27	25	24.7	0.36	150
40.7	0.16	20	40.8	0.27	285	40.2	0.36	725
58.7	0.16	515	61.7	0.27	1180	58.1	0.36	6700
						25.2	0.45	3775
						41.4	0.45	16190

** Numbers are rounded to the nearest five

The addition of roughly 11 wt% MOR to a 53wt% aqueous DGA solution increases the equilibrium partial pressure of CO₂ by a factor of 5 to 7 at high loading. The data of DGA/MOR converges with the equilibrium partial pressure of DGA at CO₂ loading below 0.2. Martin et al. (1978) obtained solubility data for CO₂ in solutions of 60 wt% DGA solutions at 50 °C and 100 °C. The data were collected for regions of high acid gas partial pressures. Their data are very helpful in studying the high loading region since our experimental data was not acquired in this region. Dingman et al. (1983) obtained a large amount of data in solutions of 65wt% DGA down to low levels of acid gas loadings. Again, their CO₂ solubility data complements the data taken in this work.

The heat of absorption, ΔH_{abs} , of 23.5 wt % MOR, 65 wt % DGA and 23.5 wt % MOR/53 wt% DGA solutions was determined at various loadings at three different temperatures using the VLE data above. Using the Clayperon equation (Smith and Van Ness, 1975), ΔH_{abs} can be calculated as;

$$\frac{d(\ln P_{\text{CO}_2}^*)}{d(1/T)} = -\frac{\Delta H_{\text{abs}}}{R} \quad (4.23)$$

Results are displayed graphically in figure 4.6, 4.7 and 4.8. The results are also given in Table 4.8.

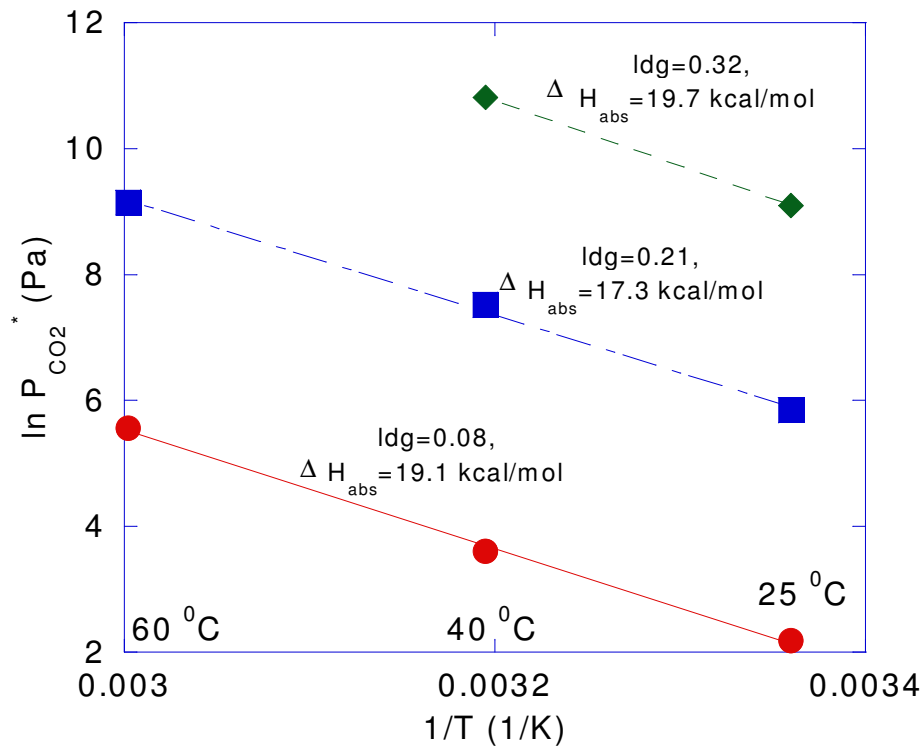


Figure 4.6 Heat of Absorption of CO₂ at various loading for 23.5 wt% MOR

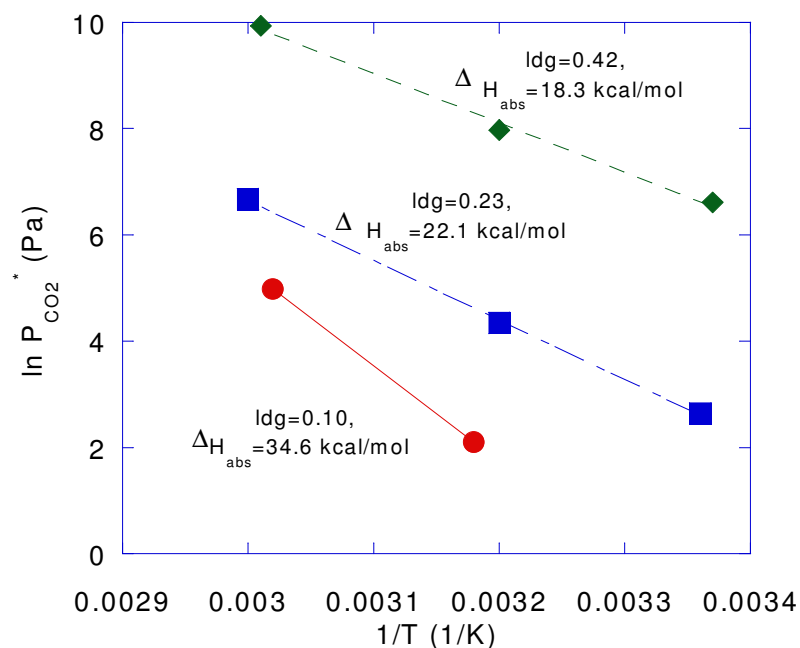


Figure 4.7 Heat of Absorption of CO₂ at various loading for 65 wt% DGA

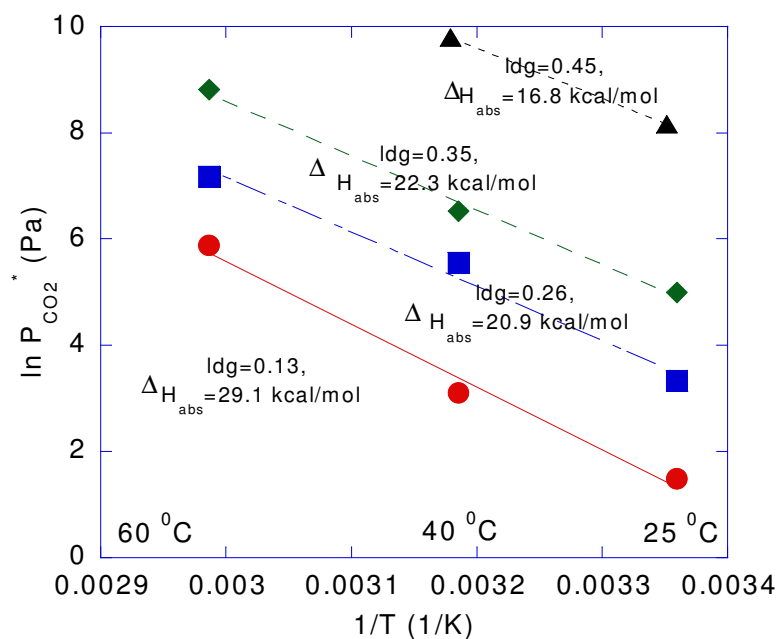


Figure 4.8 Heat of Absorption of CO₂ at various loading for 23.5 wt% MOR/53 wt% DGA.

Table ** 4.8 Heat of Absorption of CO₂ at various loading for 23.5 wt% MOR, 65 wt% DGA and 11 wt% MOR//53 wt% DGA

Solvent	Loading, mol CO ₂ /mol amine	Heat of absorption, kcal/mol
23.5 wt% MOR	0.08	19.1
23.5 wt% MOR	0.21	17.3
23.5 wt% MOR	0.32	19.7
65 wt% DGA	0.10	34.6
65 wt% DGA	0.23	22.1
65 wt% DGA	0.42	18.3
11 wt% MOR/53 wt% DGA	0.13	29.1
11 wt% MOR/53 wt% DGA	0.26	20.9
11 wt% MOR/53 wt% DGA	0.35	22.3
11 wt% MOR/53 wt% DGA	0.45	16.8

4.5 C13 NMR Data

The speciation of loaded solutions plays a critical role in determining the rate of CO₂ absorption and the solution capacity especially with primary and secondary amines. The more bicarbonate ions form in equilibrium CO₂-alkanolamine-H₂O solutions, the more free amines exist, and these free amines are able to react with CO₂ molecules again, which finally leads to a remarkable enhancement in the solution capacity. The overall reaction stoichiometry indicates that 2 mols of amine are required per mole of CO₂ reacted for the carbamate anion, whereas a one-to-one ratio is required for the bicarbonate ion. The degree of hydrolysis of the carbamate anion is determined by reaction parameters such as the amine concentration, solution pH, and chemical stability of the carbamate anion. Equation 4.24 represent the carbamate hydrolysis;



In a rich amine solution the concentration of unreacted amine depends on the carbamate stability constant. Typically the value of the carbamate stability constant is determined by regressing data on overall CO₂ solubility. Values have been determined this way for MEA, DEA, and DGA. The solution speciation has been measured more directly by C13 NMR. These measurements have been reported for MEA and a number of moderately hindered amines. In primary and secondary amines the carbamate stability constant is given by the following relationship;

$$K_{\text{carb}} = \frac{[\text{R}_2\text{NH}-\text{CO}_2^-]}{[\text{HCO}_3^-][\text{R}_2\text{NH}]} \quad (4.25)$$

In this work, the solution speciation in the aqueous 23.5wt% MOR/H₂O, 65wt% DGA/H₂O, and 11% MOR/53% DGA/H₂O solutions was measured by C13 NMR at 300K, 313K, and 333K and at CO₂ loading ranging from 0 to 0.5. Figures 4.9 to 4.14 show typical 13C NMR spectrum of 23.5wt% MOR/H₂O, 65wt% DGA/H₂O, and 11wt% MOR/53wt% DGA/H₂O solutions. Additional NMR data from this work can be found in Appendix I. Tables 4.9, 4.10 and 4.11 give the detailed NMR results of the spectrums in figures 4.9, 4.11 and 4.12. Tables 4.12, 4.13 and 4.14 also give the ratio of carbamate anion to bicarbonate ions peak areas as a function of CO₂ loading and temperature for all the NMR spectra acquired in this work.

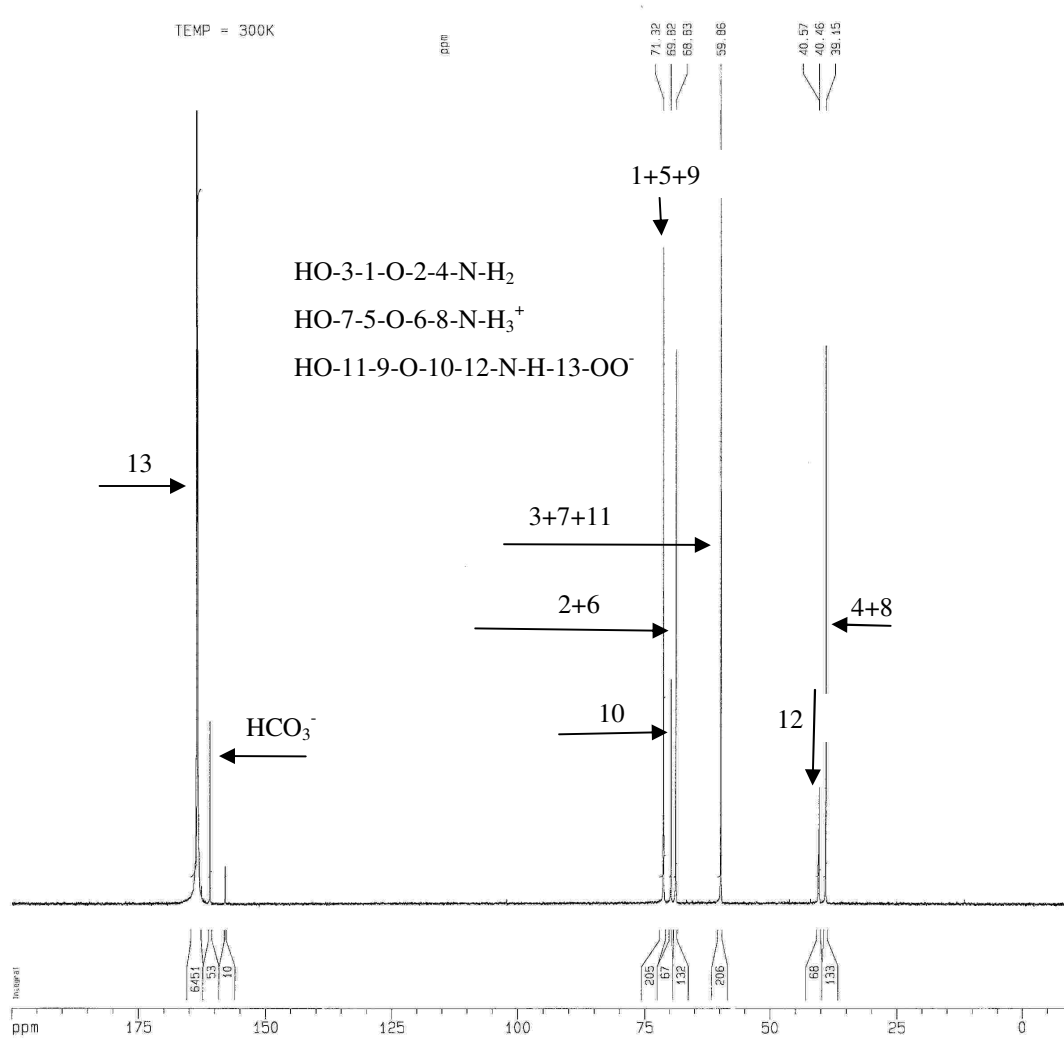


Figure 4.9 ¹³C NMR spectrum of 65 wt% DGA at 300K and 0.34 loading.

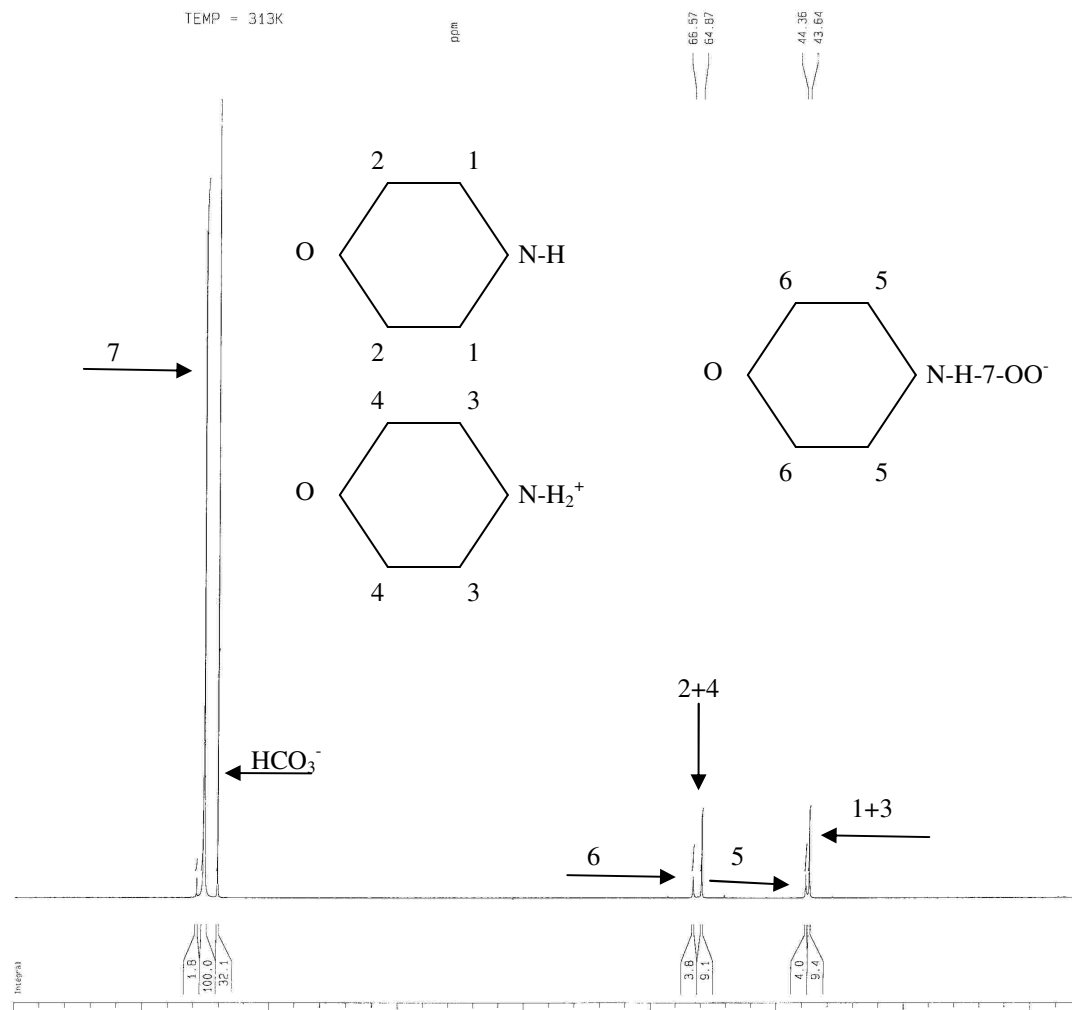


Figure 4.10 ¹³C NMR spectrum of 23.5 wt% MOR at 313K and 0.40 loading.

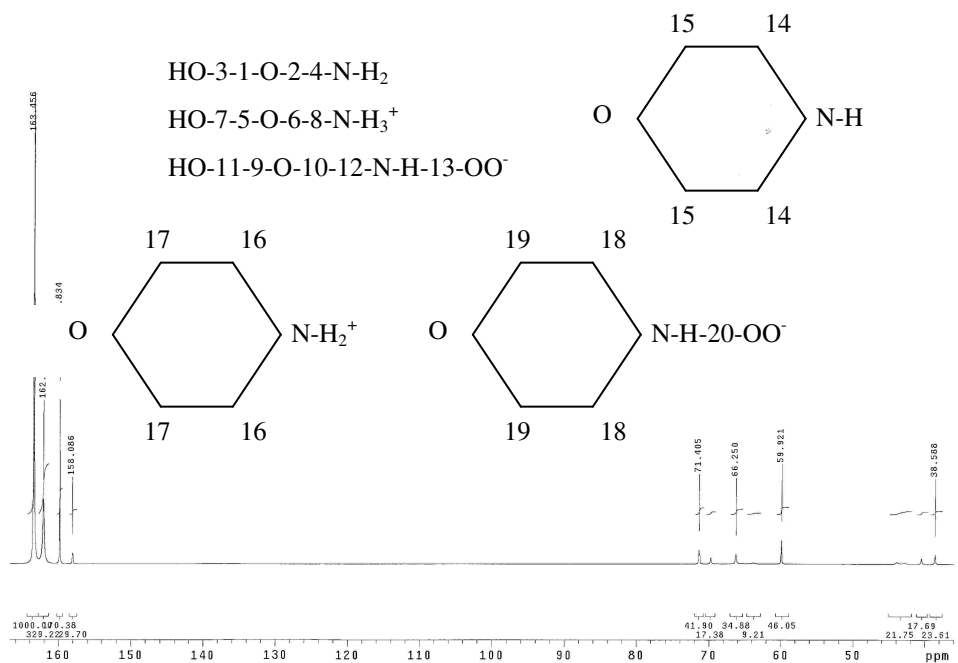


Figure 4.11 ¹³C NMR spectrum of 11 wt% MOR/53 wt% DGA at 300K and 0.52 loading.

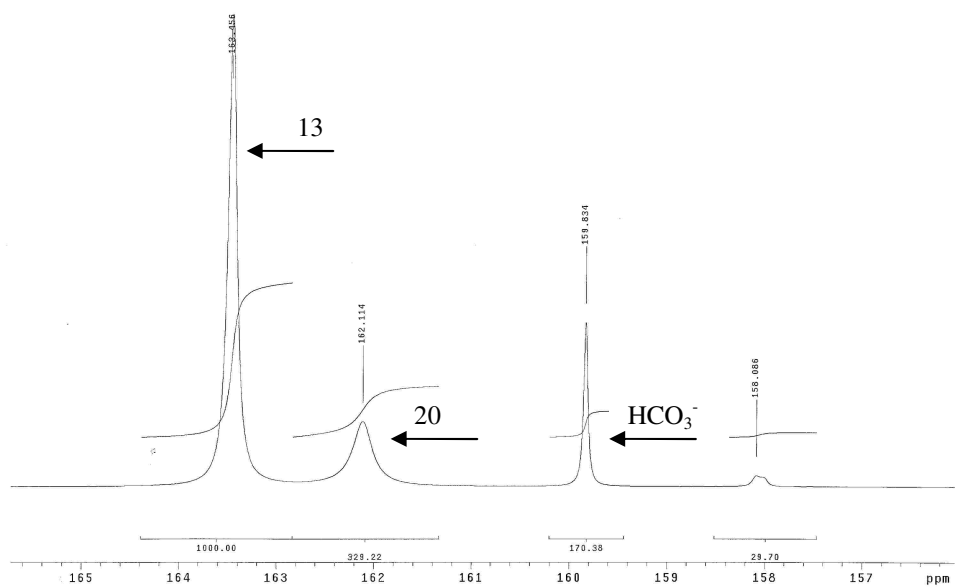


Figure 4.12 Expanded ¹³C NMR spectrum of 11 wt% MOR/53 wt% DGA at 300K and 0.52 loading.

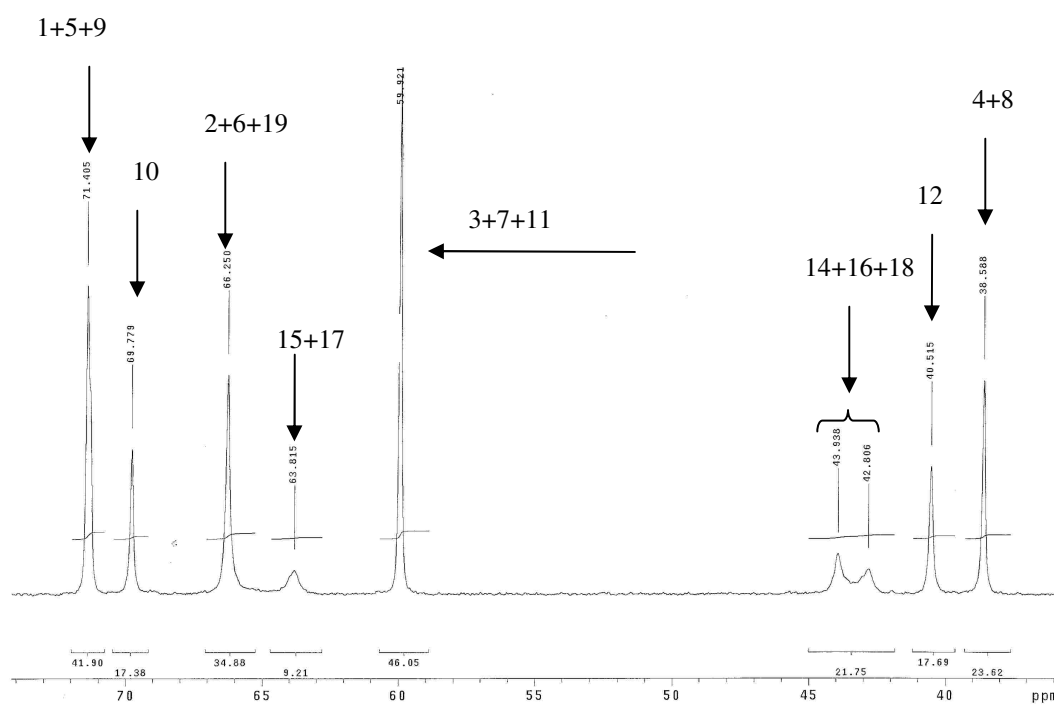


Figure 4.13 Expanded ^{13}C NMR spectrum of 11 wt% MOR/53 wt% DGA at 300K and 0.52 loading.

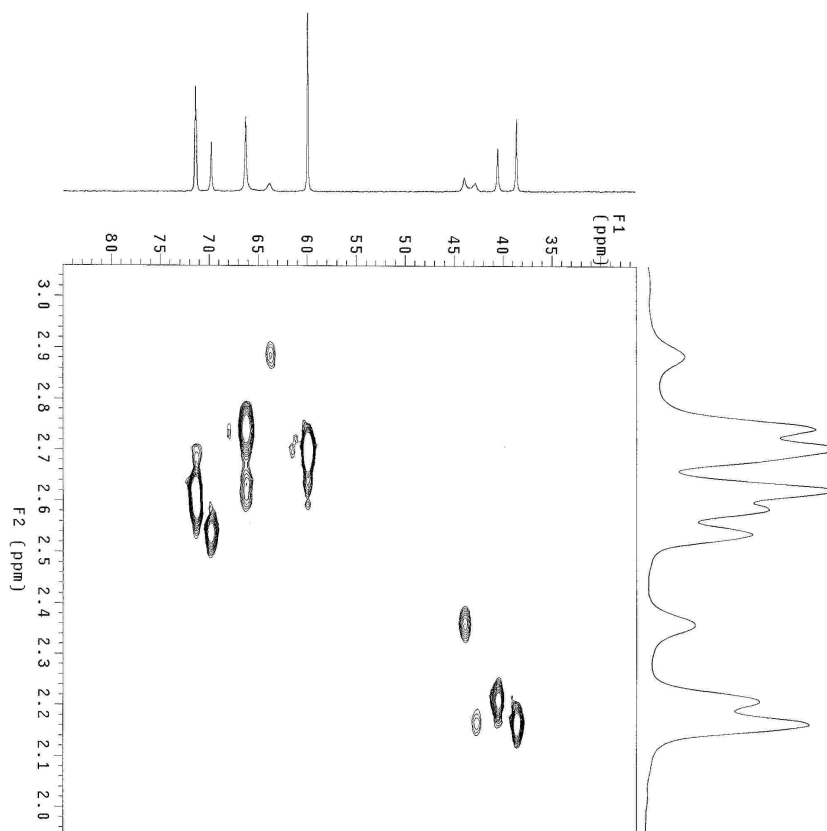


Figure 4.14 Proton, ^{13}C and short range C-H correlation NMR spectra for 11 wt% MOR/53 wt% DGA at 300K and 0.52 moles/mol amine.

Table 4.9 Detailed ^{13}C NMR Results for 65 wt% DGA and 300K and loading 0.34 mol CO_2 /mol DGA.

Species	δ (ppm)	Area
Methylene C's adjacent to nitrogen in DGA/ Protonated DGA	39.2	132.7
Methylene C's adjacent to nitrogen in DGA carbamate	40.6	67.6
Methylene C's adjacent to alcohol in DGA/ Protonated DGA & DGA carbamate	59.9	206.1
Methylene C's adjacent to oxygen in DGA/ Protonated DGA on carbamate side	68.8	131.9
Methylene C's adjacent to oxygen in DGA carbamate on carbamate side	69.8	66.7

Methylene C's adjacent to oxygen in DGA/ Protonated DGA & DGA carbamate on noncarbamate side	71.3	205.2
DGA carbamate	163.5	6451
Carbonate / Bicarbonate	160.9	53

Table 4.10 Detailed ^{13}C NMR Results for 65 wt% DGA and 313K and loading of 0.40 mol CO_2 /mol MOR.

Species	δ (ppm)	Area
Carbamate ring C's adjacent to carbamate side	44.2	3.8
Carbamate ring C's adjacent to non carbamate side	66.4	3.8
MOR / Protonated MOR on carbamate side	43.4	7.6
MOR / Protonated MOR on noncarbamate side	64.6	7.7
MOR carbamate	162.8	100.0
Carbonate / Bicarbonate	160.4	21.9

Table 4.11 Detailed ^{13}C NMR Results for 23.5 wt% MOR/65 wt% DGA and 300K.

Species	δ (ppm)	Area
Methylene C's adjacent to nitrogen in DGA/ Protonated DGA	38.6	23.6
Methylene C's adjacent to nitrogen in DGA carbamate	40.5	17.7
Methylene C's adjacent to alcohol in DGA/ Protonated DGA & DGA carbamate	59.9	46.1
Methylene C's adjacent to oxygen in DGA/ Protonated DGA on carbamate side	66.3	22.3
Methylene C's adjacent to oxygen in DGA carbamate on carbamate side	69.8	17.4
Methylene C's adjacent to oxygen in DGA/ Protonated DGA & DGA carbamate on noncarbamate side	71.4	41.9
DGA carbamate	163.5	1000
Carbonate / Bicarbonate	159.8	170.4
Carbamate ring C's adjacent to carbamate side	43.9	12.5
Carbamate ring C's adjacent to n on carbamate side	66.3	12.5
MOR / Protonated MOR on carbamate side	42.8	9.2
MOR / Protonated MOR on noncarbamate side	63.8	9.2
MOR carbamate	162.1	329.2

Table 4.12 C13 NMR in 65wt% DGA

T, °C	Loading	DGACOO ⁻ /HCO ₃ ⁻	Kcarb
27	0.167	193.1	56.5
60	0.179	78.7	25.0
27	0.337	102.4	61.2
60	0.326	42.9	25.0
27	0.362	59.5	38.5
40	0.384	52.9	37.8
60	0.382	32.6	22.2
27	0.468	6.6	63.1
40	0.481	6.1	39.3
60	0.475	5.8	25.5

Table 4.13 C13 NMR in 23.5wt% MOR

T, °C	Loading	MORCOO ⁻ /HCO ₃ ⁻	Kcarb
27	0.478	2.76	6.8
40	0.478	1.87	3.8
60	0.478	1.51	2.8
27	0.405	4.57	6.9
40	0.392	3.12	4.1
60	0.392	1.79	2.1
27	0.370	3.75	4.4
40	0.370	2.76	3.1
60	0.370	1.72	1.8
27	0.569	1.46	7.2
40	0.569	1.18	4.5
60	0.569	1.24	5.0
27	0.428	4.60	8.3
40	0.428	3.37	5.7
60	0.428	2.62	4.1
27	0.325	10.9	11.0
40	0.325	8.01	8.0
60	0.325	4.77	4.6
27	0.258	16.7	12.6
40	0.258	11.6	8.7
60	0.258	6.31	4.7

Table 4.14 C13 NMR in 11wt% MOR/53wt% DGA

T, °C	Loading	[DGACOO ⁻ +MORCOO ⁻]/HCO ₃ ⁻
27	0.524	7.80
40	0.524	7.18
60	0.524	6.50
27	0.364	54.74
40	0.374	37.67
60	0.374	24.00
27	0.271	127.1
40	0.285	73.00
60	0.285	52.11

To estimate the carbamate stability constant, the solution speciation in aqueous MOR, DGA and MOR/DGA solutions was measured. In particular, two important species in the CO₂-amine-H₂O solutions, namely, bicarbonate ion and carbamate anion, were identified by ¹³C NMR spectroscopy. To assign protonated amine and free amine in the equilibrated CO₂-amine-H₂O solutions, the NMR spectroscopic results of the aqueous amine solutions without any dissolved CO₂ were compared with those of the CO₂-amine-H₂O solutions. The chemical shifts were found nearly identical in the two ¹³C NMR spectra in the three amine solutions. For chemical shifts of 25-100 ppm, carbon peaks of protonated/free amine (AMH⁺, AM) were observed, and hence, the remaining peaks could be identified with the carbamate form of the amines (AMCO₂⁻). The carbon peaks of carbamate anion (AM¹³CO₂⁻) and bicarbonate ion (H¹³CO₃⁻) appeared at 150-175 ppm. Bicarbonate ions of the CO₂-MOR-H₂O, CO₂-DGA-H₂O, and CO₂-MOR-DGA-H₂O solutions showed similar chemical shifts at the same carbon dioxide absorbing conditions. The quantitative analysis of bicarbonate ion (H¹³CO₃⁻) was made by considering the ratio of the peak areas of the carbons in the carbamate form of the amine and the carbons in the carbamate anion. The formation of carbonate ions is not likely to occur because the basicities of amine solutions are

low enough (pH = 7-10) to guarantee that the carbonate-bicarbonate equilibrium is shifted more toward the bicarbonate side at various CO₂ loadings. The CO₂ loading can also be calculated from the peak areas of protonated/free amine, bicarbonate ion and carbamate anion peak areas. It should be noted that the peak area of the carbon attached to nitrogen and the four methylenes carbons of the carbamate have different intensities. Figures 4.9 through 4.14 give the detailed identification of the peaks. Sample calculation is also given in Appendix J of loading and species mole fractions.

After identifying the peaks, the carbamate stability constant can then be calculated using equation 4.25. Table 4.15 is a summary of the apparent carbamate stability constants obtained in the present study. Literature values of the apparent carbamate stability constants of MOR and DGA are also listed in this Table, as a reference. It is clear that the carbamate stability constant in the 65wt % aqueous DGA is greater than that of MOR. This suggests that MOR forms a very unstable carbamate upon reaction with CO₂ and requires one amine molecule for each CO₂ molecule reacted. However, the reaction of DGA with CO₂ to form very stable carbamate, which could not be converted to bicarbonate and remained in the solution, resulted in the conversion of two amine molecules for each reacted CO₂ molecule. This phenomenon might be due to the difference in the molecular structures of DGA and MOR.

The van' t Hoff equation(Smith and Van Ness, 1975) can be used to estimate the temperature dependence of the carbamate stability constant for DGA and MOR.

$$\ln K_{\text{carb}} = -\Delta H_{\text{rxn}}/RT + B \quad (4.26)$$

The results are given in Table 4.16 and figure 4.16. It is clear that the heat of reaction for DGA is higher than that of MOR since DGA carbamate is more stable compared to MOR carbamate.

Table 4.15 Comparison of carbamate stability constants (Molarity based*)

Amine	T (°C)	reference	K _{carb}
MOR	10	Caplow, 1968	8
	27	This work	8.2
	40		5.4
	60		3.6
DGA	25	Austgen, 1989 calc	12
	27	This work	61.0
	40		38.6
	60		24.4

$$* K_{CARB} = \frac{x_{AMCOO-}}{x_{AM} x_{HCO3-}}$$

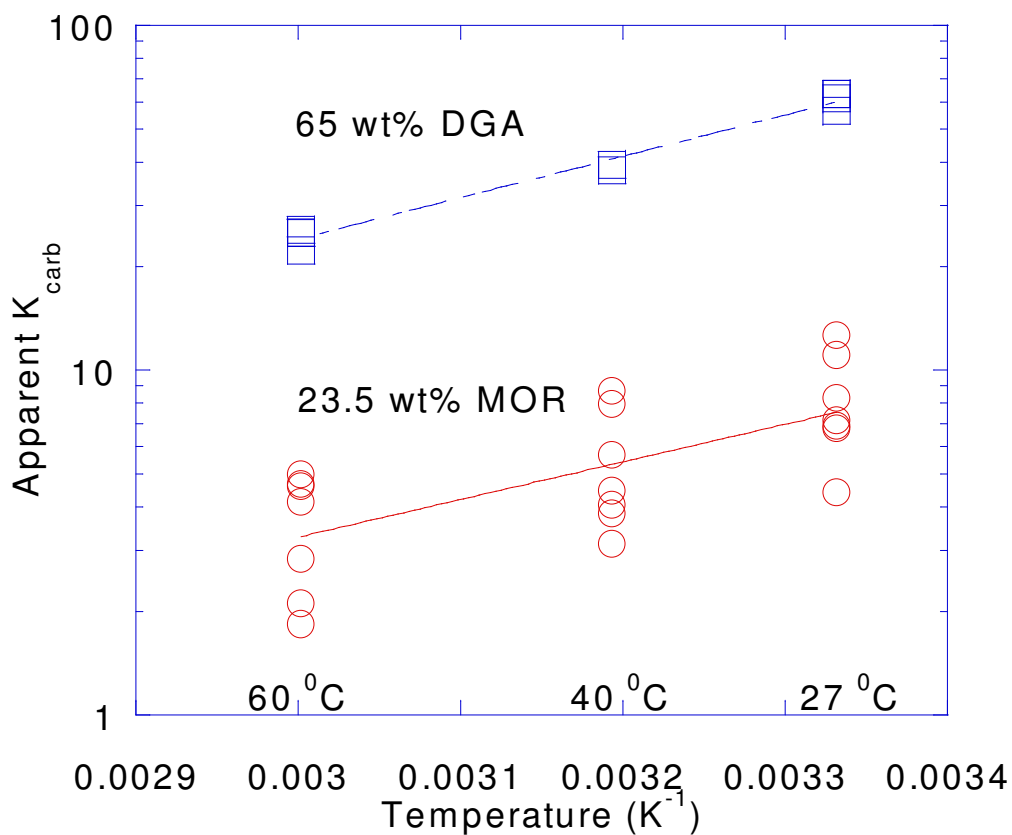


Figure 4.15 Apparent carbamate stability constant for the 23.5wt% MOR and the 65wt% DGA with 0.1 to 0.5 moles CO₂/mol Amine.

Table 4.16 Heat of reaction of carbamate for 65 wt% DGA and 23.5 wt% MOR.

Solvent	Heat of reaction (kJ/mol CO ₂)
65 wt% DGA	22.9
23.5 wt% MOR	20.9

$$* K_{CARB} = \frac{x_{AMCOO-}}{x_{AM} x_{HCO_3-}}$$

4.6 N₂O Regression Results

As can be seen in figure 4.5, the data of Versteeg and Van Swaij data showed slightly higher activity values compared to one at zero DGA® concentration. Therefore, the Henry's constant of CO₂ in water was adjusted so that it is a function of amine strength. In this way, we introduced the decrease in solubility with increasing amine strength. N₂O solubility data in unloaded DGA® and MOR solutions was then regressed.

Parameters obtained for the Henry's constant are summarized in Table 4.17 along with their standard deviation. Parameters where the standard deviation is not listed were not regressed. The results of the regression for the DGA® and MOR solutions are shown in figure 4.16 as a parity plot.

Table 4.17 Parameter Values of the Henry's Constant

Ln H _x = A + B/T + Cln(T) + DT	
A	170.7
B	-8477
C	-22.0
D	0.00578 ± 9.40E-05

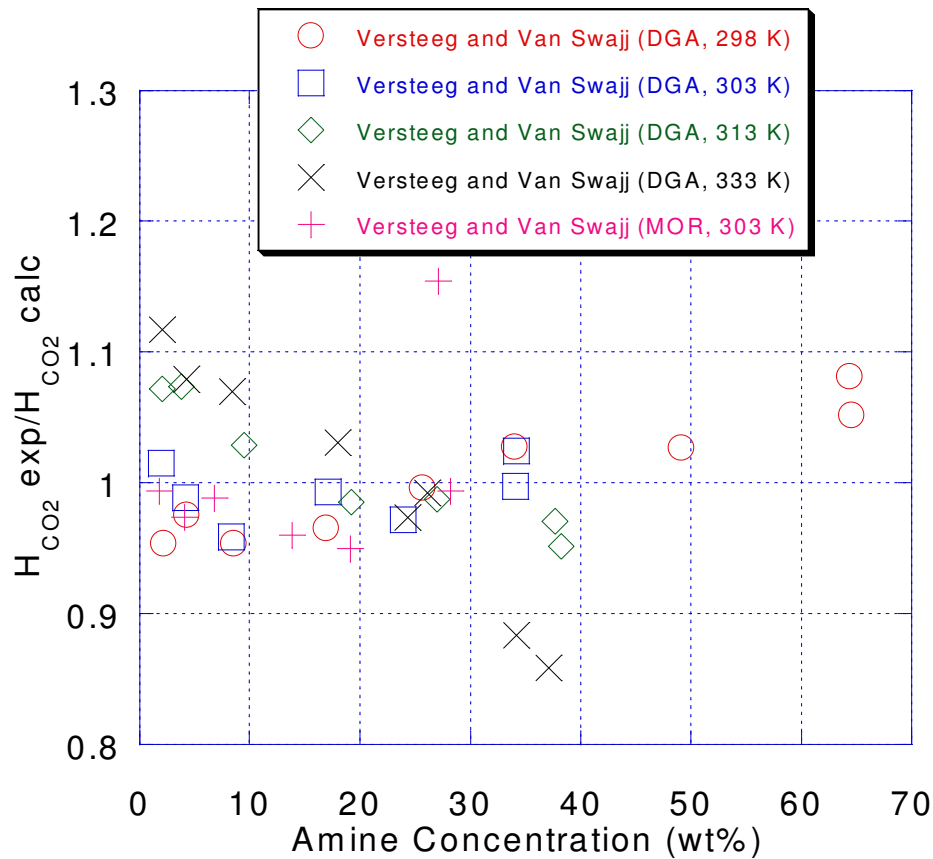


Figure 4.16 Results of Nitrous Oxide data Regression in unloaded solutions.

4.7 Activity of Diglycolamine® and Morpholine in Aqueous Mixtures

Huey et al. (1991) have measured vapor liquid equilibrium for MOR/H₂O system at 75 °C and 95 °C. Appendix A.X gives the VLE data for MOR/H₂O system at 75 °C and 95 °C. From the VLE data for MOR/H₂O system, the activity coefficients of MOR and H₂O can be calculated assuming ideal gas conditions since the total pressure is less than 1 atm;

$$\gamma_i = \frac{y_i P}{x_i p_i^{\text{sat}}} \quad (4.27)$$

where γ_i is the activity coefficient of component i , x_i and y_i are the mole fractions in the liquid and the gas phase respectively, P is the system pressure, and

p_i^{sat} is the saturation pressure of component i . Figure 4.17 shows the activity coefficients for the MOR/H₂O system. Analysis of activity coefficients at the two temperatures they studied and equation 4.28 yields an excess heat of mixing at infinite dilution of -16.7 kJ/mol for liquid MOR.

$$\ln \left(\frac{\gamma_{\text{MOR}}^{(2)}}{\gamma_{\text{MOR}}^{(1)}} \right)_{P,x} = \frac{h_2^{\text{Ex}}}{R} \left[\frac{1}{T^{(2)}} - \frac{1}{T^{(1)}} \right] \quad (4.28)$$

The absolute value of the activity coefficients should not be compared with those at temperatures of 25°C since the data of Huey et al. (1991) are at 75 to 95 °C. A comparison of the excess heat of mixing at infinite dilution is provided in Table 4.18. The value for amines is consistently negative and seems to be related to the amino group. This value of -16.7 kJ/mol is lower than the standard value of -25 kJ/mol at 25 °C. The former value is obtained by extrapolation from the high temperature data. Extrapolation is risky and should be performed with caution. The reason for us to extrapolate is because our data were obtained over the temperature range of 25 °C to 60 °C.

In addition, Huey et al. (1991) have pointed out that the predictive UNIFAC model with parameters reported in the literature results in poor predictions for the MOR/H₂O mixture. They hypothesized that the cyclic secondary amine group in MOR should be considered a different functional group from the noncyclic secondary amine group. Therefore, an attempt to use the UNIFAC model to calculate the excess heat of mixing was not pursued.

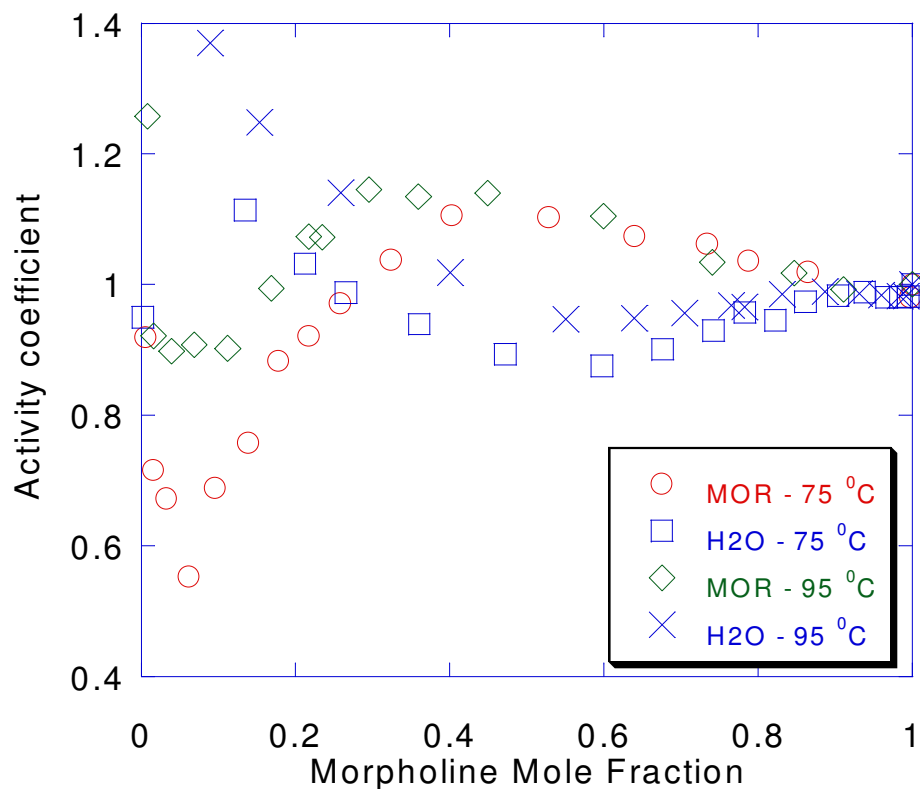


Figure 4.17 Data of Huey et al. (1991) reinterpreted as activity coefficients for the water / MOR system at elevated temperature.

Table 4.18 Excess heat of mixing at infinite dilution and 25°C

Species	$h_{AM}^{EX,\infty}$ (KJ/mol)	Source
Piperazine	-59	Dortmund Modified UNIFAC
Piperazine	-38	Wilson and Wilding (1994)
Piperidine	-26	Dohnal et al. (1994)
Morpholine	-25	Dohnal et al. (1994)
Cyclohexylamine	-23	Dohnal et al. (1994)

*All species listed are liquids in their pure state at ambient conditions except PZ

**Reference state of most components in Dortmund UNIFAC database is liquid

As noted previously, MOR is referenced to the pure component at the system temperature; therefore, the activity coefficient of MOR must be normalized in the same way that the activity coefficient of water and DGA are normalized so that

$$\gamma_{Am} \rightarrow 1 \text{ as } x_{Am} \rightarrow 1 \quad (4.29)$$

This is the normalization convention adopted for alkanolamines in this work. Using the following equation (Austgen, 1989) to relate K'_x and K_x ;

$$K'_x = K_x \gamma_{Am}^\infty \quad (4.30)$$

where γ_{Am}^∞ is the symmetrically normalized activity coefficient of MOR at infinite dilution in water, K_x is the dissociation constant expressed on the mole fraction, K'_x is the new dissociation constant after adopting the above normalization convention. The value of γ_{Am}^∞ can then be obtained from the VLE data for the binary MOR-H₂O mixture and the fact that the excess heat of mixing at infinite dilution is -25 kJ/mol.

Vistad et al. (2003) determined the dissociation constant of MOR as a function of temperature by potentiometric pH measurement of a MOR-H₂O solution (2.1:60 ratio) while varying the temperature within the range 0-50 °C. The determined temperature dependence of pK_a is the following;

$$pK_a = 1560/T + 3.52 \quad (4.31)$$

The above dissociation constant is reported on the molality scale. The pK_a is the negative logarithm (base 10) of K_m and can be converted to K_x using the following equation (Austgen, 1989);

$$\ln K_x = \ln K_m - \ln \left(\frac{1000}{M_s} \right) \quad (4.32)$$

where M_s is the molecular weight of water. The NRTL parameters for MOR/H₂O and H₂O/MOR are then fit to the infinite dilution activity coefficient values calculated by the fit to the VLE data and the excess heat of reaction at 25 °C. These parameters are reported in Table 4.19. Accurate prediction of the MOR activity coefficient is useful in two ways. It helps predict the volatility and losses

of the amine as well as correcting the equilibria that involve MOR for the effect of DGA. The results of the regression are shown in figure 4.18 and Table 4.19.

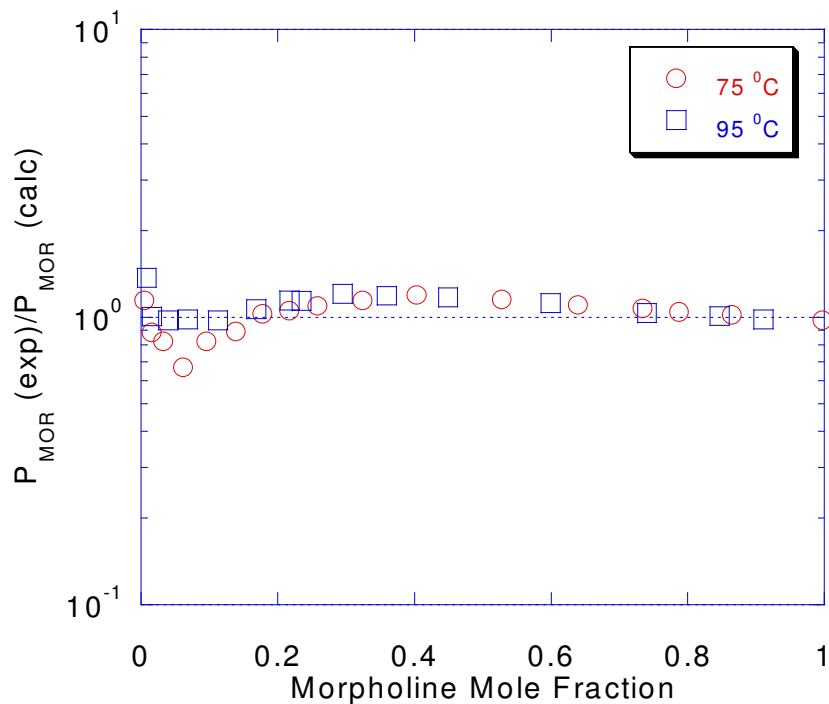


Figure 4.18 Results of regression of the equilibrium partial pressure of MOR in MOR-H₂O mixture. Fitting the excess heat of mixing at 25 °C to -25 kJ/mol

Table 4.19 Fitted values of NRTL binary interaction parameters for MOR-H₂O system.

Molecule Pair	A	B (K)
H2O-MOR	4.62 ± 0.23	0.00*
MOR-H2O	0.000*	-960 ± 1.65
DGA-H2O	1.99 ± 0.35**	0.00**
H2O-DGA	0.000**	-770 ± 62.2

** Parameters were fitted in earlier work of Austgen (1989).

* Parameters fixed at zero, could not be estimated with statistical significance

Using the NRTL model parameters shown in Table 4.19, the activity coefficient for MOR at infinite dilution can then be calculated into the common temperature form used for the equilibrium constants;

$$\ln \gamma_{\text{MOR}}^{\infty} = 8.06 - 2853/T \quad (4.33)$$

From equations 4.30, 4.31 and 4.32, the protonation equilibrium constant (mole fraction based) for MOR can be calculated as;

$$\ln K_x = -4.06 - 6445/T \quad (4.34)$$

4.8 Parameter Regression Results of CO₂ Solubility and NMR Data

4.8.1 DGA-CO₂ system

The electrolyte-NRTL parameters and the carbamate equilibrium constant for the DGA-CO₂ system were regressed to two VLE data sets and VLE and NMR data set from this work. The four data sets were simultaneously regressed and the resulting parameters are given in Table 5.20. In this work, only the partial pressure for the VLE data and the ratio of the carbamate to the bicarbonate mole fractions for the NMR data were adjusted and therefore it reflects all the error. As can be seen from figure 5.20 the ratios of experimental to calculated are well distributed about a value of unity, suggesting that the scatter is due to experimental error rather than a lack of fit by the model. In general, the model appears to represent the experimental data, as a whole, well. This is especially true in view of the fact that the VLE data used to estimate parameters vary over extremely wide ranges of CO₂ pressure and loading.

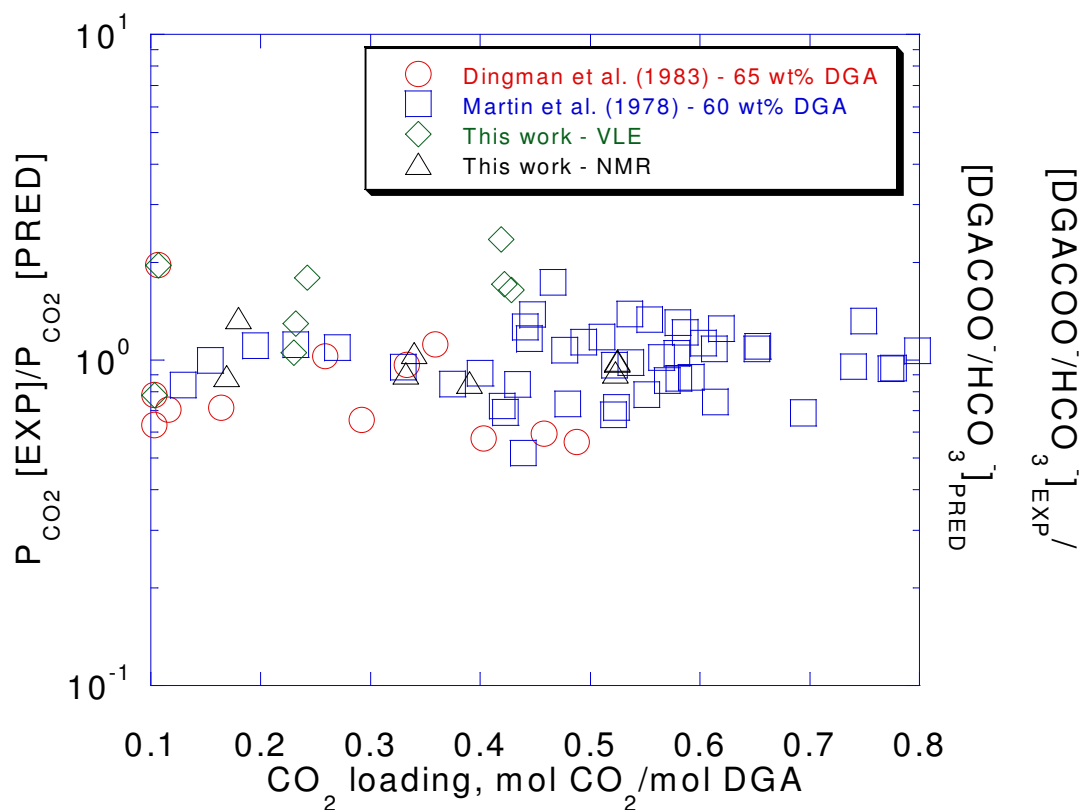


Figure 4.19 Results of VLE and C13 NMR data regression of the DGA-CO₂ system.

Table 4.20 Non-Default parameters for the NRTL model.

Parameter	A	B	τ_{40}	Default τ	ln K _x @ 40°C	
					This work	Austgen, 1989
(H ₂ O, IDGAH, IHCO ₃)	8.5 ± 0.11	787 ± 297	8.8	8		
(H ₂ O, IDGAH, IDGACOO)	10.4 ± 0.12	-5221 ± 1189	8.6	8		
(IDGAH, IHCO ₃ , H ₂ O)	-3.7*	-1713*	-4.4	-4		
(IDGAH, IDGACOO, H ₂ O)	-5.3*	2395 ± 443	-4.5	-4		
ln K _x carbamate	-7.9*	-823 ± 77			-10.5	-8.0

$$\tau = A + B \left(\frac{1}{T} - \frac{1}{T_{\text{ave}}} \right) \text{ for salt pair / molecule and molecule / salt pair}$$

$$\ln K = A + \frac{B}{T}$$

* Parameters could not be estimated with statistical significance

The binary interaction parameters of DGA-H₂O and H₂O-DGA used in this work are the same as the ones used by Austgen (1989). Most of the parameters are well predicted as indicated by the low standard deviation. The regressed τ value obtained in this work does not deviate far from the default value. This places some confidence in their absolute value.

Figure 4.20 compare partial pressure predictions from the current model to the VLE data obtained in this work. Figures 4.21, 4.22, 4.23 and 4.24 give the predicted speciation at 25 °C, 40 °C and 60 °C.

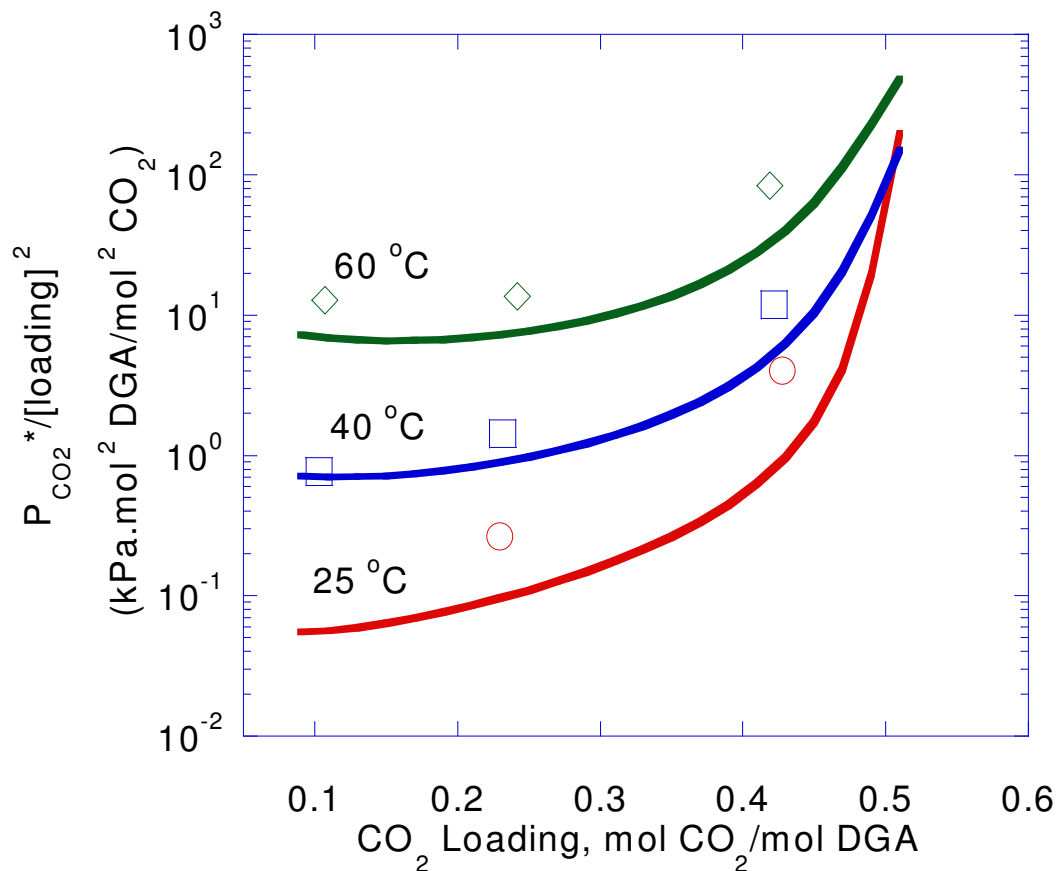


Figure 4.20 Results of regression of the equilibrium partial pressure of CO₂ in 65wt% DGA system obtained in this work.

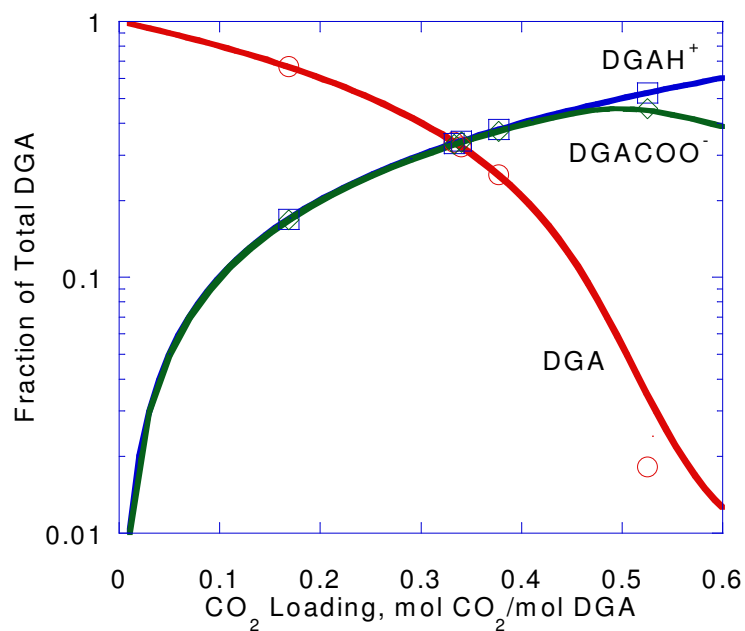


Figure 4.21 Results of regression of C13 NMR data in 65wt % DGA system at 25 °C.

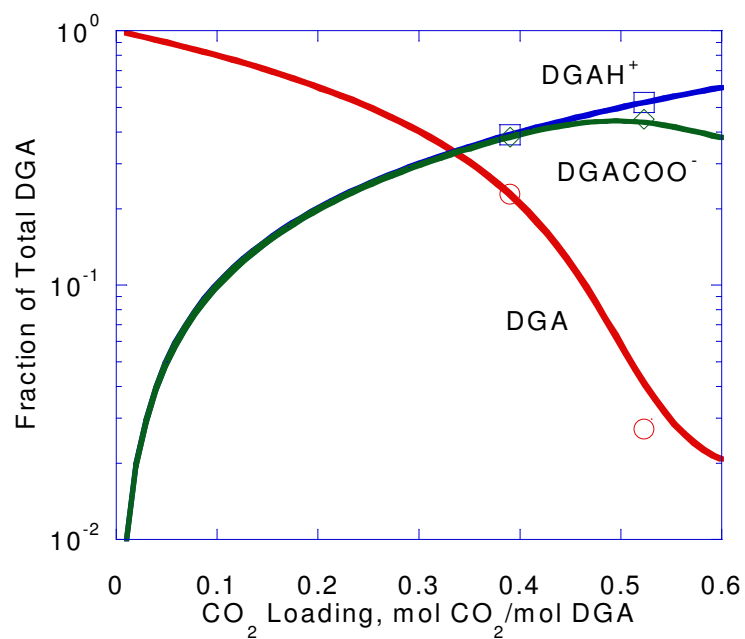


Figure 4.22 Results of regression of C13 NMR data in 65wt % DGA system at 40 °C.

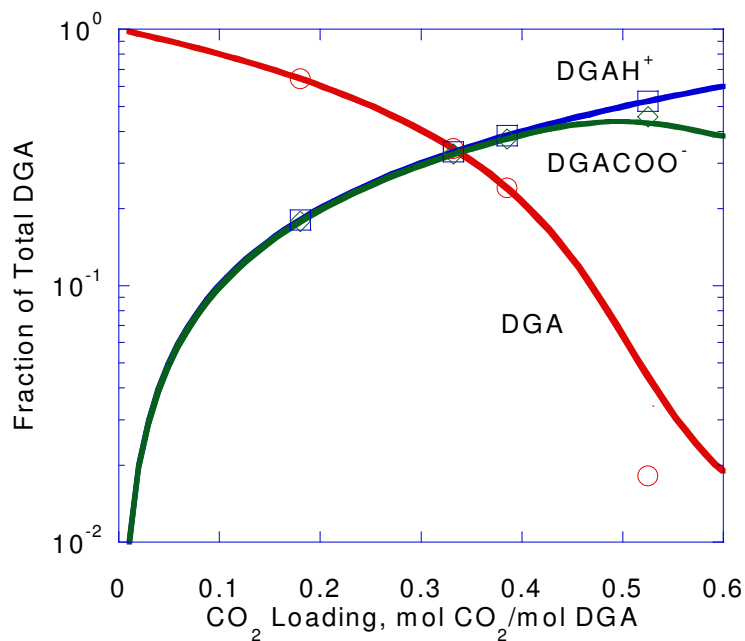


Figure 4.23 Results of regression of C13 NMR data in 65wt % DGA system at 60 °C.

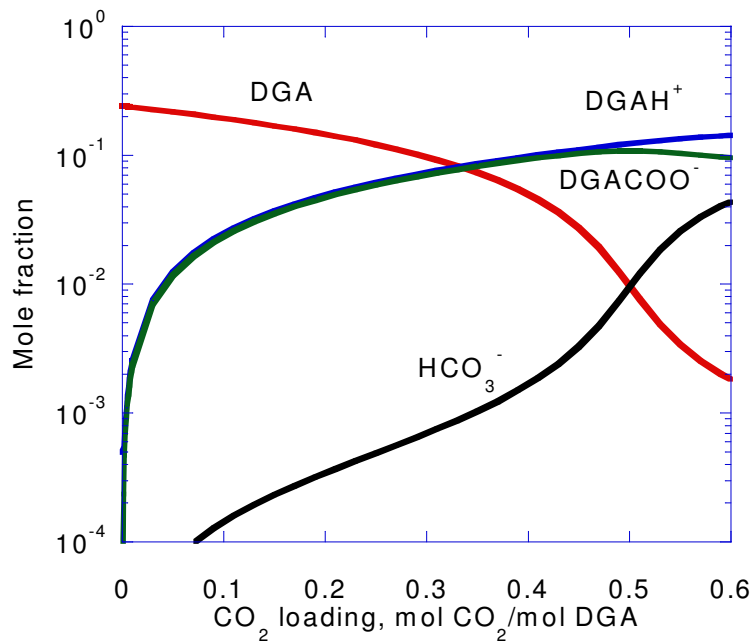


Figure 4.24 Predicted speciation of CO₂ in 65 wt% DGA at 40 °C.

4.8.2 MOR-CO₂ system

The electrolyte-NRTL parameters and the carbamate equilibrium constant for the MOR-CO₂ system were regressed to the VLE and C13 NMR data. The two data sets were simultaneously regressed and the resulting parameters are given in figure 4.25 and Table 4.21.

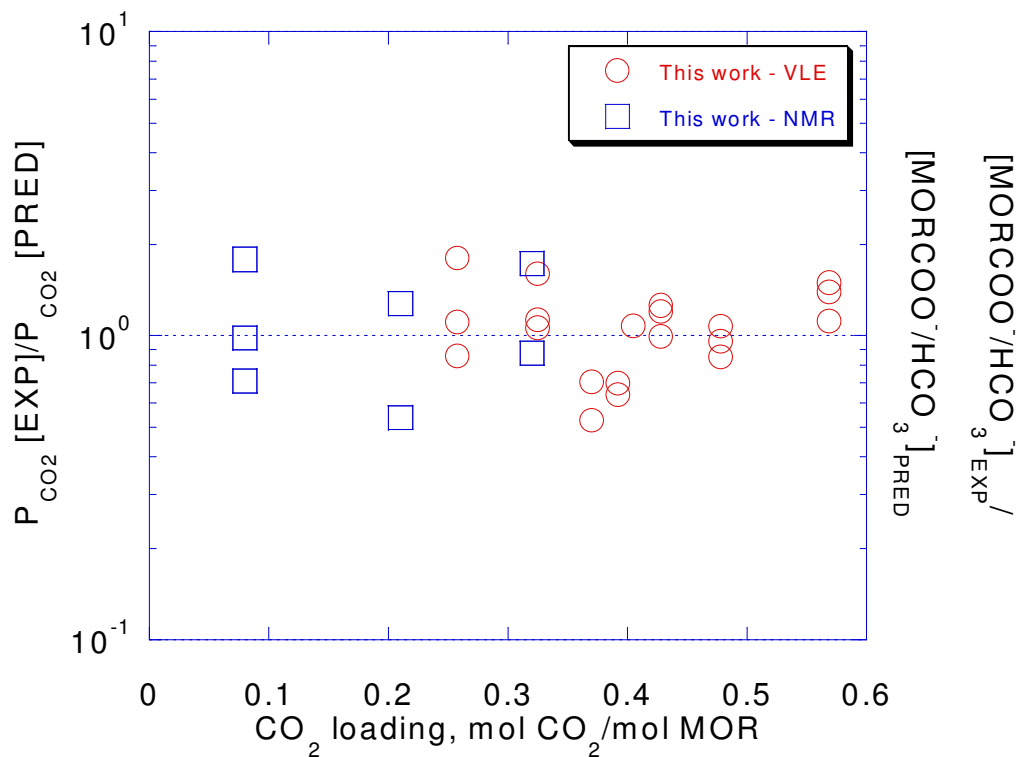


Figure 4.25 Results of VLE and NMR data regression of the MOR-CO₂ system Fixing CO₂ solubility to the N₂O Analogy.

Table 4.21 Non-Default parameters for the NRTL model.

Parameter	A	B	τ_{40}	Default τ	This work $\ln K_x @ 40^\circ\text{C}$
(H ₂ O,IMORH,IHCO ₃)	20.1 ± 1.8	- 27204*	10.3	8	
(H ₂ O,IMORH,IMORCOO)	3.91 ± 0.12	- 39885*	-10.5	8	
(IMORH,IHCO ₃ , IH ₂ O)	-8.71 ± 0.92	12722*	-4.1	-4	
(IMORH,IMORCOO, IH ₂ O)	-5.41 ± 0.22	-964*	-5.8	-4	
$\ln K_x$ carbamate	-24.9 ± 0.61	5141*			-8.5

$$\tau = A + B \left(\frac{1}{T} - \frac{1}{T_{\text{ave}}} \right) \text{ for salt pair / molecule and molecule / salt pair}$$

$$\ln K = A + \frac{B}{T}$$

* Parameters could not be estimated with statistical significance

The binary interaction parameters of MOR-H₂O and H₂O-MOR obtained in the previous section were fixed during the regression of the VLE and C13 NMR data. The regressed τ value obtained in this work does not deviate far from the default value as can be seen in Table 4.21. This places some confidence in their absolute value.

Figure 4.25 compare partial pressure predictions from the current model to the VLE data obtained in this work. Figures 4.26, 4.27, 4.28 and 4.29 give the predicted speciation at 25 °C, 40 °C and 60 °C.

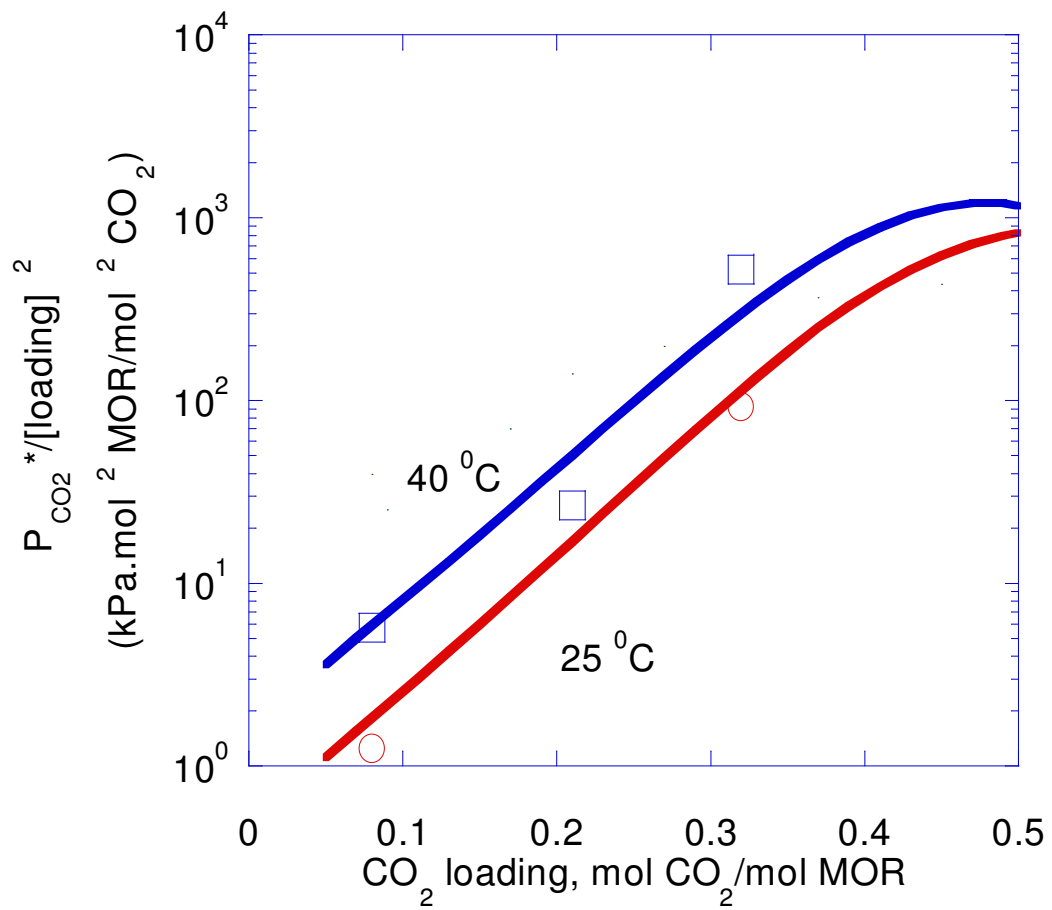


Figure 4.26 Results of regression of the equilibrium partial pressure of CO₂ in 23.5wt% DGA system.

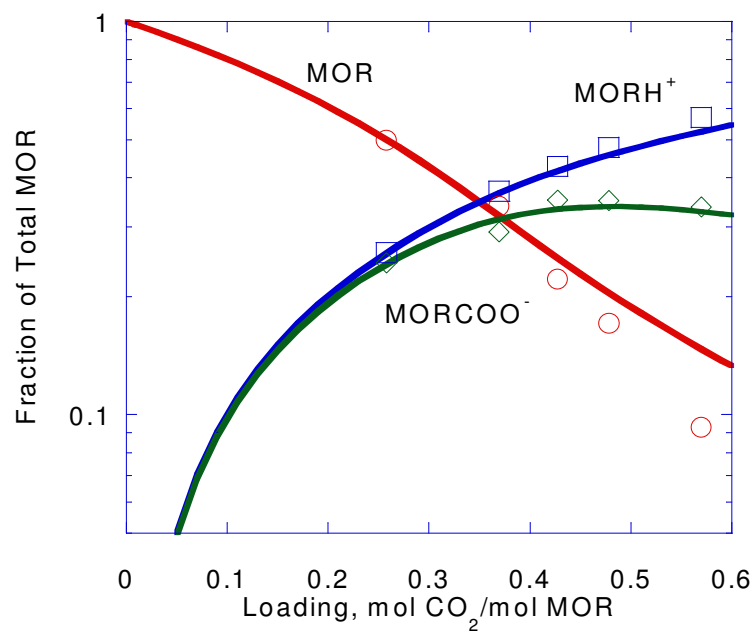


Figure 4.27 Results of regression of C13 NMR data in MOR-CO₂ system at 25 °C.

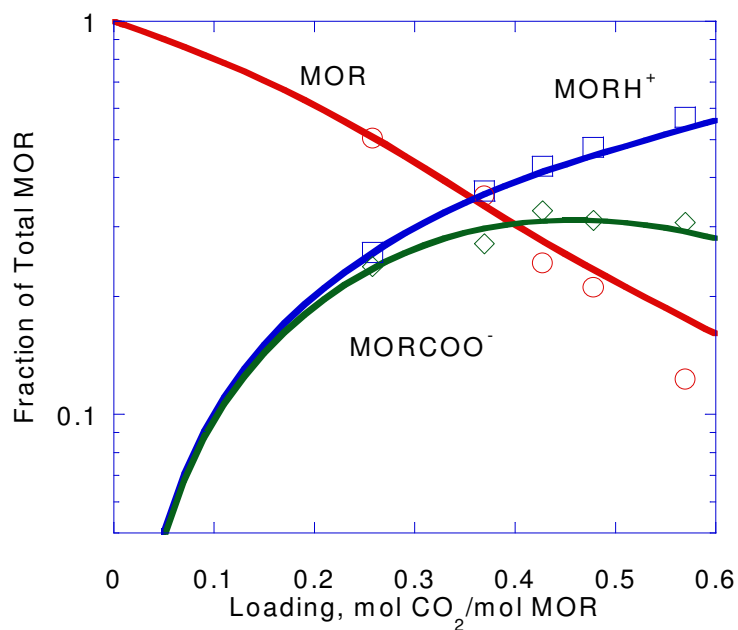


Figure 4.28 Results of regression of C13 NMR data in MOR-CO₂ system at 40 °C.

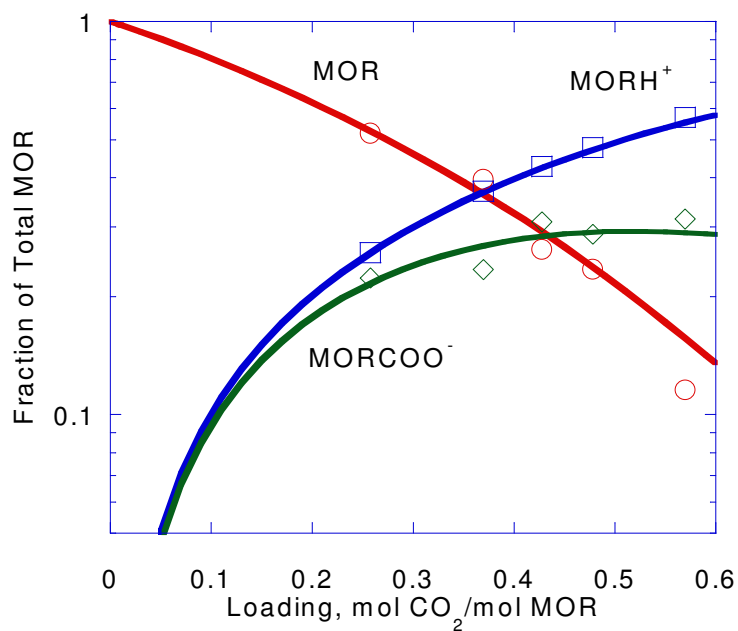


Figure 4.29 Results of regression of C13 NMR data in MOR-CO₂ system at 60 °C.

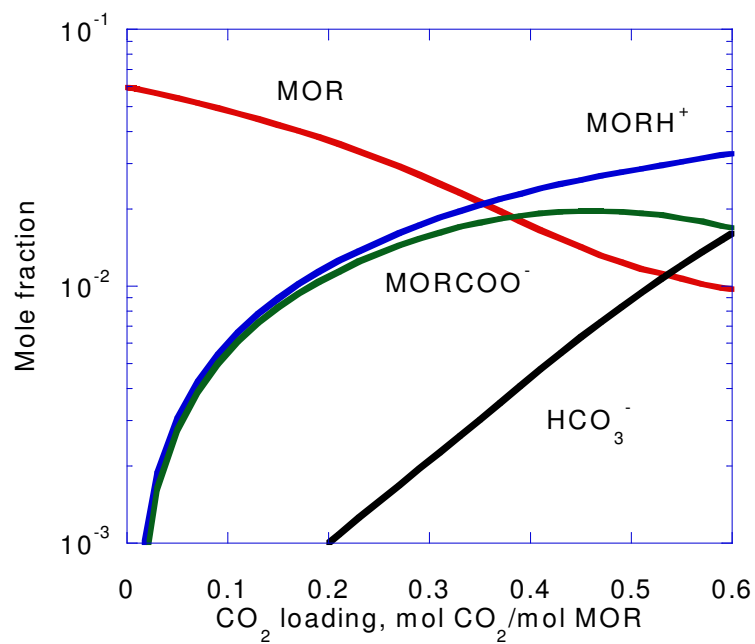


Figure 4.30 Predicted speciation of CO₂ in 23.5 wt% MOR at 25 °C.

4.8.3 MOR-DGA-CO₂ system

The parameters obtained in the single amine systems (see Tables 4.20 and 4.21) were used in the MOR-DGA-CO₂ system. Similarities can be seen in the two amine tau values. Initial model prediction of the VLE and NMR data shows a reasonably good fit. Figure 4.31 shows that the model has done a fairly good job in fitting the data considering no parameters were regressed upon this data. Parameters for the water mixed amine interactions were then regressed to improve the fit. Figure 4.32 shows the improvement in the data fitting. Table 4.22 lists the parameter values that have been used to represent interaction in the DGA-MOR systems.

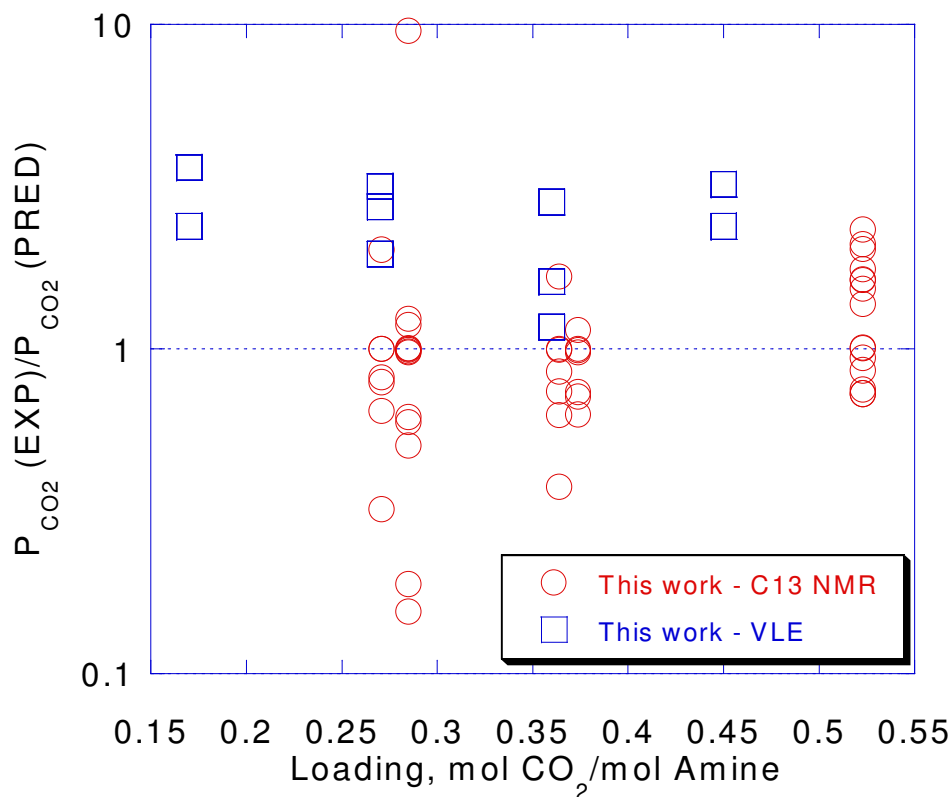


Figure 4.31 Results of model prediction for VLE and NMR data regression with no parameter adjustments of the DGA-MOR-CO₂ system.

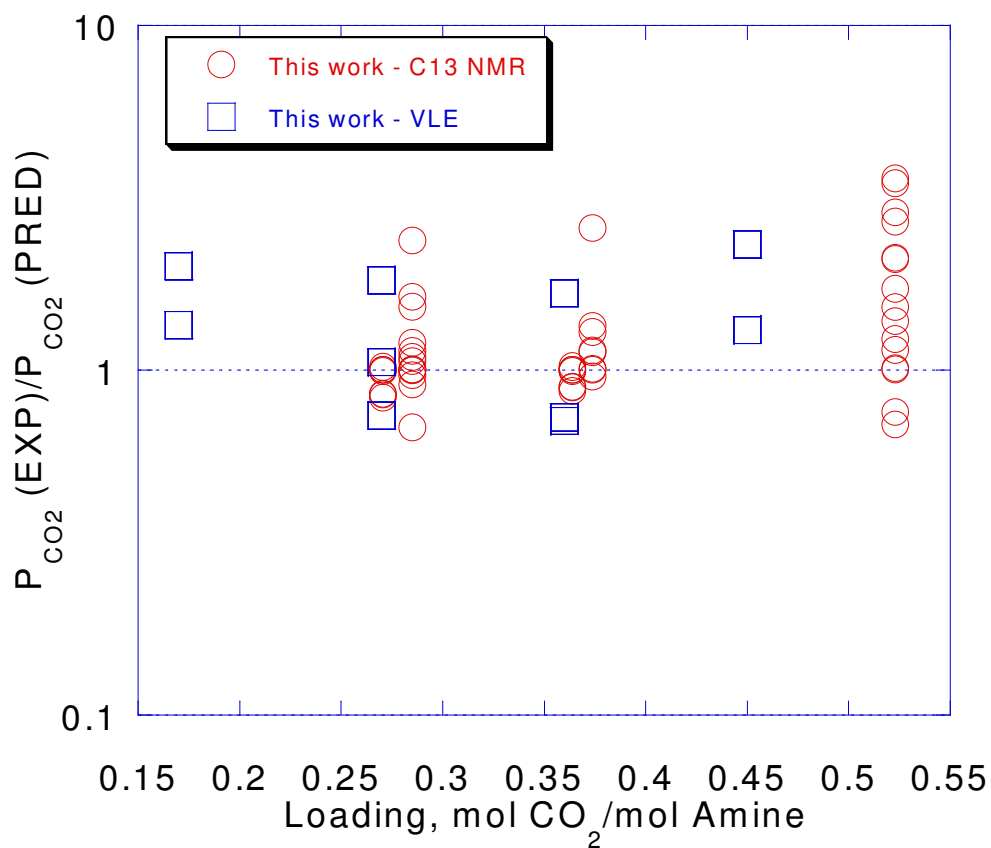


Figure 4.32 Results of VLE and NMR data regression of the DGA-CO₂ system.

Table 4.22. Non-Default parameters for DGA-MOR mixed amine parameters.

Parameter	A	B	τ_{40}	Default τ
(IH ₂ O,IMORH,IDGACOO)	-4.0	-24095	-12.7	8
(IH ₂ O,IDGAH,IMORCOO)	11.0	-24044	2.3	8
(IMORH,IDGACOO, IH ₂ O)	-3.7	-960	-4.0	-4
(IDGAH,IMORCOO, IH ₂ O)	-0.81	-1019	-1.2	-4

$$\tau = A + B \left(\frac{1}{T} - \frac{1}{T_{ave}} \right) \text{ for salt pair / molecule and molecule / salt pair}$$

Figure 4.33 compares partial pressure predictions from the current model to the VLE data obtained in this work. Figures 4.34, 4.35, 4.36 and 4.37 give the predicted speciation at 25 °C, 40 °C and 60 °C.

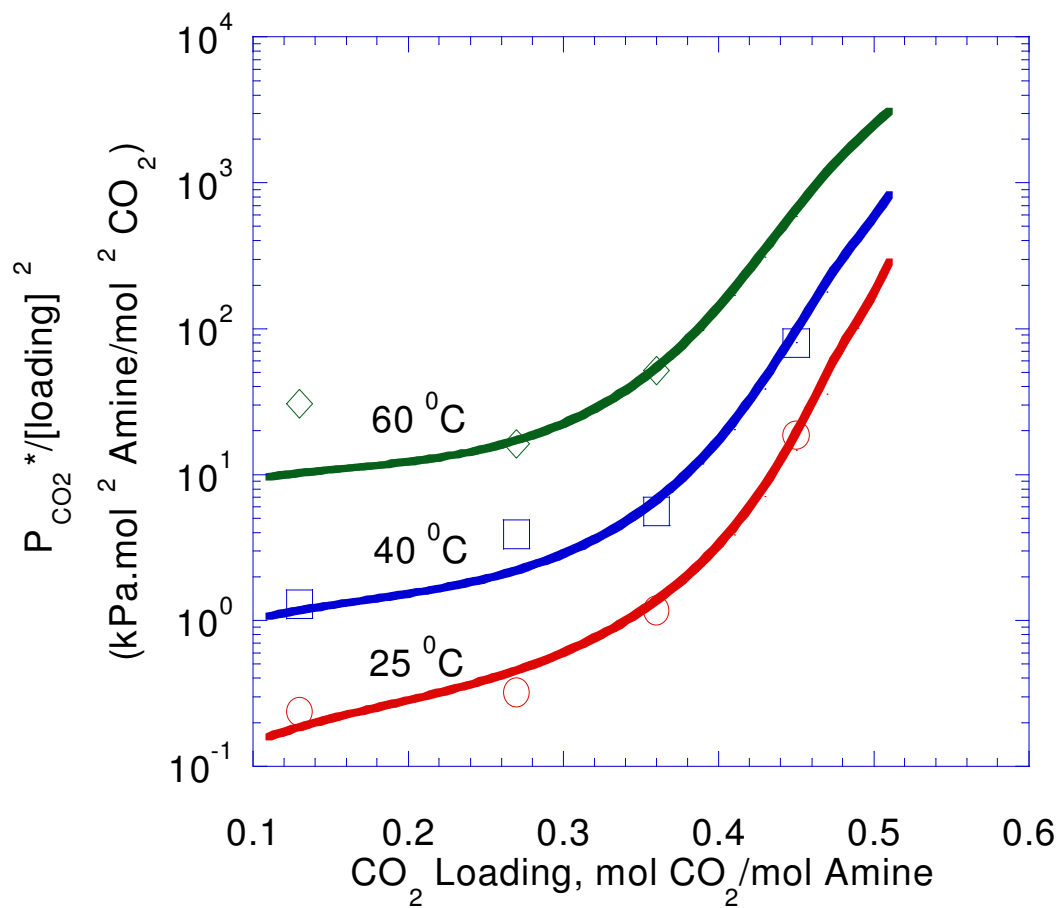


Figure 4.33 Results of VLE data regression of the 11 wt% MOR/53 wt% DGA system at 60 °C.

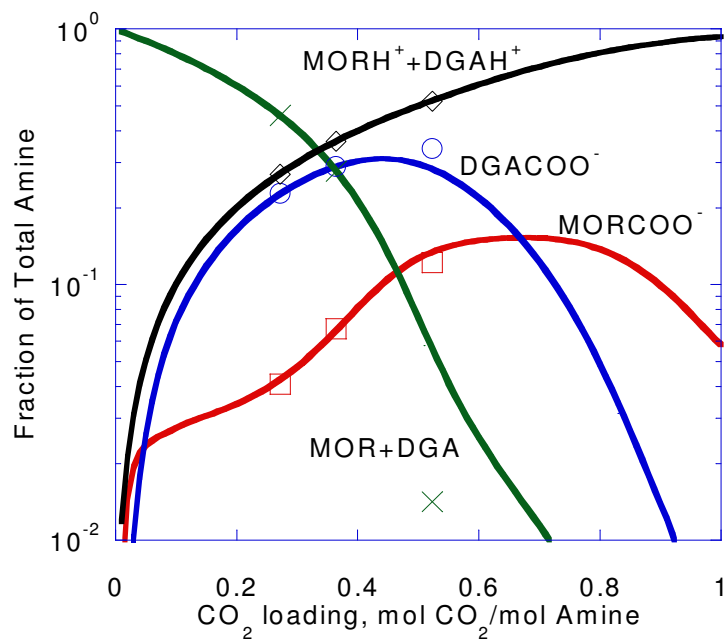


Figure 4.34 Results of regression of C13 NMR data in DGA-MOR-CO₂ system at 25 °C.

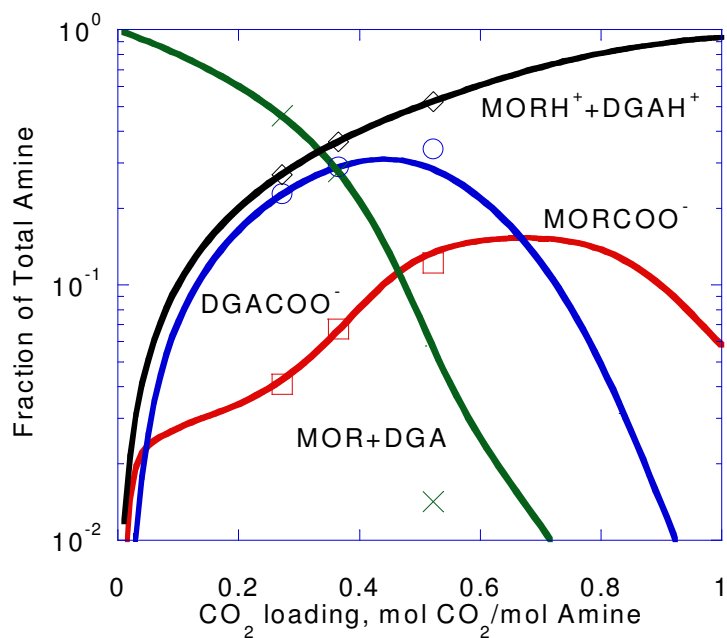


Figure 4.35 Results of regression of C13 NMR data in DGA-MOR-CO₂ system at 40 °C.

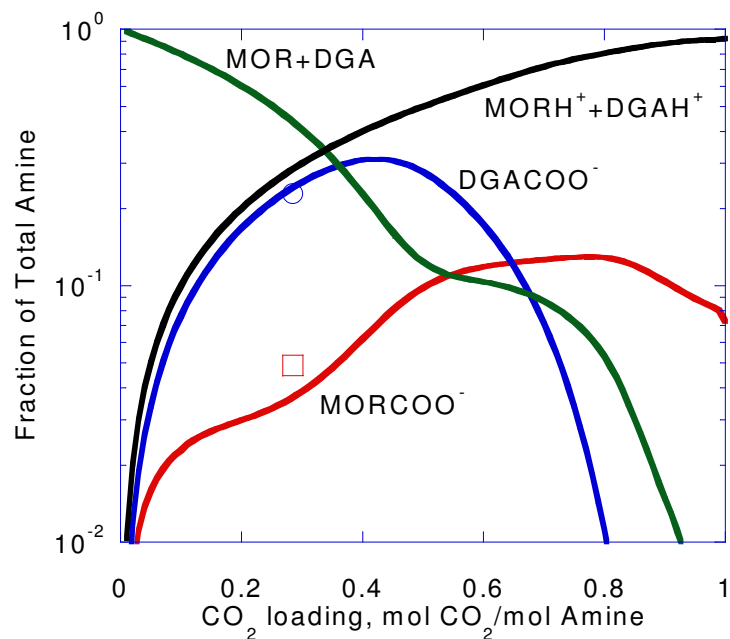


Figure 4.36 Results of regression of C13 NMR data in the 11 wt% MOR/53 wt% DGA system at 60 °C.

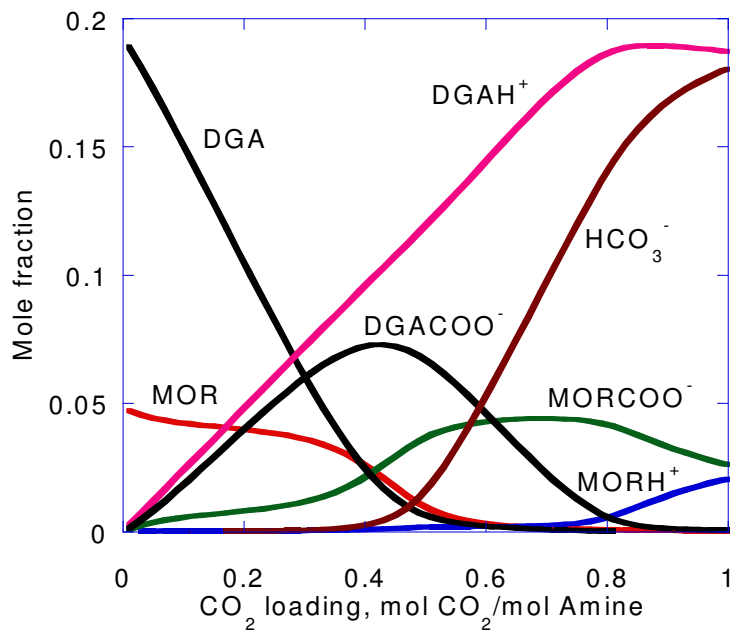


Figure 4.37 Predicted speciation of CO₂ in 11 wt% MOR/53 wt% DGA at 40 °C.

4.9 Solvent Working Capacity

Figure 4.38 shows the equilibrium CO₂ loading of the 65wt% DGA and 11wt% MOR/53 wt% DGA solutions at 25 °C, 40 °C and 60 °C. At Shedgum gas plant, the natural gas stream contains 10.3% CO₂ and is contacted with 50 wt% solvent DGA in an absorber at a total pressure of 1500 kPa and 40 to 60 °C. The corresponding CO₂ partial pressure is 155 kPa. In order to achieve maximum capacity of each volume of solution circulated, the circulation rate is set so that the maximum recommended loading can be achieved. Typically the maximum loading is represented as an approach to equilibrium set by the VLE data. Assuming that the approach to equilibrium at the bottom of the absorber is 30%, and the equilibrium partial pressure of CO₂ under regeneration conditions is 10⁻³ kPa, the solvent working capacity can then be calculated. As can be seen in figure 4.33 the blend solution shows steeper slope compared to the 65 wt% DGA. The 65 wt% DGA provides the highest equilibrium loading compared to blend mixture. The 11 wt% MOR reduces the working capacity by 11% compared to the 65 wt% DGA working capacity at 60 °C. From solvent capacity point of view, the 65 wt% DGA solution is better than the 11 wt% MOR/53 wt% DGA solution requiring a lower solvent circulation rate. Table 4.23 gives the results of the calculations at 60 °C.

Table 4.23 Comparison of working capacities at 60 °C, P_{CO₂, rich} = 50 kPa, P_{CO₂, lean} = 10⁻³ kPa .

Solvent	Lean loading (mol/mol)	Rich loading (mol/mol)	Working capacity (mol/mol)
65 wt% DGA	~0.01	0.51	0.51
11 wt% MOR/53 wt% DGA	~0.01	0.46	0.45

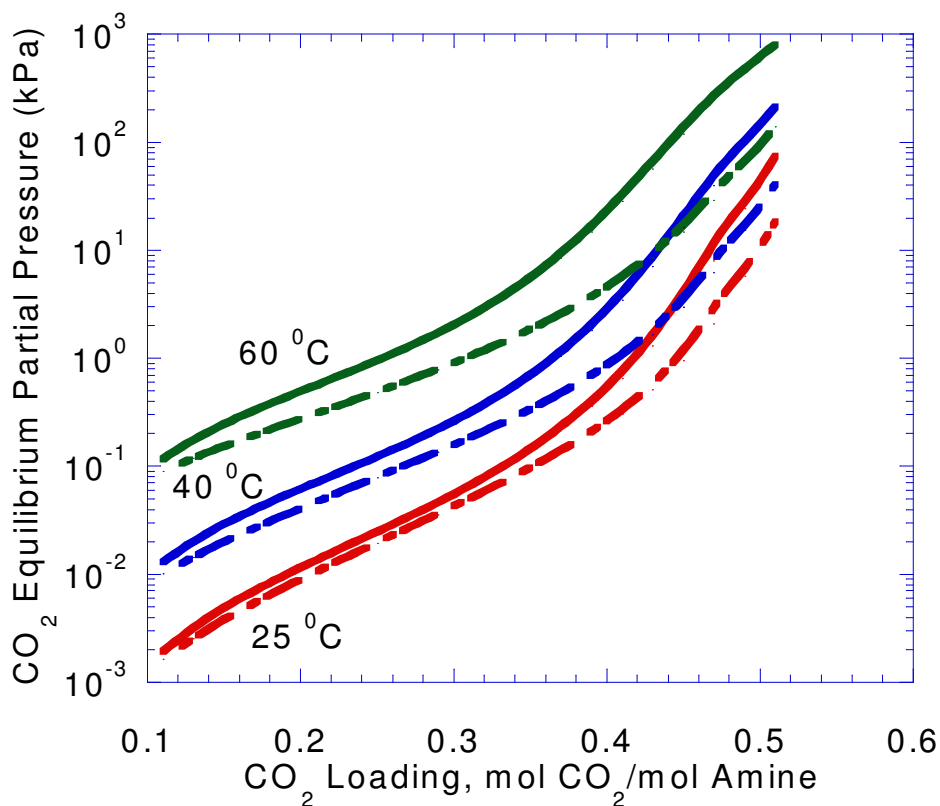


Figure 4.38 CO₂ partial pressure as a function of loading for the the 11 wt% MOR/53 wt% DGA system (solid lines) and 65 wt % DGA system (dashed lines) at 25 °C, 40 °C and 60 °C.

4.10 Regeneration Energy Requirements

The main source of energy consumption in an amine process is the regeneration step. As much as 80% of the total energy is consumed during solvent regeneration. The total energy required to regenerate a CO₂ loaded solvent can be expressed as follows:

$$\text{Total Energy} = \text{Heat of Reaction} + \text{Sensible Heat} + \text{Latent Heat of Vaporization of Water}$$

In the regeneration step, first the rich solvent temperature must be raised to the stripper temperature by sensible heat transfer. The amount of heat required for

this process is dictated by the specific heat capacity of the solvent, which does not vary much among the various solvents. In addition, the water component of the solvent must also be vaporized to generate the stripping vapor. While the specific heat capacity and the latent heat of vaporization of water remains the same for all solvents, the energy required for this step depends on the proportion of water present in a given solvent. Therefore, the energy required for the vaporization of water in the 65wt% DGA and the 11 wt% MOR/53 wt% DGA (65wt% total Amine) solutions will be the same.

Finally, sufficient heat must be provided to break up the CO₂-solvent complex formed during the absorption process. This can be accounted for by the heat of reaction. The heat of reaction, ΔH_{abs} , of 65 wt% DGA and 11 wt% MOR/53 wt% DGA solutions was determined at various loadings at 25 °C, 40 °C and 60 °C. Using the Clapeyron equation, equation 5.16, the ΔH_{abs} can be calculated. Results are displayed graphically in figure 4.39.

For the 65 wt% DGA and 11 wt% MOR/53 wt% DGA, the heat of absorption is about the same. Note that loading has a significant effect on the heat of absorption, increasing the loading decreases the heat of reaction.

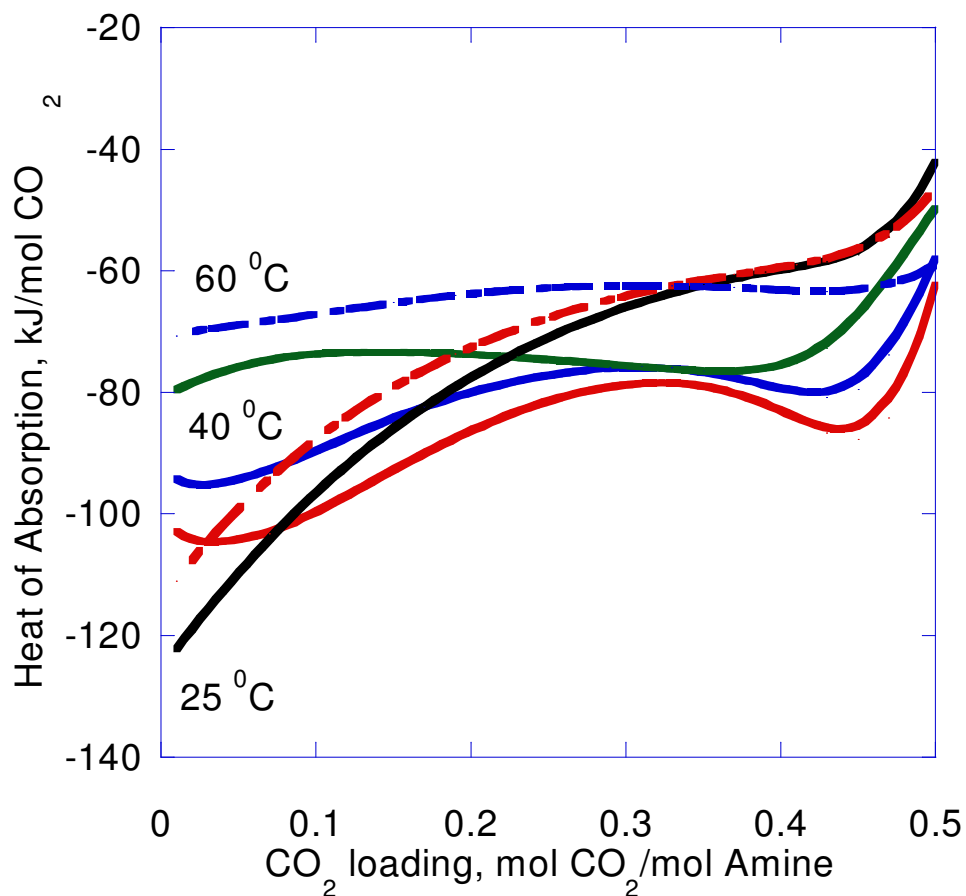


Figure 4.39 Heats of reaction of CO₂ at various CO₂ loading for 11 wt% MOR/53 wt% DGA (solid lines) and 65 wt % DGA (dashed lines) at 25 °C, 40 °C, and 60 °C.

As can be seen in figure 4.39, the 65wt% DGA heat of reaction is slightly higher than that of the 11 wt% MOR/53 wt% DGA. As a result more energy must be provided to regenerate DGA than the mixed amine solution. It should be noted that the experiential results in figures 4.7and 4.8 suggest that the heat of reaction in the blend and the 65 wt% DGA are comparable.

Based on the heats of reaction, it is clear that 11 wt% MOR/53 wt% DGA solution would have slight less energy requirements than 65wt% DGA. However, the problem is that the mixed amine solution capacity is lower than that of the

DGA solution as discussed above in section 4.9. The mass transfer rate of MOR and DGA is the subject of Chapter 5 and 6.

4.11 Solvent Vaporization losses

Amine plant losses stem from vaporization, solubility, mechanical, degradation and entrainment. Vaporization losses are a direct result of alkanolamine vapor pressure in the treating solution on the contacted gas stream. Parameters that govern the amount of vaporized amine are temperature, pressure and amine concentration. These parameters establish equilibrium between the amine vapor pressure in solution and the partial pressure of amine in the gas stream. As temperature increases and / or pressure decreases, the amount of gas phase amine increases due to higher vapor pressure exerted by the alkanolamine on the gas. Because treated gas is continuously being replaced by new gas moving up the absorber, additional amine must move into the gas phase via vaporization to maintain equilibrium.

Vaporization estimates of MOR in the 11 wt% MOR/53 wt% DGA solutions are presented in figure 4.40. Since total pressures and gas phase compositions vary widely in industrial absorbers, results are presented as the vapor side fugacity of MOR. Since the gas leaving the absorber is in contact with the lean amine solution entering the top of the column, all calculations are done at a lean loading of 0.01. MOR is seen to be very volatile compared to DGA.

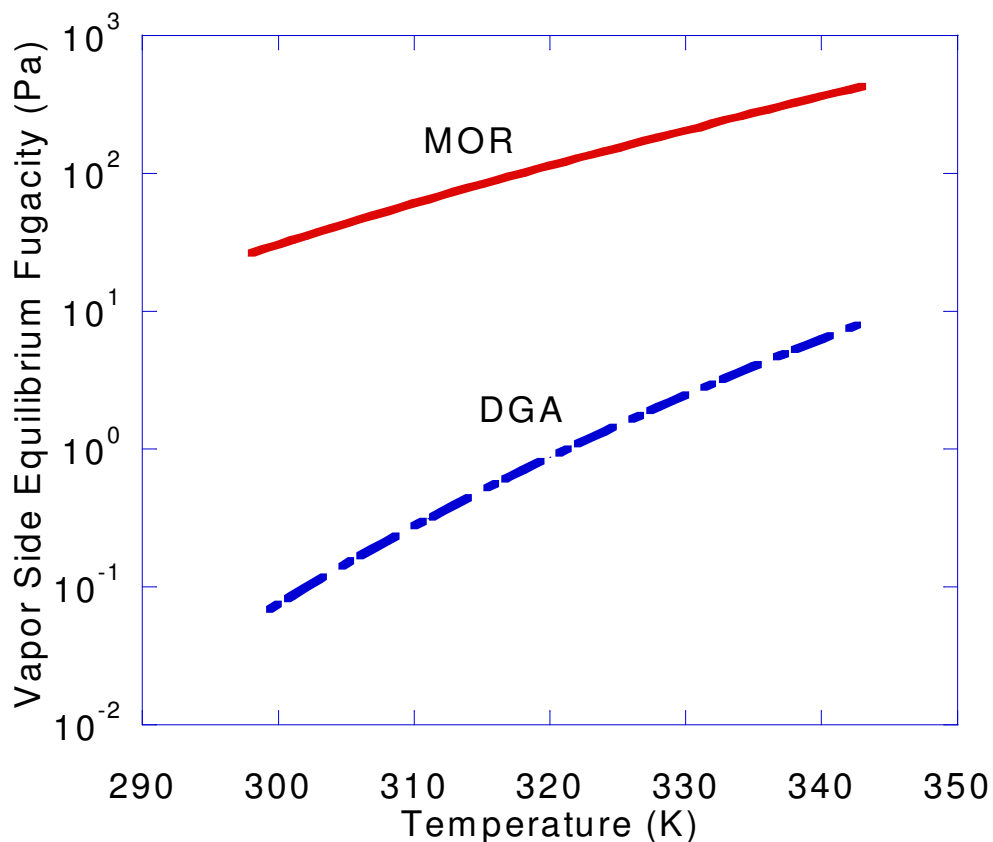


Figure 4.40 Vapor pressure of MOR over 11 wt% MOR/53 wt% DGA, and CO₂ loading of 0.01 mol CO₂ / mol amine.

4.12 Conclusions

1. Equilibrium partial pressure: The experimental solubility of CO₂ and model predictions presented in this work suggest that the 23.5 wt % MOR gives a higher CO₂ equilibrium partial pressure compared to the 65 wt% DGA and 11 wt % MOR/53 wt% DGA solutions. In addition, 11 wt%MOR/53 wt% DGA blend shows a higher equilibrium partial pressure of CO₂ at high loading by a factor of 5 to 7 than 65 wt% DGA. This is due to the low carbamate stability constant of MOR compared to DGA. Partial pressures at low loading (<0.1) in

the blend are, however, seen to be similar to those in 65 wt% DGA. This is due to the carbamate stability of each of the DGA and MOR.

2. Solvent working capacity: the 65 wt% DGA solution gives ~ 10% higher working capacity compared to the blend solution under the condition studied so far. Therefore, for a given column, the 65 wt% DGA solution will require less solvent circulation rate to achieve the separation compared to the blend solution.
3. MOR losses due to volatility: The volatility of MOR is higher than DGA. MOR vapor pressure is ~ 100 times greater than DGA vapor pressure at 313 K to 333 K. The MOR vaporization losses can be reduced by using a water-wash system. The water wash has a low concentration of MOR and a low MOR vapor pressure. The MOR partial pressure in the gas phase establishes a new equilibrium by forcing MOR into the water phase.
4. Regeneration energy requirements: the 11 wt% MOR/53 wt% DGA solution will probably require less energy to regenerate compared to the 65wt% DGA.
5. NMR has proven to be a useful technique in quantifying speciation.
6. Reaction products at different conditions: The most prevalent reaction product at high loading (>0.5 at high loading) is MOR carbamate. The existence of the protonated DGA have the effect of stabilizing the overall MOR carbamate formation
7. At loading greater than 0.4, free DGA approximately equals free MOR, therefore reaction rates in rich solutions will be dominated by MOR.
8. The carbamate species of MOR is very unstable compared to the carbamate of DGA by a factor 7 to 10 from 27 °C to 60 °C.

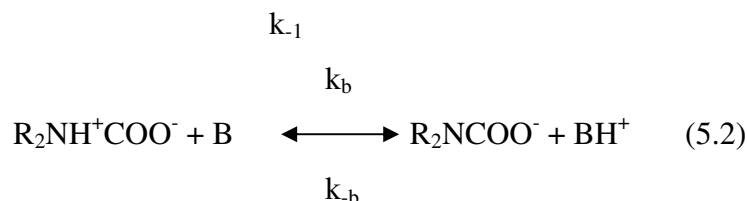
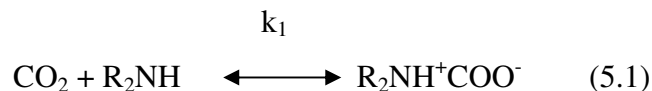
Chapter 5: Absorption of Carbon Dioxide into Aqueous Diglycolamine®

5.1 Introduction

The most widely employed gas treating process for acid gas removal in the natural gas and petroleum processing industries is the chemical solvent process, using the various alkanolamines. These processes use a solvent, either an alkanolamine or an alkali-salt (hot carbonate processes) in an aqueous solution, which reacts with the acid gas (H_2S and CO_2) to form a complex or bond. This complex is subsequently reversed in the regenerator at elevated temperatures and reduced acid gas partial pressures releasing the acid gas and regenerating the solvent for reuse. The alkanolamines most commonly used in industrial applications are monoethanolamine (MEA), diethanolamine (DEA), methyldiethanolamine (MDEA), and diglycolamine (DGA).

The use of DGA for the purpose of acid gas removal was patented by Blohm and Riesenfeld (1960) and DGA agent was commercialized in the late sixties by Fluor and Jefferson Chemical company. DGA is a primary amine, and its low vapor pressures permits its use in higher concentrations, typically 50 to 60 weight percent, resulting in significantly lower circulation rates and energy requirements. The equilibrium partial pressure of CO_2 over aqueous DGA solutions is significantly lower than that over MEA solutions, which would create more favorable driving force for mass transfer for DGA (Martin et al., 1978).

For the reaction of CO_2 with primary and secondary amines the zwitterion reaction mechanism, originally proposed by Caplow (1968) and reintroduced by Danckwerts (1979), is generally accepted as the reaction mechanism;



This mechanism comprises two steps: formation of the CO₂-amine zwitterion (reaction 1), followed by base-catalyzed deprotonation of this zwitterion (reaction 2). This mechanism leads to the following expression for CO₂:

$$R_{\text{CO}_2} = -\frac{k_2[\text{R}_2\text{NH}][\text{CO}_2]}{1 + \frac{k_{-1}}{\sum k_b[\text{B}]}} \quad (5.3)$$

where $\sum k_b[\text{B}]$ is the contribution to the removal of the proton by all bases present in the solution. For two asymptotic cases Eq. (5.3) can be simplified if,

- The second term in the denominator is much less than one. This results in simple second order kinetic expression

$$R_{\text{CO}_2} = -k_2[\text{R}_2\text{NH}][\text{CO}_2] \quad (5.4)$$

- The second term in the denominator is much greater than one. This results in the following third order kinetic expression

$$R_{\text{CO}_2} = -\frac{k_2}{k_{-1}}[\text{R}_2\text{NH}][\text{CO}_2]\sum k_b[\text{B}] \quad (5.5)$$

Although the reaction of CO₂ with primary and secondary amines has been studied extensively only limited information is available for the reaction between CO₂ and DGA.

The reaction kinetics of DGA has been studied by Pacheco (1998), Pacheco et al. (2000), Littel et al. (1991), Alper (1990), and Hikita et al. (1977). In

most cases, there is general agreement as to the order and rate of reaction with respect to DGA in the temperature range of 25°C to 40°C. However, there is disagreement on the rate data at 60°C. Hikita et al. (1977) studied the CO₂ kinetics in DGA solutions up to 40°C and at very low amine concentrations in a stopped flow reactor. Alper (1990) studied the reaction rate with 0.1 and 0.2 M DGA and at 25°C in a stopped flow reactor, and found that his results compared very well with Hikita et al. (1977). Littel et al. (1991) have extended the temperature and the concentration range by studying kinetics up to 60°C and over the concentration range of 0 to 5 M in a stirred cell reactor. Littel et al. (1991) found a value of two for the overall reaction order at temperatures below 40°C and a higher value at 60°C for the overall reaction order, and therefore used the zwitterion mechanism to explain the CO₂/DGA kinetics. They concluded that their data showed good agreement with previous authors. Overall it can be concluded that below 40°C the kinetics of DGA are well established. Recently, Pacheco (1998) and Pacheco et al. (2000) have studied DGA-CO₂ kinetics in a wetted-wall column, and their results are comparable to those of previous investigators at temperatures below 40°C; however, the activation energy was found to be higher than previously published values.

In this chapter, the work of Pacheco (1998) is reviewed and it has been extended to include more data at 65wt% DGA concentration from 25°C to 60°C at 0 to 0.4 moles CO₂/mole DGA. Unfortunately, it was not possible to evaluate the data of previous researchers because they did not publish the values of the Henry's constant and diffusivity. This work also uses the mass transfer model developed by Bishnoi (2000), based on the eddy diffusivity theory. The use of mass transfer models becomes more important especially at conditions where it is possible to significantly deplete the amine at the gas liquid interface. The rate model depends on the speciation from the VLE model. This has been verified in chapter 4 using C13 NMR measurements. Speciation is critical especially at high loading. The pseudo first order (PFO) and interface pseudo first order (IPFO) approximation

models were also compared to the rigorous model. The effect of ionic strength on the second order rate constant was also studied in this chapter. Glycolic acid and potassium formate were used to modify the ionic strength of the DGA solution.

5.2 Experimental Methods

The absorption rate of carbon dioxide was determined in a wetted wall column. The use of this apparatus to provide data for CO₂ absorption in amine solutions has been described in detail in chapter 4. Solution flowed down the outside of a stainless steel tube that was 9.1 cm long with a contact area of 38.52 cm². The column operated at 1 to 8 atm with gas rates of 4 to 6 L/min. Loaded amine solution was recirculated at 2 cm³/s from reservoirs of 1L volume. The absorption rate was determined from continuous infrared analysis of the gas leaving the system. The reported CO₂ partial pressure is the log mean average of the gas entering and leaving the contactor. The liquid film mass-transfer coefficient was determined by CO₂ desorption from water and ethylene glycol mixtures. The gas film coefficient was determined by the absorption of sulfur dioxide into sodium hydroxide solutions (Bishnoi, 2002).

5.3 Physical Properties

The Henry's law constant for CO₂ (H_{CO_2}) is obtained using the N₂O analogy with the solubility of N₂O measured by Versteeg and van Swaij (1988) in 65 wt% DGA solution at 25 °C.

$$H_{CO_2} = \frac{H_{CO_2, H_2O}}{H_{N_2O, H_2O}} H_{N_2O} \quad (5.6)$$

Pacheco (1998) correlated the Henry's Law constant for carbon dioxide in pure water measured by Versteeg and van Swaij. (1988) and reported by Al-Ghawas et al. (1989):

$$H_{\text{CO}_2}^{\circ} (\text{atm cm}^3 / \text{mol}) = 1.7107\text{E}+07 \exp \{-1886.1 / T (\text{K})\} \quad (5.7)$$

The Henry's constant for NO in loaded DGA solutions is given by Danckwerts (1979);

$$\log\left(\frac{H}{H^*}\right) = (k'_+ + k'_- + k'_g)I \quad (5.8)$$

The parameters k'_+ , k'_- , and k'_g (van-Krevelen coefficients) are specific to the cations, the anions, and the gas, respectively, and are assumed to be ion concentration independent and I_i is the partial ionic strength of each ion, given as

$$I_i = \frac{1}{2} c_i z_i^2 \quad (5.9)$$

where c_i is the ion concentration and z_i the ion charge. The superscript * refers to solubility in unloaded solution.

Table 5.1 give the values of k'_+ , k'_- , and k'_g at 25 °C, 40 °C and 60 °C.

Table 5.1 Van-Krevelen coefficients at 25 °C, 40 °C and 60 °C.

Parameter	25 °C	40 °C	60 °C
k'_+	0.043	0.043	0.043
k'_-	0.047	0.047	0.047
k'_g	-0.019	-0.026	-0.016

For applying the model equations, the ionic strength of the solution as a function of the composition must be calculated. The liquid composition can be calculated as a function of the CO_2 loading, using the equilibrium model developed in the previous chapter.

The diffusivity of CO₂ in DGA solutions was estimated using the modified Stokes-Einstein equation to correct the diffusivity of CO₂ in pure water for the change in viscosity with the addition of DGA as follows:

$$D_{\text{CO}_2} = D_{\text{CO}_2}^0 \left(\frac{\mu}{\mu_L} \right)^{0.6} \quad (5.10)$$

where $D_{\text{CO}_2}^0$ is the diffusivity of CO₂ in pure water, D_{CO_2} is the diffusivity of CO₂ in DGA solutions, μ^0 is the viscosity of pure water and μ_L is the viscosity of the DGA solution. For diffusivity of CO₂ in aqueous DGA solutions, the following equation was obtained from the data reported by Hikita et al. (1981):

$$D_{\text{DGA}} = 2.868 \times 10^{-8} \mu_L^{-0.449} T \quad (5.11)$$

where D_{DGA} in cm²/s and T in K. Diffusion coefficients of all ions are arbitrarily set at the same value as DGA. Here, the solution viscosity is calculated using the data by Jefferson (1970). The solution density is also calculated using the data by Jefferson (1970). Viscosity of DGA/glycolic acid and DGA/potassium formate solutions were measured using the Cannon-Fenske procedures for viscosity measurement. A size 150 viscometer was used to measure the viscosity of the DGA/glycolic acid and DGA/potassium formate solutions.

5.4 Model Description

5.4.1 Rigorous model

The model developed by Bishnoi (2000), based on the eddy diffusivity theory, was used in this work. The advantage of the eddy diffusivity theory over other theories, like surface renewal and penetration theory, is that it predicts the correct dependence of the mass transfer coefficient on the diffusion coefficient without introducing time as a variable. Glasscock and Rochelle (1989) have shown

that the absorption predictions from eddy theory are comparable to surface renewal and penetration theory within 5%. For a second order reaction, Glasscock and Rochelle showed that film theory deviates by 30% at enhancement factors of about 100. For this reason, the eddy diffusivity theory will be used for all rigorous modeling in this work. A full description of the model equations can be found in Bishnoi (2000).

For absorption of CO₂ into a reactive solvent, Bishnoi used the following expression to represent the material balance equation

$$\nabla\left(\left(D_i + \varepsilon x^2\right)\nabla[i]\right) = -\mathfrak{R}_i \quad (5.12)$$

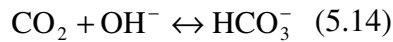
where i is a component to be included in the model, ε is the mass transfer coefficient parameter, \mathfrak{R}_i is the overall rate of the reaction of species i , and ∇ is the derivative operator with respect to the space variable x , where x represents the liquid depth away from the gas-liquid interface.

This can be simplified further as

$$\nabla^2[i] = -\mathfrak{R}_i \quad (5.13)$$

where ∇^2 can be considered the Eddy Diffusivity operator.

A proper understanding of the model used in this work begins with a discussion of all species and reactions used. The following two reactions are assumed to be kinetically controlled and reversible



For example, the rate of DGA® reaction with CO₂ is given by:

$$r = k_{\text{DGA}} \left([\text{DGA}][\text{CO}_2] - \frac{[\text{DGACOO}^-][\text{H}_3\text{O}^+]}{K} \right) \quad (5.16)$$

where k_{DGA} is given by

$$k_{\text{DGA}} = k_{25^{\circ}\text{C}} \cdot \exp\left[-\frac{\Delta H_a}{R} \left(\frac{1}{T} - \frac{1}{298.15}\right)\right] \quad (5.17)$$

and the equilibrium constant

$$K_{15} = \frac{[\text{DGACOO}^-][\text{H}_3\text{O}^+]}{[\text{DGA}][\text{CO}_2]} \quad (5.18)$$

is calculated by the ratio of the species in the bulk solution.

The rate constant for reaction 5.14 is the expression presented by Pinsent et al. (1956). The rate constant, k_{DGA} , for reaction 5.15 is fit to match absorption data into loaded and unloaded solutions.

Note that water is left out of the kinetic and equilibrium expressions since it is considered to be constant across the boundary layer and, therefore, can be lumped with the apparent rate and equilibrium constants.

In order to avoid having H_3O^+ as a species in the model, rates of reaction for carbamate formation are described as:

$$R_{15} = k_{\text{DGA}} \left([\text{DGA}][\text{CO}_2] - [\text{DGACOO}^-] \frac{K_w}{K_{15}[\text{OH}^-]} \right) \quad (5.19)$$

$$\text{where } K_w = [\text{H}_3\text{O}^+][\text{OH}^-] \quad \text{and} \quad K_{15} = \frac{[\text{DGACOO}^-][\text{H}_3\text{O}^+]}{[\text{DGA}][\text{CO}_2]}$$

Reactions involving only a proton transfer are always considered to be in equilibrium. All equilibrium constants are calculated directly from the ratio of products and reactants in the bulk solution. The bulk solution is speciated using the electrolyte NRTL model described in chapter 4. These reactions are



The equations to be solved are presented in Table 5.2. Along with these seven equations, we define boundary conditions at the interface and in the bulk solution. We use the condition that all concentrations are equal to the equilibrium

concentrations as liquid depth approaches infinity. We also assume phase equilibrium of CO₂ at the interface leading to a known concentration of CO₂ at the interface for a given interfacial partial pressure of CO₂. The concentration of species which undergo proton exchange are defined by the combined buffer system flux being zero at the interface and chemical equilibrium between the two species involved in the proton exchange. Electroneutrality is also assumed at the interface. Table 5.2 documents also the boundary conditions used in this work.

Table 5.2 Model Equations and Boundary Conditions

Conservation Equations at Each Node

Overall Species Material Balance

$$\nabla^2[\text{DGA}] + \nabla^2[\text{DGACOO}^-] + \nabla^2[\text{DGAH}^+] = 0$$

$$\nabla^2[\text{CO}_2] + \nabla^2[\text{HCO}_3^-] + \nabla^2[\text{CO}_3^{2-}] + \nabla^2[\text{DGACOO}^-] = 0$$

Equilibrium Relationships

$$K_{20} = \frac{[\text{DGAH}^+][\text{OH}^-]}{[\text{DGA}]}$$

$$K_{21} = \frac{[\text{CO}_3^{2-}]}{[\text{HCO}_3^-][\text{OH}^-]}$$

Material Balance for Molecular CO₂

$$\nabla^2[\text{CO}_2] - (R_1 + R_2) = 0$$

Carbamate Balance

$$\nabla^2[\text{DGACOO}^-] + R_2 = 0$$

Electroneutrality

$$[\text{DGAH}^+] = [\text{HCO}_3^-] + 2[\text{CO}_3^{2-}] + [\text{OH}^-] + [\text{DGACOO}^-]$$

Boundary Conditions

At $x=0$

$$[\text{CO}_2] = [\text{CO}_2]_I$$

$$\begin{aligned}
D_{\text{HCO}_3^-} \nabla[\text{HCO}_3^-] + D_{\text{CO}_3^{2-}} \nabla[\text{CO}_3^{2-}] &= 0 \\
D_{\text{DGA}} \nabla[\text{DGA}] + D_{\text{DGAH}^+} \nabla[\text{DGAH}^+] &= 0 \\
\nabla[\text{DGACOO}^-] &= 0 \\
K[\text{HCO}_3^-][\text{OH}^-] - [\text{CO}_3^{2-}] &= 0 \\
K[\text{DGA}] - [\text{DGAH}^+][\text{OH}^-] &= 0 \\
[\text{DGAH}^+] &= [\text{HCO}_3^-] + 2[\text{CO}_3^{2-}] + [\text{OH}^-] + [\text{DGACOO}^-]
\end{aligned}$$

At $x = \infty$

$[i] = [i]_0$ For all species i in solution

5.4.2 Pseudo first order models

The rigorous solution of mass transfer with chemical reaction is more complicated as seen in the last section. It requires the solution of many simultaneous equations. There are certain situations when it is not necessary to deal with a complicated large system of equations, if a few simplifying assumptions are satisfied. Assumptions 1 and 2 listed below lead to the pseudo first order (PFO) and interface pseudo first order (IPFO) approximations.

Assumption 1: The liquid phase driving force ($P_{\text{CO}_2, \text{interface}} - P_{\text{CO}_2, \text{bulk}}^*$) is very small. This means that the flux is so small that the $P_{\text{CO}_2, \text{interface}} \approx P_{\text{CO}_2, \text{bulk}}^*$ and that $[\text{DGA}]_{\text{interface}} \approx [\text{DGA}]_{\text{bulk}}$

Assumption 2: The reaction of $\text{CO}_2 + \text{DGA}$ is fast enough that CO_2 reaches equilibrium with the rest of the solution, near the interface.

The IPFO approximation requires assumption 2; the PFO approximation requires assumption 1. In assumption 1 $P_{\text{CO}_2, \text{bulk}}^*$ is the partial pressure of CO_2 that would be in equilibrium with the bulk composition at the bulk temperature and loading. Small liquid phase driving force means that the DGA is not significantly depleted at the interface and there is no accumulation of reaction products at the interface. This assumption implies that the concentrations of every component in solution, except CO_2 , can be considered constant in the liquid boundary layer at their bulk values. The assumption of small driving force is relative to the loading; at low loading there is a large amount of free DGA in solution, and a high driving

force is necessary to break the validity of the assumption; at high loading there is little free DGA in solution: a very small driving force is required for the PFO assumption to be valid.

Assumption 2 (IPFO) implies that all the reaction of CO₂ occurs in a small fraction of the boundary layer (that can be called reaction sub-layer), so that the CO₂ reaches equilibrium with the rest of the solution before the DGA and the other species in solution change significantly their concentrations from their values at the interface (CO₂ reaches an asymptote in this layer). The reaction sub-layer is controlled by the kinetics. In the diffusion region the DGA and the ions diffuse from and to the bulk; the CO₂ concentration changes, because it remains at equilibrium with all the other species.

Both the IPFO and PFO approximations assume that the concentration profiles of all the species in the reaction sub-layer, except CO₂, are constant. The IPFO differs from the PFO approximation in that the profiles are assumed constant at their interface value, different from the bulk value.

The advantage of PFO and IPFO models is that the flux of CO₂ can be derived from the analytical solution of equation 5.11, when the two following boundary conditions are applied.

$$[\text{CO}_2] = [\text{CO}_2]_i \text{ @ } x=0 \text{ for PFO and IPFO} \quad (5.22)$$

$$[\text{CO}_2] = [\text{CO}_2]_{\text{bulk}}^* \text{ for PFO or}$$

$$[\text{CO}_2] = [\text{CO}_2]_i \text{ as } x \rightarrow \infty, \text{ for IPFO} \quad (5.23)$$

The x coordinate goes from the interface into the liquid bulk.

The analytical solutions for the CO₂ flux are equations 5.23 and 5.24, as shown by Freguia (2002), for PFO and IPFO respectively. In equations 5.23 and 5.24 the CO₂+OH⁻ reaction was neglected.

$$N_{\text{CO}_2} = \sqrt{k_{2,\text{DGA}}[\text{DGA}]_{\text{bulk}} D_{\text{CO}_2}} \frac{(P_{\text{CO}_2,i} - P_{\text{CO}_2,\text{bulk}}^*)}{H_{\text{CO}_2}} \quad (5.24)$$

$$N_{\text{CO}_2} = \sqrt{k_{2,\text{DGA}}[\text{DGA}]_i D_{\text{CO}_2}} \frac{(P_{\text{CO}_2,i} - P_{\text{CO}_2,i}^*)}{H_{\text{CO}_2}} \quad (5.25)$$

$P_{\text{CO}_2,i}^*$ is the partial pressure of CO_2 that would be in equilibrium with the composition at the interface.

The results are often reported as normalized flux k_G' , defined by equation 5.26.

$$k_G' = \frac{N_{\text{CO}_2}}{(P_{\text{CO}_2,i} - P_{\text{CO}_2,\text{bulk}}^*)} \quad (5.26)$$

It is clear that equation 5.24 can be applied explicitly to calculate the flux, because $[\text{DGA}]_{\text{bulk}}$ can be calculated with the equilibrium model described in chapter 4. Equation 5.25 presents the problem that the concentration of DGA at the interface, $[\text{DGA}]_i$, is not known a priori. Diffusion of reactants and products needs to be accounted for with mass transfer coefficients for those species. The calculation of $[\text{DGA}]_i$ and $P_{\text{CO}_2,i}^*$ is performed using the equilibrium model in chapter 5 and knowing also the CO_2 loading at the interface, ldg_{int} , which can be calculated using the following equation;

$$\text{ldg}_{\text{int}} = \frac{N_{\text{CO}_2}}{k_{\ell,\text{prod}} [\text{DGA}]_i} + \text{ldg}_{\text{bulk}} \quad (5.27)$$

where $k_{\ell,\text{prod}}$ is the liquid mass transfer coefficient of the DGA products.

Generally;

$$k_{\ell,\text{prod}} = k_{\ell,\text{CO}_2} \sqrt{\frac{D_{\text{prod}}}{D_{\text{CO}_2}}} \quad (5.28)$$

where D_{prod} is the diffusion coefficient of products and is set at the same value as DGA. It should be noted that the CO_2 flux in equation 5.27 is calculated using equation 5.25. In order to make the CO_2 flux continuous across the interface, the

solution for the flux is iterated between equation 5.25 and equation 5.26 until convergence is achieved. The experimental flux can be used as an initial guess in this case. The convergence criterion is that the change in the flux from one iteration to the next is less than 10^{-5} moles/cm².sec. The same iterative procedure is also applied when using the rigorous model.

5.5 Results and Discussion

The mass transfer rates of CO₂ measured in the wetted wall column contactor were interpreted using the rigorous model described above unless otherwise noted. The model was coupled to a Generalized REGression package, GREG (Caracotsios, 1986) to estimate parameter values and confidence intervals. Reaction rate constants and diffusion coefficients of reactants and products were extracted from the experimental measurements.

5.5.1 CO₂ reactive absorption into low-loading aqueous DGA solutions

Since the reaction rate between CO₂ and DGA is very fast, the contribution of the gas-side resistance becomes more important. In order to extract the CO₂ kinetics with DGA, the interfacial mass transfer rates of CO₂ in 65 wt% DGA were measured near atmospheric pressure. High vapor flow rates, approximately 5 SLPM, were used in order to decrease the contribution of the gas-side resistance. The overall gas phase resistance was 20 to 40% for data collected in this work. Also lower CO₂ partial pressures were used to achieve lower CO₂ loading and avoid significant deviations from the kinetic controlled regime and pseudo-first order mechanism.

At low CO₂ loading, the equilibrium partial pressure will approach zero. The enhancement factor will also be much greater than one. Therefore, from equation 5.24 we can see that a plot of the flux versus interfacial partial pressure will yield a straight line. Figure 5.21 shows the results of several temperatures,

and partial pressures. The data fits a straight line with a y-intercept of approximately zero as predicted by equation 5.24. Table 5.3 presents a subset of the absorption data in 65 wt% and 25 wt% DGA obtained in this work at zero solution loading. The data analysis of the results of the 25 wt% will be discussed later in this section. The complete sets of the rate data are given in Appendix K. The second order rate constant was extracted by taking the best fit straight line of each series represented in Figure 5.1 and correcting the slope for the diffusion coefficient and Henry's law constant for carbon dioxide. Temperature dependence of the rate constant is shown in Figure 5.2 as an Arrhenius plot.

For this system the second order rate constant for the reaction between CO₂ and DGA was extracted from the experimental measurements of the interfacial mass transfer rates of CO₂.

$$k_{\text{DGA}} \left(\frac{\text{m}^3}{\text{kmol}\cdot\text{s}} \right) = k_{2(T=298\text{K})} \exp \left(- \frac{E_a}{R} \left(\frac{1}{T} - \frac{1}{298\text{K}} \right) \right) \quad (5.29)$$

$$k_{2(298\text{K})} = 1.8\text{E} + 04 \left(\frac{\text{m}^3}{\text{kmol}\cdot\text{s}} \right)$$

$$E_a = 49.1 \left(\frac{\text{kJ}}{\text{mol}} \right)$$

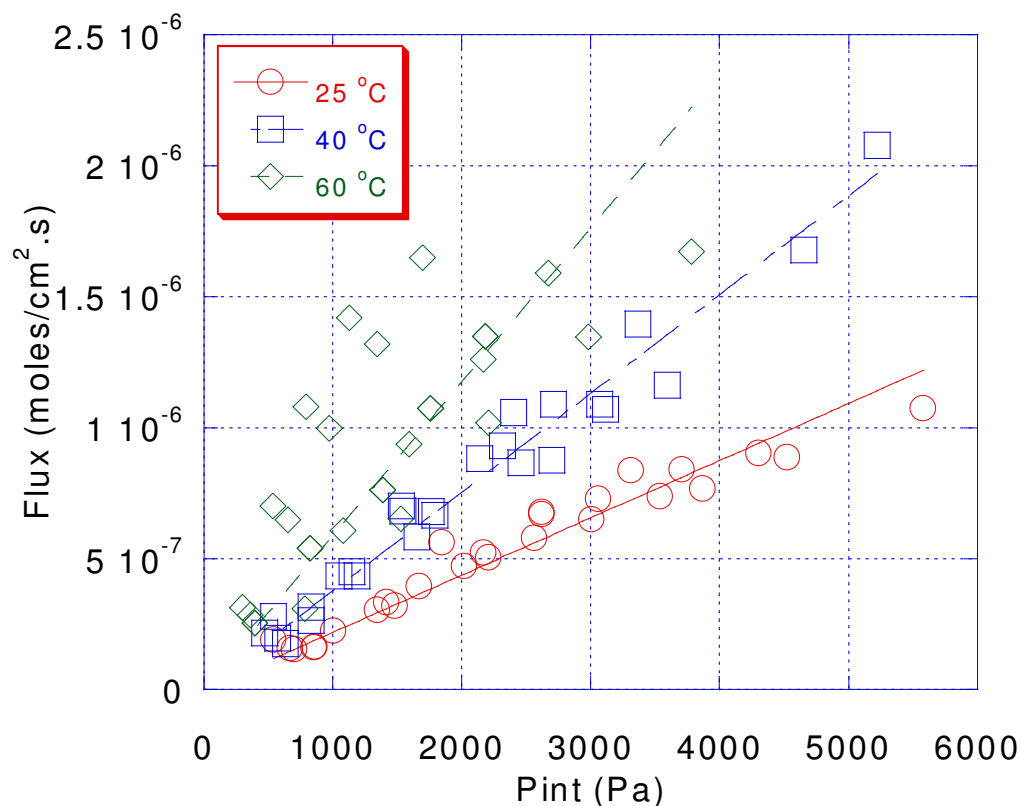


Figure 5.1 Straight line fit for rate of CO₂ absorption into aqueous 65 wt% diglycolamine solutions at low solution loading

Table 5.3 65 wt% DGA/water and 25 wt% DGA/water subset of the experimental rate measurements at zero loading. Total pressures from 0-28 psig.

$[DGA]_T$ $\frac{\text{kmol}}{\text{m}^3}$	T °C	$P_{CO_2}^{OUT} * 10^3$ Pa	Flux * 10^6 $\frac{\text{kmol}}{\text{m}^2 \cdot \text{s}}$	$k_g^o * 10^{10}$ $\frac{\text{kmol}}{\text{m}^2 \text{Pa} \cdot \text{s}}$	$k_l^o * 10^5$ m/s	$P_{CO_2}^I * 10^3$ Pa
2.5	24.5	2.5	2.7	1.94	6.6	4.1
2.5	24.5	5.2	5.8	1.96	6.6	8.5
2.5	24.5	8.0	8.7	1.98	6.6	12.8
2.5	24.6	11.0	11.1	2.00	6.6	17.0
2.5	24.9	13.8	13.8	2.02	6.6	21.1
2.5	40.2	2.2	3.0	2.07	8.9	3.9
2.5	40.9	4.6	6.4	2.09	8.9	8.0
2.5	40.8	7.2	9.6	2.06	8.9	12.4
2.5	41.0	10.1	12.4	2.04	8.9	16.8

2.5	41.1	12.9	15.1	2.06	8.9	20.8
2.5	60.9	2.3	2.5	2.28	12.2	3.5
2.5	61.0	4.7	5.6	2.24	12.2	7.5
2.5	61.2	7.4	8.3	2.21	12.2	11.6
2.5	61.2	10.2	10.5	2.23	12.2	15.3
2.5	61.3	12.8	13.1	2.25	12.2	19.0
6.5	24.1	0.7	1.9	7.91	2.5	0.9
6.5	24.3	1.6	3.1	7.95	2.5	2.0
6.5	24.7	2.3	5.6	7.99	2.5	3.0
6.5	25.2	3.1	6.8	8.04	2.5	4.0
6.5	24.7	3.9	8.4	8.07	2.5	5.0
6.5	40.0	0.6	2.2	2.60	11.5	11
6.5	40.4	1.4	4.3	2.60	11.5	11
6.5	41.0	2.0	6.8	2.60	11.5	11
6.5	41.6	2.8	8.8	2.82	11.5	76
6.5	41.7	3.5	10.9	2.98	11.4	126
6.5	61.5	111	2.69	2.89	14.4	63
6.5	60.6	182	4.22	3.04	14.3	111
6.5	60.3	138	3.12	2.93	14.3	83
6.5	60.7	160	3.73	2.99	14.3	96
6.5	60.7	11	0.20	2.66	14.3	7

The results were also reinterpreted in terms of the rigorous model to confirm the above results. The data presented in Table 5.3 were used in the parameter estimation using the rigorous model.

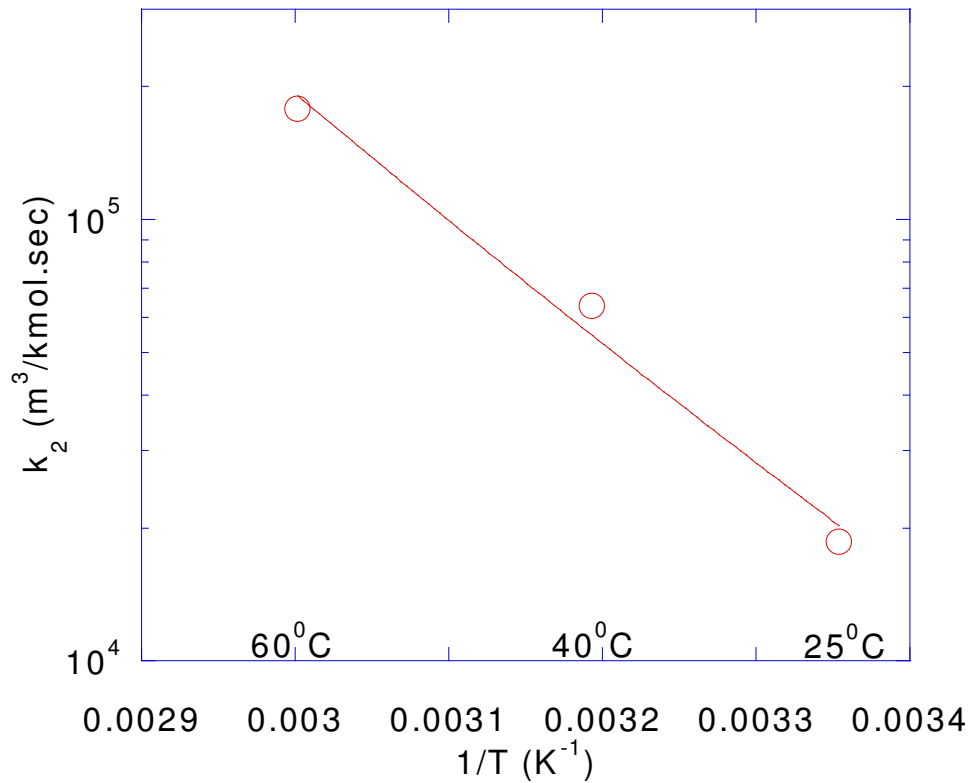


Figure 5.2 Second-order rate constant for the reaction between CO₂ and 65wt% DGA using the rigorous model, from data at zero loading.

Figure 5.3 is the parity plot for the calculated and measured fluxes of CO₂ for the DGA system. For most experiments the measured flux is within 5% of the calculated flux.

$$k_{\text{DGA}} \left(\frac{\text{m}^3}{\text{kmol.s}} \right) = k_{2(298\text{K})} \exp \left(-\frac{E_a}{R} \left(\frac{1}{T} - \frac{1}{298\text{K}} \right) \right) \quad (5.30)$$

$$k_{2(T=298\text{K})} = 2.2\text{E}+04 \left(\frac{\text{m}^3}{\text{kmol.s}} \right)$$

$$E_a = 48.5 \left(\frac{\text{kJ}}{\text{mol}} \right)$$

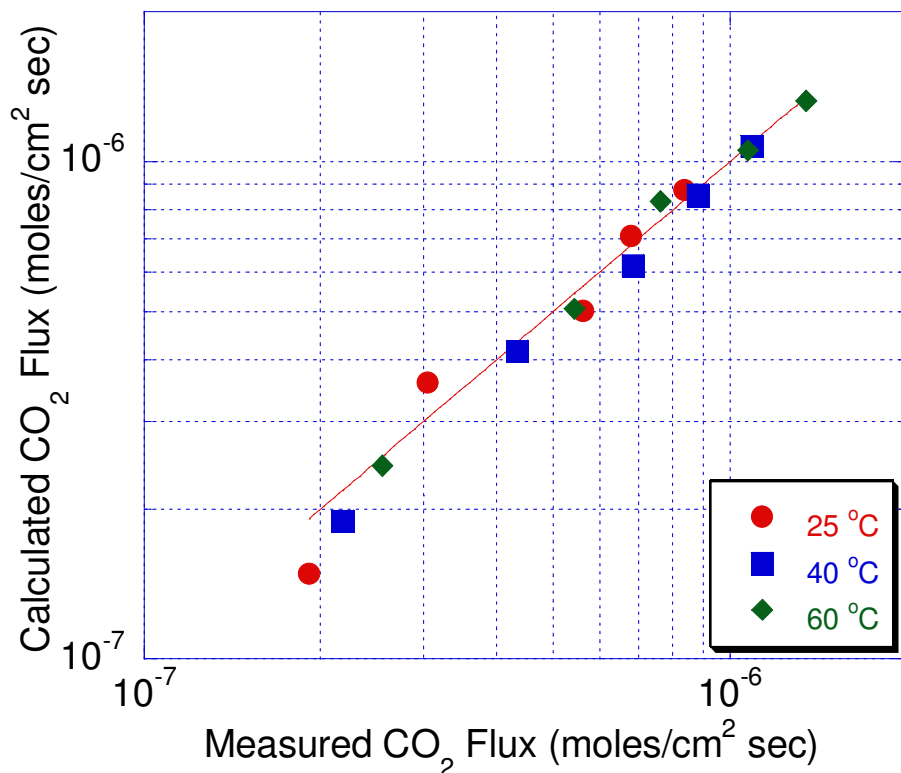


Figure 5.3 Comparison between the experimental and calculated interfacial fluxes of CO₂ using the rigorous model for the 65 wt% DGA at zero loading.

From equations 5.29 and 5.30, it can be seen that the pseudo first order model yielded results very close to those of the rigorous model. This result is due to the fact that the DGA concentration is not significantly different from that in the bulk solution. It demonstrates that the pseudo first order approximation applies at these low loading conditions.

There is a good agreement between the activation energy for the DGA reaction found in this work and those reported by other researchers. Pacheco et al (2000) obtained larger activation energy of 66.1 kJ/mol compared to other researchers.

However, the rate constant in this work is approximately four times larger than the rate constants reported by other researchers as can be seen in Table 5.4. There are two possible explanations for this observation. In the first case, the DGA reaction with CO₂ follows the zwitterions mechanism and in this case DGA catalyzes itself and therefore leads to this high value of the rate constant. In the second case, with 65 wt% DGA the wetted-wall column is operated at high vapor flow rates compared to lower DGA concentrations. It was found that, as the flow rate increased from that used at lower DGA concentrations, the film surface towards the bottom part of the column, when the gas first contacts the falling liquid, becomes less stable. This might have the effect of inducing turbulence in the gas layer close to the interface and thereby enhancing the rate of mass transfer.

In order to understand the DGA concentration effect on mass transfer, the absorption rate of CO₂ into 25wt% DGA was investigated since lower vapor flow rates can be used. Figure 5.4 shows the temperature dependence of the rate constant. There is an excellent agreement between the rate constants for the 25wt% DGA reaction and those reported by other researchers. For this system the second order rate constant is given by:

$$k_2 \left(\frac{\text{m}^3}{\text{kmol.s}} \right) = k_{2(298\text{K})} \exp \left(-\frac{E_a}{R} \left(\frac{1}{T} - \frac{1}{298\text{K}} \right) \right) \quad (5.31)$$

$$k_{2(T=298\text{K})} = 6.66\text{E} + 03 \left(\frac{\text{m}^3}{\text{kmol.s}} \right)$$

$$E_a = 40.1 \left(\frac{\text{kJ}}{\text{mol}} \right)$$

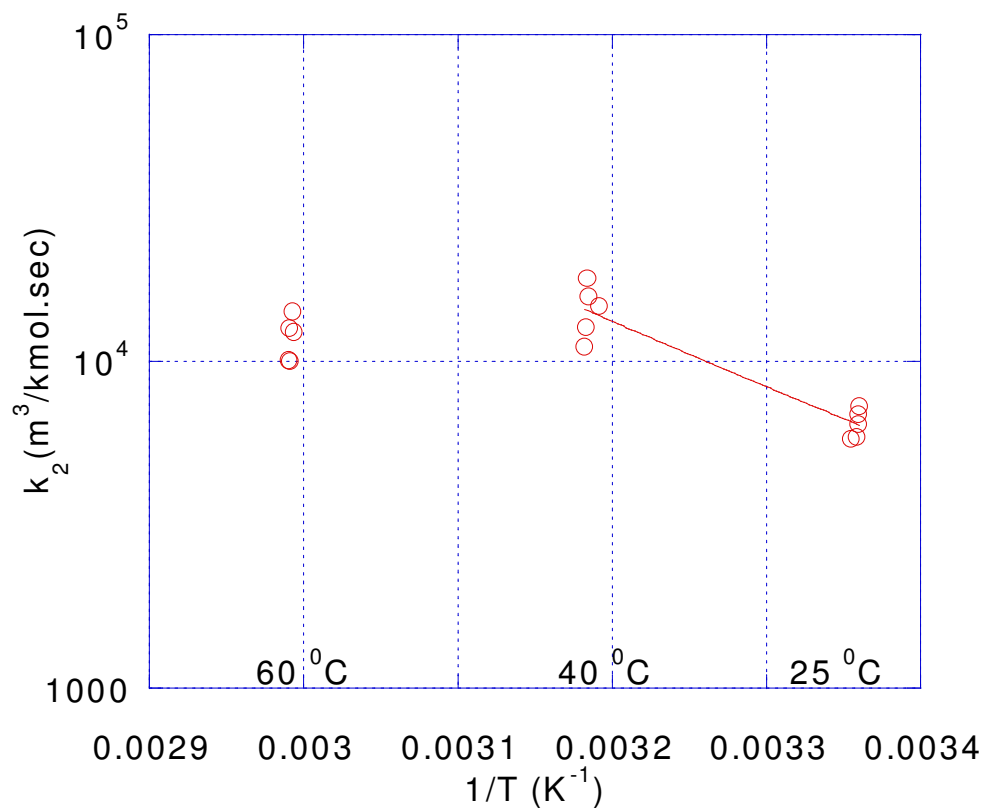


Figure 5.4 Second-order rate constant for the reaction between CO_2 and 25wt% DGA.

The results of this work and other researchers are presented in Table 5.4.

Table 5.4 Kinetic data for DGA

Reference	Temp. (range) K	DGA mol/L	$k_{298\text{K}}$ $\text{m}^3/(\text{kmole}\cdot\text{s})$	E_{act} kJ/mole	Experimental technique
Hikita et al (1977b)	278-313	0.015-0.032	5923	40.7	Stopped Flow
Barth et al., 1986	298	0-0.050	4480	-	
Alper (1990)	278-298	0.1,0.2	4517	39.4	Stopped Flow
Little et al. (1992)	298-318	0.1-3	3990	44.3	Stirred Cell
Pacheco et al. (2000)	298-333	2.4-4.8	5080	66.1	Wetted wall column
This work	298-313 298-333	2.4 6.2	6663 22947	40.1 49.1	Wetted wall column

Figure 5.5 shows also the comparison between the results of the 25wt% DGA and the 65wt% DGA in this work and other investigators.

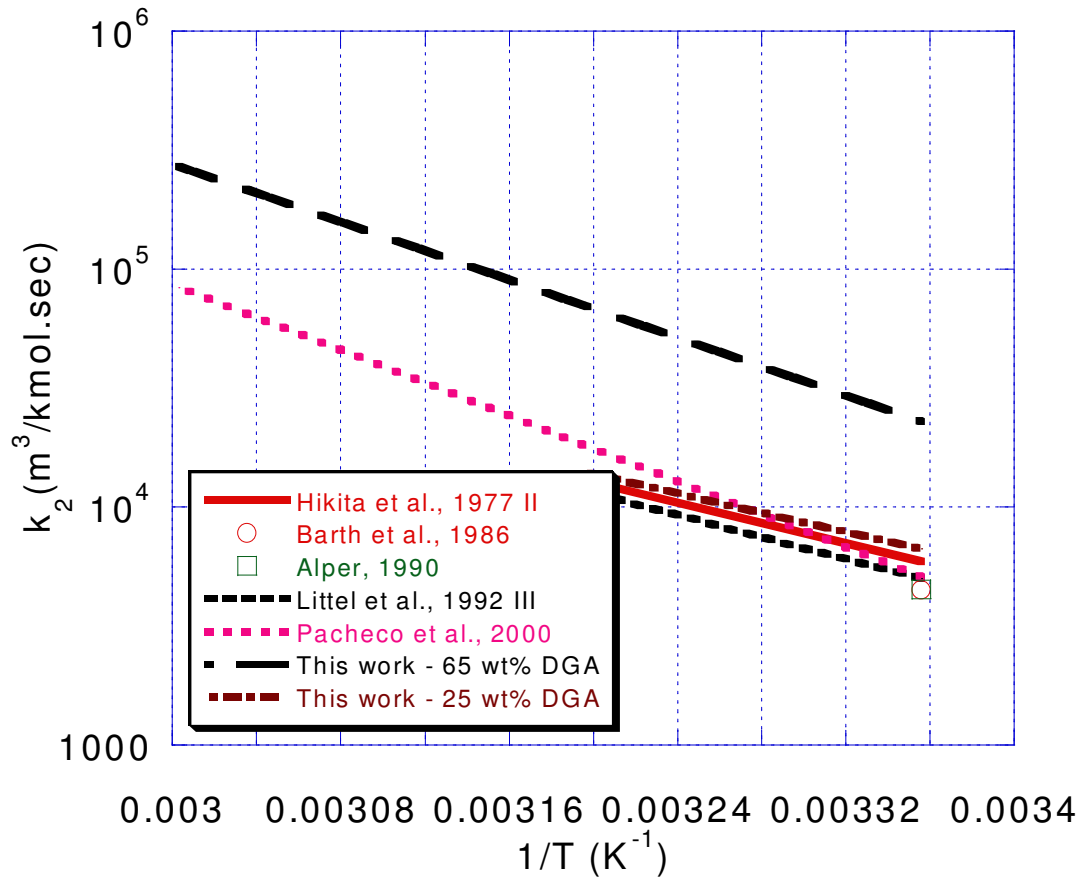


Figure 5.5 Second-order rate constant for the reaction between CO₂ and DGA at zero loading.

The above relation (6.30) for 25 wt% DGA is valid only up to 40 °C. For the 65wt% DGA the relation is valid from 25 °C to 60 °C. The data of Pacheco (1998) at low loading for 50 wt% DGA was also analyzed and the results are presented in Figure 5.6. The activation energy obtained in the 50 wt% is approximately 49.1 kJ/mol; however, the rate constant is approximately two times

greater than than previously published values. We can comment that increasing the DGA concentration increases the rate constant as seen in the 65wt% DGA and the 50 wt% DGA. An almost perfect line can be obtained if we exclude the data at 60 °C for 25 wt% DGA. The activation energy is calculated to be roughly 40.1 kJ/mol. However, the activation energy will be much smaller for 25 wt% DGA if the data set at 60 °C were included.

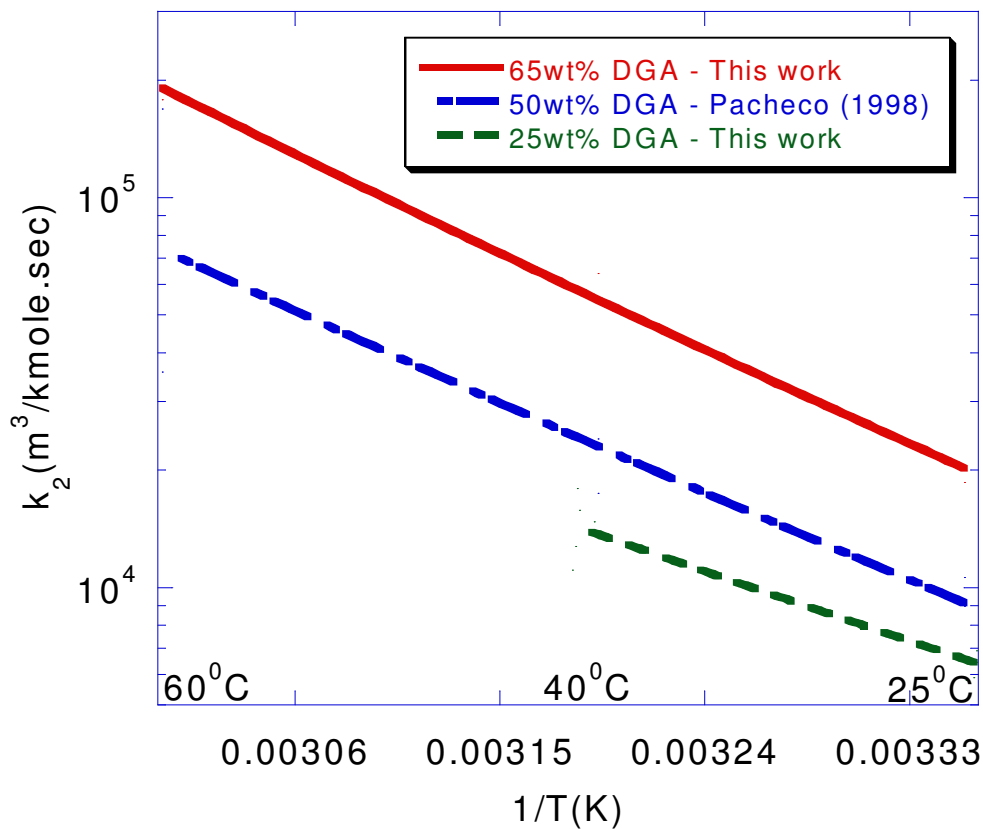


Figure 5.6 Second-order rate constant for the reaction between CO₂ and DGA.

In order to confirm the above results, we choose to plot it in terms of the raw rate data since the above analysis could change for different values of diffusivity and Henry's constants. The results with 65 wt% DGA and 25 wt% DGA at low CO₂ loading are compared to results with 50 wt% DGA by Pacheco et al.

(2000) in figure 5.7. The three data sets were plotted in terms of the normalized flux, k_G' , defined as the ratio of CO_2 flux to the partial pressure difference of the CO_2 at the interface and the CO_2 in the bulk solution. At zero loading, the partial pressure of CO_2 in the bulk solution is zero; therefore, the normalized flux is the ratio of CO_2 flux to the partial pressure of the CO_2 at the interface. As can be seen in figure 5.7 and 5.8, k_G' varies less than k_2 with DGA concentration since k_G' is proportional to the square root of k_2 .

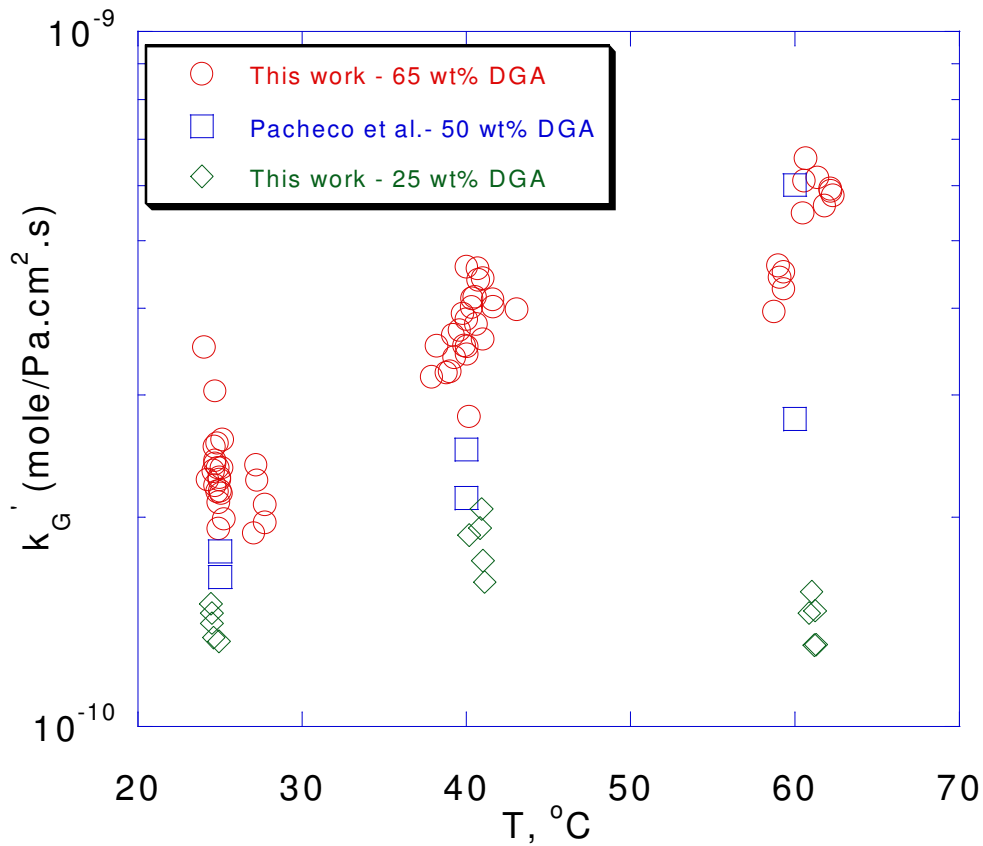


Figure 5.7 Comparison between the data obtained in this work for the 65 wt% and 25 wt% DGA solution and Pacheco et al., (2000) for the 50 wt% DGA solution at low loading.

It is clear that as the DGA concentration increases the rate increases. We are tempted by the fact that second order rate constant is a function of the DGA concentration. Although it was mentioned at the beginning of this section that instability of the film close to the bottom of the column could enhance mass transfer rates, the fact that the 50 wt% gave us a two order of magnitude higher than previously published values makes us believe that DGA concentration affects the normalized flux and second order rate constant in the same way as the 65 wt% does.

With 65wt% DGA, with an increase in temperature an increase in the rate constant is observed, following the classical Arrhenius behavior. However, for the 25wt% DGA and at temperatures below 40⁰C an Arrhenius behavior is obtained. Above 40⁰C the rate constant curve shows a clear break from the Arrhenius trend, essentially showing no activation energy for the reaction. These deviations from Arrhenius behavior may be explained in terms of reaction kinetics.

Two limiting cases for the zwitterion mechanism can be seen for the 25wt% DGA solution;

- For the 25 wt% DGA and above 40⁰C, the zwitterion formation reaction is rate-limiting and the reaction rate appears to be first-order in both the amine and carbon dioxide concentrations. Increasing the temperature increases reversibility of reaction 5.1 by increasing the rate constant of the reverse reaction. In addition, at high temperatures;

$k_{-1} \gg \{k_{DGA}[DGA] + k_{H_2O}[H_2O] + k_{OH^-}[OH^-]\}$ for the 25 wt% DGA solution and $k_{-1} \ll \{k_{DGA}[DGA] + k_{H_2O}[H_2O] + k_{OH^-}[OH^-]\}$ for the 65 wt% DGA.

- However, below 40⁰C the zwitterion deprotonation reactions are rate limiting, the overall reaction rate appears to be second order in the amine concentration. Therefore, we get the following;

$k_{-1} \ll \{k_{\text{DGA}}[\text{DGA}] + k_{\text{H}_2\text{O}}[\text{H}_2\text{O}] + k_{\text{OH}^-}[\text{OH}^-]\}$ for the 25 wt% DGA and the 65 wt% DGA.

The activation energy and pre-exponential factor were obtained with a fit to only the data points taken at 25 °C and 40 °C.

5.5.2 CO₂ reactive absorption into partially loaded aqueous DGA solutions

The rate data presented in this work is unique in that it is obtained with variation of loading instead of a zero loading like much of the other data presented in table 5.2. The quality of the rate data was analyzed for three important error parameters: gas film resistance, approach to equilibrium; and percent removal of CO₂ (Dang, 2001). Gas film resistance determines the error of the interfacial partial pressure. If it is higher than 70%, the error calculated in the interfacial partial pressure may be more than 30%. The approach to equilibrium determines the error into k_G' . Rate data measured far away from equilibrium introduces less possible error of the k_G' . The percent removal of CO₂ indicates the error of measured flux. The more percent CO₂ removal is, the less error of the measured flux. The detailed data and error analysis are in Appendix X. The data included in the analysis in this section had less than 50% gas film resistance, 20% to 50% CO₂ removal and 0 to 0.5 approach to equilibrium.

The rigorous, PFO and IPFO models were used to extract the second order rate constant from the rate data in loaded solutions. The regressions were done for each temperature instead of for all temperatures simultaneously. Figures 5.8, 5.9 and 5.10 show the second order rate constant as a function of CO₂ loading at 25 °C, 40 °C, and 60 °C respectively. As can be seen the second rate constant increases with increase in CO₂ loading for all three temperatures.

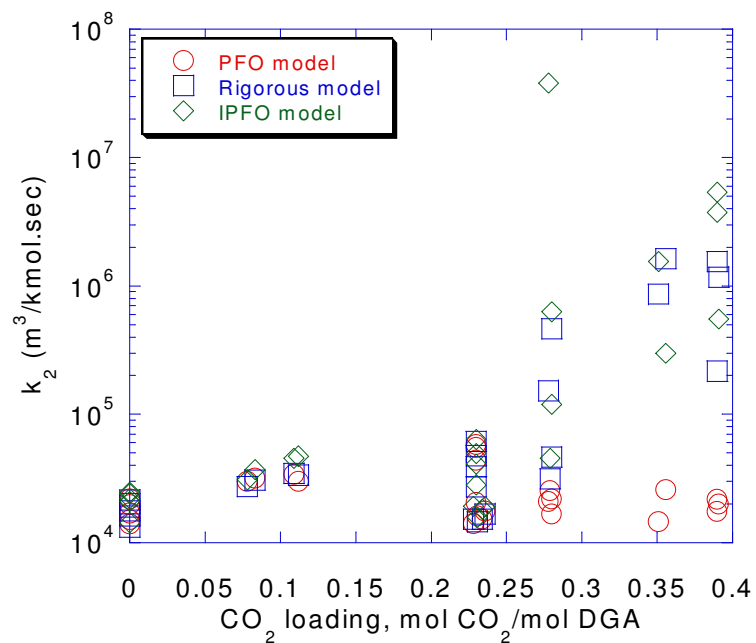


Figure 5.8 Second-order rate constant for the reaction between CO₂ and 65 wt% DGA.at 25 °C.

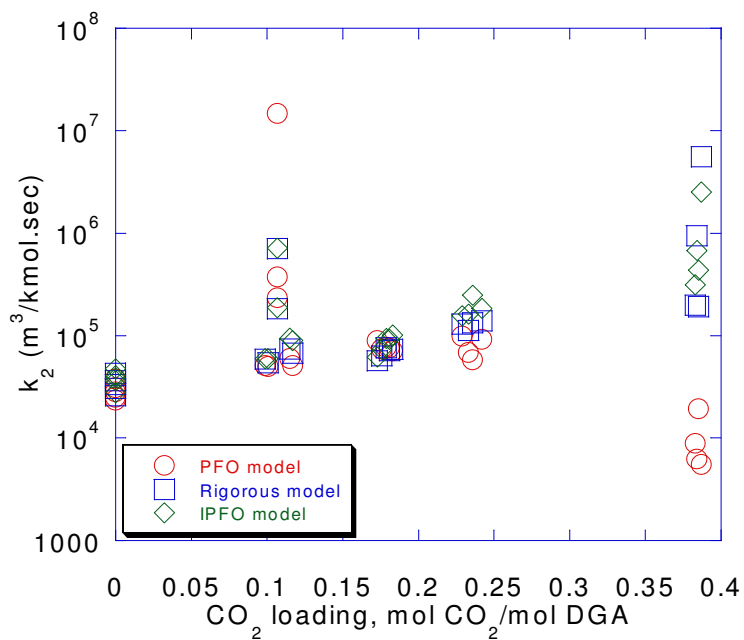


Figure 5.9 Second-order rate constant for the reaction between CO₂ and 65 wt% DGA.at 40 °C.

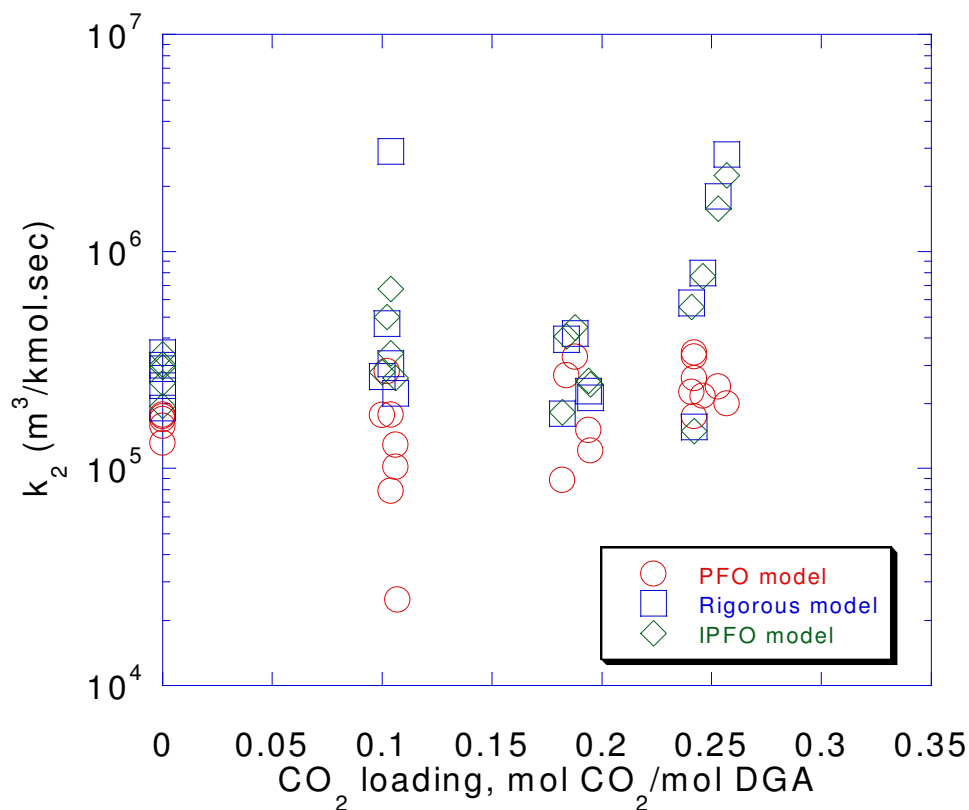


Figure 5.10 Second-order rate constant for the reaction between CO_2 and 65 wt% DGA.at 60°C .

The interesting result of the comparison of the three models is that the IPFO model matches very well the rigorous model. The knowledge of good values for the DGA diffusivities would allow the use of the IPFO model, which has the advantage of converging faster than the rigorous integration. It can be seen also that the PFO model follows the rigorous model well at low loading, as expected, whereas it underestimates rate constant at loading greater than 0.25. At low CO_2 loading the reaction rate with CO_2 is not instantaneous but fast enough for most of the reaction to occur in the boundary layer. The PFO model is valid at these conditions when the DGA concentration at the gas liquid interface is not significantly different from that in the bulk solution. At high CO_2 loading, the

DGA can be depleted at the gas liquid interface and therefore the PFO model no longer applies. Under these conditions, it is necessary to correct for the diffusion of the DGA and DGA products. The rigorous model and IPFO models account for this correction but the PFO corrects only for the diffusion of CO₂ and not for the DGA and DGA products such as bicarbonate, free DGA, and DGA carbamate. The deviation between the rigorous model, IPFO model and the PFO model is even seen more pronounced at 60 °C. This is related to the slope of the equilibrium curve that is increasing as the temperature increases, and therefore the deviation between the total concentration of the DGA at the interface and in the bulk solution increases.

Figures 5.11 and 5.12 show concentration profiles of species in the 65 wt% DGA at 313K and at loadings of 0.101 and 0.385, respectively generated using the rigorous model. These two points are in Figure 5.9. In Figure 5.10, it is easy to see that pseudo first order is a good approximation. There is not much depletion of DGA at the interface and there is still enough DGA around (about 15% depletion). This 15% depletion in the DGA concentration can be important if equilibrium matters. In the case of DGA, equilibrium is not important at such conditions. It is clear that both the DGA carbamate and protonated DGA are diffusing away from the interface since their concentration are decreasing in the direction of the bulk solution. This makes them appear as reaction products. On the other hand, Figure 6.12 shows that there is a significant amount of depletion of DGA at the interface at higher loadings (about 67% depletion). Under these conditions, the PFO does not apply.

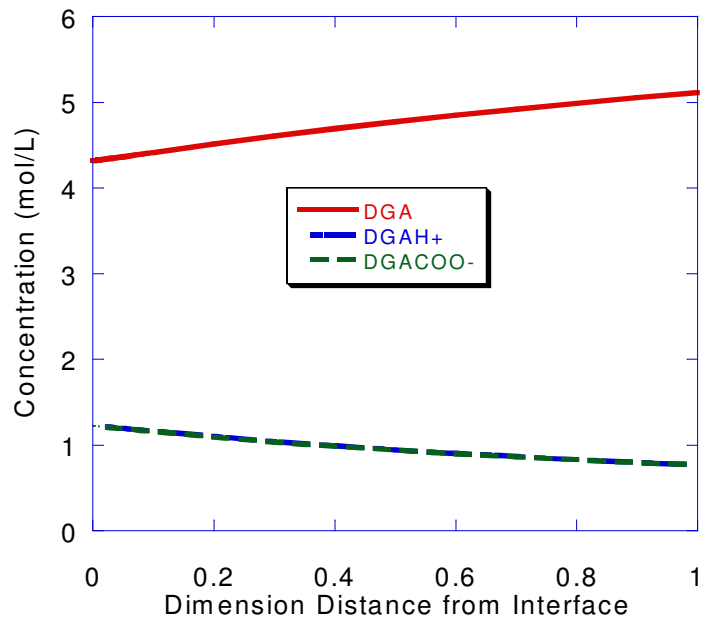


Figure 5.11 Concentration gradients for absorption of carbon dioxide into 65 wt% DGA. Loading=0.115, $k_1^0=2.79E-3$ m/s, $P^i/P^*=392.0$, $T=313K$.

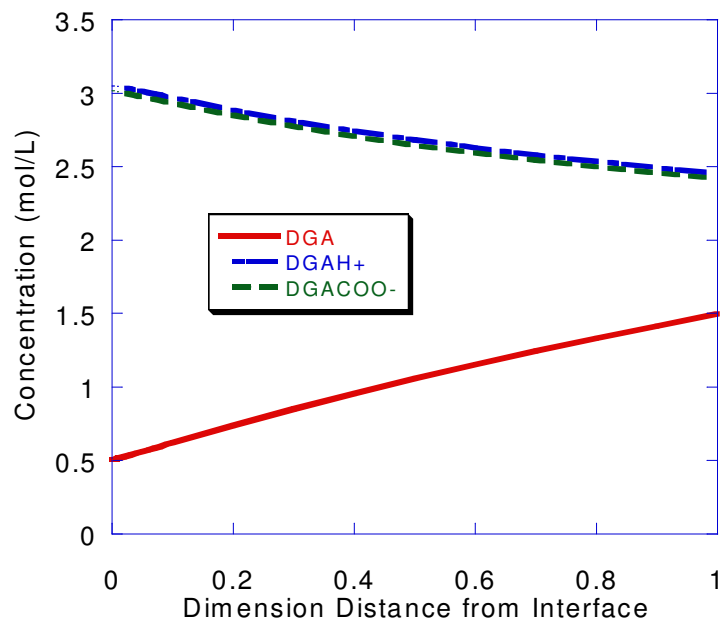


Figure 5.12 Concentration gradients for absorption of carbon dioxide into 65 wt% DGA. Loading=0.385, $k_1^0=2.45E-3$ m/s, $P^i/P^*=28.5$, $T=313K$.

The reaction rate at high CO₂ loading and high temperature becomes instantaneous. An analysis was done to estimate the relative importance of the kinetic term to the total reaction rate. The approximation is good if the fraction of the kinetic term is close to 1 and the instantaneous term is close to 0. As explained in the model development section, the IPFO approximation divides the boundary layer into two regions, one controlled by reaction rates and one controlled by diffusion of reactants and products. The liquid phase mass transfer resistance is determined by the resistances of the two regions in series.

$$R_{\text{liquid}} = R_{\text{IPFO}} + R_{\text{inst}} \quad (5.31)$$

R_{IPFO} is the resistance of the reaction sub-layer, R_{inst} is the resistance of the diffusion region, where the reactions are instantaneous. Equation 5.31 can be written in the following form in terms of normalized flux k_g^I ;

$$\frac{1}{k_g^I} = \frac{1}{k_{g,\text{IPFO}}^I} + \frac{1}{k_{g,\text{inst}}^I} \quad (5.32)$$

The IPFO (kinetic controlled) term is given by equation 5.33.

$$k_{g,\text{IPFO}}^I = \frac{\sqrt{k_2[\text{DGA}]_i D_{\text{CO}_2}}}{H_{\text{CO}_2}} \quad (5.33)$$

The instantaneous coefficient can be calculated using equation 5.34, derived in Dang (2001), and valid for small driving forces.

$$k_{g,\text{inst}}^I = \frac{1}{\frac{\partial P_{\text{CO}_2}^*}{\partial [\text{CO}_2]^*}} k_{l,\text{prod}}^0 \quad (5.34)$$

The instantaneous coefficient depends on the partial derivative of the equilibrium partial pressure with respect to the CO₂ total concentration. It also depends on the physical mass transfer coefficient of the reaction products and

DGA, $k_{l, \text{prod}}^0$. The derivative was obtained using the Electrolyte-NRTL model described in chapter 5; $k_{l, \text{prod}}^0$ was obtained using equation 5.27.

The error introduced by extracting the second order rate constant from the rate data at high loading can be estimated by calculating the fractional resistance of the kinetic term.

$$\text{fraction kinetic} = \frac{k_g^I}{k_{g, \text{kinetic}}^I} \quad (5.35)$$

Table 5.5 shows the result of the analysis, done for 25 °C, 40 °C and 60 °C. At low loading for the three temperatures the instantaneous resistance is always negligible. At high loading it accounts for 5-15% of the total resistance. These results place some confidence on the value of the rate constant estimated.

Table 5.5 Analysis of importance of the kinetics at low and high loadings for 25 °C, 40 °C and 60 °C.

T (°K)	Loading molCO ₂ /mol DGA	1/k _g ^I , _{IPFO} cm ² s atm/mol	1/k _g ^I , _{inst} cm ² s atm/mol	Fraction Kinetic
298.1	0.078	4.39E+04	1.27E+01	0.999
312.4	0.101	4.66E+04	1.26E+02	0.997
332.2	0.100	2.06E+04	9.23E+02	0.957
298.1	0.390	2.52E+05	1.13E+04	0.957
312.3	0.385	1.06E+05	1.61E+04	0.868
332.9	0.257	3.14E+04	3.57E+03	0.898

Figure 5.13 shows the sensitivity of the second order rate constant and the diffusion of products and reactants to the flux predicted by the rigorous model with 65 wt% DGA at 313K.

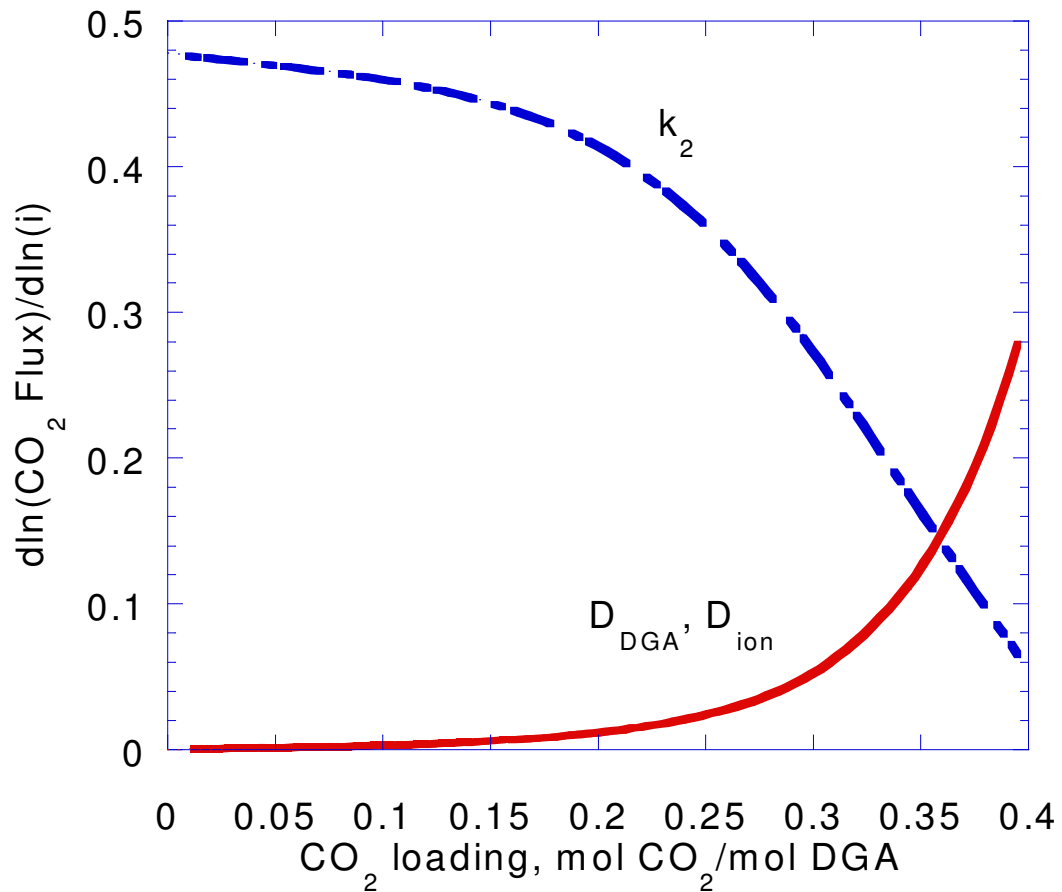


Figure 5.13 Sensitivity of calculated CO_2 flux to values of the diffusion coefficients of reactants and products and second order rate constant. 313 K, $k^0_1=2.74\text{E-}3$ m/s, $P_i=10P^*$.

The results can be divided into two regions. The first region is where the CO_2 loading is less than 0.10 (low loading). The second region is where the CO_2 loading is greater than 0.10 (high loading). At low loading (region 1), the rate constant of DGA and the diffusion of reactants and products is least sensitive. As the loading increases and the concentration of DGA drops, the rate constant of DGA and the diffusion coefficient of reactants and products becomes most sensitive (region 2). This shows that the removal of reaction products and the diffusion of DGA to the interface have become important phenomena at high

loading. The conclusion that can be drawn from this section is that the rate data at high CO₂ loading contains a source of error, that tends to overpredict the second order rate constant, since part of the resistance is neglected. This problem becomes more important as the CO₂ loading and temperature increases.

Due to the importance of the diffusion of reactants and products at high CO₂ loading, the parameters D_{ion} and D_{DGA} were regressed from the experimental data along with the second order rate constant. The second order rate constant was regressed as a function of loading and temperature as seen from Figures 5.8, 5.9 and 5.10:

$$\ln k_2 = A + B \cdot ldg + C/T \quad (5.36)$$

where A, B and C are the fitting parameters, ldg is the CO₂ loading in mol CO₂ per mol DGA. The experimental data chosen to study the effect of loading on the second rate constant are shown in Appendix K. A limited set of data was regressed to minimize the computation time using the rigorous model. This work used 38 nodes with small spacing to achieve the desired accuracy. No attempt was made, however to reduce the number of nodes. A decrease in the number of nodes used will significantly reduce the number of equations to be solved and will decrease computation time.

The values of the diffusion coefficients of the reactants and products used in the initial guess are those obtained by Pacheco (1998). We regressed these values using the same temperature and viscosity dependence as obtained by Pacheco (1998). The following equation for the diffusion of reactants and products were used in the regression:

$$D_{DGA} = 2.845E - 8 * \mathfrak{R} * \mu^{-0.5752} (cP) T(K) \quad (5.37)$$

$$D_{p,r} = 2.845E - 8 * \mathfrak{R} * \mu^{-0.5752} (cP) T(K) \quad (5.38)$$

Table 5.6 presents the regressed values and confidence intervals obtained during the regression of D_{DGA} , $D_{p,r}$, and k_2 . Figure 5.14 shows the effect of CO_2 loading and temperature on the rate constant.

Table 5.6 Results for the regression of D_{DGA} , $D_{p,r}$ and k_2 .

Parameter	Value
A	$0.30E+02 \pm 0.71E+01$
B	$0.42E+01 \pm 1.51E+00$
C	$-0.61E+04 \pm 1.60E+03$
\mathfrak{R}	$0.75E+00 \pm 0.31E+00$

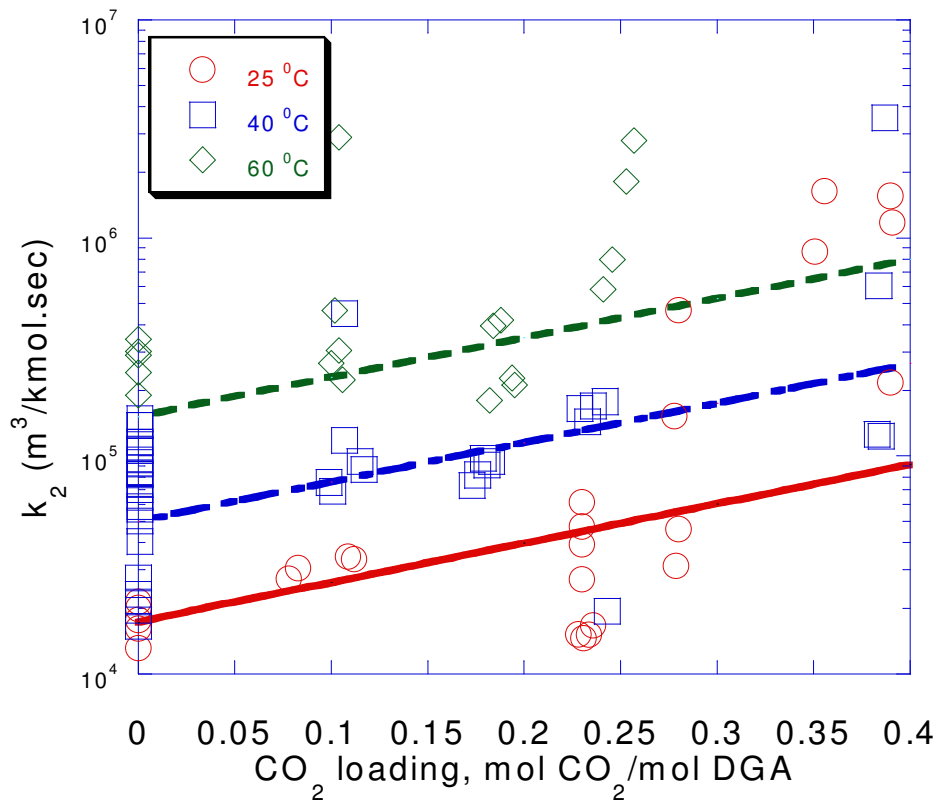


Figure 5.14 Effect of CO_2 loading on the second rate constant at $25\text{ }^{\circ}C$, $40\text{ }^{\circ}C$ and $60\text{ }^{\circ}C$ for the system DGA- water- CO_2 . Lines are model predictions.

The small confidence interval of the regressed D_{pr} and D_{DGA} places some confidence on the estimated values of the second order rate constant. The results in Figure 5.14 show that k_2 is indeed increasing with CO_2 loading since the effects of the diffusion of reactants and products are taken into account during the regression of k_2 . The data in Figures 5.8, 5.9 and 5.10 were included for comparison since most of the data were not included during regression. Figure 5.15 is the parity plot for the calculated and measured fluxes of CO_2 for the DGA® system at various CO_2 loadings and three temperatures. For most experiments the measured flux is within 15% of the calculated flux.

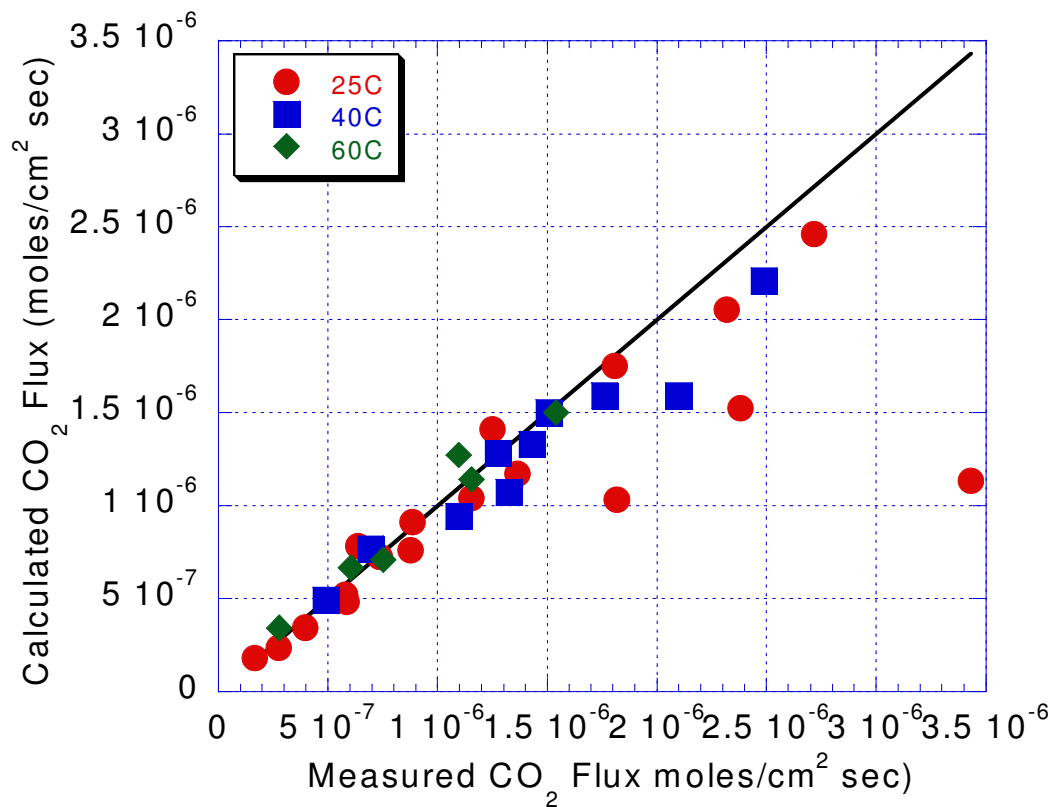


Figure 5.15 Comparison between the measured and calculated interfacial fluxes of CO_2 for the 65 wt% DGA at various CO_2 loading.

We might also choose to express the rate of reaction in terms of activity. Usually, activity is defined as ‘effective concentration’ of species. The true rate expression is a function of activity rather than concentration. The activity of a species, a_A , is defined as the product of its molar concentration, $[A]$, and a solution dependent activity coefficient, γ_A (gamma) which is dimensionless;

$$a_A = \gamma_A [A] \quad (5.39)$$

The activity coefficients vary with ionic strength such that substitution of a_A for $[A]$ in any equilibrium constant expression frees the numerical value of the constant from dependence on the ionic strength. In low loading solutions, where the ionic strength is minimal, this effectiveness becomes constant, and the activity coefficient is unity. Under such circumstances, the activity and the molar concentration of the species are identical. For most purposes, the error introduced by the assumption of unity for the activity coefficient is not large enough to lead to false conclusions. However the disregard of activity coefficients may introduce numerical error in calculations; therefore the above results for the 65 wt% DGA, were reinterpreted using activity instead of concentrations. The equilibrium model in chapter 5 was used to calculate the activity coefficients of CO_2 and DGA in the 65 wt% DGA. The results of the activity coefficients in the 50 wt% DGA and 25 wt% DGA are also included. Figures 5.16, 5.17 and 5.18 show the activity coefficients at 40 °C for the 25 wt% DGA, 50 wt% DGA and 65 wt% DGA solutions.

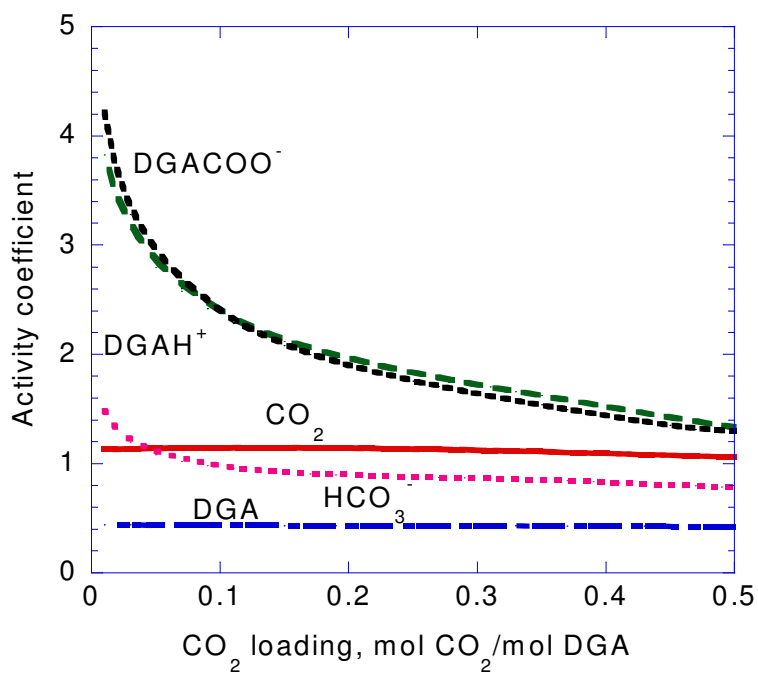


Figure 5.16 Predicted activity coefficients for 65 wt% DGA at 313K

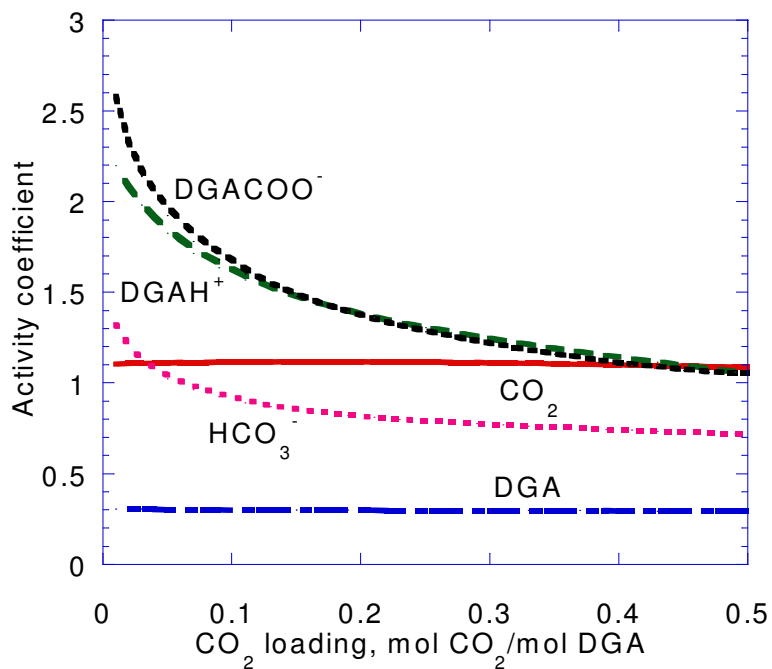


Figure 5.17 Predicted activity coefficients for 50 wt% DGA at 313K

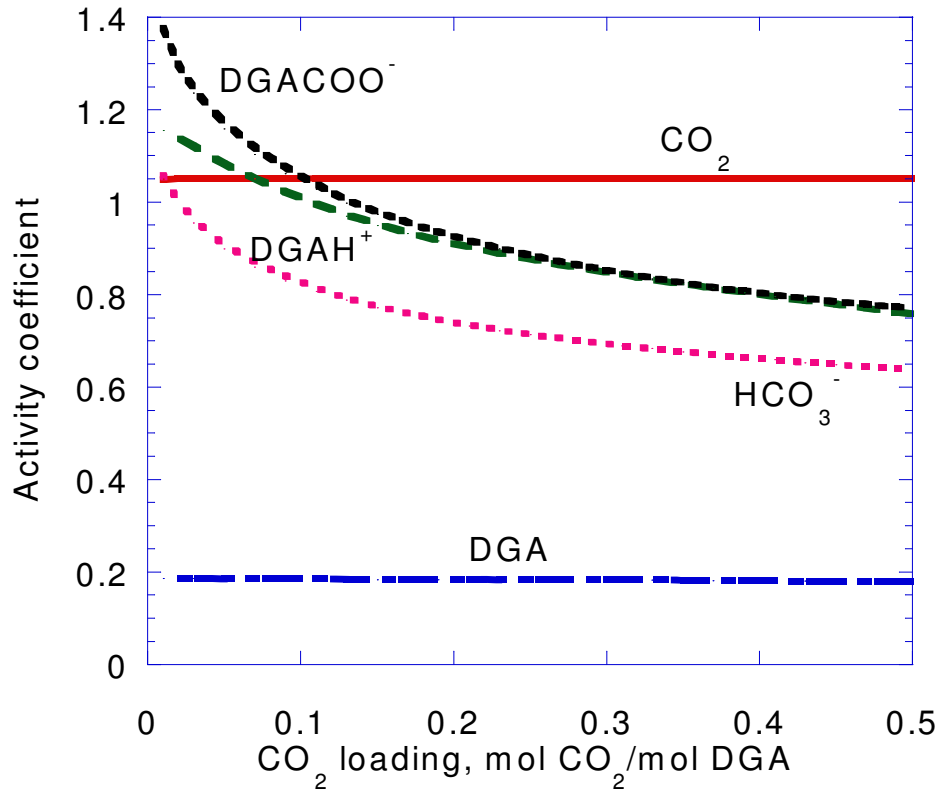


Figure 5.18 Predicted activity coefficients for 25 wt% DGA at 313K

As can be seen in figures 5.16-5.18, the activity coefficients of the ions depart farther from unity as CO_2 loading increases. From Equation 5.1 and 5.2, we can write R_{CO_2} as;

$$R_{\text{CO}_2} = k_b [\text{DGAH}^+ \text{COO}^-]$$

$$\text{where } K_{\text{eq}} = \frac{a_{\text{DGAH}^+ \text{COO}^-}}{a_{\text{DGA}} a_{\text{CO}_2}} = \frac{\gamma_{\text{DGAH}^+ \text{COO}^-} [\text{DGAH}^+ \text{COO}^-]}{\gamma_{\text{DGA}} \gamma_{\text{CO}_2} [\text{DGA}] [\text{CO}_2]}$$

Therefore,

$$R_{\text{CO}_2} = k_b K_{\text{eq}} [\text{DGA}] [\text{CO}_2] \frac{\gamma_{\text{DGA}} \gamma_{\text{CO}_2}}{\gamma_{\text{DGAH}^+ \text{COO}^-}}$$

The rate based activity constant can be written as a function of CO₂ loading as follows;

$$k_A = k_{ldg=0} \frac{\left(\frac{\gamma_{DGA} \gamma_{CO_2}}{\gamma_{DGAH^+COO^-}} \right)_{loaded}}{\left(\frac{\gamma_{DGA} \gamma_{CO_2}}{\gamma_{DGAH^+COO^-}} \right)_{unloaded}} \quad (5.40)$$

It should be noted that the CO₂ activity coefficient is calculated using the nitrous oxide analogy noted in section 5.3. Figure 5.19 shows the activity based rate constant at various loadings at 40 °C using the model fit in figure 5.14. The results in figure 5.14 are also included.

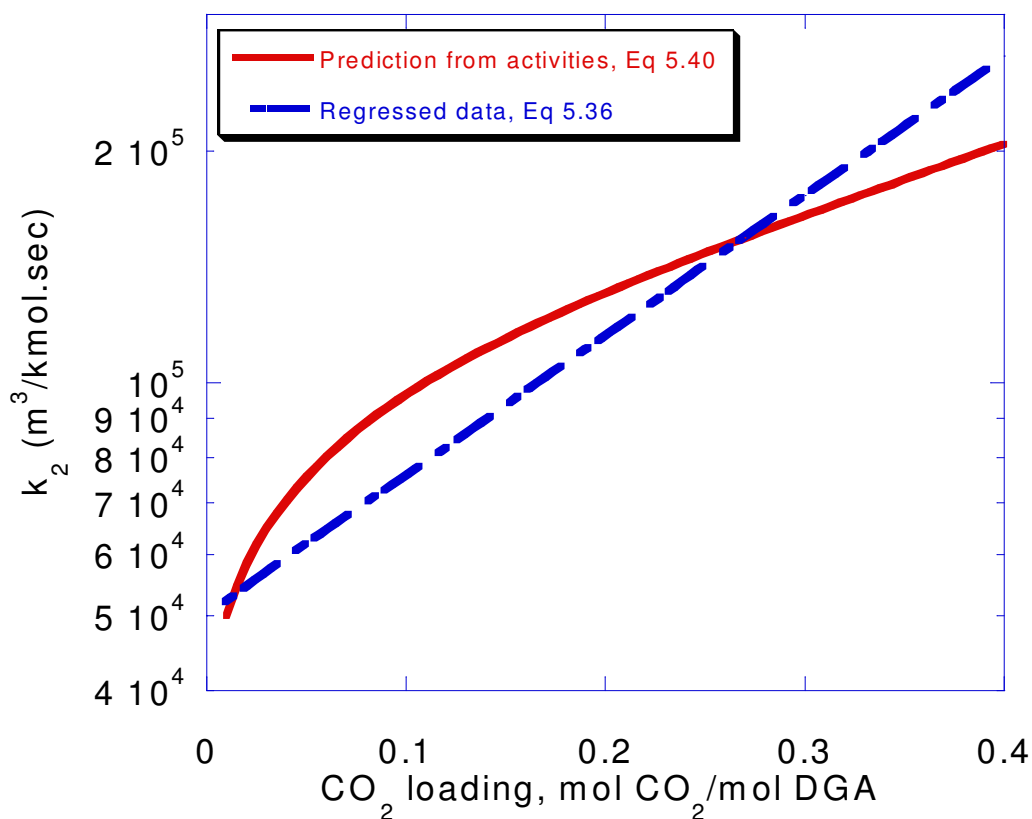


Figure 5.19 Effect of CO₂ loading on the second rate constant calculated based on concentration and on activity at 40 °C for the system DGA- water-CO₂. Lines are model predictions.

It can be seen that the concentration based rate constant calculated using Equation 5.40 shows a factor of 4 increase in k_2 compared to the second order rate constant regressed from the kinetic data.

Figures 5.20 through 5.23 show the model prediction of the normalized flux for the 65 wt% DGA solution at 40 °C. Low driving force ($1.01P^*_{CO_2}$) is considered as well as high driving force ($10P^*_{CO_2}$). Rate decreases as the loading increases; this is evident from the shape of the k_G' -loading plot. This is to be expected since the rate of the reaction depends on the concentration of the free DGA at the gas-liquid interface. Thus, increasing the CO₂ loading, the

concentration of the reactive DGA at the interface decreases; and hence the reaction rate decreases.

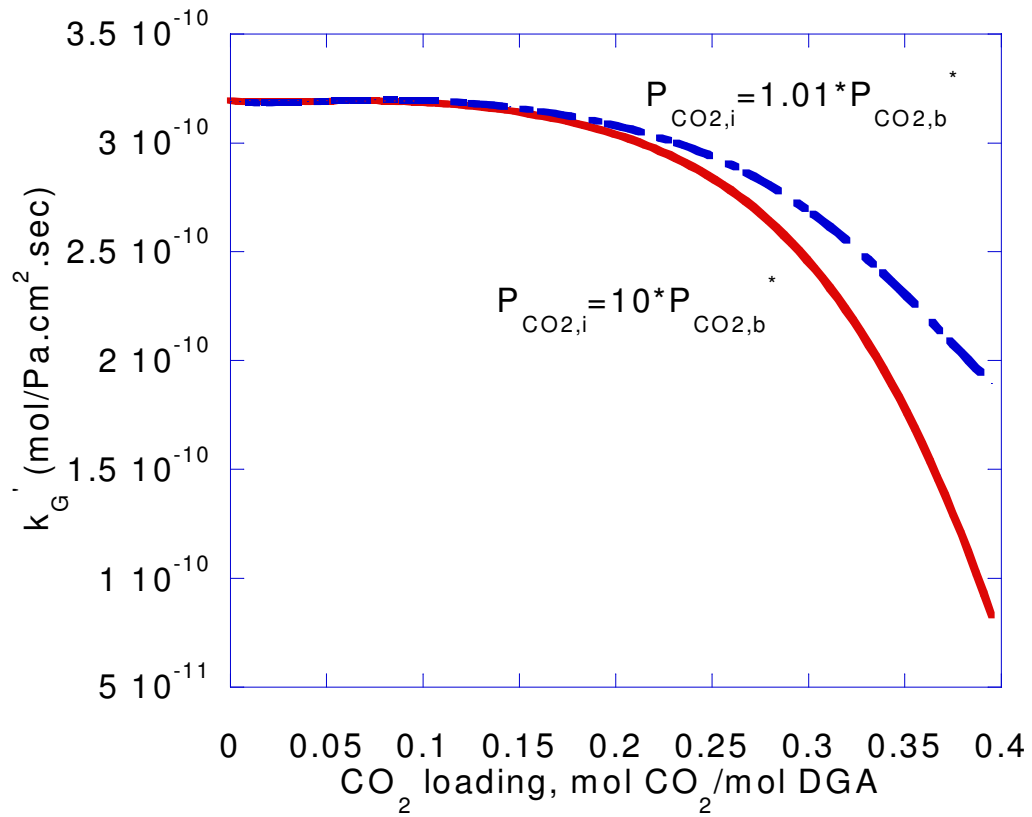


Figure. 5.20 Normalized flux of 65wt% DGA and CO_2 at low and high driving force at 313K.

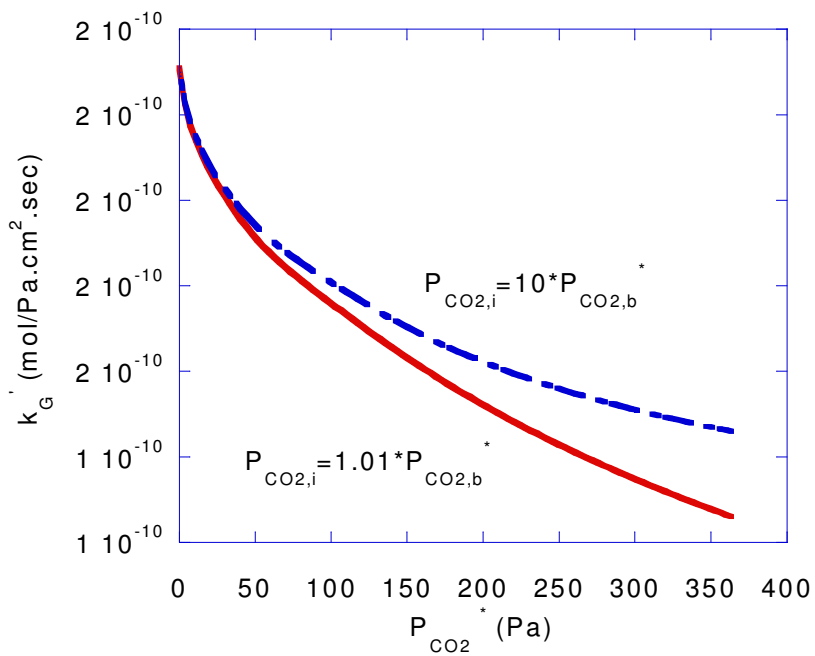


Figure. 5.21 Normalized flux of 65wt% DGA and CO₂ at low and high driving force at 298K.

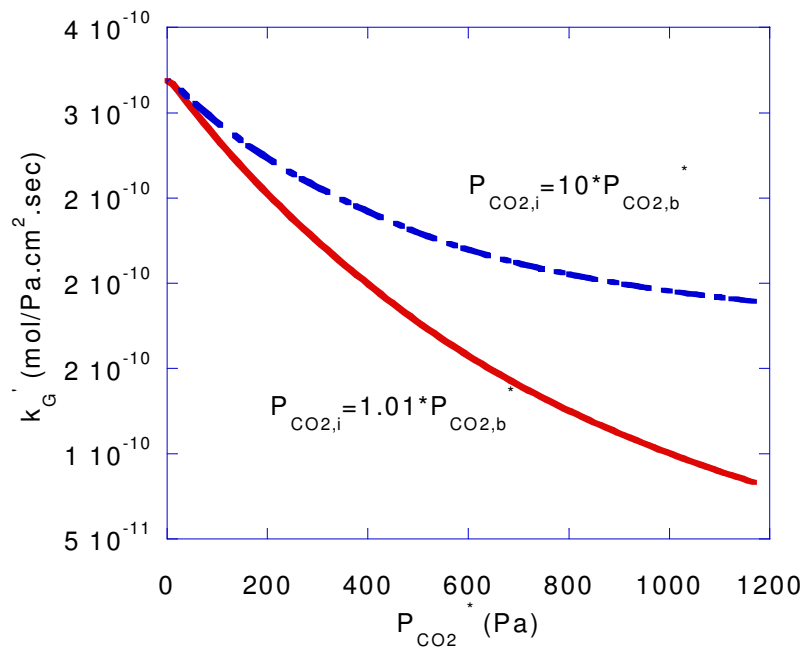


Figure. 5.22 Normalized flux of 65wt% DGA and CO₂ at low and high driving force at 313K.

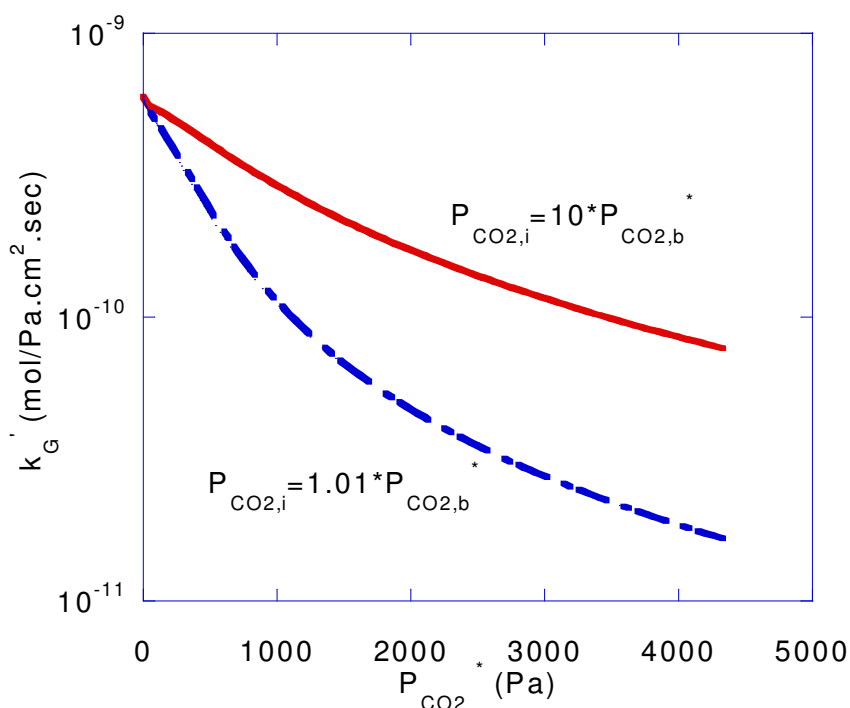


Figure. 5.23 Normalized flux of 65wt% DGA and CO₂ at low and high driving force at 333K.

5.5.3 The influence of ionic strength on the rate constant for the reaction of diglycolamine and CO₂

When CO₂ is absorbed into aqueous solutions, including alkanolamines, it combines with water and dissociates into positive and negative ions. Depending on the components in the solutions, different species may end up carrying the positive and negative charges (typically protonated amines and negatively charged carbamates, bicarbonates in DGA solutions). Usually, in such solutions, ionic strength is an important parameter, because each ion is surrounded by an extended solvation shell, which can affect ionic activities and rate constants. Davies (1963) pointed out that ion association can modify the reaction in two ways: firstly, ion pair formation affects the total ionic strength of the medium; secondly, one (or

more) such ion pairs may be involved in the rate-determining step, thus altering the charge of the activated complex and reaction rate. In accordance with the zwitterion mechanism, $R_2NH^+COO^-$ is proposed as the intermediate complex in the rate-determining step.

Although the role of ionic strength in reactions of neutral species has been known for some time, the magnitude of the effect has generally been thought to be far less than the effect of ionic strength on reactions of ions. Essentially, this effect arises from the second term in the expanded Debye-Hückel relationship for the activity coefficient, which leads to the following expression for the rate constant at any ionic strength:

$$\log k = \log k_o - \frac{-z_a z_b A \sqrt{\mu}}{1 + Ba \sqrt{\mu}} + C\mu \quad (5.41)$$

where k_o is the rate constant at zero ionic strength, μ is the ionic strength, A and B are collections of physical constants, a is the distance of closest approach, and C is an unknown constant. The other two parameters, z_a and z_b , are the charges on the reactants thus, when z_a or $z_b = 0$:

$$\log k = \log k_o + C\mu \quad (5.42)$$

and the logarithm of the rate constant is expected to show a linear dependence on the ionic strength. Although the parameters A and B can be calculated, and a estimated, there is no reliable method of calculating C , which must be determined by experiment. Kinetic studies on many different ion-ion reactions have demonstrated that for low to moderate ionic strengths, $\mu < 0.1 \text{ mol L}^{-1}$, the rate constant is proportional to $\sqrt{\mu}$, indicating that $A \gg C$.

In the last section, it was shown that the second order rate constant is increasing with CO_2 loading or ionic strength. The results in the previous section were reinterpreted in terms of equation 5.42. Figure 5.24 shows the second order

rate constant presented in Figure 5.14 as a function of ionic strength. Table 5.7 shows the values of k_0 and C constant for the three temperatures.

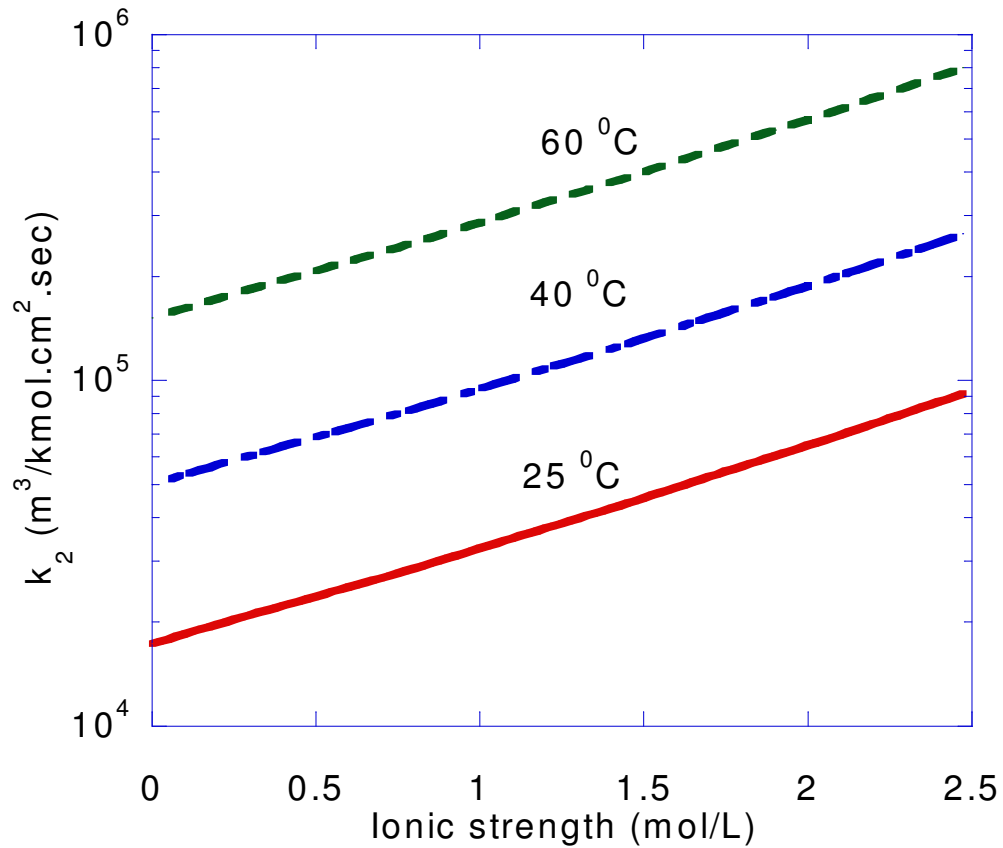


Figure 5.24 Effect of ionic strength on the second rate constant at 25 °C, 40 °C and 60 °C for the system DGA- water-CO₂

Table 5.7 Results for the fit of k_2 as a function of μ .

Temperature, °C	k_0 (m ³ /kmol.cm ² .sec)	C (m ⁶ /kmol ² .cm ² .sec)	R ²
25	1.73E+04	0.674	0.9991
40	5.00E+04	0.674	0.9991
60	1.51E+05	0.674	0.9991

To test the hypothesis that the rate constant is increasing with the ionic strength, glycolic acid was added to 65 wt% DGA solution in order to quantify the effect of ionic strength on the reaction rate constant. All of the studied solutions had a concentration of 65wt% DGA in water and zero CO₂ loading. Note that the glycolic acid will react to form DGAH⁺ glycolate⁻. The first experiment was performed with no glycolic acid to establish the base case. For the rest of the experiments, glycolic acid was added to give 0.1, 0.2, 0.3, 0.4 moles glycolic acid/mole DGA.

The data sets are given in Table 5.8. Figure 5.25 shows the normalized flux data at 40 °C. As can be seen in Figure 5.25, increasing glycolic acid concentration decreases the normalized flux. This is to be expected since the rate of the reaction depends on the concentration of the free DGA at the gas-liquid interface. Thus, increasing the acid concentration, the concentration of the reactive DGA decreases; and hence the reaction rate decreases. The data presented above have been obtained at conditions that greatly simplify the mathematical treatment of the problem. The most significant simplification arises from the pseudo-first-order assumption (PFO) for kinetics. Eq. (5.24) has been used to extract the second order rate constant of DGA/glycolic acid with carbon dioxide. Figure 5.26 shows the second order rate constant for the system DGA-Glycolic acid-CO₂-water at 40 °C.

Table 5.8 65wt%DGA/water-glycolic acid experimental rate measurements at zero loading. Total pressures from 15-42 psig

Glycolic acid/DGA $\frac{\text{mol}}{\text{mol}}$	T °C	$P^{\text{OUT}}_{\text{CO}_2} * 10^3$ Pa	Flux * 10^6 $\frac{\text{kmol}}{\text{m}^2\text{s}}$	$k_g^o * 10^9$ $\frac{\text{kmol}}{\text{m}^2\text{Pa} \cdot \text{s}}$	$k_l^o * 10^5$ m/s	$P^{\text{I}}_{\text{CO}_2} * 10^3$ Pa
0	39.5	0.84	2.49	5.50	4.39	1.29
0	39.9	1.67	5.72	5.53	4.39	2.71
0	39.9	2.54	8.71	5.56	4.39	4.10
0	39.9	3.59	11.3	5.40	4.39	5.67
0	39.8	4.67	14.1	5.25	4.39	7.31
0.1	39.6	0.98	2.50	4.69	3.95	1.52
0.1	39.7	1.99	5.58	4.71	3.95	3.18
0.1	39.7	3.00	8.61	4.73	3.95	4.82
0.1	39.8	4.15	11.3	4.69	3.95	6.53
0.1	39.6	5.31	13.9	4.64	3.95	8.27
0.2	40.4	1.12	2.50	4.09	3.42	1.74
0.2	40.3	2.28	5.58	4.11	3.42	3.65
0.2	40.0	3.45	8.61	4.13	3.42	5.53
0.2	39.8	4.76	11.3	4.09	3.42	7.48
0.2	39.8	6.08	13.9	4.06	3.42	9.46
0.3	39.2	1.30	2.15	3.79	2.89	1.88
0.3	39.8	2.57	5.31	3.77	2.89	3.98
0.3	39.6	4.06	8.01	3.66	2.89	6.25
0.3	39.9	5.45	10.7	3.67	2.89	8.34
0.3	40.1	6.91	13.1	3.69	2.89	10.4
0.4	39.2	1.60	2.56	2.84	2.61	2.51
0.4	39.7	3.20	5.84	2.86	2.61	5.26
0.4	39.6	4.85	8.95	2.87	2.61	7.97
0.4	39.7	6.70	11.5	2.88	2.61	10.6
0.4	39.7	8.40	14.3	2.90	2.61	13.3

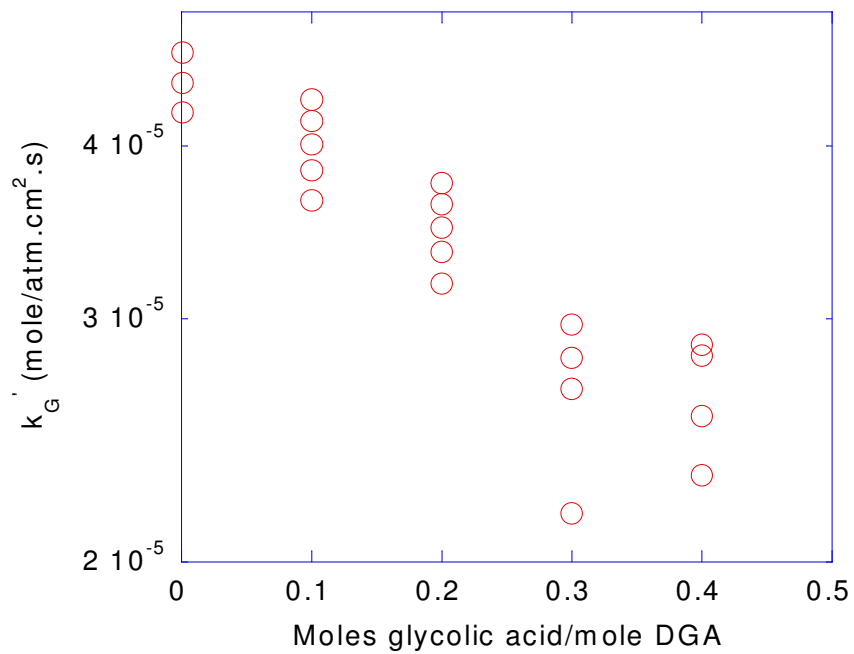


Figure 5.25 Normalized flux of 65wt% DGA and glycolic acid solvent at 40 °C.

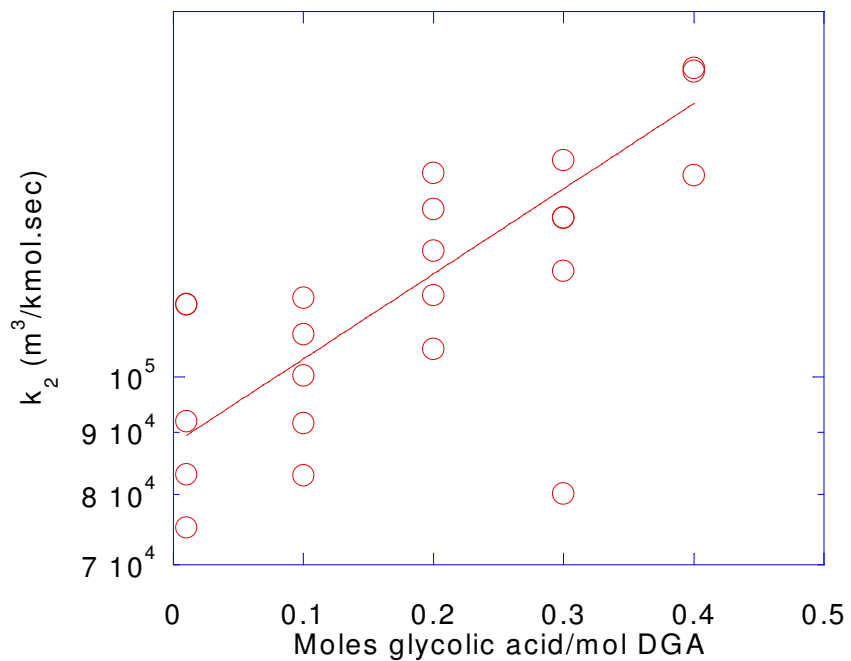


Figure 5.26 Effect of glycolic acid on the second rate constant at 40 °C for the system DGA- water- CO_2

The Henry's constants were determined using the N₂O solubility apparatus and the N₂O analogy. The viscosity of the above mentioned solutions were also measured using the Cannon-Fenske viscometer. The measured values of the Henry's constant and viscosities used in the calculation of the second order rate constant are given in Table 5.9.

Table 5.9 Measured values of Henry's constants and viscosities in glycolic acid-DGA solutions at 40 °C

Solution	H _{CO2} , atm.cm ³ /mol ⁻¹	μ, cP
0.1 glycolic acid/mol DGA	45000	8.5
0.2 glycolic acid/mol DGA	50000	11.7
0.3 glycolic acid/mol DGA	54000	16.7
0.4 glycolic acid/mol DGA	60000	20.5

It is interesting to see that increasing the glycolic acid concentration increases the second order rate constant. The rate constant increases by a factor of 2 from 0 to 0.4 moles glycolic acid per mol DGA. We also carried out systematic experiments at ionic strengths up to 3 M by adding potassium formate to 65wt% DGA solutions at zero loading. Table 5.10 summarizes the results. The results with no potassium formate added are included here for comparison.

Table 5.10 65 wt%DGA/water- potassium formate subset of the experimental rate measurements. Total pressures from 10-18 psig

Potassium formate	T °C	$P_{CO_2}^{OUT} * 10^3$ Pa	Flux $* 10^6$ $\frac{kmol}{m^2s}$	$k_g^o * 10^9$ $\frac{kmol}{m^2Pa \cdot s}$	$k_l^o * 10^5$ m/s	$P_{CO_2}^I * 10^3$ Pa
0	25.2	1.1	1.7	5.4	2.72	1.4
0	25.2	2.4	4.1	4.9	2.72	3.2
0	25.1	3.7	6.1	4.9	2.72	4.9
0	25.2	4.9	8.3	5.0	2.72	6.5
0	24.4	6.2	9.9	5.0	2.72	8.1
0	39.3	1.0	2.1	5.5	3.02	1.4
0	39.4	1.9	5.1	5.5	3.02	2.9
0	39.5	3.0	7.7	5.5	3.02	4.3
0	39.6	4.0	10.3	5.6	3.02	5.8
0	39.7	5.1	12.4	5.6	3.02	7.2
1	24.9	0.9	1.6	6.5	2.61	1.2
1	25.4	2.1	4.4	5.4	2.61	2.9
1	26.0	3.2	6.5	5.4	2.61	4.4
1	25.7	4.4	8.6	5.5	2.61	5.9
1	25.9	5.5	10.7	5.5	2.61	7.4
1	40.0	1.1	2.0	5.0	3.03	1.5
1	39.8	2.2	4.8	5.0	3.03	3.2
1	39.7	3.4	6.8	5.0	3.03	4.8
1	39.6	4.6	9.2	5.1	3.03	6.4
1	39.9	5.8	11.3	5.1	3.03	8.0
3	40.0	1.1	2.0	4.8	3.46	1.6
3	40.3	2.2	5.1	4.9	3.46	3.3
3	40.1	3.4	7.6	4.9	3.46	5.0
3	40.2	4.6	10.1	4.9	3.46	6.6
3	40.2	5.8	12.1	4.9	3.46	8.2

The measured values of the Henry's constant and viscosities in the DGA-potassium formate solutions are given in Table 5.11. Figure 5.27 and 5.28 show the normalized flux data and the second order rate constant as a function of ionic strength at 25 °C and 40 °C.

Table 5.11 Measured values of Henry's constants and viscosities in potassium formate (CHKO₂) solutions -DGA solutions

Solution	T, °C	H _{CO2} , kPa.L/mol ⁻¹	μ, cP
0M CHKO ₂ – 6.5 M DGA	25	30654	11.3
1M CHKO ₂ – 6.5 M DGA	25	36557	11.3
0M CHKO ₂ – 6.5 M DGA	40	41598	6.7
1M CHKO ₂ – 6.5 M DGA	40	48515	6.7
3M CHKO ₂ – 6.5 M DGA	40	65597	6.7

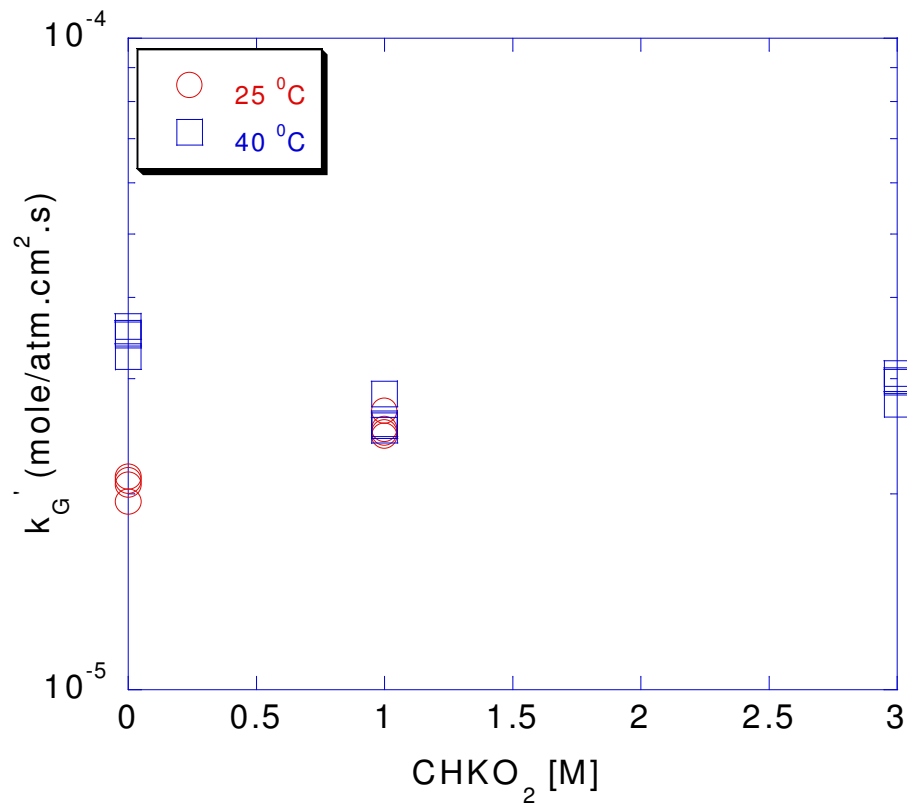


Figure 5.27 Normalized flux of fresh 65wt% DGA and potassium formate solutions.

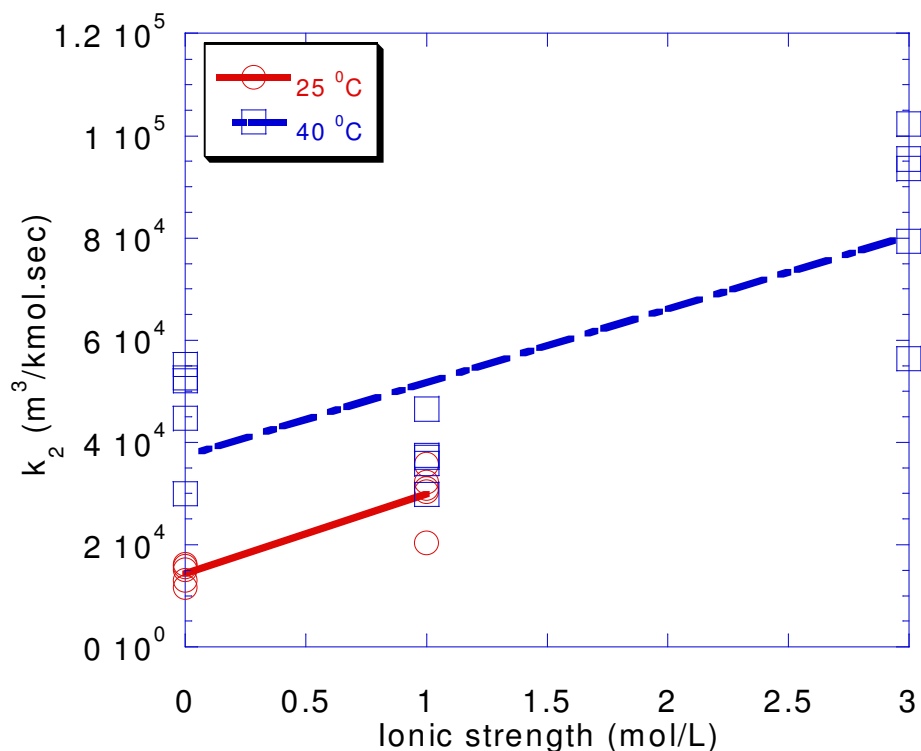


Figure 5.28 Effect of potassium formate on the second rate constant at 25 °C and 40 °C for the system DGA- water-CO₂

The present results suggest that ionic strength has strong effect on the second order rate constant. The second order rate constant increases a factor of 3. The results in the 65 wt% DGA showed increases by a factor of 5 over the range of loading from 0 to 0.4 mol CO₂/mol DGA. Figure 6.25 shows a comparison between the three results. Table 5.12 shows the slope of the line from equation 5.41. The results with potassium formate and 65 wt% DGA at 25 °C compares well to the results with 65 wt% DGA; however, at 40 °C the potassium formate and glycolic acid and 65 wt% DGA increases a factor of 2 to 3 with ionic strength compared with 65 wt% DGA which increase a factor of 5 over the range studied.

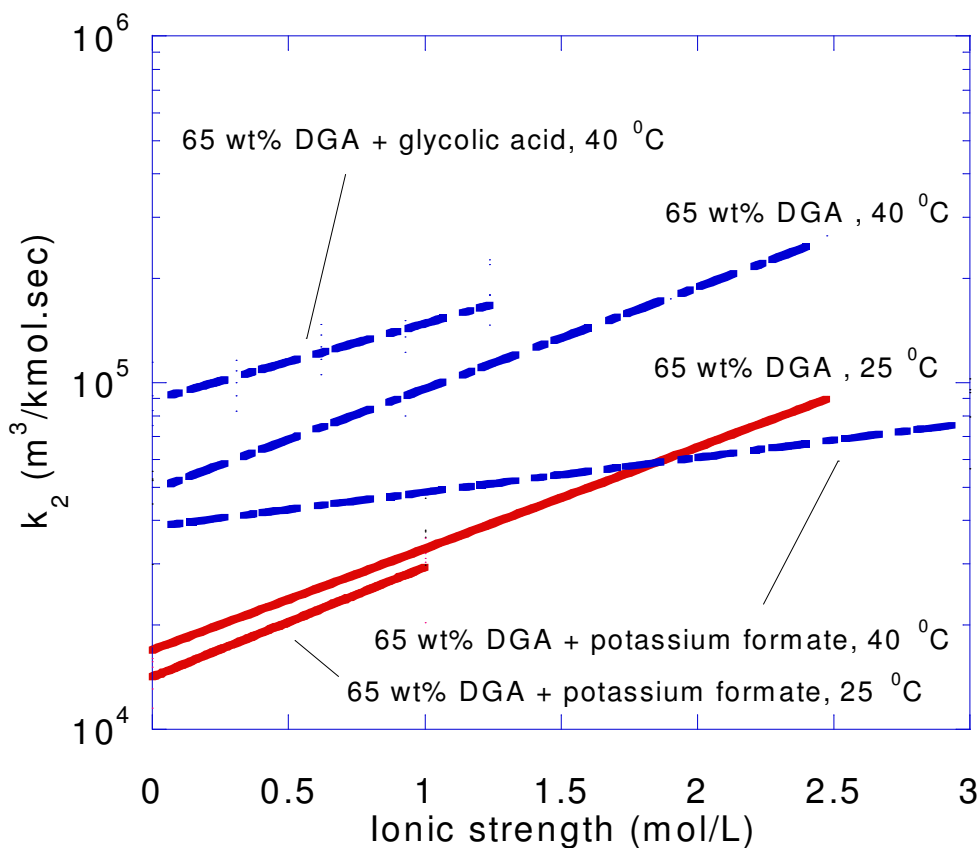


Figure 5.29 Effect of ionic strength on the second rate constant at 25 °C and 40 °C for the system DGA-water-CO₂, DGA-glycolic acid-water-CO₂, and the system DGA-potassium formate-water-CO₂

5.6 Conclusions

Absorption experiments of CO₂ into aqueous 65 wt% and 25 wt% DGA (diglycolamine) solutions were performed at 25-60°C in a wetted-wall column. The eddy diffusivity theory was used to simulate liquid-phase hydrodynamic characteristics. Two approximate models were used; the pseudo first order approximation (PFO), and the interface pseudo first order. The electrolyte-NRTL model was used to represent the activity coefficients of the species in solution. In the previous chapter, the NRTL model was verified using ¹³C NMR data, physical and chemical solubility data.

Table 5.12 Results for the fit of k_2 as a function of μ for the results

	T, °C	k_0 ($\text{m}^3/\text{kmol}\cdot\text{cm}^2\cdot\text{sec}$)	C ($\text{m}^6/\text{kmol}^2\cdot\text{cm}^2\cdot\text{sec}$)	R^2
65 wt% DGA	25	1.73E+04	0.674	0.999
65 wt% DGA	40	5.00E+04	0.674	0.999
65 wt% DGA+potassium formate	25	1.41E+04	0.730	0.834
65 wt% DGA+potassium formate	40	3.84E+04	0.230	0.521
65 wt% DGA+glycolic acid	40	8.90 E+04	0.510	0.587

Kinetic rate constants have been regressed from the currently obtained experimental data. The following conclusions can be made;

- The 65 wt% DGA shows second order kinetics.
- The IPFO model matches very well the rigorous model. The PFO model underestimates the second order rate constant, especially at high loading .
- The reaction of DGA with CO_2 is the dominant effect at low loading. At high loading, instantaneous reactions are approached and diffusion of reactants and products becomes an important phenomena.
- The natural log of the second order rate constant increases linearly with the ionic strength. The second order rate constant increases a factor of five at an ionic strength of 2.5 M.
- Experiments with 65 wt% DGA and glycolic acid and potassium formate show a comparable increase (a factor of 2 to 3) in rate constant with ionic strength as in 65 wt% DGA (a factor of 5 with ionic strength) at 25 °C and 40 °C.

Chapter 6: Absorption of CO₂ in Aqueous MOR and MOR/DGA® Blends

6.1 Introduction

Although the reaction of CO₂ with primary and secondary amines has been studied extensively only very limited information is available for the reaction between CO₂ and morpholine (MOR). There are no kinetic data for CO₂ absorption in DGA/MOR blends. Alper (1990) reported kinetic data at 298 K obtained by a stopped-flow technique for the reaction of CO₂ and MOR. Littel (1991) obtained kinetic data at 303 K with the stirred cell reactor. All the reactions can be described by the zwitterion mechanism originally proposed by Caplow (1968). The results obtained by Littel with the stirred cell reactor are considerably lower than the results obtained by Alper with stopped-flow. Littel concluded that the overall reaction rate depends on both the zwitterion formation rate and the zwitterion deprotonation rate by amine. However, Alper found that the overall reaction rate depends entirely on the zwitterion deprotonation rate. Crook and Donnellan (1989) reported kinetic data at 298 K for MOR with the stopped flow technique. They questioned the validity of the zwitterion mechanism and proposed a single step, termolecular mechanism that postulates a loosely bound complex as the initial product. For this mechanism the forward reaction rate can be calculated according to:

$$R_{\text{CO}_2} = \{k_{\text{AM}} [\text{R}_1\text{R}_2\text{NH}]^2 + k_w \{[\text{R}_1\text{R}_2\text{NH}]^2 [\text{H}_2\text{O}]\} [\text{CO}_2]\} \quad (6.1)$$

Reaction rate 6.1 for the single step, termolecular mechanism according to Crooks and Donnellan can be regarded as a limiting case of the zwitterion

mechanism, if the zwitterion deprotonation is the rate-determining step. For reactions in which the zwitterion formation is the rate-determining step such as DGA, the agreement between both methods is satisfactory.

Chapter 4 studied the equilibrium of DGA, MOR and DGA/MOR blends. Data was obtained at CO₂ loading from 0.0 to 0.5 in solutions of 23.5 wt% MOR, 65 wt% DGA and 11 wt% MOR/53 wt% DGA at 298 to 333K. In this loading region, MOR species make a significant difference on the partial pressure. The electrolyte NRTL model has been used to model partial pressure data, C13 NMR data and N₂O solubility data in the DGA, MOR and the blended amine system.

Chapter 5 studied the rate of absorption in DGA. This chapter reports results with aqueous MOR and with DGA/MOR. The rigorous model, the PFO and IPFO models discussed in the previous chapter are also used here. The rate-based model is combined with the thermodynamics model of Chapter 4 to predict rate of CO₂ absorption. Measurements for the blended amine are made at 0 to 0.4 mol CO₂/mol amine, and 25 °C to 40 °C.

6.2 Physical Properties

The Henry's law constant for CO₂ (H_{CO_2}) is obtained using the N₂O analogy. Data for N₂O solubility in MOR and DGA/MOR solutions has been determined using the data in figure 4.5, equation 5.6 and equation 5.8.

Diffusion coefficients for MOR are calculated using the diffusion coefficient of DGA corrected for molecular weight by multiplying by a factor of 1.2. Diffusion coefficients of all ions are arbitrarily set at the same value as MOR. The diffusion coefficient of CO₂ in concentrated DGA is calculated as described in chapter 5. The solution viscosity is also calculated as described in chapter 5. The absorption rate of carbon dioxide was determined in a wetted wall column as discussed in Chapter 4 and 5.

6.3 CO₂ Absorption in Aqueous MOR

The kinetic data for MOR have been obtained at conditions that greatly simplify the mathematical treatment of the mass transfer problem. The most significant simplification arises from the pseudo first order assumption for kinetics discussed in Chapter 5.

$$\begin{aligned} R_{\text{CO}_2} &= k_2 [\text{MOR}] \{ [\text{CO}_2] - [\text{CO}_2]^* \} = k_1 \{ [\text{CO}_2] - [\text{CO}_2]^* \} \\ k_1 &= k_2 [\text{MOR}]_{\text{BULK}} \end{aligned} \quad (6.2)$$

where $[\text{CO}_2]^*$ is the equilibrium concentration of carbon dioxide.

Table 6.1 presents the absorption data in 23.5 wt% MOR at zero solution loading. At low loading, the equilibrium partial pressure will approach zero. The enhancement factor will also be much greater than 1. Therefore, the CO₂ flux as seen in chapter 6 under these conditions is given by;

$$N_{\text{CO}_2} = \frac{\sqrt{k_2 [\text{MOR}] D_{\text{CO}_2}}}{H_{\text{CO}_2}} P_{\text{CO}_2}^I \quad (6.3)$$

Table 6.1 Rate of absorption data at zero loading into 23.5 wt% aqueous morpholine. Overall gas flowrates from 6.05 to 6.25 SLPM. Total pressures from 15-18 psig.

$[\text{MOR}]_T$ $\frac{\text{kmol}}{\text{m}^3}$	T °C	$P_{\text{CO}_2}^{\text{OUT}}$ Pa	Flux *10 ⁷ $\frac{\text{kmol}}{\text{m}^2\text{s}}$	$k_g^o * 10^9$ $\frac{\text{kmol}}{\text{m}^2\text{Pa} \cdot \text{s}}$	$k_l^o * 10^5$ m/s	$P_{\text{CO}_2}^I$ Pa
2.7	24.4	960	1.91	5.38	6.6	1318
2.7	24.5	1911	4.60	5.40	6.7	2762
2.7	24.4	2925	6.90	5.43	6.7	4185
2.7	24.5	4117	8.16	5.46	6.7	5589
2.7	24.5	5207	9.91	5.49	6.7	6970
2.7	40.0	932	1.96	5.51	8.9	1291
2.7	40.1	1874	4.59	5.54	8.9	2705
2.7	40.2	2877	6.83	5.56	8.9	4098
2.7	40.4	3853	9.15	5.59	8.9	5471
2.7	40.3	4917	10.9	5.62	8.9	6826
2.7	59.2	977	1.94	5.26	12.0	1349
2.7	59.2	1999	4.38	5.29	12.0	2827
2.7	59.5	3091	6.36	5.32	12.1	4280
2.7	59.6	4121	8.62	5.35	12.1	5712
2.7	59.8	5075	11.2	5.38	12.1	7122

From equation 6.3 we can see that a plot of the flux versus interfacial partial pressure will yield a straight line. Figure 6.1 shows the results at several temperatures and CO₂ partial pressures. The data fit a straight line with a y-intercept of approximately zero as predicted by equation 6.3. The second order rate constant was extracted by taking the best fit straight line of each series represented in Figure 6.1 and correcting the slope for the diffusion coefficient and Henry's law constant for carbon dioxide.

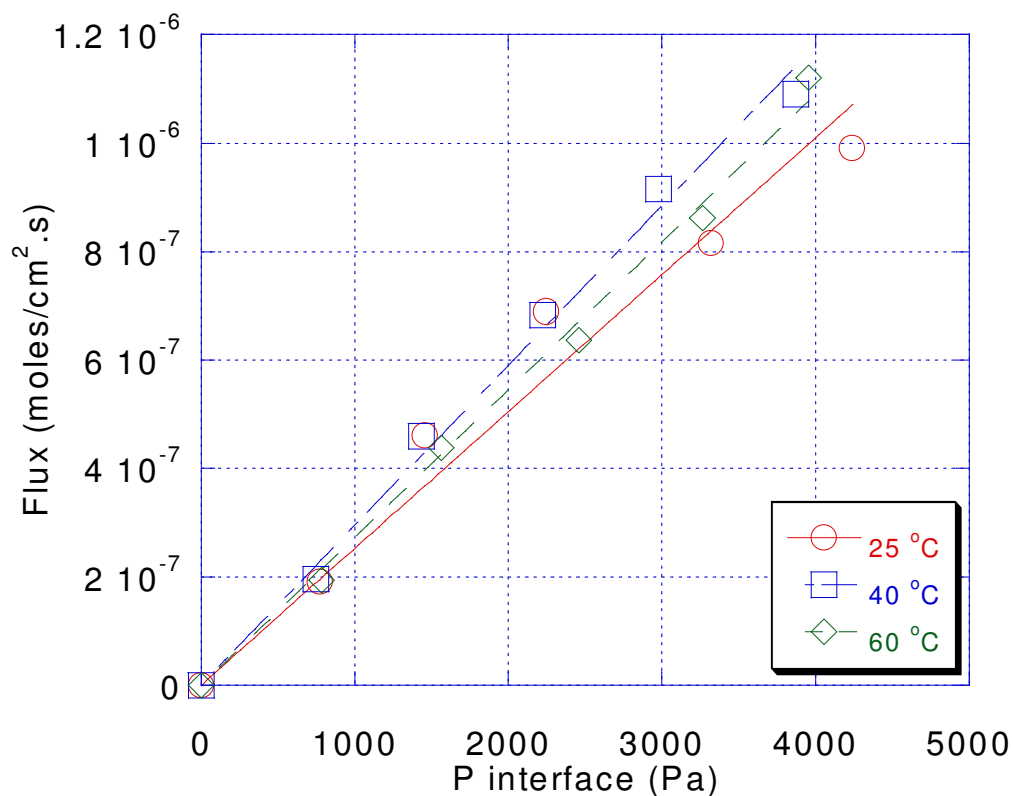


Figure 6.1 Straight line fit for rate of CO₂ absorption into aqueous 23.5 wt% MOR solutions at zero solution loading

The value of the rate constant obtained in this work is shown in Table 6.2. Several other amines are compared to morpholine in Table 6.2. The rate constant obtained in this work is a factor of 4 higher than DGA as measured in this work in the same amine concentration range (see chapter 5). It is hypothesized in this work that the high reactivity of morpholine compared to other amines with similar pKa values is due to its cyclic nature.

The temperature dependence is clearly weak consistent with the zwitterion mechanism. Temperature dependence of the rate constant is shown in Figure 6.2 as an Arrhenius plot.

Table 6.2 Bronsted Correlation of Morpholine Kinetics at 25°C

Amine	Rate Constant at 25°C (m ³ /kmol s)	pK _a at 25°C	Source
Morpholine	22259	8.70	This Work
Piperazine	53700	9.83	Bishnoi (2000)
Ethylenediamine	15000	9.90	Sharma (1966)
Diglycolamine®	6000	9.50	This work
Morpholine	20000	8.70	Sharma (1966)
Diethanolamine	1200	8.88	Sada et al. (1976)
Piperidine	60000	11.12	Sharma (1964)

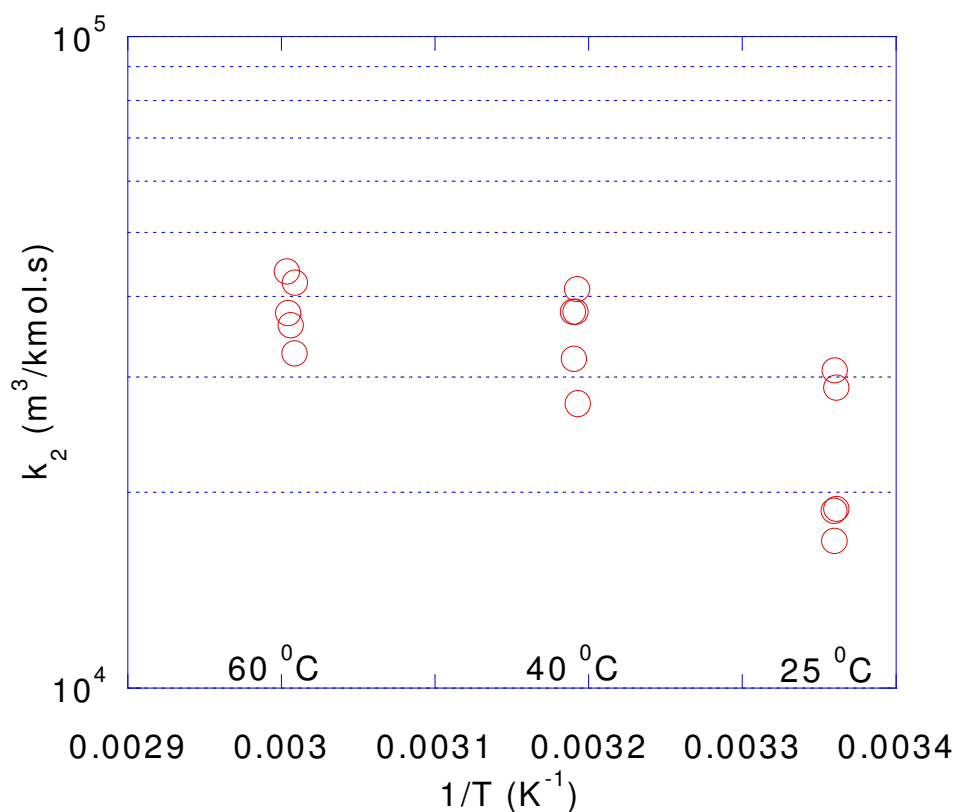


Figure 6.2 Second order rate constant of MOR and carbon dioxide.

Figure 6.3 shows the Bronsted correlation of CO₂ reaction rates with secondary amines. In most cases, it has been observed that the second order rate constant of the cyclic amines lies above the Bronsted plot for amines with similar pK_a. This is probably due to a reduction in steric hindrance around the amine group and a consequent increase in the zwitterion formation rate. Figure 6.3 shows also that the second order rate constant of the secondary amines varies as pK_b⁻¹.

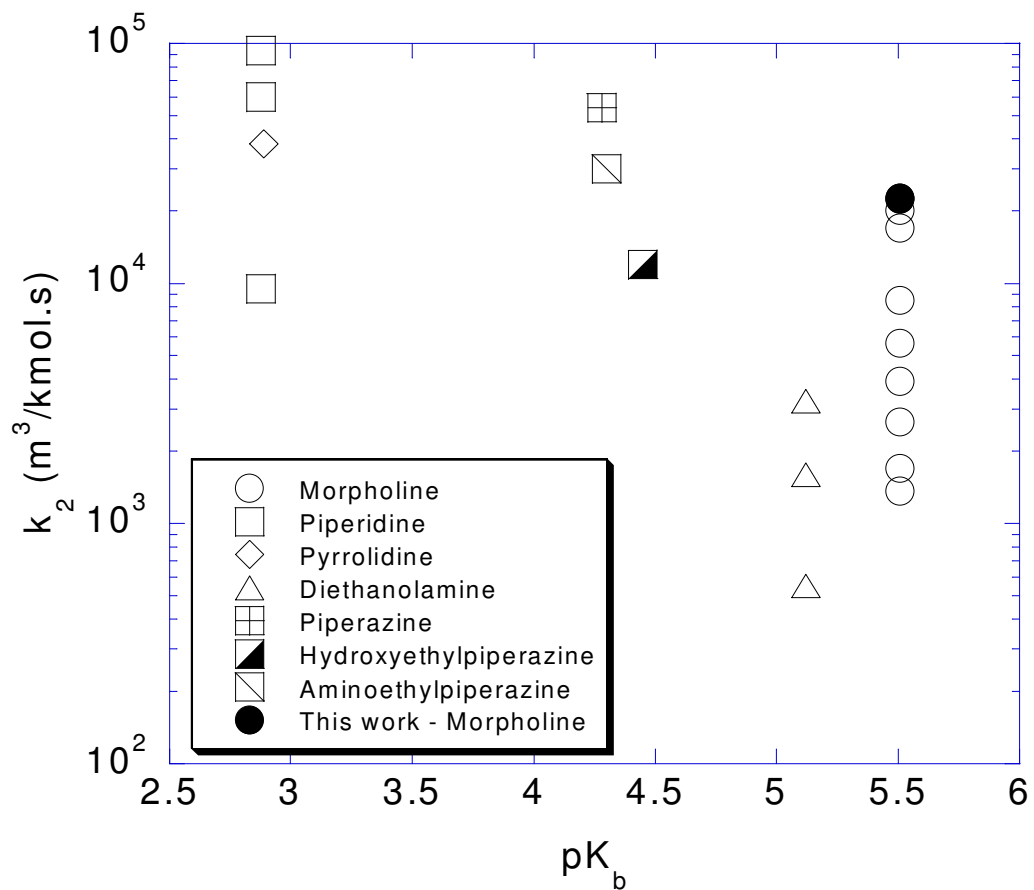


Figure 6.3 Bronsted correlation of CO₂ reaction rates with secondary amines at 25 °C. (Rochelle et al., 2000)

Table 6.3 summarizes the available rate data for morpholine. Results for piperazine are also presented since they are related to the morpholine molecule.

The overall reaction of morpholine is a second order function of amine strength and seems to follow the zwitterion mechanism, however, piperazine demonstrates second order overall kinetics.

Table 6.3 Rate Data for the Morpholine (Rochelle et al., 2000)

Reference	Amine	Temp (K)	[Amine] mol/l	$k_1 = \frac{r}{[CO_2]} \text{ s}^{-1}$	Experimental technique
Sharma (1965)	Morpholine	298	-	19952[MOR]	Stirred cell
Crooks and Donnellan (1989)	Morpholine	298	0.1-1.0	14200*[MOR] ² + 48*[MOR][H ₂ O]	Stopped Flow
Alper (1990)	Morpholine	298	0.025-0.50	3855*[MOR] + 16665*[MOR] ²	Stopped Flow
Xu et al. (1992)	Piperazine	303-333	<4 M Total	2.98*10 ¹¹ exp{-6424/T}[PZ]	Wetted Disk
Littel et al. (1992)	Morpholine	303	0.15-4	$\frac{[MOR]}{\frac{1}{12400} + \frac{1}{12.1 \cdot [MOR]}}$	Stirred Cell
Bishnoi (2000)	Piperazine	303	0.2	68000[PZ]	Stirred Cell
Bishnoi and Rochelle (2000)	Piperazine	298-333	0.2,0.6	$5.37E4 \cdot \exp\left[-\frac{3.36E4}{8.314} \left(\frac{1}{T} - \frac{1}{298.15}\right)\right]$	Wetted Wall
Seo et al. (2000)	Piperazine	303, 313	0.057 – 0.23	4096[PZ], 7075[PZ]	Wetted Sphere

6.4 Rate Results with 11 wt% MOR/53 wt% DGA

A subset of the experimental data obtained in this work for the blend is presented in Table 6.4. Figure 6.4 shows the normalized flux of CO₂ in 11 wt% OR/53 wt% DGA. Appendix K presents the detailed experimental CO₂ absorption data for the blend.

Table 6.4 Rate of absorption into aqueous 11 wt% MOR/53 wt% DGA. Overall gas flowrates from 3.05 to 6.25 SLPM. Total pressures from 15-60 psig.

$\frac{[\text{Amine}]_T}{\text{m}^3}$	T °C	$P_{\text{CO}_2}^{\text{OUT}}$ Pa	Flux *10 ⁷ $\frac{\text{kmol}}{\text{m}^2\text{s}}$	$k_g^0 * 10^9 \frac{\text{kmol}}{\text{m}^2\text{Pa} \cdot \text{s}}$	$k_l^0 * 10^5$ m/s	$P_{\text{CO}_2}^I$ Pa	CO ₂ loading
6.4	24.6	1046	2.29	5.25	2.94	1507	≈0
6.4	40.0	810	2.75	5.99	4.14	1279	≈0
6.4	59.4	650	3.42	6.38	6.09	1195	≈0
6.4	24.7	1870	2.99	2.54	2.25	3114	0.13
6.4	39.9	1824	3.05	2.59	3.32	3079	0.13
6.4	58.5	1810	2.99	2.65	5.13	3014	0.13
6.4	25.3	2089	2.46	2.55	1.95	3113	0.27
6.4	40.5	1944	2.76	2.59	2.87	3077	0.27
6.4	60.4	2492	1.55	2.54	4.68	3143	0.27
6.4	25.7	4375	2.81	1.25	1.77	6992	0.36
6.4	39.8	2530	4.43	1.42	2.54	6185	0.36
6.4	60.5	26940	7.43	1.45	4.24	32614	0.36

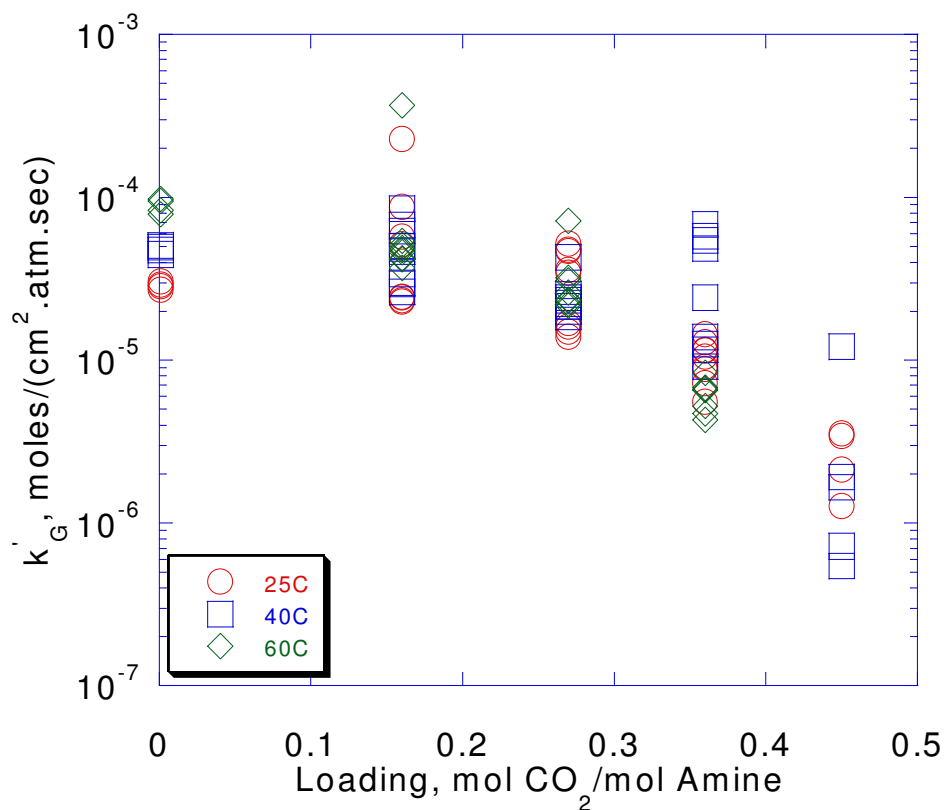
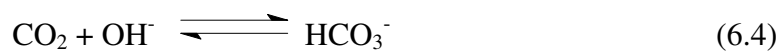


Figure 6.4 Normalized flux of 11 wt% MOR/53 wt% DGA and CO₂

6.5 Model Description

The model developed by Bishnoi (2000), based on the eddy diffusivity theory, was used in this work. The following three equations are assumed to be kinetically controlled.



For each kinetically controlled reaction, we consider the overall reversible rate of reaction. Thus, for the DGA reaction with CO₂ (reaction 6.6), we express the overall rate of reaction as:

$$R_6 = k_{\text{DGA}} \left([\text{DGA}][\text{CO}_2] - \frac{[\text{DGACOO}^-][\text{H}_3\text{O}^+]}{K_6} \right) \quad (6.7)$$

where the equilibrium constant $K_6 = \frac{[\text{DGACOO}^-][\text{H}_3\text{O}^+]}{[\text{DGA}][\text{CO}_2]}$ and is calculated by the ratio of the species in the bulk solution.

Note that water is left out of the kinetic and equilibrium expressions since it is considered to be constant across the boundary layer and, therefore, can be lumped with the apparent rate and equilibrium constants.

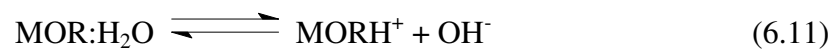
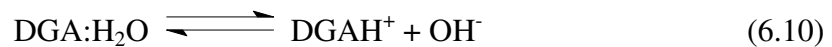
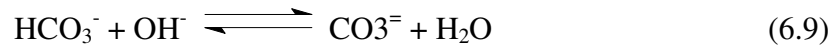
In order to avoid having H₃O⁺ as a species in the model, rates of reaction for carbamate formation are described as:

$$R_6 = k_{\text{DGA}} \left([\text{DGA}][\text{CO}_2] - [\text{DGACOO}^-] \frac{K_w}{K_6[\text{OH}^-]} \right) \quad (6.8)$$

where : $K_w = [\text{H}_3\text{O}^+][\text{OH}^-]$

Other rate expressions for equations 6.4 through 6.6 follow. The rate constant for reaction 6.4 is the expression presented by Pinsent et al. (1956).

Reactions involving only a proton transfer are considered to always be in equilibrium. These reactions are:



There are ten species that need to be considered. At each node, therefore, there are 10 unknowns that need to be determined. The equations to be solved at each node are presented in table 6.3. Along with these 10 equations at each node, we define boundary conditions at the interface and in the bulk solution. We use the condition that all concentrations are equal to the equilibrium concentrations as liquid depth approaches infinity. We also assume phase equilibrium of CO₂ at the interface leading to a known concentration of CO₂ at the interface for a given interfacial partial pressure of CO₂. The concentration of species which undergo proton exchange are defined by the combined buffer system flux being zero at the interface and chemical equilibrium between the two species involved in the proton exchange. Electroneutrality is also assumed at the interface. Table 6.5 also documents the boundary conditions used in this work.

Table 6.5 Model Equations and Boundary Conditions

Conservation Equations at Each Node

Overall Species Material Balance

$$\nabla^2[\text{MOR}] + \nabla^2[\text{MORCOO}^-] + \nabla^2[\text{MORH}^+] = 0$$

$$\nabla^2[\text{DGA}] + \nabla^2[\text{DGACOO}^-] + \nabla^2[\text{DGAH}^+] = 0$$

$$\nabla^2[\text{CO}_2] + \nabla^2[\text{HCO}_3^-] + \nabla^2[\text{CO}_3^{2-}] + \nabla^2[\text{MORCOO}^-] + \nabla^2[\text{DGACOO}^-] = 0$$

Equilibrium Relationships

$$K_9 = \frac{[\text{CO}_3^{2-}]}{[\text{HCO}_3^-][\text{OH}^-]}$$

$$K_{10} = \frac{[\text{DGAH}^+][\text{OH}^-]}{[\text{DGA}]}$$

$$K_{11} = \frac{[\text{MORH}^+][\text{OH}^-]}{[\text{MOR}]}$$

Material Balance for Molecular CO₂

$$\nabla^2[\text{CO}_2] - (R_{10} + R_{11} + R_{12}) = 0$$

Carbamate Material Balance

$$\nabla^2[\text{MORCOO}^-] + R_{11} = 0$$

$$\nabla^2[\text{DGACOO}^-] + R_{12} = 0$$

Electroneutrality

$$[\text{MORH}^+] + [\text{DGAH}^+] = [\text{HCO}_3^-] + 2[\text{CO}_3^{2-}] + [\text{OH}^-] + [\text{MORCOO}^-] + [\text{DGACOO}^-]$$

Boundary Conditions

At $x=0$

$$[\text{CO}_2] = [\text{CO}_2]_I$$

$$D_{\text{MOR}} \nabla[\text{MOR}] + D_{\text{MORH}^+} \nabla[\text{MORH}^+] = 0$$

$$D_{\text{DGA}} \nabla[\text{DGA}] + D_{\text{DGAH}^+} \nabla[\text{DGAH}^+] = 0$$

$$K_{16}[\text{MOR}] - [\text{MORH}^+][\text{OH}^-] = 0$$

$$K_{17}[\text{DGA}] - [\text{DGAH}^+][\text{OH}^-] = 0$$

$$\nabla[\text{MORCOO}^-] = 0$$

$$\nabla[\text{DGACOO}^-] = 0$$

$$K_{15}[\text{HCO}_3^-][\text{OH}^-] - [\text{CO}_3^{2-}] = 0$$

$$D_{\text{HCO}_3^-} \nabla[\text{HCO}_3^-] + D_{\text{CO}_3^{2-}} \nabla[\text{CO}_3^{2-}] = 0$$

$$[\text{MORH}^+] + [\text{DGAH}^+] = [\text{HCO}_3^-] + 2[\text{CO}_3^{2-}] + [\text{OH}^-] + [\text{MORCOO}^-] + [\text{DGACOO}^-]$$

At $x = \infty$

$$[i] = [i]_o \quad \text{For all species } i \text{ in solution}$$

The speciation was estimated using the solubility model presented in chapter 5. The rate constants used in model prediction for DGA and MOR are the rate constants estimated by the data in chapter 6 and in section 6.3 in this chapter for the single amine systems. Using these constants, the flux for each experimental point is estimated using the rigorous model described in the previous section and compared to the measured flux. Figure 6.5 compares the predicted flux to the measured flux for this series of data.

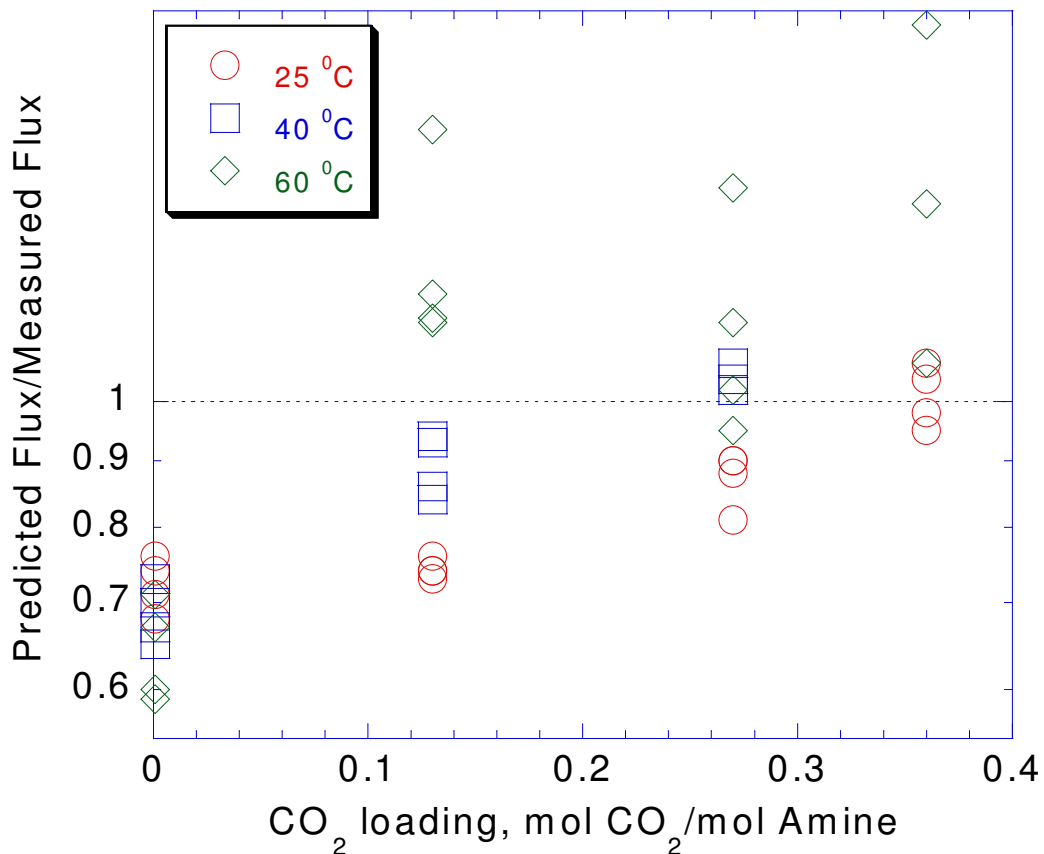
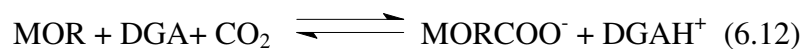


Figure 6.5 Comparison of predicted and experimental fluxes for absorption of carbon dioxide into 11 wt% MOR/53 wt% DGA.

It can be seen that rigorous model consistently underestimates the flux of carbon dioxide and that the error seems to decrease with loading. This can be attributed to the fact that DGA catalyzes the reaction of CO₂ and MOR as shown below;



This effect is consistent with the zwitterion mechanism observed for other secondary amines (Caplow, 1968; Danckwerts, 1979; Littel, 1991). The third order rate constant for the reaction of CO₂, DGA and MOR was regressed to fit the

absorption data at low loading and found to follow the Arrhenius expression as shown in figure 6.6. These kinetics are ignored by the previous model.

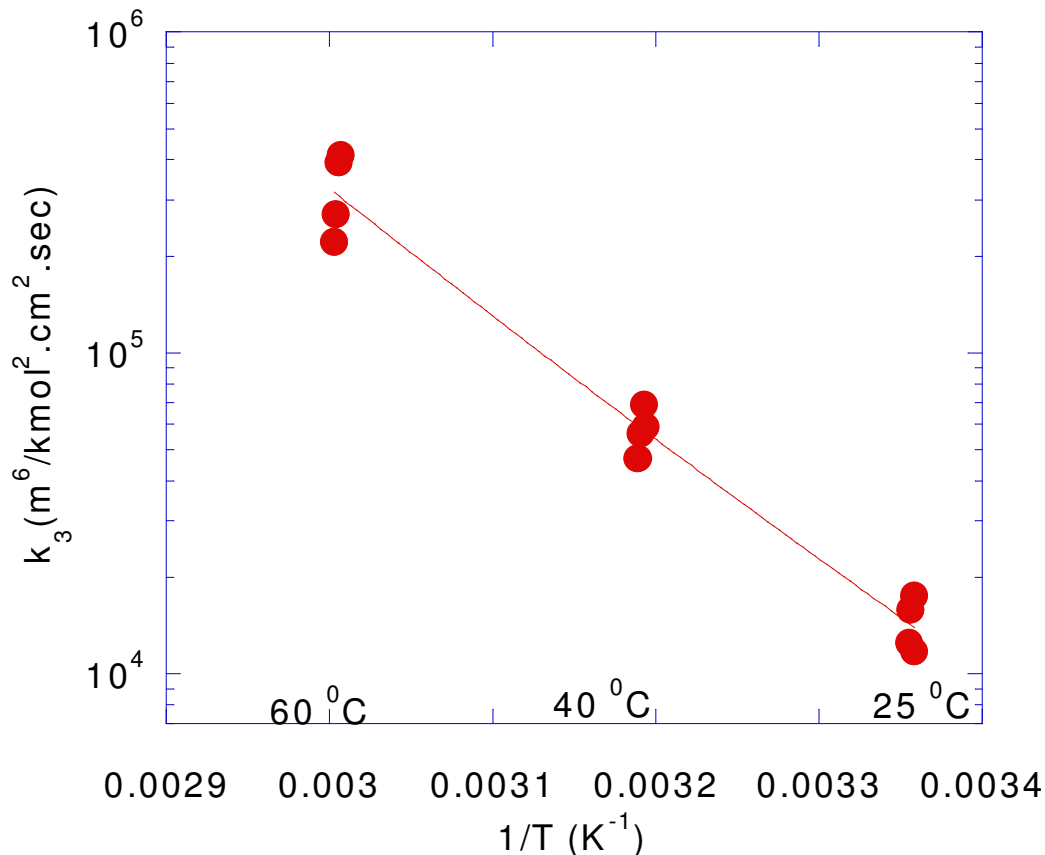


Figure 6.6 Third-order rate constant for the reaction between CO₂ and 11 wt% MOR/53 wt% DGA using the rigorous model, from data at zero loading.

As discussed in chapter 6, the third order rate constant was regressed against CO₂ loading and temperature to fit the absorption rate data at 25 °C, 40 °C and 60 °C. Equation 6.13 shows the third order rate constant equation. It is in log form, and it is similar to equation 5.36.

$$\ln k_3 = A + B \cdot l d g + C/T \quad (6.13)$$

Figure 6.7 is the parity plot for the calculated and measured fluxes of CO₂ for the 11 wt% MOR/53 wt% DGA system at various CO₂ loadings and three temperatures. For most experiments the measured flux is within 15% of the calculated flux. The fitted parameters are shown in Table 6.5.

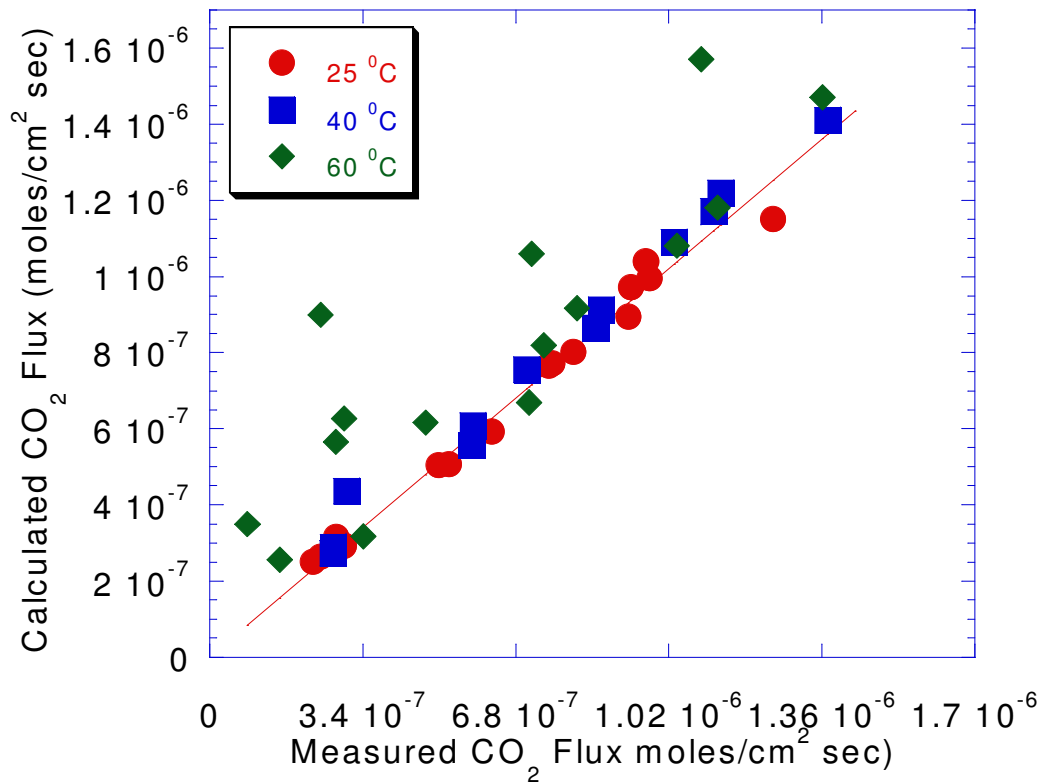


Figure 6.7 Rigorous model fit of all MOR/DGA absorption data.

Table 6.6 Results for the regression of Equation 6.13.

Parameter	Value
A	0.378E02
B	0.20E01
C	-0.84E04

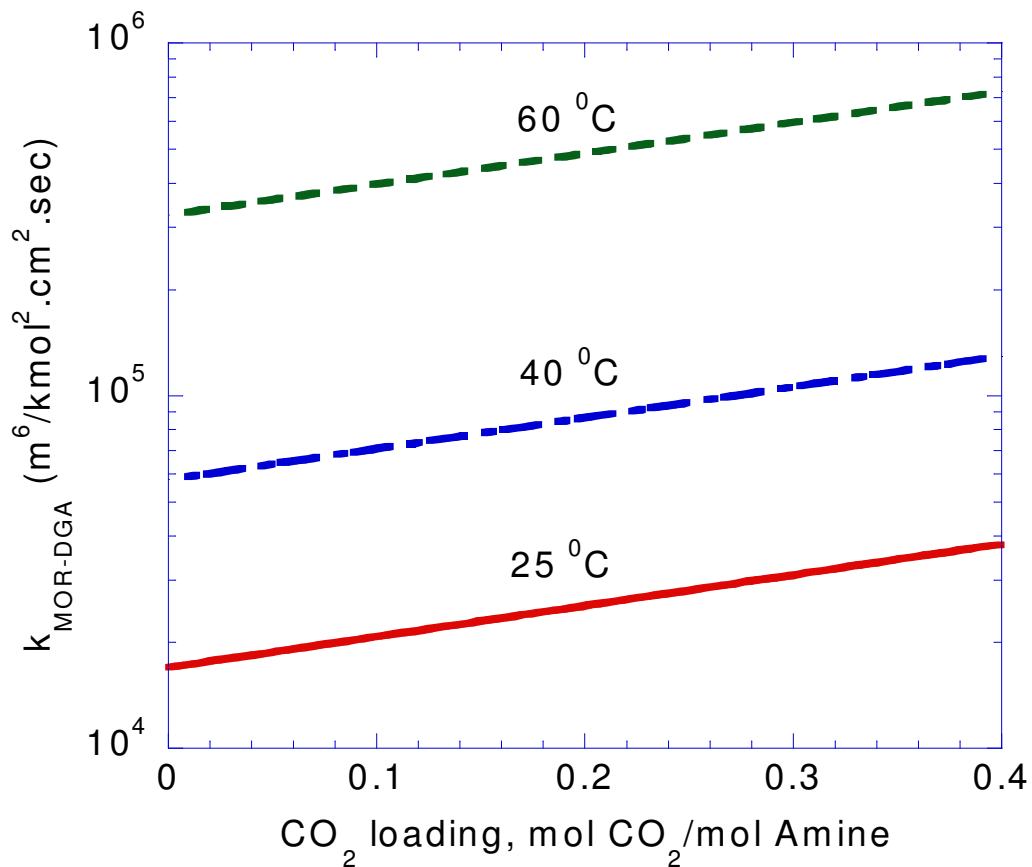


Figure 6.8 $k_{\text{MOR-DGA}}$ for absorption of carbon dioxide into 11 wt% MOR/53 wt% DGA at 25 °C, 40 °C and 60 °C.

6.6 Rate Model Predictions

Figures 6.9 to 6.11 show the model prediction of the normalized flux, k_G' , for CO₂ absorption in 65 wt% DGA and 11 wt% MOR/53 wt% DGA at 25 °C, 40 °C and 60 °C. If the MOR concentration is set to zero, the rate model can be applied to CO₂/DGA/H₂O. All the figures show that the addition of MOR to DGA can increase the CO₂ absorption rate by a factor of 1.5 compared to the DGA

solution with the same total amine concentration. The increase in the rate is more obvious at low loading than at high loading.

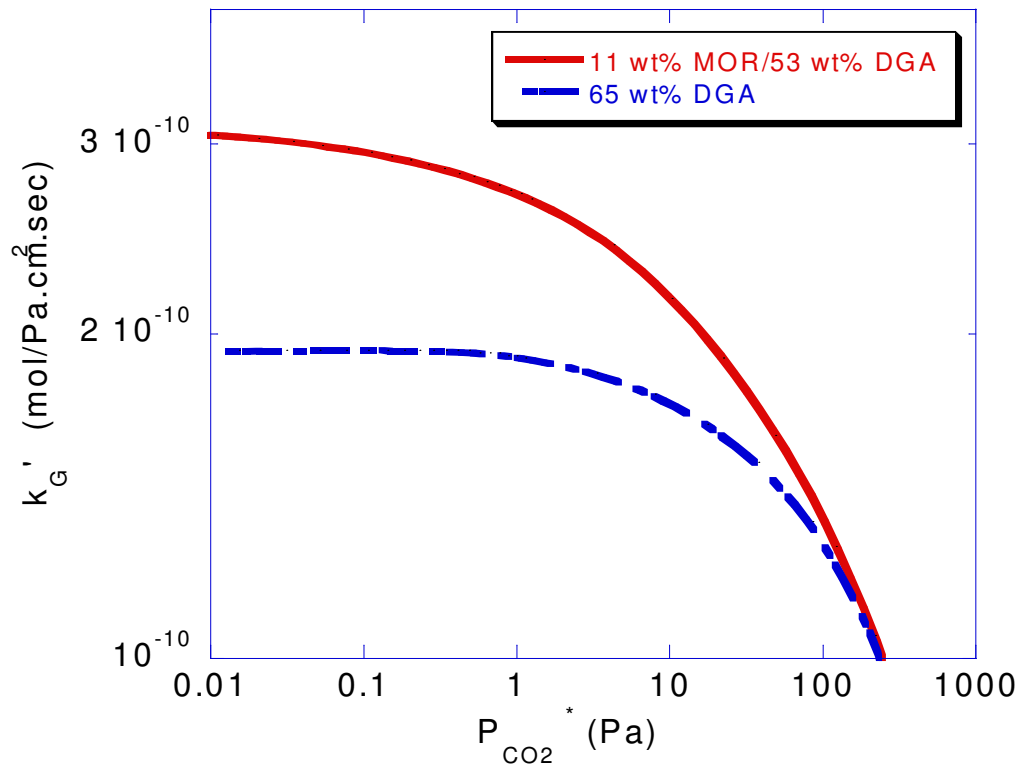


Figure 6.9 Normalized flux of CO₂ in 11 wt% MOR/53 wt% DGA and 65 wt% DGA at 25 °C, $k_i^o=1.77E-3$ m/s, $P^i=10P^*$.

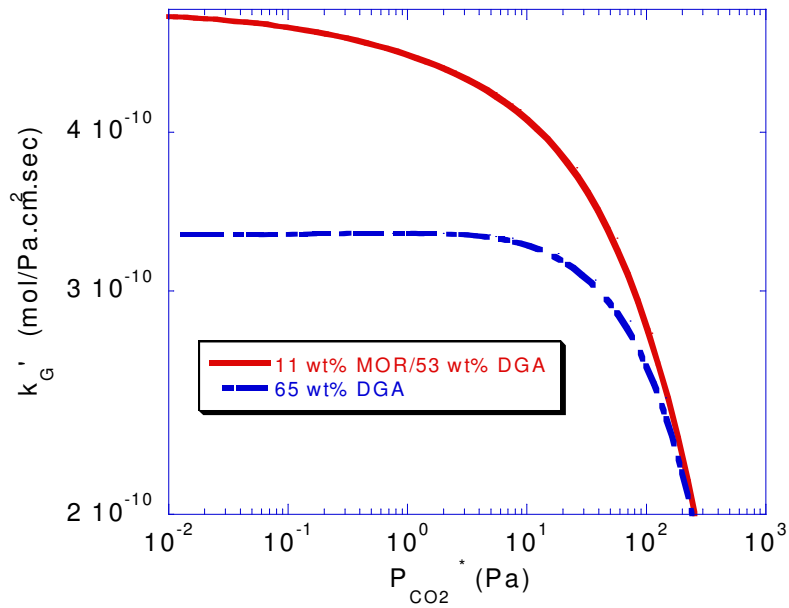


Figure 6.10 Normalized flux of CO₂ in 11 wt% MOR/53 wt% DGA and 65 wt% DGA at 40 °C, $k_i^0=1.77E-3$ m/s, $P^i=10P^*$.

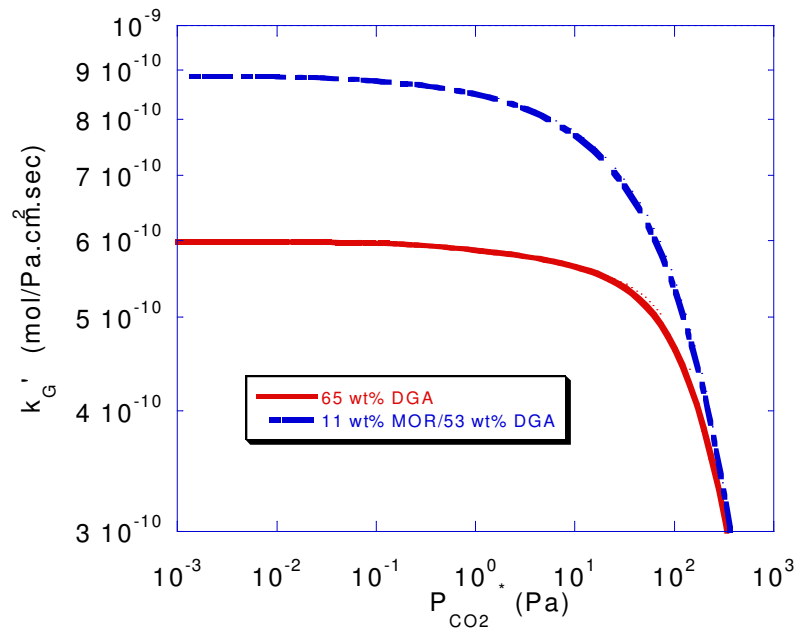


Figure 6.11 Normalized flux of CO₂ in 11 wt% MOR/53 wt% DGA and 65 wt% DGA at 60 °C, $k_i^0=1.77E-3$ m/s, $P^i=10P^*$.

6.7 Sensitivity to Model Parameters

Figure 6.12 shows the sensitivity of different parameters to the flux predicted by the rigorous model with 11 wt% MOR/53 wt% DGA at 40 °C.

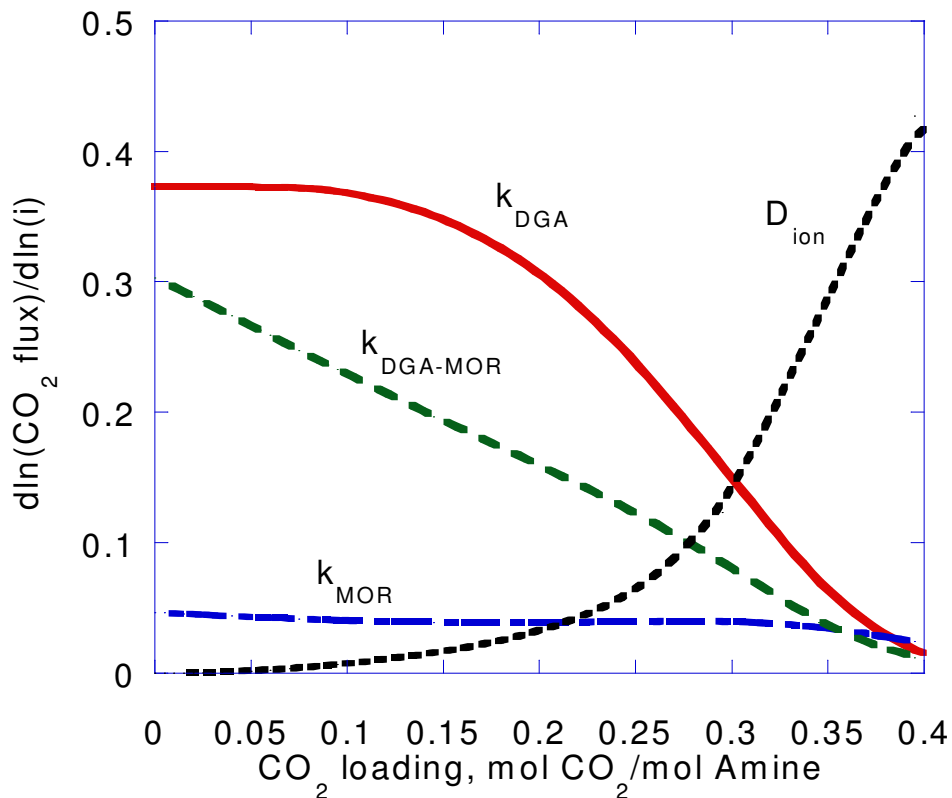


Figure 6.12 Sensitivity of calculated CO₂ flux to values of the diffusion coefficients of reactants and products and rate constants, 40 °C, $k_{ol}=1.77E-3$ m/s, $P_i=10P^*$.

The results can be divided into low and high loading regions. At low loading, the rate constant of DGA, MOR and the third-order rate constant of DGA and MOR are by far the most sensitive parameters showing that the dominant phenomenon in this region is the reaction of CO₂ with DGA and MOR. Also, it can be seen that the DGA reaction is more sensitive than the MOR reaction and the

MOR-DGA reaction. This shows that the DGA reaction is the most dominant phenomena compared to DGA and MOR-DGA reactions. As the loading increases and the concentration of DGA and MOR drops, the rate constants of DGA, MOR and MOR-DGA become less important and this is replaced by the diffusion coefficient of ions at high loading showing that the removal of reaction products and the diffusion to the interface have become the dominant phenomena.

6.8 Deviation from Approximate Solutions

Figure 6.13 and 6.14 shows the model prediction of the k_G' of CO_2 absorption into 11 wt% MOR/53 wt% DGA at 40°C and a $k_1^0=1.77\text{E-}3$ m/s using the pseudo first order approximation (PFO) and the rigorous model.

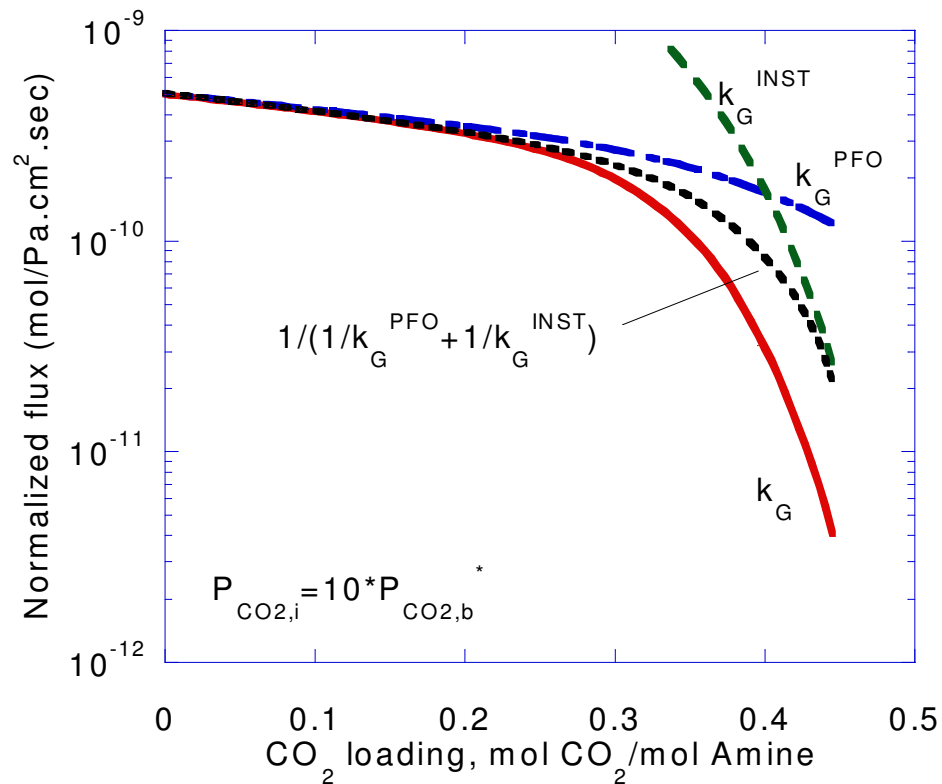


Figure 6.13 Comparison of rigorous model and PFO model for CO_2 absorption at 40°C , $k_1^0=1.77\text{E-}3$ m/s, $P_i=10P^*$.

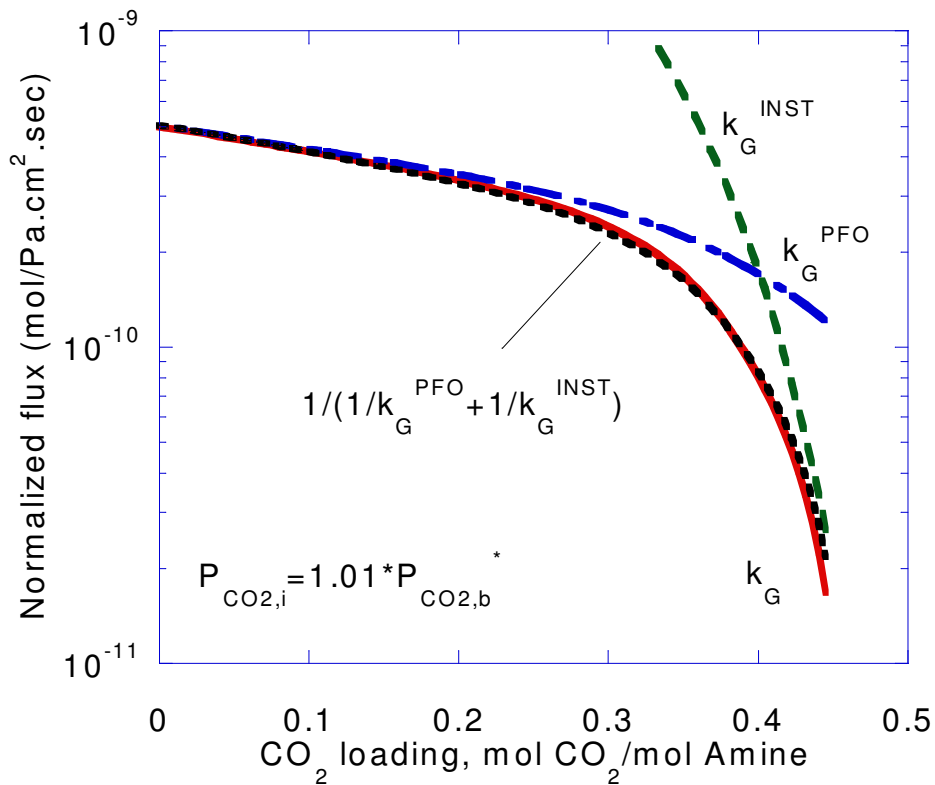


Figure 6.14 Comparison of rigorous model and PFO model for CO₂ absorption rate at 40 °C, $k_1=2.74E-3$ m/s, $P^i=1.01P^*$.

Both low driving force ($1.01 \cdot P^*_{CO_2}$) and high driving force ($10.0 \cdot P^*_{CO_2}$) are considered. At low loading, there appears to be no affect of an increase in driving force. At high loading, however, increasing the driving force from $1.01 \cdot P^*_{CO_2}$ to $10 \cdot P^*_{CO_2}$ can decrease the normalized flux by a factor of two.

We first compare pseudo first order to the rigorous model at small driving force. The model predicted the k_G ' essentially follows the pseudo first order approximation at low loading. Here, the major process occurring is the reaction of CO₂ with DGA and MOR throughout the boundary layer. At 0.2 loading, we start to see significant deviations from pseudo first order behavior even at the low driving force conditions. This is because the carbamate forming reactions are

approaching instantaneous reactions. Pseudo first order is not a good assumption at high loading.

A simple addition of the pseudo first order resistance and the instantaneous resistance ($1/k_G^{\text{PFO}} + 1/k_G^{\text{INST}}$) leads to very accurate prediction of the normalized flux with low driving force, but over predicts the normalized flux at high loading with the high driving force. This is understandable since the concentration at the interface is not significantly different from that in the bulk solution with low driving force. At high loading, the amine is significantly depleted at the interface; therefore, the concentration at the interface is significantly different from that in the bulk solution.

6.9 Conclusions

MOR Performance

The kinetics of MOR shows zwitterion behavior. The rate constant is an order of magnitude higher than primary amines such as MEA or DGA.

MOR/DGA Blend Performance

A 11/53 wt % blend of MOR/DGA provides almost 50% rate enhancement from 65 wt% wt % DGA at low loading at 25 °C, 40 °C and 60 °C.

Approximate Solutions

Pseudo first order is a good approximation to absorption into MOR/DGA blends at low loading. At high loading, instantaneous reactions are approached. A simplified model that combines the resistance of pseudo first order reactions in series with instantaneous reactions matches the rigorous model well with low driving force.

Important Phenomena at Different Conditions

The reaction of DGA with CO_2 is the dominant effect at low loading. At high loading, instantaneous reactions are approached and diffusion of reactants and products becomes an important phenomena.

Chapter 7: Conclusions and Recommendations

7.1 Effects of Heavy Hydrocarbon Impurities on Hollow Fiber Membranes Performance in Natural Gas Separation

The state-of-the-art membranes for removal of CO₂ from high-pressure natural gas are asymmetric in form and comprised of high T_g polyimide. Some previous fundamental studies have considered the effects of high pressure CO₂ on dense homogeneous membranes. Nevertheless, few fundamental studies have been published on the effects of high pressure CO₂ and only one study (White et al., 1995) with heavier hydrocarbons (C₆+) on performance of asymmetric flat sheet hollow fibers have been reported. Some actual field tests have shown extremely complex responses of hollow fiber asymmetric membranes. The goal of this work was to investigate the effect of heavy hydrocarbons in natural gas feeds on permeation and sorption in hollow fiber membranes.

Matrimid® 5218 is a polyimide that is available in the market. Its permeation properties, combined with its processability (i.e., solubility in common solvents) make it an attractive candidate for gas separation applications. Furthermore, its mechanical strength and high glass transition temperature, better suit it for more rigorous working environments than other noncellulosics such as polysulfone (Clausi and Koros, 2000). In addition, due to economic purposes, more membrane-based processes in natural gas treatments are currently running, with polyimide as membrane materials instead of cellulose acetate. The improved separation factors and high productivity of polyimide hollow fiber membranes provide a step change in natural gas processing costs compared to cellulose acetate. Therefore, the choice for our study was the Matrimid® 5218. Toluene and n-heptane were chosen as model compounds to represent aromatic and aliphatic in

natural gas streams. Permeation and sorption data were obtained using permeation and pressure decay sorption systems. The evaluation was based on a typical feed gas composition of 10% CO₂/90 % CH₄ at a given feed gas temperature of 35 °C. Parameters that were varied were the temperature, total feed pressure and toluene/n-heptane concentration. In addition to steady state tests in the presence and absence of n-heptane and toluene, hollow fiber modules were conditioned for five days with ternary mixture of CO₂, CH₄ and one or the other of these heavy hydrocarbons. Following this conditioning process, the modules were studied with the simple binary 10% CO₂/90 % CH₄ mixture. These conditioning studies provide insight into the fundamental effects induced in the membrane due to the long term exposure to the complex mixtures. By combining both gas solubility and permeation improved understanding of the complex gas/hydrocarbon/polymer interaction was achieved. From this investigation the following conclusions were reached:

- Marked hysteresis is observed in permeation levels of CO₂ and CH₄ with small losses in selectivity following conditioning with 10/90 CO₂/CH₄ + 300 ppm toluene for five days at 35 °C. Conditioning of the hollow fiber membranes with 10/90 CO₂/CH₄ + 300 ppm toluene at 35 °C and 200 psia resulted in 60% to 80% increase in the CO₂ and CH₄ permeability relative to the unconditioned fibers. At 600 psia, the permeability of CO₂ and CH₄ increased 115% and 155% respectively relative to unconditioned fibers. There was a corresponding 2-15% decrease in the selectivity of CO₂/CH₄ in the conditioned sample.
- Essentially no hysteresis was observed for hollow fiber membranes after conditioning with 10/90 CO₂/CH₄ + 500 ppm n-heptane for five days at 35 °C. The permeability of CO₂ returned essentially to its original value following conditioning with 10/90 CO₂/CH₄ + 500 ppm n-heptane at 200

psia. The selectivity loss is 2-3%. The conditioning also with 10/90 CO₂/CH₄ + 500 ppm n-heptane at 600 psia *did not* enhance the CO₂ permeance as opposed to toluene; however, the selectivity decreased 14% during conditioning. It appears that the high partial pressure of CH₄ allow a large enough sorption in the langmuir sites to enable CH₄ to compete with CO₂ and the heavier hydrocarbons for newly introduced free volume.

- Solubility measurements of CO₂ and CH₄ after conditioning with 10/90 CO₂/CH₄ + 300 ppm toluene suggest that increases in permeability after conditioning with 10/90 CO₂/CH₄ + 300 ppm toluene are not primarily due to increase in packing defects in the glass. If such an effect was at play one would expect a large shift upward in the sorption isotherm after exposure. The fact that the Langmuir capacity constant is somewhat similar on both before and after exposure suggests that any increases in Langmuir capacity are small or are accompanied by increases in dissolution capacity as well.
- The conditioning induced increase in permeability was a result of an increase in diffusivity caused by a decrease in the intersegmental resistance to mobility of the polymer chain. Conditioning, which is believed to occur because of a reduction in intersegmental steric hindrance to chain motions resulting from penetrant induced swelling of the polymer, tends to increase the diffusivity. The loosening of the polymer matrix presumably tends to increase the size and frequency of transient gaps available for diffusive jumps. Transport conditioning will preferentially increase the diffusivity of the larger penetrant, CH₄ in this case, relative to the small penetrant, CO₂ in this case, and should result in a decrease in the diffusivity selectivity. The increase in CO₂ and CH₄ diffusivity following conditioning with 10/90 CO₂/CH₄ + 300 ppm toluene at 600 psia was 150% and 177% respectively relative to unconditioned sample. Conditioning at 200 psia resulted in 75% and 87% increases relative to unconditioned samples.

- No hysteresis was observed for hollow fiber membranes conditioning with 10/90 CO₂/CH₄ + 300 ppm toluene for five days at 55 °C. This interesting result is believed to be due the reduction in the sorption level of toluene in the glassy polymer due to the increase in temperature. A similar result was found for 10/90 CO₂/CH₄ + 100 ppm toluene.
- The presence of n-heptane and toluene during exposure inhibits the transport of CO₂ and CH₄. This result is consistent with the the dual mode sorption theory which suggests the competition effect should be most apparent for highly condensable feed components, like toluene and n-heptane. For example, the CO₂ permeability during conditioning with 10/90 CO₂/CH₄ + 500 ppm n-heptane at 600 psia and 35 °C decreased 10% relative to the CO₂ permeability during conditioning with the 10/90 CO₂/CH₄. On the other hand, the CO₂ permeability during conditioning with 10/90 CO₂/CH₄ + 300 ppm toluene at the same pressure and temperature decreased 40% relative to their respective during conditioning with the 10/90 CO₂/CH₄. These results are consistent with observations for permeability hysteresis seen after conditioning with 10/90 CO₂/CH₄ + 300 ppm toluene. Toluene is strong swelling and a strong competitive agent compared to n-heptane. The term “strong competitive” is taken to mean components whose critical temperature, T_c, is greater than the measurement temperature. In this regard, the critical temperature of toluene is 591.7 K, and that of n-heptane is 540.2 K. It should be remembered also the nature of interaction of the aromatic chains of Matrimid® 5218 with the aromatic ring of toluene. In comparison to toluene, n-heptane is a straight chain aliphatic. The high T_c of toluene and its aromaticity should be responsible for its high swelling activity compared to n-heptane.
- Our results indicated that defect-free, non-nodular morphology offers advantages in performance compared to defective fibers. Earlier work

(Gunaidi, 2000) showed serious losses in selectivity of defective fibers of the same polymer compared to defect-free fibers.

Recommendations for Future Work

- The acquisition of further data at higher feed pressure, higher CO₂ composition, and higher concentration of toluene and n-heptane will increase the range of the data obtained in this work and increase our understanding of this important material.
- We suggest also doing additional sorption experiments using film materials and using quartz spring apparatus in order to characterize diffusion of toluene and n-heptane and their affinities to the membrane. Valuable future work will also include mixed gas sorption measurements. While these measurements are very difficult to perform, the results would provide valuable information about the characteristics of mixture feed streams.
- A glassy polymer has a "non-equilibrium" state resulting from the highly rigid nature of the polymers. The standard method of asymmetric membrane formation in our labs is by nonsolvent-induced phase separations. We believe this technique produces selective layers containing nanoscale pores during the phase separation, which are trapped in the glassy matrix. If this view were correct, nanoporosity of the membrane would increase the membrane's susceptibility to capillary condensation of condensable hydrocarbons. A new asymmetric membrane formation technique markedly decreases the membranes sensitivity to condensable hydrocarbons. It is believed that this new formation process suppresses nucleation and growth of nanometer scale solvent/nonsolvent-rich phases leading to essentially dense polymer films.

- Develop new polymeric materials more resistant to aromatic agents. Polyimide has been found as a good material for CO₂ removal from the natural gas streams in the absence of aromatics.
- The modeling of toluene induced swelling in glassy polymers needs more attention. There are no available models in literature that predicts plasticization in the presence of toluene. Fundamental data on sorption, dilation and diffusion needs to be collected in order to develop thermodynamic models of the gas/hydrocarbon/polymer system.

7.2 Carbon Dioxide Absorption and Solution Equilibrium in Morpholine and Diglycolamine

Our study of MOR and DGA solutions for CO₂ removal from natural gas started by examining aqueous CO₂/H₂O/MOR system, CO₂/H₂O/DGA system. Equilibrium partial pressure and absorption data for CO₂ in aqueous 23.5 wt% MOR, and 65 wt% DGA were obtained in a wetted wall column. ¹³C NMR data were acquired for the MOR/D₂O/CO₂ system and DGA/D₂O/CO₂. The NMR data were combined with CO₂ solubility data and the nitrous oxide data to determine the important ionic reaction products in the CO₂/MOR/H₂O system, CO₂/DGA/H₂O system. The absorption data in aqueous MOR, and DGA were used to obtain a second order rate constant for the MOR/CO₂ and DGA/CO₂ reactions.

Equilibrium partial pressure, NMR and absorption data were also acquired for the MOR/DGA blend. The thermodynamics of this system were modeled using the electrolyte NRTL model and the SRK equation of state along with the equilibrium constants obtained from the aqueous work. The absorption data were analyzed using a rigorous boundary layer model based on eddy diffusivity theory (Bishnoi, 2000), pseudo first order approximation model (PFO) and interface pseudo first order approximation model (IPFO). The rigorous model was used to make

predictions for the performance of MOR/DGA blends compared to 65 wt% DGA at industrial conditions.

Thermodynamic Interactions of MOR/CO₂, DGA/CO₂, MOR/DGA/CO₂

¹³C NMR data have shown that CO₂ reacts with MOR and DGA to form MOR carbamate, DGA carbamate, protonated MOR and protonated DGA.

The MOR and DGA carbamate stability constant was found comparable to other secondary amines such as DEA and primary amines such as MEA in both its absolute value and its temperature dependence. The MOR carbamate is a factor of 5 to 7 times less stable than the DGA carbamate. At low loading in the CO₂/H₂O/MOR system and CO₂/H₂O/DGA, the main reaction product is MOR carbamate and DGA carbamate. This is replaced by protonated MOR and protonated DGA at high loading.

In the MOR/DGA blend, MOR and DGA carbamate are the dominant reaction product at low loading. The main reaction products at high loading are the protonated MOR and DGA. The main difference between the blend and MOR alone is that the MOR carbamate is stabilized in the blended system. This was attributed to the equilibrium between carbamate MOR and carbamate DGA in the blend.

CO₂ solubility in DGA was found to be greater than MOR alone or MOR/DGA blends. Morpholine at 11 wt% of the total amine (65 wt% total) increases the CO₂ equilibrium partial pressure by a factor of 5 to 7 at high loading and converges below 0.2 loading. The solvent working capacity of 65 wt% DGA was found to be 10% greater than 11 wt% MOR/53 wt% DGA. The heat of reaction of 11 wt% MOR/53 wt% DGA was found to be comparable to the 65 wt% DGA. The MOR was found also to be more volatile than DGA by a factor of 100 at 60 °C

Kinetics of MOR/CO₂, DGA/CO₂, MOR/DGA/CO₂

The rate constant of MOR with CO₂ to form carbamate has been experimentally determined to be 4 times greater than DGA even though the pK_a is comparable. It is hypothesized that this large increase in the rate constant is due to the reduced hindrance around the nitrogen caused by the cyclic nature of the MOR molecule.

The second-order rate constant in 65 wt% DGA at 25⁰C for the reaction with CO₂ is 4 times larger than previously published values. On the other hand, the 25 wt% DGA yields a rate constant, which is in good agreement with literature values. The 50 wt% DGA yields a rate constant which is two times greater than the 25 wt% results. This finding suggests that the second order rate constant is probably a function of DGA concentration.

The second order rate constant in 65 wt% DGA increases by a factor of 5 over the loading range from 0 to 0.4 at 25 ⁰C, 40 ⁰C and 60 ⁰C. Experiments with 65 wt% DGA + glycolic acid and 65 wt% DGA + potassium formate at 25 ⁰C and 40 ⁰C showed similar trends. The rate constant increases a factor of 2 to 3 in these solutions. The glycolic acid and potassium formate were added to 65 wt% DGA in order to modify the ionic strength environment.

Rate of absorption into blends of MOR/DGA show that DGA kinetics increase 50% at low loading in the presence of MOR. This behavior is consistent with the zwitterion mechanism. The data at low to moderate loading cannot be fit with the single amine rate constants without considering the reaction of CO₂, DGA and MOR to MOR carbamate as a finite rate reaction.

Recommendations

The acquisition of further data for the MOR/DGA system in 50 wt% DGA and at 40 ⁰C, 60 ⁰C and 120 ⁰C will increase our understanding of this system at

industrial conditions. NMR data at higher temperature will help quantify the temperature dependence of the carbonate stability constant. Proton NMR measurements should be performed in the blend system in order to differentiate between protonated MOR and protonated DGA.

One of the concerns in the rate measurements in concentrated DGA solutions is the increase in turbulence at the gas liquid interface and possibly wave formation. Therefore, we recommend doing desorption experiments of CO₂ from 95 wt% ethylene glycol into pure nitrogen. We also recommend rate measurements in a stirred cell reactor.

The presence of MOR in DGA has two opposite effects: MOR enhances CO₂ absorption rate by 50% at low loading and decrease the working capacity by 10%. It should be noted that the higher the rate, the lower the circulation rate and the lower the working capacity, the higher the circulation rate. We recommend, therefore, system modeling of the CO₂ absorption process using DGA in the presence of MOR. The modeling will show which solvent will require less solvent circulation rate to achieve the separation. It should be noted also that DGA has the advantage of lower vapor pressure compared to DGA.

Appendix A: Modeling of Asymmetric Hollow Fiber Membrane Modules used for High-Pressure Natural Gas Purification

The use of polymeric membranes is a potential for several traditional processes used for gas separation. Separation processes of commercial interest include hydrogen recovery from hydrocarbons in refineries and petrochemical processes, oxygen/nitrogen separation from air, dehydration, and acid gas treatment of natural gas (Spillman, 1989; Loeb and Sourirajan, 1963; Spillman and Cooley, 1989; Schell et al., 1989). The inherent advantages of membrane systems include their low capital cost associated with their installation, ease of operation, potentially low energy consumption, and weight and space efficiency. Membranes are available in a wide variety of configurations such as hollow fiber, spiral-wound, plate and frame modules; however, the hollow fiber modules are often a favored configuration because of the very high membrane area which can be packed in a given package volume (Scott, 1995). Because of their widespread industrial use they have attracted considerable attention in modeling efforts.

Several mathematical models have been developed for hollow fiber membranes in the literature. Comprehensive reviews of the existing models for the various flow patterns; cocurrent, countercurrent, and crossflow are given by Shindo et al. (1985), Kowali et al. (1992) and Lipscomb (1996). Since any mathematical model must include some assumptions posed by the physical problem, evaluation of these assumptions underlying the model development is important. Successful membrane modeling and simulation can provide valuable information for the design, optimization and economics of the overall separation process. This chapter investigates the validity of the common assumption regarding a negligible bulk term in current hollow fiber membranes models.

Hollow fiber models usually include mass; momentum; energy balance equations, the relationship governing transport across the membrane, and appropriate boundary conditions. Transport equations describing permeation fluxes across the membrane usually are known to include both molecular diffusion and bulk motion given by Eq. (A.1) in the case of binary mixtures of A and B. The diffusion transport through a pore-free polymeric medium can be well described by the so-called Fick's first law of diffusion. Eqs. (A.1a) and (A.1b) shown below are the diffusion and the bulk transport equations for component A respectively. The effective diffusivity of A in the membrane medium is D_{Am} (cm²/s). The mass flux of permeant i with respect to a fixed frame of reference is n_i (g/cm².s), and ω_i is the mass fraction composition of permeant i in the membrane (g/g). The density of the system comprised of both polymer and sorbed penetrants is ρ . The mass flux of the polymer, n_p , is zero at steady state since the membrane is stationary (Kamaruddin and Koros, 1997).

$$n_A = n_A^{bulk} + n_B^{bulk} \quad (A.1)$$

$$n_A^{diff} = -\rho D_{Am} \frac{d\omega_A}{dx} \quad (A.1a)$$

$$n_A^{bulk} = (n_A + n_B + n_p)\omega_A \quad (A.1b)$$

In simulations of hollow fiber separators the contribution of bulk flow conditions is generally neglected. This assumption in some cases is completely reasonable when the sorption amount of penetrants, ω_A and ω_B , are negligible such as the sorption of simple gases H₂, He, O₂, and N₂. In a recent study, Kamaruddin and Koros (1997) have shown that for CO₂/CH₄ separation using 6FDA-TADPO polypyrrolones and phenol/water separation using a polyether-block-polyamide membranes bulk contributions are significant. Paul and Ebra-Lima (1975 I, II & III) have also shown the importance of the bulk flux term in

single component permeation in a highly swollen membrane. However, to the best of our knowledge, studies concerning the frame of reference effects on hollow fiber modules have not been reported in the literature.

The purpose of the present chapter is to investigate the influence of bulk flux contribution on the performance of membrane separators. This chapter discusses the CO₂/CH₄ separation in 6FDA-TADPA polypyrrolone membranes where a theoretical study of the influence of the frame of reference model (FM) in hollow-fiber separation modules is performed for the CO₂/CH₄ separation in direct comparison with the diffusion model (DM). The consequences of not considering the bulk flow contributions are discussed.

The model can also be extended to multicomponent mixtures as shown below, but for the present case, the binary separation illustrates the key points involved and is considered the first step for more realistic models. Methane recovery, membrane selectivity to CO₂ and stage cut are compared with those calculated by the purely diffusion model (DM). The FM model is fundamentally more correct than the DM because the convection motion is directly incorporated into the model and effects, which are neglected in the DM caused by other components are taken into account. However, the FM is more difficult to solve numerically. The dual mode model has been used to simulate the permeation of multicomponent components in hollow fiber membranes as shown by Thundyil et al. (1999). Chern et al. (1985) presented a bicomponent model on hollow fiber membranes using the dual mode model. Taveria et al. (2001) also presented a multicomponent model on hollow fiber membranes accounting for the permeability pressure and composition dependence according to the dual mode model.

A.1 Model Development

The proposed model considers a hollow fiber module as shown in Figure. A.1 for the countercurrent configuration. For CO₂/CH₄ separation, the CO₂/CH₄ feed gas enters the module where it is separated into a permeate stream and a retentate stream. The membrane acts as a CO₂ permselective barrier, so CO₂ is concentrated in the permeate and CH₄ is concentrated in the retentate stream. A one-dimensional mathematical model is solved for the case of the so-called ‘dual mode’ sorption and transport description of permeation in glassy polymers, thereby, allowing concentration dependence of the effective diffusion and sorption coefficients. .

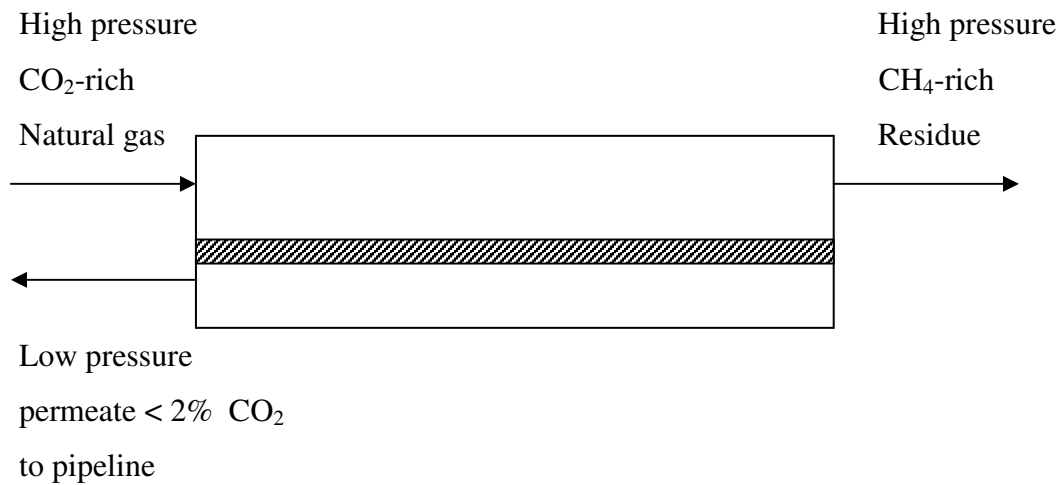


Figure A.1 Simplified block diagram of carbon dioxide/methane separation in a countercurrent hollow-fiber module.

The following assumptions are made:

- Steady state operation.
- Isothermal operation ($T=308$ K).
- Pressure change in the shell side is negligible.
- Pressure change in the tube side is given by Hagen-Poiseulle equation.
- Resistance of the porous support is negligible.
- Resistance of the shell and the tube side boundary layers is negligible.
- Uniform flow distribution within the module.
- No defects in the separating layer.
- Uniform dimensions of all the fibers.
- Plug flow conditions for the permeate and the retentate sides.
- The permeability changes along the fibers are described by the dual-mode transport model (Thundiyil et al., 1999; Chern et al., 1985; Taveira et al., 2001).
- Hollow fiber deformation is negligible.
- Negligible plasticization
- Constant membrane density.

The last assumption, constant bulk density is not seriously in error based on related sorption and dilation data from Fleming and Koros (1988). While the other above conditions are important and can cause performance to depart dramatically from expectations, they are not addressed here. According to these assumptions, the steady-state mass balance equations for species i , on both the retentate and the permeate sides, are given by;

$$\frac{d\mathfrak{R}_{Ri}}{dz} = -N_i \quad (\text{A.2a})$$

$$\frac{d\mathfrak{R}_{Pi}}{dz} = -N_i \quad (\text{A.2b})$$

where \mathfrak{R}_{Ri} and \mathfrak{R}_{Pi} are the axial molar flow rates of species i on the retentate and the permeate sides, respectively, z is the axial direction. The pressure on the shell side p_R is assumed constant and equal to the feed pressure. The pressure on the permeate side p_P is calculated for each individual stage using the Hagen-Poiseuille equation as shown below (Pan and Habgood, 1978 II):

$$\frac{dp_P^2}{dz} = \frac{-256\mu_{mix}\mathfrak{R}_pRT}{\pi d_i^4 N_F} \quad (\text{A.3})$$

where d_i is the inner diameter of the fibers; R is the universal gas constant; T is the temperature; μ_{mix} is the gas mixture viscosity calculated using Wilke's method which has an average error of less than 1% compared to the experimental values (Reid et al., 1977); \mathfrak{R}_p is the total permeate flow rate; N_F is the total number of fibers in the hollow fiber module.

The membrane is divided up into a predetermined number of stages, M small enough that the flow properties, and hence, the pressure and composition gradients are almost constant in each element. This stepwise procedure is generally referred to as succession of states method with fixed length interval (Thundyil and Koros, 1997). The first stage is at the feed end and the M_{th} stage is at the residue end. The driving force is assumed constant over each of the stages considered. At each stage, the radial permeation fluxes of species i , N_i , must be determined by solving the multicomponent mixture permeation relations. Since the membrane thickness is very small with respect to the radius of the fiber, curvature effects can be neglected and the problem can be then solved in cartesian coordinates. With

this in mind the multicomponent mixture permeation system comprises ‘ NC ’ components and the polymer as shown below;

$$\begin{aligned}
 N_1 &= -\rho D_1 \frac{d\omega_1}{dx} + \omega_1 \left(\sum_{j=1}^{nc} n_j + n_p \right) \\
 &\quad \dots \\
 &\quad \dots \\
 N_{nc} &= -\rho D_{nc} \frac{d\omega_{nc}}{dx} + \omega_{nc} \left(\sum_{j=1}^{nc} n_j + n_p \right) \\
 N_p &= -\rho D_p \frac{d\omega_p}{dx} + \omega_p \left(\sum_{j=1}^{nc} n_j + n_p \right)
 \end{aligned} \tag{A.4}$$

As noted by Paul in the context of diffusion thru elastomeric membranes, the mass flux of the polymer N_p is zero at steady state since the membrane is stationary (Paul and Ebra-Lima, 1975 I, II & III). The mass flux of component j can be obtained by integrating Eq (A.4) with the following boundary conditions;

$$\begin{aligned}
 x = 0; \quad \omega_1 &= \omega_{10} \quad \dots \quad \dots \quad \omega_{nc} = \omega_{nc0} \\
 x = \ell; \quad \omega_1 &= \omega_{1\ell} \quad \dots \quad \dots \quad \omega_{nc} = \omega_{nc\ell}
 \end{aligned} \tag{A.5}$$

A.2 Numerical Solution

Assuming constant density within the membrane and average effective diffusion coefficients evaluated between the upstream and downstream conditions; Kamaruddin and Koros (1997) analyzed the situation for a binary feed. Extending this analysis to multicomponent feeds with ‘ NC ’ components results in Eq (A.6);

$$n_j \ell = \frac{\rho D_{Dj} \ln \left[\frac{r_j - \omega_{j2} \sum_{i=1}^{nc} r_i}{r_j - \omega_{j1} \sum_{i=1}^{nc} r_i} \right]}{\sum_{i=1}^{nc} \frac{r_i}{r_j}} \quad (\text{A.6})$$

where r_j and r_i are given by;

$$r_j = \frac{n_j}{n_{ref}} \quad (\text{A.7})$$

$$r_i = \frac{n_i}{n_{ref}}$$

where n_{ref} is the reference component and can be taken to be equal to the mass flux of the slowest component in the mixture. The fraction of the bulk flux contribution of component j , Π_j^{bulk} , is the ratio of the mass flux of component j due to bulk flow relative to the total mass flux as shown in Eq. (A.8). Since the mass fraction of component j , ω_j is decreasing in the direction of the mass flux, an average mass composition, ω_j^{avg} , should be used in Eq.(A.8) when estimating the fraction of the bulk flux contribution.

$$\Pi_j^{bulk} = \frac{\omega_j^{avg} \sum_{i=1}^{nc} n_i}{n_j} = \omega_j^{avg} \sum_{i=1}^{nc} \frac{r_i}{r_j} \quad (\text{A.8})$$

Average mass composition in the membrane of component j can be calculated as follows;

$$\omega_j^{avg} = \frac{\int_0^l \omega_j(x) dx}{\int_0^l dx} \quad (\text{A.9})$$

where $\omega_j(x)$ is mass fraction profile of component j in the membrane and is a function of position and can be calculated by integrating Eq.(4.4) with the following boundary conditions;

$$\begin{aligned} x = 0; & \quad \omega_1 = \omega_{10} \quad \dots \quad \omega_{nc} = \omega_{nc0} \\ x = x; & \quad \omega_1 = \omega_1(x) \quad \dots \quad \omega_{nc} = \omega_{nc}(x) \end{aligned} \quad (\text{A.10})$$

Integrating we have,

$$\omega_j(x) = \frac{1}{\sum_{i=1}^{nc} \frac{r_i}{r_j}} \left[1 - \left[1 - \omega_{j1} \sum_{i=1}^{nc} \frac{r_i}{r_j} \right] \exp \left[\frac{n_j \sum_{i=1}^{nc} \frac{r_i}{r_j} x}{\rho D_{Dj}} \right] \right] \quad (\text{A.11})$$

When the local mass composition $\omega_j(x)$ is averaged over the membrane thickness we obtain;

$$\omega_j^{avg} = \frac{1}{\sum_{i=1}^{nc} \frac{r_i}{r_j}} \left[1 - \left[1 - \omega_{j1} \sum_{i=1}^{nc} \frac{r_i}{r_j} \right] \frac{\rho D_{Dj}}{n_j \ell \sum_{i=1}^{nc} \frac{r_i}{r_j}} \left[\exp \left[\frac{n_j \ell \sum_{i=1}^{nc} \frac{r_i}{r_j}}{\rho D_{Dj}} \right] - 1 \right] \right] \quad (\text{A.12})$$

An expression for the bulk flux contribution of component j can be obtained by substituting Eq. (A.12) into Eq.(A.8);

$$\Pi_j^{bulk} = \left[1 - \left[1 - \omega_{j1} \sum_{i=1}^{nc} \frac{r_i}{r_j} \right] \frac{\rho D_{Dj}}{n_j \ell \sum_{i=1}^{nc} \frac{r_i}{r_j}} \left[\exp \left[\frac{n_j \ell \sum_{i=1}^{nc} \frac{r_i}{r_j}}{\rho D_{Dj}} \right] - 1 \right] \right] \quad (\text{A.13})$$

The permeance $Q_{j,k}$ of component j on stage k is defined as the permeability $P_{j,k}$ divided by the skin layer thickness ℓ . Permeability can be obtained by normalizing the mass flux, diffusional or total (bulk and diffusional) flux, with the thickness and driving force (partial pressure or fugacity difference), and can be written for component j on stage k as follows;

$$Q_{j,k} = \frac{P_{j,k}}{\ell} = \frac{22400n_{j,k}\ell}{MW_j(p_{j,1} - p_{j,2})} \quad (\text{A.14})$$

where $p_{j,1}$ and $p_{j,2}$ are the partial pressures on both sides of the membrane at stage k respectively; $n_{j,k}$ is the mass flux of component j at stage k , and MW_j is the molecular weight of component j . It is more convenient to work with the mass flux units since the molar volume of gaseous penetrants are generally not known.

Using Eq. (A.13), we can calculate the diffusion based permeability, P_j^{diff} , from the observed permeability, P_j^{obs} as follows;

$$P_j^{diff} = (1 - \Pi_j^{bulk})P_j^{obs} \quad (\text{A.15})$$

The observed permeability can be obtained from Eq.(A.14) with the total observed (bulk and diffusion) mass flux. The mass fraction can be calculated using the dual mode model. The dual mode model idealizes glassy polymers as having two distinct environments, unrelaxed volume (defects) and dense matrix (Koros , 1976; Hopfenberg et al., 1973; Vieth et al., 1976; W.J. Koros, 1980). The unrelaxed volume (defects) exists because of the inability of the polymer chains to pack perfectly below their glass transition temperature (T_g). In effect, glassy polymers have not reached equilibrium packing conditions; however, the state of the polymer is metastable because the relaxation time of the polymer chains is extremely long. The population of the components sorbed in the free volume is referred to as the Langmuir's population while those occupying the dense matrix

are referred to as the Henry's population. A companion transport model assigns separate mobilities to the penetrants in the Langmuir and Henry's law populations. For the case of local equilibrium this model is mathematically equivalent to assuming that only a fraction, F , of the Langmuir's population is able to perform diffusive jumps equivalent to those of the Henry's population. The 'mobile' concentration of component j is shown in Eq. (A.16) using the dual mode transport model. As explained earlier, the mobile mass fraction ω_j^{mobile} should be used when describing permeant transport in glassy polymers.

$$\omega_j^{mobile} = \frac{k_{Dj} P_j M_j}{22400 \rho} \left(1 + \frac{F_j K_j}{1 + \sum_{i=1}^{nc} b_i f_i} \right) \quad (\text{A.16})$$

where k_{Dj} is the Henry's law constant of component j which characterizes the sorption in the dense region of the polymer matrix; b_j is a constant that is a measure of the affinity of the penetrant to the Langmuir sites. The constant F_j discussed above can be shown to be equal to the ratio of the diffusion coefficients of Langmuir's population to Henry's populations of component j ; and f_j is the fugacity of component j . The gas phase fugacity of pure and mixed CO₂/CH₄ can be calculated using the virial equation of state (Prausnitz et al., 1986). The fugacity should be used instead of partial pressure since CO₂/CH₄ is non-ideal mixture. The K_j constant can be calculated by the following equation;

$$K_j = \frac{C'_{Hj} b_j}{k_{Dj}} \quad (\text{A.17})$$

where C'_{Hj} is the Langmuir capacity constant.

Different numeric techniques have been proposed in literature for solving the differential equations of hollow-fiber models: shooting methods with initial

value algorithms (C.Y. Pan et al., 1978), weighed residues methods (Tessendorf, 1998) and finite difference methods (Chern et al., 1985) are the most commonly used. In the present work, finite difference solution technique is used.

A.3 Simulations Results and Discussion

The study was conducted for the countercurrent flow configuration. The study used data for CO₂/CH₄ separation using 6FDA-TADPO polypyrrolones. This polymer is known to its unique properties in resisting CO₂ plasticization better than most other polymers, so it was a good ideal example to illustrate the bulk flux effects at high CO₂ pressure without such plasticization complication. Table A.1 gives the dual mode parameters of the 6FDA-TADPO polypyrrolone membrane at 35 °C. The default parameters for simulation are given Table A.2. Although only counter-current flow configuration is considered, similar conclusions can be obtained for cocurrent configuration.

Table A.1 Fugacity based dual-mode and partial immobilization parameters of CO₂ and CH₄ at 35 °C in 6FDA-TADPO polypyrrolone (Kamaruddin and Koros, 1997).

	CO ₂	CH ₄
F (D _H /D _D)	0.084	0.026
D _D (cm ² s ⁻¹)	1.196e-7	1.12e-8
k _D (cm ³ (STP) cm ⁻³ atm ⁻¹)	1.526	0.327
C' _H (cm ³ (STP) cm ⁻³)	34.084	22.838
b (atm ⁻¹)	1.023	0.160

Table A.2 Default parameters for simulations.

Parameter	Default value
Thickness of membrane	0.1 micron
Feed flow rate	50 000 SCFH
Feed pressure	1000 psia
Permeate pressure (at exit)	20 psia
Temperature	308 K
Feed mole fraction	50/50 CO ₂ /CH ₄
Fiber OD	250 microns
Fiber ID	125 microns
Fiber active length	100 cm
Number of fibers	300 000

A.4 Frame of Reference Model (FM) versus Diffusion Model (DM)

In order to understand the influence of considering the bulk flux contribution, when modeling hollow-fiber permeation, one should first understand how it directly affects permeation and sorption. This has been analyzed in detail by Kamaruddin and Koros (1997) for the CO₂/CH₄ separation using 6FDA-TADPO polypyrrolone membranes. Similar conclusions can be taken for the present separation using hollow-fiber membranes, nevertheless there are some aspects worth to pinpoint.

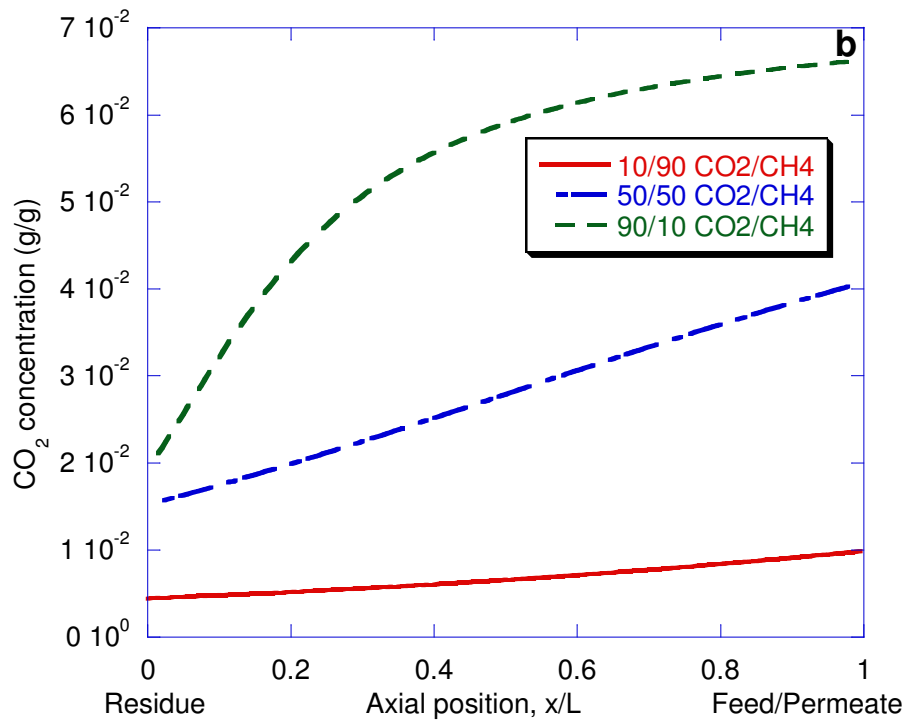
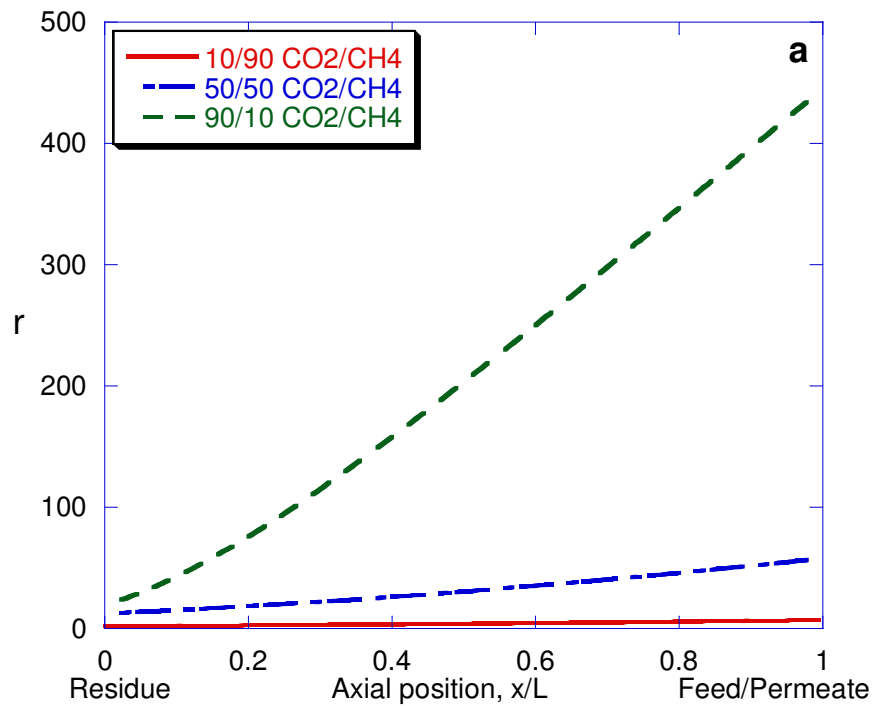
In pure component permeation, the reference term in Eq.(A.4) is a function of the sorption level of the penetrant; however, in the case of binary mixture (A and B) permeation, the reference term is a function of both the penetrant sorption level and the permeation flux of the two components as can be seen from Eq.(A.8). If the sorption level is small, neglecting the bulk flux term is a reasonable assumption; however, if the mass flux of component A is much higher

than B (r is high), then the reference term of B can be significant even though ω_B^{avg} value is small, therefore; the bulk flux term of B cannot be neglected. For component A, r has negligible effect on the bulk term as r approaches high values. In the asymptotic limit as r goes to infinity, the bulk flux contribution of A is ω_A^{avg} . Therefore, the diffusion model (DM), which neglects these coupling effects, results sometimes not only in quantitative errors but also in large qualitative deviations as discussed by Kamaruddin and Koros (1997).

In hollow-fiber modules, the partial pressure can significantly change along the fiber on each side of the membrane, affecting the amount of sorption of penetrants, ω_A^{avg} and ω_B^{avg} , and the permeation flux of both mobile components along the membrane. Therefore, a hollow-fiber model considering diffusion model is expected to lead to quite different results from the ones obtained from a more accurate permeation model, such as the frame of reference model. The differences between these results are analyzed for three different concentration scenarios.

Effect of CO₂ mole fraction

Let us consider the CO₂/CH₄ separation as shown in Figure. A.1. The CO₂ mole fraction has a significant impact on the bulk flux contribution of CO₂ and CH₄. Increasing the faster component (CO₂) feed-side mole fraction increases the value of ' r ', the mass flux ratio of CO₂ to CH₄, as can be seen in Figure A.2a. Increasing the CO₂ mole fraction increases also the CO₂ and decreases the CH₄ sorption levels in the membrane from the dual mode and competitive sorption standpoint. Figure A.2b and c shows the CO₂ and CH₄ concentration profile along the membrane for the 10/90, 50/50 and 90/10 CO₂/CH₄ mixtures. As can be seen in Figure A.2b, the CO₂ concentration decreases from the feed/permeate side to the residue side because the CO₂ is selectively permeating to the low-pressure side of the membrane.



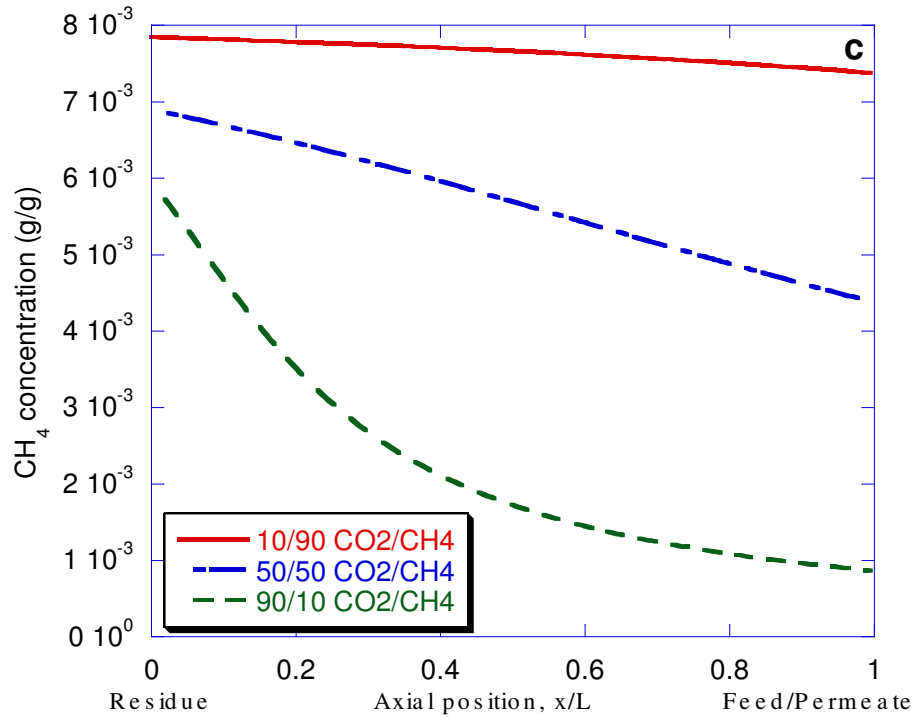


Figure A.2 Effect of CO₂ feed mole fraction on (a). ‘ \bar{r} ’; (b). CO₂ average concentration inside the membrane; (c). CH₄ average concentration inside the membrane.

The CO₂ concentration decrease in the feed side causes the CH₄ concentration to increase; hence, decreasing the average concentration of $\omega_{CO_2}^{avg}$ while increasing $\omega_{CH_4}^{avg}$ inside the membrane. Although ‘ \bar{r} ’ and $\omega_{CH_4}^{avg}$ have opposite effects, the bulk flux contribution of CH₄ can still be significant as shown in Figure. A.3b. The bulk flux contribution of CH₄ is much more sensitive to the ‘ \bar{r} ’ value than the bulk flux contribution of CO₂. This is due in part to the fact that the bulk flux contribution of CO₂ is proportional to ‘ $1/\bar{r}$ ’ while the bulk flux contribution of CH₄ is proportional to ‘ \bar{r} ’. This is quite logic when one component is much faster than the other component, the slower component is ‘swept’ along by the faster component. Looking back at Eq.(A.8), when $\omega_{CH_4}^{avg}$ value is small, the

bulk flux of CH₄ might be small compared to the total mass flux of CO₂ and CH₄; however, the bulk flux of CH₄ might still be significant relative to the diffusional flux of CH₄. Therefore, the bulk flux of CH₄ cannot be neglected. On the other hand, as discussed earlier, the impact of ‘ γ ’ on CO₂ is the opposite of CH₄; the value of the bulk flux contribution of CO₂ approaches $\omega_{CO_2}^{avg}$ when ‘ γ ’ is large; therefore, increasing the CO₂ feed-side mole fraction can increase the bulk flux contribution of CO₂ but to a lesser degree than CH₄. As a direct result, the diffusion model underestimates the permeation fluxes, therefore, predicting a lower permeability than obtainable in Figure.A.4 and Figure.A.5. It is clear that the bulk flux contribution for CH₄ has been detrimental to the separation process.

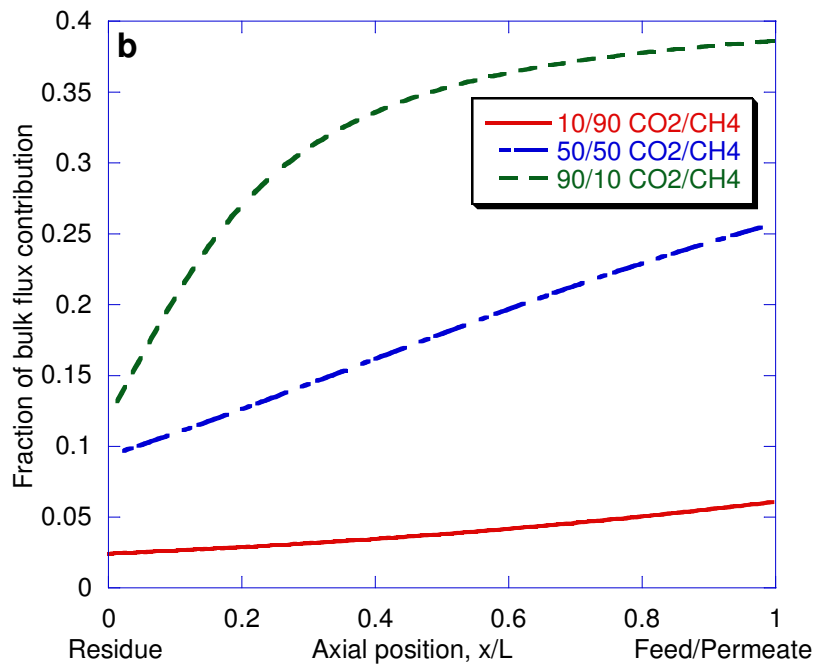
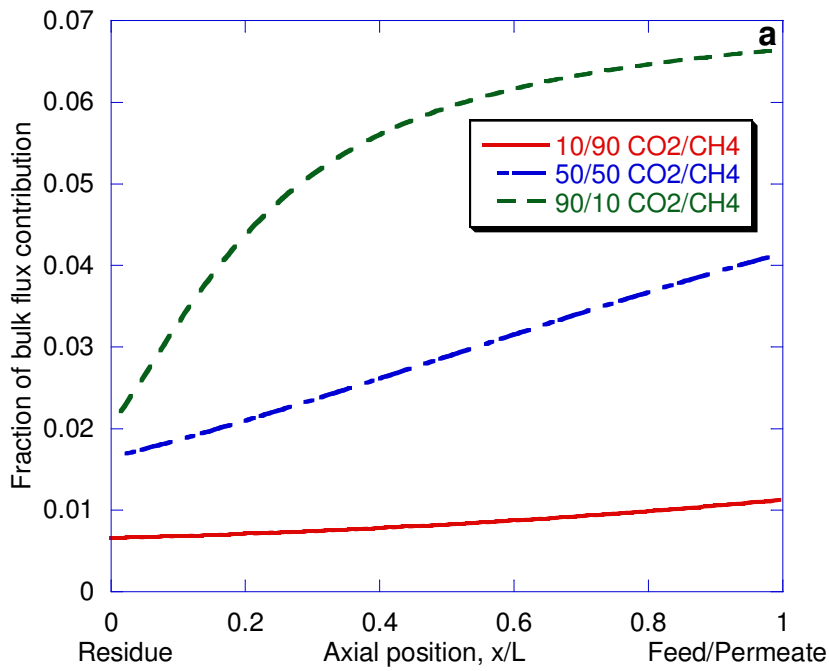
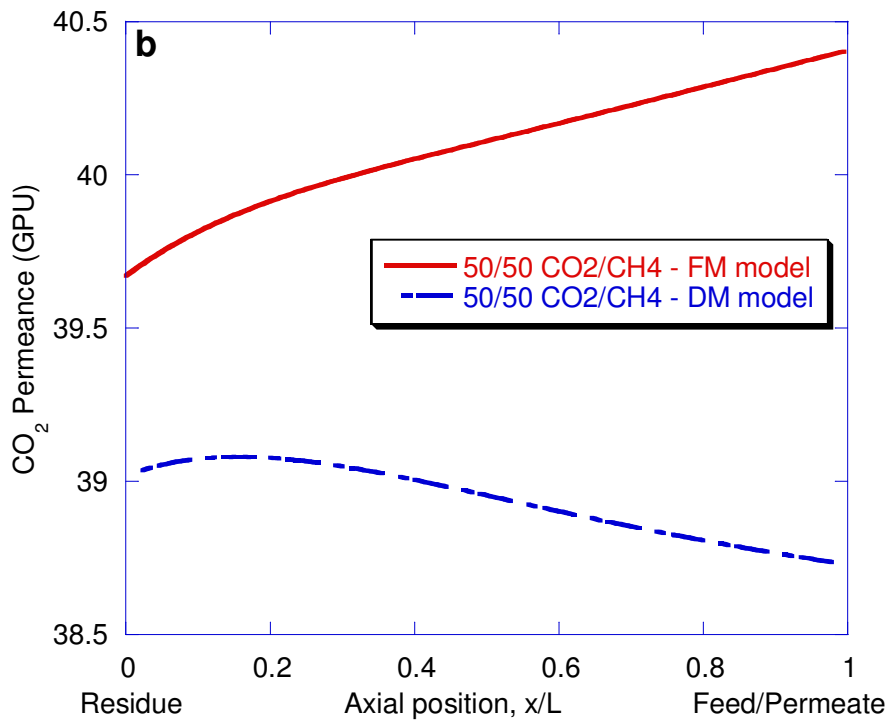
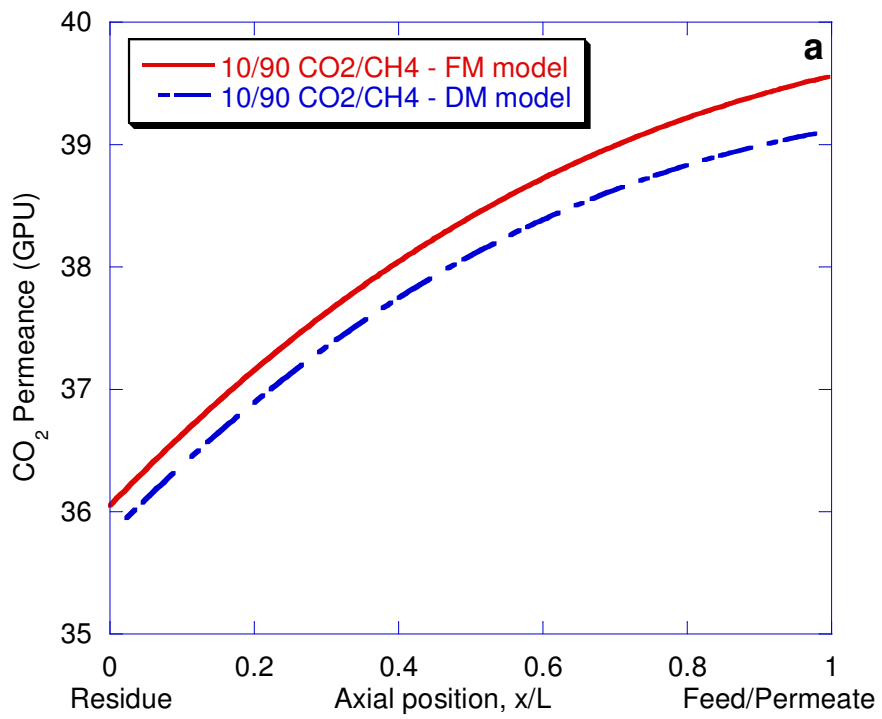


Figure A.3 Effect of CO₂ feed mole fraction on (a). CO₂ bulk flux contribution; (b). CH₄ bulk flux contribution.



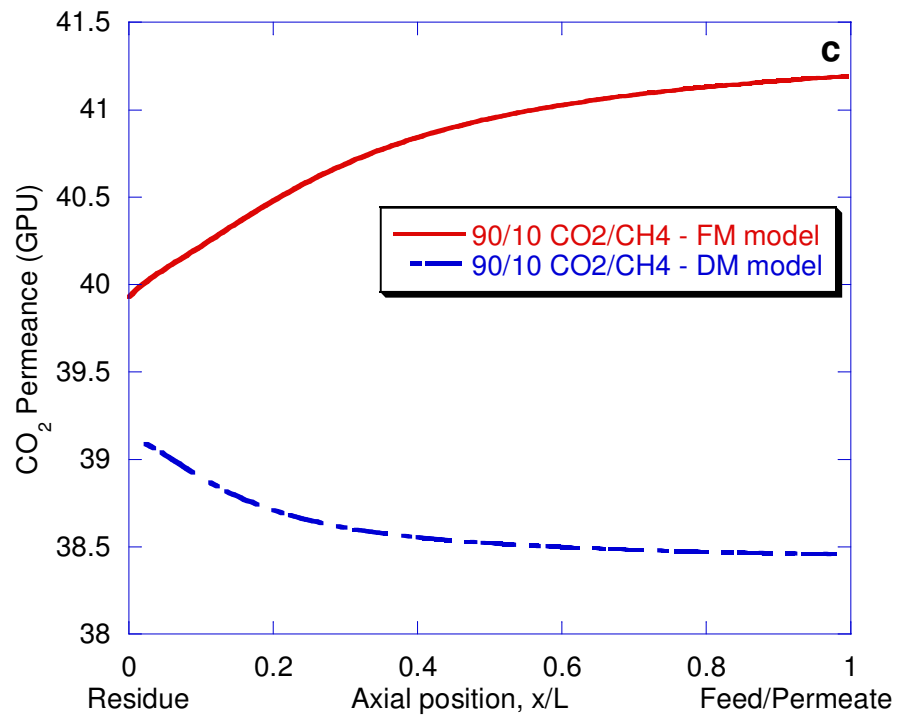
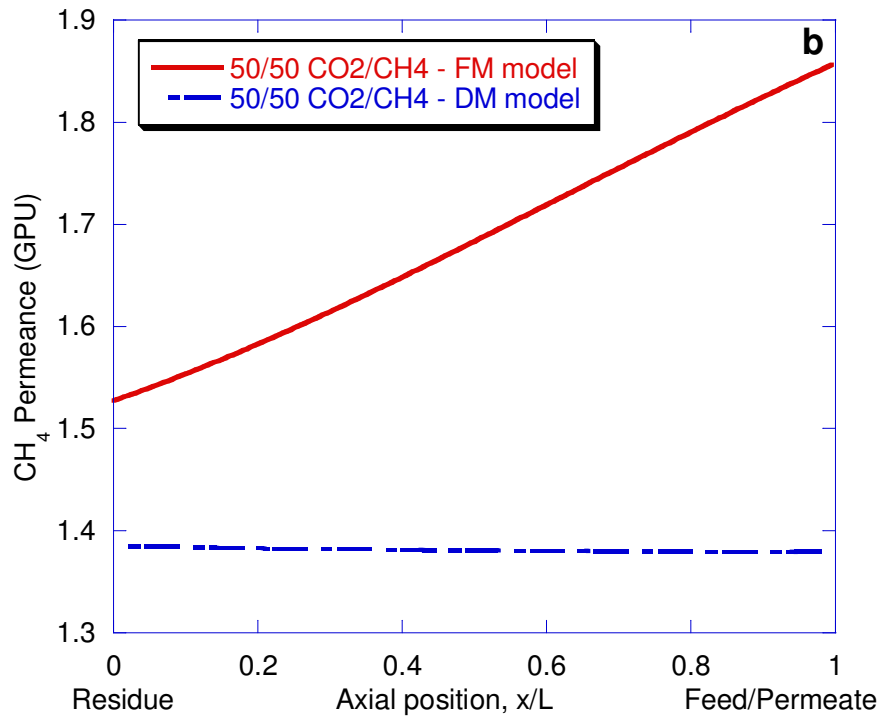
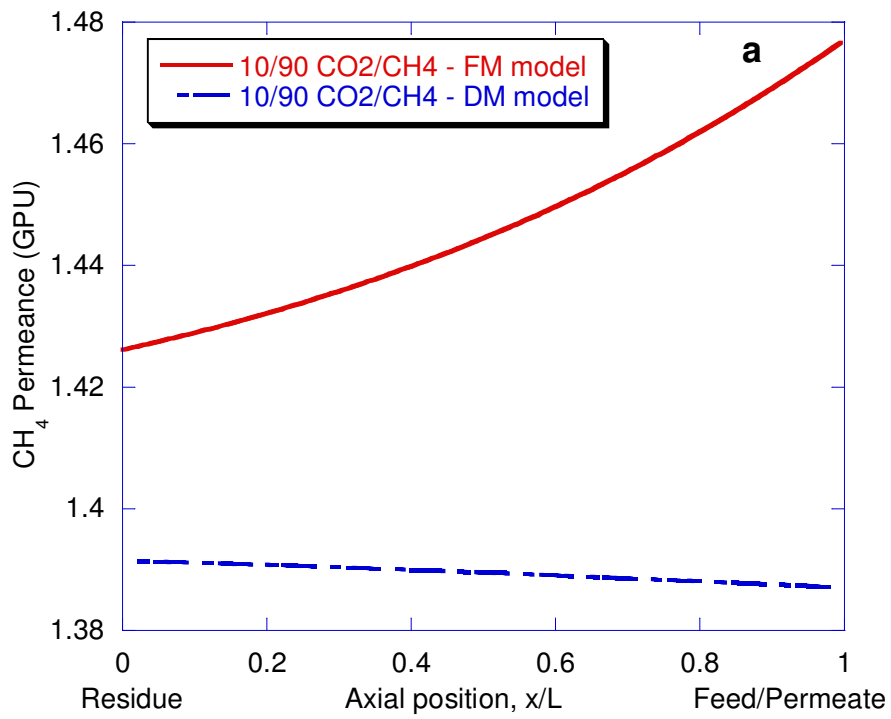


Figure A.4 Simulation of CO₂ permeance for (a) 10/90 CO₂/CH₄ feed (b) 50/50 CO₂/CH₄ feed (b) 90/10 CO₂/CH₄ feed as a function of axial position, considering the diffusion model (DM) and the frame of reference model (FM).



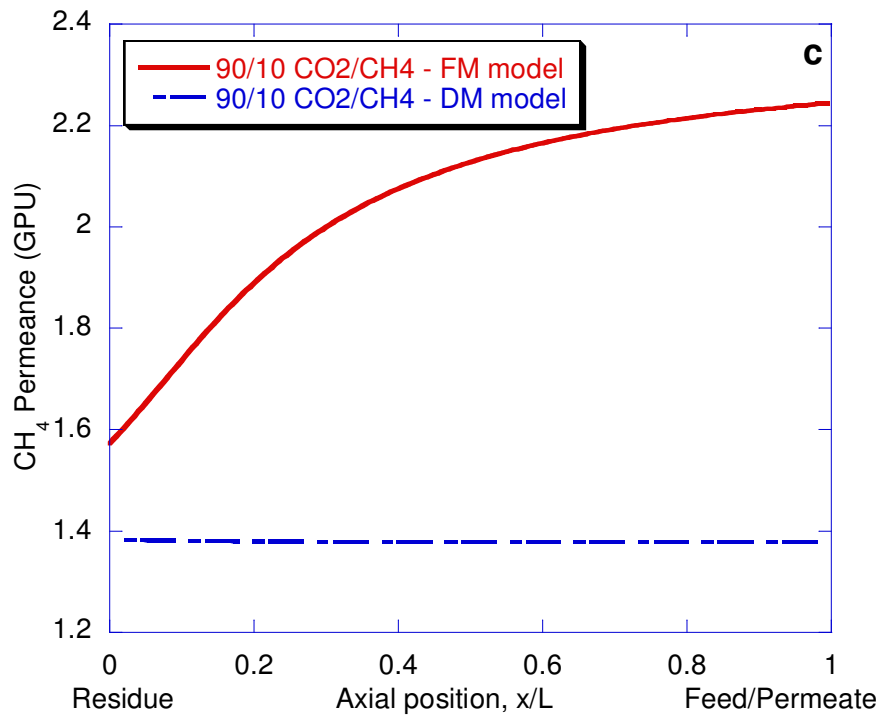


Figure A.5 Simulation of CH₄ permeance for (a) 10/90 CO₂/CH₄ feed (b) 50/50 CO₂/CH₄ feed (b) 90/10 CO₂/CH₄ feed as a function of axial position, considering the diffusion model (DM) and the frame of reference model (FM).

These observations are even more pronounced for high feed pressures, because, according to the dual-mode transport model, as discussed below, increasing the feed-side total pressure, increases the amount of sorption of penetrants, $\omega_{CO_2}^{avg}$ and $\omega_{CH_4}^{avg}$ in the membrane. Under these conditions, the diffusion model can overestimate selectivity up to 25%. The extent of the error depends on the fraction of the bulk flux contribution, the higher the bulk flux contribution the higher the inaccuracy. The bulk flux contribution effects become negligible at low CO₂ mole fractions as can be seen in (Figure. A.3) for the 10/90 CO₂/CH₄ gas mixtures case.

Following this line of reasoning, one would expect increasing membrane thickness, and decreasing membrane area, which causes the CO₂ mole fraction in

the feed side to increase thereby also increasing the bulk flux contribution of CO₂ and CH₄. But let us analyze first in more detail the effect of feed pressure on the bulk flux contribution of CO₂ and CH₄.

A.5 Effect of Feed Pressure

As the feed pressure increases, so does the ‘mobile’ sorption levels of CO₂ and CH₄, as can be seen from the dual-mode expression described by Eq. (A.16). This effect results in an increase in the bulk flux contribution of both components, $\Pi_{CO_2}^{bulk}$ and $\Pi_{CH_4}^{bulk}$. Figure A.6a and b shows the effect of increasing the total feed pressure for the 50/50 gas mixture on the total CO₂ and CH₄ concentration in the membrane, a classical dual mode response. The CH₄ concentration increases along the axial membrane length at a fixed total pressure because its partial pressure in the feed as well as the permeate sides of the membrane increases from the feed entry to the retentate exits the module. This increase results in an increase in the CH₄ total average concentration inside the membrane between the feed inlet and retentate exit. Nevertheless, the 100 psi feed pressure case shows little increase in $\omega_{CH_4}^{avg}$ along the membrane length, which can be explained in terms of the dual mode model. At low feed pressures, $\omega_{CH_4}^{avg}$ is comprised of both the Henry’s and Langmuir modes, which both have *opposite* effects on CH₄ sorption. At high feed pressures, $\omega_{CH_4}^{avg}$ is dominated by the Henry’s mode. This is why in Figure. A.6 for 500 psi and 1000 psi feed pressures, $\omega_{CH_4}^{avg}$ increases as the feed and permeate sides CH₄ partial pressure increases. On the other hand, $\omega_{CO_2}^{avg}$ concentration decreases along the membrane length from the feed side to the retentate side. In the case of 100 and 500 psi feed pressures, there was little dependence on pressure because of the competitive nature of sorption.

Similar results are also found for the 10/90, and the 90/10 CO₂/CH₄. Plasticization is assumed negligible as noted earlier because to the 6FDA-TADPO polypyrrolone has been shown to have a unique ability to resist CO₂ plasticization. Moreover, and also with CO₂ mixtures, less plasticization is observed because the CH₄ competes with the CO₂ for sorption sites as opposed to the pure CO₂ case. For cases where this assumption does not apply, even more complexity will need to be accommodated.

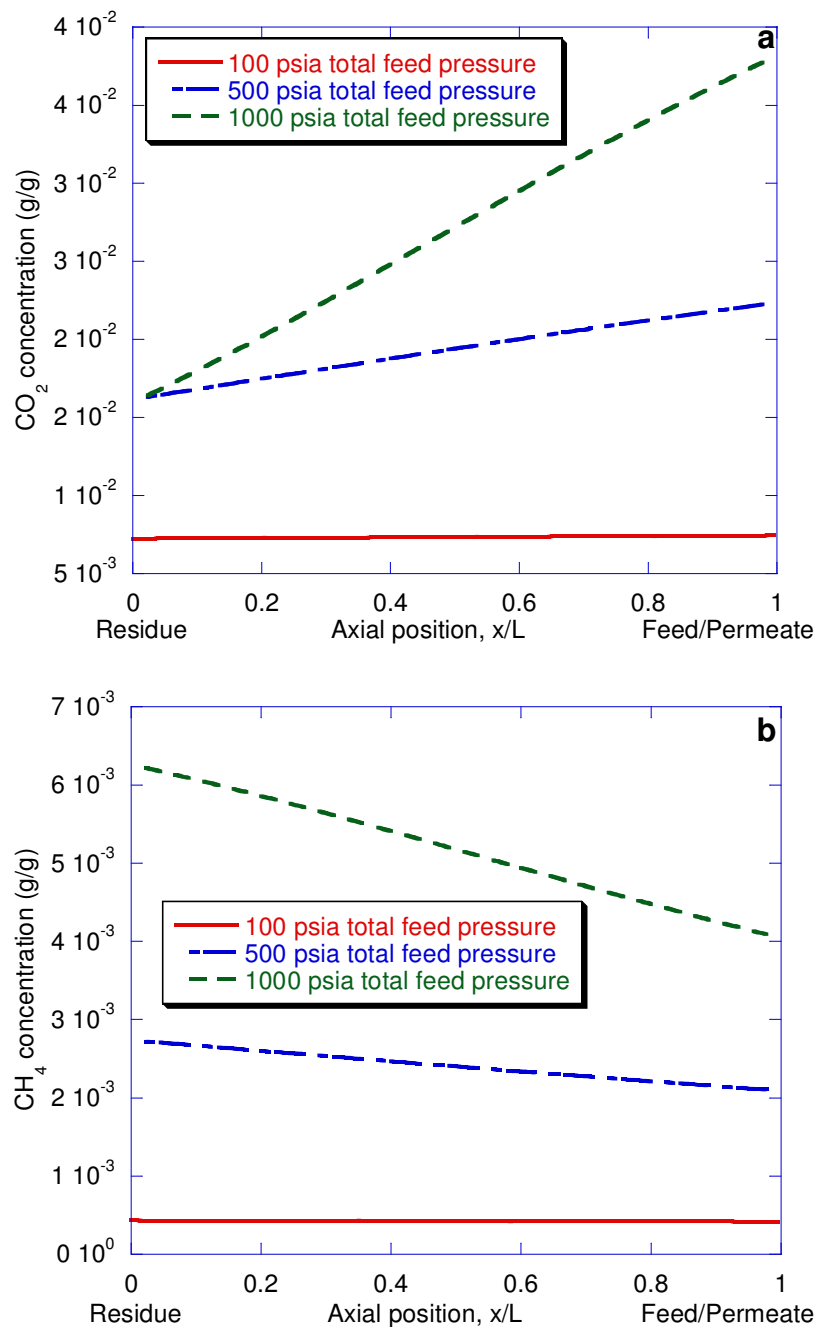
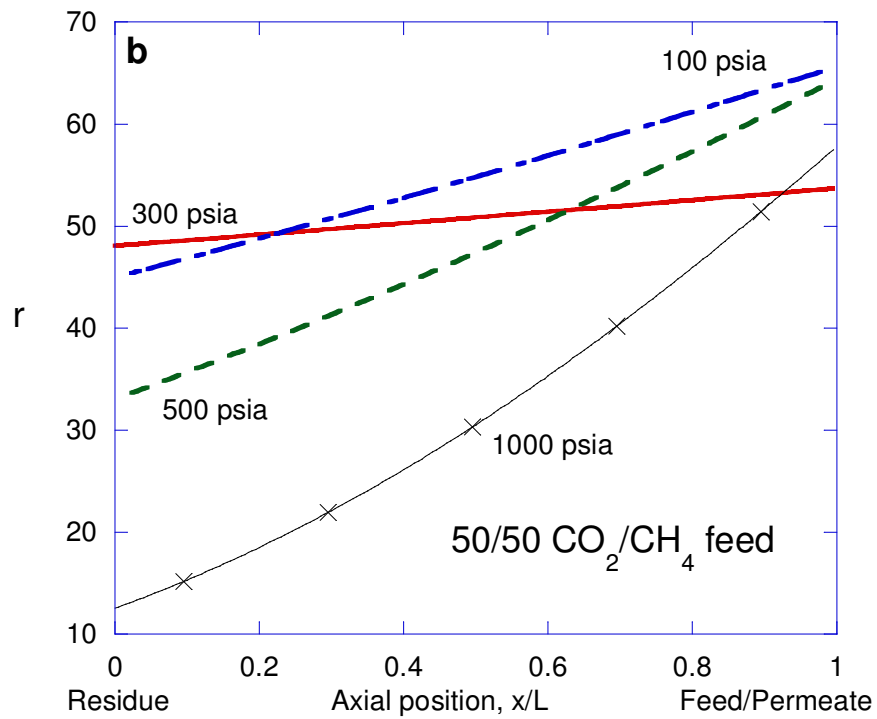
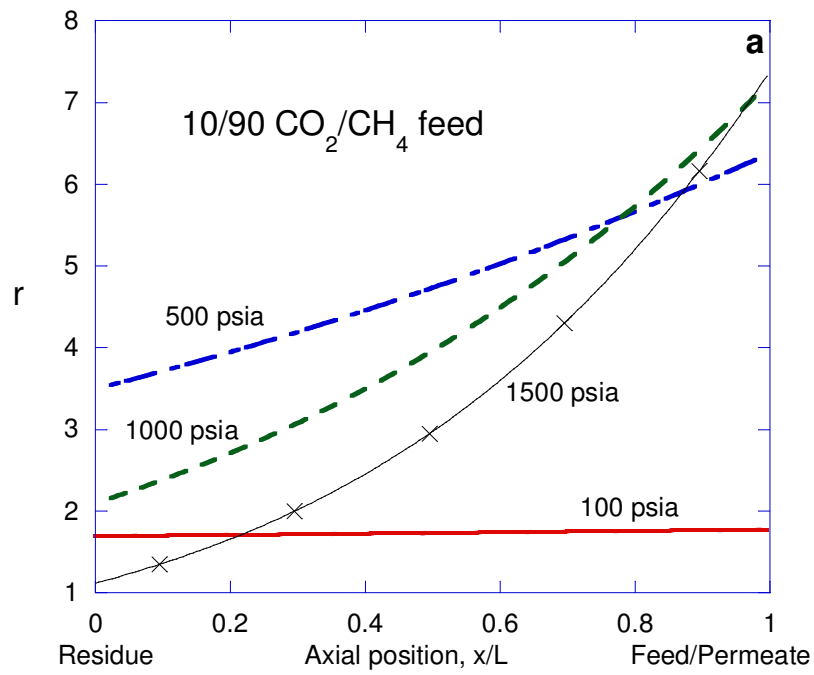


Figure A.6 Effect of total feed pressure on (a) average CO₂ concentration inside the membrane (b) average CH₄ concentration inside the membrane as a function of axial position, for 50/50 CO₂/CH₄ feed considering the frame of reference model (FM).

The effect of feed pressure on the r-value is not so straightforward. For low feed pressures, the r-value increases with pressure, a typical dual-mode response, but the opposite happens for high feed pressures (Figure. A.7). For the 10/90 gas mixture and at low feed pressures, the sorption in Langmuir sites in the permeate is greater than the sorption in the corresponding Langmuir sites in the feed side (depending on the permeate pressure) (Thundyil et al., 1999). Consequently, under this unusual case, the overall flux of the faster component will, according to the model, be lower than that contributed by the dissolved sites alone, and the permeability will be lower than $k_D D_D$. Increasing the total feed pressure, this negative gradient in the Langmuir sites is moderated by the increase in the CO₂ sorption levels in the dissolved mode on the feed side which explains why the r-value increases as the pressure goes from 100 psia to 500 psia. On the other hand, at still higher feed pressure (1000 psia) the r-value decreases.



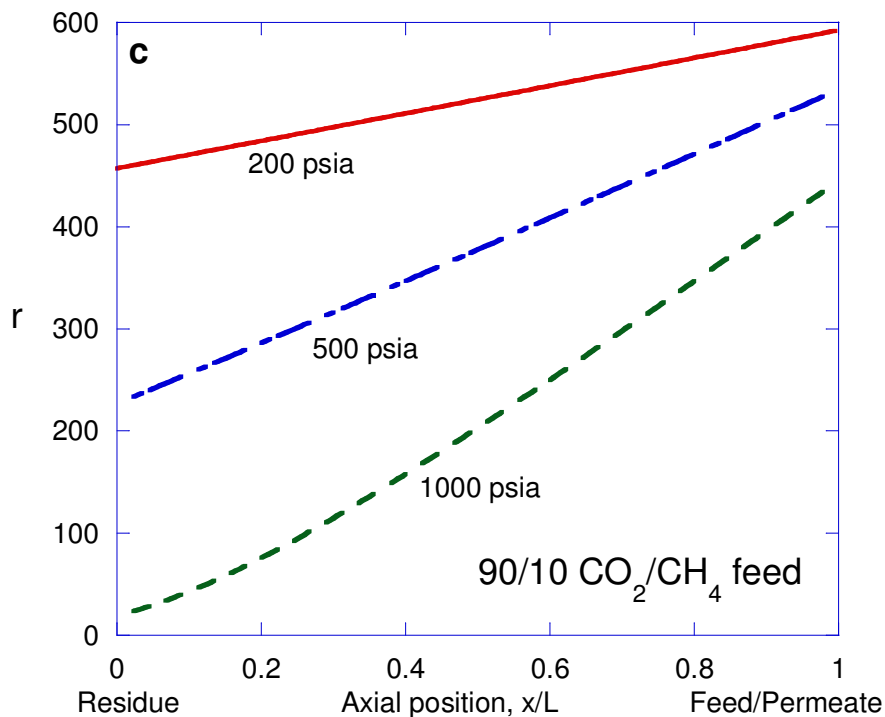


Figure A.7 Simulation of average ‘ r ’, the mass flux ratio of CO_2 to CH_4 in the membrane for (a) 10/90 CO_2/CH_4 feed (b) 50/50 CO_2/CH_4 feed (b) 90/10 CO_2/CH_4 feed as a function of axial position, considering the frame of reference model (FM).

These complex effects mean that there will be a negligible gradient for transport through the Langmuir sites and transport will be nearly governed by the dissolved mode. Therefore, for high CO_2 feed partial pressures, increasing pressure from 1000 psia to 1500 psia decreases the r -value.

This case never happens for pure gases because there is no competitive sorption, and consequently the CO_2 sorption levels on the feed side will always be greater than on the permeate side. This situation also does not happen for CH_4 because the permeate is leaner in CH_4 than the feed. In the case where there is vacuum in the permeate this case also does not happen even though the permeate is richer in CO_2 since the membrane surface in the permeate is maintained at all positions at zero pressure, the CO_2 and CH_4 sorption levels on the permeate side

will always be zero. Increasing the CO₂ concentration in the feed to 50% and 90% will increase the Langmuir sorption on the feed side relative to the sorption on the permeate side, thereby making the Langmuir gradient less negative than the 10/90 case. As a result the r-value for the 50/50 mixture decreases at lower feed pressure values as compared to the 10/90 case as can be seen in Figure A.7b. For the 90/10 CO₂/CH₄, the feed is close to the pure component and the Langmuir concentration need not be greater on the permeate side than on the feed side, as is the case when the feed stream is only 50% CO₂ or less. This is why in (Figure. A.7(c)), the r-value decreases as the feed pressure increases, a typical dual-mode response.

Clearly, the sorption level, the r-value and the bulk flux contribution are coupled. As noted before, $\omega_{CO_2}^{avg}$ and $\omega_{CH_4}^{avg}$ increases with the increase in the feed pressure as shown in (Figure. 4.8). However, the effect of feed pressure on the r-value is complicated since competitive sorption determines the sorbed concentrations on the feed and permeates side of the membrane (depending on the permeate pressure). At low CO₂ feed partial pressures, increasing the feed pressure increases the r-value, and therefore, the bulk flux contribution of both components as can be seen from Eq.8. On the other hand, high CO₂ feed partial pressures causes decreases in the r-value and in this case the $\Pi_{CH_4}^{bulk}$ can reach plateau as shown in (Figure. A.8) for the 90/10 case. One conclusion can be taken from this analysis; the bulk flux contribution is more significant for higher permeate pressures (and higher intrinsic selectivity polymers), since this implies higher negative gradients in the Langmuir mode, and therefore, higher r-values as feed pressure increases.

A.6 Effect of Membrane Thickness and Area

The bulk flux contribution of the 50/50 gas mixture was analyzed by plotting the required membrane area against the bulk flux contribution of CO₂ and CH₄. Membrane area can be increased by either increasing the fiber length or diameter. Simulations were performed here by increasing the fiber lengths. Simulations were not performed with increasing fiber diameters, because no effect would be observed, given the assumptions of the model. The active length of the fibers is varied between 10-250 cm. Clearly increasing the membrane area decreases $\Pi_{CO_2}^{bulk}$ and $\Pi_{CH_4}^{bulk}$ as can be seen in Figure A.9. The increase in the membrane area decreases the CO₂ mole fraction in the feed side, and therefore leads to lower $\Pi_{CO_2}^{bulk}$ and $\Pi_{CH_4}^{bulk}$.

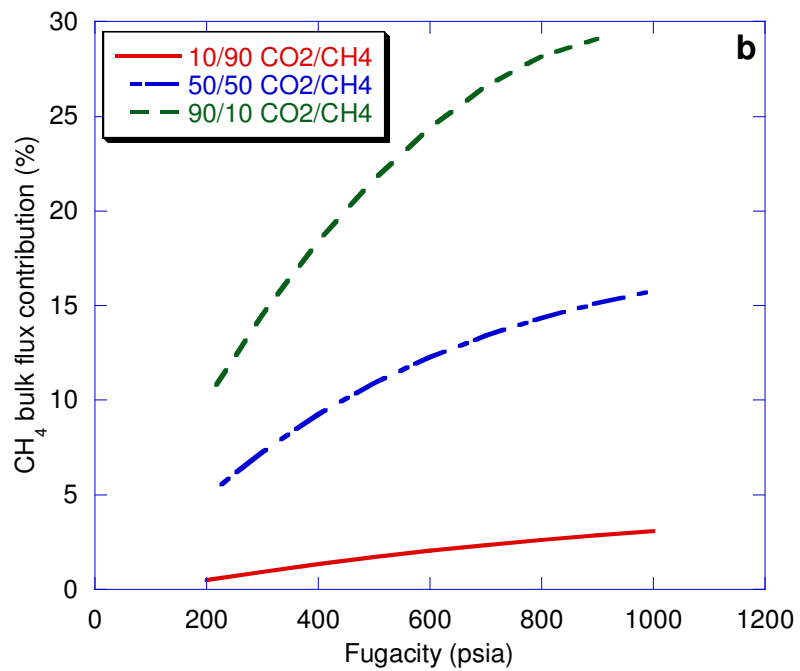
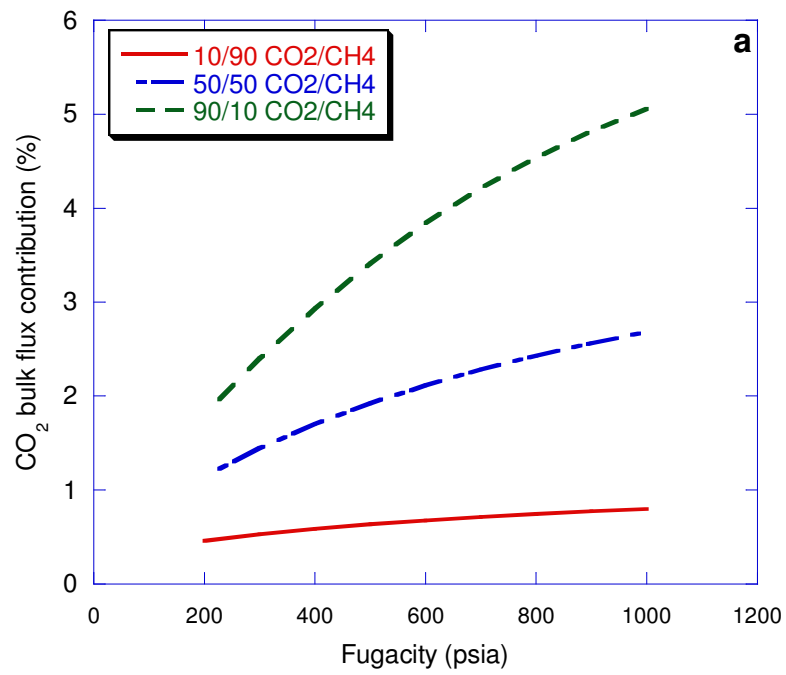


Figure A.8 Bulk flux contribution of (a) CO₂ (b) CH₄ in 10/90 CO₂/CH₄, 50/50 CO₂/CH₄ and 90/10 CO₂/CH₄ feed as a function of total feed pressure.

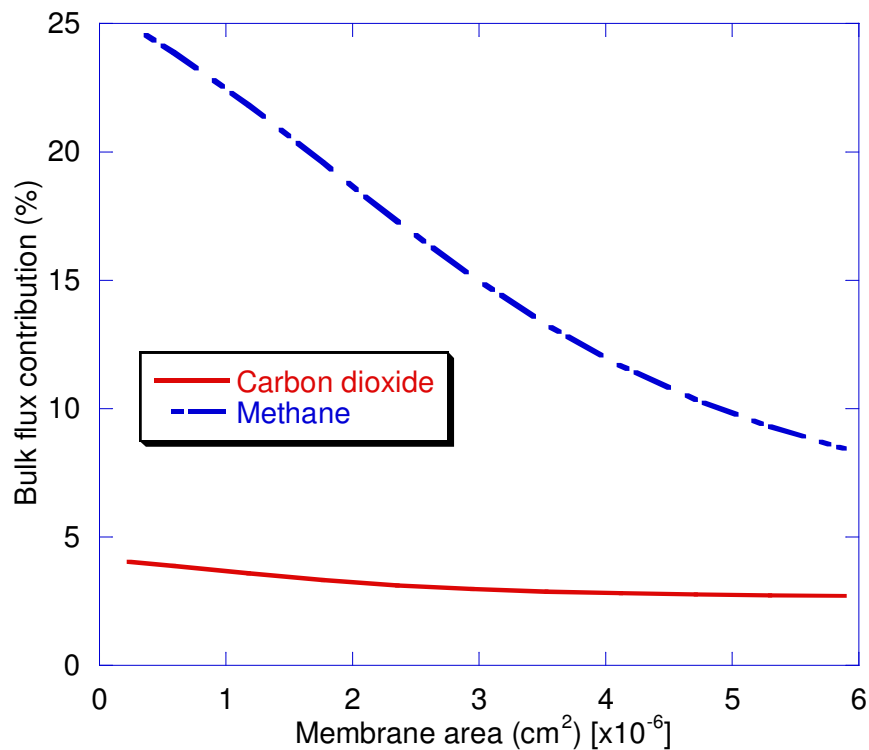


Figure A.9 Effect of membrane area on bulk flux contribution of CO₂ and CH₄ in 50/50 CO₂/CH₄ feed.

This means that nearly all of the faster gas permeates in the first stages of the membrane and, in these conditions, the faster gas mole fraction is relatively small for the rest of the membrane length. In a counter current arrangement, this means that the bulk flux contribution is only higher in a small fraction of its length, located at the very end. As a net result, the bulk flux contribution of CO₂ and CH₄ decreases with the increase of membrane area. On the other hand, low membrane area lead to high CO₂ mole fraction in the feed side and therefore, high $\Pi_{CO_2}^{bulk}$ and $\Pi_{CH_4}^{bulk}$ (Figure. A.10). This suggests that in the limit of a single stage, the bulk flux contribution of CO₂ and CH₄ is expected to reach a maximum.

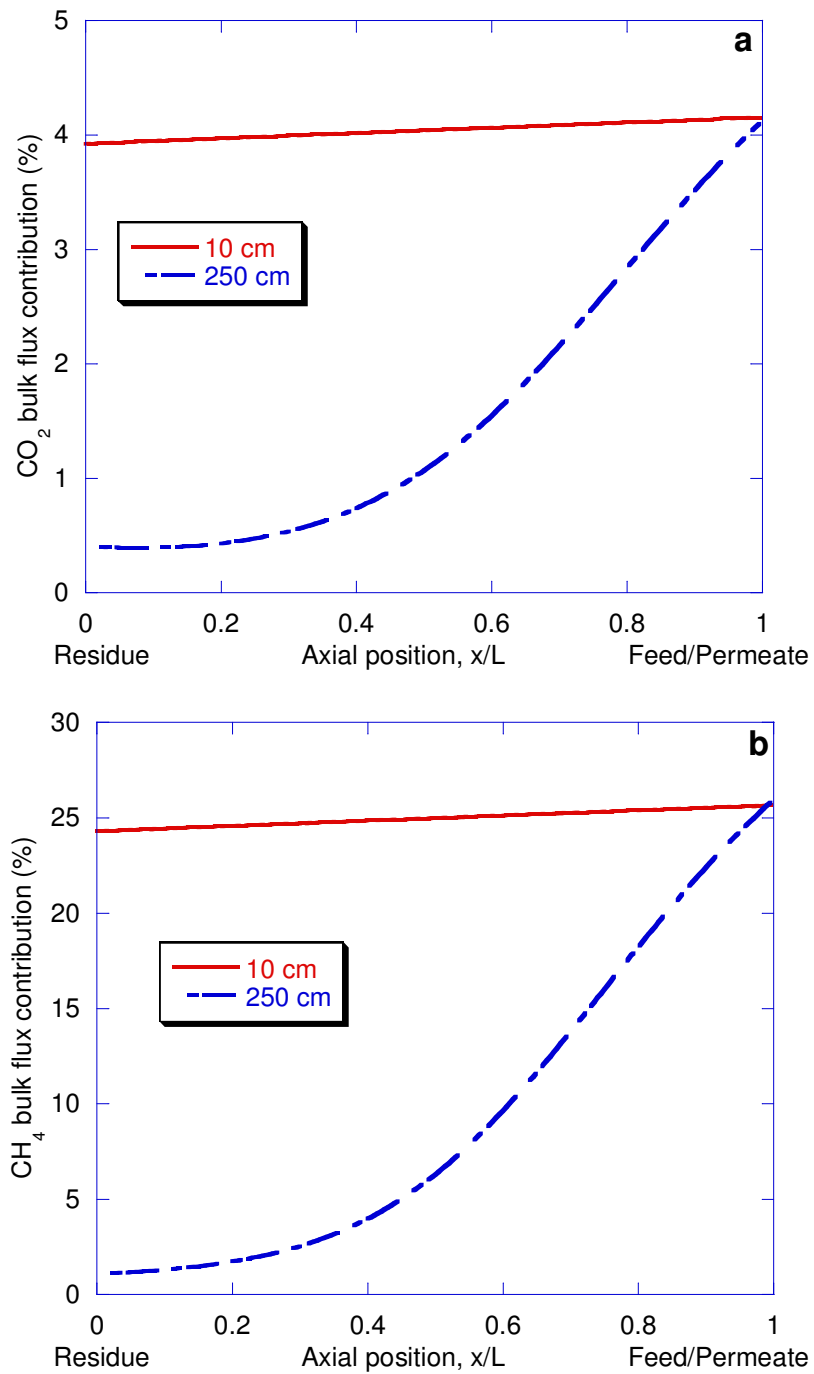


Figure A.10 Effect of membrane area on bulk flux contribution of CO_2 and CH_4 in 50/50 CO_2/CH_4 feed as a function of axial position.

This theoretical limit is consistent with observations from Kamaruddin and Koros (1997) for lab film experiments.

One should also notice that increasing the membrane thickness (Figure. A.11) has the same effect as increasing the membrane area, since a given recovery of CO₂ into the product is specified. The justification is analogous for these two cases. Figure A.12a shows the effect of increasing the membrane thickness on the bulk flux contribution of CO₂ and CH₄. Figure A.12b shows the bulk flux contribution profile of CO₂ and CH₄ along the membrane length for 0.1 μm and 1.0 μm thickness.

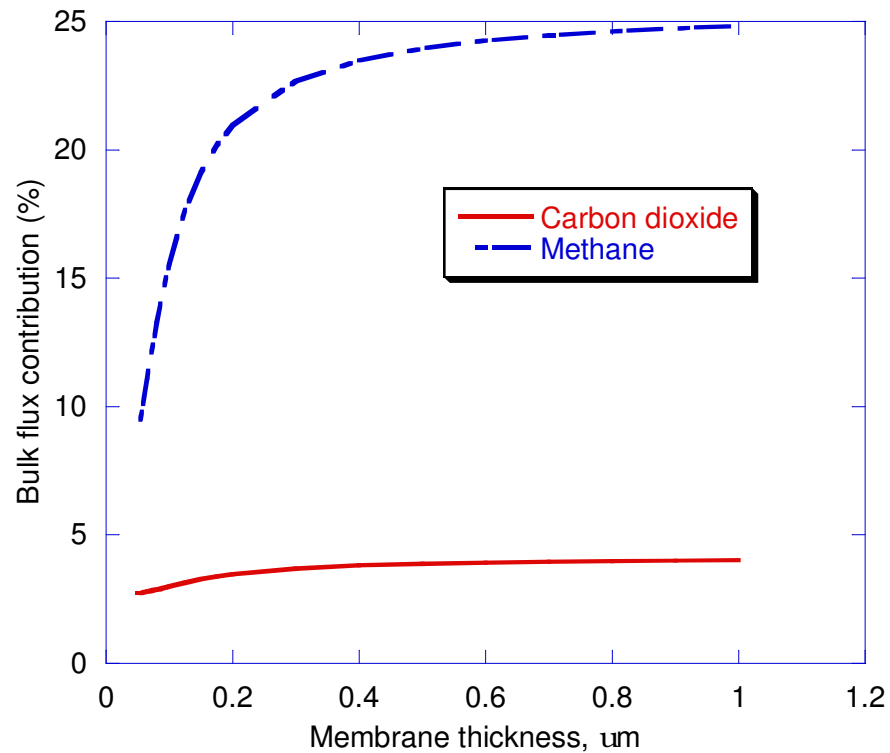


Figure A.11 Effect of membrane thickness on bulk flux contribution of CO₂ and CH₄ in 50/50 CO₂/CH₄ feed.

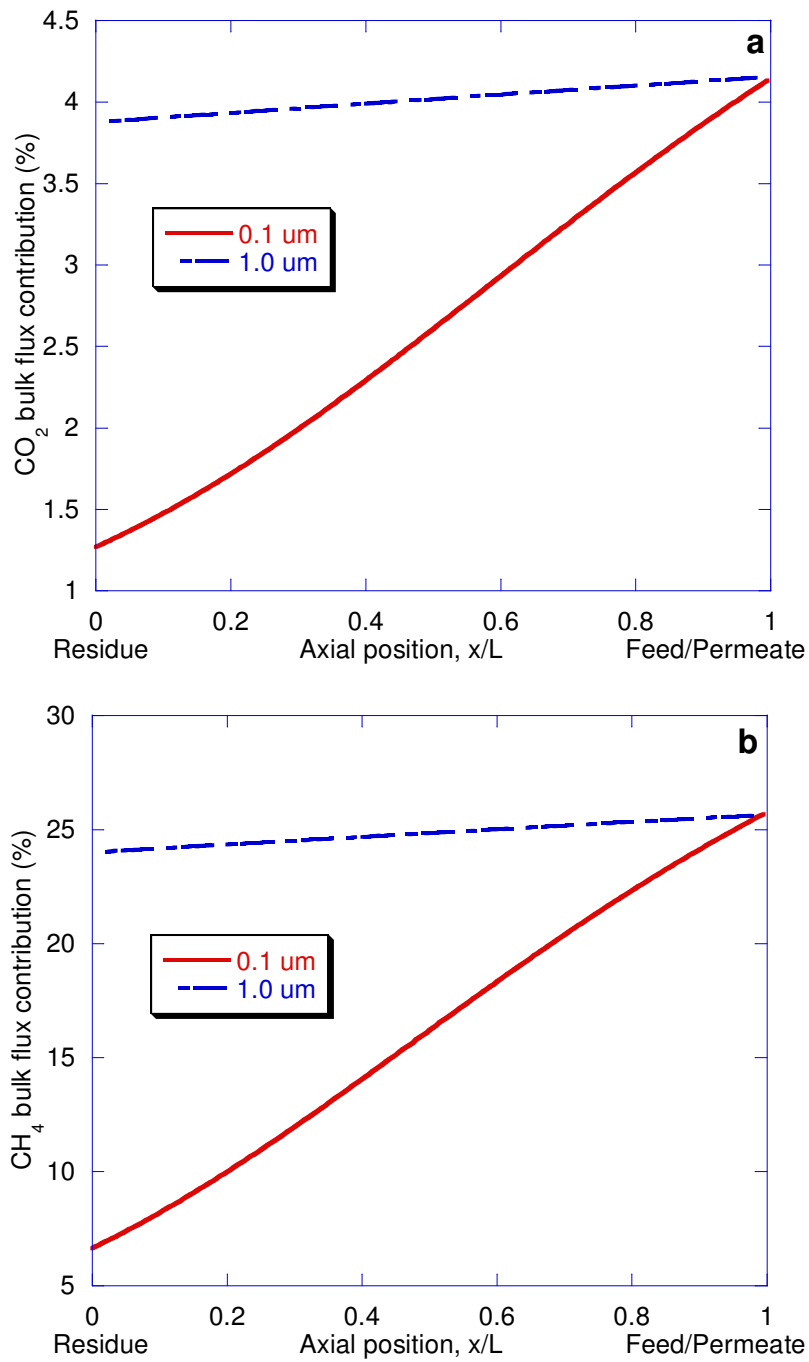
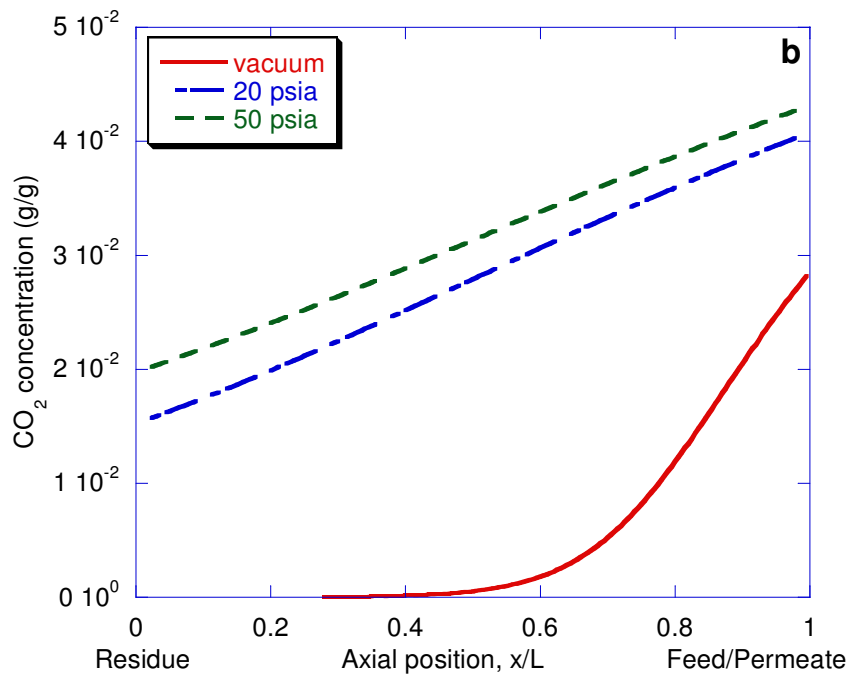
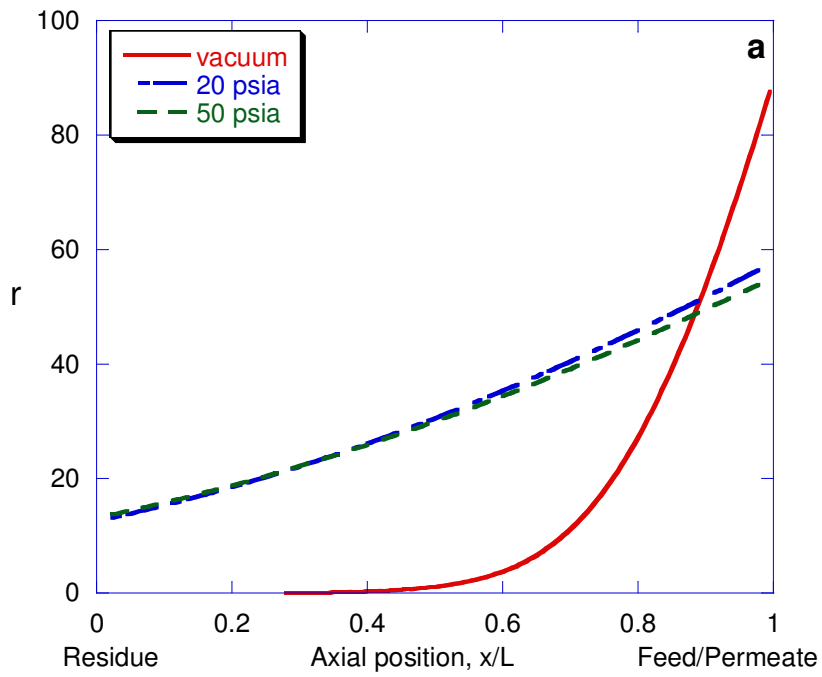


Figure A.12 Effect of of membrane thickness on bulk flux contribution of CO₂ and CH₄ in 50/50 CO₂/CH₄ feed as a function of axial position.

A.7 Effect of Permeate Pressure

Increasing the permeate pressure for the 50/50 CO₂/ CH₄ gas mixture causes the CO₂ concentration inside the membrane to increase and the CH₄ concentration to decrease (due to the higher average CO₂ mole fraction on the feed side of the membrane). Figure A.13b and c show the average mass concentration in the membrane for vacuum pressure, 20 psia and 50 psia permeate pressure along the membrane length. In the case of zero permeate pressure the flow is perpendicular to the membrane surface, cross flow type configuration and the cross flow model was used to simulate the flow pattern. As can be seen in Figure A.13b and c, the CO₂ concentration is decreasing and the CH₄ is increasing since CO₂ is permeating along the membrane length.

Increased permeate pressure reduces CO₂ permeation by decreasing its driving force across the membrane. This can be clearly seen at the permeate exit where the CO₂ permeate partial pressure is at its maximum. The CH₄ permeation flux is also affected, but not as much. Therefore, increasing permeate pressure increases the r-value. Figure A.13a shows how ‘r’, the mass flux ratio of CO₂ to CH₄, decreases from the feed/permeate end to the residue end. The effect of the permeate pressure, is clearly seen in Figure. A.13a: ‘r’ increases with the decrease of permeate pressure especially at the feed end. However, this tendency becomes small along the membrane length, due to the decrease in CO₂ permeate pressure for the three cases considered.



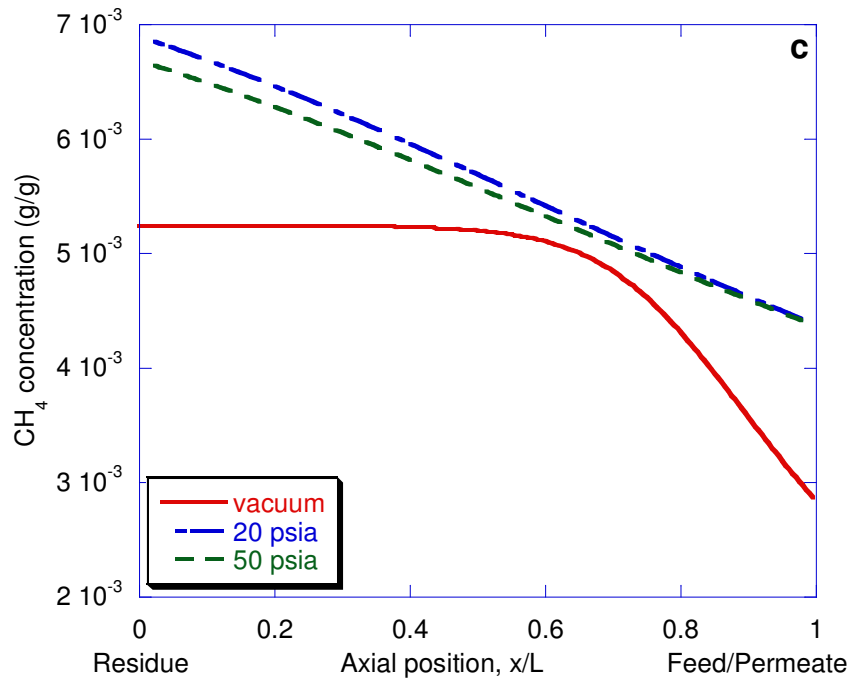


Figure A.13 Effect of permeate pressure on (a). ‘ \bar{r} ’; (b). CO_2 average concentration inside the membrane; (c). CH_4 average concentration inside the membrane in 50/50 CO_2/CH_4 feed.

As a result, the two curves for 20 psia and 50 psia overlap at the residue end as shown in Figure A.13a; however, the vacuum pressure curve crosses the other two curves because of its high CO_2 removal. This example shows that the crossflow operation at vacuum pressure outperforms the countercurrent configuration at 20 psia and 50 psia. As a net result, $\Pi_{\text{CO}_2}^{\text{bulk}}$ increases and $\Pi_{\text{CH}_4}^{\text{bulk}}$ decreases with the increase of pressure in the permeate side as shown in Figure A.14. The crossflow model shows the smallest effect of bulk flux contribution of CO_2 and CH_4 , which is 2% and 5% respectively.

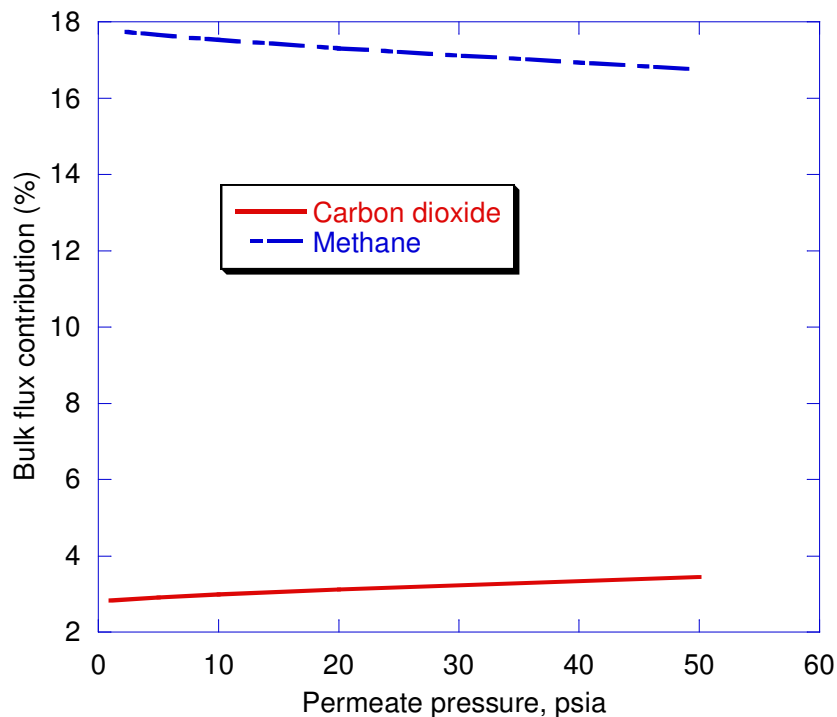
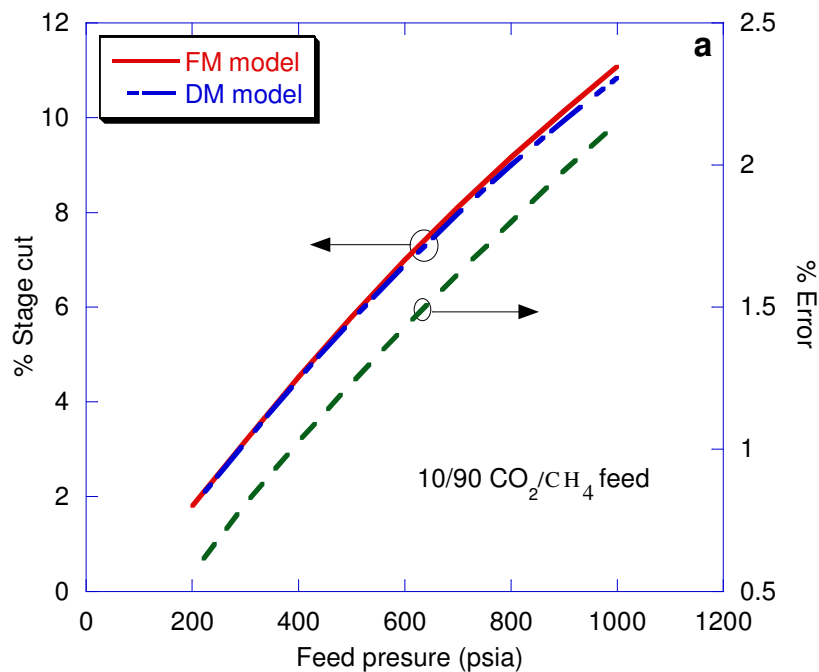


Figure A.14 Effect of permeate pressure on bulk flux contribution of CO₂ and CH₄ in 50/50 CO₂/CH₄ feed in a hollow-fiber module, operating in countercurrent.

A.8 Diffusion and Frame of Reference Models Comparisons

Let us consider the 10/90, 50/50 and 90/10 CO₂/CH₄ gas mixtures (typically shell side feed systems) based on the same gas separation as described before (Table. A.2). For the 10/90 CO₂/CH₄, bulk flux contribution of CO₂ and CH₄ was found to be negligible. Methane recovery, and percent stage cut are represented in Fig. A.15 and A.16 for the two permeation models, where a permeate pressure of 20 psia is considered, for three different concentrations. Some conclusions can be taken from Figure. A.15 and A.16, apart from whatever permeation model is used. The effect of feed pressure, is clearly seen: increasing the feed pressure increases the CO₂ and CH₄ permeation flux due to higher CO₂ and CH₄ driving across the membrane. Therefore, increasing feed pressure at fixed permeate pressure decreases methane recovery and increases percent stage cut.

The effect of not considering the frame of reference transport model is also illustrated in Figure. A.12 and Figure. A.13. Recovery is overestimated by the diffusion model by up to 7% and percent stage cut is underestimated by up to 6%. As already referred, the diffusion permeability model underestimates permeation fluxes. This difference is more significant for high CO₂ partial pressures, due to the higher bulk flux contribution of CO₂ and CH₄. Figure A.17a shows the separation factor plotted against the feed pressure for three different permeate pressures. In the case of the 10/90 CO₂/CH₄ mixtures neglecting the bulk flux contribution is a good approximation because CO₂ is present in small concentration.



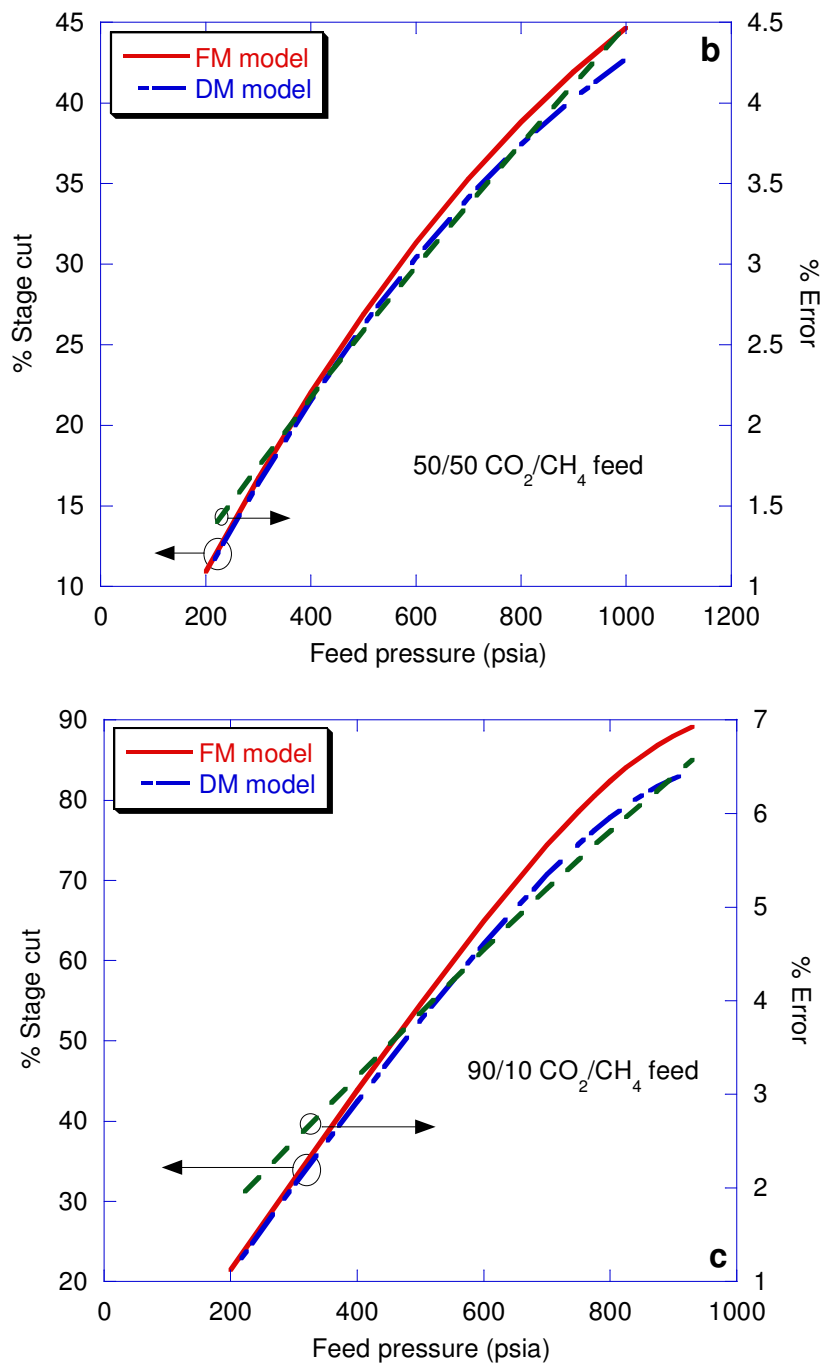


Figure A.15 Percent stage cut and percent error ($[\% \text{ stage cut}_{\text{FM}} - \% \text{ stage cut}_{\text{DM}}] / [\% \text{ stage cut}_{\text{DM}}] \times 100\%$) as a function of feed pressure for (a). 10/90 CO₂/CH₄ feed; (b). 50/50 CO₂/CH₄ feed; (c). 90/10 CO₂/CH₄ feed considering the frame of reference model (FM) and the diffusion model (DM).

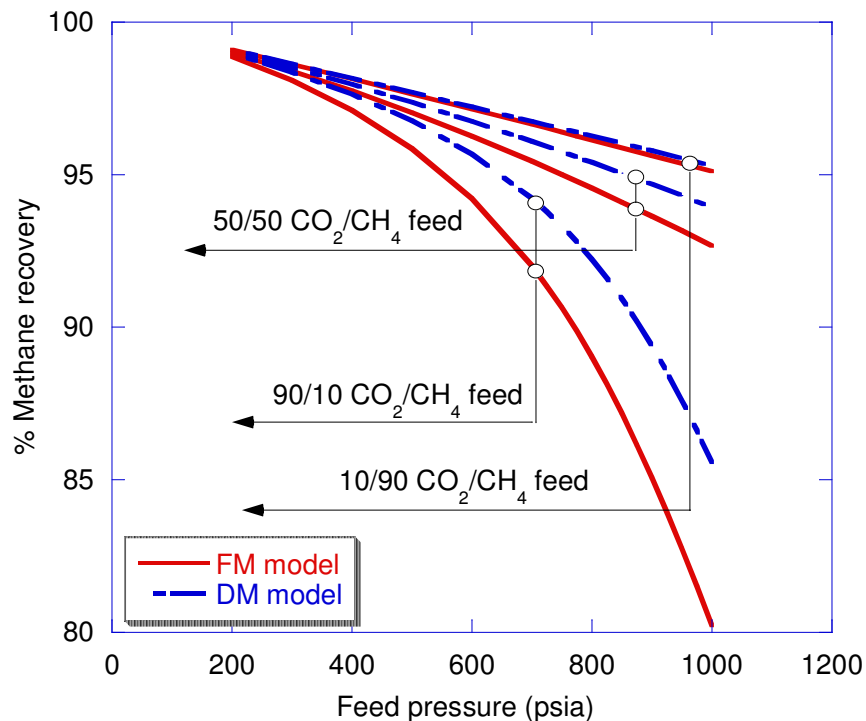


Figure A.16 Simulation of CH₄ recovery as a function of feed pressure, in a hollow-fiber module, operating in countercurrent, considering the frame of reference model (FM) and the diffusion model (DM) for 10/90 CO₂/CH₄ feed; 50/50 CO₂/CH₄ feed; and. 90/10 CO₂/CH₄ feed.

As the CO₂ concentration increases, the contribution of bulk flux contribution of both components increases and this increases the difference between the two models prediction as can be seen for the 50/50 CO₂/CH₄ case in Figure A.17b. Ignoring the bulk flux contribution could lead to incorrect results about the membrane performance. The difference also increases as the pressure increases, because of the increase in the bulk contribution of CO₂ and CH₄ as noted earlier. Under these conditions, the diffusion permeability model can overestimate selectivity up to 25% -- a rather serious error.

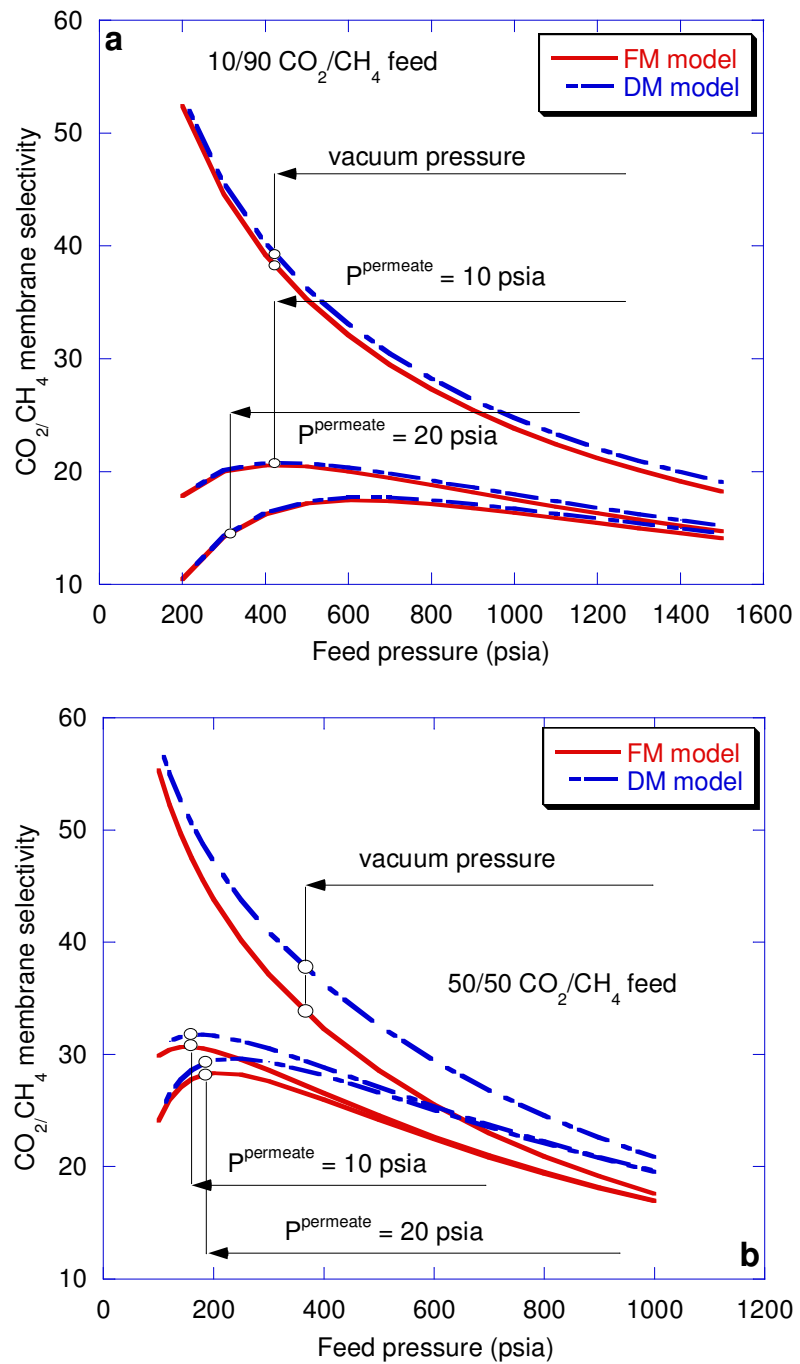


Figure A.17 Simulation of CO₂/CH₄ selectivity as a function of feed pressure for different permeate pressures, in a hollow-fiber module, operating in countercurrent, considering the frame of reference model (FM) and the diffusion model (DM) for (a). 10/90 CO₂/CH₄ feed; and (b). 50/50 CO₂/CH₄ feed.

Under a vacuum permeate, the selectivity isotherms, for material exhibiting dual mode behavior would show a uniform decreasing trend with total feed pressure as seen in Figure. A.17a and Figure. A.17b. In the case of non-zero permeate pressure, there is predicted to be a trade -off between the effects of competition and the effect of permeate pressure on the Langmuir concentration on the permeate side. At low feed pressures, the depression in separation factor caused by the permeate pressure will dominate. It is clear that permeate pressure is predicted to have the effect of reducing the selectivity of the membrane significantly. This observation has been demonstrated both experimentally and theoretically by Thundyil et al (1999).

In terms of system design the most important parameters to consider are the compression power requirements for the downstream gas, the membrane selectivity, and methane recovery in order to achieve optimal separation of the CO₂ and CH₄ gases in the natural gas mixture. Unsuccessful membrane modeling and simulation can lead to erroneous information for the design, optimization and economics of the overall separation process; thereby undermining project success. The frame of reference model is fundamentally more correct than the simple diffusion model and, therefore, should be used in all membrane design calculations. Adding effects of plasticization, while not important for this particular membrane material is expected to be necessary for cellulose acetate and some polyimides at high CO₂ feed pressures.

A.9 Conclusions

When modeling hollow-fiber membrane modules, it is common to neglect the bulk term in the transport equations. This work shows that this simplification may imply incorrect estimation of the membrane modules performance. In comparison to the frame of reference model formulation, the diffusion model overestimates CH₄ recovery, membrane selectivity and underestimates cut-

fraction. This is particularly critical for systems with high CO₂ partial pressure in the feed-side. Differences of up to 35% have been found for the present case. The simple diffusion based model was shown to overpredict membrane selectivity as high as 25% for the 90/10 CO₂/CH₄ mixture at 1000 psia feed pressure. The CH₄ recovery was also overpredicted up to 7% by the diffusion model and stage cut was also underpredicted up to 7% by the diffusion model. This is very important from the design point of view. These additional permeation fluxes resulting from the bulk motion must be taken into account when sizing the downstream compressor. The lack of proper sizing may result in premature compressor failures

The frame of reference model FM is fundamentally more correct than the diffusion model DM and therefore, it should be used in all the modeling efforts of hollow fiber membranes. Natural gas not only contains CO₂ and CH₄ but also contains significant quantities of other fast species such as H₂S and H₂O that could contribute significantly to the total bulk contribution. This study was conducted for the binary system CO₂ and CH₄ but it can be extended for multicomponent mixtures as shown earlier on the model development section. The bulk flux contribution was shown to increase as the membrane thickness increases and membrane area decreases, due to the higher CO₂ mole fraction on the feed side of the membrane. Increasing the permeate pressure also serves to increase the CO₂ concentration on the feed side of the membrane, and therefore the bulk flux contribution of CO₂ and CH₄. In the case of a single stage, the bulk flux contribution of CO₂ and CH₄ is expected to reach a maximum. This situation in fact applies in most laboratory characterization of membrane properties with mixed gases.

Appendix B: Program Documentation

B.1 Countercurrent-flow Membrane Program

```
% Code simulates COUNTERCURRENT, MULTI-COMPONENT gas
separation
% in a hollow-fiber membrane module

global Q k NC FeedPr PermPr F P FeedFl PermFl rjacob
fvalue delP

N=200;
NC=2;

kD=[0.02*76/14.7 0.006*76/14.7];
b=[0.01*76/14.7 0.001*76/14.7];
CH=[30. 20.];
DD=[2.27*1e-8 2.75*1e-9];
FF=[0.1 0.03];

K(1)=CH(1)*b(1)/kD(1);
K(2)=CH(2)*b(2)/kD(2);
%%%%%%%%%%%%%%%%%%%%%%%%%%%%%%%%%%%%%%%%%%%%%%%%%%%%%%%%%%%%%%%%%%%%%%%%%%
%%%%%%%%%%%%%%%%%%%%%%%%%%%%%%%%%%%%%%%%%%%%%%%%%%%%%%%%%%%%%%%%%%%%%%%%%%
% Pressures : psia
for i=1:N+2,
    FeedPr(i) = 200.;
    PermPr(i) = 20;
end

%%%Temperatures : Kelvin
T = 308.0;

% Flow rates : cc-STP/sec (SCFH*7.43)
for i=1:N+2,
    TotFeed(i)=0.0;
    TotPerm(i)=0.0;
end

TotFeed(N+2) = 50000.0*7.43;
```

```

% Feed Composition : mole fraction and flow rate
F(N+2,1) = 0.50;
F(N+2,2) = 0.50;
FeedFl(N+2,1) = F(N+2,1)*TotFeed(N+2);
FeedFl(N+2,2) = F(N+2,2)*TotFeed(N+2);
% input shell-side(1) or bore-side feed(2)
nval = 1;
%%%%%%%%%%%%%%%%%%%%%%%%%%%%%%%%%%%%%%%%%%%%%%%%%%%%%%%%%%%%%%%%%%%%%%%%
%%%%%%%%%%%%%%%%%%%%%%%%%%%%%%%%%%%%%%%%%%%%%%%%%%%%%%%%%%%%%%%%%%%%%%%%
% FIBER DATA
DENS=1.405;
Nfibers = 300000;
t=0.5*1d-4;
% Fiber dimensions : centimeters (microns*1e-4)
DO = 250.0*1D-4;
DI = 125.0*1D-4;
%Active fiber length : centimeters
ActiveL = 100.0;
dz = ActiveL/N;
% Mass transfer area per stage
delAk = 2*pi*DO/2*ActiveL*Nfibers/N;
%%%%%%%%%%%%%%%%%%%%%%%%%%%%%%%%%%%%%%%%%%%%%%%%%%%%%%%%%%%%%%%%%%%%%%%%
%%%%%%%%%%%%%%%%%%%%%%%%%%%%%%%%%%%%%%%%%%%%%%%%%%%%%%%%%%%%%%%%%%%%%%%%
% COMPONENT DATA
% Molecular weights lb/lbmole
MW =[44.00 16.00];
% Critical Temperatures : Kelvin
Tc =[304.2 190.6];
% Critical Pressures : bar
Pc =[73.8 46.0];
% Critical Volumes : cm3/mol
Vc =[94.0 99.0];

% Permeance : cc-STP/cm^2-sec-psia (GPU*1e-6*5.17)
% (1 GPU = 1e-6 cm3-STP / cm2-sec-cm Hg)
for i=1:N+2,
    Q(i,1) = DD(1)*kD(1)/t;
    Q(i,2) = DD(2)*kD(2)/t;
end

sum1 =0;
for j = 1:NC,

```

```

        sum1 = sum1 + Q(N+1, j) * F(N+2, j);
end

sum2 = 0;
for j = 1:NC,
    P(N+1, j) = Q(N+1, j) * F(N+2, j) / sum1;
    parF = F(N+2, j) * FeedPr(N+2);
    parP = P(N+1, j) * PermPr(N+1);
    if parP > parF
        P(N+1, j) = F(N+2, j) * FeedPr(N+2) / PermPr(N+1);
    end
    sum2 = sum2 + P(N+1, j);
end

if sum2 > 1
    for j = 1:NC,
        P(N+1, j) = P(N+1, j) / sum2;
    end
end

%%%%%%%%%%%%%%%%%%%%%%%%%%%%%%%%%%%%%%%%%%%%%%%%%%%%%%%%%%%%%%%%%%%%%%%% stage calculations begin
%%%%%%%%%%%%%%%%%%%%%%%%%%%%%%%%%%%%%%%%%%%%%%%%%%%%%%%%%%%%%%%%%%%%%%%%
for i=N+1:-1:2,
    k = i;
    newton;
    TotFeed(i)=0;
    TotPerm(i)=0;

    for j = 1:NC,
        PermFl(i, j) =
Q(i, j) * delAk * (FeedPr(i+1) * F(i+1, j) - PermPr(i) * P(i, j));
        TotPerm(i) = TotPerm(i) + PermFl(i, j);
        FeedFl(i, j) = FeedFl(i+1, j) - PermFl(i, j);
        TotFeed(i) = TotFeed(i) + FeedFl(i, j);
        P(i-1, j) = P(i, j);
    end
    F(i, 1) = FeedFl(i, 1) / TotFeed(i);
    F(i, 2) = FeedFl(i, 2) / TotFeed(i);
end

end

```

```

P(1,1)=0;
P(1,2)=0;
PermFl(1,1)=0;
PermFl(1,2)=0;

P(N+2,1)=0;
P(N+2,2)=0;
PermFl(N+2,1)=0;
PermFl(N+2,2)=0;

for i=2:N+1,
    TotPerm(i) = TotPerm(i) + TotPerm(i-1);
end

for iter=1:1000,
    % Calculate new feed flow rates
    for i=N+2:-1:2,
        for j=1:NC,
            fF(i,j) = F(i,j)*FeedPr(i);
            fP(i,j) = P(i,j)*PermPr(i);
        end
        DENF(i)=1+b(1)*fF(i,1)+b(2)*fF(i,2);
        DENP(i)=1+b(1)*fP(i,1)+b(2)*fP(i,2);
    end

    for i=N+2:-1:2,
        for j=1:NC,

wFeed(i,j)=kD(j)*fF(i,j)*MW(j)/(22400*DENS)*(1+FF(j)*K(
j)/DENF(i));

wPerm(i,j)=kD(j)*fP(i,j)*MW(j)/(22400*DENS)*(1+FF(j)*K(
j)/DENP(i));
        end
    end

    for i=2:N+1,
        for j=1:NC,
            PermFl(i,j)=FeedFl(i+1,j)-FeedFl(i,j);
            PermFl(i,j)=PermFl(i,j)*MW(j)/22400;
        end
    end
end

```

```

        end
    end

    tolr=1d-10;
    iter1=0;
    errr=10000.;

    while errr > tolr,
        iter1=iter1+1;
        errr=0;
        for ii=2:N+1,
            r1(ii)= PermFl(ii,1)/PermFl(ii,2);
            AG1=(1-wPerm(ii,1)*(1+1/r1(ii)))/(1-
wFeed(ii,1)*(1+1/r1(ii)));
            AG2=(1-wPerm(ii,2)*(1+r1(ii)))/(1-
wFeed(ii,2)*(1+r1(ii)));

PermFl(ii,1)=DENS*DD(1)*log(AG1)/(1+1/r1(ii));

PermFl(ii,2)=DENS*DD(2)*log(AG2)/(1+r1(ii));
            rvalue(ii)=PermFl(ii,1)/PermFl(ii,2)-
r1(ii);
            errr = errr + abs(rvalue(ii));
        end
    end

    for ii=2:N+1,
        ta1=(1+1/r1(ii));
        ta2=(1-wFeed(ii,1)*ta1)*DENS*DD(1);
        ta3=ta2/(PermFl(ii,1)*ta1);
        ta4=exp(PermFl(ii,1)*ta1/DENS/DD(1))-1;
        ta5=1/ta1*(1-ta3*ta4);
        wavg1(ii)=ta5;
        bulk(ii,1)=ta1*ta5;

        tb1=(1+r1(ii));
        tb2=(1-wFeed(ii,2)*tb1)*DENS*DD(2);
        tb3=tb2/(PermFl(ii,2)*tb1);
        tb4=exp(PermFl(ii,2)*tb1/DENS/DD(2))-1;
        tb5=1/tb1*(1-tb3*tb4);
        wavg2(ii)=tb5;
        bulk(ii,2)=tb1*tb5;
    end
end

```

```

end

for i=N+1:-1:2,
    deltPr(i,1)=F(i,1)*FeedPr(i)-P(i,1)*PermPr(i);
    deltPr(i,2)=F(i,2)*FeedPr(i)-P(i,2)*PermPr(i);

    Q(i,1)=
22400*PermFl(i,1)/(MW(1)*deltPr(i,1))/t;
    Q(i,2)=
22400*PermFl(i,2)/(MW(2)*deltPr(i,2))/t;
end

for j=1:NC,
    [B,C,D] =
coeffmatrix(TotPerm,TotFeed,PermPr,FeedPr,Q,delAk,j);
    r(N)=-D(N)*FeedFl(N+2,j);
    D(N) = 0.;
    B(1) = 0.;
    [r] = thomas (B,C,D,r);
    for i=2:N+1,
        FeedFl(i,j)=r(i-1);
    end
    clear r
end

for i=2:N+1,
    TotFeednew(i) = 0;
    for j=1:NC,
        TotFeednew(i) = TotFeednew(i) +
FeedFl(i,j);
    end
end
TotFeednew(N+2) = TotFeed(N+2);

% Calculate new permeate flow rates
PermFl(1,1)=0;
PermFl(1,2)=0;
for i=2:N+1,
    TotPermnew(i) = 0;
    for j=1:NC,

```

```

        PermFl(i,j)=PermFl(i-1,j)+FeedFl(i+1,j)-
FeedFl(i,j);
        end
        TotPermnew(i)= TotPermnew(i-1)+TotFeednew(i+1)-
TotFeednew(i);
        end
        TotPermnew(1) = 0;

    for i=2:N+1,
        for j=1:NC,
            F(i,j) = FeedFl(i,j)/TotFeednew(i);
            P(i,j) = PermFl(i,j)/TotPermnew(i);
        end
    end

    for k=N+1:-1:2,

        nv=-1;
        for j=1:NC,
            X(k,j) = P(k,j);
        end
        XPr(k) = PermPr(k);
        Xtotal(k) = TotPermnew(k);

        [Vmix]=viscosity(k,NC,T,MW,Tc,Pc,X);

[XPr]=pressure(k,NC,T,DI,dz,Vmix,XPr,Xtotal,Nfibers,nv)
;
        PermPr(k) = XPr(k);

    end

    % check post-iteration error
    errfeed = abs(TotFeednew(2)-TotFeed(2));
    errperm = abs(TotPermnew(N+1)-TotPerm(N+1));
    ratiof = errfeed/TotFeednew(2);
    ratiop = errperm/TotPermnew(N+1);

    if ratiof > 1e-8 | ratiop > 1e-8
        for i=N+1:-1:2,
            TotFeed(i) = TotFeednew(i);

```

```

        TotPerm(i) = TotPermnew(i);
    end
else
    dsumCO2p=0;
    dsumCH4p=0;
    rsumCO2p=0;
    rsumCH4p=0;
    for i=N+1:-1:2,
        PermFl(i,1)=FeedFl(i+1,1)-FeedFl(i,1);
        PermFl(i,2)=FeedFl(i+1,2)-FeedFl(i,2);

dsumCO2p=dsumCO2p+PermFl(i,1)*MW(1)/22400*(1-
bulk(i,1));

dsumCH4p=dsumCH4p+PermFl(i,2)*MW(2)/22400*(1-
bulk(i,2));
        rsumCO2p=rsumCO2p+PermFl(i,1)*MW(1)/22400;
        rsumCH4p=rsumCH4p+PermFl(i,2)*MW(2)/22400;

    end

dsump=dsumCO2p*22400/MW(1)+dsumCH4p*22400/MW(2);

rsump=rsumCO2p*22400/MW(1)+rsumCH4p*22400/MW(2);

    BulkCO2=(rsumCO2p-dsumCO2p)/rsumCO2p*100;
    BulkCH4=(rsumCH4p-dsumCH4p)/rsumCH4p*100;

    dyCO2=dsumCO2p*22400/MW(1)/dsump;
    dyCH4=dsumCH4p*22400/MW(2)/dsump;
    ryCO2=rsumCO2p*22400/MW(1)/rsump;
    ryCH4=rsumCH4p*22400/MW(2)/rsump;

    dse=(dyCO2/dyCH4)/(F(N+2,1)/F(N+2,2));
    rse=(ryCO2/ryCH4)/(F(N+2,1)/F(N+2,2));
    sel=[rse;dse]

    SCUTR=(rsump)/TotFeed(N+2)*100;
    SCUTD=(dsump)/TotFeed(N+2)*100;

```

```

        CH4RR=(FeedF1(N+2,2)-
rsumCH4p*22400/MW(2))/FeedF1(N+2,2)*100;
        CH4RD=(FeedF1(N+2,2)-
dsumCH4p*22400/MW(2))/FeedF1(N+2,2)*100;

        break
    end
end

x1=N+2:-1:2;
x2=N+1:-1:2;

for i=2:N+2,
    x1(i-1)=(x1(i-1)-2)/(N+2);
    y1(i-1)=F(i,1);
    y2(i-1)=F(i,2);
end
%plot(x1,y1,x1,y2)
%hold on
for i=N+1:-1:2,
    x2(i-1)=(x2(i-1)-1)/(N+1);
    PA2(i-1)=P(i,1)*PermPr(i);
    PB2(i-1)=P(i,2)*PermPr(i);
    y5(i-1)=bulk(i,1);
    y6(i-1)=bulk(i,2);
    y7(i-1)=r1(i);
    PA1(i-1)=F(i,1)*FeedPr(i);
    PB1(i-1)=F(i,2)*FeedPr(i);
    term1a(i-1)=DD(1)/(PA1(i-1)-PA2(i-1));
    term1b(i-1)=DD(2)/(PA1(i-1)-PA2(i-1));
    term2a(i-1)=kD(1)*(PA1(i-1)-PA2(i-1));
    term2b(i-1)=kD(2)*(PA1(i-1)-PA2(i-1));
    term3(i-1)=PA1(i-1)/(1+b(1)*PA1(i-1)+b(2)*PB1(i-
1));
    term4(i-1)=PA2(i-1)/(1+b(1)*PA2(i-1)+b(2)*PB2(i-
1));
    term5a(i-1)=FF(1)*CH(1)*b(1)*(term3(i-1)-term4(i-
1));
    term5b(i-1)=FF(2)*CH(2)*b(2)*(term3(i-1)-term4(i-
1));

```

```

    Pa(i-1)=term1a(i-1)*(term2a(i-1)+term5a(i-
1))*14.7/76*1e6/t;
    Pb(i-1)=term1b(i-1)*(term2b(i-1)+term5b(i-
1))*14.7/76*1e6/t;

end

%plot(x2,Pb)
%plot(x2,term2)
%plot(x2,PA2,x2,PB2)
%plot(x2,PA1,x2,PB1)
%grid on
%axis ([0 1 0 1])

%figure
%plot(x2,y5,x2,y6)
%xlabel('Feed
Axial position, x/L
Residue')
%ylabel('Fraction of Bulk Flux Contribution')
%title('Bulk Flux Contribution of CO2 and CH4 in a
90/10 CO2/CH4 mixed-gas mixture')
%gtext('CO2')
%gtext('CH4')
%grid on
%axis tight

%figure
%plot(x2,y7)
%grid on
%axis tight

function [XPr] =
pressure(k,NC,T,DI,dz,Vmix,XPr,Xtotal,Nfibers,nv)

N=200;
RI = DI/2;

convtot = Xtotal(k)*(14.7/XPr(k))*(T/273.15);
const = 8.0*Vmix/pi/(RI^4)*dz*convtot*1.45e-4/Nfibers;
XPr(k-1) = XPr(k)-const*nv;

```

```

function [r] = thomas (b, d, a, r)
%% function [r] = thomas (a, d, b, r)
%% thomas algorithm for tridag. systems
%% note: a, b, d are all of length n -
%% with a(n) = 0 and b(1) = 0.
%%
n = length(d);
for k=1:n-1
    a(k) = a(k) / d(k);
    r(k) = r(k) / d(k);
    d(k+1) = d(k+1) - b(k+1)*a(k);
    r(k+1) = r(k+1) - b(k+1)*r(k);
end
r(n) = r(n) / d(n);
for j=n-1:-1:1
    r(j) = r(j) - a(j)*r(j+1);
end

function [B,C,D] =
coeffmatrix(TotPerm,TotFeed,PermPr,FeedPr,Q,delAk,j)

N=200;
com2 = TotPerm(2)/(PermPr(2)*delAk*Q(2,j));
C(1)=1+com2*(1+Q(2,j)*delAk*FeedPr(2)/TotFeed(2));
D(1) = -1*(com2+1);
for i=3:N+1,
    com1 = TotPerm(i-1)/(PermPr(i-1)*delAk*Q(i-1,j));
    com2 = TotPerm(i)/(PermPr(i)*delAk*Q(i,j));
    B(i-1) = -1*com1*(1+Q(i-1,j)*delAk*FeedPr(i-
1)/TotFeed(i-1));
    C(i-
1)=1+com1+com2*(1+Q(i,j)*delAk*FeedPr(i)/TotFeed(i));
    D(i-1) = -1*(com2+1);
end

function yy = jacobian
global Q k NC FeedPr PermPr F P FeedFl PermFl rjacob
fvalue delP

N=200;
sumd=0;

```

```

for j=1:NC,
    sumd=sumd+Q(k,j)*(FeedPr(k+1)*F(k+1,j)-
    PermPr(k)*P(k,j));
end

for j=1:NC,
    rum = Q(k,j)*(FeedPr(k+1)*F(k+1,j)-
    PermPr(k)*P(k,j));
    for jj=1:NC,
        if j==jj
            rjacob(j,jj)= 1 - ( (-
1*sumd*PermPr(k)*Q(k,j) + rum*PermPr(k)*Q(k,j)) /
(sumd*sumd) );
        else
            rjacob(j,jj)= -
1*rum*Q(k,jj)*PermPr(k)/(sumd*sumd);
        end

    end
    fvalue(j)= P(k,j)-rum/sumd;
end

function yyyyy = gaussian
global Q k NC FeedPr PermPr F P FeedFl PermFl rjacob
fvalue delP

% modify matrices rjacob and fvalue simultaneously
for i=1:NC-1,
    for j=i+1:NC,
        quo=rjacob(j,i)/rjacob(i,i);
        for k=i:NC,
            rjacob(j,k)=rjacob(j,k)-quo*rjacob(i,k);
        end
        fvalue(j)=fvalue(j)-quo*fvalue(i);
    end
end

% solve for delP vector
delP(NC) = fvalue(NC)/rjacob(NC,NC);
for i=NC-1:-1:1,
    sum=0;

```

```

        for j=i+1:NC,
            sum=sum+rjacob(i,j)*delP(j);
        end
        delP(i)=(fvalue(i)-sum)/rjacob(i,i);
    end

function y = newton
global Q k NC FeedPr PermPr F P FeedFl PermFl rjacob
fvalue delP

tolf = NC*1D-3;
tolp = NC*1D-3;

for ntrial=1:300,
    jacobian;
    errf = 0.0;
    for j=1:NC,
        errf = errf + abs(fvalue(j));
    end
    if errf < tolf
        return
    end
    for j=1:NC,
        fvalue(j) = -fvalue(j);
    end

    fvalue=[fvalue(1);fvalue(2)];

    delP=rjacob\fvalue;

    errp = 0.0;

    for j=1:NC,
        P(k,j) = P(k,j) + delP(j);
        errp = errp + abs(delP(j));
    end
    if errp < tolp
        return
    end
end
disp('Crossflow did not converge')

```

```

function [Vmix] = viscosity(k,NC,T,MW,Tc,Pc,X)

N=200;
for i=1:NC,
    Tr(i) = T/Tc(i);
    a(i) = 5.682*((MW(i)^3)*(Pc(i)^4)/Tc(i))^(1.0/6.0);
    b(i) = 0.807*Tr(i)^0.618 - 0.357*exp(-0.449*Tr(i));
    c(i) = 0.340*exp(-4.058*Tr(i)) + 0.018;
    V(i) = a(i)*(b(i)+c(i));
end

for i=1:NC,
    for j=1:NC,
        if i==j
            phi(i,j) = 1.0;
        else
            phi(i,j) =
((1+(V(j)/V(i))^0.5*(MW(i)/MW(j))^0.25)^2)/((8*(1+MW(j)
/MW(i)))^0.5);
        end
    end
end

Vmix=0.0;
for i=1:NC,
    sump=0.0;
    for j=1:NC,
        sump = sump + X(k,j)*phi(i,j);
    end
    Vmix = Vmix + (X(k,i)*V(i))/sump;
end
% units : Pa-s (micropoise*1e-7)
Vmix = Vmix*1e-7;

```

B.2 Equilibrium Program

The rigorous VLE follows the model of Austgen (1989) and is too long to be listed here. An electronic copy is archived with Dr. Gary Rochelle.

B.3 Rigorous Rate Model for MOR / DGA

An excerpt of the rigorous rate model is shown below. Since a list of the whole program would be too long, we only show the equations that must be solved for one grid size.

C VARIABLES DICTIONARY:

C

C SCALARS:

C

C n: NUMBER OF NODES

C H1: STEPSIZE FOR GRID SIZE ONE

C R: DIMENSIONLESS DISTANCE FROM INTERFACE

C I: INTEGER COUNTER, IDENTIFIED NODE NUMBER

C C: COSINE OF $\pi/2r$ AT R

C S: SINE OF $\pi/2r$ AT R

C T: TAN OF $\pi/2r$ AT R

C T1: TERM ONE IN MATERIAL BALANCE EQUATIONS – SEE

C APPENDIX E

C T2: TERM 2

C T3: TERM 3

C T4: TERM 4

C

C VECTORS

C

C Dr(l)=DERIVATIVE OF SPECIES L

C D2r(l)=SECOND DERIVATIVE OF SPECIES L

C RR: VECTOR OF FINITE RATE REACTIONS

C 1: $\text{CO}_2 + \text{OH}^- \rightarrow \text{HCO}_3^-$

C 2: $\text{DGA} + \text{H}_2\text{O} + \text{CO}_2 \rightarrow \text{DGACOO}^- + \text{H}_3\text{O}^+$

C 6: $\text{MOR} + \text{H}_2\text{O} + \text{CO}_2 \rightarrow \text{MORCOO}^- + \text{H}_3\text{O}^+$

C 8: $\text{MOR} + \text{DGA} + \text{CO}_2 \rightarrow \text{MORCOO}^- + \text{DGAH}^+$

C DELTA(n)=RESIDUALS: THESE ARE ALL 0 AT SOLUTION.

C Y(n*11): VECTOR OF MOLEFRACTIONS. AT A GIVEN NODE,

C SPECIES COME IN THE FOLLOWING ORDER

C 1: CO_2

C 2: HCO_3^-

C 3: $\text{CO}_3^{=}$

C 4: OH^-

C 5: DGA

C 6: DGAH^+

C 7: DGACOO^-

```

C 8: MOR
C 9: MORH+
C 10: MORCOO-
C KF: FORWARD REACTION RATE CONSTANTS, SEE RR FOR
C REACTION NUMBERS
C K; EQUILIBRIUM CONSTANTS: NUMBERS ARE SAME AS RR.
C IN ADDITION:
C 3: HCO3- + OH- → CO3= + H2O
C 4: H2O → H3O+ + OH-
C 5: DGA+H2O → DGAH+ + OH-
C 7: MOR+H2O → MORH+ + OH-
C
C CALCULATE RESIDUALS FROM NODES 1 TO N1 USING GRIDSIZE
C H1
C   CALCULATE RESIDUALS FROM NODES 1 TO N1 USING
      GRIDSIZE H1
C
  do 10 i = 1,n1-1
    r=real(i)*h1

C CALCULATE FIRST AND SECOND DERIVATIVES FOR ALL
  SPECIES AT EACH NODE
C
  do 20 l=1,10
    Dr(l)=1.0/(2.0*h1)*(-y(10*(i-1)+1) +
      y(10*(i+1)+1))
    Dr2(l)=1.0/(h1*h1)*(y(10*(i-1)+1) -2.0*y(10*i+1) +
      y(10*(i+1)+1))
  20 continue
C write (12,*) 'First Derivatives'
C write (12,*) Dr
C write (12,*) 'Second Derivatives'
C write (12,*) Dr2
C
C CALCULATE THE REACTION RATES FOR FINITE RATE C
  REACTIONS
C
  RR(1)=kf(1)*y(10*i+1)*y(10*i+4) -
    kf(1)/K(1)*y(10*i+2)
  RR(2)=kf(2)*y(10*i+1)*y(10*i+5) -
    * kf(2)/K(2)*y(10*i+7)*K(4)/y(10*i+4)
  RR(3)=kf(3)*y(10*i+1)*y(10*i+8) -

```

```

      * kf(3)/K(6)*y(10*i+10)*K(4)/y(10*i+4)
RR(4)=kf(4)*y(10*i+1)*y(10*i+8)*y(10*i+5)-
      * kf(4)/K(8)*y(10*i+10)*y(10*i+6)

C CALCULATE TRIG FUNCTIONS AT R
C
c=cos(pi/2.0*r)
s=sin(pi/2.0*r)
ta=tan(pi/2.0*r)
C
C CALCULATE LEADING TERMS
C
t1=4.0*e/(pi*pi)*s*s*c*c
t2=4.0/(pi*pi)*c*c*c*c*e/D(1)
t3=-4.0/pi*e*s*s*s*c + 4.0/pi*e*ta*c*c
t4=-4.0/pi*e/D(1)*c*c*c*s
c write (12,*) 'Term 1 and 2'
c write (12,*) t1,t2
c write (12,*) 'Term 3 and 4'
c write (12,*) t3,t4
C
C RESIDUALS CORRESPONDING TO THE PIPERAZINE MATERIAL
BALANCE
C
C RESIDUALS CORRESPONDING TO TOTAL CARBON BALANCE
delta(10*i+1)=(t1+D(1)*t2)*Dr2(1) +
(t3+D(1)*t4)*Dr(1)
* + (t1+D(2)*t2)*Dr2(2) + (t3+D(2)*t4)*Dr(2)
* + (t1+D(3)*t2)*Dr2(3) + (t3+D(3)*t4)*Dr(3)
* + (t1+D(7)*t2)*Dr2(7) + (t3+D(7)*t4)*Dr(7)
* + (t1+D(10)*t2)*Dr2(10) + (t3+D(10)*t4)*Dr(10)

C RESIDUAL CORRESPONDING TO CARBON DIOXIDE MATERIAL
BALANCE
delta(10*i+2)=(t1+D(1)*t2)*Dr2(1) +
(t3+D(1)*t4)*Dr(1)
* - RR(1)- RR(2)- RR(3)- RR(4)

C RESIDUAL CORRESPONDING TO CO3= / HCO3- EQUILIBRIUM
delta(10*i+3)=K(3)*y(10*i+2)*y(10*i+4) - y(10*i+3)

```

```

C Residuals corresponding to dga balance
  delta(10*i+4)=(t1+D(5)*t2)*Dr2(5) +
  (t3+D(5)*t4)*Dr(5)+
  *      (t1+D(6)*t2)*Dr2(6) + (t3+D(6)*t4)*Dr(6)+
  *      (t1+D(7)*t2)*Dr2(7) + (t3+D(7)*t4)*Dr(7)

C      Residual corresponding to dgacoo- balance
  delta(10*i+5)=(t1+D(7)*t2)*Dr2(7) +
  (t3+D(7)*t4)*Dr(7)
  *      +RR(2)

C Residuals corresponding to dga proton equilibrium
  delta(10*i+6)=K(5)*y(10*i+5)-y(10*i+6)*y(10*i+4)

C RESIDUAL CORRESPONDING TO ELECTRONEUTRALITY
  delta(10*i+7) = y(10*i+6)+ y(10*i+9)
  *      -
  (y(10*i+2)+2.0*y(10*i+3)+y(10*i+4)+y(10*i+7)+y(10*
  i+10))

C Residuals corresponding to mor balance
  delta(10*i+8)=(t1+D(8)*t2)*Dr2(8) +
  (t3+D(8)*t4)*Dr(8)+
  *      (t1+D(9)*t2)*Dr2(9) + (t3+D(9)*t4)*Dr(9)+
  *      (t1+D(10)*t2)*Dr2(10) +
  (t3+D(10)*t4)*Dr(10)

C      Residual corresponding to dgacoo- balance
  delta(10*i+9)=(t1+D(10)*t2)*Dr2(10) +
  (t3+D(10)*t4)*Dr(10)
  *      +RR(3)+RR(4)

C Residuals corresponding to dga proton equilibrium
  delta(10*i+10)=K(7)*y(10*i+8)-y(10*i+9)*y(10*i+4)
C
C WRITE RESIDUALS FOR NODE I
C
C write (*,*) 'Residuals at Node ',i
C do 30 l=1,14
C   write (*,*) delta(14*i+l)
C30 continue
C

```

C FINISH CALCULATIONS AT NODE I
10 CONTINUE

Appendix C: Permeation Data

Table C.1 Experimental data of conditioning by 10/90 CO₂/CH₄ mixture on CO₂ permeance, CH₄ permeance and the CO₂/CH₄ selectivity at 200 psia and 35 °C. Sample # 1

	Pressure (psia)	Gas Mixture	$\alpha_{\text{CO}_2/\text{CH}_4}$	PERMEANCE (GPU)	
				CO ₂	CH ₄
before	108.7	10/90 CO ₂ /CH ₄	27.1	18.9	0.696
before	160.7	10/90 CO ₂ /CH ₄	28.2	18.2	0.644
before	215.7	10/90 CO ₂ /CH ₄	28.2	17.2	0.612
second day	215.7	10/90 CO ₂ /CH ₄	28.5	17.4	0.609
third day	215.7	10/90 CO ₂ /CH ₄	29.0	17.1	0.589
fourth day	214.7	10/90 CO ₂ /CH ₄	29.0	17.2	0.594
fifth day	214.7	10/90 CO ₂ /CH ₄	29.1	17.4	0.598
after	214.7	10/90 CO ₂ /CH ₄	28.8	17.4	0.606
after	164.7	10/90 CO ₂ /CH ₄	28.9	18.4	0.639
after	107.7	10/90 CO ₂ /CH ₄	27.5	19.4	0.702

Table C.2 Experimental data of conditioning by 10/90 CO₂/CH₄ mixture on CO₂ permeance, CH₄ permeance and the CO₂/CH₄ selectivity at 200 psia and 35 °C. Sample # 2

	Pressure (psia)	Gas Mixture	$\alpha_{\text{CO}_2/\text{CH}_4}$	PERMEANCE (GPU)	
				CO ₂	CH ₄
before	200	10/90 CO ₂ /CH ₄	33.3	8.6	0.258
first day	200	10/90 CO ₂ /CH ₄	33.4	8.9	0.267
second day	200	10/90 CO ₂ /CH ₄	32.9	8.3	0.251
third day	200	10/90 CO ₂ /CH ₄	33.0	8.2	0.249
fourth day	200	10/90 CO ₂ /CH ₄	33.1	8.3	0.250
fifth day	200	10/90 CO ₂ /CH ₄	32.8	8.3	0.254
after	200	10/90 CO ₂ /CH ₄	32.7	8.3	0.254

Table C.3 Experimental data of conditioning by 10/90 CO₂/CH₄ + 500 ppm n-heptane mixture on CO₂ permeance, CH₄ permeance and the CO₂/CH₄ selectivity at 200 psia and 35 °C. Sample # 1

	Pressure (psia)	Gas Mixture	$\alpha_{\text{CO}_2/\text{CH}_4}$	PERMEANCE (GPU)	
				CO ₂	CH ₄
before	110.7	10/90 CO ₂ /CH ₄	29.4	16.3	0.553
before	162.7	10/90 CO ₂ /CH ₄	29.8	14.7	0.492
before	215.7	10/90 CO ₂ /CH ₄	29.6	13.8	0.464
first day	204.7	10/90 CO ₂ /CH ₄ +500 ppm Heptane	29.3	12.8	0.435
second day	216.7	10/90 CO ₂ /CH ₄ +500 ppm Heptane	28.4	11.7	0.411
third day	220.7	10/90 CO ₂ /CH ₄ +500 ppm Heptane	28.2	11.5	0.407
fourth day	220.7	10/90 CO ₂ /CH ₄ +500 ppm Heptane	28.2	11.5	0.409
fifth day	220.7	10/90 CO ₂ /CH ₄ +500 ppm Heptane	28.1	11.5	0.409
after	214.7	10/90 CO ₂ /CH ₄	28.1	11.8	0.420
after	158.7	10/90 CO ₂ /CH ₄	28.4	13.4	0.471
after	100.7	10/90 CO ₂ /CH ₄	27.0	15.1	0.560

Table C.4 Experimental data of conditioning by 10/90 CO₂/CH₄ + 500 ppm n-heptane mixture CO₂ permeance, CH₄ permeance and the CO₂/CH₄ selectivity at 200 psia and 35 °C. Sample # 2

	Pressure (psia)	Gas Mixture	$\alpha_{\text{CO}_2/\text{CH}_4}$	PERMEANCE (GPU)	
				CO ₂	CH ₄
before	114.7	10/90 CO ₂ /CH ₄	28.4	14.0	0.494
before	166.7	10/90 CO ₂ /CH ₄	28.6	13.3	0.465
before	216.7	10/90 CO ₂ /CH ₄	29.0	12.6	0.437
second day	217.7	10/90 CO ₂ /CH ₄ +500 ppm Heptane	27.8	11.0	0.394
third day	218.7	10/90 CO ₂ /CH ₄ +500 ppm Heptane	27.8	10.9	0.392
fourth day	218.7	10/90 CO ₂ /CH ₄ +500 ppm Heptane	27.7	10.9	0.395
fifth day	207.0	10/90 CO ₂ /CH ₄ +500 ppm Heptane	27.5	10.9	0.396
after	212.7	10/90 CO ₂ /CH ₄	27.7	11.4	0.412
after	166.7	10/90 CO ₂ /CH ₄	28.0	13.0	0.466
after	116.7	10/90 CO ₂ /CH ₄	27.9	14.7	0.525

Table C.5 Experimental data of conditioning by 10/90 CO₂/CH₄ + 300 ppm n-heptane mixture on CO₂ permeance, CH₄ permeance and the CO₂/CH₄ selectivity at 400 psia and 35 °C. Sample # 1

	Pressure (psia)	Gas Mixture	$\alpha_{\text{CO}_2/\text{CH}_4}$	PERMEANCE (GPU)	
				CO ₂	CH ₄
before	400	10/90 CO ₂ /CH ₄	29.1	15.6	0.537
first day	400	10/90 CO ₂ /CH ₄ +300 ppm Heptane	28.7	14.3	0.499
second day	400	10/90 CO ₂ /CH ₄ +300 ppm Heptane	28.4	13.8	0.487
sixth day	400	10/90 CO ₂ /CH ₄ +300 ppm Heptane	28.9	13.6	0.471
after	400	10/90 CO ₂ /CH ₄	28.5	14.1	0.494

Table C.6 Experimental data of conditioning by 10/90 CO₂/CH₄ + 300 ppm toluene mixture on CO₂ permeance, CH₄ permeance and the CO₂/CH₄ selectivity at 200 psia and 35 °C. Sample # 1

	Pressure (psia)	Gas Mixture	$\alpha_{\text{CO}_2/\text{CH}_4}$	PERMEANCE (GPU)	
				CO ₂	CH ₄
before	114.7	10/90 CO ₂ /CH ₄	28.1	18.2	0.646
before	166.7	10/90 CO ₂ /CH ₄	28.9	17.6	0.608
before	216.7	10/90 CO ₂ /CH ₄	29.4	16.9	0.575
second day	217.7	10/90 CO ₂ /CH ₄ +300 ppm Toluene	27.3	10.7	0.391
third day	218.7	10/90 CO ₂ /CH ₄ +300 ppm Toluene	26.9	11.0	0.407
fourth day	218.7	10/90 CO ₂ /CH ₄ +300 ppm Toluene	27.0	11.1	0.412
fifth day	207.0	10/90 CO ₂ /CH ₄ +300 ppm Toluene	27.0	11.2	0.415
after	212.7	10/90 CO ₂ /CH ₄	25.9	27.1	1.046
after	166.7	10/90 CO ₂ /CH ₄	25.1	26.8	1.068
after	116.7	10/90 CO ₂ /CH ₄	24.7	27.1	1.096

Table C.7 Experimental data of conditioning by 10/90 CO₂/CH₄ + 300 ppm toluene mixture on CO₂ permeance, CH₄ permeance and the CO₂/CH₄ selectivity at 200 psia and 35 °C. Sample # 2

	Pressure (psia)	Gas Mixture	$\alpha_{\text{CO}_2/\text{CH}_4}$	PERMEANCE (GPU)	
				CO ₂	CH ₄
before	200	10/90 CO ₂ /CH ₄	30.4	11.0	0.362
second day	200	10/90 CO ₂ /CH ₄ +300 ppm Toluene	28.9	7.2	0.249
third day	200	10/90 CO ₂ /CH ₄ +300 ppm Toluene	28.4	7.3	0.257
fourth day	200	10/90 CO ₂ /CH ₄ +300 ppm Toluene	28.4	7.4	0.261
fifth day	200	10/90 CO ₂ /CH ₄ +300 ppm Toluene	28.3	7.5	0.265
after	200	10/90 CO ₂ /CH ₄	27.2	17.2	0.632

Table C.8 Experimental data of conditioning by 10/90 CO₂/CH₄ + 300 ppm toluene mixture on CO₂ permeance, CH₄ permeance and the CO₂/CH₄ selectivity at 600 psia and 35 °C. Sample # 1

	Pressure (psia)	Gas Mixture	$\alpha_{\text{CO}_2/\text{CH}_4}$	PERMEANCE (GPU)	
				CO ₂	CH ₄
before	203	10/90 CO ₂ /CH ₄	32.4	15.1	0.465
before	400	10/90 CO ₂ /CH ₄	31.0	11.4	0.368
before	604	10/90 CO ₂ /CH ₄	28.2	9.5	0.337
first day	610	10/90 CO ₂ /CH ₄ +300 ppm Toluene	22.7	6.5	0.285
second day	610	10/90 CO ₂ /CH ₄ +300 ppm Toluene	22.6	6.7	0.294
third day	611	10/90 CO ₂ /CH ₄ +300 ppm Toluene	22.6	6.5	0.290
fourth day	612	10/90 CO ₂ /CH ₄ +300 ppm Toluene	22.6	6.6	0.295
fifth day	614	10/90 CO ₂ /CH ₄ +300 ppm Toluene	22.5	6.7	0.299
after	602	10/90 CO ₂ /CH ₄	24.1	20.6	0.856
after	400	10/90 CO ₂ /CH ₄	24.8	21.3	0.861
after	206	10/90 CO ₂ /CH ₄	25.1	20.7	0.827

Table C.9 Experimental data of conditioning by 10/90 CO₂/CH₄ + 300 ppm toluene mixture on CO₂ permeance, CH₄ permeance and the CO₂/CH₄ selectivity at 600 psia and 35 °C. Sample # 2

	Pressure (psia)	Gas Mixture	$\alpha_{\text{CO}_2/\text{CH}_4}$	PERMEANCE (GPU)	
				CO ₂	CH ₄
before	600	10/90 CO ₂ /CH ₄	28.1	10.5	0.374
first day	600	10/90 CO ₂ /CH ₄ +300 ppm Toluene	22.1	7.86	0.356
second day	600	10/90 CO ₂ /CH ₄ +300 ppm Toluene	22.5	8.13	0.361
third day	600	10/90 CO ₂ /CH ₄ +300 ppm Toluene	22.5	8.15	0.362
fourth day	600	10/90 CO ₂ /CH ₄ +300 ppm Toluene	22.5	8.20	0.364
fifth day	600	10/90 CO ₂ /CH ₄ +300 ppm Toluene	22.4	8.30	0.371
after	600	10/90 CO ₂ /CH ₄	23.5	21.0	0.894

Table C.10 Experimental data of conditioning by 10/90 CO₂/CH₄ + 500 ppm n-heptane mixture on CO₂ permeance, CH₄ permeance and the CO₂/CH₄ selectivity at 600 psia and 35 °C. Sample # 1

	Pressure (psia)	Gas Mixture	$\alpha_{\text{CO}_2/\text{CH}_4}$	PERMEANCE (GPU)	
				CO ₂	CH ₄
before	216	10/90 CO ₂ /CH ₄	33.7	10.0	0.298
before	415	10/90 CO ₂ /CH ₄	35.3	8.5	0.242
before	618	10/90 CO ₂ /CH ₄	34.4	7.7	0.225
first day	605	10/90 CO ₂ /CH ₄ +500 ppm Heptane	34.1	7.6	0.224
second day	605	10/90 CO ₂ /CH ₄ +500 ppm Heptane	32.9	7.8	0.237
third day	605	10/90 CO ₂ /CH ₄ +500 ppm Heptane	31.1	7.9	0.255
fourth day	600	10/90 CO ₂ /CH ₄ +500 ppm Heptane	30.5	7.8	0.257
fifth day	610	10/90 CO ₂ /CH ₄ +500 ppm Heptane	30.0	7.9	0.263
after	212	10/90 CO ₂ /CH ₄	29.9	11.7	0.392
after	414	10/90 CO ₂ /CH ₄	29.8	9.8	0.330
after	608	10/90 CO ₂ /CH ₄	29.3	8.5	0.290

Table C.11 Experimental data of conditioning by 10/90 CO₂/CH₄ + 500 ppm n-heptane mixture on CO₂ permeance, CH₄ permeance and the CO₂/CH₄ selectivity at 600 psia and 35 °C. Sample # 2

	Pressure (psia)	Gas Mixture	$\alpha_{\text{CO}_2/\text{CH}_4}$	PERMEANCE (GPU)	
				CO ₂	CH ₄
before	600	10/90 CO ₂ /CH ₄	29.6	8.0	0.270
first day	600	10/90 CO ₂ /CH ₄ +500 ppm Heptane	29.4	8.1	0.276
second day	600	10/90 CO ₂ /CH ₄ +500 ppm Heptane	28.7	8.1	0.282
third day	600	10/90 CO ₂ /CH ₄ +500 ppm Heptane	28.1	8.2	0.292
fourth day	600	10/90 CO ₂ /CH ₄ +500 ppm Heptane	27.5	8.3	0.302
fifth day	600	10/90 CO ₂ /CH ₄ +500 ppm Heptane	26.1	8.4	0.322
after	600	10/90 CO ₂ /CH ₄	25.9	9.0	0.347

Table C.12 Experimental data of conditioning by 10/90 CO₂/CH₄ mixture on CO₂ permeance, CH₄ permeance and the CO₂/CH₄ selectivity at 600 psia and 35 °C. Sample # 1

	Pressure (psia)	Gas Mixture	$\alpha_{\text{CO}_2/\text{CH}_4}$	PERMEANCE (GPU)	
				CO ₂	CH ₄
before	210	10/90 CO ₂ /CH ₄	31.5	10.8	0.343
before	402	10/90 CO ₂ /CH ₄	29.8	9.4	0.315
before	614	10/90 CO ₂ /CH ₄	27.4	8.6	0.315
first day	614	10/90 CO ₂ /CH ₄	27.4	8.6	0.315
first day	611	10/90 CO ₂ /CH ₄	28.4	9.6	0.339
second day	606	10/90 CO ₂ /CH ₄	28.2	8.4	0.297
third day	602	10/90 CO ₂ /CH ₄	28.2	9.7	0.343
fourth day	600	10/90 CO ₂ /CH ₄	29.1	9.8	0.336
fifth day	600	10/90 CO ₂ /CH ₄	28.4	9.9	0.349
after	600	10/90 CO ₂ /CH ₄	30.3	10.4	0.342
after	400	10/90 CO ₂ /CH ₄	30.1	13.5	0.449
after	200	10/90 CO ₂ /CH ₄	28.4	9.9	0.349

Table C.13 Experimental data of conditioning by 10/90 CO₂/CH₄ + 100 ppm toluene mixture on CO₂ permeance, CH₄ permeance and the CO₂/CH₄ selectivity at 400 psia and 55 °C. Sample # 1

	Pressure (psia)	Gas Mixture	$\alpha_{\text{CO}_2/\text{CH}_4}$	PERMEANCE (GPU)	
				CO ₂	CH ₄
before	200	10/90 CO ₂ /CH ₄	20.6	23.4	1.139
first day	200	10/90 CO ₂ /CH ₄ +300 ppm Toluene	21.7	18.2	0.838
second day	200	10/90 CO ₂ /CH ₄ +300 ppm Toluene	21.6	18.0	0.834
third day	200	10/90 CO ₂ /CH ₄ +300 ppm Toluene	21.4	18.0	0.843
fourth day	200	10/90 CO ₂ /CH ₄ +300 ppm Toluene	21.3	17.8	0.839
fifth day	200	10/90 CO ₂ /CH ₄ +300 ppm Toluene	21.1	17.6	0.837
after	200	10/90 CO ₂ /CH ₄	20.5	23.3	1.138

Table C.14 Experimental data of conditioning by 10/90 CO₂/CH₄ + 300 ppm toluene mixture on CO₂ permeance, CH₄ permeance and the CO₂/CH₄ selectivity at 200 psia and 55 °C. Sample # 1

	Pressure (psia)	Gas Mixture	$\alpha_{\text{CO}_2/\text{CH}_4}$	PERMEANCE (GPU)	
				CO ₂	CH ₄
before	200	10/90 CO ₂ /CH ₄	20.4	18.0	0.884
first day	200	10/90 CO ₂ /CH ₄ +300 ppm Toluene	22.5	12.6	0.560
second day	200	10/90 CO ₂ /CH ₄ +300 ppm Toluene	22.6	12.4	0.550
third day	200	10/90 CO ₂ /CH ₄ +300 ppm Toluene	22.4	12.3	0.547
fourth day	200	10/90 CO ₂ /CH ₄ +300 ppm Toluene	23.1	12.2	0.529
fifth day	200	10/90 CO ₂ /CH ₄ +300 ppm Toluene	22.6	12.3	0.544
after	200	10/90 CO ₂ /CH ₄	20.6	17.7	0.861

Table C.15 Experimental data of conditioning by 10/90 CO₂/CH₄ + 100 ppm toluene mixture on CO₂ permeance, CH₄ permeance and the CO₂/CH₄ selectivity at 200 psia and 55 °C. Sample # 1

	Pressure (psia)	Gas Mixture	$\alpha_{\text{CO}_2/\text{CH}_4}$	PERMEANCE (GPU)	
				CO ₂	CH ₄
before	200	10/90 CO ₂ /CH ₄	23.4	16.4	0.700
second day	200	10/90 CO ₂ /CH ₄ +300 ppm Toluene	24.5	13.3	0.543
third day	200	10/90 CO ₂ /CH ₄ +300 ppm Toluene	24.4	13.3	0.547
fourth day	200	10/90 CO ₂ /CH ₄ +300 ppm Toluene	24.4	13.5	0.553
fifth day	200	10/90 CO ₂ /CH ₄ +300 ppm Toluene	24.3	13.7	0.562
after	200	10/90 CO ₂ /CH ₄	22.6	16.9	0.747

Table C.16 Experimental data of conditioning by 10/90 CO₂/CH₄ + 500 ppm toluene mixture on CO₂ permeance, CH₄ permeance and the CO₂/CH₄ selectivity at 200 psia and 55 °C. Sample # 1

	Pressure (psia)	Gas Mixture	$\alpha_{\text{CO}_2/\text{CH}_4}$	PERMEANCE (GPU)	
				CO ₂	CH ₄
before	100	10/90 CO ₂ /CH ₄	18.5	20.0	1.084
before	150	10/90 CO ₂ /CH ₄	19.5	19.1	0.976
before	200	10/90 CO ₂ /CH ₄	19.6	18.3	0.932
first day	200	10/90 CO ₂ /CH ₄ +500 ppm Heptane	18.9	14.3	0.754
second day	200	10/90 CO ₂ /CH ₄ +500 ppm Heptane	19.1	14.4	0.754
third day	200	10/90 CO ₂ /CH ₄ +500 ppm Heptane	19.1	14.4	0.754
fourth day	200	10/90 CO ₂ /CH ₄ +500 ppm Heptane	19.1	14.3	0.746
fifth day	200	10/90 CO ₂ /CH ₄ +500 ppm Heptane	19.0	14.3	0.748
after	200	10/90 CO ₂ /CH ₄	19.2	17.6	0.947
after	150	10/90 CO ₂ /CH ₄	19.3	18.3	1.012
after	100	10/90 CO ₂ /CH ₄	17.5	19.3	1.017

Appendix D: Equation for Compressibility Factors for Penetrants at 35 °C

The following were derived from least square curve fits on pressure and temperature dependent compressibility factor data for each of the penetrants [reference 13 in Anshu's thesis].

D.1 Nitrogen

$$Z = 1 - 8.59 \times 10^{-6} p + 1.08 \times 10^{-9} p^2 + 1.07 \times 10^{-13} p^3$$

D.2 Carbon Dioxide

$$Z = 1 - 3.38 \times 10^{-4} p + 6.17 \times 10^{-8} p^2 - 1.69 \times 10^{-10} p^3$$

D.3 Methane

$$Z = 1 - 1.05 \times 10^{-4} p + 3.82 \times 10^{-9} p^2 + 5.20 \times 10^{-12} p^3$$

Appendix E: Desorption Isotherm Sample Calculation

The following is a sample calculation for the desorption isotherm after conditioning with 10/90 CO₂/CH₄ + 500 ppm n-heptane and then probing with CO₂. Using equations D.2, F.1, F.2, F.3 and Table E.1, P_R, P_C, z_R and z_C can be calculated as shown in Table E.2 and E.3.

Table E.1 Voltage Measurements

E _{vacuum,PS} (V)	E _{vacuum,R} (mV)	E _{vacuum,C} (mV)	E _{PS} (V)	E _R (mV)	E _C (mV)
10.337	0.393	-0.438	10.337	1.669	1.457
10.337	0.393	-0.438	10.337	1.897	1.165
10.337	0.393	-0.438	10.337	1.466	1.166
10.337	0.393	-0.438	10.337	1.662	0.916
10.337	0.393	-0.438	10.337	1.038	0.918
10.337	0.393	-0.438	10.337	1.321	0.560
10.337	0.393	-0.438	10.337	0.731	0.563
10.337	0.393	-0.438	10.337	1.006	0.226
10.337	0.393	-0.438	10.337	0.392	0.226
10.337	0.393	-0.438	10.337	0.684	-0.113
10.337	0.393	-0.438	10.337	0.393	-0.112
10.337	0.393	-0.438	10.337	0.540	-0.267
10.337	0.393	-0.438	10.337	0.393	-0.271
10.337	0.393	-0.438	10.337	0.470	-0.349
10.337	0.393	-0.438	10.337	0.390	-0.349
10.337	0.393	-0.438	10.337	0.434	-0.388
10.337	0.393	-0.438	10.337	0.394	-0.389
10.337	0.393	-0.438	10.337	0.417	-0.408
10.337	0.393	-0.438	10.337	0.392	-0.411
10.337	0.393	-0.438	10.337	0.406	-0.419

Table E.2 Pressure and moles desorbed calculations

P _R (psia)	P _C (psia)	z _R	z _C	- Δn _p
36.168	50.789	0.989	0.985	
42.631	42.963	0.988	0.987	-0.499
30.414	42.990	0.991	0.987	
35.970	36.290	0.990	0.989	-0.453
18.282	36.343	0.995	0.989	
26.304	26.748	0.992	0.992	-0.699
9.581	26.829	0.997	0.992	

17.375	17.796	0.995	0.995	-0.905
-0.028	17.796	1.000	0.995	
8.248	8.711	0.998	0.998	-1.345
0.000	8.737	1.000	0.997	
4.167	4.583	0.999	0.999	-1.009
0.000	4.476	1.000	0.999	
2.183	2.385	0.999	0.999	-0.596
-0.085	2.385	1.000	0.999	
1.162	1.340	1.000	1.000	-0.456
0.028	1.313	1.000	1.000	
0.680	0.804	1.000	1.000	-0.267
-0.028	0.724	1.000	1.000	
0.368	0.509	1.000	1.000	-0.236
$\sum \Delta n_p = \text{moles sorbed}$				-6.47

Table E.3 Concentration Calculation, polymer sample volume = 0.239 cc.

P_c (psia)	$-\Delta n_p$	Moles sorbed $= \sum \Delta n_p - \Delta n_p$	C , cc(STP/cc polymer)
50.8	-	6.47	27.05
43.0	-0.499	5.97	24.96
36.3	-0.453	5.51	23.07
26.7	-0.699	4.81	20.14
17.8	-0.905	3.91	16.36
8.7	-1.345	2.56	10.73
4.6	-1.009	1.55	6.51
2.4	-0.596	0.96	4.01
1.3	-0.456	0.50	2.10
0.8	-0.267	0.24	0.99
0.5	-0.236	0.00	0.00
0	$\sum \Delta n_p = 6.47$		0

Appendix F: Working Equations for Sorption Isotherm Calculations

When converting voltages to pressures, we take into account two deviations from ideal transducer performance:

1. Non-zero signal at vacuum. The transducer will give a non-zero voltage reading when the system is essentially at vacuum.
2. Variable DC voltage from power supply. The transducers are powered by a DC voltage supply which is designed to output ~10V. However, this output voltage may fluctuate due to changes in ambient conditions (mainly temperature)

The working equation for converting voltage to pressure (psia) :

$$P = \frac{1}{C.F} \left(\frac{E}{E_{PS}} - \frac{E_{vacuum}}{E_{vacuu,PS}} \right) \quad (F.1)$$

P = pressure, psia

C.F. = calibration factor; unique for each transducer; obtain from vendor

E = voltage reading from transducer, V

E_{PS} = voltage reading from power source, V

E_{vacuum} = voltage reading from transducer at vacuum, V

$E_{vacuum,PS}$ = voltage reading from power source at conditions of vacuum reading, V

Table F.1 Channel 1 Calibration

P, psia	$E_{\text{vacuum,PS}}$	E_{vacuum}	E_{PS}	E	$\frac{E}{E_{\text{PS}}} - \frac{V_{\text{vacuum}}}{E_{\text{vacuum,PS}}}$
0	10.356	0.432	10.356	0.432	0.00000
65.5	10.356	0.432	10.356	2.748	0.22364
114.9	10.356	0.432	10.356	4.492	0.39204
219.6	10.356	0.432	10.356	8.2	0.75010
427.6	10.356	0.432	10.356	15.543	1.45915
623	10.356	0.432	10.356	22.444	2.12553
823	10.356	0.432	10.356	29.522	2.80900

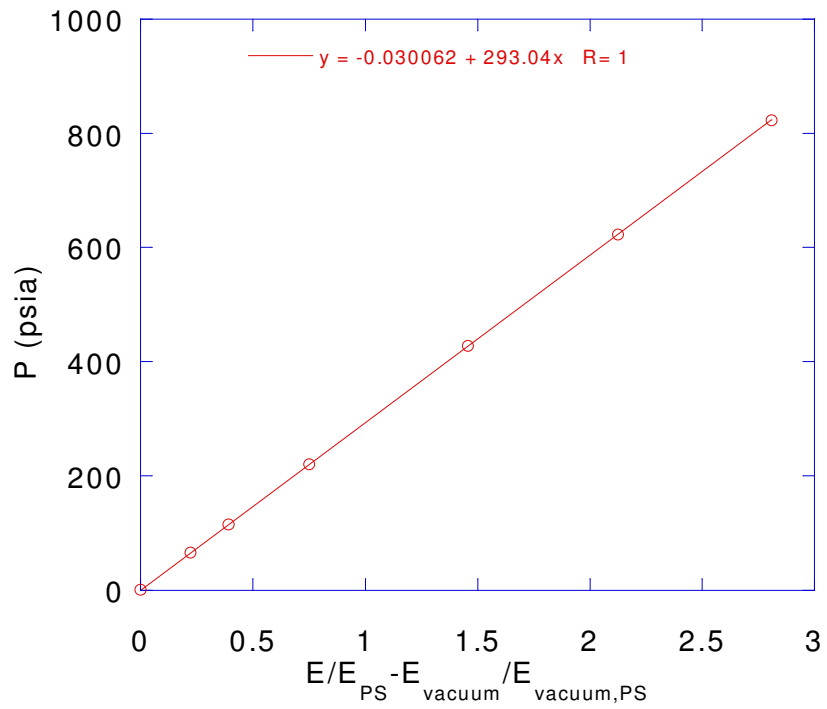


Figure F.1 Calibration curve for channel # 1

Table F.2 Channel 2 Calibration

P, psia	$E_{\text{vacuum,PS}}$	E_{vacuum}	E_{PS}	E	$\frac{E/E_{\text{PS}} - E_{\text{vacuum}}/E_{\text{vacuum,PS}}}{V_{\text{vacuum}}/E_{\text{vacuum,PS}}}$
0	10.356	-0.427	10.356	-0.427	0.00000
65.5	10.356	-0.427	10.356	2.02	0.23629
114.9	10.356	-0.427	10.356	3.862	0.41416
219.6	10.356	-0.427	10.356	7.776	0.79210
427.6	10.356	-0.427	10.356	15.543	1.54210
623	10.356	-0.427	10.356	22.861	2.24874
823	10.356	-0.427	10.356	30.345	2.97142

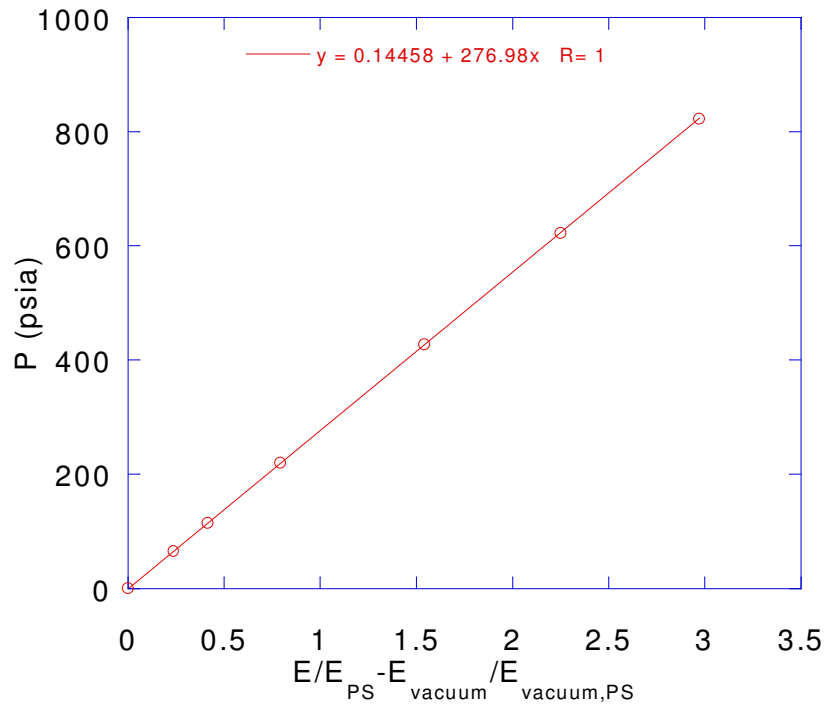


Figure F.2 Calibration curve for channel # 2

Therefore,

$$C.F_R = 1/293 \text{ and } C.F_C = 1/277. \quad (\text{F.2})$$

The equation of state:

$$PV = znRT$$

P = pressure (from transducer) [psia]

V = volume (must be calibrated) [ml]

z = compressibility factor (a function of pressure, see appendix D)

R = ideal gas constant [ml psia / mol K]

T = temperature [K]

n = number of moles [mol]

We utilize the fact that the number of sorbate moles initially introduced into the system remains constant.

Initial :

$$n_{T,I} = n_{R,I} + n_{C,I} + n_{P,I}$$

Final :

$$n_{T,F} = n_{R,F} + n_{C,F} + n_{P,F}$$

where:

R = Reservoir (or volume A) C = Sample cell (or volume B)

P = Polymer sample T = Total

I = Initial F = Final

Since $n_T = \text{constant}$, then

$$\Delta n_T = 0 = (n_{R,I} + n_{C,I} + n_{P,I}) - (n_{R,F} + n_{C,F} + n_{P,F})$$

$$= \Delta n_R + \Delta n_C + \Delta n_P$$

$$\Delta n_P = - \Delta n_C - \Delta n_R$$

We can express Δn_C and Δn_R in terms of pressure using:

$$\Delta n = \frac{V}{RT} \Delta \left(\frac{P}{z} \right)$$

Therefore,

$$\Delta n_P = \frac{1}{RT} \left[(V_C - V_P) * \left(\frac{P_{C,I}}{z_{P_{C,I}}} - \frac{P_{C,F}}{z_{P_{C,F}}} \right) + V_R * \left(\frac{P_{R,I}}{z_{P_{R,I}}} - \frac{P_{R,F}}{z_{P_{R,F}}} \right) \right] \quad (F.3)$$

where,

V_R = volume of the reservoir

$V_C - V_P$ = volume of sample cell - volume of sample

V_C and V_R were determined from calibration by using a ball of known volume.

Finally, to get the sorbate concentration, simply divide moles sorbed by the sample volume.

Table F.3 Expansion – No ball

E_{PS} (V)	E_R (mV)	E_C (mV)	P_R (psia)	P_C (psia)	z_R	z_C	V_R/V_C
10.336	4.909	-0.431	128.188	0.027	0.987	1.000	1.28391
10.336	2.950	2.265	72.655	72.291	0.992	0.992	
10.336	9.942	2.265	270.861	72.291	0.972	0.992	1.28641
10.336	6.923	6.458	185.279	184.682	0.981	0.981	
10.336	13.519	6.458	372.260	184.682	0.962	0.981	1.29011
10.336	10.677	10.411	291.696	290.640	0.970	0.970	
10.336	17.122	10.411	474.396	290.640	0.952	0.970	1.29322
10.336	14.350	14.273	395.816	394.158	0.959	0.960	
10.336	21.088	14.273	586.822	394.158	0.941	0.960	1.29479
10.336	18.173	18.340	504.189	503.172	0.949	0.949	
10.336	24.652	18.341	687.853	503.198	0.931	0.949	1.29368
Average							1.29035
Standard deviation							0.00438

Table F.4 Expansion – with ball ($V_B = 0.719 \text{ cm}^3$)

E_{PS} (V)	E_R (mV)	E_C (mV)	P_R (psia)	P_C (psia)	z_R	z_C	$V_R/(V_C - V_B)$
10.336	4.515	-0.433	117.019	0.000	0.988	1.000	1.36620
10.336	2.786	2.096	68.006	67.788	0.993	0.993	
10.336	9.930	2.095	270.520	67.761	0.972	0.993	1.36451
10.336	6.950	6.487	186.045	185.486	0.981	0.981	
10.336	13.667	6.486	376.455	185.459	0.961	0.981	1.36576
10.336	10.861	10.619	296.912	296.242	0.969	0.969	
10.336	17.383	10.620	481.795	296.269	0.951	0.969	1.37145
10.336	14.674	14.623	405.001	403.567	0.958	0.959	
10.336	20.968	14.621	583.420	403.513	0.941	0.959	1.36874
10.336	18.323	18.517	508.441	507.943	0.948	0.948	
10.336	24.886	18.518	694.486	507.970	0.931	0.948	1.37070
Average							1.368
Standard deviation							0.003

$V_R/V_C = 1.29035$ and $V_R/(V_C - V_B) = 1.368$, therefore;
 $V_R = 16.355 \text{ cm}^3$ and $V_C = 12.675 \text{ cm}^3$

Appendix G: Polynomial Fitting Parameters for Permeation and Sorption Results

G.1 Permeation Results Fitting

Table G.1 Summary of fitting parameters, A, B, C, D and E, for CO₂ and CH₄ in unconditioned and conditioned samples with 10/90 CO₂/CH₄ mixture at 200 psia and 35 °C

Parameter	CO ₂		CH ₄	
	Uncond	Cond	Uncond	Cond
A	19.593	20.882	0.87297	0.89485
B	-0.015769	-0.11291	-0.002281	-0.0024876
C	-0.0044115	-0.0022955	4.825e-06	5.1375e-06
R	1	1	1	1

Table G.2 Summary of fitting parameters, A, B, C, D and E, for CO₂ and CH₄ in unconditioned and conditioned samples with 10/90 CO₂/CH₄ + 500 ppm n-heptane mixture at 200 psia and 35 °C

Parameter	CO ₂		CH ₄	
	Uncond	Cond	Uncond	Cond
A	15.443	18.509	0.55753	0.66394
B	-0.11976	-0.3169	-0.00061258	-0.0013311
C	-0.0005279	-0.00081523	-2.7934e-08	7.8276e-08
R	1	1	1	1

Table G.3 Summary of fitting parameters, A, B, C, D and E, for CO₂ and CH₄ in unconditioned and conditioned samples with 10/90 CO₂/CH₄ + 300 ppm toluene mixture at 200 psia and 35 °C

Parameter	CO ₂		CH ₄	
	Uncond	Cond	Uncond	Cond
A	19.062	30.338	0.74309	1.1779
B	-0.047475	-0.42965	-0.0010289	-0.00089034
C	-0.0024133	0.013044	8.5658e-07	1.0512e-06
R	1	1	1	1

Table G.4 Summary of fitting parameters, A, B, C, D and E, for CO₂ and CH₄ in unconditioned and conditioned samples with 10/90 CO₂/CH₄ mixture at 600 psia and 35 °C

Parameter	CO ₂		CH ₄	
	Uncond	Cond	Uncond	Cond
A	13.066	19.2	0.4041	0.67
B	-0.12621	-0.35	-0.0004075	-0.0015444
C	0.00087081	0.00325	4.4565e-07	1.7593e-06
R	1	1	1	1

Table G.5 Summary of fitting parameters, A, B, C, D and E, for CO₂ and CH₄ in unconditioned and conditioned samples with 10/90 CO₂/CH₄ + 500 ppm n-heptane mixture at 600 psia and 35 °C

Parameter	CO ₂		CH ₄	
	Uncond	Cond	Uncond	Cond
A	12.293	14.416	0.39639	0.48313
B	-0.13167	-0.14933	-0.00065157	-0.0005618
C	0.00092086	0.00084802	6.1861e-07	3.79e-07
R	1	1	1	1

Table G.6 Summary of fitting parameters, A, B, C, D and E, for CO₂ and CH₄ in unconditioned and conditioned samples with 10/90 CO₂/CH₄ + 300 ppm toluene mixture at 600 psia and 35 °C

Parameter	CO ₂		CH ₄	
	Uncond	Cond	Uncond	Cond
A	21.175	18.612	0.64493	0.7483
B	-0.33086	0.1337	-0.0011254	0.00052793
C	0.0022969	-0.0016612	1.028e-06	-6.0509e-07
R	1	1	1	1

G.2 Sorption Results Fitting

Table G.7 Summary of fitting parameters, A, B, C, D and E, for CO₂ and CH₄ in unconditioned and conditioned samples with 10/90 CO₂/CH₄ at 600 psia and 35 °C

Parameter	CO ₂		CH ₄	
	Uncond	Cond	Uncond	Cond
A	-0.10954	-0.39815	-0.029384	-0.32924
B	1.4012	1.2557	0.14833	0.15835
C	-0.054667	-0.032233	-0.00044169	-0.00050493
D	0.0012007	0.0004567	8.1322e-07	1.0129e-06
E	-9.6909e-06	-2.5049e-06	-5.8692e-10	-8.1267e-10
R	0.99945	0.99963	0.9997	0.99984

Table G.8 Summary of fitting parameters, A, B, C, D and E, for CO₂ and CH₄ in unconditioned and conditioned samples with 10/90 CO₂/CH₄ + 300 ppm toluene mixture at 600 psia and 35 °C.

Parameter	CO ₂		CH ₄	
	Uncond	Cond	Uncond	Cond
A	-0.35637	-0.38796	-0.092317	-0.2926
B	1.1234	1.3136	0.12099	0.159
C	-0.033667	-0.04227	-0.00036429	-0.00060642
D	0.00064854	0.00075903	7.612e-07	1.3311e-06
E	-4.8373e-06	-5.1031e-06	-6.2818e-10	-1.0739e-09
R	0.99977	0.99967	0.99981	0.99981

Table G.9 Summary of fitting parameters, A, B, C, D and E, for CO₂ and CH₄ in unconditioned and conditioned samples with 10/90 CO₂/CH₄ + 500 ppm n-heptane mixture at 600 psia and 35 °C

Parameter	CO ₂		CH ₄	
	Uncond	Cond	Uncond	Cond
A	-0.2029	-0.16018	-0.3261	-0.20857
B	1.2471	1.4831	0.14692	0.15863
C	-0.038751	-0.059473	-0.00047941	-0.00053159
D	0.00068818	0.0012957	1.0072e-06	1.1122e-06
E	-4.5684e-06	-1.0294e-05	-8.1374e-10	-8.9353e-10
R	0.99967	0.99923	0.99983	0.99987

Appendix H: CO₂ Solubility and Rate Data

In this Appendix, the gas film resistance, % CO₂ removal and % approach to equilibrium are calculated as;

$$\% \text{ Gas film resistance} = (\mathbf{P}_{\text{CO}_2}^{\text{bulk}} - \mathbf{P}_{\text{CO}_2}^{\text{int}}) / (\mathbf{P}_{\text{CO}_2}^{\text{bulk}} - \mathbf{P}_{\text{CO}_2}^*) * 100\%$$

$$\% \text{ CO}_2 \text{ removal} = (\mathbf{P}_{\text{CO}_2}^{\text{IN}} - \mathbf{P}_{\text{CO}_2}^{\text{OUT}}) / \mathbf{P}_{\text{CO}_2}^{\text{IN}} * 100\%$$

$$\% \text{ Approach to equilibrium} = \mathbf{P}_{\text{CO}_2}^{\text{int}} / \mathbf{P}_{\text{CO}_2}^* * 100\%$$

Table H.1 65 wt% DGA solubility and rate

T, °C	27.05	27.20	27.25	27.75	27.73
N _{CO₂} moles/(cm ² .sec)	1.64E-07	3.97E-07	5.79E-07	7.37E-07	8.88E-07
P _{CO₂} ^{bulk} , atm	1.16E-02	2.38E-02	3.58E-02	4.82E-02	6.05E-02
P _{CO₂} ^{int} , atm	8.53E-03	1.65E-02	2.53E-02	3.49E-02	4.46E-02
P _{CO₂} [*] , atm	0.00E+00	0.00E+00	0.00E+00	0.00E+00	0.00E+00
P _{CO₂} ^{IN} , atm	1.32E-02	2.77E-02	4.12E-02	5.50E-02	6.86E-02
P _{CO₂} ^{OUT} , atm	1.01E-02	2.03E-02	3.08E-02	4.19E-02	5.31E-02
% Gas phase resistance	26	31	29	28	26
% CO ₂ Removal	23	27	25	24	23
% Approach to Equilibrium	0.00	0.00	0.00	0.00	0.00
k _{g,CO₂} moles/(cm ² .atm.sec)	5.37E-05	5.40E-05	5.52E-05	5.55E-05	5.58E-05
k _l , m/s	2.47E-05	2.47E-05	2.47E-05	2.47E-05	2.47E-05
CO ₂ ldg	0	0	0	0	0
μ, cp	11.5	11.4	11.4	11.1	11.1
ρ, g/cm ³	1.06	1.06	1.06	1.06	1.06

T, °C	40.85	41.10	41.10	41.10	41.08
N _{CO₂} moles/(cm ² .sec)	1.61E-07	3.92E-07	5.56E-07	7.22E-07	8.71E-07
P _{CO₂} ^{bulk} , atm	1.14E-02	2.34E-02	3.52E-02	4.74E-02	5.95E-02
P _{CO₂} ^{int} , atm	8.46E-03	1.63E-02	2.54E-02	3.47E-02	4.42E-02
P _{CO₂} [*] , atm	0.00E+00	0.00E+00	0.00E+00	0.00E+00	0.00E+00
P _{CO₂} ^{IN} , atm	1.29E-02	2.71E-02	4.04E-02	5.39E-02	6.73E-02
P _{CO₂} ^{OUT} , atm	9.97E-03	2.00E-02	3.06E-02	4.14E-02	5.23E-02
% Gas phase resistance	26	30	28	27	26
% CO ₂ Removal	23	26	24	23	22
% Approach to Equilibrium	0.00	0.00	0.00	0.00	0.00

k_{g,CO_2} moles/(cm ² .atm.sec)	5.50E-05	5.53E-05	5.65E-05	5.68E-05	5.71E-05
k_l m/s	3.20E-05	3.23E-05	3.23E-05	3.23E-05	3.23E-05
CO ₂ ldg	0	0	0	0	0
μ , cp	6.5	6.5	6.5	6.5	6.5
ρ , g/cm ³	1.05	1.05	1.05	1.05	1.05

T, °C	61.98	61.83	62.20	62.33	62.15
N_{CO_2} moles/(cm ² .sec)	2.78E-07	6.06E-07	9.38E-07	1.26E-06	1.59E-06
$P_{CO_2}^{bulk}$ atm	1.07E-02	2.22E-02	3.35E-02	4.55E-02	5.68E-02
$P_{CO_2}^{int}$, atm	5.36E-03	1.07E-02	1.57E-02	2.14E-02	2.64E-02
$P_{CO_2}^*$, atm	0.00E+00	0.00E+00	0.00E+00	0.00E+00	0.00E+00
$P_{CO_2}^{IN}$, atm	1.36E-02	2.85E-02	4.31E-02	5.85E-02	7.31E-02
$P_{CO_2}^{OUT}$, atm	8.22E-03	1.69E-02	2.54E-02	3.46E-02	4.32E-02
% GFR	50	52	53	53	54
% CO ₂ Removal	40	41	41	41	41
% Approach to Equilibrium	0.00	0.00	0.00	0.00	0.00
k_{g,CO_2} moles/(cm ² .atm.sec)	5.22E-05	5.24E-05	5.27E-05	5.21E-05	5.23E-05
k_l m/s	6.16E-05	6.13E-05	6.19E-05	6.21E-05	6.19E-05
CO ₂ ldg	0	0	0	0	0
μ , cp	3.3	3.3	3.3	3.3	3.3
ρ , g/cm ³	1.03	1.03	1.03	1.03	1.03

T, °C	24.05	24.25	24.70	25.15	24.65
N_{CO_2} moles/(cm ² .sec)	1.91E-07	3.05E-07	5.61E-07	6.78E-07	8.36E-07
$P_{CO_2}^{bulk}$ atm	7.95E-03	1.74E-02	2.57E-02	3.49E-02	4.38E-02
$P_{CO_2}^{int}$, atm	5.37E-03	1.33E-02	1.82E-02	2.59E-02	3.27E-02
$P_{CO_2}^*$, atm	0.00E+00	0.00E+00	0.00E+00	0.00E+00	0.00E+00
$P_{CO_2}^{IN}$, atm	9.28E-03	1.95E-02	2.95E-02	3.94E-02	4.93E-02
$P_{CO_2}^{OUT}$, atm	6.76E-03	1.55E-02	2.23E-02	3.08E-02	3.87E-02
% Gas phase resistance	33	24	29	26	25
% CO ₂ Removal	27	20	25	22	21
% Approach to Equilibrium	0.00	0.00	0.00	0.00	0.00
k_{g,CO_2} moles/(cm ² .atm.sec)	7.40E-05	7.44E-05	7.48E-05	7.52E-05	7.54E-05
k_l m/s	2.54E-05	2.53E-05	2.52E-05	2.50E-05	2.52E-05
CO ₂ ldg	0	0	0	0	0

μ , cp	13.1	13.0	12.7	12.5	12.8
ρ , g/cm ³	1.1	1.1	1.1	1.1	1.1

T, °C	40.00	40.35	41.00	41.60	41.65
N _{CO2} moles/(cm ² .sec)	2.18E-07	4.34E-07	6.84E-07	8.82E-07	1.09E-06
P ^{bulk} _{CO2} , atm	7.55E-03	1.60E-02	2.41E-02	3.25E-02	4.08E-02
P ^{int} _{CO2} , atm	4.69E-03	1.04E-02	1.53E-02	2.11E-02	2.68E-02
P [*] _{CO2} , atm	0.00E+00	0.00E+00	0.00E+00	0.00E+00	0.00E+00
P ^{IN} _{CO2} , atm	9.04E-03	1.89E-02	2.87E-02	3.83E-02	4.78E-02
P ^{OUT} _{CO2} , atm	6.24E-03	1.34E-02	2.01E-02	2.74E-02	3.44E-02
% Gas phase resistance	38	35	37	35	34
% CO2 Removal	31	29	30	29	28
% Approach to Equilibrium	0.00	0.00	0.00	0.00	0.00
k _{g,CO2} moles/(cm ² .atm.sec)	7.62E-05	7.66E-05	7.71E-05	7.75E-05	7.78E-05
k _i , m/s	3.26E-05	3.30E-05	3.38E-05	3.45E-05	3.45E-05
CO ₂ ldg	0	0	0	0	0
μ , cp	6.7	6.6	6.5	6.3	6.3
ρ , g/cm ³	1.05	1.05	1.05	1.05	1.05

T, °C	60.55	60.65	60.50	60.55	61.40
N _{CO2} moles/(cm ² .sec)	2.55E-07	5.42E-07	7.63E-07	1.07E-06	1.35E-06
P ^{bulk} _{CO2} , atm	7.31E-03	1.53E-02	2.38E-02	3.14E-02	3.91E-02
P ^{int} _{CO2} , atm	3.93E-03	8.16E-03	1.37E-02	1.74E-02	2.16E-02
P [*] _{CO2} , atm	0.00E+00	0.00E+00	0.00E+00	0.00E+00	0.00E+00
P ^{IN} _{CO2} , atm	9.08E-03	1.90E-02	2.89E-02	3.86E-02	4.80E-02
P ^{OUT} _{CO2} , atm	5.79E-03	1.21E-02	1.92E-02	2.52E-02	3.13E-02
% Gas phase resistance	46	47	42	45	45
% CO2 Removal	36	36	33	35	35
% Approach to Equilibrium	0.00	0.00	0.00	0.00	0.00
k _{g,CO2} moles/(cm ² .atm.sec)	7.55E-05	7.58E-05	7.61E-05	7.64E-05	7.70E-05
k _i , m/s	6.20E-05	6.35E-05	6.32E-05	6.28E-05	6.44E-05
CO ₂ ldg	0	0	0	0	0
μ , cp	3.4	3.4	3.4	3.4	3.3
ρ , g/cm ³	1.03	1.03	1.03	1.03	1.03

T, °C	25.10	24.88	24.68	24.83	24.95
N _{CO2} moles/(cm ² .sec)	1.59E-07	3.34E-07	5.23E-07	6.71E-07	8.40E-07
P ^{bulk} _{CO2} atm	8.92E-03	1.87E-02	2.89E-02	3.89E-02	4.86E-02
P ^{int} _{CO2} , atm	6.65E-03	1.40E-02	2.14E-02	2.93E-02	3.66E-02
P [*] _{CO2} , atm	0.00E+00	0.00E+00	0.00E+00	0.00E+00	0.00E+00
P ^{IN} _{CO2} , atm	1.01E-02	2.12E-02	3.29E-02	4.39E-02	5.47E-02
P ^{OUT} _{CO2} , atm	7.83E-03	1.65E-02	2.54E-02	3.44E-02	4.30E-02
% Gas phase resistance	25	25	26	25	25
% CO2 Removal	23	22	23	22	21
% Approach to Equilibrium	0.00	0.00	0.00	0.00	0.00
k _{g,CO2} moles/(cm ² .atm.sec)	7.00E-05	7.04E-05	6.92E-05	6.95E-05	6.99E-05
k _l m/s	2.54E-05	2.53E-05	2.53E-05	2.53E-05	2.52E-05
CO ₂ ldg	0	0	0	0	0
μ, cp	12.5	12.6	12.8	12.7	12.6
ρ, g/cm ³	1.06	1.06	1.06	1.06	1.06

T, °C	39.28	39.20	39.60	40.05	40.05
N _{CO2} moles/(cm ² .sec)	1.96E-07	4.34E-07	6.67E-07	8.67E-07	1.07E-06
P ^{bulk} _{CO2} atm	8.42E-03	1.79E-02	2.71E-02	3.64E-02	4.56E-02
P ^{int} _{CO2} , atm	5.69E-03	1.17E-02	1.77E-02	2.43E-02	3.08E-02
P [*] _{CO2} , atm	0.00E+00	0.00E+00	0.00E+00	0.00E+00	0.00E+00
P ^{IN} _{CO2} , atm	9.86E-03	2.11E-02	3.20E-02	4.27E-02	5.33E-02
P ^{OUT} _{CO2} , atm	7.12E-03	1.50E-02	2.27E-02	3.07E-02	3.87E-02
% Gas phase resistance	32	34	35	33	33
% CO2 Removal	28	29	29	28	27
% Approach to Equilibrium	0.00	0.00	0.00	0.00	0.00
k _{g,CO2} moles/(cm ² .atm.sec)	7.19E-05	7.07E-05	7.11E-05	7.15E-05	7.19E-05
k _l m/s	3.22E-05	3.28E-05	3.32E-05	3.37E-05	3.37E-05
CO ₂ ldg	0	0	0	0	0
μ, cp	6.9	6.9	6.8	6.7	6.7
ρ, g/cm ³	1.05	1.05	1.05	1.05	1.05

T, °C	59.30	59.45	59.58	59.95	59.80
N _{CO2} moles/(cm ² .sec)	2.85E-07	6.49E-07	9.99E-07	1.32E-06	1.65E-06
P ^{bulk} _{CO2} atm	7.43E-03	1.52E-02	2.30E-02	3.08E-02	3.86E-02

$P_{CO_2}^{int}$, atm	3.59E-03	6.47E-03	9.62E-03	1.33E-02	1.67E-02
$P_{CO_2}^*$, atm	0.00E+00	0.00E+00	0.00E+00	0.00E+00	0.00E+00
$P_{CO_2}^{IN}$, atm	9.52E-03	2.00E-02	3.02E-02	4.03E-02	5.03E-02
$P_{CO_2}^{OUT}$, atm	5.67E-03	1.13E-02	1.70E-02	2.30E-02	2.89E-02
% Gas phase resistance	52	57	58	57	57
% CO2 Removal	40	44	44	43	43
% Approach to Equilibrium	0.00	0.00	0.00	0.00	0.00
k_{g,CO_2} moles/(cm ² .atm.sec)	7.40E-05	7.44E-05	7.48E-05	7.53E-05	7.55E-05
k_l m/s	5.72E-05	5.81E-05	5.76E-05	5.82E-05	5.89E-05
CO ₂ ldg	0	0	0	0	0
μ , cp	3.6	3.5	3.5	3.5	3.5
ρ , g/cm ³	1.03	1.03	1.03	1.03	1.03

T, °C	25.00	24.83	24.95	25.08	25.23
N_{CO_2} moles/(cm ² .sec)	1.53E-07	3.21E-07	5.04E-07	6.51E-07	7.69E-07
$P_{CO_2}^{bulk}$ atm	9.17E-03	1.93E-02	2.91E-02	3.91E-02	4.91E-02
$P_{CO_2}^{int}$, atm	6.93E-03	1.46E-02	2.18E-02	2.97E-02	3.81E-02
$P_{CO_2}^*$, atm	0.00E+00	0.00E+00	0.00E+00	0.00E+00	0.00E+00
$P_{CO_2}^{IN}$, atm	1.03E-02	2.17E-02	3.28E-02	4.38E-02	5.47E-02
$P_{CO_2}^{OUT}$, atm	8.09E-03	1.70E-02	2.56E-02	3.46E-02	4.40E-02
% Gas phase resistance	24	24	25	24	22
% CO2 Removal	22	21	22	21	20
% Approach to Equilibrium	0.00	0.00	0.00	0.00	0.00
k_{g,CO_2} moles/(cm ² .atm.sec)	6.85E-05	6.88E-05	6.92E-05	6.96E-05	7.00E-05
k_l m/s	2.53E-05	2.53E-05	2.53E-05	2.52E-05	2.52E-05
CO ₂ ldg	0	0	0	0	0
μ , cp	12.6	12.7	12.6	12.5	12.4
ρ , g/cm ³	1.06	1.06	1.06	1.06	1.06

T, °C	40.18	39.78	40.00	40.33	39.88
N_{CO_2} moles/(cm ² .sec)	1.77E-07	4.52E-07	6.80E-07	9.31E-07	1.09E-06
$P_{CO_2}^{bulk}$ atm	8.74E-03	1.77E-02	2.70E-02	3.59E-02	4.55E-02
$P_{CO_2}^{int}$, atm	6.24E-03	1.13E-02	1.74E-02	2.29E-02	3.03E-02
$P_{CO_2}^*$, atm	0.00E+00	0.00E+00	0.00E+00	0.00E+00	0.00E+00
$P_{CO_2}^{IN}$, atm	1.01E-02	2.11E-02	3.20E-02	4.27E-02	5.33E-02
$P_{CO_2}^{OUT}$, atm	7.54E-03	1.47E-02	2.25E-02	2.98E-02	3.85E-02

% Gas phase resistance	29	36	35	36	33
% CO2 Removal	25	30	30	30	28
% Approach to Equilibrium	0.00	0.00	0.00	0.00	0.00
k_{g,CO_2} moles/(cm ² .atm.sec)	7.05E-05	7.08E-05	7.12E-05	7.16E-05	7.19E-05
k_l , m/s	3.38E-05	3.33E-05	3.36E-05	3.40E-05	3.34E-05
CO ₂ ldg	0	0	0	0	0
μ , cp	6.7	6.8	6.7	6.6	6.8
ρ , g/cm ³	1.05	1.05	1.05	1.05	1.05

T, °C	59.78	60.08	60.25	59.93
N_{CO_2} moles/(cm ² .sec)	3.13E-07	7.01E-07	1.08E-06	1.42E-06
$P_{CO_2}^{bulk}$, atm	7.17E-03	1.47E-02	2.22E-02	3.00E-02
$P_{CO_2}^{int}$, atm	2.95E-03	5.31E-03	7.81E-03	1.11E-02
$P_{CO_2}^*$, atm	0.00E+00	0.00E+00	0.00E+00	0.00E+00
$P_{CO_2}^{IN}$, atm	9.50E-03	1.99E-02	3.01E-02	4.03E-02
$P_{CO_2}^{OUT}$, atm	5.27E-03	1.05E-02	1.58E-02	2.17E-02
% Gas phase resistance	59	64	65	63
% CO2 Removal	45	47	47	46
% Approach to Equilibrium	0.00	0.00	0.00	0.00
k_{g,CO_2} moles/(cm ² .atm.sec)	7.42E-05	7.46E-05	7.50E-05	7.52E-05
k_l , m/s	6.24E-05	6.29E-05	6.32E-05	6.26E-05
CO ₂ ldg	0	0	0	0
μ , cp	3.5	3.5	3.5	3.5
ρ , g/cm ³	1.03	1.03	1.03	1.03

T, °C	24.70	24.60	24.70	24.90	24.90
N_{CO_2} moles/(cm ² .sec)	2.24E-07	4.72E-07	7.30E-07	9.04E-07	1.07E-06
$P_{CO_2}^{int}$, atm	9.93E-03	1.99E-02	3.02E-02	4.25E-02	5.50E-02
$P_{CO_2}^*$, atm	0.00E+00	0.00E+00	0.00E+00	0.00E+00	0.00E+00
k_l , m/s	2.62E-05	2.61E-05	2.62E-05	2.64E-05	2.64E-05
CO ₂ ldg	0	0	0	0	0
μ , cp	14.9	15.0	15.0	14.7	14.7
ρ , g/cm ³	1.07	1.07	1.07	1.07	1.07

T, °C	37.90	38.20	39.00	38.80
-------	-------	-------	-------	-------

N_{CO_2} moles/(cm ² .sec)	2.65E-07	5.84E-07	8.75E-07	1.16E-06
$P_{CO_2}^{int}$, atm	8.22E-03	1.63E-02	2.67E-02	3.55E-02
$P_{CO_2}^*$, atm	0.00E+00	0.00E+00	0.00E+00	0.00E+00
k_l , m/s	3.76E-05	3.78E-05	3.84E-05	3.82E-05
CO ₂ ldg	0	0	0	0
μ , cp	7.6	7.6	7.6	7.6
ρ , g/cm ³	1.06	1.06	1.06	1.06

T, °C	58.70	59.30	59.00	59.30	59.10
N_{CO_2} moles/(cm ² .sec)	3.10E-07	6.51E-07	1.02E-06	1.35E-06	1.67E-06
$P_{CO_2}^{int}$, atm	7.74E-03	1.51E-02	2.18E-02	2.94E-02	3.73E-02
$P_{CO_2}^*$, atm	0.00E+00	0.00E+00	0.00E+00	0.00E+00	0.00E+00
k_l , m/s	5.76E-05	5.84E-05	5.80E-05	5.84E-05	5.82E-05
CO ₂ ldg	0	0	0	0	0
μ , cp	4.1	4.1	4.1	4.1	4.1
ρ , g/cm ³	1.05	1.05	1.05	1.05	1.05

T, °C	25.08	25.05	25.90	26.18
N_{CO_2} moles/(cm ² .sec)	2.76E-07	5.88E-07	8.78E-07	1.15E-06
$P_{CO_2}^{bulk}$, atm	2.39E-02	5.08E-02	7.75E-02	1.04E-01
$P_{CO_2}^{int}$, atm	1.21E-02	2.54E-02	3.98E-02	5.49E-02
$P_{CO_2}^*$, atm	4.49E-06	5.10E-06	1.22E-05	1.36E-05
$P_{CO_2}^{IN}$, atm	3.04E-02	6.46E-02	9.78E-02	1.31E-01
$P_{CO_2}^{OUT}$, atm	1.85E-02	3.91E-02	6.03E-02	8.18E-02
% Gas phase resistance	49	50	49	47
% CO ₂ Removal	39	39	38	37
% Approach to Equilibrium	0.00	0.00	0.00	0.00
k_{g,CO_2} moles/(cm ² .atm.sec)	2.34E-05	2.32E-05	2.33E-05	2.34E-05
k_l , m/s	2.73E-05	2.77E-05	2.81E-05	2.68E-05
CO ₂ ldg	0.078496	0.082639	0.109048	0.11185
μ , cp	15.1	15.5	15.7	14.4
ρ , g/cm ³	1.09	1.10	1.12	1.10

T, °C	39.40	39.85	40.20	40.60
N_{CO_2} moles/(cm ² .sec)	2.70E-07	5.71E-07	8.78E-07	1.14E-06

$P_{CO_2}^{bulk}$, atm	2.42E-02	5.08E-02	7.69E-02	1.04E-01
$P_{CO_2}^{int}$, atm	1.27E-02	2.64E-02	3.97E-02	5.55E-02
$P_{CO_2}^*$, atm	6.57E-05	6.75E-05	1.01E-04	1.11E-04
$P_{CO_2}^{IN}$, atm	3.05E-02	6.40E-02	9.70E-02	1.29E-01
$P_{CO_2}^{OUT}$, atm	1.88E-02	3.95E-02	5.97E-02	8.15E-02
% Gas phase resistance	48	48	48	47
% CO2 Removal	38	38	38	37
% Approach to Equilibrium	0.01	0.00	0.00	0.00
k_{g,CO_2} moles/(cm ² .atm.sec)	2.34E-05	2.35E-05	2.36E-05	2.37E-05
k_l , m/s	2.79E-05	2.80E-05	2.74E-05	2.84E-05
CO ₂ ldg	0.100509	0.098915	0.11512	0.116795
μ , cp	8.5	8.5	8.8	8.3
ρ , g/cm ³	1.09	1.10	1.11	1.10

T, °C	59.15	58.75	59.18	58.83
N_{CO_2} moles/(cm ² .sec)	3.32E-07	7.52E-07	1.10E-06	1.42E-06
$P_{CO_2}^{bulk}$, atm	2.23E-02	4.59E-02	7.20E-02	9.85E-02
$P_{CO_2}^{int}$, atm	8.31E-03	1.40E-02	2.51E-02	3.77E-02
$P_{CO_2}^*$, atm	1.12E-03	1.09E-03	1.22E-03	1.20E-03
$P_{CO_2}^{IN}$, atm	3.02E-02	6.39E-02	9.81E-02	1.32E-01
$P_{CO_2}^{OUT}$, atm	1.59E-02	3.16E-02	5.10E-02	7.12E-02
% Gas phase resistance	66	71	66	62
% CO2 Removal	47	50	48	46
% Approach to Equilibrium	0.14	0.08	0.05	0.03
k_{g,CO_2} moles/(cm ² .atm.sec)	2.37E-05	2.36E-05	2.34E-05	2.33E-05
k_l , m/s	5.16E-05	5.08E-05	5.13E-05	5.07E-05
CO ₂ ldg	0.099954	0.101709	0.104342	0.105935
μ , cp	4.3	4.4	4.4	4.4
ρ , g/cm ³	1.08	1.08	1.08	1.09

T, °C	23.63	23.75	23.95	24.03
N_{CO_2} moles/(cm ² .sec)	2.41E-07	5.10E-07	7.51E-07	1.00E-06
$P_{CO_2}^{bulk}$, atm	3.87E-02	8.05E-02	1.23E-01	1.67E-01
$P_{CO_2}^{int}$, atm	2.46E-02	5.10E-02	7.99E-02	1.08E-01
$P_{CO_2}^*$, atm	1.29E-04	1.44E-04	1.41E-04	1.27E-04
$P_{CO_2}^{IN}$, atm	4.66E-02	9.71E-02	1.48E-01	1.99E-01

$P_{CO_2}^{OUT}$, atm	3.17E-02	6.60E-02	1.02E-01	1.39E-01
% Gas phase resistance	36	37	35	35
% CO2 Removal	32	32	31	30
% Approach to Equilibrium	0.01	0.00	0.00	0.00
k_{g,CO_2} moles/(cm ² .atm.sec)	1.71E-05	1.72E-05	1.72E-05	1.71E-05
k_l , m/s	3.77E-05	3.79E-05	3.76E-05	3.71E-05
CO ₂ ldg	0.231037	0.236329	0.233932	0.228127
μ , cp	27.5	27.8	27.2	26.5
ρ , g/cm ³	1.11	1.11	1.11	1.11

T, °C	38.75	38.88	39.28	39.38
N_{CO_2} moles/(cm ² .sec)	7.11E-07	1.36E-06	1.99E-06	1.06E-06
$P_{CO_2}^{bulk}$ atm	8.29E-02	1.75E-01	2.68E-01	1.30E-01
$P_{CO_2}^{int}$, atm	3.74E-02	8.70E-02	1.39E-01	6.09E-02
$P_{CO_2}^*$, atm	6.20E-04	6.70E-04	7.34E-04	8.14E-04
$P_{CO_2}^{IN}$, atm	1.10E-01	2.25E-01	3.41E-01	1.71E-01
$P_{CO_2}^{OUT}$, atm	6.07E-02	1.32E-01	2.07E-01	9.65E-02
% Gas phase resistance	55	50	48	54
% CO2 Removal	45	41	39	44
% Approach to Equilibrium	0.02	0.01	0.01	0.01
k_{g,CO_2} moles/(cm ² .atm.sec)	1.57E-05	1.56E-05	1.55E-05	1.53E-05
k_l , m/s	2.85E-05	2.87E-05	2.87E-05	2.89E-05
CO ₂ ldg	0.229324	0.232747	0.236161	0.24247
μ , cp	13.8	13.9	13.8	14.1
ρ , g/cm ³	1.10	1.10	1.10	1.10

T, °C	59.18	59.50	60.10	59.88
N_{CO_2} moles/(cm ² .sec)	3.23E-07	7.40E-07	1.15E-06	1.54E-06
$P_{CO_2}^{bulk}$ atm	3.82E-02	7.87E-02	1.18E-01	1.59E-01
$P_{CO_2}^{int}$, atm	1.86E-02	3.34E-02	4.77E-02	6.52E-02
$P_{CO_2}^*$, atm	8.61E-03	9.57E-03	1.13E-02	1.16E-02
$P_{CO_2}^{IN}$, atm	5.00E-02	1.06E-01	1.60E-01	2.14E-01
$P_{CO_2}^{OUT}$, atm	2.85E-02	5.66E-02	8.42E-02	1.14E-01
% Gas phase resistance	66	66	66	64
% CO2 Removal	43	47	48	47
% Approach	0.46	0.29	0.24	0.18

to Equilibrium				
k_{g,CO_2} moles/(cm ² .atm.sec)	1.65E-05	1.63E-05	1.64E-05	1.64E-05
k_l m/s	3.95E-05	3.94E-05	3.97E-05	3.90E-05
CO ₂ ldg	0.240598	0.246212	0.253177	0.257245
μ , cp	6.3	6.4	6.3	6.5
ρ , g/cm ³	1.09	1.09	1.09	1.10

T, °C	23.33	24.43	24.08	24.40
N_{CO_2} moles/(cm ² .sec)	6.38E-07	1.25E-06	1.81E-06	2.32E-06
$P_{CO_2}^{int}$, atm	6.34E-02	1.34E-01	1.96E-01	2.82E-01
$P_{CO_2}^*$, atm	3.15E-04	3.54E-04	3.30E-04	3.53E-04
k_l m/s	1.76E-05	1.83E-05	1.81E-05	1.83E-05
CO ₂ ldg	0.279	0.28	0.278	0.28
μ , cp	32.9	30.6	31.1	30.7
ρ , g/cm ³	1.12	1.12	1.12	1.12

T, °C	39.73	40.30	40.40	40.53
N_{CO_2} moles/(cm ² .sec)	2.52E-07	5.36E-07	7.46E-07	9.50E-07
$P_{CO_2}^{int}$, atm	3.48E-02	7.26E-02	1.18E-01	1.64E-01
$P_{CO_2}^*$, atm	2.31E-03	3.60E-03	2.55E-03	1.99E-03
k_l m/s	2.51E-05	2.48E-05	2.54E-05	2.60E-05
CO ₂ ldg	0.306	0.33	0.308	0.291
μ , cp	16.5	17.2	16.2	15.4
ρ , g/cm ³	1.12	1.12	1.12	1.12

T, °C	58.80	59.13	59.18	59.28
N_{CO_2} moles/(cm ² .sec)	2.33E-07	5.47E-07	9.03E-07	1.16E-06
$P_{CO_2}^{int}$, atm	4.13E-02	7.12E-02	9.99E-02	1.41E-01
$P_{CO_2}^*$, atm	1.74E-02	1.86E-02	1.98E-02	2.03E-02
k_l m/s	4.20E-05	4.22E-05	4.21E-05	4.22E-05
CO ₂ ldg	0.297	0.299	0.303	0.304
μ , cp	7.5	7.5	7.5	7.5
ρ , g/cm ³	1.11	1.11	1.11	1.11

T, °C	25.10	25.40	25.40	25.60	25.90
N_{CO_2}	2.82E-07	5.87E-07	9.12E-07	1.18E-06	1.45E-06

moles/(cm ² .sec)					
P ^{int} _{CO2} , atm	4.96E-03	1.06E-02	1.88E-02	2.63E-02	3.80E-02
P [*] _{CO2} , atm	4.29E-05	4.84E-05	5.81E-05	2.64E-04	3.29E-04
k _f m/s	2.21E-05	2.24E-05	2.23E-05	2.24E-05	2.26E-05
CO ₂ ldg	0.167	0.164	0.171	0.177	0.177
μ, cp	21.2	20.7	20.9	20.8	20.4
ρ, g/cm ³	1.1	1.1	1.1	1.1	1.1

T, °C	38.80	38.70	39.30	39.80	40.00
N _{CO2} moles/(cm ² .sec)	4.23E-07	8.68E-07	1.30E-06	1.72E-06	2.10E-06
P ^{int} _{CO2} , atm	1.70E-02	3.45E-02	5.17E-02	7.19E-02	9.13E-02
P [*] _{CO2} , atm	4.08E-03	4.66E-03	5.19E-03	3.54E-04	3.30E-04
k _f m/s	3.12E-05	3.10E-05	3.14E-05	3.18E-05	3.18E-05
CO ₂ ldg	0.173	0.176	0.179	0.181	0.183
μ, cp	12.0	12.1	11.9	11.7	11.6
ρ, g/cm ³	1.09	1.09	1.09	1.09	1.09

T, °C	59.20	59.50	59.60	59.90	59.70
N _{CO2} moles/(cm ² .sec)	2.96E-07	7.14E-07	1.09E-06	1.36E-06	1.68E-06
P ^{int} _{CO2} , atm	1.46E-02	2.33E-02	3.49E-02	5.69E-02	7.37E-02
P [*] _{CO2} , atm	3.53E-04	2.31E-03	3.60E-03	2.55E-03	1.99E-03
k _f m/s	5.06E-05	5.09E-05	5.09E-05	5.11E-05	5.09E-05
CO ₂ ldg	0.182	0.184	0.188	0.194	0.195
μ, cp	5.4	5.4	5.4	5.4	5.4
ρ, g/cm ³	1.08	1.08	1.08	1.08	1.08

T, °C	24.4	24.8	25.1	24.8	25.0
N _{CO2} moles/(cm ² .sec)	1.36E-06	2.38E-06	3.43E-06	1.82E-06	2.72E-06
P ^{bulk} _{CO2} atm	3.34E-01	6.67E-01	9.53E-01	5.52E-01	8.16E-01
P ^{int} _{CO2} , atm	1.91E-01	4.29E-01	6.28E-01	3.51E-01	5.55E-01
P [*] _{CO2} , atm	1.48E-03	1.38E-03	3.22E-03	3.22E-03	3.18E-03
P ^{LN} _{CO2} , atm	4.27E-01	8.09E-01	1.13E+00	6.77E-01	9.64E-01
P ^{OUT} _{CO2} , atm	2.55E-01	5.43E-01	7.94E-01	4.43E-01	6.84E-01
% Gas phase resistance	43	36	34	37	32
% CO2 Removal	40	33	30	34	29
% Approach to Equilibrium	0.01	0.00	0.01	0.01	0.01

k_{g,CO_2} moles/(cm ² .atm.sec)	9.54E-06	1.00E-05	1.06E-05	9.03E-06	1.04E-05
k_l , m/s	1.68E-05	1.73E-05	1.67E-05	1.65E-05	1.66E-05
CO ₂ ldg	0.36	0.35	0.39	0.39	0.39
μ , cp	37.9	36.2	38.9	40.0	39.4
ρ , g/cm ³	1.14	1.14	1.15	1.15	1.15

T, °C	39.3	39.4	40.0	40.0
N_{CO_2} moles/(cm ² .sec)	1.02E-06	1.21E-06	1.41E-06	1.68E-06
$P_{CO_2}^{bulk}$, atm	3.50E-01	5.36E-01	7.24E-01	9.15E-01
$P_{CO_2}^{int}$, atm	2.47E-01	4.18E-01	5.86E-01	7.49E-01
$P_{CO_2}^*$, atm	8.66E-03	8.40E-03	9.07E-03	9.59E-03
$P_{CO_2}^{IN}$, atm	4.16E-01	6.08E-01	8.03E-01	1.01E+00
$P_{CO_2}^{OUT}$, atm	2.91E-01	4.71E-01	6.50E-01	8.30E-01
% Gas phase resistance	30	22	19	18
% CO ₂ Removal	30	23	19	18
% Approach to Equilibrium	0.04	0.02	0.02	0.01
k_{g,CO_2} moles/(cm ² .atm.sec)	9.89E-06	1.02E-05	1.02E-05	1.01E-05
k_l , m/s	2.45E-05	2.46E-05	2.50E-05	2.48E-05
CO ₂ ldg	0.38	0.38	0.38	0.39
μ , cp	20.3	20.1	19.7	19.9
ρ , g/cm ³	1.14	1.14	1.14	1.14

T, °C	41.3	41.1	41.2
N_{CO_2} moles/(cm ² .sec)	-2.33E-09	3.54E-10	2.02E-09
$P_{CO_2}^{bulk}$, atm	3.75E-07	8.45E-05	1.57E-04
$P_{CO_2}^{int}$, atm	3.86E-05	7.87E-05	1.25E-04
$P_{CO_2}^*$, atm	7.97E-05	7.97E-05	7.97E-05
$P_{CO_2}^{IN}$, atm	4.21E-48	8.74E-05	1.74E-04
$P_{CO_2}^{OUT}$, atm	3.71E-05	8.17E-05	1.42E-04
% Gas phase resistance	48	121	42
% CO ₂ Removal	-100	7	19
% Approach to Equilibrium	2.06	1.01	0.64
k_{g,CO_2} moles/(cm ² .atm.sec)	6.08E-05	6.12E-05	6.16E-05
k_l , m/s	3.02E-05	3.00E-05	3.01E-05
CO ₂ ldg	0.107	0.107	0.107

μ , cp	8.2	8.2	8.2
ρ , g/cm ³	1.07	1.07	1.07

T, °C	58.5	58.7	58.3
N_{CO_2} moles/(cm ² .sec)	-2.87E-08	-8.19E-09	-1.32E-09
$P_{CO_2}^{bulk}$, atm	4.81E-06	1.08E-03	1.35E-03
$P_{CO_2}^{int}$, atm	5.00E-04	1.21E-03	1.37E-03
$P_{CO_2}^*$, atm	1.45E-03	1.45E-03	1.45E-03
$P_{CO_2}^{IN}$, atm	4.42E-48	1.02E-03	1.34E-03
$P_{CO_2}^{OUT}$, atm	4.88E-04	1.14E-03	1.36E-03
% Gas phase resistance	34	35	21
% CO2 Removal	-100	-12	-2
% Approach to Equilibrium	2.89	1.20	1.06
k_{g,CO_2} moles/(cm ² .atm.sec)	5.79E-05	6.25E-05	6.29E-05
k_l , m/s	5.15E-06	5.18E-06	5.12E-06
CO ₂ ldg	0.104	0.106	0.107
μ , cp	4.6	4.5	4.6
ρ , g/cm ³	1.06	1.06	1.06

T, °C	23.8	24.1	24.5	24.6
N_{CO_2} moles/(cm ² .sec)	-1.92E-09	-3.44E-10	3.02E-09	1.72E-09
$P_{CO_2}^{bulk}$, atm	3.55E-07	1.01E-04	3.59E-04	2.76E-04
$P_{CO_2}^{int}$, atm	3.60E-05	1.08E-04	3.04E-04	2.45E-04
$P_{CO_2}^*$, atm	1.39E-04	1.39E-04	1.39E-04	1.39E-04
$P_{CO_2}^{IN}$, atm	4.74E-48	9.83E-05	3.86E-04	2.92E-04
$P_{CO_2}^{OUT}$, atm	3.50E-05	1.05E-04	3.33E-04	2.61E-04
% Gas phase resistance	26	17	25	23
% CO2 Removal	-100	-6	14	11
% Approach to Equilibrium	3.85	1.29	0.46	0.57
k_{g,CO_2} moles/(cm ² .atm.sec)	5.38E-05	5.42E-05	5.53E-05	5.49E-05
k_l , m/s	1.96E-05	1.98E-05	2.01E-05	2.02E-05
CO ₂ ldg	0.230	0.230	0.230	0.230
μ , cp	27.0	26.5	25.9	25.6
ρ , g/cm ³	1.11	1.11	1.11	1.11

T, °C	39.5	39.7	39.6	39.4
N _{CO2} moles/(cm ² .sec)	-6.39E-09	-4.75E-09	4.03E-09	-9.63E-10
P ^{bulk} _{CO2} atm	2.37E-04	4.12E-04	1.04E-03	7.32E-04
P ^{int} _{CO2} , atm	3.48E-04	4.95E-04	9.69E-04	7.49E-04
P [*] _{CO2} , atm	7.60E-04	7.60E-04	7.60E-04	7.60E-04
P ^{IN} _{CO2} , atm	1.86E-04	3.73E-04	1.07E-03	7.24E-04
P ^{OUT} _{CO2} , atm	2.96E-04	4.54E-04	1.00E-03	7.40E-04
% GFR	21	24	24	59
% CO2 Removal	-59	-22	6	-2
% Approach to Equilibrium	2.19	1.54	0.78	1.02
k _{g,CO2} moles/(cm ² .atm.sec)	5.75E-05	5.74E-05	5.94E-05	5.88E-05
k _l m/s	2.91E-05	2.90E-05	2.90E-05	2.91E-05
CO ₂ ldg	0.232	0.232	0.232	0.232
μ, cp	13.5	13.4	13.5	13.6
ρ, g/cm ³	1.10	1.10	1.10	1.10

T, °C	60.3	60.2	60.1	60.1
N _{CO2} moles/(cm ² .sec)	2.34E-08	-2.41E-08	7.06E-08	-8.16E-08
P ^{bulk} _{CO2} atm	8.80E-03	6.63E-03	1.10E-02	4.51E-03
P ^{int} _{CO2} , atm	8.44E-03	7.00E-03	9.89E-03	5.76E-03
P [*] _{CO2} , atm	7.85E-03	7.85E-03	7.85E-03	7.85E-03
P ^{IN} _{CO2} , atm	8.98E-03	6.45E-03	1.15E-02	3.91E-03
P ^{OUT} _{CO2} , atm	8.62E-03	6.82E-03	1.04E-02	5.17E-03
% Gas phase resistance	38	30	35	37
% CO2 Removal	4	-6	9	-32
% Approach to Equilibrium	0.93	1.12	0.79	1.36
k _{g,CO2} moles/(cm ² .atm.sec)	6.53E-05	6.52E-05	6.53E-05	6.51E-05
k _l m/s	4.29E-05	4.29E-05	4.27E-05	4.27E-05
CO ₂ ldg	0.242	0.242	0.242	0.242
μ, cp	6.1	6.1	6.1	6.1
ρ, g/cm ³	1.09	1.09	1.09	1.09

T, °C	41.6	41.4	41.9	41.8	41.8
N _{CO2} moles/(cm ² .sec)	1.17E-08	-3.43E-10	-5.32E-09	6.56E-09	-7.86E-09
P ^{bulk} _{CO2} atm	3.08E-03	1.95E-03	1.25E-03	2.57E-03	8.44E-04

$P_{CO_2}^{int}$, atm	2.24E-03	1.98E-03	1.67E-03	2.07E-03	1.49E-03
$P_{CO_2}^*$, atm	1.83E-03	1.83E-03	1.83E-03	1.83E-03	1.83E-03
$P_{CO_2}^{IN}$, atm	3.58E-03	1.94E-03	1.02E-03	2.86E-03	5.22E-04
$P_{CO_2}^{OUT}$, atm	2.62E-03	1.97E-03	1.51E-03	2.29E-03	1.28E-03
% Gas phase resistance	67	-22	73	68	66
% CO2 Removal	27	-2	-49	20	-145
% Approach to Equilibrium	0.82	0.92	1.09	0.89	1.23
k_{g,CO_2} moles/(cm ² .atm.sec)	1.39E-05	1.30E-05	1.25E-05	1.31E-05	1.21E-05
k_l , m/s	2.73E-05	2.73E-05	2.74E-05	2.74E-05	2.74E-05
CO ₂ ldg	0.243	0.248	0.250	0.261	0.255
μ , cp	12.1	12.1	12.1	12.1	12.1
ρ , g/cm ³	1.11	1.11	1.11	1.11	1.11

Table H.2 23.5 wt% MOR solubility and rate

T, °C	24.93	25.03	25.43	25.28	25.58
N_{CO_2} moles/(cm ² .sec)	1.91E-07	4.60E-07	6.90E-07	8.16E-07	9.91E-07
$P_{CO_2}^{bulk}$ atm	1.11E-02	2.28E-02	3.47E-02	4.75E-02	5.97E-02
$P_{CO_2}^{int}$, atm	7.64E-03	1.44E-02	2.22E-02	3.28E-02	4.19E-02
$P_{CO_2}^*$, atm	0.00E+00	0.00E+00	0.00E+00	0.00E+00	0.00E+00
$P_{CO_2}^{IN}$, atm	1.30E-02	2.73E-02	4.13E-02	5.52E-02	6.88E-02
$P_{CO_2}^{OUT}$, atm	9.47E-03	1.89E-02	2.89E-02	4.06E-02	5.14E-02
% Gas phase resistance	32	37	36	31	30
% CO2 Removal	27	31	30	26	25
% Approach to Equilibrium	0.00	0.00	0.00	0.00	0.00
k_{g,CO_2} moles/(cm ² .atm.sec)	5.45E-05	5.47E-05	5.50E-05	5.53E-05	5.56E-05
k_l , m/s	6.65E-05	6.65E-05	6.67E-05	6.66E-05	6.67E-05
CO ₂ ldg	0.03	0.03	0.03	0.03	0.03
μ , cp	2.0	2.0	2.0	2.0	2.0

T, °C	40.03	40.05	40.15	40.35	40.28
N_{CO_2} moles/(cm ² .sec)	1.96E-07	4.59E-07	6.83E-07	9.15E-07	1.09E-06
$P_{CO_2}^{bulk}$ atm	1.09E-02	2.23E-02	3.41E-02	4.55E-02	5.74E-02
$P_{CO_2}^{int}$, atm	7.36E-03	1.42E-02	2.20E-02	2.94E-02	3.82E-02
$P_{CO_2}^*$, atm	0.00E+00	0.00E+00	0.00E+00	0.00E+00	0.00E+00
$P_{CO_2}^{IN}$, atm	1.27E-02	2.67E-02	4.04E-02	5.40E-02	6.74E-02

$P_{CO_2}^{OUT}$, atm	9.20E-03	1.85E-02	2.84E-02	3.80E-02	4.85E-02
% Gas phase resistance	32	37	36	35	33
% CO2 Removal	28	31	30	30	28
% Approach to Equilibrium	0.00	0.00	0.00	0.00	0.00
k_{g,CO_2} moles/(cm ² .atm.sec)	5.58E-05	5.61E-05	5.64E-05	5.67E-05	5.70E-05
k_f , m/s	8.87E-05	8.87E-05	8.88E-05	8.89E-05	8.88E-05
CO ₂ ldg	0.03	0.03	0.03	0.03	0.03
μ , cp	1.3	1.3	1.3	1.3	1.3

T, °C	59.20	59.18	59.48	59.63	59.78
N_{CO_2} moles/(cm ² .sec)	1.94E-07	4.38E-07	6.36E-07	8.62E-07	1.12E-06
$P_{CO_2}^{bulk}$ atm	1.14E-02	2.36E-02	3.61E-02	4.81E-02	5.96E-02
$P_{CO_2}^{int}$, atm	7.74E-03	1.54E-02	2.43E-02	3.22E-02	3.90E-02
$P_{CO_2}^*$, atm	9.87E-04	9.87E-04	9.87E-04	9.87E-04	9.87E-04
$P_{CO_2}^{IN}$, atm	1.33E-02	2.79E-02	4.22E-02	5.64E-02	7.03E-02
$P_{CO_2}^{OUT}$, atm	9.64E-03	1.97E-02	3.05E-02	4.07E-02	5.01E-02
% Gas phase resistance	35	36	34	34	35
% CO2 Removal	28	29	28	28	29
% Approach to Equilibrium	0.13	0.06	0.04	0.03	0.03
k_{g,CO_2} moles/(cm ² .atm.sec)	5.33E-05	5.36E-05	5.39E-05	5.42E-05	5.45E-05
k_f , m/s	1.20E-04	1.20E-04	1.21E-04	1.21E-04	1.21E-04
CO ₂ ldg	0.03	0.03	0.03	0.03	0.03
μ , cp	0.90	0.90	0.90	0.90	0.90

T, °C	24.23	24.80	24.23	24.48	24.43
N_{CO_2} moles/(cm ² .sec)	-1.59E-09	3.78E-10	1.99E-09	3.75E-09	5.44E-09
$P_{CO_2}^{bulk}$ atm	3.01E-07	9.70E-05	1.81E-04	2.62E-04	3.42E-04
$P_{CO_2}^{int}$, atm	2.96E-05	9.01E-05	1.45E-04	1.94E-04	2.47E-04
$P_{CO_2}^*$, atm	7.93E-05	7.93E-05	7.93E-05	7.93E-05	7.93E-05
$P_{CO_2}^{IN}$, atm	4.85E-48	1.01E-04	2.00E-04	2.98E-04	3.93E-04
$P_{CO_2}^{OUT}$, atm	2.97E-05	9.35E-05	1.64E-04	2.29E-04	2.95E-04
% Gas phase resistance	37	39	36	37	36
% CO2 Removal		7	18	23	25
% Approach to Equilibrium	2.68	0.88	0.55	0.41	0.32
k_{g,CO_2}	5.42E-05	5.46E-05	5.50E-05	5.54E-05	5.70E-05

moles/(cm ² .atm.sec)						
k _i , m/s	6.62E-05	6.64E-05	6.62E-05	6.63E-05	6.63E-05	
CO ₂ ldg	0.08	0.08	0.08	0.08	0.08	

T, °C	40.03	39.83	39.83	39.70	39.68	39.65	39.7
N _{CO2} moles/(cm ² .sec)	6.46E-12	3.77E-09	- 4.00E-09	9.02E-09	- 6.10E-09	1.15E-08	- 8.00E-09
P ^{bulk} _{CO2} , atm	3.85E-04	5.34E-04	2.30E-04	6.64E-04	1.47E-04	8.14E-04	1.46E-06
P ^{int} _{CO2} , atm	3.85E-04	4.69E-04	3.01E-04	5.11E-04	2.55E-04	6.12E-04	1.53E-04
P [*] _{CO2} , atm	3.62E-04	3.62E-04	3.62E-04	3.62E-04	3.62E-04	3.62E-04	3.62E-04
P ^{IN} _{CO2} , atm	3.85E-04	5.68E-04	1.96E-04	7.44E-04	9.85E-05	9.14E-04	4.75E-48
P ^{OUT} _{CO2} , atm	3.85E-04	5.02E-04	2.68E-04	5.90E-04	2.09E-04	7.22E-04	1.46E-04
% Gas phase resistance	0	38	54	51	50	45	42
% CO2 Removal	0	11	-37	21	-112	21	
% Approach to Equilibrium	0.94	0.77	1.20	0.71	1.42	0.59	2.37
k _{g,CO2} moles/(cm ² .atm.sec)	5.73E-05	5.81E-05	5.64E-05	5.89E-05	5.62E-05	5.7E-05	5.3E-05
k _i , m/s	8.87E-05	8.86E-05	8.86E-05	8.85E-05	8.85E-05	8.85E-05	8.85E-05
CO ₂ ldg	0.08	0.08	0.08	0.08	0.08	0.08	0.08

T, °C	59.80	59.78	59.95	60.05	60.00	60.125
N _{CO2} moles/(cm ² .sec)	-1.82E-11	-6.03E-09	-2.76E-09	6.68E-09	-6.03E-09	-1.34E-08
P ^{bulk} _{CO2} , atm	2.46E-03	1.67E-03	2.13E-03	3.37E-03	1.67E-03	1.66E-05
P ^{int} _{CO2} , atm	2.46E-03	2.25E-03	2.40E-03	2.75E-03	2.25E-03	1.34E-03

$P_{CO_2}^*$, atm	2.49E-03	2.49E-03	2.49E-03	2.49E-03	2.49E-03	2.49E-03
$P_{CO_2}^{IN}$, atm	4.97E-48	1.42E-02	2.96E-02	4.48E-02	5.97E-02	7.44E-02
$P_{CO_2}^{OUT}$, atm	2.41E-03	1.15E-02	2.22E-02	3.34E-02	4.44E-02	5.45E-02
% Gas phase resistance	5	71	75	70	71	53
% CO2 Removal		19	25	25	26	27
% Approach to Equilibrium	1.01	1.10	1.04	0.91	1.10	1.86
k_{g,CO_2} moles/(cm ² .atm.sec)	1.11E-05	1.03E-05	1.04E-05	1.07E-05	1.03E-05	1.02E-05
k_l , m/s	1.21E-04	1.21E-04	1.21E-04	1.21E-04	1.21E-04	0.000121
CO ₂ ldg	0.08	0.08	0.08	0.08	0.08	0.08

T, °C	39.30	39.95	40.03	40.05
N_{CO_2} moles/(cm ² .sec)	2.39E-07	6.37E-07	9.82E-07	1.32E-06
$P_{CO_2}^{bulk}$, atm	4.28E-02	8.38E-02	1.27E-01	1.70E-01
$P_{CO_2}^{int}$, atm	2.78E-02	4.41E-02	6.59E-02	8.82E-02
$P_{CO_2}^*$, atm	1.16E-02	1.16E-02	1.16E-02	1.16E-02
$P_{CO_2}^{IN}$, atm	5.15E-02	1.07E-01	1.63E-01	2.18E-01
$P_{CO_2}^{OUT}$, atm	3.51E-02	6.41E-02	9.71E-02	1.30E-01
% Gas phase resistance	48	55	53	52
% CO2 Removal	32	40	40	40
% Approach to Equilibrium	0.42	0.26	0.18	0.13
k_{g,CO_2} moles/(cm ² .atm.sec)	1.59E-05	1.61E-05	1.61E-05	1.61E-05
k_l , m/s	8.83E-05	8.87E-05	8.87E-05	8.87E-05
CO ₂ ldg	0.21	0.21	0.21	0.21

T, °C	59.25	59.30	59.18	60.00	59.90
N_{CO_2} moles/(cm ² .sec)	-7.40E-07	1.77E-06	4.19E-07	1.27E-06	8.28E-07
$P_{CO_2}^{bulk}$, atm	4.77E-04	2.04E-01	9.08E-02	1.69E-01	1.32E-01
$P_{CO_2}^{int}$, atm	4.57E-02	9.68E-02	6.53E-02	9.24E-02	8.10E-02
$P_{CO_2}^*$, atm	6.07E-02	6.07E-02	6.07E-02	6.07E-02	6.07E-02
$P_{CO_2}^{IN}$, atm	1.77E-47	2.66E-01	1.05E-01	2.14E-01	1.61E-01
$P_{CO_2}^{OUT}$, atm	4.99E-02	1.53E-01	7.76E-02	1.32E-01	1.06E-01
% Gas phase	75	75	85	71	71

resistance					
% CO2 Removal		43	26	38	34
% Approach to Equilibrium	1.33	0.63	0.93	0.66	0.75
k_{g,CO_2} moles/(cm ² .atm.sec)	1.64E-05	1.65E-05	1.64E-05	1.64E-05	1.63E-05
k_l , m/s	1.20E-04	1.20E-04	1.20E-04	1.21E-04	1.21E-04
CO ₂ ldg	0.21	0.21	0.21	0.21	0.21

T, °C	23.88	23.95	24.25	24.28	24.10	23.65
N_{CO_2} moles/(cm ² .sec)	3.64E-07	2.44E-07	7.09E-08	-1.19E-07	3.27E-07	-2.90E-07
$P_{CO_2}^{bulk}$, atm	2.26E-01	1.72E-01	1.17E-01	2.92E-02	2.82E-01	1.06E-04
$P_{CO_2}^{int}$, atm	2.13E-01	1.63E-01	1.15E-01	3.35E-02	2.70E-01	1.09E-02
$P_{CO_2}^*$, atm	9.42E-02	9.42E-02	9.42E-02	9.42E-02	9.42E-02	9.42E-02
$P_{CO_2}^{IN}$, atm	2.33E-01	1.76E-01	1.18E-01	2.71E-02	2.87E-01	9.85E-48
$P_{CO_2}^{OUT}$, atm	2.20E-01	1.68E-01	1.16E-01	3.14E-02	2.77E-01	1.10E-02
% Gas phase resistance	10	11	11	7	6	12
% CO2 Removal	5	5	2	-16	4	
% Approach to Equilibrium	0.44	0.58	0.82	2.81	0.35	8.61
k_{g,CO_2} moles/(cm ² .atm.sec)	2.80E-05	2.77E-05	2.74E-05	2.78E-05	2.83E-05	2.68E-05
k_l , m/s	6.61E-05	6.61E-05	6.62E-05	6.62E-05	6.62E-05	6.6E-05
CO ₂ ldg	0.32	0.32	0.32	0.32	0.32	0.32

T, °C	39.78	40.55	39.93	40.13
N_{CO_2} moles/(cm ² .sec)	8.05E-07	-1.43E-07	1.01E-06	-6.52E-07
$P_{CO_2}^{bulk}$, atm	1.21E+00	3.31E-01	1.51E+00	8.57E-04
$P_{CO_2}^{int}$, atm	1.12E+00	3.46E-01	1.40E+00	7.23E-02
$P_{CO_2}^*$, atm	5.30E-01	5.30E-01	5.30E-01	5.30E-01
$P_{CO_2}^{IN}$, atm	1.25E+00	3.22E-01	1.56E+00	3.63E-47
$P_{CO_2}^{OUT}$, atm	1.17E+00	3.40E-01	1.46E+00	8.96E-02
% Gas phase resistance	13	8	11	14
% CO2 Removal	7	-6	6	

% Approach to Equilibrium	0.47	1.53	0.38	7.32
k_{g,CO_2} moles/(cm ² .atm.sec)	9.38E-06	9.30E-06	9.34E-06	9.12E-06
k_l , m/s	8.86E-05	8.90E-05	8.86E-05	8.87E-05
CO ₂ ldg	0.32	0.32	0.32	0.32

Table H.3 11 wt% MOR/53 wt% DGA solubility and rate

T, °C	24.6	24.6	24.8	24.9
N_{CO_2} moles/(cm ² .sec)	2.29E-07	5.09E-07	7.54E-07	9.69E-07
$P_{CO_2}^{bulk}$, atm	1.25E-02	2.67E-02	4.06E-02	5.47E-02
$P_{CO_2}^{int}$, atm	8.10E-03	1.67E-02	2.59E-02	3.59E-02
$P_{CO_2}^*$, atm	0.00E+00	0.00E+00	0.00E+00	0.00E+00
$P_{CO_2}^{IN}$, atm	1.49E-02	3.22E-02	4.86E-02	6.48E-02
$P_{CO_2}^{OUT}$, atm	1.03E-02	2.19E-02	3.36E-02	4.57E-02
% Gas phase resistance	35	37	36	34
% CO ₂ Removal	31	32	31	29
% Approach to Equilibrium	0.00	0.00	0.00	0.00
k_{g,CO_2} moles/(cm ² .atm.sec)	5.25E-05	5.09E-05	5.12E-05	5.15E-05
k_l , m/s	2.94E-05	2.95E-05	2.95E-05	2.99E-05
CO ₂ ldg	0.001	0.001	0.001	0.001
μ , cp	11.5	11.4	11.4	11.1
ρ , g/cm ³	1.06	1.06	1.06	1.06

T, °C	40.0	40.1	40.3	40.5
N_{CO_2} moles/(cm ² .sec)	2.75E-07	5.83E-07	8.57E-07	1.12E-06
$P_{CO_2}^{bulk}$, atm	1.01E-02	2.11E-02	3.23E-02	4.34E-02
$P_{CO_2}^{int}$, atm	5.54E-03	1.14E-02	1.81E-02	2.51E-02
$P_{CO_2}^*$, atm	0.00E+00	0.00E+00	0.00E+00	0.00E+00
$P_{CO_2}^{IN}$, atm	1.26E-02	2.64E-02	3.99E-02	5.32E-02
$P_{CO_2}^{OUT}$, atm	7.99E-03	1.66E-02	2.58E-02	3.50E-02
% Gas phase resistance	45	46	44	42
% CO ₂ Removal	37	37	35	34
% Approach to Equilibrium	0.00	0.00	0.00	0.00
k_{g,CO_2} moles/(cm ² .atm.sec)	5.99E-05	6.02E-05	6.05E-05	6.08E-05

k_L , m/s	4.14E-05	4.15E-05	4.16E-05	4.17E-05
CO ₂ ldg	0.001	0.001	0.001	0.001
μ , cp	6.6	6.6	6.6	6.6
ρ , g/cm ³	1.05	1.05	1.05	1.05

T, °C	59.4	59.6	59.8	59.9
N _{CO₂} moles/(cm ² .sec)	3.42E-07	7.10E-07	1.04E-06	1.36E-06
P ^{bulk} _{CO₂} , atm	8.83E-03	1.85E-02	2.85E-02	3.84E-02
P ^{int} _{CO₂} , atm	3.48E-03	7.48E-03	1.24E-02	1.73E-02
P [*] _{CO₂} , atm	0.00E+00	0.00E+00	0.00E+00	0.00E+00
P ^{IN} _{CO₂} , atm	1.18E-02	2.46E-02	3.72E-02	4.97E-02
P ^{OUT} _{CO₂} , atm	6.41E-03	1.36E-02	2.12E-02	2.89E-02
% Gas phase resistance	61	60	57	55
% CO ₂ Removal	46	45	43	42
% Approach to Equilibrium	0.00	0.00	0.00	0.00
k _{g,CO₂} moles/(cm ² .atm.sec)	6.38E-05	6.41E-05	6.45E-05	6.48E-05
k_L , m/s	6.09E-05	6.11E-05	6.14E-05	6.16E-05
CO ₂ ldg	0.001	0.001	0.001	0.001
μ , cp	3.7	3.7	3.6	3.6
ρ , g/cm ³	1.03	1.03	1.03	1.03

T, °C	24.7	24.8	24.8	25.0
N _{CO₂} moles/(cm ² .sec)	2.99E-07	6.26E-07	9.30E-07	1.25E-06
P ^{bulk} _{CO₂} , atm	2.41E-02	5.04E-02	7.68E-02	1.02E-01
P ^{int} _{CO₂} , atm	1.23E-02	2.59E-02	4.07E-02	5.41E-02
P [*] _{CO₂} , atm	3.96E-05	3.96E-05	3.96E-05	3.96E-05
P ^{IN} _{CO₂} , atm	3.07E-02	6.41E-02	9.68E-02	1.29E-01
P ^{OUT} _{CO₂} , atm	1.85E-02	3.87E-02	5.98E-02	7.98E-02
% Gas phase resistance	49	49	47	47
% CO ₂ Removal	40	40	38	38
% Approach to Equilibrium	0.00	0.00	0.00	0.00
k _{g,CO₂} moles/(cm ² .atm.sec)	2.54E-05	2.56E-05	2.57E-05	2.59E-05
k_L , m/s	2.25E-05	2.26E-05	2.26E-05	2.27E-05
CO ₂ ldg	0.130	0.130	0.130	0.130
μ , cp	20.2	20.1	20.0	19.9
ρ , g/cm ³	1.07	1.07	1.07	1.07

T, °C	39.9	39.7	39.5	39.6
N _{CO2} moles/(cm ² .sec)	3.05E-07	7.04E-07	1.03E-06	1.37E-06
P ^{bulk} _{CO2} atm	2.37E-02	4.84E-02	7.49E-02	9.94E-02
P ^{int} _{CO2} , atm	1.19E-02	2.11E-02	3.47E-02	4.67E-02
P [*] _{CO2} , atm	2.43E-04	2.43E-04	2.43E-04	2.43E-04
P ^{IN} _{CO2} , atm	3.04E-02	6.40E-02	9.76E-02	1.29E-01
P ^{OUT} _{CO2} , atm	1.80E-02	3.55E-02	5.61E-02	7.49E-02
% Gas phase resistance	50	57	54	53
% CO2 Removal	41	44	43	42
% Approach to Equilibrium	0.02	0.01	0.01	0.01
k _{g,CO2} moles/(cm ² .atm.sec)	2.59E-05	2.58E-05	2.57E-05	2.61E-05
k _l m/s	3.32E-05	3.30E-05	3.29E-05	3.29E-05
CO ₂ ldg	0.130	0.130	0.130	0.130
μ, cp	10.5	10.7	10.7	10.7
ρ, g/cm ³	1.06	1.06	1.06	1.06

T, °C	58.5	58.5	58.4	58.5	58.7
N _{CO2} moles/(cm ² .sec)	-1.19E-07	2.99E-07	7.15E-07	1.09E-06	1.43E-06
P ^{bulk} _{CO2} atm	4.59E-05	2.33E-02	4.71E-02	7.26E-02	9.94E-02
P ^{int} _{CO2} , atm	4.50E-03	1.20E-02	1.99E-02	3.06E-02	4.37E-02
P [*] _{CO2} , atm	4.83E-03	4.83E-03	4.83E-03	4.83E-03	4.83E-03
P ^{IN} _{CO2} , atm	1.03E-47	2.98E-02	6.26E-02	9.64E-02	1.31E-01
P ^{OUT} _{CO2} , atm	4.72E-03	1.79E-02	3.43E-02	5.30E-02	7.35E-02
% Gas phase resistance	93	61	64	62	59
% CO2 Removal		40	45	45	44
% Approach to Equilibrium	1.07	0.40	0.24	0.16	0.11
k _{g,CO2} moles/(cm ² .atm.sec)	2.66E-05	2.65E-05	2.64E-05	2.60E-05	2.57E-05
k _l m/s	5.14E-05	5.13E-05	5.12E-05	5.13E-05	5.14E-05
CO ₂ ldg	0.130	0.130	0.130	0.130	0.130
μ, cp	5.2	5.2	5.2	5.2	5.2
ρ, g/cm ³	1.05	1.05	1.05	1.05	1.05

T, °C	25.3	25.1	25.7	25.5
N _{CO2}	2.46E-07	5.31E-07	7.62E-07	9.78E-07

moles/(cm ² .sec)				
P ^{bulk} _{CO2} atm	2.53E-02	5.26E-02	8.07E-02	1.09E-01
P ^{int} _{CO2} , atm	1.57E-02	3.19E-02	5.12E-02	7.10E-02
P [*] _{CO2} , atm	2.29E-04	2.29E-04	2.29E-04	2.29E-04
P ^{IN} _{CO2} , atm	3.07E-02	6.41E-02	9.68E-02	1.29E-01
P ^{OUT} _{CO2} , atm	2.06E-02	4.26E-02	6.65E-02	9.07E-02
% Gas phase resistance	39	40	37	35
% CO2 Removal	33	33	31	30
% Approach to Equilibrium	0.01	0.01	0.00	0.00
k _{g,CO2} moles/(cm ² .atm.sec)	2.55E-05	2.56E-05	2.58E-05	2.59E-05
k _l m/s	1.95E-05	1.93E-05	1.98E-05	1.96E-05
CO ₂ ldg	0.270	0.270	0.270	0.270
μ, cp	27.9	28.3	27.2	27.6
ρ, g/cm ³	1.12	1.12	1.12	1.12

T, °C	40.5	40.6	40.8	41.5
N _{CO2} moles/(cm ² .sec)	2.76E-07	5.85E-07	8.70E-07	1.14E-06
P ^{bulk} _{CO2} atm	2.44E-02	5.12E-02	7.87E-02	1.08E-01
P ^{int} _{CO2} , atm	1.37E-02	2.85E-02	4.49E-02	6.30E-02
P [*] _{CO2} , atm	1.31E-03	1.31E-03	1.31E-03	1.31E-03
P ^{IN} _{CO2} , atm	3.04E-02	6.39E-02	9.74E-02	1.32E-01
P ^{OUT} _{CO2} , atm	1.92E-02	4.03E-02	6.26E-02	8.64E-02
% Gas phase resistance	46	45	44	42
% CO2 Removal	37	37	36	35
% Approach to Equilibrium	0.10	0.05	0.03	0.02
k _{g,CO2} moles/(cm ² .atm.sec)	2.59E-05	2.58E-05	2.57E-05	2.54E-05
k _l m/s	2.87E-05	2.88E-05	2.90E-05	2.94E-05
CO ₂ ldg	0.270	0.270	0.270	0.270
μ, cp	14.6	14.5	14.4	14.0
ρ, g/cm ³	1.11	1.11	1.11	1.11

T, °C	60.2	60.4	60.8	60.6	60.6
N _{CO2} moles/(cm ² .sec)	-1.72E-07	1.55E-07	4.80E-07	8.16E-07	1.13E-06
P ^{bulk} _{CO2} atm	6.78E-05	2.77E-02	5.53E-02	8.24E-02	1.09E-01
P ^{int} _{CO2} , atm	6.68E-03	2.16E-02	3.62E-02	4.99E-02	6.44E-02
P [*] _{CO2} , atm	1.46E-02	1.46E-02	1.46E-02	1.46E-02	1.46E-02

$P_{CO_2}^{IN}$, atm	1.06E-47	3.10E-02	6.58E-02	1.00E-01	1.34E-01
$P_{CO_2}^{OUT}$, atm	7.00E-03	2.46E-02	4.59E-02	6.67E-02	8.78E-02
% Gas phase resistance	45	47	47	48	47
% CO2 Removal		21	30	34	34
% Approach to Equilibrium	2.19	0.68	0.40	0.29	0.23
k_{g,CO_2} moles/(cm ² .atm.sec)	2.60E-05	2.54E-05	2.51E-05	2.50E-05	2.52E-05
k_l m/s	4.65E-05	4.68E-05	4.72E-05	4.70E-05	4.70E-05
CO ₂ ldg	0.270	0.270	0.270	0.270	0.270
μ , cp	6.6	6.5	6.4	6.5	6.5
ρ , g/cm ³	1.10	1.10	1.10	1.10	1.10

T, °C	25.7	25.5	25.4	24.9
N_{CO_2} moles/(cm ² .sec)	2.81E-07	5.88E-07	8.08E-07	9.37E-07
$P_{CO_2}^{bulk}$ atm	5.51E-02	1.15E-01	1.77E-01	2.43E-01
$P_{CO_2}^{int}$, atm	3.26E-02	6.82E-02	1.14E-01	1.70E-01
$P_{CO_2}^*$, atm	1.49E-03	1.49E-03	1.49E-03	1.49E-03
$P_{CO_2}^{IN}$, atm	6.90E-02	1.43E-01	2.15E-01	2.85E-01
$P_{CO_2}^{OUT}$, atm	4.32E-02	9.04E-02	1.44E-01	2.05E-01
% Gas phase resistance	42	41	36	30
% CO2 Removal	37	37	33	28
% Approach to Equilibrium	0.05	0.02	0.01	0.01
k_{g,CO_2} moles/(cm ² .atm.sec)	1.25E-05	1.26E-05	1.28E-05	1.29E-05
k_l m/s	1.77E-05	1.75E-05	1.74E-05	1.71E-05
CO ₂ ldg	0.360	0.360	0.360	0.360
μ , cp	34.7	35.2	35.6	36.8
ρ , g/cm ³	1.14	1.14	1.14	1.14

T, °C	39.7	39.8	40.2	40.5	40.3
N_{CO_2} moles/(cm ² .sec)	-5.72E-08	4.43E-07	9.28E-07	1.43E-06	1.88E-06
$P_{CO_2}^{bulk}$ atm	4.64E-05	4.04E-02	8.55E-02	1.28E-01	1.74E-01
$P_{CO_2}^{int}$, atm	4.10E-03	9.17E-03	1.97E-02	2.74E-02	4.15E-02
$P_{CO_2}^*$, atm	2.65E-03	2.65E-03	2.65E-03	2.65E-03	2.65E-03
$P_{CO_2}^{IN}$, atm	2.15E-47	6.10E-02	1.28E-01	1.93E-01	2.59E-01
$P_{CO_2}^{OUT}$, atm	4.74E-03	2.50E-02	5.33E-02	7.95E-02	1.11E-01
% Gas phase resistance	156	83	79	80	77
% CO2 Removal		59	58	59	57

% Approach to Equilibrium	0.65	0.29	0.13	0.10	0.06
k_{g,CO_2} moles/(cm ² .atm.sec)	1.41E-05	1.42E-05	1.41E-05	1.42E-05	1.42E-05
k_f , m/s	2.54E-05	2.54E-05	2.56E-05	2.58E-05	2.57E-05
CO ₂ ldg	0.360	0.360	0.360	0.360	0.360
μ , cp	18.9	18.9	18.6	18.4	18.5
ρ , g/cm ³	1.13	1.13	1.13	1.13	1.13

T, °C	60.3	60.5	60.4	60.4	60.9
N_{CO_2} moles/(cm ² .sec)	-3.53E-07	7.43E-07	2.80E-07	8.36E-08	-1.20E-07
$P_{CO_2}^{bulk}$, atm	2.77E-04	2.93E-01	1.85E-01	1.25E-01	6.68E-02
$P_{CO_2}^{int}$, atm	2.48E-02	2.42E-01	1.65E-01	1.19E-01	7.53E-02
$P_{CO_2}^*$, atm	9.98E-02	9.98E-02	9.98E-02	9.98E-02	9.98E-02
$P_{CO_2}^{IN}$, atm	2.13E-47	3.22E-01	1.96E-01	1.29E-01	6.20E-02
$P_{CO_2}^{OUT}$, atm	2.87E-02	2.66E-01	1.74E-01	1.22E-01	7.18E-02
% Gas phase resistance	25	27	23	23	26
% CO ₂ Removal		17	11	5	-16
% Approach to Equilibrium	4.02	0.41	0.60	0.84	1.33
k_{g,CO_2} moles/(cm ² .atm.sec)	1.44E-05	1.45E-05	1.42E-05	1.42E-05	1.41E-05
k_f , m/s	4.22E-05	4.24E-05	4.23E-05	4.23E-05	4.30E-05
CO ₂ ldg	0.360	0.360	0.360	0.360	0.360
μ , cp	8.2	8.1	8.1	8.1	7.9
ρ , g/cm ³	1.12	1.12	1.12	1.12	1.12

T, °C	25.8	25.6	25.8	25.7	25.8
N_{CO_2} moles/(cm ² .sec)	-1.86E-09	3.82E-09	1.71E-09	5.14E-09	7.44E-09
$P_{CO_2}^{bulk}$, atm	3.15E-07	1.46E-04	7.51E-05	2.22E-04	2.88E-04
$P_{CO_2}^{int}$, atm	3.10E-05	8.34E-05	4.71E-05	1.39E-04	1.69E-04
$P_{CO_2}^*$, atm	3.96E-05	3.96E-05	3.96E-05	3.96E-05	3.96E-05
$P_{CO_2}^{IN}$, atm	4.35E-48	1.79E-04	9.01E-05	2.67E-04	3.53E-04
$P_{CO_2}^{OUT}$, atm	3.11E-05	1.16E-04	6.18E-05	1.83E-04	2.33E-04
% Gas phase resistance	78	59	79	45	48
% CO ₂ Removal		35	31	31	34
% Approach to Equilibrium	1.28	0.47	0.84	0.28	0.23
k_{g,CO_2} moles/(cm ² .atm.sec)	6.05E-05	6.14E-05	6.09E-05	6.18E-05	6.23E-05

k_l , m/s	2.35E-05	2.33E-05	2.35E-05	2.34E-05	2.35E-05
CO ₂ ldg	0.130	0.130	0.130	0.130	0.130

T, °C	40.6	40.7	40.8	40.7	40.7	40.8
N _{CO₂} moles/(cm ² .sec)	-5.71E-09	-1.06E-09	2.93E-09	7.38E-09	1.04E-08	-3.65E-09
P ^{bulk} _{CO₂} , atm	9.35E-07	1.83E-04	3.20E-04	4.48E-04	5.82E-04	1.15E-04
P ^{int} _{CO₂} , atm	9.28E-05	2.00E-04	2.75E-04	3.34E-04	4.24E-04	1.73E-04
P* _{CO₂} , atm	2.16E-04	2.16E-04	2.16E-04	2.16E-04	2.16E-04	2.16E-04
P ^{IN} _{CO₂} , atm	4.25E-48	1.75E-04	3.44E-04	5.07E-04	6.64E-04	8.80E-05
P ^{OUT} _{CO₂} , atm	9.33E-05	1.92E-04	2.98E-04	3.93E-04	5.06E-04	1.47E-04
% Gas phase resistance	43	52	44	49	43	58
% CO ₂ Removal		-10	13	22	24	-67
% Approach to Equilibrium	2.33	1.08	0.79	0.65	0.51	1.25
k _{g,CO₂} moles/(cm ² .atm.sec)	6.21E-05	6.31E-05	6.40E-05	6.49E-05	6.59E-05	6.27E-05
k_l , m/s	3.38E-05	3.39E-05	3.39E-05	3.39E-05	3.39E-05	3.4E-05
CO ₂ ldg	0.130	0.130	0.130	0.130	0.130	0.130

T, °C	59.3	59.1	58.3	58.1
N _{CO₂} moles/(cm ² .sec)	-1.41E-07	1.55E-07	4.76E-07	7.51E-07
P ^{bulk} _{CO₂} , atm	2.27E-05	1.10E-02	2.17E-02	3.26E-02
P ^{int} _{CO₂} , atm	2.33E-03	8.45E-03	1.39E-02	2.04E-02
P* _{CO₂} , atm	5.09E-03	5.09E-03	5.09E-03	5.09E-03
P ^{IN} _{CO₂} , atm	4.31E-48	1.23E-02	2.58E-02	3.90E-02
P ^{OUT} _{CO₂} , atm	2.34E-03	9.75E-03	1.80E-02	2.69E-02
% Gas phase resistance	46	43	47	44
% CO ₂ Removal		21	30	31
% Approach to Equilibrium	2.18	0.60	0.37	0.25
k _{g,CO₂} moles/(cm ² .atm.sec)	6.11E-05	6.13E-05	6.14E-05	6.16E-05
k_l , m/s	5.22E-05	5.20E-05	5.11E-05	5.10E-05
CO ₂ ldg	0.130	0.130	0.130	0.130

T, °C	24.2	24.7	24.8	25.1	24.9
N _{CO2} moles/(cm ² .sec)	-6.10E-09	-2.71E-09	6.14E-09	6.59E-10	8.43E-09
P ^{bulk} _{CO2} atm	9.85E-07	1.07E-04	4.52E-04	2.52E-04	5.90E-04
P ^{int} _{CO2} , atm	9.82E-05	1.50E-04	3.58E-04	2.41E-04	4.63E-04
P* _{CO2} , atm	2.29E-04	2.29E-04	2.29E-04	2.29E-04	2.29E-04
P ^{IN} _{CO2} , atm	4.19E-48	8.68E-05	5.00E-04	2.57E-04	6.55E-04
P ^{OUT} _{CO2} , atm	9.84E-05	1.30E-04	4.07E-04	2.46E-04	5.29E-04
% Gas phase resistance	43	35	42	45	35
% CO2 Removal		-50	19	4	19
% Approach to Equilibrium	2.33	1.53	0.64	0.95	0.49
k _{g,CO2} moles/(cm ² .atm.sec)	6.27E-05	6.32E-05	6.56E-05	6.42E-05	6.66E-05
k _l m/s	1.87E-05	1.90E-05	1.91E-05	1.92E-05	1.91E-05
CO ₂ l/dg	0.270	0.270	0.270	0.270	0.270

T, °C	40.8	40.9	40.7	40.5	41.0
N _{CO2} moles/(cm ² .sec)	-6.90E-08	1.52E-07	3.73E-07	5.60E-07	7.24E-07
P ^{bulk} _{CO2} atm	1.19E-05	1.17E-02	2.39E-02	3.64E-02	4.88E-02
P ^{int} _{CO2} , atm	1.21E-03	9.08E-03	1.75E-02	2.68E-02	3.65E-02
P* _{CO2} , atm	2.82E-03	2.82E-03	2.82E-03	2.82E-03	2.82E-03
P ^{IN} _{CO2} , atm	4.59E-48	1.31E-02	2.73E-02	4.13E-02	5.51E-02
P ^{OUT} _{CO2} , atm	1.22E-03	1.04E-02	2.09E-02	3.18E-02	4.30E-02
% Gas phase resistance	43	30	30	29	27
% CO2 Removal		20	24	23	22
% Approach to Equilibrium	2.33	0.31	0.16	0.11	0.08
k _{g,CO2} moles/(cm ² .atm.sec)	5.76E-05	5.79E-05	5.81E-05	5.85E-05	5.89E-05
k _l m/s	2.89E-05	2.90E-05	2.89E-05	2.87E-05	2.90E-05
CO ₂ l/dg	0.270	0.270	0.270	0.270	0.270

T, °C	61.6	61.6	61.9	61.8	61.5
N _{CO2} moles/(cm ² .sec)	-2.36E-07	2.49E-08	2.60E-07	4.44E-07	6.14E-07
P ^{bulk} _{CO2} atm	3.88E-05	1.24E-02	2.41E-02	3.60E-02	4.80E-02

$P_{CO_2}^{int}$, atm	4.01E-03	1.20E-02	1.98E-02	2.87E-02	3.77E-02
$P_{CO_2}^*$, atm	1.16E-02	1.16E-02	1.16E-02	1.16E-02	1.16E-02
$P_{CO_2}^{IN}$, atm	4.42E-48	1.26E-02	2.63E-02	3.98E-02	5.32E-02
$P_{CO_2}^{OUT}$, atm	4.02E-03	1.22E-02	2.20E-02	3.25E-02	4.32E-02
% Gas phase resistance	34	55	35	30	28
% CO2 Removal		3	16	18	19
% Approach to Equilibrium	2.90	0.97	0.59	0.41	0.31
k_{g,CO_2} moles/(cm ² .atm.sec)	5.95E-05	5.98E-05	6.01E-05	6.04E-05	5.95E-05
k_l , m/s	4.83E-05	4.83E-05	4.87E-05	4.86E-05	4.82E-05
CO ₂ ldg	0.270	0.270	0.270	0.270	0.270

T, °C	24.8	25.0	25.0	24.6	24.4
N_{CO_2} moles/(cm ² .sec)	6.33E-09	-1.75E-09	1.11E-09	4.07E-09	-4.32E-09
$P_{CO_2}^{bulk}$, atm	2.27E-03	1.30E-03	1.64E-03	1.95E-03	9.47E-04
$P_{CO_2}^{int}$, atm	2.04E-03	1.37E-03	1.59E-03	1.81E-03	1.11E-03
$P_{CO_2}^*$, atm	1.49E-03	1.49E-03	1.49E-03	1.49E-03	1.49E-03
$P_{CO_2}^{IN}$, atm	2.39E-03	1.27E-03	1.66E-03	2.03E-03	8.64E-04
$P_{CO_2}^{OUT}$, atm	2.16E-03	1.34E-03	1.61E-03	1.88E-03	1.03E-03
% Gas phase resistance	29	35	28	32	30
% CO2 Removal	10	-5	3	7	-20
% Approach to Equilibrium	0.73	1.09	0.93	0.82	1.34
k_{g,CO_2} moles/(cm ² .atm.sec)	2.82E-05	2.68E-05	2.73E-05	2.77E-05	2.63E-05
k_l , m/s	1.70E-05	1.72E-05	1.72E-05	1.70E-05	1.67E-05
CO ₂ ldg	0.360	0.360	0.360	0.360	0.360

T, °C	40.6	40.7	40.6	39.6	39.5
N_{CO_2} moles/(cm ² .sec)	-1.08E-07	1.17E-07	2.96E-07	4.52E-07	5.26E-07
$P_{CO_2}^{bulk}$, atm	2.85E-05	1.85E-02	3.79E-02	5.72E-02	7.73E-02
$P_{CO_2}^{int}$, atm	2.69E-03	1.56E-02	3.06E-02	4.62E-02	6.46E-02
$P_{CO_2}^*$, atm	7.15E-03	7.15E-03	7.15E-03	7.15E-03	7.15E-03
$P_{CO_2}^{IN}$, atm	7.08E-48	2.01E-02	4.19E-02	6.33E-02	8.41E-02
$P_{CO_2}^{OUT}$, atm	2.93E-03	1.70E-02	3.41E-02	5.16E-02	7.08E-02

% Gas phase resistance	37	25	24	22	18
% CO2 Removal		16	19	18	16
% Approach to Equilibrium	2.65	0.46	0.23	0.15	0.11
k_{g,CO_2} moles/(cm ² .atm.sec)	4.04E-05	4.06E-05	4.08E-05	4.10E-05	4.14E-05
k_i m/s	2.59E-05	2.60E-05	2.59E-05	2.53E-05	2.53E-05
CO ₂ ldg	0.360	0.360	0.360	0.360	0.360

T, °C	57.6	57.9	57.6	58.7	58.9
N_{CO_2} moles/(cm ² .sec)	-4.55E-07	-2.46E-07	-1.24E-07	4.81E-09	2.11E-07
$P_{CO_2}^{bulk}$ atm	1.21E-04	2.36E-02	4.43E-02	6.39E-02	1.03E-01
$P_{CO_2}^{int}$ atm	1.16E-02	2.98E-02	4.73E-02	6.38E-02	9.78E-02
$P_{CO_2}^*$ atm	6.61E-02	6.61E-02	6.61E-02	6.61E-02	6.61E-02
$P_{CO_2}^{IN}$ atm	7.21E-48	2.05E-02	4.26E-02	6.40E-02	1.06E-01
$P_{CO_2}^{OUT}$ atm	1.26E-02	2.71E-02	4.59E-02	6.39E-02	1.00E-01
% Gas phase resistance	17	14	14	-5	14
% CO2 Removal		-33	-8	0	5
% Approach to Equilibrium	5.70	2.22	1.40	1.04	0.68
k_{g,CO_2} moles/(cm ² .atm.sec)	3.97E-05	4.00E-05	4.03E-05	4.08E-05	4.08E-05
k_i m/s	3.92E-05	3.95E-05	3.92E-05	4.03E-05	4.05E-05
CO ₂ ldg	0.360	0.360	0.360	0.360	0.360

T, °C	24.7	25.2	25.4	25.5
N_{CO_2} moles/(cm ² .sec)	-1.01E-07	7.16E-08	1.74E-07	2.57E-07
$P_{CO_2}^{bulk}$ atm	8.58E-05	6.30E-02	1.33E-01	2.59E-01
$P_{CO_2}^{int}$ atm	7.67E-03	5.75E-02	1.20E-01	2.40E-01
$P_{CO_2}^*$ atm	3.73E-02	3.73E-02	3.73E-02	3.73E-02
$P_{CO_2}^{IN}$ atm	2.27E-47	6.62E-02	1.41E-01	2.69E-01
$P_{CO_2}^{OUT}$ atm	8.81E-03	5.99E-02	1.26E-01	2.49E-01
% Gas phase resistance	20	21	14	8
% CO2 Removal		9	11	8
% Approach to Equilibrium	4.86	0.65	0.31	0.16
k_{g,CO_2} moles/(cm ² .atm.sec)	1.33E-05	1.31E-05	1.28E-05	1.37E-05
k_i m/s	1.55E-05	1.58E-05	1.60E-05	1.60E-05
CO ₂ ldg	0.450	0.450	0.450	0.450

T, °C	40.9	41.2	41.5	41.7	41.7
N_{CO_2} moles/(cm ² .sec)	-2.73E-07	-5.38E-08	1.00E-07	2.02E-07	2.11E-07
$P_{CO_2}^{bulk}$, atm	1.94E-04	5.73E-02	1.75E-01	2.95E-01	4.67E-01
$P_{CO_2}^{int}$, atm	1.75E-02	6.07E-02	1.68E-01	2.81E-01	4.53E-01
$P_{CO_2}^*$, atm	1.60E-01	1.60E-01	1.60E-01	1.60E-01	1.60E-01
$P_{CO_2}^{IN}$, atm	1.92E-47	5.54E-02	1.78E-01	3.02E-01	4.74E-01
$P_{CO_2}^{OUT}$, atm	2.01E-02	5.93E-02	1.71E-01	2.88E-01	4.60E-01
% Gas phase resistance	11	3	44	10	4
% CO2 Removal		-7	4	5	3
% Approach to Equilibrium	9.15	2.63	0.95	0.57	0.35
k_{g,CO_2} moles/(cm ² .atm.sec)	1.58E-05	1.57E-05	1.56E-05	1.54E-05	1.57E-05
k_l , m/s	2.39E-05	2.41E-05	2.43E-05	2.43E-05	2.43E-05
CO ₂ ldg	0.450	0.450	0.450	0.450	0.450

Appendix I: Additional C13 NMR Data

I.1 65 wt% DGA

Table I.1 C13 NMR of 65 wt% DGA, Loading = 0.377 mol CO₂/mol DGA, T=27 °C

Species	δ (ppm)	Area
Methylene C's adjacent to nitrogen in DGA/ Protonated DGA	39.327	28.53
Methylene C's adjacent to nitrogen in DGA carbamate	40.874	16.53
Methylene C's adjacent to alcohol in DGA/ Protonated DGA & DGA carbamate	60.233	49.55
Methylene C's adjacent to oxygen in DGA/ Protonated DGA on carbamate side	68.435	27.17
Methylene C's adjacent to oxygen in DGA carbamate on carbamate side	70.176	16.35
Methylene C's adjacent to oxygen in DGA/ Protonated DGA & DGA carbamate on noncarbamate side	71.700	45.69
Carbonate / Bicarbonate	160.697	16.80
DGA carbamate	163.831	1000.00

Table I.2 C13 NMR of 65 wt% DGA, Loading = 0.525 mol CO₂/mol DGA, T=27 °C

Species	Area	Area
Methylene C's adjacent to nitrogen in DGA/ Protonated DGA	38.463	18.47
Methylene C's adjacent to nitrogen in DGA carbamate	40.365	15.33
Methylene C's adjacent to alcohol in DGA/ Protonated DGA & DGA carbamate	59.795	38.74
Methylene C's adjacent to oxygen in DGA/ Protonated DGA on carbamate side	66.100	17.98
Methylene C's adjacent to oxygen in DGA carbamate on carbamate side	69.649	15.28
Methylene C's adjacent to oxygen in DGA/ Protonated DGA & DGA carbamate on noncarbamate side	71.28	35.79

Carbonate / Bicarbonate	159.791	151.08
DGA carbamate	163.349	1000.00

Table I.3 C13 NMR of 65 wt% DGA, Loading = 0.523 mol CO₂/mol DGA, T=40 °C

Species	Area	Area
Methylene C's adjacent to nitrogen in DGA/ Protonated DGA	38.790	23.16
Methylene C's adjacent to nitrogen in DGA carbamate	40.674	18.57
Methylene C's adjacent to alcohol in DGA/ Protonated DGA & DGA carbamate	60.090	43.0
Methylene C's adjacent to oxygen in DGA/ Protonated DGA on carbamate side	66.480	21.02
Methylene C's adjacent to oxygen in DGA carbamate on carbamate side	69.927	17.55
Methylene C's adjacent to oxygen in DGA/ Protonated DGA & DGA carbamate on noncarbamate side	71.526	39.46
Carbonate / Bicarbonate	159.842	162.98
DGA carbamate	163.515	1000.00

Table I.4 C13 NMR of 65 wt% DGA, Loading = 0.332 mol CO₂/mol DGA, T=60 °C

Species	Area	Area
Methylene C's adjacent to nitrogen in DGA/ Protonated DGA	39.56	46.22
Methylene C's adjacent to nitrogen in DGA carbamate	40.94	22.19
Methylene C's adjacent to alcohol in DGA/ Protonated DGA & DGA carbamate	60.28	71.50
Methylene C's adjacent to oxygen in DGA/ Protonated DGA on carbamate side	69.24	45.42
Methylene C's adjacent to oxygen in DGA carbamate on carbamate side	70.21	21.62
Methylene C's adjacent to oxygen in DGA/ Protonated DGA & DGA carbamate on noncarbamate side	71.69	69.66
Carbonate / Bicarbonate	160.19	44
DGA carbamate	163.82	2313

Table I.5 ^{13}C NMR of 65 wt% DGA, Loading = 0.390 mol CO_2 /mol DGA, $T=40^\circ\text{C}$

Species	Area	Area
Methylene C's adjacent to nitrogen in DGA/ Protonated DGA	39.513	30.51
Methylene C's adjacent to nitrogen in DGA carbamate	41.077	19.04
Methylene C's adjacent to alcohol in DGA/ Protonated DGA & DGA carbamate	60.418	51.90
Methylene C's adjacent to oxygen in DGA/ Protonated DGA on carbamate side	68.627	30.13
Methylene C's adjacent to oxygen in DGA carbamate on carbamate side	70.352	18.54
Methylene C's adjacent to oxygen in DGA/ Protonated DGA & DGA carbamate on noncarbamate side	71.870	48.12
Carbonate / Bicarbonate	160.510	18.91
DGA carbamate	163.983	1000.00

Table I.6 ^{13}C NMR of 65 wt% DGA, Loading = 0.385 mol CO_2 /mol DGA, $T=60^\circ\text{C}$

Species	Area	Area
Methylene C's adjacent to nitrogen in DGA/ Protonated DGA + Methylene C's adjacent to nitrogen in DGA carbamate	41.280/39.751	48.99
Methylene C's adjacent to alcohol in DGA/ Protonated DGA & DGA carbamate	60.626	49.59
Methylene C's adjacent to oxygen in DGA/ Protonated DGA on carbamate side	68.877	30.24
Methylene C's adjacent to oxygen in DGA carbamate on carbamate side	70.520	18.07
Methylene C's adjacent to oxygen in DGA/ Protonated DGA & DGA carbamate on noncarbamate side	72.042	46.61
Carbonate / Bicarbonate	160.295	30.65
DGA carbamate	164.123	1000.00

Table I.7 ^{13}C NMR of 65 wt% DGA, Loading = 0.168 mol CO_2 /mol DGA, $T=27^\circ\text{C}$

Species	Area	Area
Methylene C's adjacent to nitrogen in DGA/ Protonated DGA	40.043	120.4
Methylene C's adjacent to nitrogen in DGA carbamate	41.002/40.899	24.3
Methylene C's adjacent to alcohol in DGA/ Protonated DGA & DGA carbamate	60.222	150.9
Methylene C's adjacent to oxygen in DGA/ Protonated DGA on carbamate side + Methylene C's adjacent to oxygen in DGA carbamate on carbamate side + Methylene C's adjacent to oxygen in DGA/ Protonated DGA & DGA carbamate on noncarbamate side	70.307/71.031 /71.743	295.7
Carbonate / Bicarbonate	161.43	10
DGA carbamate	163.83	2316

Table I.8 ^{13}C NMR of 65 wt% DGA, Loading = 0.180 mol CO_2 /mol DGA, $T=60^\circ\text{C}$

Species	Area	Area
Methylene C's adjacent to nitrogen in DGA/ Protonated DGA	40.491	52.0
Methylene C's adjacent to nitrogen in DGA carbamate	41.404	11.3
Methylene C's adjacent to alcohol in DGA/ Protonated DGA & DGA carbamate	60.679	65.1
Methylene C's adjacent to oxygen in DGA/ Protonated DGA on carbamate side + Methylene C's adjacent to oxygen in DGA carbamate on carbamate side + Methylene C's adjacent to oxygen in DGA/ Protonated DGA & DGA carbamate on noncarbamate side	72.146/71.476 /70.731	127.0
Carbonate / Bicarbonate	160.63	10.0
DGA carbamate	164.52/164.21	988.6

I.2 23.5 wt% MOR

Table I.9 C13 NMR of 23.5 wt% MOR, Loading = 0.370 mol CO₂/mol MOR, T=27 °C

Species	δ (ppm)	Area
Carbamate ring C's adjacent to carbamate side	44.182	2.172
Carbamate ring C's adjacent to non carbamate side	66.440	2.049
MOR / Protonated MOR on carbamate side	43.633	5.177
MOR / Protonated MOR on noncarbamate side	65.083	4.961
Carbonate / Bicarbonate	160.62	26.7
MOR carbamate	162.87	100.0

Table I.10 C13 NMR of 23.5 wt% MOR, Loading = 0.569 mol CO₂/mol MOR, T=27 °C

Species	δ (ppm)	Area
Carbamate ring C's adjacent to carbamate side	44.5	62.74
Carbamate ring C's adjacent to non carbamate side	66.5	58.37
MOR / Protonated MOR on carbamate side	43.0	122.87
MOR / Protonated MOR on noncarbamate side	64.0	114.78
Carbonate / Bicarbonate	160.4	1000.00
MOR carbamate	163.0	1455.82

Table I.11 C13 NMR of 23.5 wt% MOR, Loading = 0.478 mol CO₂/mol MOR, T=27 °C

Species	δ (ppm)	Area
Carbamate ring C's adjacent to carbamate side	44.492	18.85
Carbamate ring C's adjacent to non carbamate side	66.753	18.29
MOR / Protonated MOR on carbamate side	43.553	34.68
MOR / Protonated MOR on noncarbamate side	64.526	34.00
Carbonate / Bicarbonate	160.678	362.09
MOR carbamate	163.146	1000.00

Table I.12 C13 NMR of 23.5 wt% MOR, Loading = 0.258 mol CO₂/mol MOR, T=27 °C

Species	δ (ppm)	Area
Carbamate ring C's adjacent to carbamate side + MOR / Protonated MOR on carbamate side	44.4	166.13
Carbamate ring C's adjacent to non carbamate side	67.0	39.00
MOR / Protonated MOR on noncarbamate side	63.0	121.19
Carbonate / Bicarbonate	161.0	59.92
MOR carbamate	163.0	1000.00

Table I.13 C13 NMR of 23.5 wt% MOR, Loading = 0.427 mol CO₂/mol MOR, T=27 °C

Species	δ (ppm)	Area
Carbamate ring C's adjacent to non carbamate side	67.0	43.35
MOR / Protonated MOR on noncarbamate side	63.0	80.06
Carbonate / Bicarbonate	161	217.38
MOR carbamate	163	1000.0

Table I.14 C13 NMR of 23.5 wt% MOR, Loading = 0.325 mol CO₂/mol MOR, T=27 °C

Species	δ (ppm)	Area
Carbamate ring C's adjacent to non carbamate side	67.0	39.16
MOR / Protonated MOR on noncarbamate side	63.0	92.42
Carbonate / Bicarbonate	161	91.41
MOR carbamate	163	1000.0

Table I.15 C13 NMR of 23.5 wt% MOR, Loading = 0.392 mol CO₂/mol MOR, T=40 °C

Species	δ (ppm)	Area
Carbamate ring C's adjacent to carbamate side	44.360	4.037
Carbamate ring C's adjacent to non carbamate side	66.571	3.835
MOR / Protonated MOR on carbamate side	43.640	9.446
MOR / Protonated MOR on noncarbamate side	64.867	9.094
Carbonate / Bicarbonate	160.34	32.1
MOR carbamate	163.01	100.0

Table I.16 C13 NMR of 23.5 wt% MOR, Loading = 0.370 mol CO₂/mol MOR, T=40 °C

Species	δ (ppm)	Area
Carbamate ring C's adjacent to carbamate side	44.385	2.304
Carbamate ring C's adjacent to non carbamate side	66.595	2.045
MOR / Protonated MOR on carbamate side	43.856	5.807
MOR / Protonated MOR on noncarbamate side	65.314	5.675
Carbonate / Bicarbonate	160.45	36.2
MOR carbamate	163.06	100.0

Table I.17 C13 NMR of 23.5 wt% MOR, Loading = 0.569 mol CO₂/mol MOR, T=40 °C

Species	δ (ppm)	Area
Carbamate ring C's adjacent to carbamate side + MOR / Protonated MOR on carbamate side	44.965	216.79
Carbamate ring C's adjacent to non carbamate side + MOR / Protonated MOR on noncarbamate side	65.997	183.32
Carbonate / Bicarbonate	161.036	1000.0
MOR carbamate	163.590	1175.15

Table I.18 C13 NMR of 23.5 wt% MOR, Loading = 0.478 mol CO₂/mol MOR, T=40 °C

Species	δ (ppm)	Area
Carbamate ring C's adjacent to carbamate side + MOR / Protonated MOR on carbamate side	44.133	164.99
Carbamate ring C's adjacent to non carbamate side + MOR / Protonated MOR on noncarbamate side	67.027	149.64
Carbonate / Bicarbonate	160.568	534.97
MOR carbamate	163.373	1000.00

Table I.19 C13 NMR of 23.5 wt% MOR, Loading = 0.258 mol CO₂/mol MOR, T=40 °C

Species	δ (ppm)	Area
Carbamate ring C's adjacent to carbamate side + MOR / Protonated MOR on carbamate side	45	220.64
Carbamate ring C's adjacent to non carbamate side + MOR / Protonated MOR on noncarbamate side	67	211.75
Carbonate / Bicarbonate	160.9	86.35
MOR carbamate	163.4	1000.00

I.3 11 wt% MOR/53 wt% DGA

Table I.20 C13 NMR of 11 wt% MOR/53 wt% DGA, Loading = 0.364 mol CO₂/mol MOR, T=27 °C

Species	δ (ppm)	Area
DGA carbamate	164	100
MOR carbamate	162.1	23.17
Carbonate / Bicarbonate	162.5	2.25
Methylene C's adjacent to oxygen in DGA/ Protonated DGA & DGA carbamate on noncarbamate side	72.0	4.76
Methylene C's adjacent to oxygen in DGA carbamate on carbamate side	70.0	1.81
Carbamate ring C's adjacent to non carbamate side + Methylene C's adjacent to oxygen in DGA/ Protonated DGA on carbamate side	68.0	3.08
Ring C's adjacent to non carbamate side in MOR/ Protonated MOR & MOR carbamate	66.0	2.63
Methylene C's adjacent to alcohol in DGA/ Protonated DGA & DGA carbamate	60.0	5.25
Ring C's adjacent to carbamate side in MOR/ Protonated MOR & MOR carbamate	44.0	2.55
Methylene C's adjacent to nitrogen in DGA/ Protonated DGA	41.0	1.77

Methylene C's adjacent to nitrogen in DGA carbamate	39.0	3.07
---	------	------

Table I.21 C13 NMR of 11 wt% MOR/53 wt% DGA, Loading = 0.271 mol CO₂/mol MOR, T=27 °C

Species	δ (ppm)	Area
DGA carbamate	165	1000
MOR carbamate	162.6	179.65
Carbonate / Bicarbonate	161	9.28
Methylene C's adjacent to oxygen in DGA/ Protonated DGA & DGA carbamate on noncarbamate side	72.0	63.35
Methylene C's adjacent to oxygen in DGA carbamate on carbamate side	70.5	18.73
Methylene C's adjacent to oxygen in DGA/ Protonated DGA on carbamate side	70.0	45.68
Ring C's adjacent to non carbamate side in MOR/ Protonated MOR & MOR carbamate	67.0	33.71
Methylene C's adjacent to alcohol in DGA/ Protonated DGA & DGA carbamate	60.5	68.95
Ring C's adjacent to carbamate side in MOR/ Protonated MOR & MOR carbamate	45.0	34.71
Methylene C's adjacent to nitrogen in DGA/ Protonated DGA	41.0	18.50
Methylene C's adjacent to nitrogen in DGA carbamate	39.0	46.03

Table I.22 C13 NMR of 11 wt% MOR/53 wt% DGA, Loading = 0.521 mol CO₂/mol MOR, T=40 °C

Species	δ (ppm)	Area
DGA carbamate + MOR carbamate	163.4	1000.0
Carbonate / Bicarbonate	159.8	139.32
Methylene C's adjacent to oxygen in DGA/ Protonated DGA & DGA carbamate on noncarbamate side	72.0	33.42

Methylene C's adjacent to oxygen in DGA carbamate on carbamate side	70.5	15.78
Methylene C's adjacent to oxygen in DGA/ Protonated DGA on carbamate side + Ring C's adjacent to non carbamate side in MOR/ Protonated MOR & MOR carbamate	65.0	37.96
Methylene C's adjacent to alcohol in DGA/ Protonated DGA & DGA carbamate	60.5	36.48
Ring C's adjacent to carbamate side in MOR/ Protonated MOR & MOR carbamate	44.0	17.76
Methylene C's adjacent to nitrogen in DGA/ Protonated DGA	41.0	15.49
Methylene C's adjacent to nitrogen in DGA carbamate	38.0	19.68

Table I.23 C13 NMR of 11 wt% MOR/53 wt% DGA, Loading = 0.374 mol CO₂/mol MOR, T=40 °C

Species	δ (ppm)	Area
DGA carbamate	164	1000
MOR carbamate	162.6	242.09
Carbonate / Bicarbonate	161	32.97
Methylene C's adjacent to oxygen in DGA/ Protonated DGA & DGA carbamate on noncarbamate side	72.0	48.48
Methylene C's adjacent to oxygen in DGA carbamate on carbamate side	70.5	18.38
Methylene C's adjacent to oxygen in DGA/ Protonated DGA on carbamate side	68.0	31.30
Ring C's adjacent to non carbamate side in MOR/ Protonated MOR & MOR carbamate	66.0	26.74
Methylene C's adjacent to alcohol in DGA/ Protonated DGA & DGA carbamate	60.5	52.28
Ring C's adjacent to carbamate side in MOR/ Protonated MOR & MOR carbamate	44.0	25.78

Methylene C's adjacent to nitrogen in DGA/ Protonated DGA	41.0	18.54
Methylene C's adjacent to nitrogen in DGA carbamate	39.0	31.46

Table I.24 C13 NMR of 11 wt% MOR/53 wt% DGA, Loading = 0.285 mol CO₂/mol MOR, T=40 °C

Species	δ (ppm)	Area
DGA carbamate	164.2	1000
MOR carbamate	162.8	187.69
Carbonate / Bicarbonate	160.8	16.27
Methylene C's adjacent to oxygen in DGA/ Protonated DGA & DGA carbamate on noncarbamate side	72.5	63.44
Methylene C's adjacent to oxygen in DGA carbamate on carbamate side	70.5	19.28
Methylene C's adjacent to oxygen in DGA/ Protonated DGA on carbamate side	70.0	44.98
Ring C's adjacent to non carbamate side in MOR/ Protonated MOR & MOR carbamate	67.0	33.48
Methylene C's adjacent to alcohol in DGA/ Protonated DGA & DGA carbamate	60.5	66.64
Ring C's adjacent to carbamate side in MOR/ Protonated MOR & MOR carbamate	45.0	33.52
Methylene C's adjacent to nitrogen in DGA/ Protonated DGA	41.0	18.98
Methylene C's adjacent to nitrogen in DGA carbamate	40.0	45.15

Table I.25 C13 NMR of 11 wt% MOR/53 wt% DGA, Loading = 0.522 mol CO₂/mol MOR, T=60 °C

Species	δ (ppm)	Area
DGA carbamate	163.0	1000
MOR carbamate	159.8	153.96
Carbonate / Bicarbonate	158.2	30.66
Methylene C's adjacent to oxygen in DGA/ Protonated DGA & DGA carbamate on noncarbamate side	72.0	34.34

Methylene C's adjacent to oxygen in DGA carbamate on carbamate side + Methylene C's adjacent to oxygen in DGA/ Protonated DGA on carbamate side + Ring C's adjacent to non carbamate side in MOR/ Protonated MOR & MOR carbamate	67.0	54.74
Methylene C's adjacent to alcohol in DGA/ Protonated DGA & DGA carbamate	60.5	36.27
Ring C's adjacent to carbamate side in MOR/ Protonated MOR & MOR carbamate	44.0	17.82
Methylene C's adjacent to nitrogen in DGA/ Protonated DGA + Methylene C's adjacent to nitrogen in DGA carbamate	40.0	37.07

Table I.26 C13 NMR of 11 wt% MOR/53 wt% DGA, Loading = 0.285 mol CO₂/mol MOR, T=60 °C

Species	δ (ppm)	Area
DGA carbamate + MOR carbamate	164.4	1000.0
Carbonate / Bicarbonate	160.6	19.19
Methylene C's adjacent to oxygen in DGA/ Protonated DGA & DGA carbamate on noncarbamate side	72.5	52.21
Methylene C's adjacent to oxygen in DGA carbamate on carbamate side + Methylene C's adjacent to oxygen in DGA/ Protonated DGA on carbamate side	70.5	53.99
Ring C's adjacent to non carbamate side in MOR/ Protonated MOR & MOR carbamate	67.0	27.65
Methylene C's adjacent to alcohol in DGA/ Protonated DGA & DGA carbamate	60.5	54.60

Ring C's adjacent to carbamate side in MOR/ Protonated MOR & MOR carbamate	45.0	27.77
Methylene C's adjacent to nitrogen in DGA/ Protonated DGA	41.0	15.54
Methylene C's adjacent to nitrogen in DGA carbamate	40.0	38.42

Table I.27 C13 NMR of 11 wt% MOR/53 wt% DGA, Loading = 0.374 mol CO₂/mol MOR, T=60 °C

Species	δ (ppm)	Area
DGA carbamate	163.0	1000
MOR carbamate	159.8	153.96
Carbonate / Bicarbonate	158.2	41.66
Methylene C's adjacent to oxygen in DGA/ Protonated DGA & DGA carbamate on noncarbamate side	72.0	37.34
Methylene C's adjacent to oxygen in DGA carbamate on carbamate side + Methylene C's adjacent to oxygen in DGA/ Protonated DGA on carbamate side + Ring C's adjacent to non carbamate side in MOR/ Protonated MOR & MOR carbamate	67.0	54.74
Methylene C's adjacent to alcohol in DGA/ Protonated DGA & DGA carbamate	60.5	40.05
Ring C's adjacent to carbamate side in MOR/ Protonated MOR & MOR carbamate	44.0	20.76
Methylene C's adjacent to nitrogen in DGA/ Protonated DGA + Methylene C's adjacent to nitrogen in DGA carbamate	40.0	39.91

Appendix J: ^{13}C NMR Sample Calculation

J.1 65 wt% DGA

In Figure 4.9, the following quantities can be calculated;

From peaks 10 and 12;

$$A_{\text{DGACOO}^-} = (67+68)/2=67.5 \quad (\text{J.1})$$

From peaks 4+8 and 2+6;

$$A_{\text{DGA/DGAH}^+} = (132+133)/2=132.5$$

From peaks 13, HCO_3^- , and (J.1);

$$A_{\text{HCO}_3^-} = 53/6451*67.5=0.55 \text{ (To correct for intensity of } ^{13}\text{CO}_2 \text{ and normal } ^{13}\text{C)}$$

Therefore,

$$\text{Loading} = (0.55+67.5)/(67.5+132.5) = 0.340 \text{ mol CO}_2/\text{mol DGA}$$

Assuming that $\text{CO}_3^{=}$ and CO_2 are negligible fraction of total CO_2

$$A_{\text{DGAH}^+} = A_{\text{DGACOO}^-} + A_{\text{HCO}_3^-} = 68.1$$

$$A_{\text{DGA}} = A_{\text{DGA/DGAH}^+} - A_{\text{DGAH}^+} = 64.4$$

$$\text{Fraction of Total DGA} = 64.4 / (67.5+132.5) = 0.322$$

$$K_{\text{carb}} = [\text{DGACOO}^-]/([\text{HCO}_3^-][\text{DGA}])$$

This gives ;

$$K_{\text{carb}} = 67.5/(0.55*64.4) * 1/(6.18 \text{ M}) = 61.2 \text{ M}^{-1}$$

J.2 23.5 wt% MOR

In Figure 4.10, the following quantities can be calculated;

From peaks 6 and 5;

$$A_{\text{MORCOO}^-} = (4.0+3.8)/4=1.95 \quad (\text{J.2})$$

From peaks 2+4 and 1+3;

$$A_{\text{MOR/MORH}^+} = (9.1+9.4)/4=4.6$$

From peaks 7, HCO₃⁻, and (J.2);

$$A_{\text{HCO}_3^-} = 32.1/100.0*1.95=0.63$$

Therefore,

$$\text{Loading} = (0.63+1.95)/(1.95+4.6) = 0.392 \text{ mol CO}_2/\text{mol MOR}$$

$$A_{\text{MORH}^+} = A_{\text{MORCOO}^-} + A_{\text{HCO}_3^-} = 2.58$$

$$A_{\text{MOR}} = A_{\text{MOR/MORH}^+} - A_{\text{MORH}^+} = 2.05$$

$$\text{Fraction of Total MOR} = 2.05/ (4.6+1.95) = 0.312$$

$$K_{\text{carb}} = [\text{MORCOO}^-]/([\text{HCO}_3^-][\text{MOR}])$$

This gives ;

$$K_{\text{carb}} = 1.95/(0.63*2.05) * 1/(2.70 \text{ M}) = 4.05 \text{ M}^{-1}$$

J.3 11 wt% MOR/53 wt% DGA

In Figures 4.11-4.13, the following quantities can be calculated;

From peaks 10 and 12;

$$A_{\text{DGACOO}^-} = (17.69+17.38)/2=17.53 \quad (\text{J.3})$$

$$\text{Peak 2+6} = \text{Peaks 2+6+19} - \text{Peaks 15+17} = 34.88 - 9.21= 22.34 \quad (\text{I.4})$$

From Peak 4+8 and (I.4), we get;

$$A_{\text{DGA/DGAH}^+} = (23.62+22.34)/2=22.98$$

$$\text{Peak 19} = \text{Peak 18} = \text{Peak 14+16+18} - \text{Peak 15+17} = 21.75 - 9.21 = 12.54$$

$$A_{\text{MORCOO}^-} = 12.54/2 = 6.7 \quad (\text{J.5})$$

$$A_{\text{MOR/MORH}^+} = 9.21/2 = 4.6$$

From peaks 13, 20, HCO₃⁻, (J.3) and (J.5);

$$A_{\text{HCO}_3^-} = 170.38 / (1000.0 + 329.22) * (6.7 + 17.53) = 3.05$$

Therefore,

$$\begin{aligned} \text{Loading} &= (17.53 + 6.7 + 3.05) / (17.53 + 6.7 + 22.98 + 4.6) \\ &= 0.522 \text{ mol CO}_2 / \text{mol Amine} \end{aligned}$$

Bibliography

Al-Ghawas, H.A., Hagewiesche, D.P., Ruiz-Ibanez and G. Sandall, O.C., "Physicochemical Properties Important for Carbon Dioxide Absorption in Aqueous Methyldiethanolamine," *J.Chem. Eng.Data*, 34, 385-391, 1989

Alper, E., "Kinetics of Reactions of Carbon Dioxide with Diglycolamine and Morpholine," *Chem. Eng. J.*, 44, 107-111, 1990.

Austgen, D.M., A Model for Vapor-Liquid Equilibrium for Acid gas-Alkanolamine-Water Systems. Ph.D. Dissertation, The University of Texas at Austin, 1989.

Austgen, D.M., Rochelle, G.T. and Chen, C.C., "A Model of Vapor-Liquid Equilibria for Aqueous Acid Gas-Alkanolamine Systems Using the Electrolyte-NRTL Equation," *Ind Eng. Chem. Res.*, 28(7), 1060, 1989

Bhide, B.D. and Stern, S.A., "Membrane Processes for the Removal of Acid Gases from Natural Gas. I. Process Configurations and Optimization of Operating Conditions," *J. Membr. Sci.*, 81, 209-237, 1993.

Bhide, B.D. and Stern, S.A., "Membrane Processes for the Removal of Acid Gases from Natural Gas. II. Effects of Operating Conditions, Economic Parameters and Membrane Properties," *J. Membr. Sci.*, 81, 209-237, 1993.

Bird, R.B., Steward, W.E., Lightfoot, E.N., *Transport Phenomena.*, John Wiley and Sons, Inc., New York, 1960.

Bishnoi, S. and Rochelle, G.T., "Absorption of Carbon Dioxide into Aqueous Piperazine: Reaction Kinetics, Solubility and Mass Transfer," *Chem. Eng. Sci.*, 55, 5531-5543, 2000.

Bishnoi, S. Carbon Dioxide Absorption and Solution Equilibrium in Piperazine Activated Methyldiethanolamine. Ph.D. Dissertation, The University of Texas at Austin, 2000.

Bishnoi, S., and Rochelle, G.T., "Physical and Chemical Solubility of Carbon Dioxide in Aqueous Methyldiethanolamine," *Fluid Phase Equilibria*, 168, 241-258, 2000.

- Blohm, C. L., & Riesenfeld, F. C. (1955). U.S. Patent 2712978, July 12.
- Brelvi, S.W. and O'Connell, J.P., "Corresponding States Correlations for Liquid Compressibility and Partial Molal Volumes of Gases at Infinite Dilution in Liquids," *AICHE J.*, 18(6), 1239-1242, 1972.
- Browning, G. J. and Weiland, R. H., "Physical Solubility of Carbon Dioxide in Aqueous Alkanolamines via Nitrous Oxide Analogy," *J. Chem. Eng. Data*, 39, 817-822, 1994.
- Caplow, M., "Kinetics of Carbamate Formation and Breakdown," *J. Am. Chem. Soc.*, 90, 6795-6803, 1968.
- Caracotsios, M., Model Parametric Sensitivity Analysis and Nonlinear Parameter Estimation. Theory and Applications. Ph.D. Dissertation, The University of Wisconsin – Madison, 1986.
- Carruthers, S., Integral Skin Formation in Hollow Fiber Membranes for Gas Separations. Ph.D. Dissertation, The University of Texas at Austin, 2001.
- Chan, A.H., Koros, W.J. and Paul, D.R., "Analysis of Hydrocarbon Gas Sorption and Transport in Ethyl Cellulose using the Dual Sorption/Partial Immobilization Models," *J. Membr. Sci.*, 3, 117-130, 1978.
- Chen, C.C. and Evans, L.B. "A Local Composition Model for the Excess Gibbs Energy of Aqueous Electrolyte Systems," *AICHE J.*, 32(3), 444-454, 1986.
- Chen, C.C., Britt, H.I., Boston, J.F. and Evans, L.B. "Extension and Application of the Pitzer Equation for Vapor-Liquid Equilibrium of Aqueous Electrolyte Systems with Molecular Solutes," *AICHE J.*, 25(5), 820, 1979.
- Chen, C.C., Britt, H.I., Boston, J.F. and Evans, L.B. "Local Composition Model for Excess Gibbs Energy of Electrolyte Systems, Part I: Single Solvent, Single Completely Dissociated Electrolyte," *AICHE J.*, 28(4), 588-596, 1982.
- Chern, R. T., W. J. Koros, E. S. Sanders and R. Yui, "Second component effects in sorption and permeation of gases in glassy polymers," *J. Membr. Sci.*, 152, 29-40, 1999.
- Chern, R.T., Koros, W.J., O.C. Sandall, "Simulation of a hollow-fiber gas separator: the effects of process and design variables," *Ind. Eng. Chem. Process Des. Dev.*, 24, 1015, 1985.

Chung, D.K. and Mills, A.F., "Experimental Study of Gas Absorption into Turbulent Falling Films of Water and Ethylene Glycol-Water Mixtures," *Int. J. Heat Mass Transfer*, 19, 51-59, 1976.

Clausi, D.T. and Koros, W.J., "Formation of Defect-Free Polyimide Hollow Fiber Membranes for Gas Separations," *J. Membr. Sci.*, 167, 79-89, 2000.

Clausi, D.T., Formation and Characterization of Asymmetric Polyimide Hollow Fiber Membranes for Gas Separations. Ph.D. Dissertation, The University of Texas at Austin, 1998.

Coleman, M.R. and Koros, W.J., "Isomeric Polyimides Based on Fluorinated Dianhydrides and Diamines for Gas Separation Applications," *J. Membr. Sci.*, 50, 285-297, 1990.

Coleman, M.R. Isomers Of Fluorine-Containing Polyimides For Gas Separation Membranes Glassy Polymers. Ph.D. Dissertation, The University of Texas at Austin, 1992.

Crank, J. *The Mathematics of Diffusion*, 2nd ed., Clarendon Press, Oxford, 1975.

Crause, J. C. and Nieuwoudt, I., "Mass Transfer in a Short Wetted-Wall Column. 1. Pure Components," *Ind. Eng. Chem. Res.*, 38, 4928, 1999.

Critchfield, J.E., CO₂ Absorption/Desorption in Methyl-diethanolamine Solutions Promoted With Monoethanolamine and Diethanolamine: Mass Transfer and Reaction Kinetics. Ph.D. Dissertation, The University of Texas at Austin, 1988.

Crooks, J.E. and Donnellan, J.P., "Kinetics and Mechanism of the Reaction between Carbon Dioxide and Amines in Aqueous Solutions," *J. Chem. Soc. Perkin. Trans. II*, 331, 1989.

Cullinane, T. Master's Thesis, The University of Texas at Austin, 2002.

Curry, R. N, Fundamentals of natural gas conditioning, PennWell Pub. Co., Oklahoma, 1981.

Danckwerts, P.V., "The Reaction of CO₂ with Ethanolamines," *Chem. Eng. Sci.*, 34, 443-446, 1979.

Dang, H. Master's Thesis, The University of Texas at Austin, 2001.

- Dankwerts, P.V., Gas-liquid Reactions , McGraw-Hill, New York (1970)
- Davies, C. W. Progr. React. Kin. 1, 163, 1961.
- Dingman, J.D., Jackson, J.L., Moore, T. F and Branson, J.A., "Equilibrium Data for the H₂S-CO₂-Diglycolamine Agent-Water System," Proceedings of the Sixty-Second Annual Convention, 1981.
- Dortmundt, D. and K. Doshi, "Recent Developments in CO₂ Removal Membrane Technology," UOP LLC, Des Plaines, Illinois, 1999.
- Ebra-Lima, O.M. and D.R. Paul, "Hydraulic permeation of liquids through swollen polymers networks. I. Poly(vinylalcohol)-water," *J. Appl. Polym. Sci.*, 19 1975.
- Echt, W., "Hybrid Systems: Combining Technologies Leads to More Efficient Gas Conditioning," Laurance Reid Gas Conditioning Conference, 2002.
- Emmert, R.E. and Pigford, R.L., "A Study of Gas Absorption in Falling Liquid Films," *Chem. Eng. Prog.*, 50, 87-93, 1954.
- Energy Information Administration, International Energy Outlook, 2001.
- Erasmus, A.B. and Nieuwoudt, I., "Mass Transfer in Structured Packing: A Wetted-Wall Study" *Ind. Eng. Chem. Res.*, 40(10), 2310-2321, 2001.
- Fleming, G. K. and Koros, W. J., "Carbon Dioxide Conditioning Effects on Sorption and Volume Dilation Behavior for Bis-Phenol-A-Polycarbonate," *Macromolecules*, 23, 1353, 1990.
- Fleming, G. K. Dilation of Silicone Rubber and Glassy Polycarbonates Due to High Pressure Gas Sorption. Ph.D Dissertation, The University of Texas at Austin, 1988.
- Fournie, F.J.C. and Agostini, J.P., "Permeation Membranes Can Efficiently Replace Conventional Gas Treatment Processes," *J. Petr. Tech.*, 707-712, 1987.
- Fujita, H., Fortschr, Hochpolym. Forsch., 3, 1, 1961.
- Glasscock, D. A., and G. T. Rochelle, "Numerical Simulation of Theories for Gas Absorption with Chemical Reaction," *AI ChEJ.*, 35, 8, 1719

Glasscock, D.A. Modelling and Experimental Study of Carbon Dioxide Absorption into Aqueous Alkanolamines. Ph.D. Dissertation, The University of Texas at Austin, 1990.

Gunaidi, D.. Characterization and Analysis of Asymmetric Hollow Fiber Membranes for Natural Gas Purification in the Presence of Hydrocarbons. M.S. Thesis, The University of Texas at Austin, 2000.

Haimour, N. and Sandall, O. C., "Absorption of Carbon Dioxide into Aqueous Methyl-diethanolamine," *Chem. Eng. Sci.*, 39, 1791- 1796, 1984.

Harruff, L.G, "Saudi Arabian Experience with DGA Units and Related Sulfur Plants," First International Conference on Chemistry in Industry, Manama, Bahrain, Nov. 1992.

Harruff, L.G., "The Origin of Morpholine in Diglycolamine Gas Sweetening Plants", First International Conference on Chemistry in Industry, Manama, Bahrain, Nov. 1992.

Henstock, W.H. and Hanratty, T.J., "Gas Absorption by A Liquid Layer Flowing on the Wall of A Pipe," *AIChE J.*, 25, 122–131, 1979.

Hikita, H., Asai, S., Ishikawa, H. and M.Honda, "The Kinetics of Reactions of Carbon Dioxide with Monoisopropanolamine, Diglycolamine, and Ethylenediamine by a Rapid Mixing Method," *Chem. Eng. J.*, 14, 27-30, 1977.

Ho, W.S.W. and K.K. Sirkar, eds. Membrane Handbook. Van Nostrand Reinhold: New York, NY, 1992.

Hopfenberg, H.B., Stannet, V. and R.N. Haward (Ed.), The physics of Glassy state, Appl. Sci. Publ. Ltd., London, 1973.

Huntsman Gas Treating website. DGA® Agent Reclaimer Design and Operations.

Jeferson Chemical Company (1970). Technical Bulletin.

Jonsson, G., "The Influence Of Pressure in the Compaction of Asymmetric Cellulose Acetate Membranes," *Proceedings of the 6th International Symposium in Fresh Water from Sea*, Athens, 1978.

Joosten, G. E. H. and Danckwerts, P. V. "Solubility and Diffusivity of Nitrous Oxide in Equimolar Potassium Carbonate-Potassium Bicarbonate Solutions at 25 °C and 1 atm," *J. Chem. Eng. Data*, 17, 452-454, 1972.

Jordan, S. M. and W. J. Koros, "Characterization of Carbon Dioxide Induced Permeation Conditioning of Substituted Polycarbonates using Various 'Exchange' Penetrants," *J. Membr. Sci.*, 51, 233, 1990.

Jordan, S. M. and W. J. Koros, "Permeability of Pure and Mixed Gases in Silicone Rubber at Elevated Pressures," *J. Polym. Sci., Polym. Phys. Ed.*, 28, 795 1990.

Jordan, S. M., M. A. Henson and W. J. Koros, "The effects of carbon dioxide conditioning on the permeation behavior of hollow fiber asymmetric membranes," *J. Membr. Sci.*, 54, 103-118, 1990.

Jordan, S. M., W. J. Koros and G. K. Fleming, "Permeability of Carbon Dioxide at Elevated Pressures in Substituted Polycarbonates," *J. Polym. Sci., Polym. Phys. Ed.*, 28, 2305, 1990.

Jordan, S.M., Ph.D. Thesis, The University of Texas at Austin, 1989.

K. Scott, Handbook of Industrial Membranes, Elsevier, Amsterdam, 1995.

Kamaruddin, H. D. and W.J. Koros, "Some Observations about the Application of Fick's First Law for Membrane Separation of Multicomponent Mixtures," *J. Membr. Sci.*, 135, 147-159, 1997.

Kamei, S. and Oishi, J., 1955. Mass and Heat Transfer in A Falling Liquid Film of Wetted Wall Tower. Mem. Fac. Eng. (Kyoto Univ.) 17, p. 277.

Kesting, R.E. and A.K. Fritzsche, "Polymeric Gas Separation Membranes," 1993, New York: John Wiley and Sons, Inc.

Kim, T.H., *et al.*, "Relationship Between Gas Separation Properties and Chemical Structure in A Series of Aromatic Polyimide," *J. Membr. Sci.*, 37, 45-62, 1988.

Kim, T.H., W.J. Koros and G.R. Husk, "Temperature Effects on Gas Permselection Properties in Hexafluoro Aromatic Polyimides," *J. Membr. Sci.*, 46, 43-56, 1989.

- Kohl, A.L. and Nielsen, R.B., Gas Purification, 5th edition, Houston, 1997.
- Koros, W. J. and M. W. Hellums, Transport properties. Encyclopedia of Polymer Science, 2nd Edition, Ed. by J. I. Kroschwitz, Wiley-Interscience Publishers, New York, Supplement Volume 724 (1989).
- Koros, W. J., G. K. Fleming, S. M. Jordan, T. H. Kim and H. H. Hoehn, "Polymeric membrane materials for solution-diffusion based permeation separations" *Progress in Polymer Science*, 13, 339-401, 1988.
- Koros, W.J, Ph.D. Thesis, The University of Texas at Austin, 1977.
- Koros, W.J. and D.R. Paul, "Design Considerations for Measurement of Gas Sorption in Polymers by Pressure Decay," *J. Polym. Sci., Polym. Phys. Ed.*, 14, 1903, 1976.
- Koros, W.J. Ph.D. Thesis, Sorption and transport in glassy polymers, The University of Texas at Austin, 1977.
- Koros, W.J., "Model for sorption of mixed gasses in glassy polymers," *J. Polym. Phys. Ed.*, 18, 981, 1980.
- Kowali, A. S., S. Vemury, K. R. Krowidi, and A. A. Khan, "Models and Analyses of Membrane Gas Permeators," *J. Memb. Sci.*, 73, 1, 1992.
- Lamurelle, A.P. and Sandall, O.C., "Gas Absorption into A Turbulent Liquid," *Chem. Eng. Sci.* , 19, 1035–1042, 1972.
- Lee, S. Y., Minhas, B. S. and M.D. Donohue, "Effect of gas composition and pressure on permeation through cellulose acetate membranes," *AIChE Symposium Series*, 84, 93-101, 1988.
- Li, M., Lai, M., "Solubility and Diffusivity of N₂O and CO₂ in (Monoethanolamine + N-Methyldiethanolamine + Water) and in (Monoethanolamine + 2-Amino-2-methyl-1-propanol + Water)," *J. Chem. Eng. Data*, 40, 486-492, 1995.
- Lieberman, N. P, Troubleshooting Natural Gas Processing, PennWell Books, Oklahoma, 1987.

Lipscomb, G. G., "Design of Hollow Fiber Contactors for Membrane Gas Separations," 17th 1996 Memb. Technol. Rev., D. Mulloy, ed., Business Communications Co., Norwalk, CT, p. 23 (1996).

Littel, R.J. Selective Carbonyl Sulfide Removal in Acid Gas Treating Processes. Ph.D. Dissertation, Twente University, 1991.

Littel, R.J., Versteeg, G.F., Van Swaaij, W.P.M., "Kinetics of CO₂ with primary and secondary amines in aqueous solutions –I. Zwitterion deprotonation kinetics for DEA and DIPA in aqueous blends of alkanolamines," *Chem. Eng. Sci.*, 47(8), 2027-2035, 1992.

Littel, R.J., Versteeg, G.F., Van Swaaij, W.P.M., "Kinetics of CO₂ with primary and secondary amines in aqueous solutions –II. Influence of temperature on zwitterion formation and deprotonation rates," *Chem. Eng. Sci.* 47(8), 2037-2045, 1992.

Liu, J., G. Pope, and K. Sepehrnoori, "A High Resolution FiniteDifference Scheme for Non-uniform Grids," *Appl. Math. Modelling*, 19, 162 (1995).

Loeb, S. and S. Sourirajan, In Advances in chemistry series: Saline water conversion II; R. F. Gould, Ed.; American Chemical Society: Washington DC, 117, 1963.

LRGCC 2003 Conference Fundamentals Manual.

Markham, A. E. and Kobe, K. A., "The Solubility of Carbon Dioxide and Nitrous Oxide in Aqueous Salt Solutions," *J. Am. Chem. Soc.*, 63, 449-454, 1941.

Martin, J.L., Otto, F.D. and Mather, A.E., "Solubility of Hydrogen Sulfide and Carbon Dioxide in a Diglycolamine Solution," *J. Chem. Eng. Data*, 23, 163, 1978.

Matsumoto, K. and P. Xu, "Gas permeation of aromatic polyimides. II. Influence of chemical structure," *J. Membr. Sci.*, 81, 23-30, 1993.

Mock, B., Evans, L.B., Chen, C.C., "Thermodynamic Representation of Phase Equilibria of Mixed-Solvent Electrolyte Systems," *AIChE J.*, 32(10), 1655-1664, 1986.

Mshewa, M. M. Carbon dioxide desorption/absorption with aqueous mixtures of methyldiethanolamine and diethanolamine at 40 to 120 °C. Ph.D. dissertation, The University of Texas at Austin, 1995.

Mulder, M., Basic principles of membrane technology. Dordrecht: Kluwer Academic Publishers, 1991.

Newman, S. A, Acid and sour gas treating processes : latest data and methods for designing and operating today' s gas treating facilities, Gulf Pub. Co., Houston, 1985.

Pacheco, M.A. Mass Transfer, Kinetics and Rate-Based Modeling of Reactive Absorption. Ph.D. Dissertation, The University of Texas at Austin., 1998.

Pacheco, M.A., Kaganoi, S., Rochelle, G.T., "CO₂ Absorption into Aqueous Mixtures of Diglycolamine and Methyldiethanolamine," *Chem. Eng. Sci.*, 55, 5125-5140, 2000.

Pan, C.Y., Habgood, H.W. and Ohlrogge, K., "Gas Separation by Permeation: Part II. Effect of Permeate Pressure Drop and Choice of Permeate Pressure," *Can. J. Chem. Eng.*, 56, 210-217, 1978.

Paul, D.R. and Ebra-Lima, O.M., "Hydraulic Permeation of Liquids Through Swollen Polymers Networks. III. A Generalized Correlation," *J. Appl. Polym. Sci.*, 19, 2759, 1975.

Paul, D.R. and Y.P. Yampol' skii, eds. Polymeric Gas Separation Membranes. 1994, CRC Press: Boca Raton, FL.

Paul, D.R., Paciotti, J.D. and Ebra-Lima, O.M., "Hydraulic Permeation of Liquids Through Swollen Polymers Networks. II. Liquid Mixtures," *J. Appl. Polym. Sci.*, 19 1837, 1975.

Peramanu, S. and Sharma, A., "Nonlinear instabilities of falling films on a heated vertical plane with gas absorption," *Can. J. Chem. Eng.*, 76, 211, 1998.

Pinsent, B.R., Pearson, L., Roughton, F.J.W., "The kinetics of combinati on of carbon dioxide with hydroxide ions," *Trans. Faraday Soc.*, 52,1512, 1956.

Pope, D., Ph.D. Thesis, The University of Texas at Austin, 1991.

Porter, M.C., ed. Handbook of Industrial Membrane Technology. 1990, Noyes Publications: Park Ridge, NJ.

Posey, M.L. Thermodynamic model for acid gas loaded aqueous alkanolamine solutions. Ph.D. Dissertation, The University of Texas at Austin, 1996.

Posey, M.L., Rochelle, G.T. "A Thermodynamic Model of Methyl-diethanolamine-CO₂-H₂S-Water," *Ind. Eng. Chem. Res.*, 36, 3944-3958, 1997.

Prasher, B. D., and A. L. Fricke, "Mass Transfer at a Free Gas Liquid Interface in Turbulent Thin Films," *Ind. Eng. Chem. Process. Des. Dev.*, 13, 4, 336 (1974).

Prausnitz, J. M. , R. N. Lichtenthaler and E. G. de Azevedo. *Molecular Thermodynamics for Fluid-Phase Equilibria*, 2nd Edn., Prentice-Hall Inc.: New Jersey, 1986.

Press, W.H., et al., *Numerical Recipes in C, The Art of Scientific Computing*. 1988, New York: Cambridge University Press.

Punsalan, D., A Sorption and Dilation Investigation of Amorphous Glassy Polymers and Physical Aging. Ph.D. Dissertation, The University of Texas at Austin, 2001.

Reid, R. C., Sherwood, T. K. and J. M. Prausnitz, *The Properties of Gases and Liquids*, McGraw-Hill, New York, 1977.

Rochelle, G.T., Bishnoi, S., Chi, S., Dang, H., "Research needs for CO₂ capture from flue gas by aqueous absorption/stripping," Final report, U.S. Dept. of Energy, Federal Energy Technology Center, P.O. No. DE-AF26-99FT01029, 2000.

Rojey, A., *et al.*, eds. *Natural gas: production, processing, transport*. Paris: Editions Technip, 1997.

Rowley, R.L., Wilding, W.V., Oscarson, J.L., Adams, M.E., Marshall, T.L., *Physical and thermodynamic properties of pure chemicals*.

Sada, E., Kumazawa, H. and M.A. Butt, "Gas Absorption with Consecutive Chemical Reaction: Absorption of Carbon Dioxide into Aqueous Amine Solutions," *Can. J. Chem. Eng.*, 54, 421, 1976.

Sada, E., Kumazawa, H., Butt, M. A. "Solubilities of Gases in Aqueous Solutions of Amine," *J. Chem. Eng. Data*, 22, 277- 278, 1977.

Saha, A. K., Bandyopadhyay, S. S., Biswas, A. K. "Solubility and Diffusivity of N₂O and CO₂ in Aqueous Solutions of 2-Amino-2- methyl-1-propanol," *J. Chem. Eng. Data*, 38, 78-82, 1993.

Schell, W. J., Wensley, C. G., Chen, M. S. K., Venugopal, K. G., Miller, B. D., J. A. Stuart, "Recent advances in cellulosic membranes for gas separation and pervaporation," *Gas Separation and Purification*, 3, 162-169, 1989.

Schumpe, A. The Estimation of Gas Solubilities in Salt Solutions. *Chem. Eng. Sci.* 1993, 48 (1), 153-158. 1978.

Seban, R. and Faghri, A., "Wave effects on the transport of falling laminar liquid films," *Trans. ASME J. Heat Transfer* 100, p. 1.

Seo, D.J., Hong, W.H., "Effect of piperazine on the kinetics of carbon dioxide with aqueous solutions of 2-amino-2-methyl-1-propanol," *Ind. Eng. Chem. Res.*, 39, 2062, 2000.

Sharma, M.M., "Kinetics on Reactions of Carbonyl Sulphide and Carbon Dioxide with Amines and Catalysis by Bronsted Bases of the Hydrolysis of COS," *Transactions of the Faraday Society*, 61, 681-687, 1965.

Sharma, M.M., Thesis, Cambridge University (1964).

Shindo, Y., T. Hakuta, H. Yoshitome, and H. Inoue, "Calculation Methods for Multicomponent Gas Separation by Permeation," *Sep. Sci. and Tech.*, 20, 445 1985.

Smith, J. M., Van Ness, H.C., Introduction to chemical engineering thermodynamics. McGraw Hill Book Company, New York, 1975.

Smith, W.R. Missen, R.W., "Strategies for Solving The Chemical Equilibrium Problem and an Efficient Microcomputer Based Algorithm," *Can. J. Chem. Eng.*, 66, 591, 1988.

Soave, G., "Equilibrium Constants from a Modified Redlich-Kwong Equation of State," *Chem. Eng. Sci.*, 27, 1197, 1972.

Spillman, R. W. and T. E. Cooley, Membrane gas treating. Proceedings of the sixty-eighth Gas Processors Association Annual Convention, 1989.

Spillman, R. W., "Economics of gas separation membranes," *Chemical Engineering Progress*, 41-62, .1989.

Spillman, R.W. and M.B. Sherwin, "Gas Separation Membranes: The First Decade," *ChemTech*, 378-384, 1990.

Spillman, R.W. and T.E. Cooley. Membrane Gas Treating. in *the sixty-eight Gas Processors Association Annual Convention*. 1989.

Stephenson, R.M., Malanowski, S., *Handbook of the thermodynamics of organic compounds*, Elsevier Science Publishing Co., New York, 1987.

Stern, S.A., *et al.*, "Structure/permeability relationships of polyimide membranes: Applications to the separation of gas mixtures," *Journal of Polymer Science. Part B: Polymer Physics*, 27, 1887-1909, 1989.

Stirba, C. and Hurt, D. M., Turbulence in falling liquid films. *A.I.Ch.E. J.* 1, 178-184, 1955.

Tanaka, K., *et al.*, "Gas permeability and permselectivity in polyimides based on 3,3',4,4'-biphenyltetracarboxylic dianhydride," *J. Membr. Sci.*, 47, 203-215, 1989.

Taveira, P., P. Cruz, A. Mendes, C. Costa and F. Magalhães, "Considerations on the performance of hollow-fiber modules with glassy polymeric membranes," *J. Membr. Sci.*, 188, 263-277, 2001.

Tessendorf, S. Modelling analysis and design of membrane-based gas separation system, Ph.D. Thesis, Department of Chemical Engineering, Technical University of Denmark, Denmark, 1998.

Thundiyil, M.J., Characterization and Analysis of Non-Ideal Transport in Polymeric Membranes and Modeling of Membrane Modules for Natural Gas Processing, Ph.D. Dissertation. The University of Texas at Austin: Austin, TX. 1998.

Thundiyil, M.J., Y.H. Jois, and W.J. Koros, "Effect of permeate pressure on the mixed gas permeation of carbon dioxide and methane in a glassy polyimide," *J. Membr. Sci.*, 15, 157-169, 1983.

Thundiyil, M.T. and W.J. Koros, "Mathematical modeling of gas separation permeators — for radial crossflow, countercurrent, and cocurrent hollow-fiber membrane modules," *J. Membr. Sci.*, 125, 275, 1997.

Versteeg, G. F., "Mass Transfer and Chemical Reaction Kinetics in Acid Gas Treating Processes," PhD Diss., Twente University, The Netherlands (1987).

Versteeg, G. F., Swaaij, W. P. M., "Solubility and Diffusivity of Acid Gases (CO₂,N₂O) in Aqueous Alkanolamine Solutions," *J. Chem. Eng. Data*, 33,29-34,1988.

Vieth, W.R., Howell, J.M. and J.H. Hsieh, "Dual sorption theory," *J. Membr. Sci.*, 1, 177-220, 1976.

Vistad, O.B, Akporiaye, D.E., Taulelle, F, Lillerud, K.P., "Morpholine, an in situ ¹³C NMR pH meter for hydrothermal crystallogensis of SAPO-34," *Chemistry of Materials*, 15 (8), 1650-1654, 2003.

Vrentas, J. S. and J. L Duda., "Diffusion in Polymer-Solvent Systems I Reexammatlon of the Free-Volume Theory, II A Predictive Theory for the Dependence of Slon Coefficiente On Temperature, Concentration and Molecular Weight," *J Polym Sci , Polym Phys Ed*, 15, 403-417, 1977.

Vrentas, J. S. and J. L Duda., "Solvent and Temperature Effects on Diffusion M Polymer-Solvent Systems," *J Appl Polym Scl*, 21, 1715, 1977.

White, L. S., T. A. Blinka, H. A. Kloczewski and I.-f. Wang, "Properties of A Polyimide Gas Separation Membrane in Natural Gas Streams," *J. Membr. Sci.*, 103, 73-82, 1995.

Wu, H.S., Locke, W.E, Sandler, S.I., "Isothermal vapor-liquid equilibrium of binary mixtures containing morpholine," *J.Chem. Eng.Data*, 36, 127-130, 1991.

Xu, G-W. Zhang, C-F. Qin, S-J. Wang, Y-W., "Kinetics Study on Absorption of Carbon Dioxide into Solutions of Activated Methyldiethanolamine," *Industrial and Engineering Chemistry Research*, 31, 921-927., 1992.

Yih, S.M. and Chen, C.H., Heat transfer in the thermal entrance region of a turbulent falling liquid film undergoing heat or evaporation. *Proc. Seventh Int. Heat Transfer Conf.* 3, 125-130, 1982.

Zimmerman, C.M. Advanced gas separation membrane materials; hyprid rigid polymers and molecular sieve-polymer matrices. PhD Dissertation, The University of Texas at Austin, 1998.

Vita

Mohammed Awad Al-Juaied was born on February 15, 1972 in Taif, Saudi Arabia as the son of Awad Al-Juaied. He graduated from Taif High School in Taif, Saudi Arabia in 1989. He entered King Fhad University of Petroleum and Minerals and graduated with a Bachelor of Science in Chemical Engineering in 1995. He worked for Saudi Aramco as a Lab Scientist at the Research and Development Center during 1996 and 1997. He entered the graduate school of Chemical Engineering at the University of Notre Dame in 1998 and graduated with a Master of Science degree in Chemical Engineering in 1999. In January of 2000 he entered the graduate school at the University of Texas at Austin as a PhD student working under Dr. William Koros and Dr. Gary Rochelle. In Fall of 2003 he graduated with a Master of Science degree in Petroleum Engineering.

Permanent Address: 600 West & 26th ST APT A213
Austin, TX 78705

This dissertation was typed by the author.